université de BORDEAUX

THÈSE PRÉSENTÉE

POUR OBTENIR LE GRADE DE

DOCTEURE DE L'UNIVERSITÉ DE BORDEAUX

ÉCOLE DOCTORALE DES SCIENCES CHIMIQUES
SPÉCIALITÉ POLYMÈRES

Par Hannah BEAUSEROY

Auto-assemblage induit par polymérisation par ouverture de cycle des *N*-carboxyanhydrides en milieux aqueux vers une application en nanomédecine

Aqueous ring-opening polymerization-induced self-assembly of *N*-carboxyanhydrides towards nanomedicine

Sous la direction du Dr. Colin BONDUELLE et du Pr. Sébastien LECOMMANDOUX

Soutenue le 5 juin 2025

Membres du jury :

M. DEMING Timothy J.	Professeur – University of California (Los Angeles, CA, ETATS-UNIS)	Président du jury
Mme BOUCHEMAL Kawthar	Professeure – IRCP, ChimieParisTech (Paris)	Rapporteure
M. FERJI Khalid	Maître de Conférences – Université de Lorraine (Nancy)	Rapporteur
M. KATAOKA Kazunori	Professeur – University of Tokyo (Tokyo, JAPON)	Examinateur
Mme VICENT Maria J.	Professeure – CIPF (Valence, ESPAGNE)	Examinatrice
M. BONDUELLE Colin	Directeur de Recherche – CNRS (Pessac)	Directeur de thèse
M. LECOMMANDOUX Sébastien	Professeur – Bordeaux INP (Pessac)	Directeur de thèse

Remerciements

Tout d'abord, je souhaite exprimer ma profonde gratitude à mes directeurs de thèse.
À Colin Bonduelle, directeur de recherche au CNRS au LCPO, merci de m'avoir accordé ta confiance pour réaliser cette thèse. Malgré ma candidature déposée à la dernière minute (un jour avant la date limite, si je me souviens bien !), tu as su voir en moi la doctorante capable de travailler sur la ROPISA. Déjà familière avec la PISA grâce à mon stage de M2, tu m'as très vite donné confiance et autonomie pour travailler sur ce sujet, en étroite collaboration avec Ségolène Antoine, qui m'a particulièrement encadrée durant mes premiers mois de thèse. Merci pour ta disponibilité, ton accompagnement au laboratoire, pour nos nombreuses discussions scientifiques (et d'autres, plus farfelues !). Ta curiosité sans limites et ta rigueur scientifique resteront pour moi des modèles précieux. Merci également d'avoir initié les collaborations qui ont enrichi ce projet, de m'avoir permis de travailler avec des chercheurs du monde entier, et de m'avoir donné l'opportunité de participer à des conférences nationales et internationales. Tu m'as toujours poussée à aller plus loin et à m'affirmer en tant que chercheuse. Je garderai en mémoire ta bienveillance et ton écoute.
À Sébastien Lecommandoux, professeur et actuel directeur du LCPO, merci aussi pour ta confiance dans le cadre de cette co-direction. Merci de m'avoir accueillie dans ton équipe et dans le laboratoire. Alors que Colin m'a particulièrement guidée sur les aspects de chimie, tu m'as transmis tes connaissances et offert l'encadrement nécessaire sur la physico-chimie et la nanomédecine, un domaine qui me tient tout particulièrement à cœur. Merci d'avoir trouvé du temps pour moi malgré un emploi du temps (très) chargé et de m'avoir permis d'explorer cette voie. Je te serai toujours reconnaissante de m'avoir donné la chance de partir au Japon, à l'iCONM, pour y réaliser les expériences biologiques. Tu m'as permis de réaliser un rêve en travaillant dans un institut d'excellence. Cette expérience a marqué ma vie de manière indélébile, autant sur le plan professionnel que personnel, et cela grâce à ta confiance et à celle de Colin. Je t'en suis infiniment reconnaissante. Merci également de m'avoir donné l'opportunité de poursuivre à tes côtés, au sein de Doxanano, pour continuer à travailler dans le domaine qui me passionne, la nanomédecine.
Je remercie également chaleureusement les membres du jury pour l'honneur qu'ils m'ont fait en acceptant d'évaluer ce travail et d'assister à ma soutenance malgré la distance. Merci à mes rapporteurs, Kawthar Bouchemal et Khalid Ferji, ainsi qu'aux examinateurs Kazunori Kataoka, Maria Vicent, et au président du jury Timothy Deming.

Un immense merci à Annie Brûlet pour son expertise en diffusion de rayons X petits et grands angles, avant, pendant et après notre manip' à SOLEIL, ainsi qu'à Guillaume Fleury pour ses conseils. Merci également à Thomas Bizien pour son aide précieuse avec le montage expérimental et les mesures sur la ligne SWING, ainsi que pour son assistance sur Foxtrot, et à Frank Wien pour son aide sur la ligne DISCO.

Merci à Sabina Quader, pour son accueil chaleureux à l'iCONM au Japon : j'ai tellement appris grâce à toi, scientifiquement (techniques de culture cellulaire 2D et 3D) mais aussi humainement, au fil de nos nombreuses discussions sur nos cultures respectives. Merci à Xueying Liu (Liu-san) pour le confocal, sa patience avec les cellules capricieuses et pour son aide précieuse sur les expériences *in vivo*, sans oublier la découverte de la cuisine chinoise ! Merci à Thi Kim Dung Doan pour sa gentillesse, son aide en TEM et la découverte de la cuisine vietnamienne. Merci à Hiroaki Kinoh (Kinoh-sensei) de m'avoir accueillie dans son équipe, prêté des modèles cellulaires et appris à utiliser le FACS. Et bien sûr, merci à Kazunori Kataoka pour son accueil dans son prestigieux institut, pour sa confiance et pour avoir accepté de faire partie de mon jury.
Je remercie également les autres collaborateurs avec qui j'ai eu la chance d'échanger : Elizabeth Gillies (Western University, Canada), Sébastien Perrier (Université de Warwick, Royaume-Uni) et Khalid Ferji (LCPM, Nancy).
Merci également à Sisareuth Tan, pour son accompagnement avec la cryo-TEM au CBMN et Sabrina Lacomme avec la TEM au BIC.

Au LCPO, un grand merci à tous les experts qui facilitent nos caractérisations : Léna Alembik, Sylvain Bourasseau, Amélie Vax-Weber, Christophe Velours, Paul Marque, Benjamin Cabannes-Boué, Mélanie Bousquet, Frédérique Ham-Pichavant, Emmanuel Ibarboure, Cédric Le Coz. Merci également à toutes celles et ceux qui facilitent notre quotidien au laboratoire : Florian Lacaze, Olivier Fihey, Emilie Lalande, Claude Le Pierres, Mame Mbacke, Séverine Saint-Drenant.

Merci à Angela Mutschler pour son implication dans le projet, notamment sur la partie encapsulation. Merci aussi aux chercheurs permanents de l'équipe 3 du LCPO : Elisabeth Garanger, Olivier Sandre, Christophe Schatz, Jean-François Le Meins, Bertrand Garbay, toujours disponibles pour donner d'excellents conseils scientifiques et pour partager des discussions enrichissantes. Merci également à Chloé Grazon, la pionnière de ROPISA.
Je remercie également les stagiaires que j'ai eu la chance d'encadrer :

- Thomas Barbeau, pour son stage de BTS, son aide précieuse sur les nombreuses ROPISA, son implication et sa curiosité.
- Fatemeh Salimi, pour son stage de M2: tu as permis de générer un grand nombre de données, notamment sur la nanoprécipitation et le système phénylalanine. Bonne chance pour ta thèse !

Bon courage aussi à ma successeuse, Maura Martinez Morales, qui reprend le « bébé » ROPISA et le mènera, j'en suis sûre, encore plus loin vers des applications thérapeutiques. Ta rigueur et ta patience seront des atouts précieux, je te souhaite beaucoup de succès !

Merci à toutes celles et ceux qui ont partagé ces années avec moi.

- Ségolène : merci de m'avoir prise sous ton aile dès le départ et de m'avoir appris tant de choses sur la ROPISA.
- Leslie : ma voisine de bureau et désormais collègue ! Merci pour ta bonne humeur, ton enthousiasme contagieux et tes encouragements : « c'est vous les experts ! ».
- Anouk : merci pour nos séances de fitness et ce passage mémorable à SOLEIL.
- Eloïse : pour toutes ces soirées tardives au bureau et les moments festifs en dehors autour d'un cocktail ou sur une piste de danse.
- Elise : pour les ragots et les apéros dans ton immense appartement.
- Mostafa : pour ton aide quotidienne et ton humour noir.
- Antoine : pour les innombrables cafés et les discussions league of legendèsque…
- Roro : pour ta gentillesse, ta patience et ta douceur, et pour tous ces cafés au labo ou ailleurs.

Merci également à toute l'équipe 3, anciens et nouveaux membres, ainsi qu'aux autres membres du LCPO : Sifan, Yupei, Marie, Martin, Valentin M., Sarah, Amin, Rocio, Enzo, Margaux, Carolina, Auriane, Alice, Anissa, Chloé, Megi, Diana, Arthur, Julien, Dongxu, Yue, Karine, Nadia, Zoi, Yelin, Bastien, Valentin, Clément, Florent, Nicholas, Alexandre, Maéva… et sûrement d'autres que j'oublie !

Merci à celles et ceux qui sont devenus ma famille ici.

Lou, on a commencé cette thèse ensemble, on a souffert ensemble. A ces nombreux verres, d'abord à la Victoire, puis transposés à Saint-Michel (Tripletta dans mon cœur) …. A ces nombreux vocaux envoyés, parfois beaucoup trop long. A ces nombreux conseils prodigués. A ces nombreuses larmes versées. A ces nombreux moments partagés. Le chœur voyageur, les concerts, Twilight, le Brat summer pendant les JO… Merci d'être toi, merci d'être aussi généreuse et passionnée, d'être comme une sœur. Je nous souhaite encore beaucoup d'années d'amitié.

Léna, merci pour ton énergie solaire. Tu es un rayon de bonheur, toujours positive et souriante. Tu m'as permis de m'accrocher dans les moments les plus durs durant cette thèse. Merci de m'avoir écouté de trop nombreuses fois me plaindre de mes tracas quotidiens, que ça soit à propos de la thèse ou d'autres sujets encore plus futiles (…). Merci de m'avoir fait découvert LoL (j'aurais jamais cru écrire ça un jour !!), mais aussi le crochet, la linogravure, ta passion pour Shay et les tatouages… Tu es et tu seras toujours d'une grande source d'inspiration.

Théophile évidemment, ton cher et tendre. Merci de me faire toujours autant rire, et merci de me carry sur LoL.

Clémence, merci pour ta douceur, merci d'être un peu notre maman, de nous accueillir chez toi avec les bons petits plats concoctés par Julien… Merci de m'avoir transmis ta passion pour les show drags, et d'être la personne solaire et créative que tu es. Et surtout merci à vous deux pour votre service traiteur lors de mon pot de thèse qui a été très grandement apprécié !

Paul, à toutes ces pauses clopes/cafés, ces nombreuses discussions tocardesques que nous adorons tant, des références de télé-réalité obscures, aux spritz et aux soirées folles…

Aurèle, pour ta douceur, tes ronrons et ta force de caractère et de persévérance qui m'impressionne tant…

Merci à mes colocs, Pierre et Amanda, et Hugo avant elle, de me supporter au quotidien depuis presque 1 an maintenant.
Merci à Noémie, retrouvée à Bordeaux, pour tous ces bons moments passés ensemble, que ça soit en blindtest, en terrasse ou à la salle de sport…

Merci aux Titouans et Titouanas de m'accompagner depuis la JC1A à CP: notre groupe ne s'est jamais lâché. Des premières soirées Kfet jusqu'au mariage de Léo, j'espère que nos aventures continueront longtemps à Collonges, à Aix, à Paris, ou ailleurs… Merci Julie, Camille, Marie, Constance, Léo, Julien, Maxime, Maia (et aux nombreux +1).

Merci aux Sanglichons ardennais pour cette amitié encore plus ancienne : depuis la 6e pour certains, depuis la 2nde4 pour d'autres. Même si l'on se voit rarement, chaque rencontre donne l'impression que rien n'a changé. À nous encore plein de pintes au Temple et de soirées au Cab. Merci Allan, Clément, Arthur, Camille, Corentin, Elise, Eugénie.

Merci à ma mère, de m'avoir toujours poussé à faire des études et de m'avoir accompagnée dans cette réussite. Merci à mon frère, pour l'exemple d'excellence et d'intelligence qu'il représente. Merci à Michel, d'être là pour ma mère et d'apporter un peu de calme dans cette famille excentrique. Merci à mon oncle et ma tante, grâce à qui j'ai pu suivre une prépa parisienne dans d'excellentes conditions, à l'internat Jean Zay. A mon cousin, d'être toujours là même après tout ce temps.
Un merci tout particulier à ma sœur, toujours là pour m'écouter et me rassurer, partager les joies comme les peines. Je t'aime.
Merci à ma famille de cœur, les Boumaraf, de m'avoir accueillie comme leur propre fille et transmis des valeurs de générosité et de partage.
Merci à Renée, d'être un amour de petit chat, qui m'a tant apportée de tendresse durant la rédaction de ce manuscrit.

Enfin, merci à toutes les autres personnes qui ont traversé ma vie avant ou pendant cette thèse. Même si nos chemins se sont séparés, vous avez, d'une manière ou d'une autre, marqué ma vie et contribué à faire de moi la personne que je suis aujourd'hui.

Table of contents

Résumé étendu en français _____ *i*

List of abbreviations _____ *viii*

List of symbols _____ *xiv*

General introduction _____ *xv*

Chapter I. Literature review _____ *1*

I.1. Introduction _____ **3**

I.2. Nanomedicine and cancer therapy _____ **3**

I.2.1. General concept of nanomedicine 3

I.2.2. Passive targeting and the enhanced permeability retention effect 5

I.2.3. Active targeting 8

I.2.4. The effect of particle shape 10

I.3. Polypeptide-based polymers as nanocarriers _____ **14**

I.3.1. Polypeptide, a simplified analogue of protein 14

I.3.2. Synthesis of polypeptides 18

I.3.3. Self-assembly of polypeptide-based copolymers 25

I.4. Polymerization-induced self-assembly _____ **39**

I.4.1. General definition 39

I.4.2. Design of nanocarriers by PISA 41

I.5. Conclusion _____ **64**

I.6. References _____ **67**

Chapter II. Elucidating the aqueous ROPISA of NCA mechanism _____ *76*

II.1. Introduction _____ **78**

II.2. Presentation of the study _____ **79**

II.2.1. Kinetics of polymerization 79

II.2.2. Presentation of the SAXS/WAXS experiment 82

II.3. Nucleation – a critical phase _____ **86**

II.3.1. SAXS/WAXS analysis 86

II.3.2. Pre-micellization hypothesis 87

II.4. Confinement-driven nucleophilicity _____ **89**

II.4.1. Acidification overtime 89

II.4.2. Initial pH effect 89

II.5. Monomer solubilization as the rate limiting factor ____ **90**

II.6. Nanoparticle growth via conformational maturation ____ **93**

II.6.1. β-sheet driven self-assembly ... 93

II.6.2. Conformational maturation ... 96

II.6.3. Chain configuration evolution within nanoparticles ... 99

II.7. Overall Mechanism ____ **101**

II.8. Conclusion ____ **102**

II.9. Experimental section ____ **104**

II.9.1. Materials ... 104

II.9.2. Instruments and methods ... 104

II.9.3. Synthesis ... 106

II.9.4. SAXS models ... 107

II.9.5. Calculations details ... 107

II.10. References ____ **109**

Chapter III. Tailoring anisotropic nanoparticles through NCA monomer selection in aqueous ROPISA ____ ***111***

III.1. Introduction ____ **114**

III.1.1. π−π interactions ... 114

III.1.2. H-bonding ... 116

III.1.3. Others driving forces ... 118

III.2. Influence of the chemical nature of protecting groups ____ **120**

III.2.1. [M]/[I] = 20 ... 120

III.2.2. [M]/[I] from 10 to 40 ... 124

III.3. Influence of the hydrophobicity of the amino-acid side chain ____ **128**

III.3.1. Aqueous ROPISA of Gly, Ala, Tyr, Leu and Phe-NCA ... 128

III.3.2. Kinetic studies ... 133

III.4. π-π interactions versus hydrophilic content: phenylalanine NCA ____ **134**

III.4.1. From low… ... 135

III.4.2. … to high hydrophilic fractions ... 138

III.5. Towards more functional π-π interactions: tyrosine NCA ____ **141**

III.6. Conclusion ____ **147**

III.7. Experimental Section ____ **149**

III.7.1. Materials ... 149

III.7.2. Instrumentation and methods ... 149

III.7.3. Synthesis ... 151

III.8. Supplementary Figures 155

III.9. References 167

Chapter IV. Modulation of stabilizing blocks in aqueous ROPISA to diversify nanoparticle surfaces 170

IV.1. Introduction 173

IV.2. Aqueous ROPISA initiated by poly(sarcosine) 174

IV.2.1. Poly(sarcosine)-glycine synthesis 174

IV.2.2. Aqueous ROPISA initiated by poly(sarcosine) of BLG-NCA 176

IV.3. Aqueous ROPISA initiated by poly(*L*-proline) 177

IV.3.1. Poly(*L*-proline) synthesis 179

IV.3.2. Aqueous ROPISA initiated by poly(*L*-proline) of various NCAs 179

IV.3.3. Thermoresponsive properties 184

IV.4. Aqueous ROPISA initiated by elastin-like polypeptide 186

IV.4.1. Aqueous ROPISA initiated by elastin-like polypeptide of various chain length 187

IV.4.2. Thermoresponsive properties 190

IV.5. Enzyme-polypeptide conjugates via aqueous ROPISA 191

IV.5.1. Presentation of the enzymes 192

IV.5.2. Aqueous ROPISA initiated by metalloenzymes of Gly-NCA and BLG-NCA 193

IV.6. Perspectives: other macroinitiators of interest 197

IV.6.1. Poly(ethylene glycol)-cyclic peptide conjugate (PEG-CP) 197

IV.6.2. Self-Immolative Polymers (SIP) 201

IV.6.3. Polysaccharides 204

IV.7. Conclusion 210

IV.8. Experimental section 212

IV.8.1. Materials 212

IV.8.2. Instrumentation and methods 212

IV.8.3. Synthesis 216

IV.9. Supplementary figures 220

IV.10. References 230

Chapter V. In vitro and in vivo evaluation of nanoparticles obtained by aqueous ROPISA *233*

V.1. Introduction 236

V.2. Nanoparticles preparation 238

V.2.1. Worm-like micelles preparation with covalent attachment of cyanine 238

V.2.2. Spherical nanoparticles obtention via solvent displacement 242

V.3. Cell internalization in 2D monolayer cell cultures 245

V.3.1. Cell viability in HUVEC 245
V.3.2. Cell association study in monolayer CT26 and 4T1 cells 245

V.4. Spheroids penetration 251
V.4.1. Preparation of multicellular tumor spheroids (MCTS) 251
V.4.2. CLSM 253
V.4.3. Flow cytometry 256

V.5. Biodistribution 259
V.5.1. Circulation time in healthy BALB/c nude mice 259
V.5.2. Accumulation of fluorescent NPs in CT26 and 4T1 tumors 260

V.6. Conclusion 263

V.7. Experimental section 265
V.7.1. Materials 265
V.7.2. Instrumentation and methods 265
V.7.3. Synthesis 270

V.8. References 272

Chapter VI. Aqueous ROPISA for drug delivery: encapsulation strategies 274

VI.1. Introduction 276
VI.1.1. *In situ* encapsulation 276
VI.1.2. *Post*-PISA encapsulation 283

VI.2. *In-situ* ROPISA encapsulation 287
VI.2.1. Ellipticine 287
VI.2.2. Mitoxantrone 290
VI.2.3. Doxorubicin 293

VI.3. Post-ROPISA encapsulation 298

VI.4. Conclusion 303

VI.5. Experimental section 304
VI.5.1. Materials 304
VI.5.2. Instrumentation and methods 304
VI.5.3. Encapsulation procedures 306

VI.6. References 308

General conclusion 310

Perspectives 312

Modulating morphology by copolymerization and enhanced drug loading 312

Towards active targeting with hyaluronan as stabilizer block 315

Encapsulation optimization and further *in vitro* / *in vivo* evaluation _____ **316**

References _____ **317**

Résumé étendu en français

Ces dernières années, un intérêt croissant s'est porté sur le développement de nanoparticules pour la vectorisation de médicaments anticancéreux, en raison de leur capacité à cibler spécifiquement les tumeurs via l'effet de perméabilité et de rétention accrue (EPR), tout en limitant la toxicité systémique et la dégradation prématurée des principes actifs. Toutefois, malgré les avancées technologiques, la majorité des nanomédicaments anticancéreux n'ont pas conduit à des améliorations significatives en clinique. Ces limitations sont principalement attribuées à une accumulation tumorale insuffisante et à des profils pharmacocinétiques défavorables, en lien avec la complexité des barrières biologiques et les différences entre les modèles animaux et les tumeurs humaines.

Dans ce contexte, la morphologie des nanoparticules est apparue comme un paramètre clé influençant leurs performances thérapeutiques. En particulier, les particules de forme allongée ont démontré une circulation sanguine prolongée, une meilleure pénétration tumorale et une internalisation cellulaire accrue.[1] L'auto-assemblage de copolymères à blocs amphiphiles, en particulier ceux constitués de polypeptides, biocompatibles et biodégradables, constitue une stratégie prometteuse pour générer ces objets anisotropes. Grâce à leur capacité à adopter des structures secondaires bien définies (hélices α ou feuillets β), ces polypeptides dirigent des comportements d'auto-assemblage uniques. Plusieurs de ces systèmes sont déjà utilisés cliniquement ou en cours d'évaluation dans des essais clinique de phase avancée, mais ils restent majoritairement confinés à des morphologies sphériques.[2]

La polymérisation par ouverture de cycle (ROP) des *N*-carboxyanhydrides (NCA) représente une méthode efficace pour la synthèse de tels polypeptides amphiphiles. Néanmoins, les procédés conventionnels reposent sur des conditions rigoureusement anhydres, des étapes de purification fastidieuses et l'emploi de solvants toxiques. Des travaux récents ont permis d'explorer des stratégies alternatives en milieu aqueux, notamment par l'usage de co-solvants ou de systèmes en émulsion, rendant possible une polymérisation contrôlée des NCA. Toutefois, la formation des nanoparticules reste le plus souvent fondée sur des procédés de déplacement de solvant, peu adaptés à une montée en échelle et nécessitant l'utilisation de solvants organiques délétères.

À l'inverse, le concept d'auto-assemblage induit par polymérisation (PISA) permet la synthèse directe de nanovecteurs aux formes variées à haute concentration, tout en réduisant les étapes de synthèse. Si cette approche a révolutionné le domaine de la polymérisation radicalaire contrôlée, son extension aux polypeptides, en particulier *via* la ROP aqueuse des NCA, reste encore très peu explorée. De plus, les stratégies d'encapsulation, qu'elles soient physiques ou chimiques, sont encore rares dans ce contexte. La formation de morphologies anisotropes, bien que prometteuse, reste limitée à une fenêtre expérimentale étroite et souvent dépendante de systèmes non biodégradables.

Ces travaux de recherche de doctorat s'inscrivent dans ce contexte et avaient pour but d'explorer le potentiel de l'auto-assemblage induit par polymérisation par ouverture de cycle (ROPISA) des NCA en

milieux aqueux pour des applications en nanomédecine. Ce procédé en une étape, réalisé en conditions douces et aqueuses, permet la formation de nanoparticules de polypeptides à morphologies allongées et à concentration élevée.[3] L'objectif principal fut de mieux comprendre les mécanismes de polymérisation et d'auto-assemblage impliqués, de diversifier les structures obtenues via l'emploi de différents monomères et macro-amorceurs, puis de démontrer leur pertinence en vectorisation de principes actifs anticancéreux, *via* des évaluations *in vitro* et *in vivo* ainsi que des stratégies d'encapsulations variées.

Le **Chapitre I** propose une revue approfondie de la littérature sur les nanoparticules polymères et polypeptidiques appliquées à la nanomédecine, en mettant particulièrement l'accent sur l'importance des morphologies anisotropes et sur les stratégies PISA pour le développement de nanovecteurs dégradables et fonctionnels.

Le **Chapitre II** s'attache à explorer en profondeur les mécanismes de polymérisation et d'auto-assemblage mis en jeu au cours du procédé ROPISA en milieu aqueux, appliqué au γ-benzyl-*L*-glutamate *N*-carboxyanhydride (BLG-NCA) amorcé par une amino-poly(éthylène glycol) (PEG_{5k}-NH_2). Ce procédé, encore peu documenté, soulève des interrogations en raison de la sensibilité à l'humidité des NCA, qui pourrait compromettre la polymérisation contrôlée en favorisant l'hydrolyse au détriment de l'aminolyse. Une première étude cinétique a toutefois révélé une polymérisation rapide suggérant l'existence de conditions favorables à une aminolyse plus rapide que l'hydrolyse. L'analyse en temps réel par diffusion des rayons X aux petits et grands angles (SAXS/WAXS) a permis de suivre simultanément la cinétique d'auto-assemblage et l'évolution de la conformation des chaînes polypeptidiques. Les résultats montrent que la nucléation des premières micelles intervient dès les premières étapes de la polymérisation. Des mesures complémentaires, notamment la détermination de la concentration d'agrégation critique (CAC) du PEG, ont mis en évidence la formation de pré-micelles dès que la concentration en PEG dépasse cette valeur. Ces pré-micelles génèrent un environnement confiné favorable à la réaction, en concentrant localement le monomère et en stabilisant l'état de protonation de l'amorceur (NH_2), même en milieu progressivement acidifié. Ce phénomène a été confirmée par un suivi pHmétrique, et l'étude du pH initial a montré qu'un pH trop acide compromet l'amorçage. Le confinement favorise ainsi la nucléophilie de l'amorceur et accélère la polymérisation en augmentant localement la concentration en monomère. Nous avons également démontré que la solubilité du NCA est un facteur clé influençant la cinétique de polymérisation. De plus, la formation précoce de feuillets β montré par WAXS oriente l'auto-assemblage vers des nanostructures anisotropes, notamment fibreuses, via des mécanismes d'addition ou de fusion de chaînes. Une proposition mécanistique a été avancée pour décrire la formation des nanoparticules, positionnant ce procédé hétérogène entre la polymérisation en émulsion, par ses effets interfaciaux,[4] et l'auto-assemblage induit par cristallisation et par polymérisation par ouverture de cycle (ROPI-CDSA), grâce à son mécanisme d'auto-assemblage structuré.[5] Enfin, nous avons identifié les paramètres clés de la réaction à maîtriser pour optimiser la polymérisation : le taux de solide, qui assure une bonne concentration en amorceur pour forcer la formation des pré-micelles, l'agitation pour une dispersion efficace du

monomère dans les nanoréacteurs micellaires, et un pH initial suffisamment basique pour maintenir un état optimal de protonation de l'amine et garantir la nucléophilicité de l'amorceur.

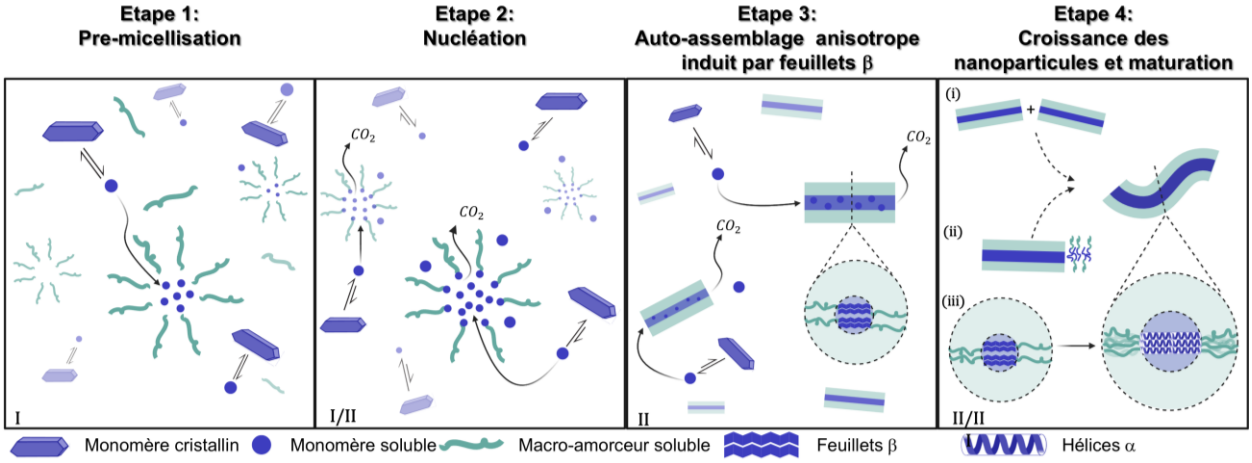

Scheme 1. Représentation schématique du mécanisme de ROPISA. **Étape 1** : Le mélange réactionnel initial est hétérogène, composé de monomères cristallins (cristaux bleus) en équilibre avec des monomères solubles (sphères bleues), et d'un macro-amorceur soluble (courbes vertes) formant des pré-micelles. Ces pré-micelles facilitent l'amorçage de la polymérisation des monomères solubles qui diffusent dans leur cœur par aminolyse *(Intervalle I)*. **Étape 2** : La nucléation micellaire débute lorsque le second bloc, hydrophobe et insoluble, commence à se former avec quelques unités répétées. Les monomères solubles diffusent et sont séquestrés au sein des cœurs micellaires, déplaçant ainsi l'équilibre de solubilisation du monomère cristallin. La polymérisation par ouverture de cycle (ROP) génère du CO_2 relargué dans la phase aqueuse continue, mais l'environnement confiné des micelles permet de préserver la nucléophilie du site amine réactif tout en limitant l'intrusion d'eau *(Intervalle I-II)*. **Étape 3** : Les nanoparticules s'allongent en fibres sous l'effet de la formation de feuillets β dans les peptides courts, stabilisant davantage les structures micellaires *(Intervalle II)*. **Étape 4** : Les nanoparticules continuent de croître en structures anisotropes plus longues via (i) la fusion de petites fibres ou (ii) l'élongation progressive des chaînes en croissance. Parallèlement, (iii) une transition conformationnelle lente des feuillets β vers des hélices α a lieu, conduisant à une augmentation du rayon du cœur hydrophobe.

Dans le **Chapitre III**, nous avons élargi notre étude en variant de manière systématique les monomères NCA, soumis à une polymérisation ROPISA amorcée par le PEG_{5k}-NH_2. Dans un premier temps, différents NCA de lysine ont été testés en ROPISA, révélant une meilleure régularité pour ε-benzyloxycarbonyl-*L*-lysine (Lys(Z))-NCA. L'étude a ensuite été élargie à des monomères variés (glycine, alanine, leucine, phénylalanine, tyrosine), afin d'explorer l'impact de l'hydrophobicité, de l'empilement π-π et des liaisons hydrogène sur la cinétique de polymérisation et l'anisotropie des nanoparticules. L'impact de l'hydrophobicité sur la cinétique de polymérisation a été clairement mis en évidence : plus le monomère est hydrophile, plus sa polymérisation est rapide, ce qui vient conforter l'hypothèse émise au **Chapitre II** quant au rôle déterminant de la solubilité sur la vitesse de polymérisation. Ainsi, un monomère diffusant rapidement au sein du nanoréacteur micellaire est rapidement polymérisé. Concernant leur influence sur l'auto-assemblage, la glycine induit la formation de fibrilles flexibles, tandis que l'alanine et la phénylalanine induisent des structures plus rigides et anisotropes. Enfin, une étude plus approfondie sur la phénylalanine et la tyrosine, deux acides aminés d'intérêt dans le contexte de la délivrance de principes actifs, a été menée en faisant varier la taille des blocs hydrophiles et hydrophobes, modifiant la morphologie, même si la morphologie anisotrope reste omniprésente. Ainsi, l'équilibre hydrophile/hydrophobe, les interactions de type π-π et les liaisons hydrogène se sont révélés être des paramètres clés influençant à la fois la cinétique de polymérisation et les dynamiques d'auto-assemblage,

et déterminant *in fine* le rapport d'aspect des nanostructures formées. Ce chapitre met ainsi en lumière la grande versatilité du procédé ROPISA, démontrant sa capacité unique à générer des nanoparticules aux morphologies variées, là où les autres stratégies PISA présentent des fenêtres expérimentales beaucoup plus restreintes.

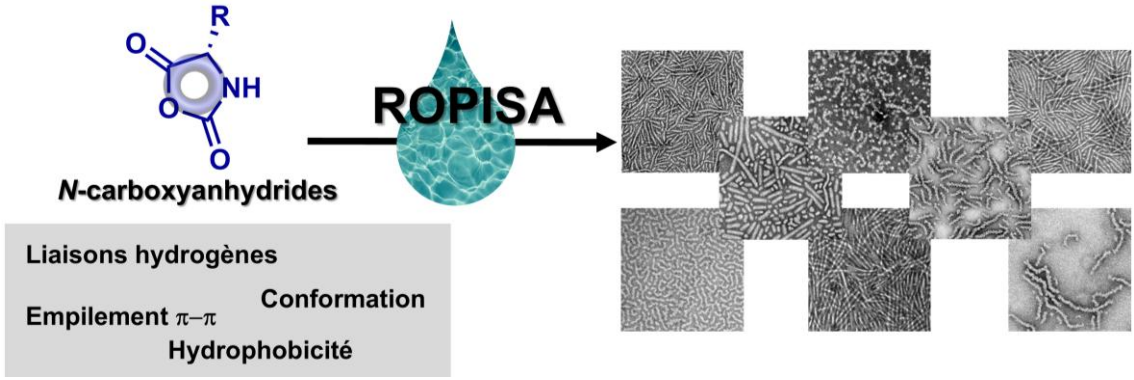

Figure 1. Obtention de nanoparticules avec différentes anisotropie grâce à l'utilisation de *N*-carboxyanhydrides d'acides aminés variés en ROPISA.

Dans le **Chapitre IV**, nous avons exploré l'utilisation de divers macroamorceurs (bio)dégradables et fonctionnels comme blocs stabilisants pour la ROPISA aqueuse de NCA. Dans un premier temps, des amorceurs peptidiques ont été étudiés. Par exemple, la poly(sarcosine), un analogue du poly(éthylène glycol), a permis la formation de nanoparticules allongées, ce qui est prometteur pour la délivrance de principes actifs, notamment en réponse aux controverses croissantes autour du PEG. La poly(proline) et les polypeptides de type élastine (ELPs) ont conduit à la formation de nanoparticules anisotropes bien définies, tout en conservant leurs propriétés intrinsèques, telles que leur réponse thermique.[6] Cette stratégie a ensuite été étendue à des conjugués enzyme-polypeptide : bien que la polymérisation ait été efficace, une baisse d'activité enzymatique a été observée, vraisemblablement due à des encombrements stériques. D'autres amorceurs innovants ont également été évalués, notamment des peptides cycliques, des polymères auto-immolables (SIPs) et des dérivés du dextrane. Les peptides cycliques ont mené à la formation de nanoparticules sphériques, bien que le mécanisme sous-jacent reste à élucider. Les SIPs ont permis l'obtention de nanoparticules, sans qu'un allongement de chaîne puisse être démontré. Enfin, la fonctionnalité des extrémités du dextrane s'est révélée déterminante pour l'efficacité de la polymérisation, soulignant l'importance de la nucléophilie de l'amorceur. L'ensemble de ces résultats met en lumière le rôle crucial du bloc stabilisant dans la régulation de la morphologie des nanoparticules. Ce chapitre illustre une nouvelle fois la grande versatilité du procédé ROPISA, ouvrant la voie à la conception de nanoparticules peptidiques fonctionnelles adaptées à des applications en vectorisation thérapeutique.

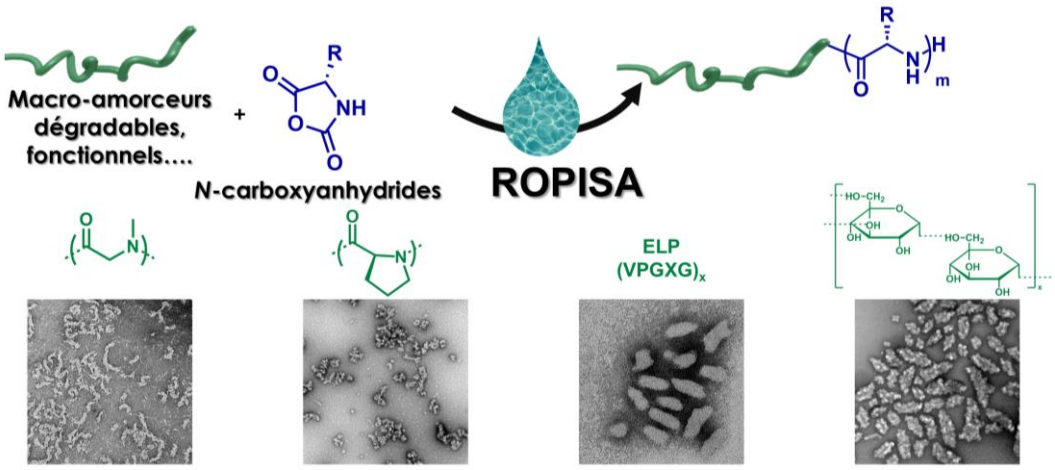

Figure 2. Utilisation de blocs stabilisants variés, fonctionnels et/ou dégradables, pour moduler la surface des nanoparticules obtenues par ROPISA.

Afin de démontrer le potentiel thérapeutique des nanoparticules obtenues par ROPISA, il est essentiel d'évaluer leur comportement en milieu biologique. Dans cette optique, une comparaison a été réalisée avec des nanoparticules sphériques, dans la mesure où plusieurs études ont déjà mis en lumière les avantages potentiels des nanoparticules anisotropes. Ainsi, dans le **Chapitre V**, nous avons synthétisé avec succès des nanoparticules filamenteuses fluorescentes à base de polypeptides *via* une polymérisation ROPISA aqueuse en une seule étape du BLG-NCA, intégrant une stratégie optimisée de couplage d'une sonde fluorescente directement au cours de la réaction. En parallèle, des nanoparticules sphériques analogues ont été préparées par déplacement de solvant, servant de référence. L'internalisation cellulaire et la biodistribution *in vivo* ont été évaluées dans deux modèles tumoraux murins, CT26 (carcinome colorectal) et 4T1 (cancer du sein), présentant des architectures vasculaires distinctes et influençant de manière différenciée l'effet EPR et l'accumulation passive des nanovecteurs. Les deux morphologies, sphérique et filamenteuse, ont montré une internalisation efficace en culture cellulaire 2D, avec une cinétique plus rapide dans les cellules CT26, tandis que les cellules 4T1 ont révélé une accumulation plus importante. Aucune différence significative n'a été observée entre les morphologies, soulignant la robustesse des nanoparticules issues de la ROPISA pour le ciblage tumoral. Ces résultats ont été confirmés dans des modèles tridimensionnels de sphéroïdes, où les deux types de nanoparticules ont démontré une bonne capacité de pénétration, bien que plus lente dans les sphéroïdes 4T1, conduisant malgré tout à une accumulation finale plus élevée. Plus important encore, les études *in vivo* menées chez des souris saines ont mis en évidence un temps de circulation prolongé, confirmant la stabilité des nanovecteurs dans des conditions physiologiques. Chez les souris porteuses de tumeurs CT26 ou 4T1, une accumulation tumorale significative a été observée, validant le potentiel des nanoparticules issues de la ROPISA pour des applications en vectorisation de médicaments. L'accumulation particulièrement marquée observée dans les tumeurs 4T1 souligne l'intérêt des nanoparticules filamenteuses pour le ciblage d'environnements tumoraux complexes, notamment ceux caractérisés par une forte pression intratumorale. Ces résultats constituent une première démonstration convaincante du potentiel de la ROPISA aqueuse de NCA en

nanomédecine. Ce travail jette ainsi les bases du développement de nanovecteurs de nouvelle génération, chargés en médicament par encapsulation physique, tel qu'exploré au **Chapitre VI.**

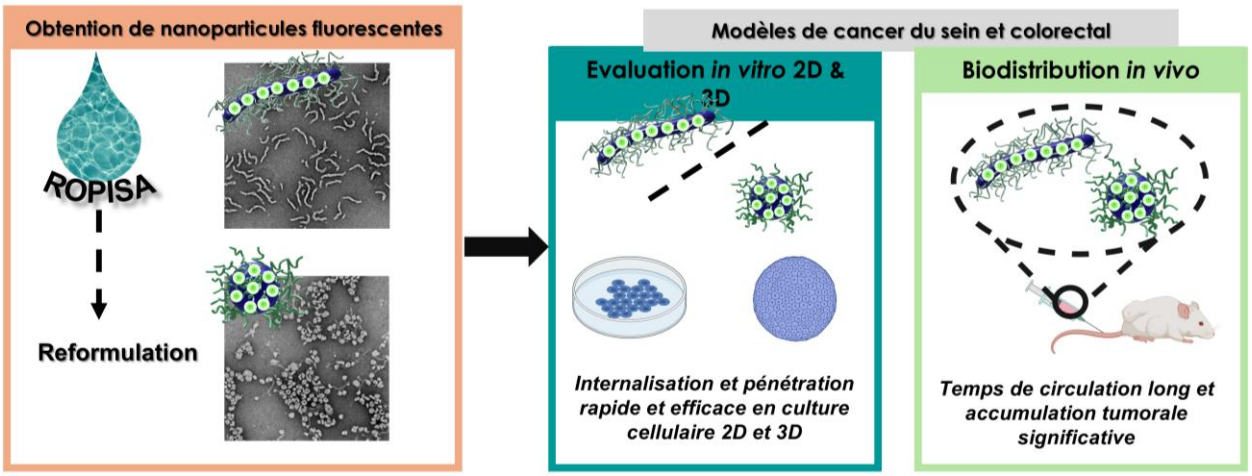

Figure 3. Evaluation biologique des nanoparticules obtenues par ROPISA et comparaison à des analogues sphériques.

Dans ce **Chapitre VI**, nous avons démontré que de fortes efficacités d'encapsulation de médicaments anticancéreux, aux hydrophobicités variées, peuvent être obtenues *via* deux stratégies complémentaires : l'encapsulation *in situ* lors de la polymérisation ROPISA aqueuse, et l'encapsulation *post*-polymérisation (*post*-ROPISA). Nos résultats indiquent que, pour des composés peu réactifs comme la mitoxantrone, l'encapsulation *in situ* est particulièrement efficace. En revanche, pour des molécules plus réactives telles que la doxorubicine, dont les groupes fonctionnels nucléophiles peuvent induire des réactions secondaires indésirables pendant la polymérisation, une stratégie *post*-ROPISA s'avère plus adaptée pour confiner la molécule au sein du cœur hydrophobe. Par ailleurs, l'encapsulation *in situ* de l'ellipticine, un agent hautement hydrophobe mais chimiquement inerte, a également été démontrée ; cependant, son efficacité d'encapsulation s'est révélée limitée par sa faible solubilité dans le DMSO et l'eau, entraînant une charge médicamenteuse réduite. Ces observations soulignent l'influence déterminante de la nature chimique et de la solubilité du principe actif sur l'efficacité du processus d'encapsulation, et fournissent un cadre pour la conception rationnelle de nanovecteurs à base de polypeptides, alliant chargement optimisé et morphologie contrôlée pour des applications en oncologie. Ainsi, cette étude met en lumière la capacité unique du procédé ROPISA à générer, en une seule étape, des nanomédicaments peptidiques hautement concentrés, à rendement élevé, et à forte charge médicamenteuse, le tout dans des conditions douces 100 % aqueuses.

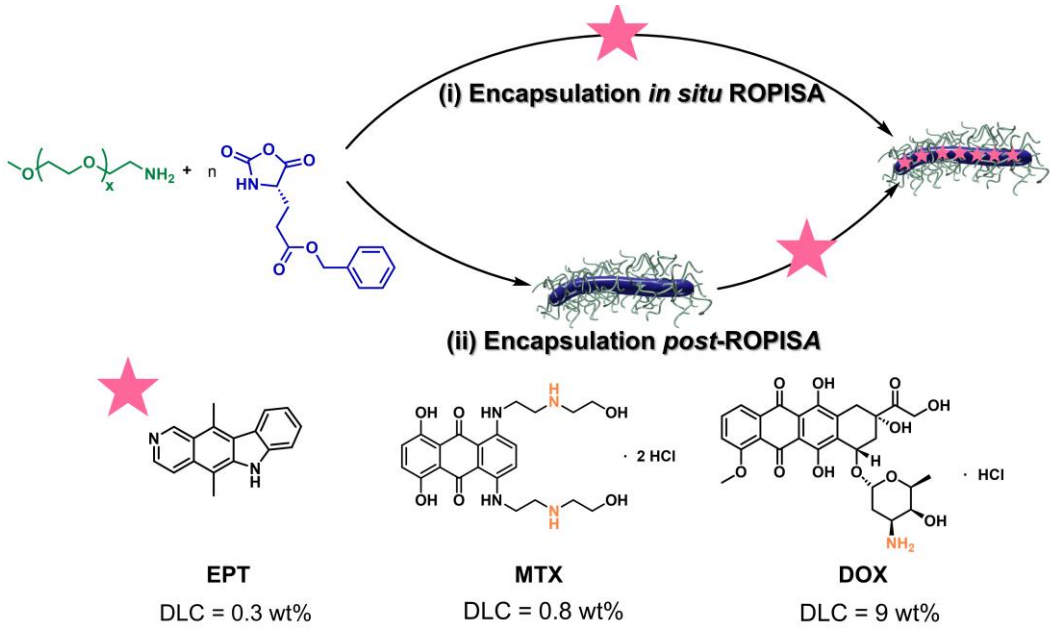

Figure 4. Encapsulation de principes actifs anticancéreux hydrophobes dans les nanoparticules produites par ROPISA par deux stratégies d'encapsulation, simultanément à l'auto-assemblage (*in situ*) et *post*-ROPISA.

Les travaux futurs viseront à améliorer encore la capacité d'encapsulation en sélectionnant des monomères présentant une meilleure affinité pour les principes actifs, comme la tyrosine, connue pour ses interactions de type π–π et liaisons hydrogène avec les composés hydrophobes. Des efforts seront également menés pour affiner les profils de relargage des principes actifs et évaluer l'efficacité thérapeutique de ces nanovecteurs dans des modèles biologiques pertinents. Au-delà de l'encapsulation physique, la conjugaison chimique constitue également une stratégie prometteuse, comme introduit en début de chapitre. Forts des résultats obtenus au **Chapitre V** sur le couplage carbodiimide dans le cœur hydrophobe à l'aide d'une sonde fluorescente, cette approche de fonctionnalisation pourrait être étendue à des principes actifs thérapeutiques d'intérêt.

Références :

[1] H. Hadji, K. Bouchemal, *J. Control. Release.***2022**, *342*, 93–110.
[2] T. Melnyk, S. Đorđević, I. Conejos-Sánchez, M. J. Vicent, *Adv. Drug Deliv. Rev.* **2020**, *160*, 136–169.
[3] C. Grazon, P. Salas-Ambrosio, E. Ibarboure, A. Buol, E. Garanger, M. W. Grinstaff, S. Lecommandoux, C. Bonduelle, *Angew. Chem. Int. Ed.* **2020**, *59*, 622–626.
[4] A. Czajka, S. P. Armes, *J. Am. Chem. Soc.* **2021**, *143*, 1474–1484.
[5] P. J. Hurst, A. A. Graham, J. P. Patterson, *ACS Polym Au* **2022**, *2*, 501–509.
[6] H. Beauseroy, C. Grazon, S. Antoine, M. Badreldin, P. Salas-Ambrosio, S. Harrisson, E. Garanger, S. Lecommandoux, C. Bonduelle, *Macromol. Rapid Commun.***2024**, *45*, 2400079.

List of abbreviations

Aac	Acrylic acid
Aam	Acrylamide
ABC	Accelerated Blood Clearance phenomenon
ABTS	2,2'-azino-bis(3-ethylbenzothiazoline-6-sulfonic acid
ACN	Acetonitrile
ADH	Adipic acid dihydrazide
AFM	Atomic Force Microscopy
AMM	Activated monomer mechanism
APC-A	Allophycocyanin
API	Active Pharmaceutical Ingredients
APTAC	3-acrylamidopropyl trimethylammonium chloride
Asp	Aspartic acid
ATR	Attenuated Total Reflectance
ATMP	Atom Transfer Radical Polymerization
BCP	Block copolymer
BD	Brownian Dynamic
BLA	*L*-aspartic acid β-benzyl ester
BLG	γ-benzyl-*L*-glutamate
BMDO	5,6-benzo-2-methylene-1,3-dioxepane
Boc	ε-tert-butyloxycarbonyl
BSA	Bovin Serum Albumin
BzMA	Benzyl methacrylate
CA	Cellulose acetate
CAC	Critical Aggregation Concentration
CBMA	*N,N*-cystaminebismethacrylamide
CCK-8	Cell counting kit-8
$CDCl_3$	Deuterated chloroform
CDSA	Crystallization-Driven Self-Assembly
CH_2Cl_2	Dichloromethane
$CHCl_3$	Chloroform
CKA	Cyclic ketene acetal
CMC	Critical Micelle Concentration
CONACYT	Consejo Nacional de Ciencia y Tecnología
CO_2	Carbon dioxide

$COCl_2$	Phosgene
CPT	Camptothecin
Cryo-TEM	Cryo-Transmission Electron Microscopy
CSLM	Confocal Scanning Laser Microscopy
CTA	Thiocarbonylthio chain-transfer agent
COT	Cyclooctatetraene
Cy	Cyanine
CWC	Critical Water Content
D_2O	Deuterium oxide
DAPI	4′,6-diamidino-2-phenylindole
DCR	Derived count rate
Dde	1-(4,4-dimethyl-2,6-dioxocyclohex-1-ylidene)ethyl
Dex	Dextran
DMA	*N,N*-dimethylacrylamide
DMAc	Diacetone acrylamide
DMAEA	2-(*N,N*-dimethylamino)ethyl acrylate
DMEM	Dulbecco's modified Eagle's medium
DMF	*N,N*-dimethylformamide
DMSO	Dimethylsulfoxide
DMSO-d_6	Deuterated dimethylsulfoxide
DNA	Deoxyribonucleic acid
DLS	Dynamic Light Scattering
DLC	Drug Loading Content
DOX	Doxorubicin
DOSY	Diffusion-ordered spectroscopy
DOT	Dibenzo[c,e]oxepane-5-thione
DP	Degree of polymerization
DPD	Dissipative particle dynamics
DTT	*DL*-dithiothreitol
EBM-2	Endothelial Basal Medium-2
EDC	1-ethyl-3-carbodiimide hydrochloride
EE	Encapsulation efficiency
ECM	Extracellular matrix
ELP	Elastin-like polypeptide
EPR	Enhanced Permeability and Retention effect
EPT	Ellipticine
FDA	Food and drug administration
FBS	Fetal bovine serum

FITC	Fluorescein isothiocyanate
FITR	Fourier Infrared Transformer spectroscopy
FNA	Functional nucleic acids
FTMC	Fluorene trimethylene carbonate
GFP	Freen fluorescent protein
Glu	Flutamic acid
GOx	Flucose oxidase
GTP	Group-Transfer Polymerization
HA	Hyaluronan
HCl	Hydrochloride acid
HEMA	2-hydroxyethyl methacrylate
HFIP	Hexafluoro-2-propanol
HHH	Hexagonally packed hollow hoop
HOBt	1-hydroxybenzotriazole hydrate
HPMA	2-hydroxypropyl methacrylate
HRP	Horseradish peroxidase
HSA	Human serum albumin
IFN	Interferon-α
iCONM	Innovation Center of Nanomedicine
IVIS	*In vivo* imaging system
KOH	Potassium hydroxide
Lac	Laccase
LAP	Living anionic polymerization
LCDSA	Liquid crystallization-driven self-assembly
LC	Liquid crystal
Leu	Leucine
LiHMDS	Lithium hexamethyldisilazide
Lys	Lysine
LCTS	Lower Critical Solution Temperature
MA	Methylacrylate
MAEAC	2-(methacryloyloxy)ethyl anthracene-9-carboxylate
MAEB	2-(methacryloyloxy)ethyl benzoate
MALS	Multiangle light scattering
MCTS	Multicellular tumor spheroids
MEA	2-methoxyethyl acrylate
Met	Methionine
MeOH	Methanol
MDO	2-methylene-1,3-dioxepane

MFI	Mean fluorescent intensity
MMA	Methylmethacrylate
MPA	Mycophenolic acid
MPDL	2-methylene-4-phenyl-1,3-dioxolane
MPC	2-methacryloyloxyethyl phosphorylcholine
MTC	3-methylene-1,9-dioxa-5,12,13-trithiacyclopentadecane-2,8-dione
MTX	Mitoxantrone
NAM	Normal amine mechanism
NB	n-Butyl acrylate
NCA	*N*-carboxyanhydrides
NHS	N-hydroxysuccinimide ester
NIR	Near infrared
NMP	Nitroxide Mediated Polymerization
NNCA	*N*-alkylated NCA
NP	Nanoparticles
NR	Nile Red
NMR	Nuclear Magnetic Resonance
NTA	*N*-thiocarboxyanhydride
O/W	Oil-in-water emulsion
PAM	Polyacrylamides
PAA	Poly(acrylic acid)
PBMA	Poly(butyl methacrylate)
PCL	Polycaprolactone
PDMAPMA	Poly(*N*-[3-(dimethylamino)propyl] methacrylamide)
PDMAEMA	Poly(dimethylaminoethylmethacrylate)
PEG	Polyethylene glycol
PEE	Polyethylethylene
PFTMC	Poly(fluorenetrimethylcarbonate)
Phe	Phenylalanine
PI-CDSA	Polymerization-Induced Crystallization-Driven Self-Assembly
PISA	Polymerization-Induced Self-Assembly
PLA	Poly(lactide)
PLMA	Poly(lauryl methacrylate)
PLP	Poly(proline)
PMeOx	Poly(2-methyl-2-oxazoline)
PMeOz	Poly(2-methyl-2-oxazine)
PMPC	Poly(2-(methacryloyloxy)ethylphosphorylcholine)
PNAM	Poly(*N*-acryloylmorpholine)

PNB	Poly(norbornene)
PNIPAM	Poly(*N*-isopropylacrylamide)
POEGMA	Poly[oligo(ethylene glycol) methacrylate]
POx	Polyoxazolines
PBS	Phosphate-buffered saline
P/S	Penicillin/streptomycin
PSar	Poly(sarcosine)
PTMC	Poly(trimethylene carbonate)
PTX	Paclitaxel
PVP	Poly(*N*-vinylpyrrolidone)
RAFT	Reversible Addition-Fragmentation Chain Transfer
RDRP	Reversible Deactivation Radical Polymerization
ROI	Region of interest
ROMP	Ring-Opening Metathesis Polymerization
ROP	Ring Opening Polymerization
ROPI-CDSA	Ring-Opening Polymerization-Induced Crystallization-Driven Self-Assembly
ROS	Reactive oxygen species
RPMI	Roswell Park Memorial Institute medium
rROP	Radical Ring-Opening Polymerization
SAXS	Small-angle X-ray scattering
SAOCA	Salicylic acid *O*-carboxyanhydride
SD	Standard deviation
SEC	Steric Exclusion Chromatography
SDS-PAGE	Sodium dodecyl-sulfate polyacrylamide gel electrophoresis
SEM	Scanning Electron Microscopy
SIP	Self-immolative polymers
$SOCl_2$	Thionyl chloride
SPPS	Solid-Phase Peptide Synthesis
TARO	Thiocarbonyl addition ring-opening
TBA	*N*-tert-butylacrylamide
TCEP	Tris(2-carboxyethyl)phosphine
TERP	Organotellurium-Mediated Radical Polymerization
THF	Tetrahydrofuran
TFA	Trifluoracetic acid
TFA-*d*	Deuterated trifluoracetic acid
TMS	Trimethylsilyl
TPP	Triphenylphosphonium
Tyr	Tyrosine

UNAM	Universidad Nacional Autónoma de México
UV-vis	Ultraviolet-visible
VP	Versatile peroxidase
WAXS	Wide-angle X-ray scattering
WHO	World Health Organization
Z	ε-benzyloxycarbonyl

List of symbols

A	Surface area
a	Contact area of the head group
D	Distance between chains, diffusion coefficient
$Đ$	Dispersity index
D_Z	Hydroynamic Z-average diameter
$I(q)$	Scattering intensity
L	Length, layer thickness
M	Molar mass
M_n	Number average molar mass
M_w	Mass average molar mass
N	Number of repeating units in the polymer
R_f	Flory radius
R_g	Radius of gyration
T	Temperature
T_{CL}	Clear point temperature
T_{CP}	Cloud point temperature
T_g	Glass transition temperature
T_t	Transition temperature
V	Volume
χ	Interaction parameter
χ^2	Fitting error
dn/dc	Refractive index increment
f	Hydrophilic fraction
λ	Wavelength
P	Packing parameter
q	Wave vector
ρ	Scattering length density
σ	Polydispersity index, surface density
Σ	Reduced grafting density
τ_s	Solid content
w	Width

General introduction

In recent years, considerable attention has been directed towards the development of nanoparticles for drug delivery due to their capacity to target tumors *via* the Enhanced Permeability and Retention (EPR) effect, while concurrently reducing drug toxicity and degradation. However, the majority of cancer nanomedicines have not demonstrated substantial improvement in clinical outcomes, primarily due to limited tumor accumulation and unfavorable pharmacokinetics resulting from biological barriers and discrepancies between animal models and human tumors. Alternatively, nanoparticle shape has been demonstrated to play a crucial role in therapeutic performance, with elongated particles exhibiting prolonged circulation times, enhanced tumor penetration, and improved cellular uptake. In this regard, the self-assembly of amphiphilic block copolymers emerges as a promising approach to generate such nanocarriers, particularly when using biocompatible and biodegradable polypeptides that can form specific secondary structures (α-helix or β-sheet) and direct anisotropic self-assembly. These materials hold particular value in the field of drug delivery, with several systems already in clinical use or undergoing phase 3 trials; however, these materials are typically constrained to spherical morphologies.

Ring-opening polymerization (ROP) of *N*-carboxyanhydrides (NCAs) has been identified as a highly effective method for the synthesis of amphiphilic polypeptides. However, conventional processes are often hindered by the necessity of extensive purification and the use of harmful solvents. Recent studies have demonstrated the potential for controlled polymerization of NCAs in aqueous media using co-solvents or emulsion techniques. Polypeptide-based nanoparticles are typically formed *via* a solvent-displacement process, which uses toxic solvents and diluted conditions, thereby presenting challenges in terms of scalability. Conversely, the advent of polymerization-induced self-assembly (PISA) has emerged as a more direct approach for the synthesis of nanocarriers exhibiting a wide range of shapes and compositions at high concentrations. However, the encapsulation of drugs *via* physical or chemical loading remains an under-explored field. The formation of anisotropic morphologies is typically limited to a narrow experimental window and often relies on non-degradable polymer systems. In this PhD project, we investigated the recently developed aqueous ring-opening polymerization-induced self-assembly (ROPISA) of NCAs for nanomedicine applications. This one-pot, aqueous process enables the synthesis of elongated polypeptide-based nanoparticles at high concentrations. Despite its promising potential, ROPISA remains underexplored, with few monomers investigated, a limited mechanistic understanding, and no established applications in nanomedicine to date.

This thesis manuscript summarizes our findings in six chapters. **Chapter I** reviews the literature on polymer and polypeptide nanoparticles in nanomedicine, with a specific focus on anisotropic nanoparticles' importance and polymerization-induced self-assembly strategies for the development of degradable/functional nanocarriers. **Chapter II** examines the mechanism of polymerization and self-

assembly using PEG-*b*-PBLG as a model. This chapter uses time-resolved small and wide-angle X-ray scattering (SAXS/WAXS) with complementary techniques like size exclusion chromatography (SEC) and transmission electron microscopy (TEM) to analyze the kinetics of self-assembly and proposes a mechanism for this heterogeneous process. In **Chapter III**, a diverse array of amino-acid NCAs, functioning as monomers, undergo ROPISA to diversify the structures obtained and to study the impact of the specific properties of each peptide on polymerization and self-assembly. **Chapter IV** explores a range of macroinitiators of interest, including biodegradable and/or functional, for ROPISA and characterizes the resulting nanoparticles. Finally, **Chapter V** appraises the behavior of fluorescent PEG-*b*-PBLG nanoparticles *in vitro* and *in vivo* with tumor models, while **Chapter VI** assesses drug delivery strategies by comparing *in situ* and *post*-polymerization encapsulation of anticancer agents.

Chapter I. Literature review

Table of Contents

Chapter I. Literature review

I.1. Introduction 3

I.2. Nanomedicine and cancer therapy 3

I.2.1. General concept of nanomedicine 3

I.2.2. Passive targeting and the enhanced permeability retention effect 5

I.2.3. Active targeting 8

I.2.4. The effect of particle shape 10

I.3. Polypeptide-based polymers as nanocarriers 14

I.3.1. Polypeptide, a simplified analogue of protein 14

I.3.1.1. Primary structure: amino acids 15

I.3.1.2. Secondary structure 16

I.3.2. Synthesis of polypeptides 18

I.3.2.1. Ring-opening polymerization of *N*-carboxyanhydrides 18

I.3.2.1.1. NCA synthesis 18

I.3.2.1.2. Mechanism of polymerization 19

I.3.2.1.3. NCA polymerization in presence of water 21

I.3.3. Self-assembly of polypeptide-based copolymers 25

I.3.3.1. Basic principle of self-assembly 26

I.3.3.2. Self-assembly of amphiphilic block copolymers 27

I.3.3.2.1. Conventional self-assembly 28

I.3.3.2.2. Crystallization-driven self-assembly 30

I.3.3.2.3. Application to polypeptide-based copolymers 33

I.4. Polymerization-induced self-assembly 39

I.4.1. General definition 39

I.4.2. Design of nanocarriers by PISA 41

I.4.2.1. Biomolecule as stabilizer block in PISA 41

I.4.2.1.1. Poly(sarcosine) 41

I.4.2.1.2. Peptides 42

I.4.2.1.3. Proteins 43

I.4.2.1.4. Functional nucleic acids 46

I.4.2.1.5. Polysaccharides 46

I.4.2.2. Degradable core: apply ROP with PISA 48

I.4.2.2.1. rROPISA 48

I.4.2.2.1.1. CKAs 48

I.4.2.2.1.2. DOT 52

I.4.2.2.1.3. Disulfide-based cyclic monomers 54

I.4.2.2.2. ROPI-CDSA 56

I.4.2.2.3. ROPISA 58

I.5. Conclusion _____ **64**

I.6. References _____ **67**

I.1. Introduction

This chapter aims at providing the essential knowledge required to understand the key concepts and challenges addressed in my PhD project, as detailed in this manuscript. A broad, but not exhaustive overview of relevant research areas is presented in this literature review. The discussion starts with an introduction to nanomedicine and drug delivery, specifically in the context of cancer therapy, followed by an exploration of how nanocarrier properties, particularly their shape, influence their performance. The advantages of anisotropic nanoparticles as drug carriers are highlighted. Next, synthetic polypeptides are reviewed as a promising material for nanocarrier design, including their synthesis and their unique ability to form anisotropic nanoparticles through various self-assembly mechanisms. Finally, special attention is given to polymerization-induced self-assembly (PISA) as a promising and versatile approach for the design of nanocarriers with potential applications in nanomedicine.

I.2. Nanomedicine and cancer therapy

I.2.1. General concept of nanomedicine

Effective drug delivery is a fundamental aspect of achieving successful therapy and accurate diagnosis in various healthcare fields.[1] One major challenge is ensuring that therapeutic agents, including biotherapeutics and small bioactive molecules, accumulate in diseased tissues and are internalized by target cells when necessary, although some agents exert their effects *via* extracellular receptor activation and do not require internalization. This specific delivery is essential for drugs to exert their intended therapeutic or diagnostic effects. However, several obstacles make this process challenging:

1. Limited solubility and/or high toxicity of drugs under physiological conditions.[2]
2. Degradation by the host metabolism, which can lead to the loss of drug functionality before reaching the target site.
3. Interactions with the biological environment and non-targeted cells, reducing therapeutic efficacy and potentially causing side effects.
4. Premature elimination of the drug before it reaches the target tissue.
5. Ineffective cellular entry due to the physicochemical properties of the drugs.

To address the limitations of free therapeutics and the complexity of biological barriers, significant efforts have been directed toward the development of advanced drug delivery systems capable of protecting, encapsulating, and precisely delivering therapeutic agents. Nanomedicine, the use of nanotechnology for medical applications, employs nanoparticles (NPs) as drug carriers. These nanoparticles serve as versatile tools for navigating systemic, microenvironmental, and cellular barriers that vary across patient populations and disease types.

To be used in nanomedicine, these nanocarriers should:[3]

1. Be made of a biocompatible material, well purified and characterized, and easily functionalized to avoid any side reaction with the organism (toxicity, inflammation or immune response).
2. Be soluble or colloidally stable in aqueous media for enhanced efficacy.
3. Demonstrate high differential uptake efficiency in target cells compared to normal cells or tissues.
4. Have an extended circulation time, low aggregation rate and long shelf life.

Following these criteria, a variety of materials have been used to design nanocarriers, each with unique properties. These range from early liposomes[4] to more advanced metallic nanoparticles (*e.g.*, quantum dots, gold nanoparticles, iron oxide nanoparticles),[5] as well as lipid nanoparticles (LNPs),[6] polymeric micelles,[7] polymersomes,[8] dendrimers,[9] and silica nanoparticles.[10] The ideal size of nanoparticles ranges from 10 to 100 nm, to avoid elimination in the kidney (particles < 6 nm)[11] and the spleen (particles > 150 nm).[7] Shapes can vary from spheres, rods, worms, cubes, and disks. Nanocarriers are typically coated with hydrophilic, neutral, zwitterionic or negatively charged materials on their surface to enhance solubility, improve stealth properties, and prevent enzymatic degradation and protein corona formation. Meanwhile, their hydrophobic core facilitates drug encapsulation and controlled release (Figure I-1).[12]

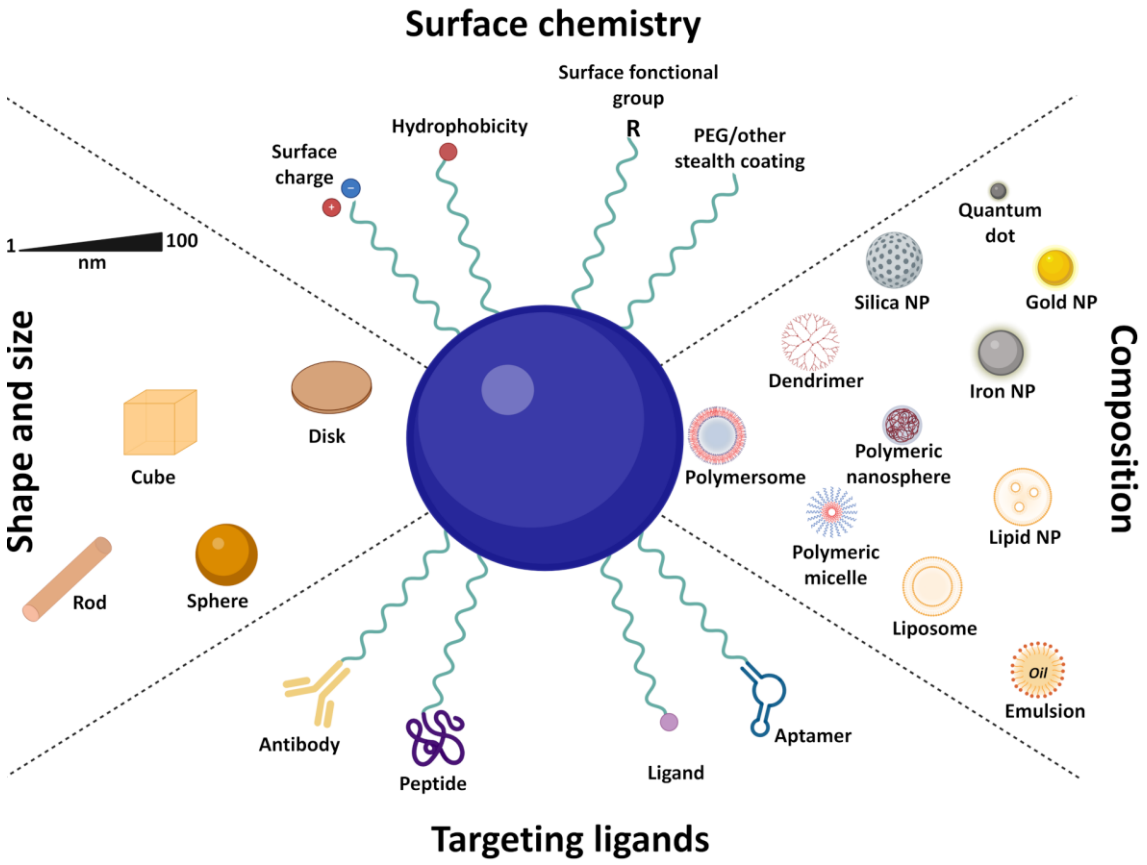

Figure I-1. Design of nanocarriers for drug delivery. Size, shape et composition can be tailored, and they can exhibit different surfaces and targeting ligands. Adapted from Scheper *et al*.[13]

The most common application of nanocarriers concern the treatment of cancer, which will be further discussed in the following section.[14] Indeed, cancer accounts for more than 10 million new cases each year and is the leading cause of death worldwide, according to the World Health Organization (WHO).[15] Despite advances in cancer treatment, controlling the biological fate of active pharmaceutical ingredients (APIs) remains a significant challenge, as current therapies are limited by poor stability, solubility, and metabolism, resulting in suboptimal pharmacokinetics. Furthermore, off-target effects cause unwanted toxicities that reduce treatment tolerability and often result in treatment failure due to inadequate drug delivery to the tumor site.

I.2.2. Passive targeting and the enhanced permeability retention effect

Since Paul Ehrlich's "magic bullet" concept in the early 20th century, which suggested that specific therapeutic agents could target and destroy pathogens or diseased cells without harming surrounding healthy cells,[16] the use of nanomedicine in oncology has been widely explored.[14] The main strategy for targeting tumor tissue has been to exploit the enhanced permeability and retention (EPR) effect. In fact, in 1986, Matsumura and Maeda showed that solid tumors have increased permeability to macromolecules and prolonged retention compared to healthy tissues. They observed that nanoparticles could preferentially accumulate in tumors due to increased vascular permeability and impaired lymphatic drainage (Figure I-2).[17] Later, the EPR effect was described more precisely, showing that it occurs in solid tumors when they reach 1-2 cm in size, and can no longer feed all their cells through diffusion from peripheral capillaries.[18]

Capillary formation by the cancer becomes haphazard, resulting in leaky junctions between endothelial cells and pores as large as 200 nm.[19] Due to their relatively large size, nanoparticles evade renal clearance and cannot penetrate the tight endothelial junctions of normal blood vessels. However, they can extravasate through the leaky vasculature of tumors and accumulate in the tumor microenvironment. This microenvironment plays a critical role in the passive delivery of nanomedicines. A notable feature is its acidic nature, a result of glycolysis, the primary metabolic process of cancer cells, which lowers the pH to support their rapid proliferation.[20]

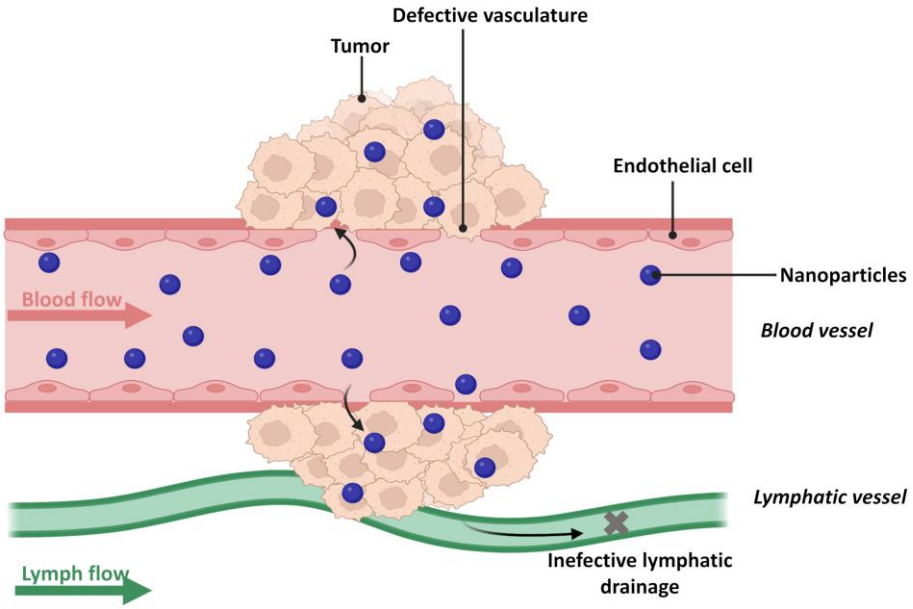

Figure I-2. Enhanced permeability and retention (EPR) effect in solid tumors and passive targeting. Adapted from Peer *et al.* [3]

The EPR effect has then served as the cornerstone for the development of cancer nanotheranostics. Their accumulation in the tumor due to the EPR effect is called *passive targeting* and can be achieved by using simple drug-loaded nanoparticles that can circulate in the blood long enough to reach and penetrate the tumor site. However, the interpretation of this EPR effect can be oversimplified, as it does not consider the multiple biological steps involved in the systemic delivery of nanoparticles. Specifically, after intravenous administration, nanoparticles interact with plasma proteins, especially opsonin, that are adsorbed onto the surface *via* the opsonization process.[21,22] The immune response subsequently marks the nanoparticles as exogenous and initiates a cascade that triggers their recognition and rapid clearance by phagocytic cells, primarily Kupffer cells, following their redirection to the liver.[23,24] This immune-mediated clearance and preferential hepatic accumulation has been applied to treat liver metastasis or to reduce drug toxicity by hijacking nanoparticles from tissues to which they are toxic.[25–27]

To target other tissues and organs, this first generation of nanoparticles was improved by changing their composition, size or surface. To avoid opsonization, a stealth coating on the surface of nanoparticles, mostly using poly(ethylene glycol) (PEG), a hydrophilic and flexible polymer, was envisaged to avoid interactions with plasmatic proteins and opsonin *via* steric repulsion. Indeed, in 1977, Abuchowski *et al.* reported that covalent conjugation of 2 kDa or 5 kDa PEG to bovine liver catalase decreased immunogenicity of the protein and prolonged its circulation time in the blood.[28] This so-called PEGylation process was subsequently applied to various nanoparticle systems, including liposomes, polymeric nanoparticles, and micelles.[29]

The chain length, shape, and grafting density of PEG on nanoparticles directly influence surface hydrophilicity and phagocytosis. Specifically, these parameters determine whether the PEG surface adopts a mushroom or brush model as described in Figure I-3. Depending on both PEG molar mass and chain

density at the interface, mushroom, brush or extended brush conformation can be obtained. The brush conformation is particularly effective in preventing opsonization, as reported by Landfester *et al.* who studied the effect of PEG conformation on protein adsorption on ovalbumin NPs by grafting different PEG with different length and in different ratios. In particular, the dense brush conformation plays a crucial role in reducing cellular interactions, regulating opsonin adsorption, and influencing the biological fate of PEGylated nanocarriers.[30] It is important to emphasize that no single PEG length optimally prevents opsonization; rather, it is the precise combination of PEG length and grafting density that determines the proper PEG brush conformation.

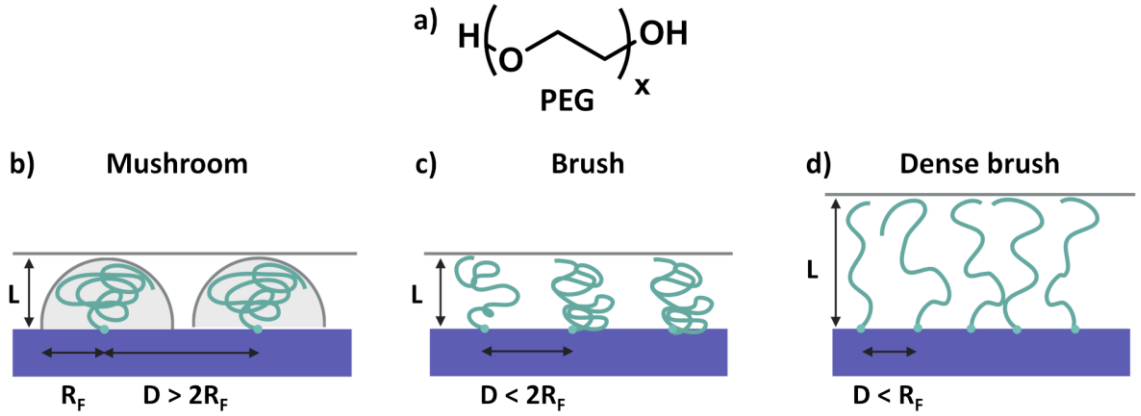

Figure I-3. PEG conformations on a particle surface: (a) Chemical structure of PEG, (b) Mushroom regime, (c) Brush regime, (d) Dense brush regime. D refers to grafting spacing, L for the length/thickness of the PEG layer and R_F stands for Flory radius of PEG chains. Adapted from Shi *et al.*[31]

Thus, this second generation of nanoparticles has stealth properties which make them undetectable by the immune system or macrophages. As a result, they have a longer circulation time in the bloodstream and can better exploit the EPR effect. As shown by Verrechia *et al.* in rat models, PEGylated NPs show higher plasma concentrations and lower liver accumulation than non-PEGylated NPs, with a plasma half-life of 6 hours instead of a few minutes for non-PEGylated NPs.[32] Consequently, PEGylated liposomal doxorubicin (*Doxil*®) was developed and became the first FDA-approved anticancer nanomedicine in 1995, using passive targeting and stealth coating to deliver doxorubicin, an anticancer drug compound.[33–36] This success story initiated global efforts to design and develop other PEG-coated long circulating NPs. However, the "PEG safety dilemma" soon emerged, with concerns about biodegradability. Studies suggest that the immune system may produce anti-PEG immunoglobulin (Ig) M antibodies, or anti-PEG IgM that bind to PEG, leading to an "accelerated blood clearance (ABC) phenomenon" after repeated administration of PEGylated substances and nanoparticles.[37–39] Alternative coating polymers were then explored. PEG-like polymers, such as poly(*N*-vinylpyrrolidone) (PVP),[40–42] polyacrylamides (PAM),[43] polybetaines,[44,45] polyoxazolines (POx),[46] polysaccharides,[47] polyesters[48] and poly(sarcosine) (PSar)[49–52] were comprehensively investigated for this purpose (Figure I-4). Regarding the last three candidates, their specific biocompatibility and biodegradability make them the most promising substitution candidates.

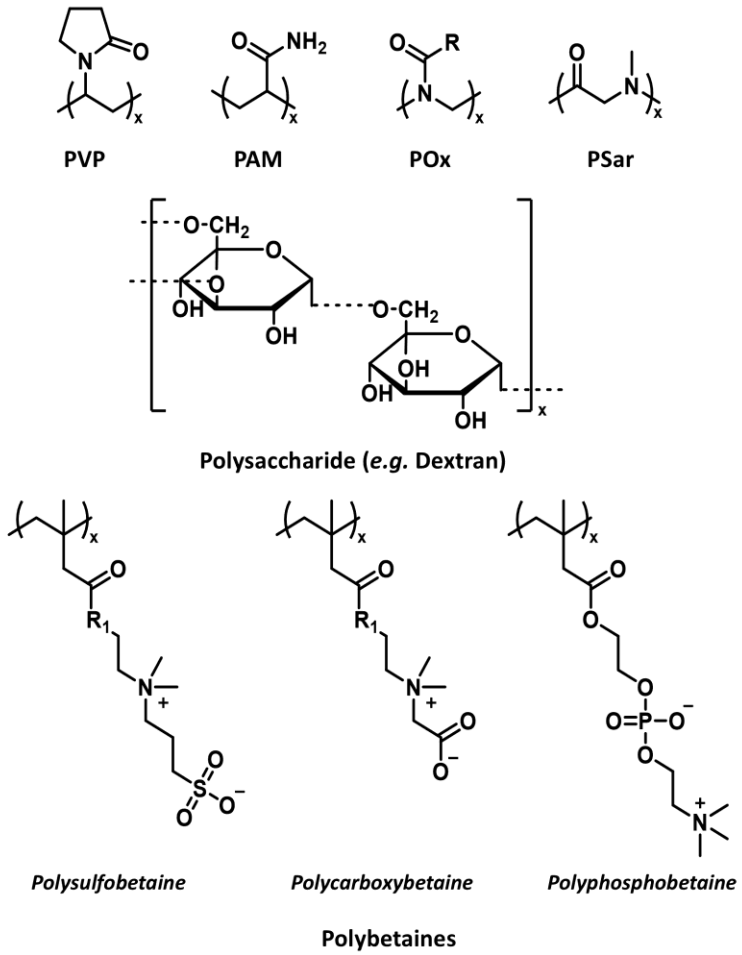

.

Figure I-4. Chemical structures of the different polymers as PEG alternatives in NPs design for drug delivery.

I.2.3. Active targeting

The EPR effect has then been considered the gold standard in cancer therapy, yet only 15 nanoparticle-based cancer nanomedicines have been approved worldwide.[53] The majority of cancer nanomedicines have failed to significantly improve clinical efficacy. Factors explaining this lack of efficacy have been attributed to too low accumulation of nanoparticles in tumors as well as insufficient pharmacokinetics improvement. In fact, after reviewing nanomedicine articles published in the literature over a ten-year period in 2016, Chan's group pointed out that an average of 0.7% of administered nanoparticles reached solid tumors,[54] and only 0.0014% reached cancer cells.[55] One factor that could explain this failure is the EPR effect controversy, despite evidence that the drug fraction in the tumor compared to the blood is improved with nanoparticles delivery.[56] This is primarily due to differences between cancer in mouse models and humans, including variations in vascular density observed in several mouse models compared to human tumors, which often complicates the translation of promising preclinical results into clinical outcomes.[57] Moreover, in more advanced tumor stages, high intratumoral pressure, if it exceeds the pressure in the capillaries, may impede nanoparticle penetration into the tumor.[58] In addition,

cancer cells are embedded in a complex and tumor-specific microenvironment, consisting of endothelial cells, stromal fibroblasts, collagen, and immune cells that collectively act as a biological barrier to nanoparticle infiltration.[59] However, given that this meta-analysis is now almost ten years old, these figures should be interpreted with caution, as significant advances in nanoparticle design, targeting strategies, and delivery mechanisms have since emerged.

A promising approach to overcome this issue is the use of targeting ligands. A third generation has emerged in which PEGylated NPs are surface functionalized with various targeting ligands, such as antibodies and antibody fragments, aptamers, proteins, peptides, carbohydrates, and small molecules. They selectively bind to tumor-specific and/or overexpressed antigens or receptors on the cell surface, thereby improving tumor tissue retention and enhancing tumor cell internalization of the nanocarriers.[60]

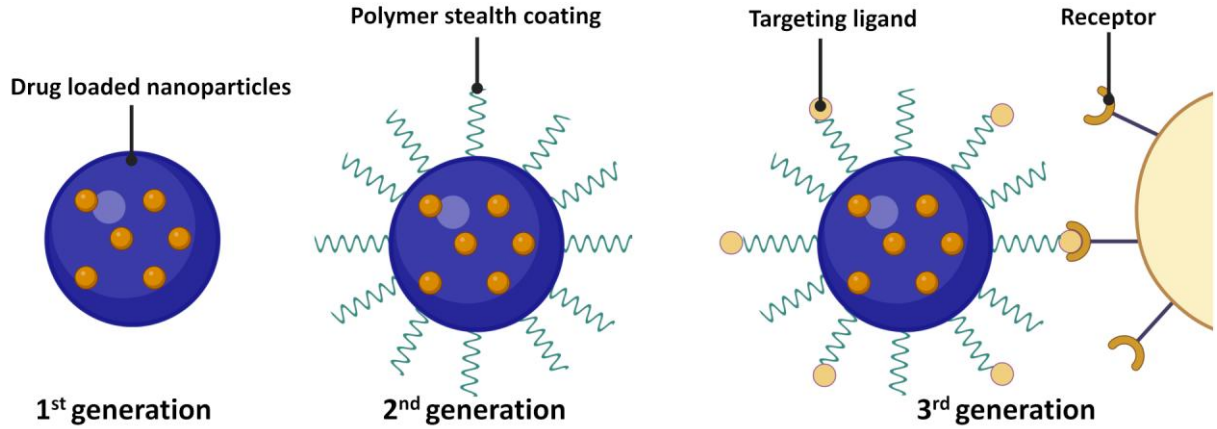

Figure I-5. The three first generations of nanocarriers in nanomedicine. 1st generation corresponds to drug-loaded nanoparticles using passive targeting. 2nd generation nanoparticles are coated with stealth polymers on the surface to allow longer circulation in blood, to promote accumulation in tumor site by passive targeting. 3rd generation nanoparticles use active targeting *via* functionalization on their surface with specific ligand to promote cell recognition and adhesion to specific receptors overexpressed on the tumor cell surface.

Once nanocarriers bind to target cells, they can: i) release their cargo upon approaching the target cells; ii) attach to the cell membrane and gradually release their cargo extracellularly; or iii) internalize into the cell through mechanisms such as endocytosis or pinocytosis (Figure I-6).[57]

Although numerous nanocarrier systems functionalized with targeting ligands have shown promising results *in vitro* and *in vivo*, their clinical translation remains a challenge. An alternative strategy involves the development of nanoparticles that respond to external physical stimuli, offering a promising approach to enhance tumor accumulation and improve therapeutic outcomes. These stimuli can be exogenous (*e.g.*, temperature changes, magnetic fields, light exposure, ultrasound or electrical pulses) or endogenous (*e.g.*, pH changes, enzymatic activity, potential differences, or redox conditions).[61]

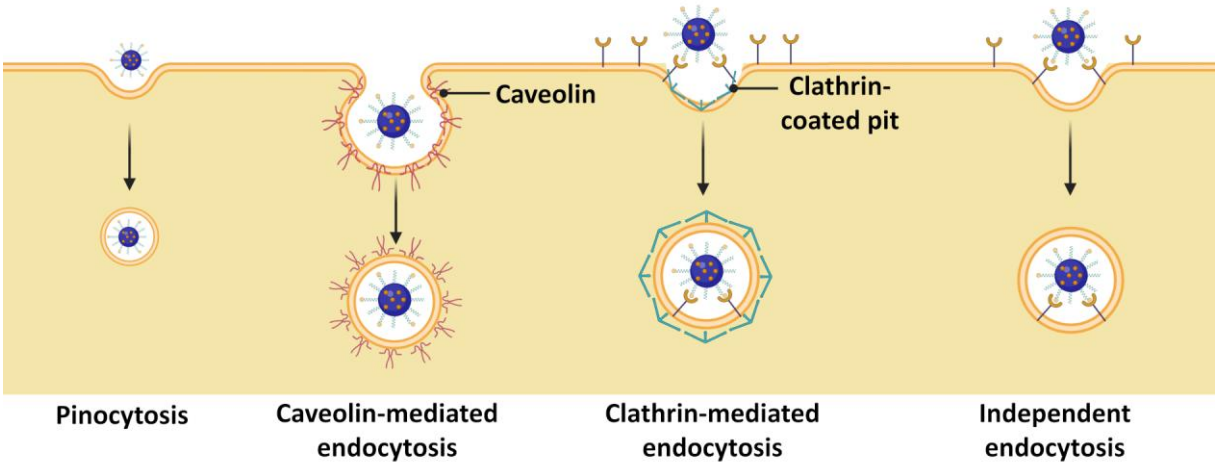

Figure I-6. Different pathways of cellular internalization. Adapted from Fan *et al.*[62]

Nanoparticle design, including size, shape, and surface characteristics, must be tailored to the specific tumor type and its location. While size and surface have been extensively studied in this context, shape also plays an important role and represents a promising parameter to optimize for advancing the design of next-generation nanomedicines.

I.2.4. The effect of particle shape

Particle shape has recently emerged as a critical parameter for modulating biological interactions and thereby enhancing the therapeutic efficacy of nanocarriers. Shape influences several key factors, including nanoparticle motion in biological fluids under static and dynamic conditions, interactions with cell membranes, endocytic pathways, and intracellular distribution.[63,64] In addition, opsonization, which varies with morphology, affects macrophage uptake, circulation time, biodistribution, and ultimately tumor accumulation.[65]

While nanoparticles are typically spherical, anisotropic nanoparticles, characterized by a length-to-width ratio different from 1, particularly elongated particles, have attracted significant interest in various therapeutic applications (Figure I-7).



Figure I-7. Most common anisotropic morphologies found in drug delivery applications.

These particles exhibit prolonged circulation times,[66] attributed to their ability to align and stretch under flow conditions within blood vessels and during spleen filtration. As a result, elongated nanoparticles evade macrophage uptake and subsequent clearance, allowing them to remain in the systemic circulation longer (Figure I-8).[67–69] However, Vasilev and coworkers demonstrated significant protein corona

formation on rod-like nanoparticles, with a higher amount of plasma and serum proteins binding to these elongated particles compared to their spherical counterparts, which could influence their biodistribution.[65]

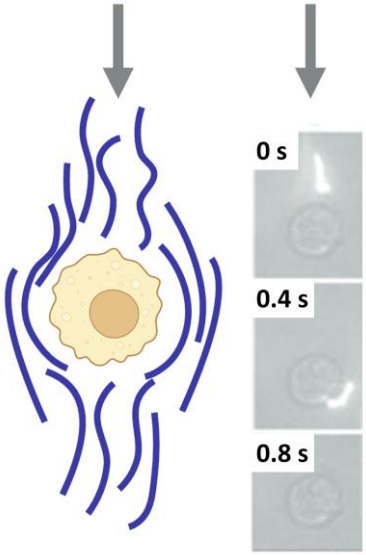

Figure I-8. Elongated worm-like micelles exhibit streamlined flow properties, pass macrophages and avoid phagocytic uptake. Adapted from Discher *et al*.[66]

After escaping phagocytosis and reaching the target site, nanoparticles must be able to escape the blood stream and marginate against the vessel wall to recognize and bind to diseased sites and cells. The translational and rotational motions that govern margination are influenced by factors such as buoyancy, gravity, drag, and weak interactions. Due to their elongated shape, nanoparticles experience variable drag and torque forces in flow, which increases their likelihood of interacting with vessel walls, as compared to spherical nanoparticles (Figure I-9).[64,70]

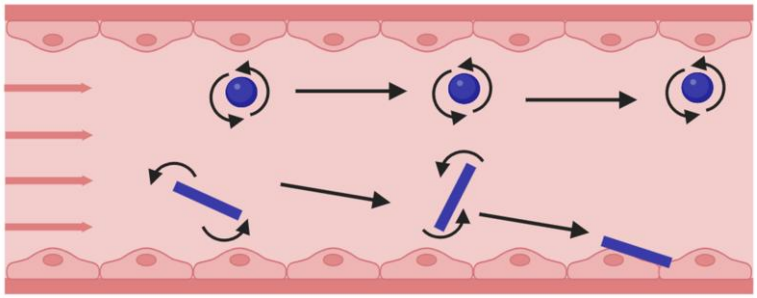

Figure I-9. Margination of nanoparticles in the blood stream. Rod-like nanoparticles tend to marginate more readily to the wall of the blood vessel than spherical particles, due to particle rotation. Adapted from Stenzel *et al*.[70]

The rate of internalization of a non-spherical nanoparticle depends on its angular orientation relative to the cell membrane, especially for rigid rod-like nanoparticles.

After margination, nanoparticles, especially those with ligands, must be able to bind to their target of interest. The number of ligands on their surface affects their binding affinity, and this can be influenced by increasing the size of the NPs or changing its shape. These changes in shape can modify the presentation of the ligands, thereby influencing the way they interact with the target (Figure I-10). Overall, shape, in addition to ligand length and polymer flexibility, plays a role in the active fractional area of a nanocarrier.

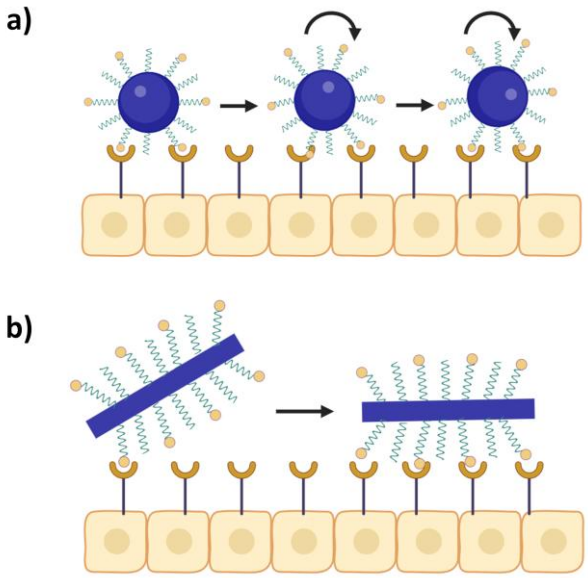

Figure I-10. Carrier shape modulates efficiency and dynamics of ligand-mediated on endothelium. Adapted from Muzykantov *et al*.[71]

For example, ovalbumin-targeted rods have twice as many specific binding interactions as ovalbumin-targeted spheres.[72] On the other hand, hyaluronan-coated ellipsoidal nanoparticles showed lower internalization in macrophages than spheres, despite having comparable surface potentials.[73]

Due to their prolonged circulation and efficient margination, elongated nanoparticles exhibit improved tumor penetration.[74] Moreover, their small diameter, typically ranging from 10 to 50 nm, enables them to extravasate through leaky vascular networks *via* the EPR effect without requiring deformation, unlike their spherical counterparts (Figure I-11).[75] Discher and colleagues also observed this passive accumulation of elongated nanoparticles. After injecting near-infrared fluorescent worm-like nanoparticles into tumor-bearing mice, they detected a highly luminescent tumor. This indicated an abnormally high concentration of micelles in the xenograft tumor, just 10 minutes after intravenous injection.[76] Similarly, DeSimone and coworkers using docetaxel-loaded nanorods reported higher drug accumulation in SKOV-3 human ovarian cancer xenograft tumor than with *Taxotere*®, the clinical formulation of docetaxel.[77]

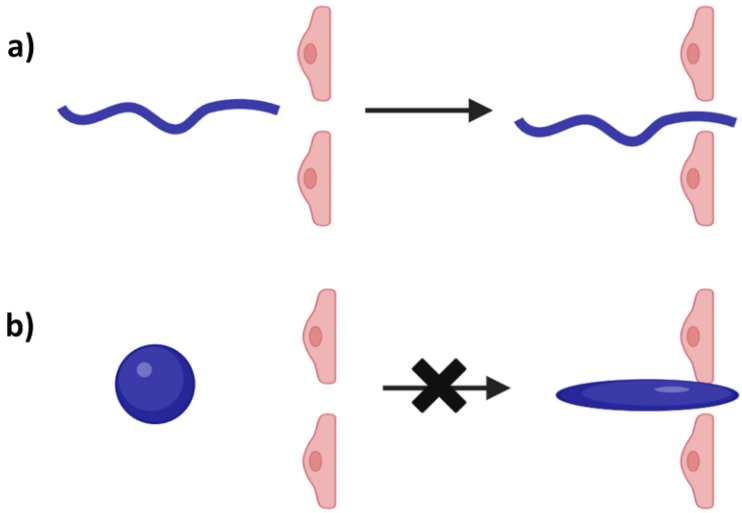

Figure I-11. Schematic comparison of vascular pore-to-tumor translocation between (a) worm-like nanocarriers and (b) spherical nanocarriers, both possessing equivalent hydrodynamic volumes. Adapted from Davis *et al.*[75]

In addition to passive tumor accumulation, elongated nanoparticles can also penetrate deeper into the tumor than their spherical counterparts. Using multicellular tumor spheroids (MCTSs) as a model of the tumor microenvironment, Steinmetz and coworkers observed enhanced tumor penetration for rod-shaped nanoparticles compared to nanospheres.[78] Similarly, Winnik and coworkers observed deeper penetration of rod-like polymeric nanoparticles in porous spheroid compared to spherical ones (Figure I-12).[79] *In vivo* studies also confirmed deeper penetration of elongated nanoparticles in xenograft tumors.[76,80] These observations may be attributed to the enhanced mobility of elongated nanoparticles in dense environments, such as the tumor microenvironment. Their unique shape allows them to navigate obstacles more efficiently than spherical nanoparticles, facilitating deeper penetration into the complex and heterogeneous tumor stroma. This enhanced ability to traverse such barriers increases their likelihood of reaching and interacting with cancer cells.[81]

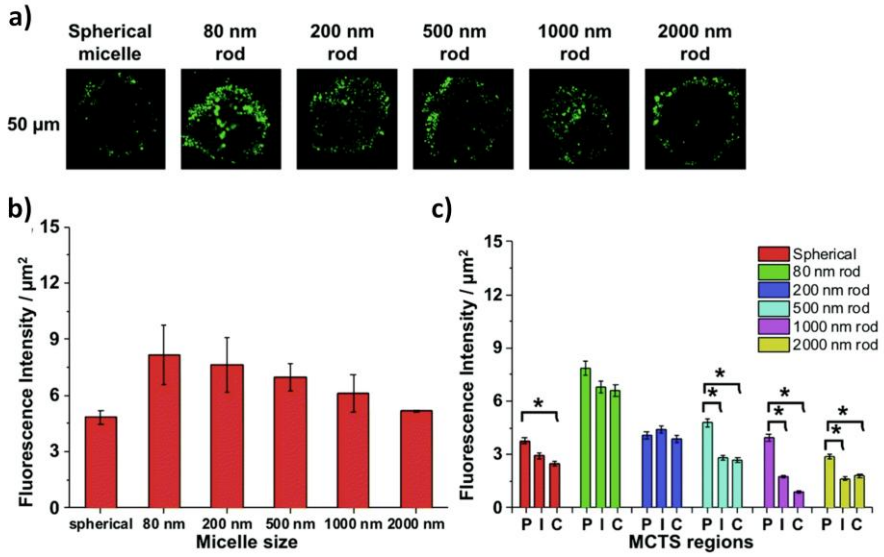

Figure I-12. Micelle accumulation depending on their anisotropy in MDA-MB-436 multicellular tumor spheroid (MCTS) with (a) confocal microscopy, images taken at 50 µm depth from the spheroid surface, (b) total fluorescence intensities per unit area and (c) penetration in MCTS in periphery, intermediate and core regions of the spheroids, at 50 µm depth. Adapted from Winnick *et al.* [79]

Drug encapsulation and delivery are also significantly influenced by the geometry of nanocarriers. Elongated nanoparticles offer higher drug encapsulation capacities compared to spherical counterparts due to their higher surface-to-volume ratio. In addition, their typically higher packing parameter results in larger hydrophobic blocks, which enhances drug-polymer interactions and ultimately improves the final drug partition coefficient.[82–84]

Overall, precise control over morphology and the engineering of nanoparticles toward anisotropic shapes can serve as a powerful strategy to enhance the therapeutic efficiency of drug-loaded nanocarriers. Among the various materials available for the construction of nanometric architectures, polymers stand out as the most versatile due to their adjustable chemical composition, tunable length, customizable physical properties, and functional adaptability, allowing them to meet specific design requirements.

I.3. Polypeptide-based polymers as nanocarriers

The self-assembly of block copolymers (BCPs) enables the formation of diverse and well-defined morphologies, including spherical micelles, worm-like micelles, rod-like micelles, and polymersomes, by controlling the balance between hydrophilicity and hydrophobicity, or by changing the nature of the blocks. This adaptability allows fine-tuning of key characteristics, such as size, shape, rigidity, porosity and surface properties, making BCPs ideal candidates for engineering nanoparticles with tailored functionalities for nanomedicine applications.[85] However, as mentioned above, nanoparticles, and consequently polymers, must be biocompatible and (bio)degradable for healthcare applications, which significantly limits the choice of suitable polymers.[86] Furthermore, the dominance of liposomes in the market, due to their low cost and ease of production, has resulted in only a limited number of polymer-based nanoparticles reaching the market.

In this context, poly(amino acids), or polypeptides, are a class of biomimetic macromolecules that are particularly attractive due to their ability to mimic key protein properties, such as biocompatibility, biodegradability, and hierarchical organization. Their unique properties make them highly promising for applications in nanomedicine, and this section will discuss their nature and specificity, their synthesis and their self-assembly into the nanocarriers of tomorrow.

I.3.1. Polypeptide, a simplified analogue of protein

Proteins are among the most important biomacromolecules in living organisms. These large, complex molecules play critical roles, including:

- Providing mechanical support to cells, tissues, and organs (*e.g.*, collagen, actin).[87]
- Acting as catalysts for various biochemical reactions (*e.g.*, enzymes).[88]
- Regulating processes such as cell signaling, cell adhesion, and the immune response.[89]

Structurally, proteins are composed of amino acid units linked by peptide bonds to form polypeptide chains, known as their primary structure. This primary structure can further self-assemble into more complex configurations through hydrogen bonding, resulting in the formation of secondary structures, such as α-helices and β-sheets. These secondary structures can then fold into even more complex shapes, known as the tertiary structure, which can further organize into a quaternary structure when multiple polypeptide chains interact (Figure I-13).[90] Through this hierarchical self-assembly process, each protein possesses a unique sequence and folding pattern that determines its function. Polypeptides share the same backbone as natural proteins. They are therefore one of the most important classes of (bio)polymers. Thus, researchers in chemistry and biology have developed synthetic polypeptides, biomimetic polymers that are simplified analogues of natural proteins. These synthetic polypeptides composed of amino acid residues, natural or non-natural, linked by peptide bonds, can assemble hierarchically into stable and ordered secondary structures. In the following sections, the characteristics of polypeptides will be developed in more detail, by looking at natural amino acids and conformational properties.

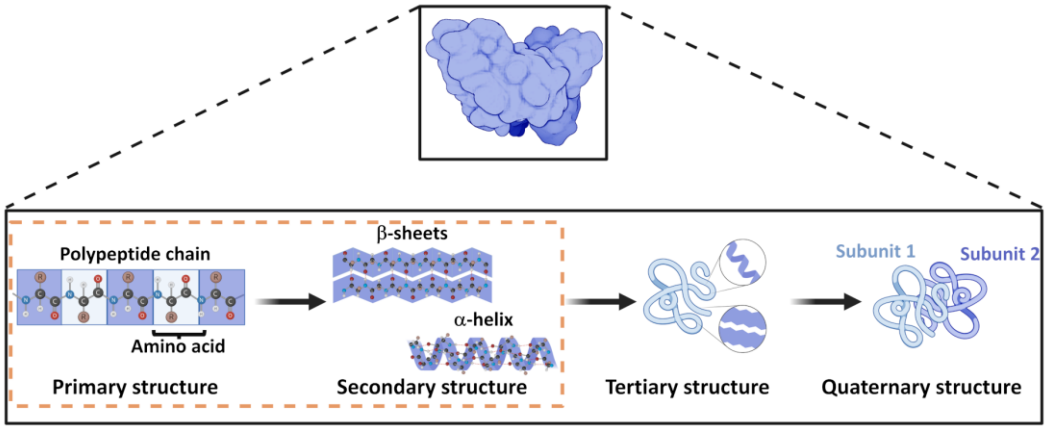

Figure I-13. Protein folding and structural hierarchy. On top, folded structure of the bovine serum albumin (BSA). In the orange box, conformations found in synthetic polypeptide.

I.3.1.1. Primary structure: amino acids

There are 20 standard canonical amino acids, each of which makes a unique contribution to the structure and function of polypeptides and proteins. These monomers are composed of an amine group (-NH_2) and a carboxylic acid group (-COOH) linked by a central α-carbon (C_α), which is also linked to a distinctive side chain (R group). This side chain is what differentiates one amino acid from another and greatly influences the properties of the resulting polypeptide.

Natural amino acids are all found in the *L*-configuration, which corresponds to the *S*-absolute configuration, except for cysteine, which adopts the *R*-configuration due to the priority of its sulphur-containing side chain. Glycine is the only achiral amino acid, as its side chain consists of a single hydrogen atom. The R groups can be classified according to their chemical nature, which affects how they interact with the environment (Figure I-14).

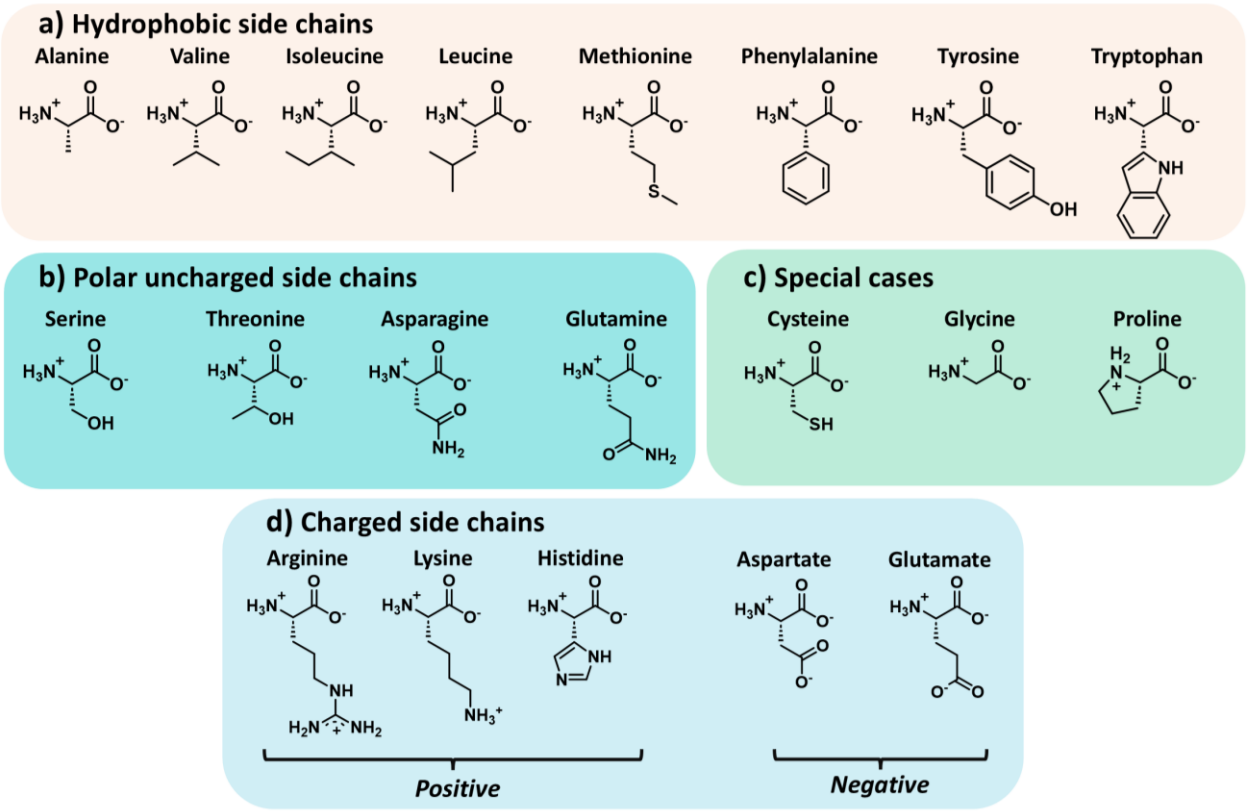

Figure I-14. Canonical amino acids found in the human proteome, classified according to the nature of their side chains. Protonation is shown at physiological conditions (pH = 7.4).

Hydrophilic side chains, such as those found in serine, threonine, or glutamine, can form hydrogen bonds with water, increasing the solubility and stability of polypeptides in aqueous environments. On the other hand, hydrophobic side chains, such as those of leucine, valine, and phenylalanine, tend to cluster together and avoid water. This hydrophobic effect plays a critical role in the folding and stability of the tertiary structure of the protein by driving the formation of a non-polar core. Charged side chains, such as those of lysine (positively charged) and glutamate (negatively charged), vary in ionization state depending on the pH of the surrounding environment, influencing the solubility and overall charge of the polypeptide. These side chains participate in forming salt bridges and electrostatic interactions, which are pivotal for stabilizing higher-order structures and interactions with other biomolecules.[91]

Beyond natural amino acids, non-natural amino acids have been developed to expand the functional repertoire of polypeptides. These synthetic or modified amino acids can confer unique properties that are not found in Nature, such as enhanced stability, novel catalytic functions, or improved binding affinities. The incorporation of non-natural amino acids can be achieved through genetic engineering or chemical synthesis and has opened new avenues for the design of biomimetic materials and therapeutic proteins.[92]

I.3.1.2. Secondary structure

Polypeptide chains are made of amino acids linked by an amide bond, commonly called a peptide bond. The chains thus organize themselves *via* hydrogen bonding between these amides. However, the nature of the peptide bonds limits conformational flexibility. Polypeptide chains are composed of repeating

units, each consisting of two adjacent planes connected by a single C_α carbon atom. The possible conformations of these chains are determined by the average values of the torsion angles, φ and ψ (Figure I-15a). Given the electronic configuration and steric hindrance in the polypeptide chain, little rotational freedom is allowed. Thus, two main low energy regions of angle values can be determined, as given by the Ramachandron plot, attributed to alpha helices or beta sheets conformation (Figure I-15b).

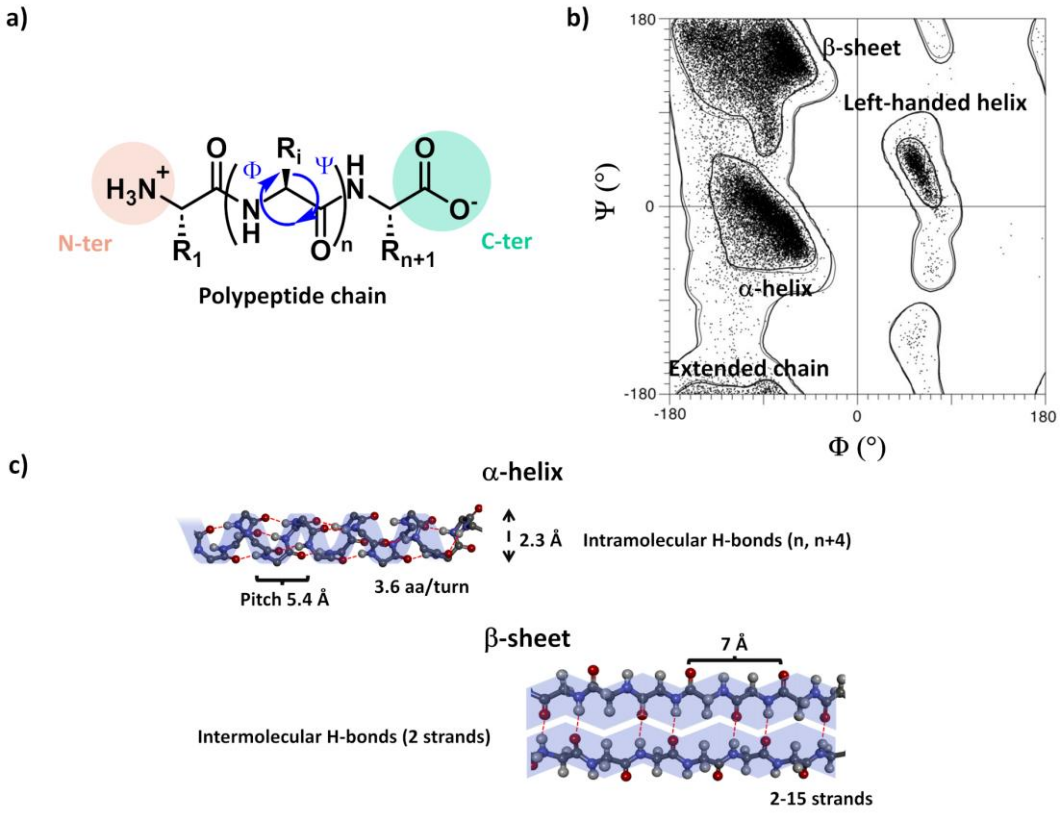

Figure I-15. (a) General structure of a polypeptide chain, at physiological conditions (pH = 7.4), with the torsion angles ϕ and φ of the backbone represented around the C_α of an amino acid. (b) Example of Ramachandran plot, adapted from Lovell *et al.*[93] (c) Balls and sticks molecular structures and their schematic representation of the α-helix (top) and the β-sheet (bottom).

In the α-helix geometry, hydrogen bonding occurs between the oxygen atom of the carbonyl group in one peptide bond and the hydrogen atom of the amine group located four amino acid residues further along the chain. This regular pattern of intramolecular hydrogen bonding stabilizes the helical structure, with the main chain at the center of the helix, and the side chains pointing outwards (Figure I-15c). The average torsion angles for an α-helix are of – 60 ° for φ and – 45 ° for ψ.

In a β-sheet, hydrogen bonding occurs between the carbonyl oxygens of one strand and the amino hydrogens of an adjacent strand. The strands can be arranged in either a parallel or antiparallel configuration, with the antiparallel arrangement being more stable due to the optimal alignment of the hydrogen bonds. This conformation is fully extended, with alternating amino acid side chains pointing in opposite directions (Figure I-15c). The typical torsion angles for β-sheets are approximately – 130 ° for φ and 120 ° for ψ. Notably, this structure can form with as few as three or four residues, making it one of the simplest secondary structures.

When none of these criteria are fulfilled by a peptide chain, they are usually considered to be in an extended conformation, which corresponds to a random coil disordered state of a polymer in solution. Other conformations exist but are less commonly found and will not be discussed in this section.

I.3.2. Synthesis of polypeptides

Synthetic polypeptides can be produced by three main approaches: engineered protein production, solid-phase peptide synthesis (SPPS), and α-amino acid *N*-carboxyanhydride (NCA) ring-opening polymerization (ROP). In the first method, an engineered recombinant plasmid is inserted into a bacterial host, typically *Escherichia coli*, to produce polypeptides with precise sequences and chain lengths. However, this technique often suffers from low yields, limited capacity for post-translational modifications, and complex production processes. As a result, it is primarily used for the development of therapeutic proteins and polypeptides rather than for materials science applications.[94]

The second approach, solid-phase peptide synthesis (SPPS), was developed by Merrifield and coworkers in 1963.[95] This method involves the sequential addition of amino acids through repeated cycles of deprotection, washing, coupling, and washing, using a functionalized resin as the reactive site. Each amino acid must have two reactive groups, one of which is protected. The first monomer reacts with functional groups on the resin in excess, and unreacted residues are washed away. After deprotection, the next monomer can be added and coupled. Repeating this cycle *n* times yields oligomers or polymers with *n* repeating units, all identical in sequence and length. Despite its precision, SPPS has limitations, including sequence length constraints, low yield, poor scalability, and high cost. As a result, this method is mainly used for the synthesis of therapeutic peptides or short polypeptides.

For the synthesis of peptide-based materials, the ROP of α-amino acid NCAs, cyclic derivatives of amino acids, represents a more economical and efficient alternative, which will be further explored in the following section.

I.3.2.1. Ring-opening polymerization of *N*-carboxyanhydrides

NCA ring-opening polymerization is an efficient and cost-effective one-step process for synthesizing high-molecular-weight polypeptides with biomimetic secondary structures, using simple reagents and conventional chemicals.

I.3.2.1.1. NCA synthesis

α-Amino acid NCAs, the monomers involved in the ROP, are five-membered anhydrides, highly reactive due to the highly electrophilic 5-position carbonyl and the acidity of the nitrogen proton, but also unstable. Indeed, they are susceptible to ring-opening by impurities, such as water, and their preparation requires strict anhydrous reaction conditions. Leuchs was the first to synthesize NCAs or "Leuchs's anhydrides" by exposing *N*-alkyloxylcarbonyl amino acids to thionyl chloride ($SOCl_2$) and other halogenating agents (PBr_3, PCl_3, PCl_5) in vacuum at 50-70°C (Scheme I-1a).[96] Later in the 1920s, Fuchs

obtained *N*-alkylated NCA (*N*NCA) by reacting *N*-benzylglycine with phosgene ($COCl_2$).[97] Adapted to other amino acids by Farthing,[98] this so-called "Fuchs-Farthing" method using phosgene or non-gaseous phosgene substitutes became the gold standard to yield NCA, because it does not involve amino acid derivatives, thus reducing the number of steps (Scheme I-1b).[99] However, this method generates HCl related byproducts that may decomposed NCA and induce side-reactions. Some acid scavengers, such as triethylamine, (+)-limonene, the cyclic monoterpenes alpha-pinene or triethyloxonium tetrafluoroborate can be added in the cyclization step to reduce the amount of HCl.[100]

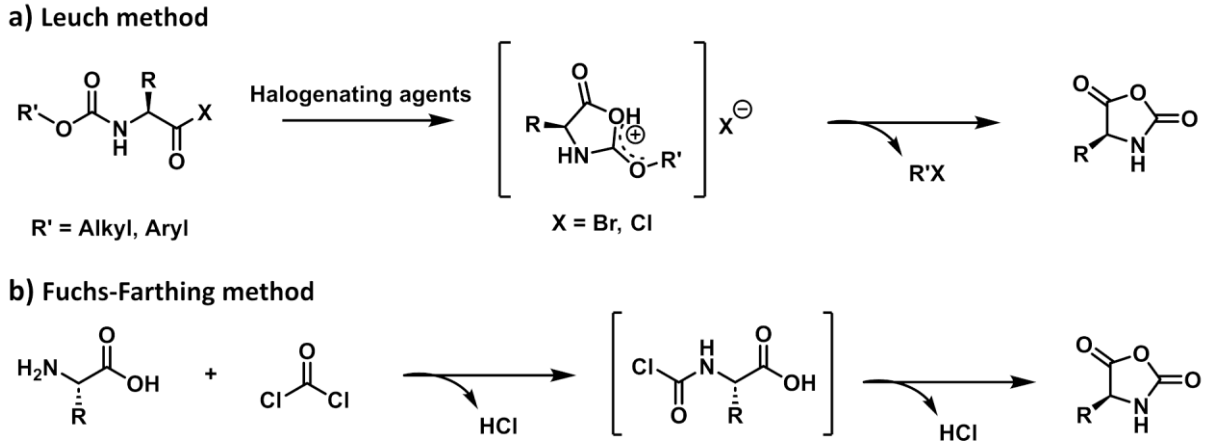

Scheme I-1. Method for the synthesis of NCA monomers. (a) Leuchs method, (b) Fuchs-Farthing method.

There is significant interest in developing greener and safer NCA syntheses that avoid the use of phosgene, which is highly toxic, aside from the Leuchs method. Alternative approaches using di-tert-butyltricarbonate (DBTC),[101] bisaryl carbonate,[102,103] *n*-propanephosphonic acid anhydride (T3P)[104] or cyanuric chloride[105] have been explored to address reactant toxicity, reduce stringent moisture control requirements and improve preparation efficiency. However, traditional phosgene-based methods remain the most widely used due to their high reactivity and universality. In addition to the formation of NCAs, the formation of byproduct and their purification must be controlled, since NCA monomer purity plays a crucial role during the ring-opening polymerization. Typically, this is achieved by laborious purification involving aqueous washing, recrystallization or column chromatography.[106]

Scarce examples of direct polymerization in very specific conditions have been recently reported where crude NCA monomers were used without prior purification thanks to superfast polymerization.[107,108] The *in situ* generation of NCAs by activation of amino acids into urethane-type derivatives[109] or NCA precursors[110] have also been reported, offering a more direct route to polymerization, but still little explored as compared to traditional NCA monomers.

I.3.2.1.2. Mechanism of polymerization

There are two recognized reaction mechanisms for NCA ring-opening polymerization. The normal amine mechanism (NAM) involves a nucleophilic attack, typically from a primary amine, an alcohol or a sulfhydryl group, on the electrophilic 5-position carbonyl of the NCA, causing ring opening (Scheme I-2a). An unstable carbamic acid intermediate is then formed, which undergoes decarboxylation, releasing carbon

dioxide. The resulting primary amine at the chain end can initiate further nucleophilic attack on another NCA, leading to the sequential formation of amide or peptide bonds and allowing chain propagation.[111]

The activated monomer mechanism (AMM), on the other hand, is initiated by deprotonation of an NCA. The activated monomer becomes nucleophilic and initiates chain growth (Scheme I-2b). These two mechanisms can coexist in the same polymerization. This ambivalence between the two mechanisms can induce different structures than those predicted by the monomer feed compositions. AMM typically results in faster polymerization rates but compromises control over the ROP, resulting in polymers with broader molecular weight distributions. To promote NAM, which provides better control and narrower dispersities, primary amines are preferred as initiators because of their higher nucleophilicity and lower basicity compared to secondary or tertiary amines.

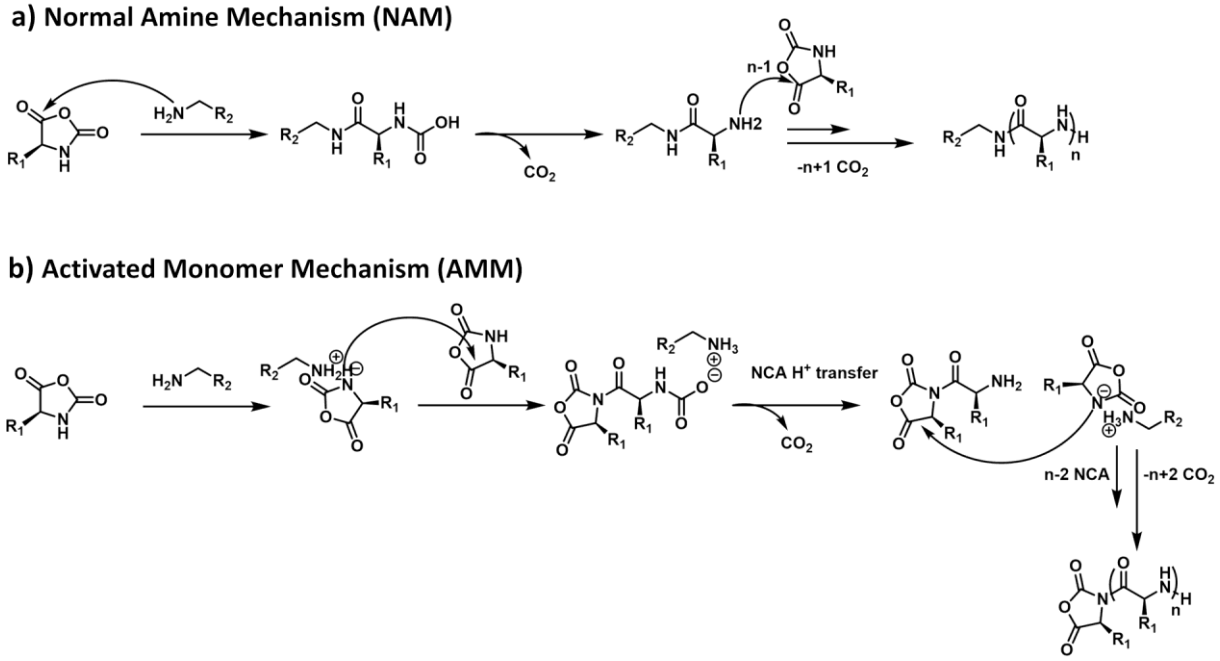

Scheme I-2. Traditional mechanisms occurring during ROP of NCA. (a) Normal amine mechanism (NAM), (b) Activated monomer mechanism (AMM).

Even when using primary amine initiators, achieving a well-defined polypeptide architecture remains a challenge. Once an initiator reacts with an NCA monomer, it is no longer active, and the resulting end group, primary amine, carbamate or NCA anion, can undergo undesirable side reactions. In addition, impurities such as acids, acid chlorides, isocyanates or water, commonly found in NCA monomers or reaction media, can quench propagating chains, act as chain transfer agent, or even catalyze side reactions. As a result, many strategies have then been explored to better control NCA polymerization and eliminate side reactions. For example, Deming and coworkers used transition metal complexes as initiators.[112] The protonated amines, or ammonium salts, also offer a stable and easy-to-handle alternative to amines for initiating NCA polymerization. The mechanism involves a balance between dormant ammonium salts and active amine chain ends, allowing for controlled propagation while suppressing AMM by protonating NCA anions.[113] However, polymerization kinetics are slower, and monomer conversion may remain incomplete

due to the reduced reactivity of the active site. Catalytic approaches have also been explored to achieve faster polymerization while using conventional amine initiators.[114] Certain reaction conditions, such as removing CO_2 by conducting the polymerization under high vacuum,[115] or increasing the flow of inert gas,[116] have also been shown to improve control and accelerate polymerization kinetics. Lowering the reaction temperature to 0°C has also been reported by Giani *et al*. to improve control of the ROP of ε-trifluoroacetyl-*L*-lysine-NCA (Lys(TFA)-NCA) in *N,N*-dimethylformamide (DMF).[117] Cryo-polymerization has also been investigated in dimethylsulfoxide (DMSO) or dioxane below freezing point, with good control of the molar mass.[118] However, conducting NCA polymerization at low temperatures may slow the kinetics and result in long reaction times.

I.3.2.1.3. NCA polymerization in presence of water

Despite all these efforts, and as previously mentioned, the high electrophilicity of NCA makes them particularly sensitive to moisture, and typical ROP are processed under dry conditions. Although aminolysis is faster than hydrolysis,[119,120] in most of the mechanisms, strict water removal from the medium is required to eliminate possible water-induced NCA hydrolysis and polymerization in the case of NAM (Scheme I-3), and termination in the case of AMM or degradation of moisture-sensitive catalysts.[121,122]

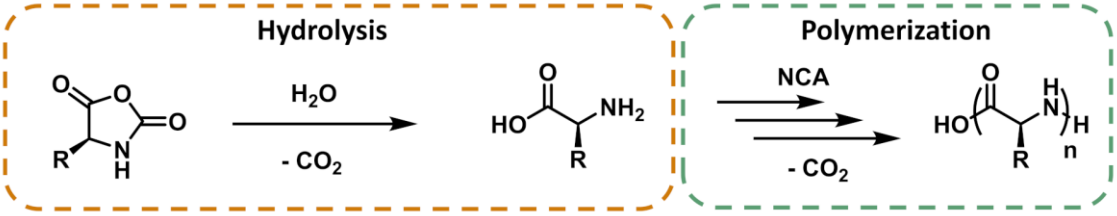

Scheme I-3. Schematic representation of the water-initiated polymerization of NCA.

Interestingly, recent studies have shown that controlled polymerization under less stringent conditions can be achieved by minimizing NCA degradation through the promotion of rapid aminolysis and ROP kinetics. For example, open vessel ROP of NCA has been achieved by using lithium hexamethyldisilazide (LiHMDS), which initiates an extremely rapid NCA polymerization, in an environment of at least 60% relative humidity in untreated tetrahydrofuran (THF).[123] By deprotonating the amine and forming an anionic NCA that initiates polymerization *via* nucleophilic attack and propagation through a lithium carbamate intermediate, a controlled AMM has been achieved that allows for the rapid synthesis of high molar mass with low dispersity.

Similarly, tetraalkylammonium carboxylate has been shown to be an efficient initiator for superfast NCA polymerization in open vessels at ambient conditions, even with unpurified NCA.[124] Mechanistically, it has been shown that the carboxylate initiates NCA polymerization by nucleophilic addition to the carbonyl carbon on the NCA ring and propagates in one concerted step using the terminal tetraalkylammonium carbamate as a reactive center.

Crown ethers, and more specifically 18-crown-6 ether, were first shown to catalyze the polymerization of NCAs initiated by conventional primary amines in dry solvents. They were also shown

to be effective in catalyzing ROP in biphasic systems involving dichloromethane and aqueous buffers, demonstrating compatibility with unpurified NCAs.[125] This catalytic effect was attributed to crown ethers promoting proximity and interactions between propagating amino groups and NCA monomers, thereby facilitating the reaction. The same group highlighted how cooperative polymerization (CCP) in a crowded environment accelerates chain propagation and facilitates rapid monomer consumption. The folding of polypeptides into α-helices plays a critical role in this process. As the monomer units are incorporated, the growing polypeptide chain transitions to a brush-like structure. Upon reaching a critical length, the chain adopts an α-helical conformation, which enhances the polymerization rate through cooperative macrodipole interactions between adjacent helices. First demonstrated with the trimethylsilyl (TMS) amine macroinitiator poly(norbonene)-TMS (PNB_n),[126] it was further observed when dendritic polyamines were used as spherical surface brush macroinitiators. Fast NCA polymerization leading to the formation of spherical monomolecular micelles was also reported.[127] This approach was applied in a water/dichloromethane biphasic system using amine-terminated poly(ethylene glycol)-*block*-poly(γ-benzyl-*L*-glutamate) (PEG-*b*-PBLG) localized at the interface, enabling fast polymerization unaffected by the presence of water (Figure I-16a).[107] Various initiators have been identified to initiate similar biphasic interfacial polymerization, including amino-functionalized polysaccharides for the preparation of polysaccharide-polypeptide conjugates (Figure I-16b).[128] Polypeptide/inorganic nanohybrids have also been prepared by helix-accelerated polymerization using amino-modified mesoporous silica nanoparticles in a dichloromethane/water (CH_2Cl_2/H_2O) biphasic system.[129] Nanoscale metal-organic frameworks (MOFs) can also be used as heterostructures where coordinated water molecules on their surfaces can initiate NCA polymerization to yield polypeptides or MOF@polypeptide hybrids (Figure I-16c).[130]

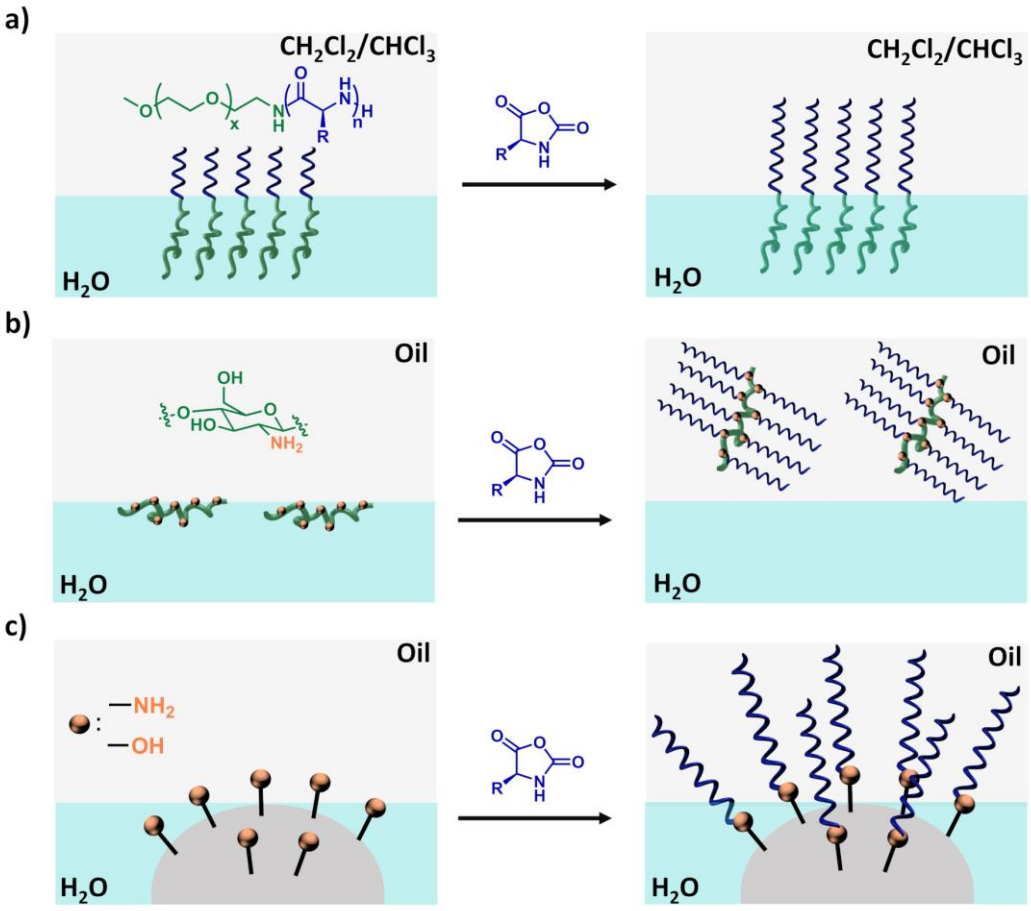

Figure I-16. Biphasic helix-accelerated cooperative NCA polymerization in low-polarity solvents and in presence of water, using (a) PEG-*b*-PBLG, (b) polysaccharide, (c) amine-modified mesoporous silica nanoparticles or MOFs, as initiators respectively. Adapted from Wu *et al*.[131]

In this context, water is no longer avoided but used to promote helix-accelerated polymerization, which represents a promising biomimetic approach for the efficient synthesis of polypeptides. However, this method requires the use of preformed α-helical macroinitiators and solvents with low dielectric constants. In addition, the two-phase kinetics observed in this polymerization process often result in significant deviations from the expected molecular weights.

From another perspective, in the specific case of proline polymerization, water acts as a "catalyst", facilitating the rapid formation of well-defined poly(proline) II helices (PPII) within minutes. This impressive behavior was demonstrated by Lu and coworkers, who used a mixed acetonitrile (ACN)/water solvent system in which water promotes nucleophilic attack and hydrogen migration, lowering the overall energy barrier by 7.1 kcal.mol^{-1}. This approach contrasts sharply with traditional ROP methods, which typically yield precipitated poly(proline) type I helices (PPI), resulting in slower polymerization rates and limited control over the process (Figure I-17).[132]

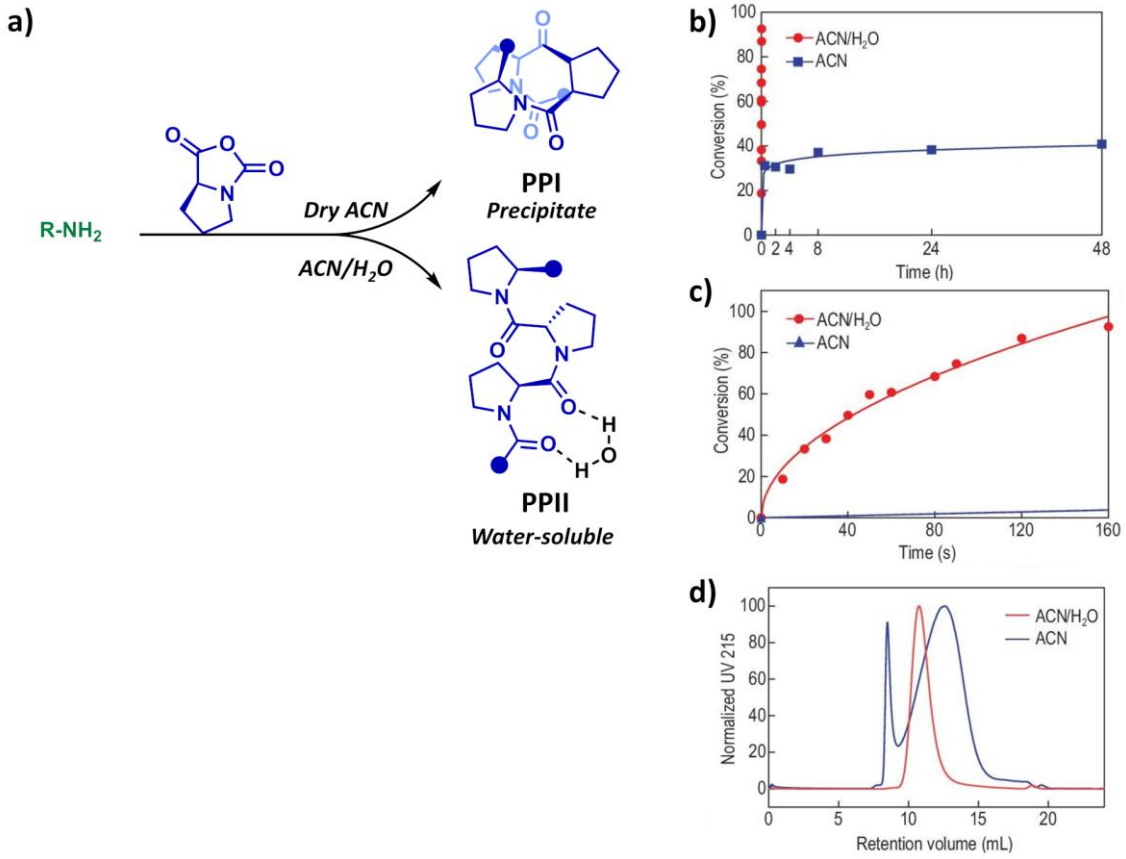

Figure I-17. Water-assisted ROP of Proline-NCA (Pro-NCA). (a) Comparison between synthesis in pure ACN and mixed ACN/H_2O. (b) Conversions of Pro-NCA over-time and (c) zoomed-in period of the first 160 s. d) Steric exclusion chromatograms (SEC) of the PLP produced in ACN and mixed ACN/H_2O. Adapted from Hu *et al.* [132]

Water also plays a critical role in emulsion polymerization, where monomers are dispersed in water to form an emulsion stabilized by emulsifiers and mechanical agitation. Heise and coworkers demonstrated the successful synthesis of polypeptide nanoparticles through emulsion polymerization of NCAs, using triethylamine as an initiator. In this system, glycosylated amphiphilic polypeptides act as surfactants and form protective micelles around the NCAs. These micelles protected the NCAs from hydrolysis, allowing efficient and controlled polymerization (Figure I-18).[133]

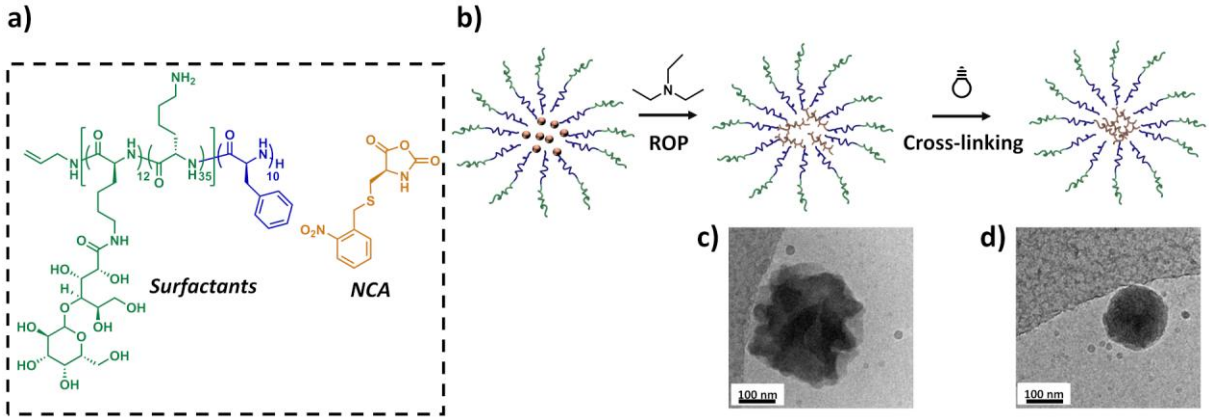

Figure I-18. Emulsion polymerization of NCA. (a) Structure of the polypeptide surfactants and the NCA employed. (b) Schematic representation of the ROP followed by cross-linking to form polypeptide nanoparticles. Cryo-transmission electron microscopy (Cryo-TEM) of (c) nanoparticles before and (d) after cross-linking. Adapted from Heise *et al.* [133]

In our group, recent research has enabled the suppression of water-induced NCA polymerization under aqueous conditions by selecting a specific medium in which aminolysis outpaces hydrolysis and by using α-amino-poly(ethylene glycol) (PEG-NH_2) as a macroinitiator to promote the formation of protective micelles.[134,135] This new process has been termed ring-opening polymerization-induced self-assembly (ROPISA) because it enables amphiphilic copolymers and nanomaterials in a single step.

Overall, recent studies have shown that it is feasible to circumvent the hydrolytic sensitivity of NCA by promoting faster aminolysis is feasible, thanks to secondary structure and/or clustered systems. However, and so far, a limited number of studies have reported the possible use of ROP in presence of water as reported in Table I-1.

Table I-1. Recent reported NCA polymerizations in the presence of water.

Reaction conditions	Polymers	Initiators	Advantages (+) Disadvantages (-)	Key refs
THF, open vessel	PBLG	LiHMDS	(+): Superfast, water insensitive, high MW, various types of NCAs (−): Complex macromolecular structures, challenges in controlled polymerization	[123]
Oil/water biphasic mixture	PBLG-based copolymers	Macromolecular primary amine	(+): Superfast, water insensitive, *in situ* removal of impurities (−): Low dielectric constant solvents	[107]
ACN/water mixture	PLP	Benzylamine, hexylamine	(+): Superfast, water-assisted and controlled polymerization (−): Limited to specific NCA monomers	[132]
Oil/water emulsion	pNBC (poly-cysteine based-polymers)	Triethylamine	(+): In situ obtention of nanoparticles (−): Complex reaction conditions, need a surfactant, limited to specific NCA monomers	[133]
Aqueous solution	PBLG, PLeu, PLys(Boc)	PEG-NH_2	(+): No organic solvent, fast, *in situ* self-assembly, (-): Limited to specific NCA monomers, low MW	[134,135]

I.3.3. Self-assembly of polypeptide-based copolymers

The main approach to the design of polymer-based nanocarriers relies on the self-assembly of amphiphilic diblock copolymers (BCPs) capable of encapsulating drugs. Controlled/“living” ROP of NCA techniques, as discussed earlier, provide the versatility and precision needed to synthesize well-defined block copolypeptides. This is typically achieved by initiating ROP with a macroinitiator bearing an

appropriate functional group,[136] although the conjugation of two different polymer segments *via* click chemistry is also a commonly used method.[137]

The following sections will discuss the fundamental principles governing the self-assembly of BCPs, highlighting recent examples that yield nanocarriers, particularly anisotropic structures such as wormlike and rod-like micelles. Special attention will then be given to the self-assembly of polypeptide-based BCPs, which exhibit unique behaviors and often result in nanoparticles with promising morphologies for nanomedicine applications.

I.3.3.1. Basic principle of self-assembly

Various strategies can be used to produce polymeric nanoparticles, and this discussion will focus specifically on self-assembly approaches.[138] Self-assembly of amphiphilic molecules, or surfactants, containing a hydrophilic head group and a hydrophobic tail, has been studied in bulk and in aqueous solutions for many decades.[139] Various morphologies have been observed, including spherical micelles, or spheres, cylindrical micelles, or cylinders, and vesicles. The packing parameter, $p = \frac{V}{a.l}$, where V is the volume of the hydrophobic segment, a is the contact area of the head group, and l is the length of the hydrophobic segment, has been found to determine the morphology of the aggregates.[139] Similarly, block copolymers can self-assemble into various morphologies in solution, similar to those adopted by surfactant molecules. Amphiphilic block copolymers are defined as polymers that have one hydrophilic and one hydrophobic segment, A and B, covalently linked to each other. When diluted in a solvent selective for one of its blocks and at a concentration above the critical micelle concentration (CMC), these AB diblock copolymers will self-assemble into aggregated structures. This self-assembly is driven by several thermodynamic and entropic parameters. The main force is the minimization of the free energy between the two blocks in solution (polymer-polymer interaction parameter, χ_{AB}) and between each block and the surrounding solvent (polymer-solvent interaction parameters, χ_{AS} and χ_{BS}).[140] These parameters are determined by the relative volume fractions, the solvophobicity, the degree of polymerization (DP) of each block, and are strongly related to the packing parameter p introduced for surfactant micellization. For amphiphilic block copolymers, spherical micelles are formed when $p < 1/3$, cylinders between $1/3 < p < 1/2$, and vesicles when $1/2 < p < 1$ (Figure I-19). While this applies to equilibrium structures typical of surfactants, block copolymers can also form kinetically trapped, out-of-equilibrium structures that are influenced by the macromolecular properties of their solvophobic blocks (*e.g.* glass transition temperature, T_g), the self-assembly process and solvent conditions.[141]

In summary, morphologies can be tailored by adjusting chemical compositions, such as the hydrophilic fraction (f) defined as $f = \frac{M_{hydrophilic\ block}}{M_{copolymer}}$ where M is the molar mass,[142] the DP of the constituent blocks and their molar mass dispersity, with additional factors such as specific non-covalent interactions, external additives, chirality, chain conformation and macromolecular architectures also

playing critical role.[143] In the following section, we will explore the methods for obtaining anisotropic nanoparticles, such as worm-like micelles and rod-like micelles, through self-assembly in solution.

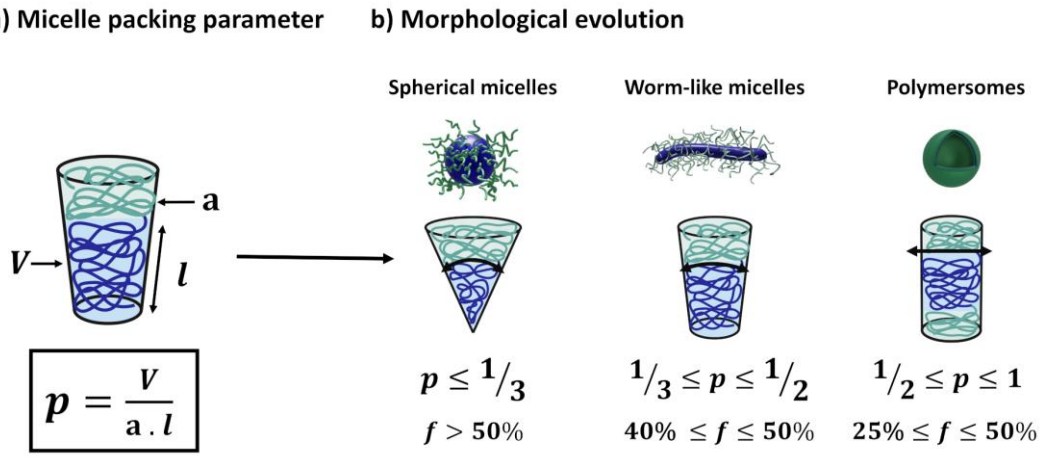

Figure I-19. Schematic representation of different nanoparticle morphologies made through the self-assembly of amphiphilic BCPs (hydrophilic part in green, hydrophobic in blue). (a) Packing parameter formula and (b) hydrophilic fraction or packing parameters theoretically predicting morphology of amphiphilic aggregates. Adapted from Ryan *et al*.[144] and Discher and Ahmed.[142]

I.3.3.2. Self-assembly of amphiphilic block copolymers

In practice, self-assembly of amphiphilic block copolymers can be achieved through a wide range of techniques, depending on the chemical nature of the polymers, and the desired nanoparticle properties.[145] These properties include shape, size, concentration, functionality, stability and drug loading efficiency. For drug loading, self-assembly is simply performed in the presence of the active ingredient to enable its encapsulation. The main strategies for self-assembly and simultaneous drug encapsulation have been summarized by Hochreiner and van Ravensteijn[146] and are listed in Table I-2.

Among the available methods, only a limited number enable the controlled preparation of non-spherical nanoparticles. This section examines some examples of the preparation of such nanoparticles through self-assembly processes, including solvent displacement which is referred to as conventional self-assembly. In addition, crystallization-driven self-assembly, which has been reported to produce non-spherical nanoparticles and nanocarriers, will be discussed.

Table I-2. Self-assembly and drug loading strategies for block copolymer (BCP) nanoparticles. Adapted from Hochreiner and van Ravensteijn.[146]

Method	Concept	Advantages (+) Disadvantages (-)
Direct dissolution	BCP and cargo are directly dissolved in aqueous medium (C ≥ CMC)	(+): Simple, fast, no organic solvent (−): BCP requires to be soluble enough in aqueous medium, low cargo loading
Solvent-displacement	BCP and cargo are dissolved in water-miscible organic solvent, which is gradually or rapidly replaced by water	(+): High cargo loading (−): Time-consuming, limited up-scaling, large amount of water, chances of kinetically trapping depending on the speed/order of water addition
Thin film hydration	BCP and cargo are casted onto a surface by evaporating the organic solvent, followed by rehydration with aqueous solvent	(+): High cargo loading, upscaling (−): Time-consuming
Oil-in-water (O/W) emulsion	Cargo is dissolved in water-immiscible solvent droplets, while the BCP localizes at the solvent-water interface. Cargo is encapsulated upon solvent evaporation.	(+): High cargo loading (−): Chlorinated solvents are often required, limited up-scaling
Crystallization-driven self-assembly (CDSA)	BCP with a semicrystalline block crystallises upon solvent exchange	(+): Non-spherical and complex, hierarchical assemblies (−): Requires semicrystalline core-forming block, limited cargo loading
Polymerization-induced self-assembly (PISA)	BCP synthesis and nanoparticle self-assembly in one-pot with simultaneous cargo encapsulation	(+): One-pot procedure, higher-order morphologies accessible (−): Monomer/polymer restrained choice, many parameters to considered

I.3.3.2.1. Conventional self-assembly

By exploiting the amphiphilic behavior of BCP, nanoparticles can be obtained in a given solvent when one block (the solvophilic block) is soluble, while the other is insoluble (the solvophobic block). In the solvent displacement process, the diblock copolymer is first dissolved in a good solvent (typically in an organic solvent) for both blocks. A poor solvent (typically water) that solubilizes only the solvophilic block is then added to the solution until the critical water content (CWC) is reached, at which point the solvophobic block becomes insoluble leading to the aggregation of the solvophobic blocks (Figure I-20). Finally, the organic solvent is removed either by evaporation or by dialysis. The type of organic solvent, the order of addition of the aqueous phase, the rate of addition, the temperature, and the polymer concentration can be adjusted to obtain different sizes and morphologies of nanoparticles.[147]

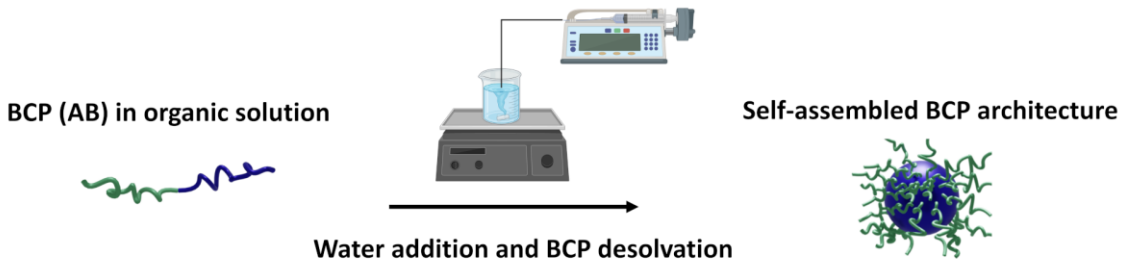

Figure I-20. Schematic representation of solvent-displacement process to self-assemble diblock copolymer.

First reported and patented by Fessi *et al.* in 1989 for the formation of polymeric nanoparticles and simultaneous encapsulation,[148] it was then has been extensively studied by Eisenberg and colleagues to form various types of nanoparticles by self-assembly of amphiphilic block copolymers.

They first reported self-assembled worm-like micelles in 1995 using a polystyrene-*block*-poly(acrylic acid) (PS-*b*-PAA) diblock copolymer.[149] This BCP was dissolved in DMF, a good solvent for both blocks at a concentration of 2 wt%, followed by gradual addition of water (good solvent for PAA, poor for PS) under vigorous stirring. Stable nanoparticles were then obtained at a water content of 25 wt%, where transmission electron microscopy (TEM) revealed worm-like morphologies when the DP was 200 for PS and 15 for PAA. Spheres and vesicles were obtained by slightly varying the DP of PAA while keeping the DP of PS constant (Figure I-21). The same group also demonstrated the formation of rod-like nanoparticles from polystyrene-*block*-poly(ethylene glycol) (PS-*b*-PEG).[150] Later, investigations have optimized the self-assembly conditions to produce anisotropic nanoparticles by conventional self-assembly. For example, worm-like micelles with diameters between 22 and 60 nm and lengths between 1 and 18 µm were prepared from poly(ethylene glycol)-*block*-polyethylethylene (PEG_{42}-*b*-PEE_{35}), poly(ethylene glycol)-*block*-polycaprolactone (PEG_{44}-*b*-PCL_{24} and PEG_{110}-*b*-PCL_{58}),[66] poly(ethylene glycol)-*block*-poly(propylene sulfide) (PEG_{45}-*b*-PPS_{44})[151] and series of poly(ethylene glycol)-*block*-poly(lactide) (PEG-*b*-PLA)[152] linear diblock copolymers. In terms of drug loading, various non-spherical nanocarriers for drug delivery applications, especially in cancer therapy, have been obtained during the last two decades.[81] For example, PEG-*b*-PCL-based worm-like micelles have demonstrated higher drug loading content (DLC, wt%) and encapsulation efficiency (EE, %) compared to their spherical counterparts, especially with paclitaxel (PTX), one of the most studied anticancer drugs.[153–155]

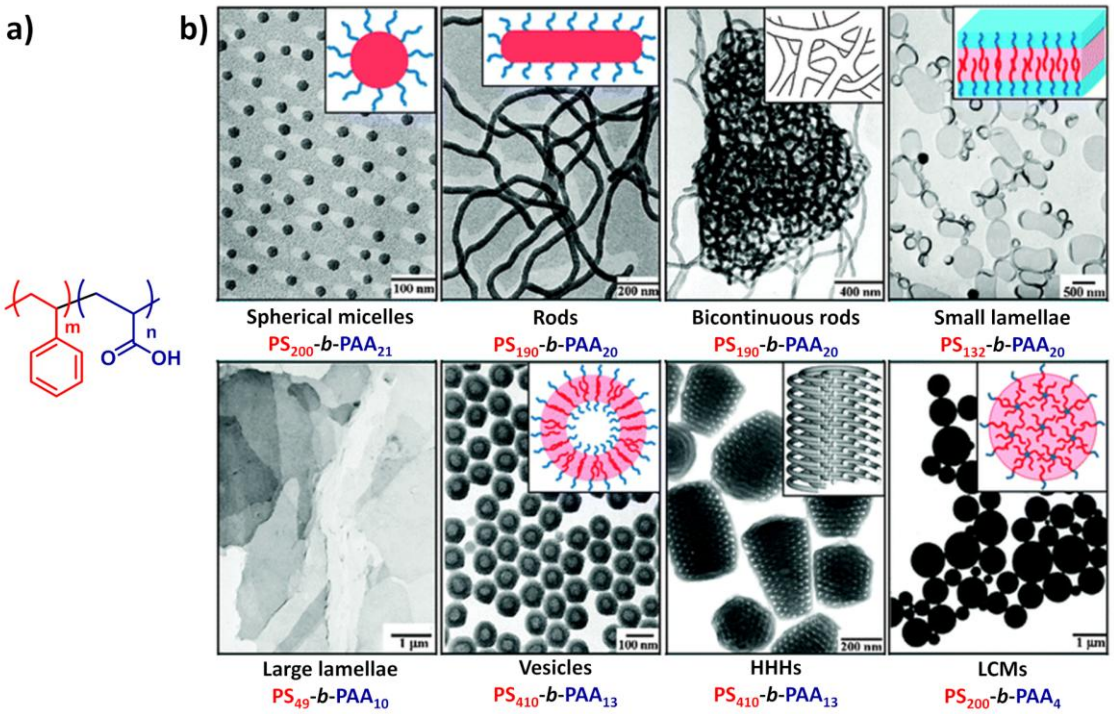

Figure I-21. (a) Chemical structure of PS-*b*-PAA BCP. (b) Representative transmission electron microscopy (TEM) images and schematic diagrams of obtained nanoparticle morphologies from PS-*b*-PAA self-assembly. HHHs: hexagonally packed hollow hoops; LCMs: large compound micelles. From Mai and Eisenberg.[156]

Although these self-assembled systems have been obtained by conventional process using "coil-coil" block copolymers with an amorphous core-forming block, the formation of non-spherical micellar

nanoparticles is still limited to specific compositions and conditions. These nanoparticles often coexist with other morphologies, and even when pure forms are obtained, controlling their dimensions and dispersities remains challenging. In fact, micellar nanoparticles obtained by self-assembly of polymeric amphiphiles are generally kinetically trapped, where the exchange of BCPs between the micelles is very slow, or non-existent, in contrast to the low molar mass surfactants based micelles.[157] Predicting the resulting morphologies is then tedious, and the same BCP can even yield different morphologies in the same solvent medium by using different processing conditions.[147]

I.3.3.2.2. Crystallization-driven self-assembly

The use of BCPs containing a semicrystalline block as the solvophobic block, rather than amorphous, offers promising strategies for achieving controlled anisotropic nanoparticles. The introduction of a poor solvent for the crystalline block promotes core crystallization, shifting the self-assembly process from traditional spherical morphologies to 1D cylindrical and 2D platelet structures. This method, known as crystallization-driven self-assembly (CDSA), has been extensively studied by Winnick and Manners.[158,159] It has been shown to be a robust and versatile approach for fabricating kinetically controlled and colloidally stable crystalline nanostructures in solution. Unlike the self-assembly of coil-coil BCPs, which is primarily driven by solvophobic interactions, the phase separation of crystalline-coil BCPs results from a combination of solvophobic interactions and core-crystallization. Several factors influence this self-assembly process, including the molecular structure of the polymers, block length, soluble/insoluble ratio, solvent type, concentration, and temperature.[160]

In living CDSA, seed particles nucleate the assembly, allowing for controlled epitaxial growth upon polymer addition. This approach ensures precise size control and low polydispersity (Figure I-22),[161] making it highly relevant for nanomedicine. Unfortunately, a potential barrier to their use as nanocarriers is that encapsulation within the crystalline core is cumbersome due to the tight packing of polymer chains, which can disrupt crystallinity and ultimately lead to particle disassembly.[162]

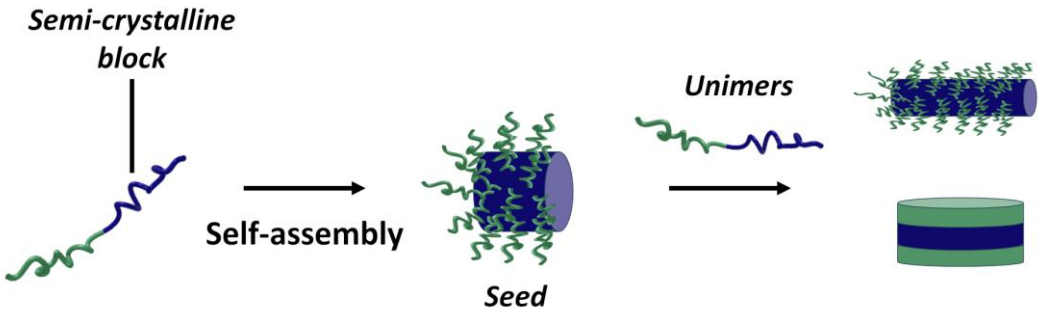

Figure I-22. Schematic illustration of the living CDSA process to generate 1D and 2D micelles from a semi-crystalline BCP.

To facilitate drug loading in nanofibers obtain by living CDSA, Manners and coworkers designed a triblock copolymer with a crystallizable poly(fluorenetrimethylcarbonate) (PFTMC) core-forming block (A), a hydrophobic amorphous poly(butyl methacrylate) (PBMA) middle block (B), and a hydrophilic poly(*N*-isopropylacrylamide) (PNIPAM) corona-forming block (C).[163] This BCP can undergo living

CDSA in polar organic media, yielding nanofibers with a crystalline PFTMC core and a solvated PBMA-*b*-PNIPAM corona. A solvent switch, namely preformed nanoparticle solvent switch loading (PNSL), enabled the formation of nanofibers with a crystalline PFTMC core, an amorphous PBMA layer, and a PNIPAM corona, allowing efficient encapsulation and release of the hydrophobic cargo Nile Red (NR) in the PBMA layer (Figure I-23).

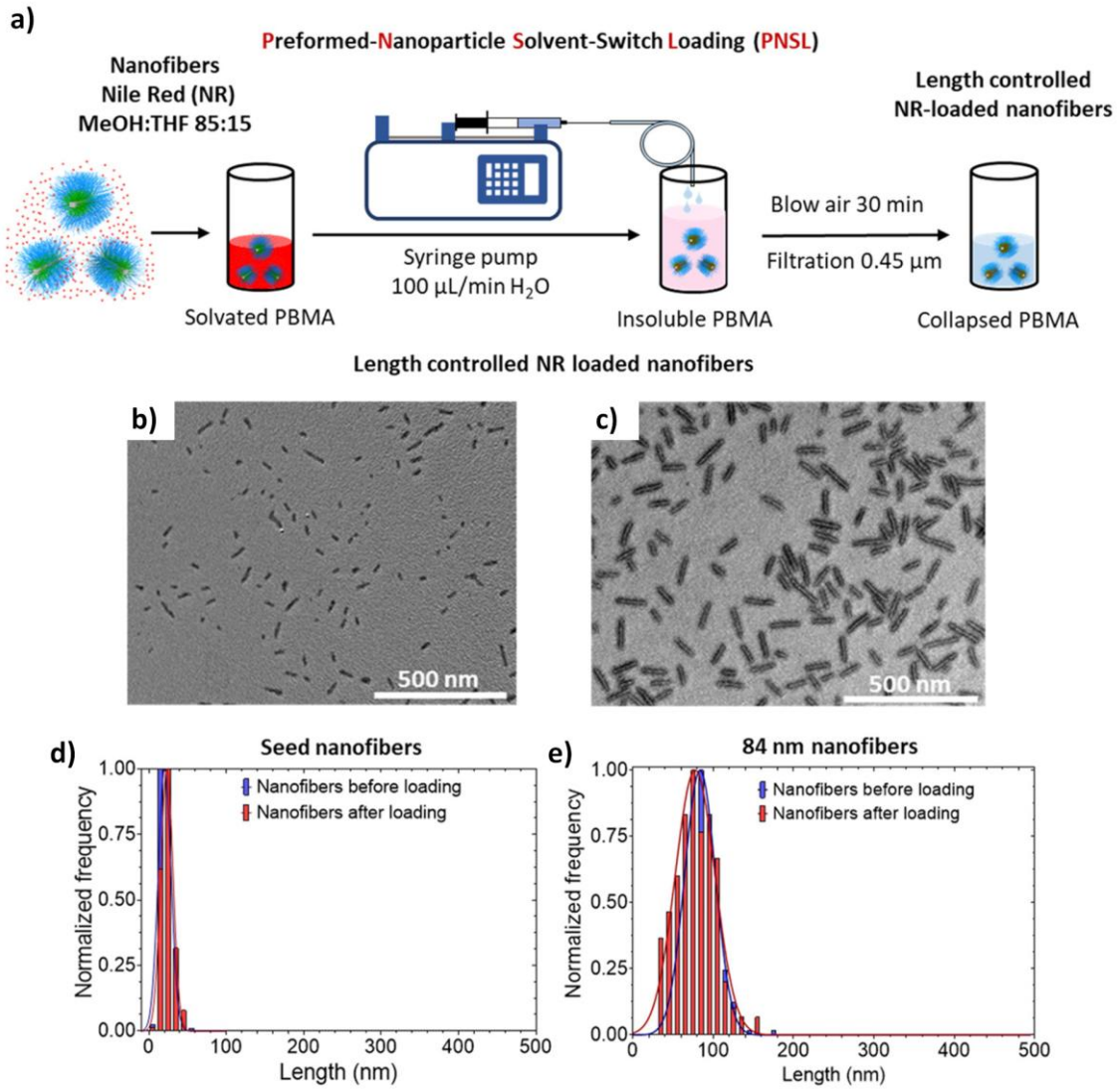

Figure I-23. (a) Loading of Nile Red (NR) into preformed nanofibers *via* the PNSL method. (b,c) Representative TEM images of the NR-loaded nanofibers in water. (d,e) Contour length histograms of the NR-loaded nanofibers in water before and after loading. From Manners *et al.*[163]

Manners' group also incorporated paclitaxel (PTX) into the core-corona interface of nanofiber seeds composed of poly-(fluorenetrimethylcarbonate)-*block*-poly(dimethylaminoethylmethacrylate) (PFTMC-*b*-PDMAEMA).[164] This was achieved by adding a PTX solution in ethanol to the nanofiber self-assembly solvent mixture. When water was added and the organic solvent evaporated, PTX was successfully loaded at 20 wt%. *In vitro* toxicity studies using 2D and 3D U87 MG GBM tumor models showed promising results compared to the conventional therapy *Abraxane*® which consists of PTX encapsulated in an albumin shell.

Other examples of non-covalent corona loading include loading of 2D crystalline platelets with doxorubicin,[165] and loading of PFTMC-*b*-PDMAEMA nanorods with tetracycline,[166] by using a solvent switch method to load the drugs at the core-corona interface.

Stenzel and coworkers overcame the limitations of crystalline cores for drug loading by using covalent attachment methods. They used the living CDSA of polycaprolactone (PCL)-based block copolymers to fabricate glycoplatelets. They functionalized these particles with doxorubicin (DOX) or cyanine 5 (Cy5) fluorescent dye, either directly on the corona prior to the self-assembly or by post-modification of the pre-assembled glycoplatelets (Figure I-24).[167] However, this process required many laborious steps and complex co-solvents for the assembly, and the platelets were not challenged under biological conditions.

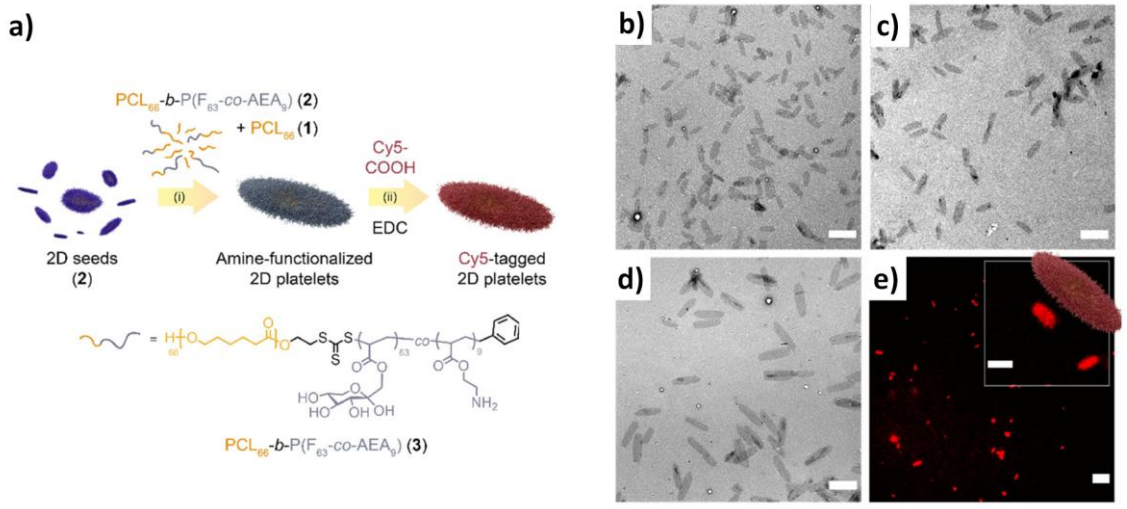

Figure I-24. (a) Fluorescent labelling of pre-assembled glycoplatelets with amine functionalities. The seeds are subjected to (i) unimer addition (3) and (ii) fluorescent labelling by amidation coupling with Cy5-COOH. (b-d) Representative TEM images of Cy5-tagged platelets in water. The unimer/seed ratios used were (b) 2.5, (c) 5 and (d) 10 (w/w). Scale-bar: 5 µm. (e) Confocal laser scanning microscopy (CLSM) ($\lambda_{exc.}$ = 633 nm) of Cy5-tagged platelets in water made by using unimer/seed ratio = 5/1. Scale bars: 5 and 2 µm (inset). Adapted from Stenzel *et al.*[167]

Similarly, Kempe and colleagues used drug conjugation of the cytostatic drug mycophenolic acid (MPA) onto BCP unimers made of poly(2-isopropyl-2-oxazoline)-*block*-poly(2-methyl-2-oxazine) (PiPrOx-*b*-PMeOz) and poly(2-isopropyl-2-oxazoline)-*block*-poly(2-methyl-2-oxazoline) (PiPrOx-*b*-PMeOx) to obtain drug-loaded nanorods.[168] This CDSA phenomenon in the all-oxazoline-based block copolymer has also been previously investigated by our group.[169] PiPrOx formed the core, while PMeOz or PMeOx formed the corona, which was terminated *in situ* with MPA, a nucleophilic drug. These pre-functionalized BCPs were used in living CDSA to create drug-nanorod conjugates that showed reduced off-target effects in human immune cells compared to free MPA *in vitro* assays.

Despite advances in drug loading within anisotropic nanoparticles obtained by CDSA, examples remain limited, and the encapsulation process is often challenging. In addition, biological evaluations are still scarce, and the impact of drug positioning within the corona requires thorough investigation.

I.3.3.2.3. Application to polypeptide-based copolymers

Polypeptide copolymers can also self-assemble into various structures, including spherical micelles, cylindrical micelles, vesicles, and hierarchical architectures, in selective solvents or aqueous media.[170] Unlike conventional synthetic polymers, peptide polymers benefit from stable secondary structures in solution, which, together with hydrophobic, electrostatic, and dipolar interactions, drive the self-assembly process. In these systems, the polypeptide block can form a rigid "rod" structure, as opposed to the more flexible "coil" block typically found in synthetic polymers. Typically, rod-coil polymers consist of hydrophilic "coil" segments and hydrophobic "rod" segments that facilitate self-assembly into organized nanostructures. The self-assembly behavior of rod-coil copolymers, driven by the ordering of the rod segments and their transition between different chain conformations, results in unique nanostructures. While helical polypeptide (with the α-helix conformation) - solvophilic polymer conjugates are a prime example of rod-coil copolymers, the self-assembly of these systems remains less explored compared to the extensively studied coil-coil block copolymers. However, in the rod-coil polymer field, the self-assembly behavior of PBLG-based copolymer has been extensively studied,[171–175] as PBLG serves as a typical hydrophobic rod segment due to its helical conformation above a DP of 20.[176] Notably, amphiphilic block copolymers composed of PBLG and PEG have been extensively studied for biomedical applications. Their self-assembled nanoparticles form a hydrophobic core rich in aromatic benzyl groups, enabling π-π stacking interactions that facilitate the encapsulation of various hydrophobic drugs, such as clonazepam,[177,178] paclitaxel[179] or doxorubicin.[180,181]

For example, Yang *et al.* studied the self-assembly behavior of PBLG-*b*-PEG-*b*-PBLG triblock copolymers, as a function of the PBLG block length and preparation conditions, with a PEG size of 5kDa.[182] The DP of PBLG varied from 80 to 210, forming a hydrophobic block and adopting a rigid helical conformation. Thus, this rod-coil-rod triblock copolymers self-assembled either into vesicles when the PBLG block length was short, or into spheres when the DP was increased. Dissipative particle dynamics (DPD) simulations were performed on model rod-coil-rod triblock copolymers to better understand the structure of the vesicles. They showed that the rigid PBLG blocks align parallel to each other to form the monolayer vesicle wall.

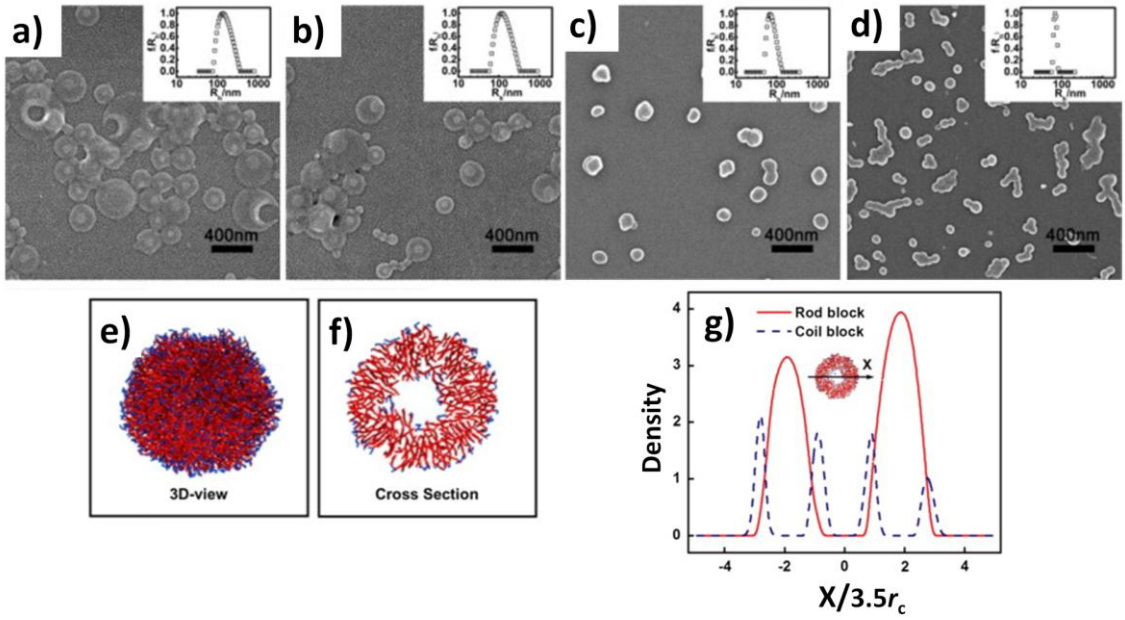

Figure I-25. (a-d) Representative scanning electron microscopy (SEM) images of particles formed by: (a) $PBLG_{80}$-*b*-PEG_{5k}-*b*-$PBLG_{80}$ at 0.5 mg.mL^{-1}; (b) $PBLG_{150}$-*b*-PEG_{5k}-*b*-$PBLG_{150}$ at 0.5 mg.mL^{-1}; (c) $PBLG_{120}$-*b*-PEG_{5k}-*b*-$PBLG_{120}$ at 0.5 mg.mL^{-1}; and (d) $PBLG_{80}$-*b*-PEG_{5k}-*b*-$PBLG_{80}$ at 1 mg.mL^{-1}. (e-g) DPD simulations of the vesicle structure self-assembled from rod-coil-rod triblock copolymers model: (e) 3D-view of a vesicle, (f) cross-section of a vesicle and (g) one-dimensional density profile of rod and coil blocks along the x-arrow of the vesicles. Adapted from Yang *et al.*[182]

This peculiar rod-coil behavior may be of interest for the formation of anisotropic morphologies. Disk-like nanoparticles were obtained by our group by the self-assembly of a mixture of "tree-like" glycopolypeptides (dextran-*grafted*-PBLG), and homopolymers of PBLG.[183] Using traditional solvent-displacement process through nanoprecipitation using DMSO as good solvent and water as poor solvent, the incorporation of 30 % of rod-like PBLG "dilute" the dendritic dextran blocks leading to high local curvature and spherical morphologies by inducing rod-rod interactions responsible for a flat interface, as it can be observed in Figure I-26.

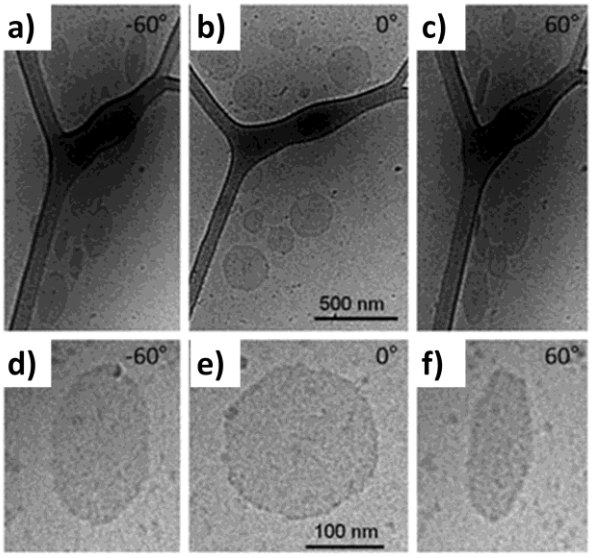

Figure I-26. Cryo-TEM imaging of dextran-*grafted*-PBLG with 30 wt% PBLG at different magnifications (scale bar indicated in the images). The sample grid was tilted from −60° (images (a) and (d)) to +60° (images (c) and (f)) to reveal the disk-shape structure of the sample. Adapted from Lecommandoux *et al.* [183]

Similarly, disk-like nanoobjects were obtained by the self-assembly of PEG_{2k}-*b*-$PBLG_{150}$ copolymers *via* solvent displacement processed by dialysis.[184] The copolymer was dissolved in THF at a concentration of 0.5 $mg.mL^{-1}$, stirred overnight and water was slowly added until the water content reached 50% by volume. After quenching with 10-fold amount of water and dialysis, microscopy imaging revealed a disk-like morphology with a diameter of about 0.5 – 1 µm, with some cylindrical pores. Cai *et al* also obtained non-spherical nanoparticles with the self-assembly of PEG-*b*-PBLG *via* similar solvent-displacement process, where the copolymer was dissolved in chloroform, and ethanol, a selective solvent for PEG, was added drop by drop.[185] Long cylindrical micelles with a length in the range of 150 nm – 1 µm and a diameter of about 90 nm were obtained in the $CHCl_3$/ethanol mixture. DPD simulations showed that the rod blocks are regularly packed into the core and are interdigitated, with their long axes oriented to form a twisted structure, while the coil blocks cover the cores to form the shell. The arrangement of the rigid blocks is characteristic of the chiral liquid crystal (LC) structure. In fact, liquid crystals are materials characterized by long-range orientation or positional order in at least one direction, while maintaining a high degree of mobility for individual molecules. They can be found in two main regimes : smectic, where molecules are arranged in layers with orientational order within each layer, and nematic, where molecules are oriented in the same direction but without layer formation (Figure I-27).[186] PBLG, which forms a rigid rod due to its helical conformation in organic solvent, exhibits liquid crystalline ordering.[174]

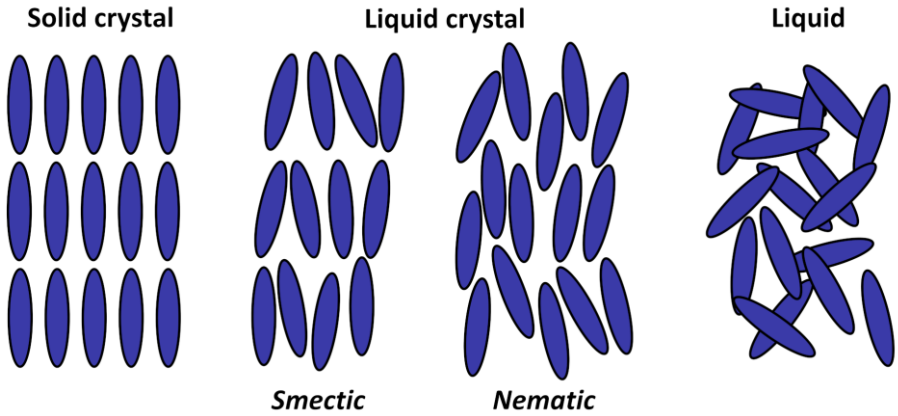

Figure I-27. Schematic representations of the arrangement of molecules in a solid crystal, a liquid or a liquid crystal (in a smectic or nematic phase). Adapted from Asdonk & Kouwer.[187]

As explained in section I.3.3.2.2, CDSA concerns the self-assembly of semicrystalline BCP in solution, which provides access to well-defined hierarchical micellar structures based on epitaxial crystallization. In this area of research, Liquid Crystallization-Driven Self-Assembly (LCDSA) of block copolymers with a liquid crystalline block has recently emerged.[188] As representative example, polypeptide-based rod-coil block copolymers, such as PNIPAM-*b*-PBLG, have been successfully self-assembled by LCDSA in THF/methanol (MeOH) mixed solution as reported by Lin *et al*, where cylinders were obtained (Figure I-28).[189] When polypeptide block copolymer unimers are introduced into a seed solution containing cylindrical micelles with LC-like cores, the micelles can elongate by incorporating these unimers at both ends. This growth is driven by the formation of the LC-like structure within the polypeptide

blocks in the micelle cores. Homogeneous, elongated micelles can then be obtained due to the hydrophobic nature of the polypeptide core.

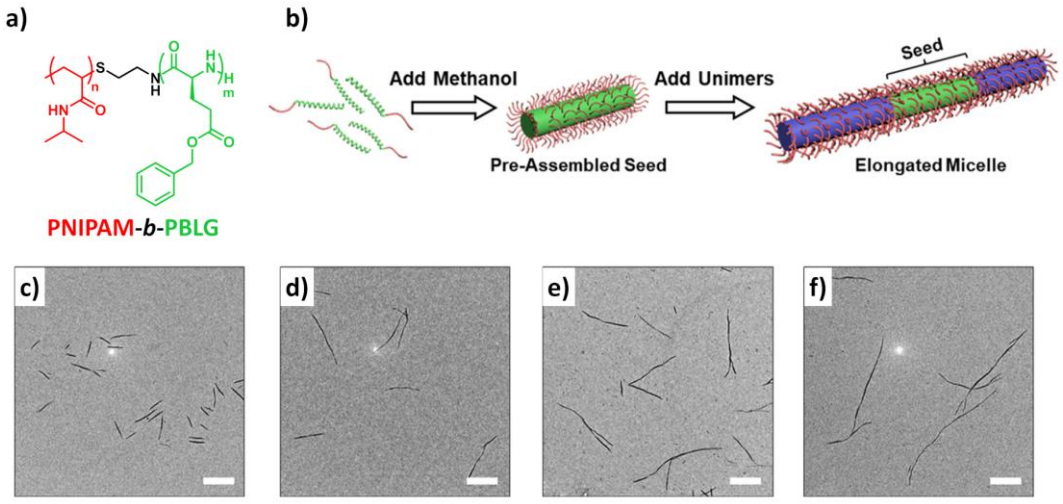

Figure I-28. (a) Chemical structure of the PBLG-*b*-PNIPAM. (b) Preparation of micelle seeds and the growth of cylindrical seeds. (c-f) Representative TEM images of the seeds (c) and the elongated micelles after adding unimers in DMF to the seed solutions in THF/MeOH for various aging times: (d) 6, (e) 12 and (f) 48 hours. Scale bar: 1 µm. Adapted from Lin *et al*.[189]

Also using LCDSA, Gao and coworkers used disk-like micelles of PEG-*b*-PBLG as seeds and added unimers to epitaxially grow the disk-like micelles (Figure I-29).[190] The added unimers initially formed small aggregates that later fused with the seed edges. During this process, the rod blocks rearranged to align with the LC-like core of the seeds, while the copolymers within the disk-like micelles simultaneously adjusted their structure, as revealed by Brownian dynamic (BD) simulations by modeling the copolymer as a coarse-grained rod-coil BCP. This work extends LCDSA from 1D to 2D thanks to the LC behavior of the polypeptide rod block.

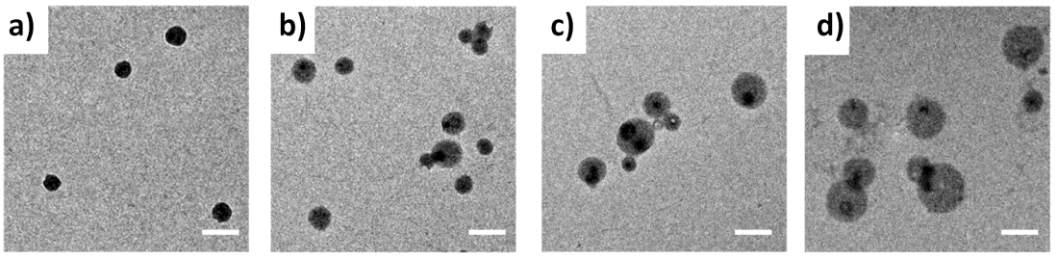

Figure I-29. Growth of disklike micelles for by PEG-*b*-PBLG. (a) Representative TEM image of dislike seed micelles. (b-d) Representative TEM images of the dislike micelles after unimers were added to the seed solutions for various aging times: (b) 30, (c) 90 and (d) 180 min. Scale-bar: 500 nm. Adapted from Gao *et al*.[190]

These few examples highlight the potential for achieving anisotropic morphologies through the self-assembly of polypeptide-based BCPs, leveraging the rod-coil behavior of polypeptides with helical conformations. Alternatively, anisotropic structures can also arise from the self-assembly of polypeptides adopting β-sheet conformations, which inherently favor fibrillar organization. This tendency is well-documented in amyloid-forming peptides, where β-sheet stacking drives aggregation into fibrils.[191,192] For block copolymer, the short peptide sequence of phenylalanine in the peptide BCP PEG_{5k}-*b*-$PPhe_4$ can for instance self-assemble into nanofibrils thanks to hydrophobic interactions of aromatic phenylalanine

residues occurring at low concentration and well-defined β-sheets at higher concentration, in aqueous medium (Figure I-30).[193]

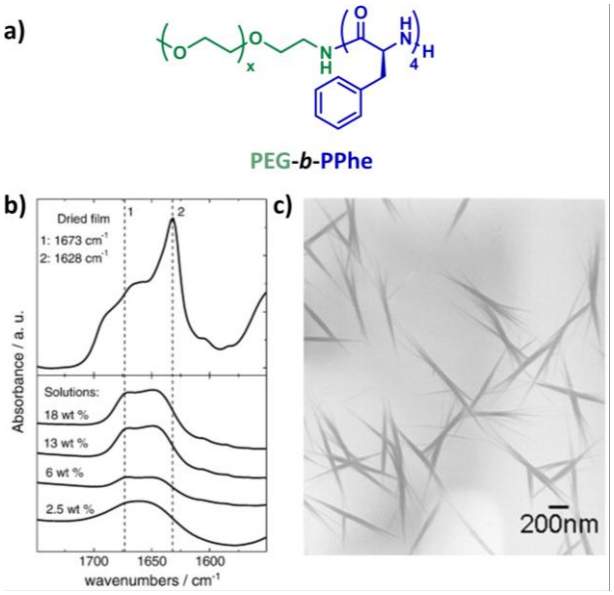

Figure I-30. (a) Chemical structure of PEG_{5k}-*b*-$PPhe_4$ peptide BCP. (b) FTIR spectra of the amide I region of a dried film of PEG_{5k}-*b*-$PPhe_4$ solution (top) and PEG_{5k}-*b*-$PPhe_4$ D2O solutions at 2.5, 6, 13 and 18 wt% (bottom). The peak positions 1 (1673 cm^{-1}) and 2 (1628 cm^{-1}) are associated with secondary structure in the dried film. (c) Representative TEM image of fibrils formed by PEG_{5k}-*b*-$PPhe_4$ at 5 wt%. Adapted from Castelletto and Hamley.[193]

Beyond anisotropic structures, the self-assembly of block copolymers with polypeptides as hydrophilic, hydrophobic, or double blocks has been extensively studied in nanomedicine, although primarily in the form of spheres.[194,195] In fact, polymeric micelles made of polypeptides and obtained by self-assembly, are currently undergoing human clinical evaluation for the treatment of various solid tumors. The first polymeric micelles to enter clinical evaluation were developed by the Kataoka group in 2001. These micelles were composed of PEG-*b*-poly(α,β-aspartic acid) (PEG-*b*-PAsp) and incorporated doxorubicin (NK911, Nippon Kayaku, Co.).[196] The nanocarrier consists of the self-assembly of a diblock copolymer composed of PEG (5 kDa) and PAsp (DP ~ 30), partially conjugated with doxorubicin to form polymeric micelles of approximately 40 nm in size. The doxorubicin is loaded into the hydrophobic core of the micelles. While conjugated doxorubicin has no intrinsic antitumor activity, it helps stabilize the micelles, prolongs the release of doxorubicin, and acts as a drug reservoir, enabling gradual release through cleavage of the conjugate bond.[197] Subsequently, several other micellar formulations loaded with anticancer agents entered human trials (Table I-3). These polymeric micelles are mainly composed of a PEG corona and a poly(*L*-glutamic acid) (PGlu) or PAsp core.

Table I-3. Current clinical status of PEG-*b*-polypeptide micelles

Name	Drug	Block copolymers	Drug loading (wt%)	Loading method	Size (nm)	Development phase	Ref
NK105	Paclitaxel	PEG-*b*-PAsp	23	Physical encapsulation after 4-phenyl-1-butanol grafting to enhance affinity with Ptx	85	Phase II (Phase III fails against metastatic or recurrent breast cancer)	[198,199]
NK012	SN-38	PEG-*b*-PGlu	20	Conjugation with Glu in hydrophobic core (ester bond cleavable in PBS)	20	Phase II	[200]
NK911	Doxorubicin	PEG-*b*-Asp	17	Physical encapsulation (hydrophobic and Dox-Dox interaction)	40	Phase II	[196]
NC-6004	Cisplatin	PEG-*b*-PGlu	30	Metal complexation with carboxylates	20	Phase III	[201]
NC-4016	Oxaliplatin	PEG-*b*-PAsp	30	Metal complexation with carboxylates	30	Phase I	[201]
NC-6300	Epirubicin	PEG-*b*-poly(aspartate-hydrazone)	20	Conjugation with hydrazone bound on aspartate (pH sensitive bond)	60	Phase I	[202]

In addition to others, such as the Vicent group specializing in polypeptide-drug conjugates,[203–205] our group has also significantly contributed to the design of polypeptide-based amphiphilic block copolymer nanoparticles, especially based on PEG-PBLG,[180] poly(trimethylene carbonate)-poly(*L*-glutamic acid) (PTMC-PGlu)[206,207] and PBLG-hyaluronan (PBLG-HA).[208–212]

However, despite their potential as drug delivery systems, no polypeptide-based nanodrugs have received regulatory approval so far and only two polypeptides from ROP have been approved as therapeutic agents: *Vivagel*®, a topically administered polylysine dendrimer used as an antibacterial and antiviral agent against HIV-1 and HSV-2,[213,214] and *Copaxone*®, a copolymer composed of *L*-glutamic acid (Glu), *L*-alanine (Ala), *L*-lysine (Lys), and *L*-tyrosine (Tyr), used in the treatment of multiple sclerosis.[215]

In conclusion, while self-assembly of synthetic amphiphilic BCP from polypeptide offers a promising approach to obtaining anisotropic nanoparticles, its limitations are evident. The multi-step nature of the process involving sequential polymerization and self-assembly inherently limits scalability due to the low concentrations of nanoparticles produced. Furthermore, although anisotropic morphologies can be achieved, their formation remains limited to specific cases, making it difficult to establish general predictive rules for their design. Importantly, to the best of our knowledge, there are no reported examples of anisotropic morphologies composed of synthetic polypeptides that have successfully loaded therapeutic agents and undergo preclinical evaluation, highlighting a significant gap in the field. On the other hand,

polymerization-induced self-assembly (PISA) has recently emerged as an alternative process for the preparation of aqueous suspensions of polymer assemblies of different morphologies, at high concentrations (10 - 50 wt%), with good reproducibility and without additional surfactant.[216–221] This process holds significant potential for applications in nanomedicine, particularly in the development of nanocarriers, which will be explored in more detail in the following section.

I.4. Polymerization-induced self-assembly

I.4.1. General definition

In a PISA process, a solvophilic living precursor block is chain extended with a second monomer, or core-forming monomer, whose homopolymer becomes solvophobic in the given solvent after reaching a certain DP. The process can take place in either dispersion or emulsion systems, depending on the reaction conditions and solvent properties. This block copolymer becomes amphiphilic and self-assembles into spherical micelles when the core-forming block exceeds a certain DP. Then, the monomers concentrated in the core of the micelles will continue to polymerize, and as the DP increases, the morphology of the polymer assemblies will evolve from spherical micelles to worm-like micelles, to vesicles (Figure I-31). The morphology of the assemblies can be theoretically predicted with the same packing parameter p that has been defined previously in section I.3.3.1.

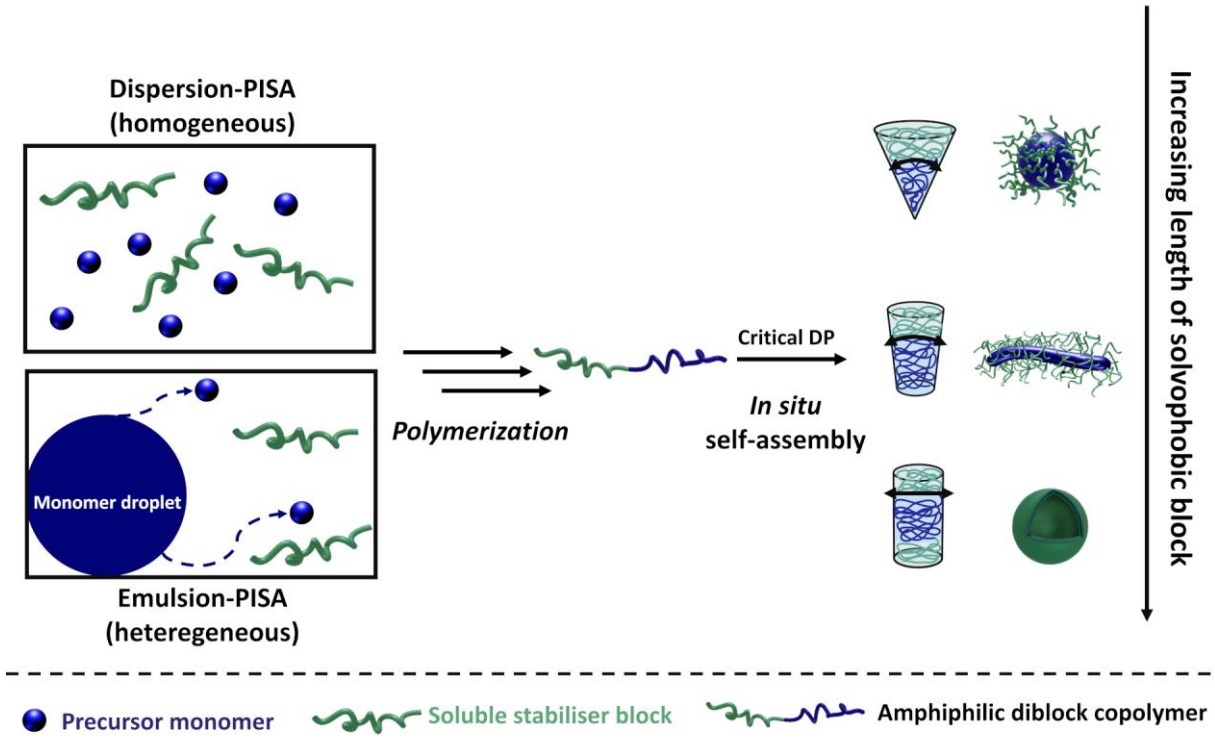

Figure I-31. Schematic representation of the Polymerization-Induced Self-Assembly (PISA) process, starting from a dispersion or an emulsion.

Living step-growth polymerizations, such as reversible deactivation radical polymerization (RDRP), are primarily used in PISA due to their ability to provide precise control over polymer architecture.

Among RDRP methods, reversible addition-fragmentation chain transfer (RAFT) polymerization is the most widely utilized in PISA due to its broad monomer compatibility, suitability for aqueous solvents, and operation under mild reaction conditions.[222,223] Other controlled/"living" polymerization techniques have also been used in PISA to date, as these polymerizations exhibit a linear increase in second block length with increasing conversion, and are summarized in Table I-4 adapted from the reviews of Pan and coworkers,[224] and Du and coworkers.[225] Some key references are mentioned in the table. Given this versatility, PISA has significant potential for biomedical applications, particularly in the development of polymeric nanocarriers for drug delivery.

Table I-4. Main polymerization techniques in PISA.

Process	Stabilizer block	Monomer	Morphologies	Limits	Ref
RAFT	Thiocarbonylthio chain-transfer agent (CTA)	Methacrylate, acrylate, methacrylamide, acrylamide, styrene	Spheres, worms, lamellae, vesicles, jellyfish	Sulfur-containing polymer, non-degradable vinylic polymer	[218,219,226,227]
NMP	Alkoxyamine	Methacrylate, acrylate, acrylamide, styrene	Spheres, worms, vesicles	High temperature/pressure required, non-degradable vinylic polymer	[228–230]
ATRP	Bromide-based initiator	Methacrylate, acrylate, acrylamide, styrene	Spheres, worms, vesicles	Cu catalyst, poor control, non-degradable vinylic polymer	[231–233]
ROMP	Ruthenium-based initiator	Norbornene, cyclooctatetraene, 1,5-cyclooctadiene	Spheres, worms, vesicles	Non degradable polymer	[234–236]
LAP	Lithium-based initiator	Isoprene, styrene, styrenic	Spheres, worms, vesicles	Strict anhydrous conditions, non-degradable vinylic polymer	[237,238]
TERP	Organotellurium-based initiator	Methacrylate, acrylate, styrene	Spheres	Limited morphologies, non-degradable vinylic polymer	[239]
GTP	Silyl ketene acetal	Methacrylate	Spheres, worms, vesicles	Non-polar media, non-degradable vinylic polymer	[240,241]
ROP	Amine-/ hydroxyl-based initiators	*N*-Carboxyanhydrides, Salicylic *O*-Carboxyanhydrides, Lactones, *L*-lactides, carbonates	Spheres, worms, rods, platelets, vesicles	Few monomers appliable	[134,242–246]

Abbreviation: RAFT: reversible addition-fragmentation chain transfer; NMP: nitroxide mediated polymerization; ATRP: atom transfer radical polymerization; ROMP: ring-opening metathesis polymerization; LAP: living anionic polymerization; TERP: organotellurium-mediated radical polymerization; GTP: group-transfer polymerization; ROP: ring-opening polymerization.

I.4.2. Design of nanocarriers by PISA

The *in situ* formation of nanoparticle suspensions during polymerization allows direct encapsulation of active ingredients by adding them at different stages of the process. The development of effective nanocarriers *via* PISA requires that several key considerations be addressed. First, the nanoparticles must be (bio)degradable or (bio)compatible. Since PISA relies predominantly on radical polymerization, which produces non-degradable carbon-carbon backbones, alternative strategies are needed to introduce degradability. Functionalization with biomolecules is also essential for active targeting. In addition, nanoparticles must demonstrate water stability, either through direct PISA in aqueous media or through successful transfer and stabilization in water. Second, drug encapsulation methods must be optimized. Finally, it is desirable to achieve non-spherical morphologies as these structures often enhance therapeutic efficacy. However, integrating degradability, water stability, drug encapsulation, and morphological control into a single system remains a complex challenge. The following sections will examine these aspects in detail, beginning with the use of biomolecules as stabilizer blocks in PISA to impart degradability and functionality to nanostructures. Next, the potential for achieving degradability through ring-opening polymerization in PISA will be explored, along with an analysis of the resulting morphologies. Specific driving forces driving the formation of anisotropic nanoparticles *via* PISA are discussed separately in **Chapter III**, while drug encapsulation strategies are presented in **Chapter VI**.

I.4.2.1. Biomolecule as stabilizer block in PISA

Biomolecule-polymer conjugated nanoparticles combine the distinct advantages of biomolecules with the versatility of synthetic polymers. Their self-assembly in aqueous environments results in multivalent, high-density biomolecule shells that enhance stability and enable targeted cancer therapy. In addition, these biomolecules can impart partial degradability to the nanostructures, as they are (bio)degradable and metabolized by the organism. This section explores some examples of the range of biomolecules, from simple peptides and polypeptoids to enzymes, used in the hydrophilic shells of PISA nanoparticles, and highlights their significance in drug delivery applications.

I.4.2.1.1. Poly(sarcosine)

Poly(sarcosine) (PSar), an α-polypeptoid, derived from polyglycine with a methyl group on the amine, shares “stealth” properties with PEG, making it a promising material for long-circulating nanoparticles.[50] PSar was used as a macro-chain transfer agent (CTA) to prepare PSar-based nano-objects *via* photo-RAFT PISA. Synthetized by ROP of Sar NCA and conjugated to a trithiocarbonate RAFT agent, photo-PISA of 2-hydroxypropyl methacrylate (HPMA) in water initiated by PSar-CTA was achieved yielding various morphologies based on solid content and PHPMA chain length (Figure I-32). Notably, PSar-*b*-PHPMA unilamellar vesicles exhibited exceptional proteolytic resistance to enzymes such as α-chymotrypsin, trypsin, and pepsin, demonstrating their stability. While resistant to enzymatic degradation, the hydrolytic degradation of PSar enhances its potential for biomedical applications.[247] A comparison of

empty and horseradish peroxidase (HRP)-loaded PSar-stabilized vesicles with PEG-based counterparts showed superior colloidal stability and resistance to proteolytic degradation. These results highlight the potential of PSar as a promising alternative to PEG in nanomaterials.

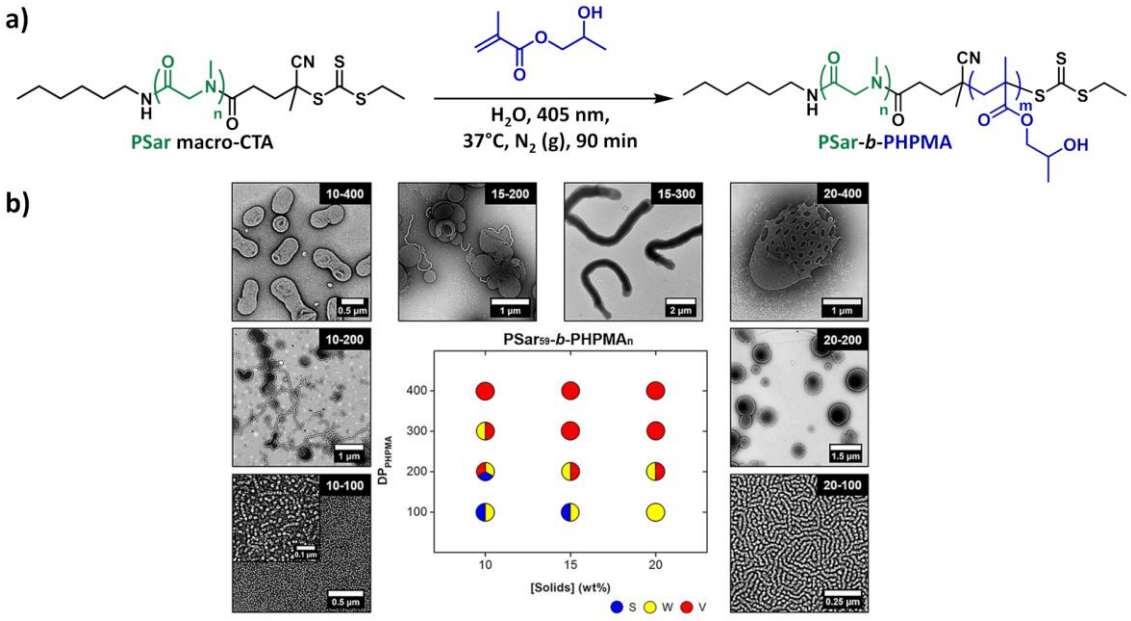

Figure I-32. (a) Aqueous RAFT-mediated Photo-PISA using a PSar based macro-CTA of HPMA. (b) Phase diagram for PSar-*b*-PHPMA diblock copolymer nano-objects by varying the solid content and DP of PHPMA with representative TEM images. Legend: S, spherical micelles (blue); W, worm-like micelles (yellow); V, vesicles (red). Adapted from O'Reilly *et al.*[247]

I.4.2.1.2. Peptides

Peptide-polymer nanoparticles are of biomedical interest because of their stimulus-responsive behavior, *e.g.* in the presence of specific enzymes, improved stability and biocompatibility, but also because of enhanced cell binding and penetration through multivalent effects.[248]

Peptide-based solvophilic stabilizers were used by Gianneschi and coworkers using ROMPISA of norbornenyl monomers in DMF/MeOH mixtures. The corresponding *L*-amino acid-based norbornene monomer was first synthesized, resulting in a ruthenium-based macroinitiator with multiple pendant peptides bearing the sequence GPLGLAGGWGERDGS, which are cleavable by thermolysin. A quaternary amine-based phenyl norbornene dicarboximide was then used as the core-forming monomer. Chain extension by ROMPISA resulted in the formation of spherical peptide-polymer nanoparticles that underwent a morphological transition from spheres to worms and vesicles upon incubation with thermolysin (Figure I-33).[234]

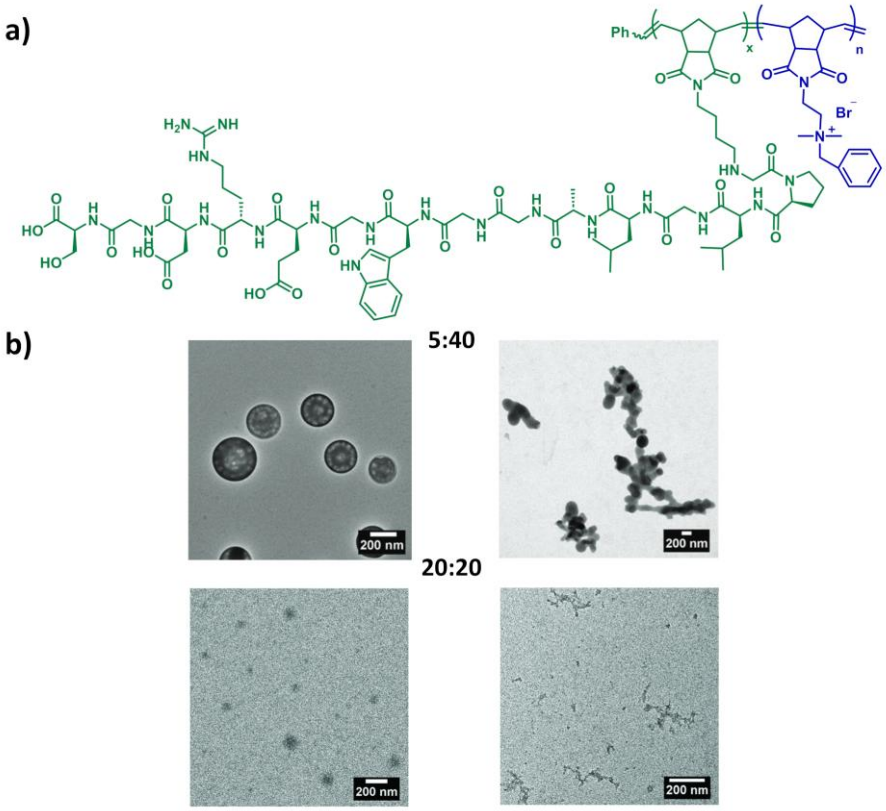

Figure I-33. (a) Structure of the peptide-polymer amphiphile obtained *via* ROMPISA. (b) Representative TEM images of nano-objects (left) before enzyme incubation and (right) after enzyme incubation for diblock copolymer nanoparticles with relative DP of 5 or 20 for hydrophilic block and 40 or 20 for hydrophobic block. Adapted from Gianneschi *et al.* [234]

Photocontrolled RAFT PISA was also performed using a macro-CTA functionalized with proapoptotic peptide side groups having the sequence KLAKLAKKLAKLAK, which are considered as anticancer therapeutics with hindered efficacy due to its low proteolytic stability as well as poor cell uptake efficiency.[249] Spherical nanoparticles were synthesized by chain extending the peptide-based macro-CTA with diacetone acrylamide (DMAc) and *N*,*N*-dimethylacrylamide (DMA), resulting in a high peptide density at high concentrations. These micelles showed improved proteolytic stability and increased cellular uptake in HeLa cells but also exhibited increased toxicity due to mitochondrial depolarization.

I.4.2.1.3. Proteins

Protein-conjugated nanoparticles offer the dual benefit of stabilizing proteins, thereby enhancing their bioactivity, and facilitating the crossing of biological barriers to enhance cellular uptake.[250] To synthesize these conjugated nanoparticles using PISA, several critical requirements must be met. First, the process must take place in aqueous media, which limits the choice of suitable core-forming monomers. Secondly, polymerization cannot be performed at high temperatures, as this can destabilize the protein.[251] Photoinitiated polymerization processes are therefore preferred. In addition, oxygen tolerance is highly desirable because conventional degassing methods, such as inert gas sparging or freeze–pump–thaw degassing, run the risk of reducing enzymatic activity and causing protein denaturation.

With these considerations in mind, bovine serum albumin (BSA) conjugated to a RAFT agent was used as a solvophilic macroinitiator for the polymerization of HPMA *via* photo-RAFT PISA. The resulting system retained 80% of its esterase-like activity towards aryl esters and showed no toxicity to NIH3T3 cells at concentrations up to 15 $mg.mL^{-1}$. In addition, hydrophilic and hydrophobic drugs, including doxorubicin, Nile Red, and deoxyribonucleic acid (DNA), were successfully encapsulated in the resulting vesicles, with protease-mediated release being demonstrated.[252]

BSA was also chain extended with DAAm and DMA *via* photo-RAFT PISA to produce worm-like and spherical nanoparticles. The morphology was influenced by factors such as the size and nature of the hydrophobic block, grafting density, and solid content. The resulting nanoparticles exhibited reduction-responsive behavior, enabling their disassembly under reductive conditions.[253]

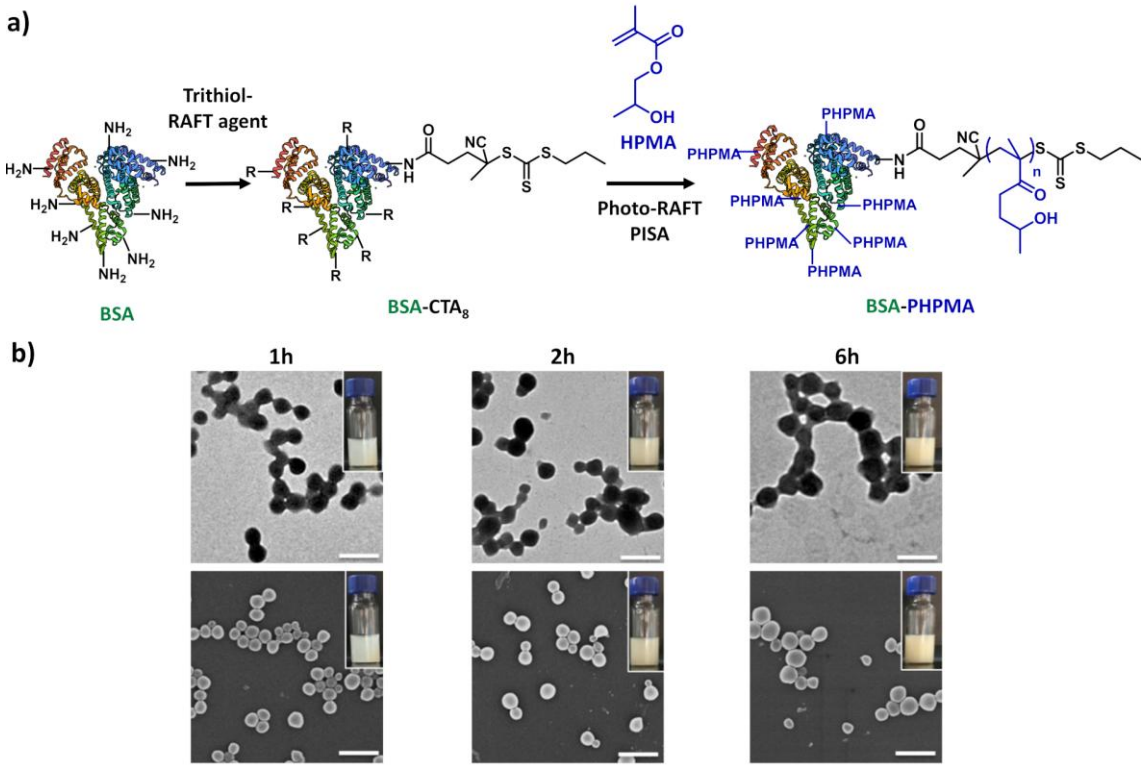

Figure I-34. (a) BSA macro-CTAs synthesis and photoinitiated PISA of HPMA for BSA-based nanoparticles synthesis. (b) (top) Representative TEM images of the BSA-PHPMA nanoparticles for a series of polymerization time and (bottom) corresponding SEM images. Scale bars = 500 nm. Adapted from Huang *et al.*[252]

Similarly, human serum albumin (HSA) was used as a stabilizer block after modification with an ATRP initiator. SDS-PAGE and steric exclusion chromatography (SEC) analysis of the hydrolyzed PHPMA chains confirmed successful chain extension with HPMA, yielding various morphologies ranging from spheres to vesicles (Figure I-35). The protein retained its activity, and no toxicity was observed towards healthy MCF-10A cells or MCF-7 cancer cells. Encapsulation of Green Fluorescent Protein (GFP) at concentrations up to 5 wt% was achieved within the vesicles, with MCF-7 cells showing improved uptake efficiency compared to GFP alone.[254]

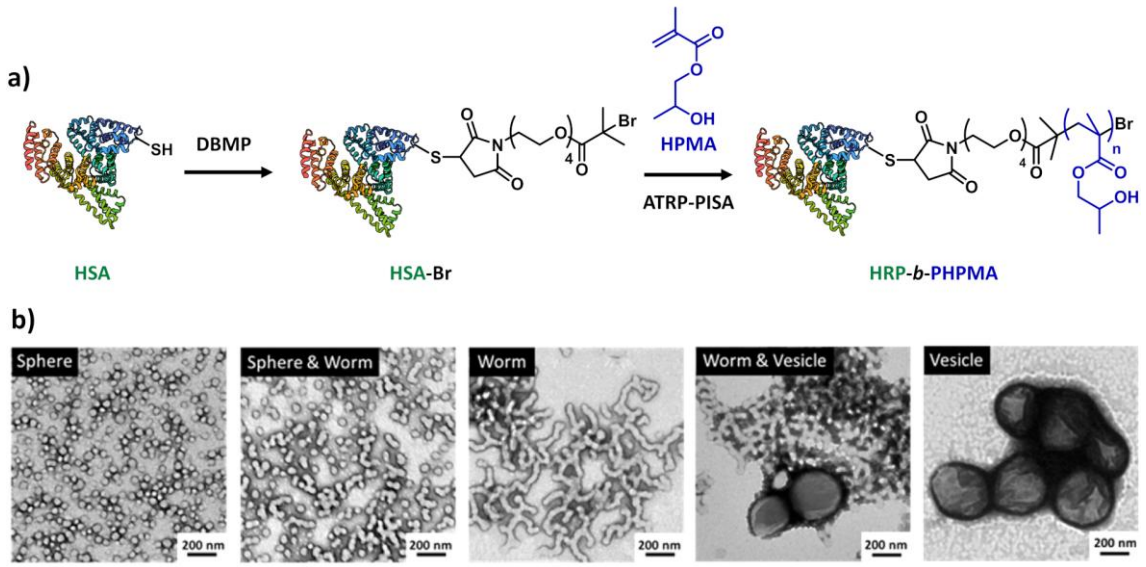

Figure I-35. (a) HRP-Br synthesis and ATRP-PISA of HPMA for HRP-based nanoparticles synthesis. (b) Representative TEM images of the HRP-PHPMA nanostructures. Adapted from Gao *et al*.[254]

Therapeutic proteins can also be used to form protein conjugated micelles. For instance, an amphiphilic block copolymer poly[oligo(ethylene glycol) methacrylate]-*block*-poly(2-hydroxypropyl methacrylate) (POEGMA-*b*-PHPMA) was grown directly from the C-terminus of the therapeutic protein interferon-α (IFN) functionalized with an ATRP initiator. The resulting IFN-conjugate micelles exhibited an *in vivo* half-life of approximately 84 hours, significantly longer than previously reported protein-polymer conjugates. In addition, the micelles retained bioactivity, demonstrated greater tumor accumulation, and effectively inhibited tumor growth, all without inducing systemic toxicity.[255] IFN was also non-covalently PEGylated by *in situ* polymerization-induced co-assembly of IFN and PEG functionalized with ATRP initiators, chain-extended with HPMA. This method preserved the bioactivity of IFN and increased its in vivo circulation half-life from 1 hour (free IFN) to 5 hours, thereby enhancing its therapeutic efficacy.[256]

Genetic encoding of an isobutyryl bromide functionality, which acts as an ATRP initiator, directly onto a superfolder (sf) GFP protein has been demonstrated. This innovative approach, demonstrated by Savin and coworkers, allowed sfGFP to function as a macroinitiator for the photo-PISA of HPMA, resulting in successful micelle formation.[257]

Enzymes such as glucose oxidase (GOx) and horseradish peroxidase (HRP) were conjugated to an ATRP initiator and chain extended together to form co-micelles. These co-micelles exhibited tunable and enhanced cascade enzymatic activity.[258] Candida antarctica lipase B based spherical nanoparticles were also synthesized using Cu(0)-mediated reversible deactivation radical polymerization (RDRP-PISA). This method involved the chain extension of *N*-tert-butylacrylamide (TBA) and methyl acrylate (MA) in a MeOH/water mixture. The resulting nanoparticles exhibited preserved and even enhanced activity compared to the native lipase in the hydrolysis of p-nitrophenyl palmitate due to specific interfacial behavior.[259]

I.4.2.1.4. Functional nucleic acids

Functional nucleic acids (FNA), including aptamers, DNAzymes, and CpG oligodeoxynucleotides, possess molecular recognition, catalytic activities, and therapeutic potential, making them critical in biomedical applications. When conjugated to nanoparticles, their stability is improved, and their activity is enhanced, offering significant potential for effective targeting of tumor cells.[260]

Sgc8 aptamer and CpG oligonucleotide functionalized into a RAFT macro-CTA were successfully chain extended with HPMA and exhibited different morphologies by PISA. They exhibited higher nuclease resistance as well as greater cellular uptake efficiency and increased bioactivity.[261] A 19-mer single-stranded DNA (3′-ATC ATC CAC CAT CTC TTT T-5') functionalized with a RAFT chain transfer agent was also used as a macroinitiator to polymerize acrylamide and acrylate monomers. This acrylamide-based approach resulted in the formation of spherical and worm-like micelles capable of hybridizing with complementary ssDNA' on the PISA worm structures (Figure I-36).[262]

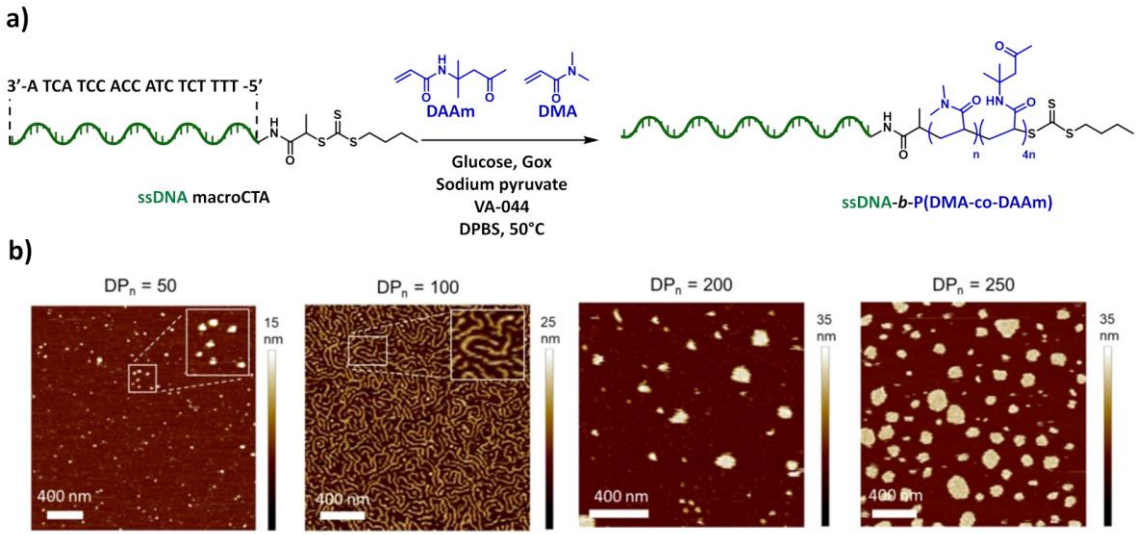

Figure I-36. (a) PISA from ssDNA as macroinitiator using DMA and DAAm as the monomers. (b) Representative AFM images recorded by liquid AFM after PISA using a [DAAm]/[DMA] ratio of 80:20, with different DP targeted. Adapted from Weil *et al*.[262]

I.4.2.1.5. Polysaccharides

Polysaccharides, known for their biocompatibility, bioactivity, and stability, also serve as promising solvophilic blocks for targeting tumor cells due to the overexpression of sugar receptors on their surface.[263]

The first PISA synthesis of polysaccharide-polymer nanoparticles was achieved in 2008 by Charleux's group and consisted of the synthesis of dextran-polymer nano-objects *via* RAFT-PISA. The dextran was end-functionalized with a xanthate moiety by click chemistry and was used as a RAFT agent in surfactant-free emulsion PISA of vinyl acetate, resulting in latex particles.[264]

Alginate polymer nanoparticles were also obtained by ATRP-PISA by incorporating ATRP initiators onto the side chains of the alginate fragment *via* esterification reaction. Methyl methacrylate (MMA) was then chain extended under ATRP conditions in a water/MeOH mixture, resulting in brush-like

alginate-PMMA conjugates that simultaneously self-assembled into spherical micelles.[265] From another perspective, glycuronan, from alginate, was functionalized and copolymerized with *N*-acryloylmorpholine by aqueous RAFT to be used as a macro-CTA to initiate emulsion RAFT-mediated PISA of styrene in water. Polystyrene-latex decorated with alginate were then obtained in quantitative yield and short polymerization time.[266]

Xyloglucan after being functionalized into a RAFT macro-CTA by reducing its chain end to carry a dithioester moiety was also chain-extended with MMA in water, resulting in stable latex nanoparticles with a xyloglucan shell and a PMMA core.[267]

In the above examples, polysaccharide-initiated PISA resulted in predominantly spherical nanoparticles. However, Ferji and coworkers achieved higher-order hierarchical structures by synthesizing dextran-*grafted*-PHPMA nanoparticles *via* photo-initiated RAFT-PISA. By varying the graft length and solid content, they successfully produced spherical, worm-like, and vesicular nanoparticles, and were able to tune membrane thickness with grafts length (Figure I-37).[268,269] This example stands out as the only demonstration of vesicle formation with a polysaccharide shell, a morphology of considerable interest for biomedical applications.[142] However, because the system relies on a graft copolymer, the number and distribution of initiator sites cannot be precisely controlled, potentially affecting the reproducibility of higher order morphologies.

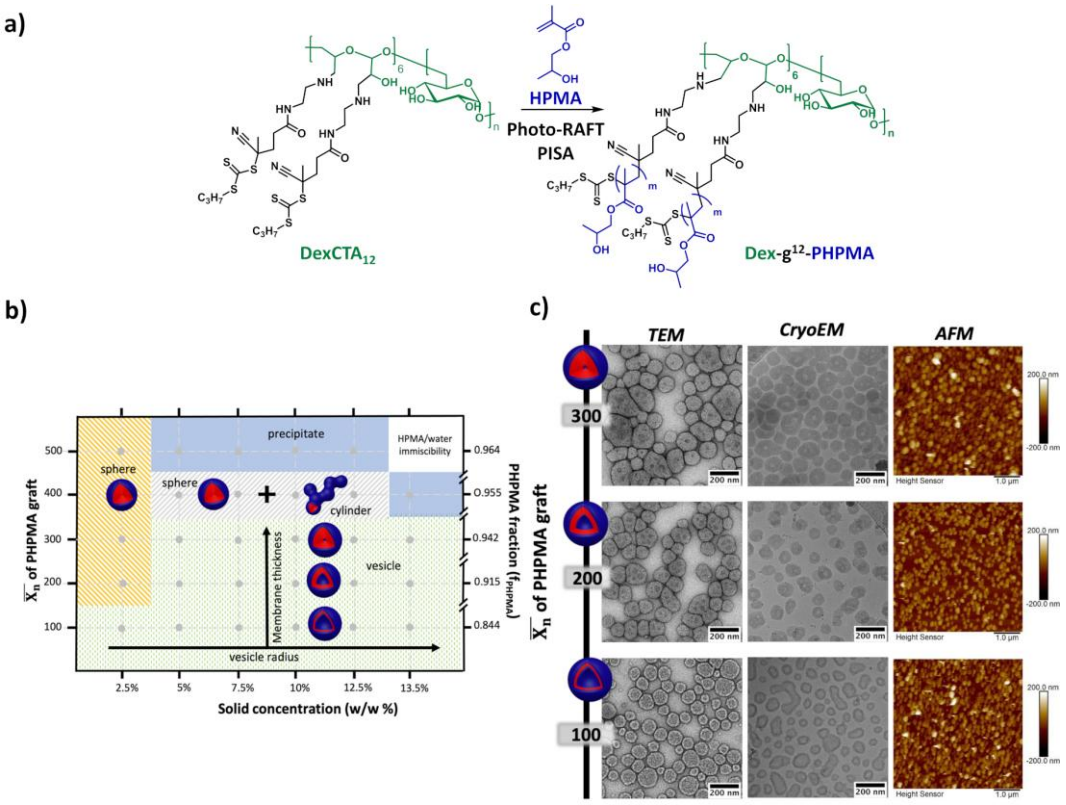

Figure I-37. (a) Nano-objects of Dex-g_{12}-PHPMA obtained *via* aqueous photo-raft mediated PISA of HPMA from $DexCTA_{12}$. (b) Phase diagram of the obtained nano-objects morphologies by tuning the solid content and the DP of each PHPMA graft. c) Representative TEM, CryoTEM and AFM of obtained vesicles at 7.5 wt% showing an increase in membrane thickness with the DP of PHPMA. Adapted from Ferji *et al*.[268]

I.4.2.2. Degradable core: apply ROP with PISA

I.4.2.2.1. rROPISA

While the incorporation of biomacromolecules into the nanoparticle shell to provide functionality and degradability has attracted considerable interest in drug delivery applications, the degradability of the nanoparticle core is equally critical. As mentioned above, the primary polymerization techniques employed in PISA are radical polymerizations that produce vinyl-based polymer nanoparticles. However, the non-degradability of these materials limits their applicability in most biomedical contexts. Their inability to be metabolized or excreted raises concerns about potential toxic accumulation of foreign materials in the body.[270] Significant efforts have therefore been made to introduce degradability into vinyl polymer nanoparticles while retaining the key features of radical polymerization and PISA. These include the controlled/"living" nature of the polymerization, which allows the synthesis of well-defined, narrowly dispersed polymers, and the *in situ* self-assembly of highly concentrated nanoparticles.

Radical ring-opening polymerization (rROP) of cyclic ketene acetal (CKA), dibenzo[c,e]oxepane-5-thione (DOT), or 3-methylene-1,9-dioxa-5,12,13-trithiacyclopentadecane-2,8-dione (MTC) represents an efficient strategy for incorporating degradable moieties, such as ester, thioester, or disulfide groups, into the polymer backbone. The combination of rROP with PISA then offers a promising strategy to produce degradable nanoparticles for biomedical applications.[271]

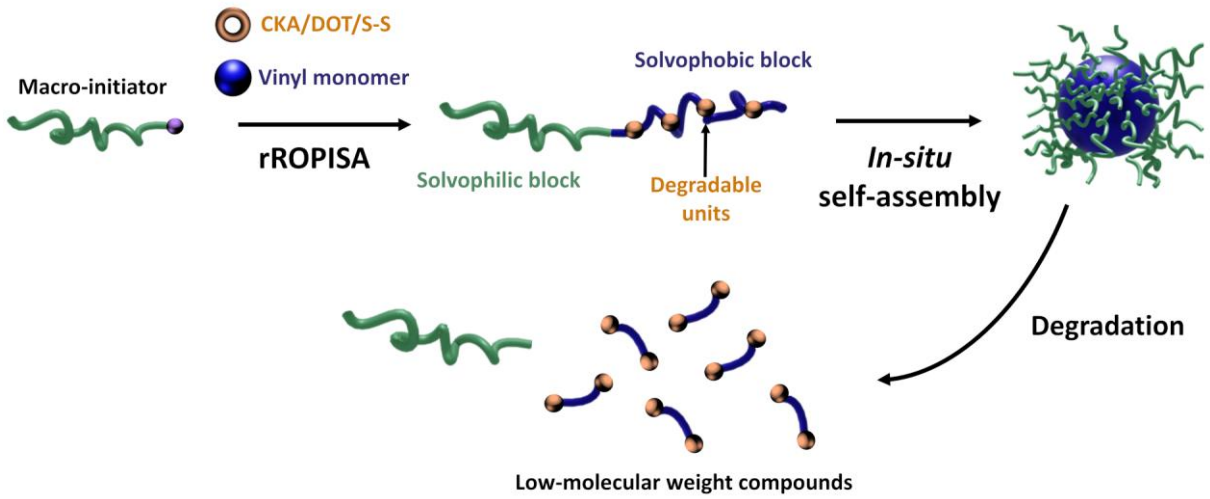

Figure I-38. General strategy for radical ring-opening polymerization-induced self-assembly (rROPISA), allowing the *in situ* obtention of nanoparticles with degradable units, *via* the incorporation of ester, thioester moieties or disulfide bonds.

I.4.2.2.1.1. CKAs

Radical ring-opening polymerization (rROP) of cyclic ketene acetals (CKAs) is an approach to impart degradability to the vinyl polymers obtained in most PISA processes. In fact, it is a simple way to introduce labile groups into the copolymer chain (Figure I-39a).[270–275] CKA monomers can, under the right conditions, polymerize by an rROP mechanism and provide ester groups in the copolymer backbone, that can be further degraded by hydrolysis or enzymatic pathways, resulting in a decrease in the molar mass of

the initial copolymer. Three main CKAs are used: 2-methylene-1,3-dioxepane (MDO), 5,6-benzo-2-methylene-1,3-dioxepane (BMDO) and 2-methylene-4-phenyl-1,3-dioxolane (MPDL) (Figure I-39b).

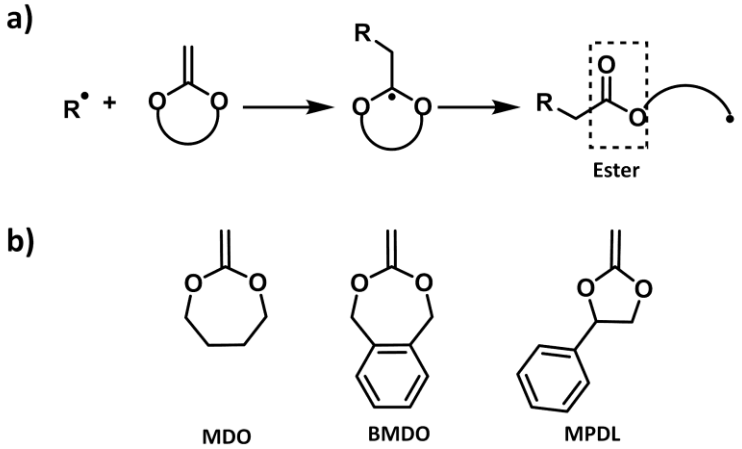

Figure I-39. (a) Radical ring-opening polymerization (rROP) of cyclic ketene acetal (CKA). (b) Three main cyclic ketene acetals (CKAs) employed to confer degradability by rROP.

The first radical ring-opening polymerization-induced self-assembly (rROPISA), which combined rROP with PISA, was reported by Nicolas and colleagues in 2019.[276] CKAs were copolymerized with benzyl methacrylate (BzMA) in heptane at 90°C during chain extension of a poly(lauryl methacrylate) (PLMA) macro-CTA. This process was applied to MPDL, BMDO and MDO.[277] rROPISA was performed in heptane to avoid hydrolysis of CKA monomers. Degradable sites were successfully obtained in the vinylic copolymer nanoparticles thanks to the incorporation of CKA units in the solvophobic block. Stable spherical nanoparticles were obtained, regardless of the block length ratio or the fraction of CKA in the core, in contrast to the analogous PISA system without CKA reported by Armes and colleagues, as shown in Figure I-40.[278] This was attributed to the influence of CKA and RAFT agent on the self-assembly. The degradability of the copolymers and films formed by solvent casting was confirmed under accelerated conditions (2.5 wt% KOH), but the degradation of the nanoparticles was not evaluated.

Nicolas and colleagues went a step further by positioning the CKA either at the surface, the core or both sites of the nanoparticles to enhance the degradability.[277] By incorporating BMDO or MPDL into the macro-CTAs of poly(laury methacrylate), P(LMA-*co*-MPDL) and P(LMA-*co*-BMDO) macro-CTAs were chain extended by BzMA under PISA conditions, with or without CKA, to obtain “all-degradable” nanoparticles. Stable spherical nanoparticles were obtained despite poor control of the polymerization during chain extension and poor livingness of the macro-CTAs. An accelerated degradation study confirmed the presence of ester groups at the desired sites.

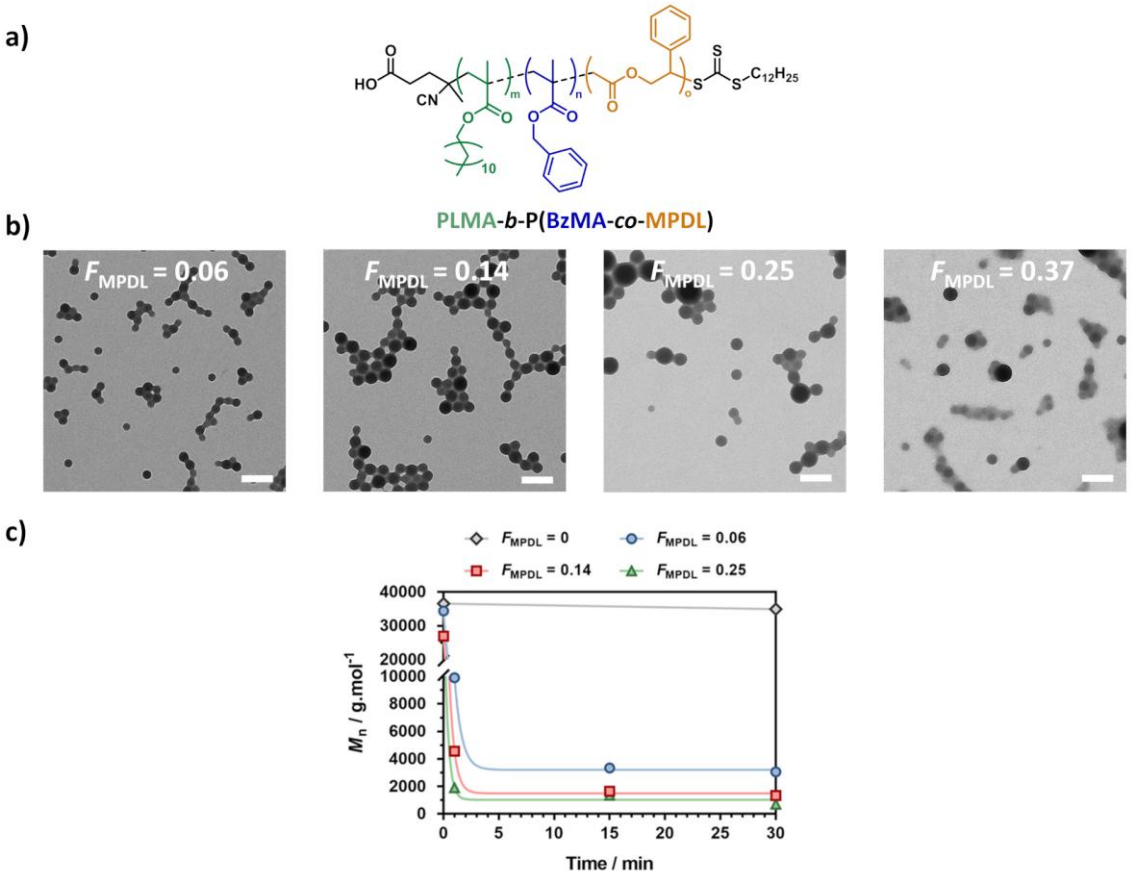

Figure I-40. (a) Obtained copolymer after rROPISA of BzMA and MPDL by PLMA macro-CTA. (b) Representative TEM images of PLMA-*b*-P(BzMA-*co*-MPDL) nanoparticles as function of the molar fraction of MPDL (F_{MPDL}). Scale-bars = 200 nm. (c) Number-average molar mass (M_n) overtime during degradation under accelerated conditions (THF/MeOH, 2.5% KOH) of PLMA-*b*-P(BzMA-*co*-MPDL) as a function of F_{MPDL}. Adapted from Nicolas *et al*.[276]

Despite the progress in introducing partial degradability to vinyl polymer nanoparticles synthesized *via* PISA, this approach has not been directly implemented in aqueous dispersed media due to the extreme sensitivity of CKA. In addition, the transfer of this method to PLMA-based nanoparticles has been unsuccessful due to their hydrophobic nature. A two-step rROPISA process was then developed to obtain aqueous nanoparticle suspensions (Figure I-41).[279] First, poly[oligo(ethylene glycol) methyl ether methacrylate]-*block*-poly(lauryl methacrylate-*co*-cyclic ketene acetal) (POEGMA-*b*-P(LMA-*co*-CKA)) diblock copolymer nanoparticles were synthesized in DMF at 15 wt% solid content from a solvophilic POEGMA macro-CTA. The resulting suspension was then dialyzed into water. The colloidal properties remained unchanged due to the effective stabilization provided by the POEGMA shell, which has PEG-like properties. As in previous studies, the resulting nanoparticles remained spherical regardless of the relative volume fraction of the blocks and the amount of CKA incorporated. The three major CKAs were successfully incorporated into the core of the nanoparticles, and their degradation was confirmed under accelerated conditions. Cell viability was also investigated on macrophages (J774.A1), endothelial cells (HUVEC) and fibroblasts (NIH/3T3) for three representative nanoparticle libraries: $POEGMA_{23}$-*b*-$P(LMA_{150}$-*co*-MPDL), $POEGMA_{23}$-*b*-$P(LMA_{150}$-*co*-MDO) and $POEGMA_{52}$-*b*-$P(LMA_{300}$-*co*-MPDL). The study investigated the effects of CKA with initial molar fractions ranging from 0 to 0.7, as well as the influence of POEGMA block length. Viability was maintained in all cell lines and no adverse effects were

observed for any combination of CKA type, POEGMA chain length, or content, confirming the biocompatibility of the nanoparticles and their potential for drug delivery applications. The same system was therefore used to synthesize degradable polymeric prodrug nanoparticles.[280] Paclitaxel and gemcitabine were chemically modified into methacrylate derivatives for incorporation into the PISA process *via* copolymerization with a $POEGMA_{28}$ macro-CTA. The resulting nanoparticles had a spherical morphology, although excess drug disrupted the self-assembly. The drugs incorporated into the polymer backbone exhibited slower degradation, probably due to hydrophobic effects and steric hindrance. Both drugs exhibited cytotoxicity against cancer cells, with lower IC50 values in A549 cells compared to free drugs, indicating delayed release from the polymer prodrugs.

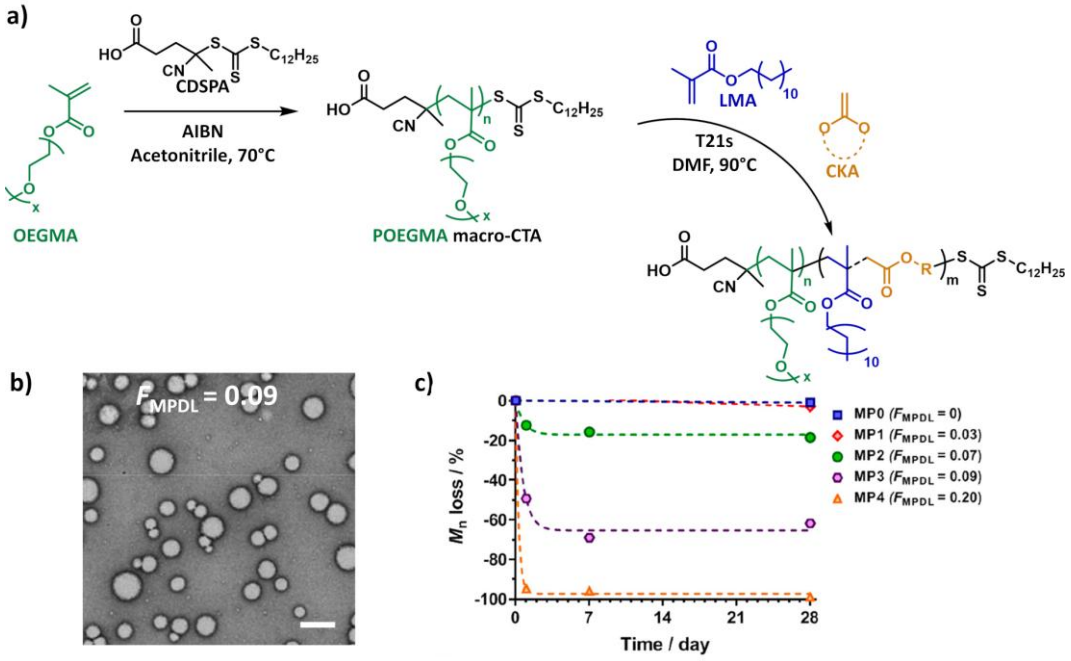

Figure I-41. (a) RAFT-mediated polymerization of oligo(ethylene glycol)methyl ether methacrylate (OEGMA) followed by radical ring-opening copolymerization-induced self-assembly (rROPISA) of lauryl methacrylate (LMA) and cyclic ketane acetal (CKA) to produce degradable POEGMA-*b*-P(LMA-*co*-CKA) diblock copolymer nanoparticles. (b) Representative TEM image of $POEGMA_{23}$-*b*-P(LMA_{150}-*co*-$MPDL_{0.09}$). Scale-bar: 200 nm. (c) Number-average molar mass (M_n) overtime during degradation under accelerated conditions (THF/MeOH, 2.5% KOH) of POEGMA-*b*-P(LMA-*co*-MPDL) as a function of F_{MPDL}. Adapted from Nicolas *et al.* [279]

The application of rROPISA to copolymerize CKA monomers with a PLMA or POEGMA macro-CTA and its use to obtain degradable prodrug nanoparticles represented a significant step forward in obtaining degradable drug delivery systems *via* PISA. However, this approach was limited to spherical morphologies, probably due to the influence of the CKA and the CTA used. To diversify the morphologies, Xiao *et al.* performed rROPISA of styrene and BMDO in MeOH, using poly(4-vinylpyridine) (P4VP) as macro-CTA (Figure I-42).[281] Various morphologies of core degradable nanoparticles were obtained, including spheres, worms, vesicles. Degradation experiments under accelerated conditions (THF/MeOH, 5 wt% KOH) confirmed the degradability behavior of the nanoparticles, although the degradation rate was relatively low (35.6% degradation in 7 days). This may be due to the incorporation of CKA, which is mainly located at the end of the polymer chain. As they have low polymerization reactivity, their copolymerization

with more activated monomers results in the formation of a gradient along the polymer backbone. Degradation typically results in oligomers of different molar masses. This process is even more challenging in nanoparticles, where degradable blocks are embedded in the core, due to the uneven distribution of ester groups.

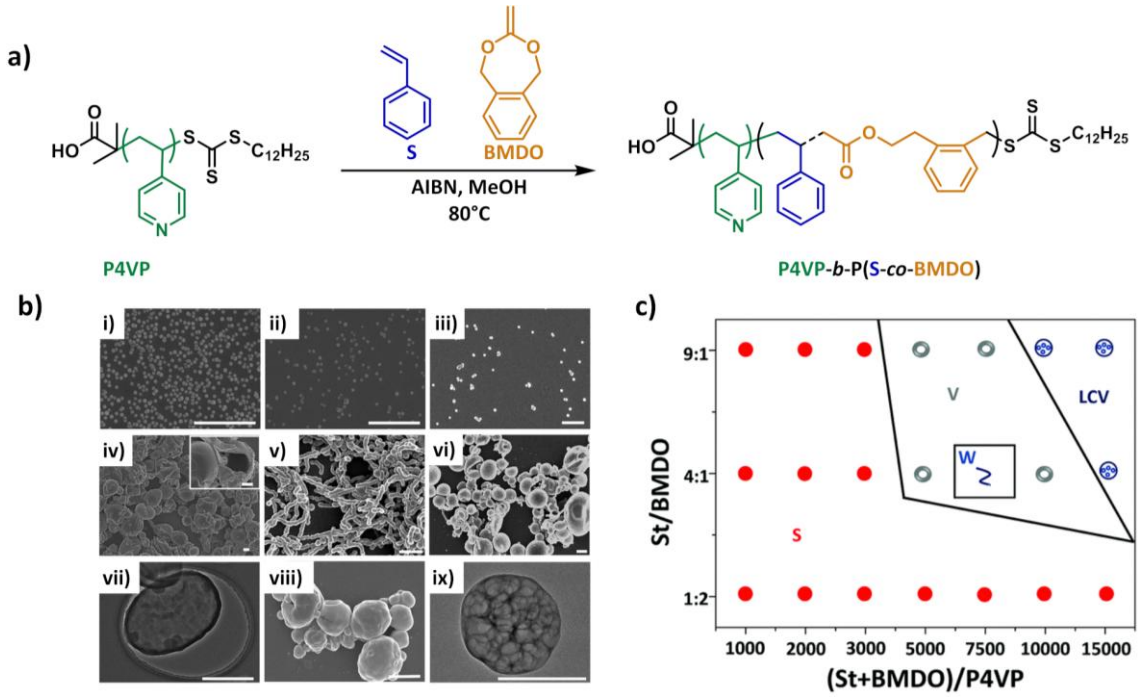

Figure I-42. (a) Radical ring-opening copolymerization-induced self-assembly (rROPISA) of styrene (S) and 5,6-benzo-2methylene-1,3-dioxepane (BMDO) by chain extension of poly(4-vinylpyridine) (P4VP) macro-CTA to produce degradable P4VP-*b*-P(S-*co*-BMDO) diblock copolymer nanoparticles. (b) Representative SEM (i – vii) and TEM (viii – ix) images P4VP-*b*-P(St-*co*-BMDO) aggregates. Scale-bar: 1 µm. (c) Overall phase diagram for polymeric nanomaterials obtained *via* rROPISA. S: spheres, V: vesicles, and W: worms. Adapted from Xiao *et al*.[281]

I.4.2.2.1.2. DOT

Despite the progress and potential application of rROPISA of CKAs in drug delivery through prodrug synthesis, direct aqueous polymerization remains not feasible. In addition, CKAs exhibit low reactivity and radical competition mechanisms between radical ring opening and ring retention propagation, leading to the incorporation of non-degradable ketal units in the chain.[282] In this context, another method of rROPISA has been developed by using thionolactone, in particular dibenzo[c,e]oxepane-5-thione (DOT), which can be polymerized *via* thiocarbonyl addition ring-opening (TARO),[283] and copolymerized with vinyl monomers, the insertion of which leads to cleavable thioester units in the backbone (Scheme I-4). [271]

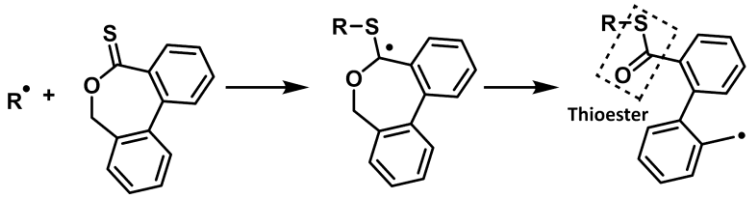

Scheme I-4. Thiocarbonyl addition – ring-opening (TARO) copolymerization of dibenzo[c,e]oxepan-5thione (DOT).

DOT monomers are known for their high stability in protic solvents, ease of synthesis, and ability to incorporate significant degradable fractions when copolymerized with acrylates or styrene.[284] Of great

interest compared to CKAs, is that DOT are not subject to hydrolysis, making them easier to use in aqueous dispersion media.[284] Nicolas and colleagues applied the rROP of DOT under aqueous conditions *via* nitroxide-mediated polymerization with vinyl monomers such as styrene or *n*-butyl acrylate (*n*BA), using a poly(acrylic acid) macroalkoxyamine as a macroinitiator (Figure I-43).[285] This aqueous emulsion rROPISA method produced spherical latex nanoparticles with DOT incorporation of up to 3 mol%, achieving effective polymer degradation under aminolytic or basic conditions (up to a 79% decrease in number average molar mass (M_n) for dry extracts). However, degradation of the nanoparticles was less efficient, with M_n loss of up to 56% for *n*BA-based particles, possibly due to the protective PANa shell preventing adequate swelling by the TBD base. Interestingly, copolymers formed from *n*BA and DOT exhibited greater degradability than those formed from DOT and styrene, likely due to differences in the placement of thioester units along the polymer backbone, driven by the different copolymerization mechanisms of the two comonomers.

RAFT-mediated emulsion copolymerization of DOT with *n*-butyl acrylate or styrene, using biocompatible poly(*N*-acryloylmorpholine) (PNAM) and PEG as macro-CTAs, was then achieved to obtain core-degradable nanoparticles that exhibited better degradability than latexes obtained with poly(acrylic acid) macro-CTA.[286] This work demonstrated that nanoparticles with a biocompatible shell and a degradable vinylic core can be obtained directly in water, paving the way for the use of DOT-rROPISA to design nanocarriers.

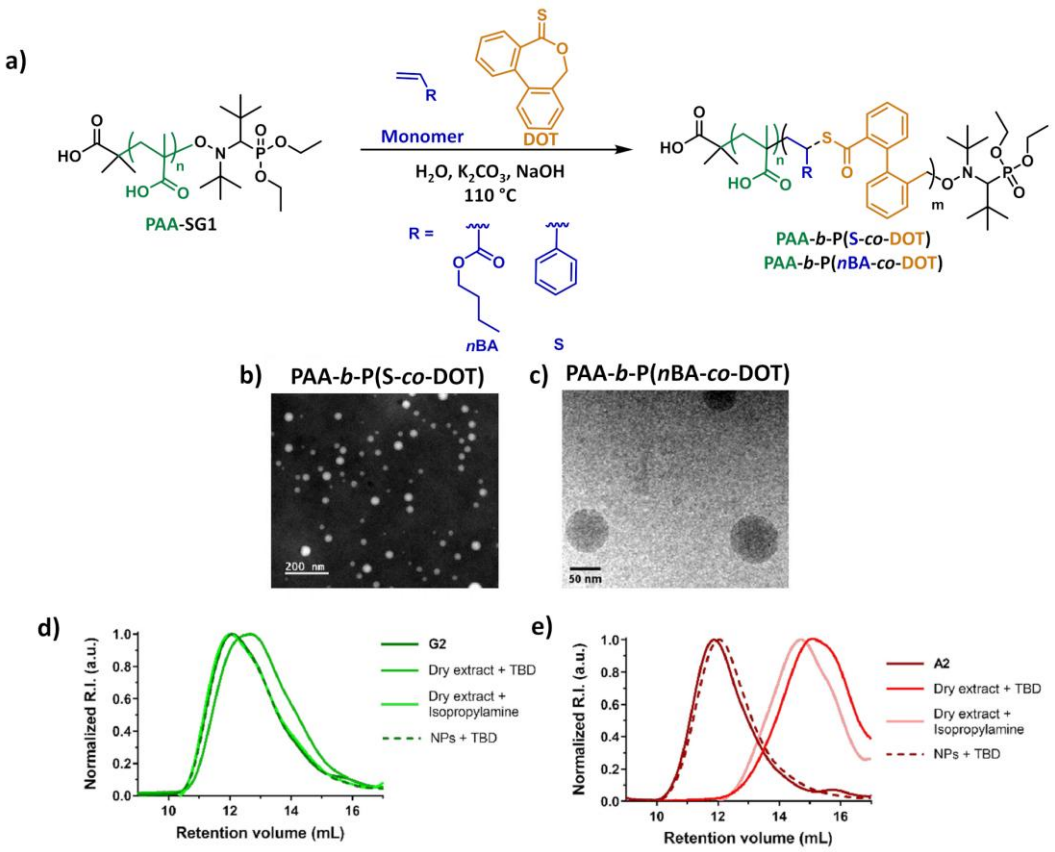

Figure I-43. (a) Synthesis of degradable vinyl polymer nanoparticles *via* aqueous nitroxide-mediated radical ring-opening copolymerization-induced self-assembly (rROPISA) of DOT and vinyl monomers (*n*-butyl acrylate *n*BA, styrene S) from poly(acrylic acid) macroinitiator. (b) Representative TEM image of PAA-*b*-P(S-*co*-DOT) nanoparticles. (c) Representative cryo-TEM image of PAA-*b*-P(*n*BA-*co*-DOT) nanoparticles. (d) Evolution of SEC chromatograms of PAA-*b*-P(S-*co*-DOT) copolymer after degradation of dry extracts or nanoparticles with isopropylamine or TBD. (e) Evolution of SEC chromatograms of PAA-*b*-P(*n*BA-*co*-DOT) copolymer after degradation of dry extracts or nanoparticles with isopropylamine or TBD. Adapted from Nicolas *et al*.[285]

Despite the promise of DOT copolymerization, current DOT-containing PISA formulations are limited to spherical morphologies, highlighting the need for further research to achieve more complex, higher order structures with degradable properties. In addition, these formulations have not yet been explored for drug loading applications.

I.4.2.2.1.3. Disulfide-based cyclic monomers

Incorporation of disulfide bonds into the polymer backbone is another strategy for creating degradable nanoparticles *via* rROPISA. In this approach, disulfide-containing cyclic monomers, such as 3-methylidene-1,9-dioxa-5,12,13-trithiacyclopentadecane-2,8-dione (MTC) are copolymerized with HPMA using a biocompatible poly(glycerol monomethacrylate) (PGMA) macro-CTA in water, as demonstrated by Paulusse and colleagues (Figure I-44).[287] Spherical, worm-like and vesicle-like nanoparticles were obtained by adjusting the hydrophobic/hydrophilic fraction, but only 1 mol% of MTC was incorporated to avoid side reactions. Even though the incorporation of MTC was low, degradation by addition of tris(2-carboxyethyl)phosphine (TCEP) was assessed by a reduction of M_n of nearly 50% after 16 hours, as well as a worm-to-sphere transformation for TCEP-treated nanoparticles after 8 days. However, a high incorporation of MTC results in increased molecular weight dispersity, while low incorporation results in

a lack of disulfide bonds in the polymer chain. The development of new cyclic monomers with improved polymerization activity and reduced side reactions may provide better control over the polymerization process and facilitate degradation.

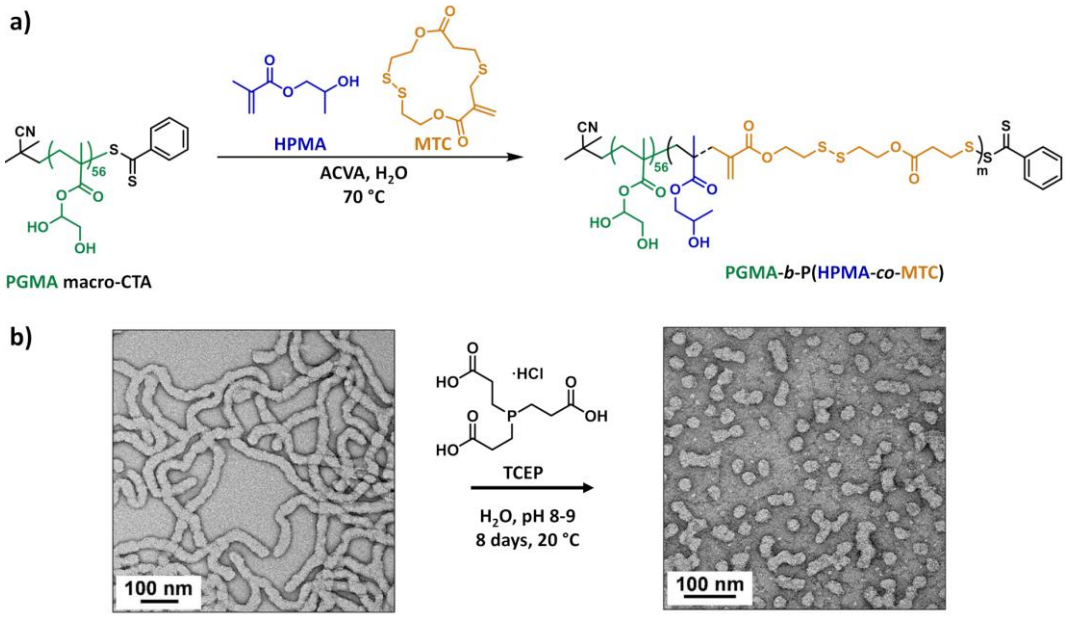

Figure I-44. (a) Synthesis of $PGMA_{56}$-*b*-P(HPMA-*co*-MTC) diblock copolymer nano-objects *via* rROPISA of HPMA with MTC from a PGMA macro-CTA in aqueous solution at 70 °C. (b) Representative TEM images before (left) and after (right) exposure to TCEP at pH 8-9 for 8 days at 20°C showing a worm-to-sphere transition by disulfide bond cleavage. Adapted from Paulusse *et al*.[287]

Overall, the combination of radical ring-opening polymerization with polymerization-induced self-assembly represents a promising strategy for the integration of degradable moieties into well-established PISA systems. This approach allows the design of nanoparticles with inherent degradability, in aqueous media, and the generation of prodrug nanoparticles, paving the way for nanomedicine applications. However, the incorporation of degradable units such as CKA, DOT groups, or disulfide bonds into the polymer backbone poses significant challenges. The synthesis requires strict control of reaction conditions to minimize side reactions, such as incomplete ring opening or radical termination events, which can lead to poor reproducibility and loss of control over the polymerization process. In addition, the lower polymerization reactivity of these degradable units complicates their incorporation into the copolymer chain, often resulting in uneven copolymerization. This leads to a gradient distribution of monomers within the polymer, causing partial degradation, with segments of the polymer chain remaining intact. Such residual polymer chains, particularly those of high molar mass, could accumulate in biological systems without being efficiently metabolized, potentially leading to toxicological concerns. In addition, degradability is often demonstrated under alkaline conditions, which do not accurately reflect the biological environment, where acidic conditions prevail within cellular compartments.[288] The persistence of these non- or slowly degradable chains *in vivo* represents a significant barrier to the broader application of rROPISA-based degradable polymer systems in drug delivery. Finally, anisotropic morphologies, such as rod- or worm-like micelles, are rarely achieved, and when they are, they often coexist with other morphologies.

I.4.2.2.2. ROPI-CDSA

The ROP of cyclic esters and carbonates yields degradable polyesters and polycarbonates, many of which exhibit semi-crystalline properties. When coupled with CDSA, these materials can leverage their semi-crystallinity to form anisotropic 1D and 2D nanostructures, with crystallization serving as the driving force for self-assembly, as discussed in section I.3.3.2.2. This approach is particularly advantageous for drug delivery applications, allowing the production of non-spherical nanoparticles with degradable cores, such as those based on poly(lactic acid) or poly(caprolactone).[289] However, like traditional self-assembly, CDSA typically occurs in dilute solutions.

With the advent of polymerization-induced crystallization-driven self-assembly (PI-CDSA) with sequential living anionic polymerization,[290] and the ring-opening metathesis of organometallic polymers (ROMPI-CDSA),[291] ring-opening PI-CDSA (ROPI-CDSA) was investigated by Patterson *et al.* to obtain high-concentration polylactide-based crystalline nanoparticles in a single step (Figure I-45).[242] In this approach, polymerization and self-assembly of a block copolymer with a crystallizable core-forming block occur simultaneously *in situ*. This strategy effectively combines the advantages of CDSA, such as the ability to access micelle morphologies with low interfacial curvature, and those of PISA, including scalability and practical feasibility. By using PEG as macroinitiator and TBD as catalyst, ROPI-CDSA of *L*-lactide was carried out in toluene, resulting in poly(ethylene glycol)-*b*-poly(*L*-lactide) block copolymer nanoparticles with 1D, 2D and 3D structures at concentrations ranging from 5 to 20 wt% due to the non-equilibrium self-assembly process. They hypothesized that the kinetics of polymerization was faster than that of self-assembly, resulting in "kinetically frozen" morphologies.

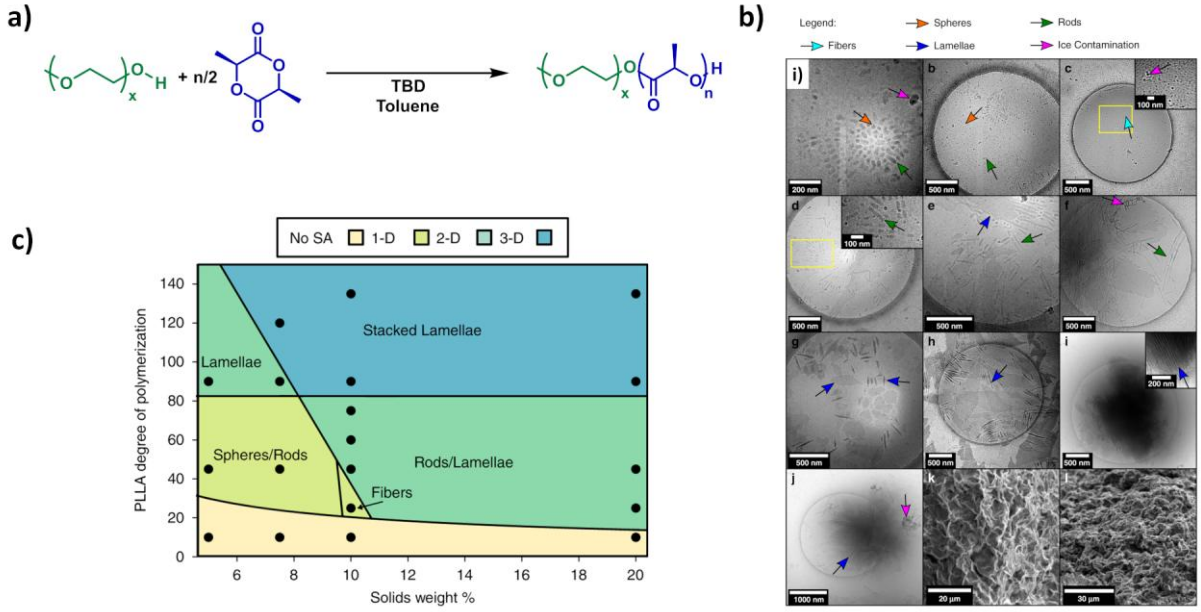

Figure I-45. (a) Synthesis of PEG-*b*-PLLA copolymer nanoparticles *via* ROPI-CDSA of *L*-lactide in toluene from a poly(ethylene glycol) macro-initiator, catalyzed by TBD. (b) Representative images of ROPI-CDSA morphologies. (a-j): Cryo-TEM; (k-l): SEM. (c) ROPI-CDSA phase diagram. No SA: no self-assembly. Adapted from Patterson *et al.*[242]

To verify this hypothesis, Patterson's group performed kinetic studies of polymerization and self-assembly using two ROP catalytic systems, one fast and one slow, to tune the polymerization rate of *L*-lactide.[292] They showed that fast reactions favored the formation of 2D lamellae, whereas the slow reactions led to the formation of 3D networks and strong gels (Figure I-46).

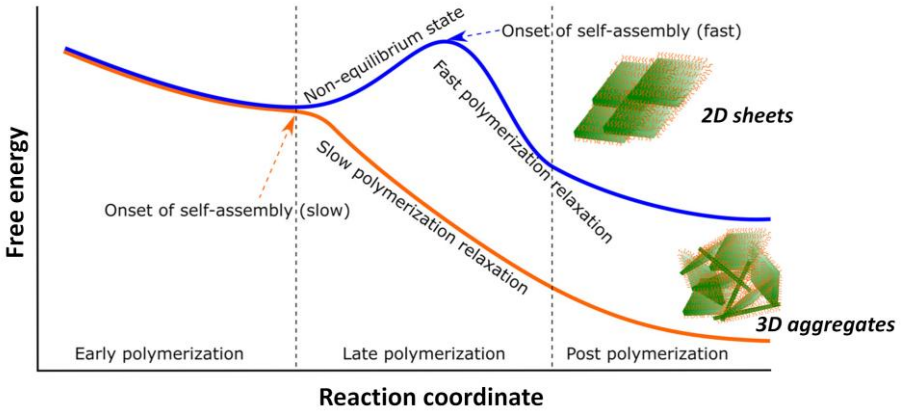

Figure I-46. Free energy diagram illustrating the impact of polymerization rate on the ROPI-CDSA process and the resulting morphologies. Polymerization occurs in three distinct stages: (i) early polymerization, where polymers lack the thermodynamic driving force for self-assembly; (ii) late polymerization, where self-assembly becomes thermodynamically favorable; and (iii) *post*-polymerization. The relative rates of polymerization and self-assembly dictate the final morphology: rapid polymerization leads to a transient nonequilibrium state, favoring kinetically trapped 2D sheet-like structures, whereas slower polymerization allows for the formation of 3D aggregates. Adapted from Patterson *et al*.[292]

Moving towards drug delivery applications, Patterson and colleagues also used drugs with functional groups similar to those of the ROP organocatalyst, such as trimethoprim and chlorhexidine, to catalyze the ROPI-CDSA of *L*-lactide (*L*-LA) *via* chain extension of a PEG macroinitiator.[293] This process resulted in the formation of two different types of drug delivery systems with different morphologies and antibacterial properties. In the case of chlorhexidine, it acted as both a catalyst and a co-initiator, resulting in the formation of drug-conjugated polymers within the nanoparticle suspensions. For trimethoprim, no drug conjugation occurred, but effective drug loading was achieved within the core of the nanoparticles, with a high encapsulation efficiency (EE > 80%), and the resulting drug nanocarriers exhibited significant antibacterial activity.

Fully degradable nanoparticles can also be obtained by ROPI-CDSA. Sequential ROP of *D*-*L*-lactic acid (*D*,*L*-LA) and *L*-lactid acid monomers in toluene was reported by Weng and colleagues, where the crystalline PLLA served as the core-forming block, while the amorphous PDLLA acted as a stabilizer block.[246] Various morphologies, ranging from spherical micelles to platelets, were obtained depending on the solid content, solvent, and relative volume fraction between the two blocks. Nano-objects with polycaprolactone and poly(δ-valerolactone) as the stabilizer block have also been obtained. Unfortunately, these methods showed poor size control.

With the synthesis of poly(*N*,*N*-dimethylacrylamide)-*block*-poly(*L*)-lactide (PDMA-*b*-PLLA) by ROPI-CDSA, Patterson and coworkers,[294] inspired by the earlier work on CDSA by O'Reilly *et al,*[295,296] successfully obtained uniform nanorods. Fluorene trimethylene carbonate (FTMC), a carbonate monomer,

can also undergo ROPI-CDSA when initiated by poly(ethylene glycol). This process yields nanofibers with tunable lengths, depending on the solid content and monomer conversion. In addition, uniform 1D nanofibers can be generated by a living PI-CDSA approach using preformed poly(ethylene glycol)-*b*-poly(fluorenetrimethylene carbonate) (PEG_{205}-*b*-$PFTMC_{17}$) seeds, which are nanofibers fragmented by sonication. The length of the nanofibers can be precisely adjusted by varying the monomer to seed ratio.[297]

In conclusion, ROPI-CDSA is a promising approach to produce degradable, anisotropic nanostructures suitable for drug delivery applications. However, it faces similar challenges to traditional CDSA in terms of drug loading, with only a few examples reported to date. Furthermore, as this process is relatively new, its underlying mechanisms are still under investigation, and a deeper understanding could help to optimize drug loading strategies.

I.4.2.2.3. ROPISA

The combination of ROP of NCA with PISA represents an exciting opportunity to obtain functional, biocompatible and biodegradable nanoparticles based on polypeptides or polyesters. Apart from semicrystalline core-forming polymer and CDSA associated with ROP, the first ROPISA of NCA was reported by Du and coworkers with the open-to-air chain-extension of PEG-NH_2 with *L*-phenylalanine and *L*-aspartic acid β-benzyl ester (BLA) NCAs in THF.[244] Complete conversion of Phe-NCA was observed after 8 hours of reaction. Spherical nanoparticles and vesicles were obtained by adjusting monomer to initiator ratio and the solid content. Spheres were formed at 10 wt% and vesicles were observed when a longer core forming block DP was used at 20 wt%. The biodegradability of the obtained vesicles after transfer to aqueous solution was evaluated with *in vitro* enzymatic degradation experiments using trypsin, showing degradation after 96 hours from dynamic light scattering (DLS) and TEM monitoring. The same group later demonstrated that monomer chirality significantly influences nanoparticle morphology in ROPISA.[298] Using PEG-*b*-P(*D/L*-Phe) block copolymers with a core-forming PPhe block DP ranging from 5 to 20, they performed ROPISA in THF at 15 wt% solid content (Figure I-47a). Homochiral formulations produced vesicles, while blending 40–60% of the *L*-Phe enantiomer with the *D*-enantiomer resulted in dissolved block copolymer chains without self-assembly. Heterochiral mixtures outside this range produced various morphologies, including vesicles, compound micelles, disrupted micelles, and swollen micelles (Figure I-47b,c). This behavior was attributed to the secondary structure of the nanoparticles, which included both α-helix and β-sheet configurations. Increased heterochirality resulted in a larger β-sheet fraction, leading to more solvated and morphologically diverse nanoparticles. In the non-self-assembly regime, the β-sheet fraction exceeded the α-helix fraction, weakening the π-π stacking interactions (Figure I-47c). The study concluded that in ROPISA in THF, nanoparticle secondary structure and morphology can be tuned by adjusting monomer chirality. This affects polymer self-assembly, which is primarily driven by intermolecular peptide-peptide interactions rather than traditional polymer-solvent interactions.

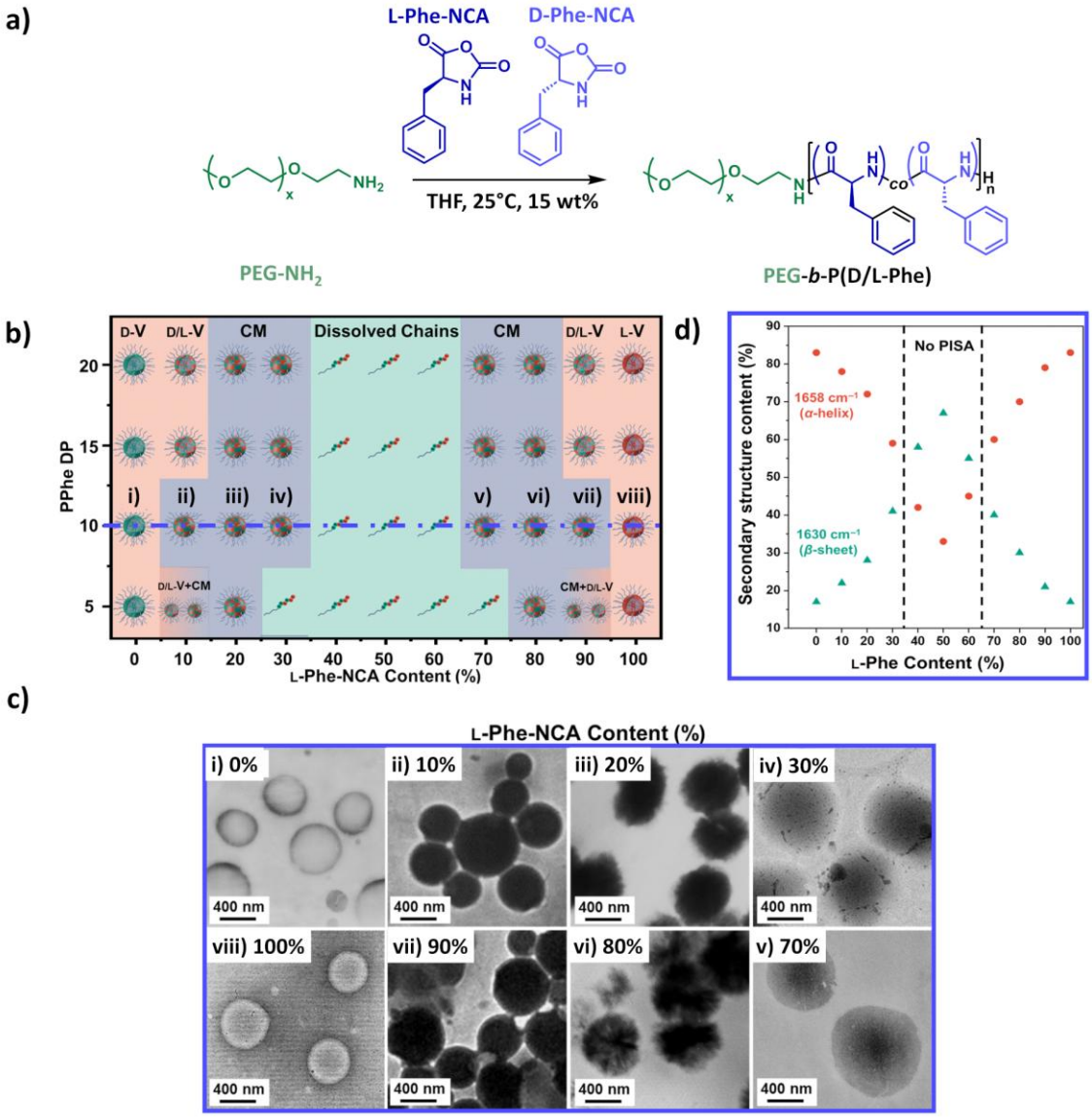

Figure I-47. (a) Ring-opening polymerization-induced self-assembly (ROPISA) of *L*-Phe-NCA and/or *D*-Phe-NCA in THF (15 wt%) at 25°C. (b). Pseudo-phase diagram of PEG_{2k}-*b*-P(*D*/*L*-Phe)$_x$ assemblies by adjusting the DP and the L-Phe-NCA content. D-V = D-Vesicles, D/L-V = D/L-Vesicles, CM = Compound Micelles, and L-V = L-Vesicles. (Chiral composition of the polymer, not the nanoparticle chirality). (c) Representative TEM images obtained for PEG_{2k}-*b*-P(*D*/*L*-Phe)$_{10}$ nanoparticles; the numbers correspond to the samples in the pseudo-diagram. (d) Deconvoluted amide I band areas from FTIR spectra of PEG_{2k}-*b*-P(*D*/*L*-Phe)$_{10}$ copolymer nanoparticles plotted against the *L*-Phe content. Adapted from Du *et al.*[298]

Battaglia and coworkers reported the ROPISA of methionine-NCA (Met-NCA) using PEG-NH_2 as both the stabilizing block and macroinitiator, with Met-NCA generated *in situ via* an activated urethane precursor at 60°C in the polar aprotic solvent DMSO (Figure I-48a).[299] By adjusting the DP from 5 to 120 units and the solid content from 8 to 45 wt%, different nanoparticle morphologies were obtained, ranging from spherical micelles to worm-like micelles and vesicular structures, all of which remained stable after transfer to water (Figure I-48b, c). However, the phase diagram was dominated by cylindrical assemblies, as spherical micelles were not obtained for methionine block lengths exceeding five units. This behavior was attributed to the propensity of methionine to form α-helices, which induce twisted structures displaying helical patterns rather than smooth linear worms. These worm-like micelles were also able to into self-

standing gels. In addition, the reactive oxygen species (ROS)-responsiveness of the methionine block enabled controlled degradation of the nanoparticles under oxidative conditions or by electron beam irradiation.

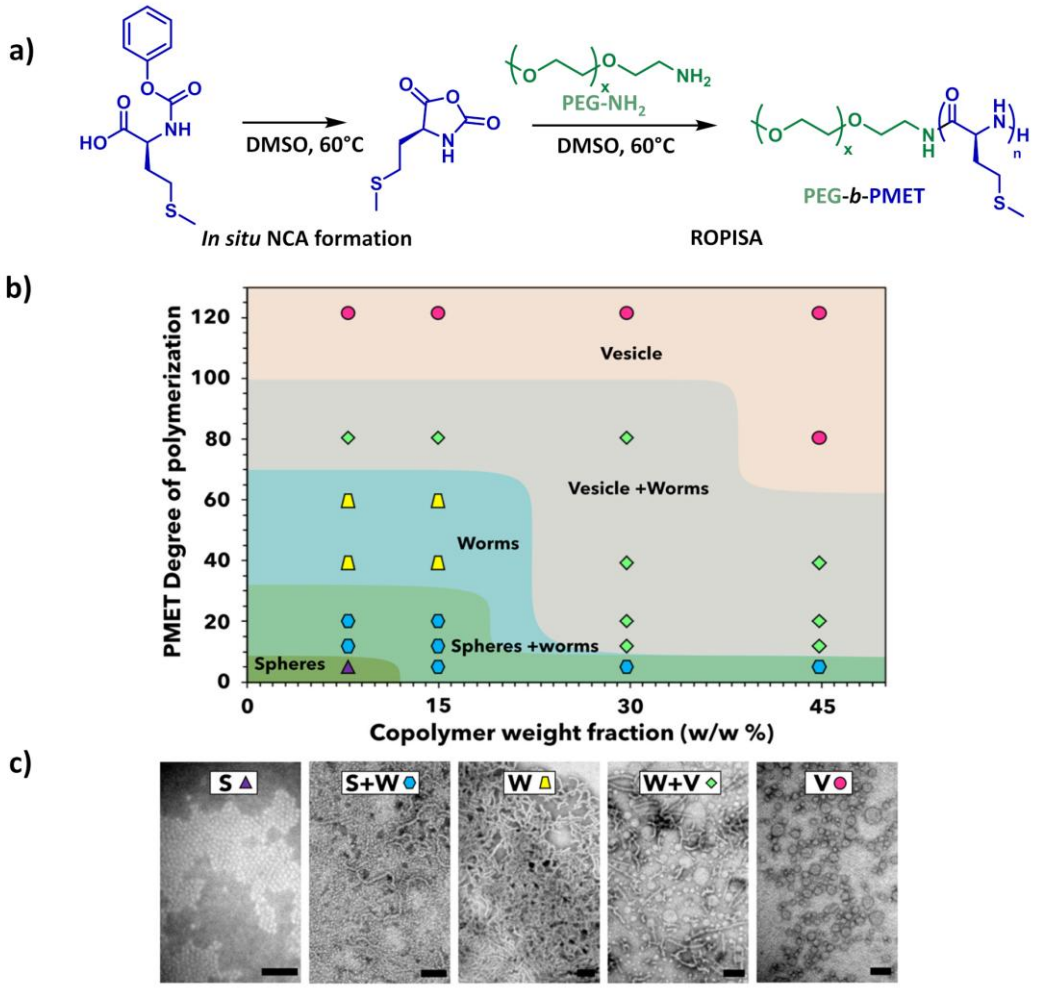

Figure I-48. (a) Ring-opening polymerization-induced self-assembly (ROPISA) of activated urethane of methionine in DMSO. (b) Phase diagram of obtained nanoparticle morphologies after transfer to water by dialysis, for polymerization conducted under various solid contents (w/w%) and degrees of polymerization (DP) of the methionine block (PMET). Symbol legend: purple triangle = spheres (i.e., spherical micelles) (S); blue hexagon = spheres + worms (i.e., wormlike micelles) (S + W); yellow trapeze = worms (W); green diamond = worms + vesicles (W + V); pink circle = vesicles (V). (c) Representative TEM images of PEG_{5k}-*b*-$PMET_n$ aqueous suspensions. Scale-bar: 100 nm. Adapted from Battaglia *et al.*[299]

Polyesters are an attractive class of polymeric materials due to their excellent biodegradability and biocompatibility, making them widely used in biomedical engineering.[300] In this context, Yang's group developed the ROPISA of six-membered cyclic salicylic acid *O*-carboxyanhydride (SAOCA) initiated by poly(ethylene glycol) in THF using the phosphazene base BEMP and urea (U-1) as cooperative catalysts.[243] The high reactivity of SAOCA combined with the solvophobic switch of the growing PSA block in THF, enabled rapid polymerization within minutes, yielding predominantly worm-like micelles along with spherical nanoparticles.

Further studies developed by the same group investigated the ROPISA of SAOCA initiated by PEG with TBD as the catalyst (Figure I-49).[301] This work revealed a range of metastable morphologies,

including spherical, worm-like, and toroidal micelles, with worm-like structures still predominant at concentrations of 5 to 20 wt%. The authors attributed this behavior to the kinetically-driven nature of the process, where polymerization proceeds faster than self-assembly, which is driven by hydrophobic and π–π interactions, resulting in initial assemblies that are far from thermodynamic equilibrium.

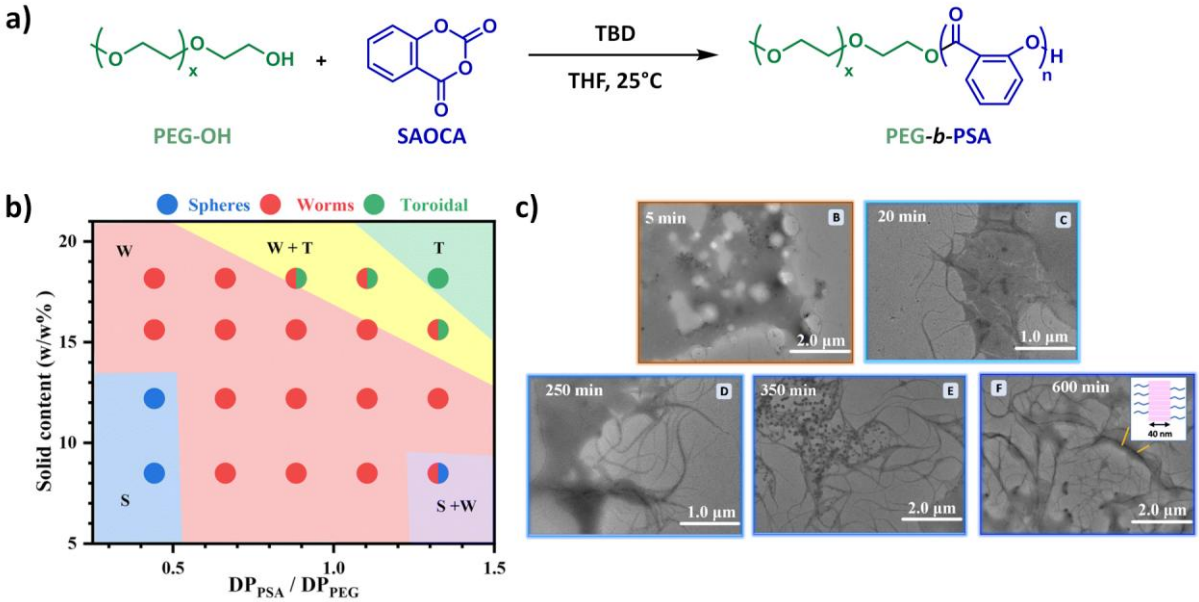

Figure I-49. (a) Ring-opening polymerization-induced self-assembly (ROPISA) of SAOCA in THF with TBD as the catalyst. (b) Phase diagram of obtained morphologies depending on the solid content and the DP ratio of PSA to PEG. Spheres: S, worms: W, and toroidal: T. (c) Representative TEM images of the nanoparticles at different polymerization times. Adapted from Yang *et al.*[301]

In this stimulating context, at LCPO, we have recently demonstrated that ROP of NCA can be performed in aqueous solution *via* a ROPISA process under specific conditions, as mentioned in section I.3.2.1.3. Using α-amino-poly(ethylene glycol) as the macroinitiator, we achieved the chain extension of BLG-NCA and ε-tert-butyloxycarbonyl-*L*-lysine NCA (Lys(Boc)-NCA) resulting in the formation of amphiphilic diblock copolymer nanoparticles with worm-like morphology (Figure I-50). The controlled NCA polymerization was mainly driven by the self-assembly process, which protected NCAs from hydrolysis by forming micelles during polymerization. This effect was further supported by adjusting the pH to 8.5 with a 50 mM $NaHCO_3$ buffer, which enhanced aminolysis and polymerization rates over hydrolysis.[134] The same conditions were later applied to Leu-NCA and compared to BLG-NCA, and the results have shown that the secondary structure, β-sheets in the case of *L*-leucine and α-helix in the case of BLG, have an impact on the obtained nanoparticle morphology, where β-sheet resulted in rod-like nanoparticles while α-helix resulted in more flexible worm-like nanoparticles.[135]

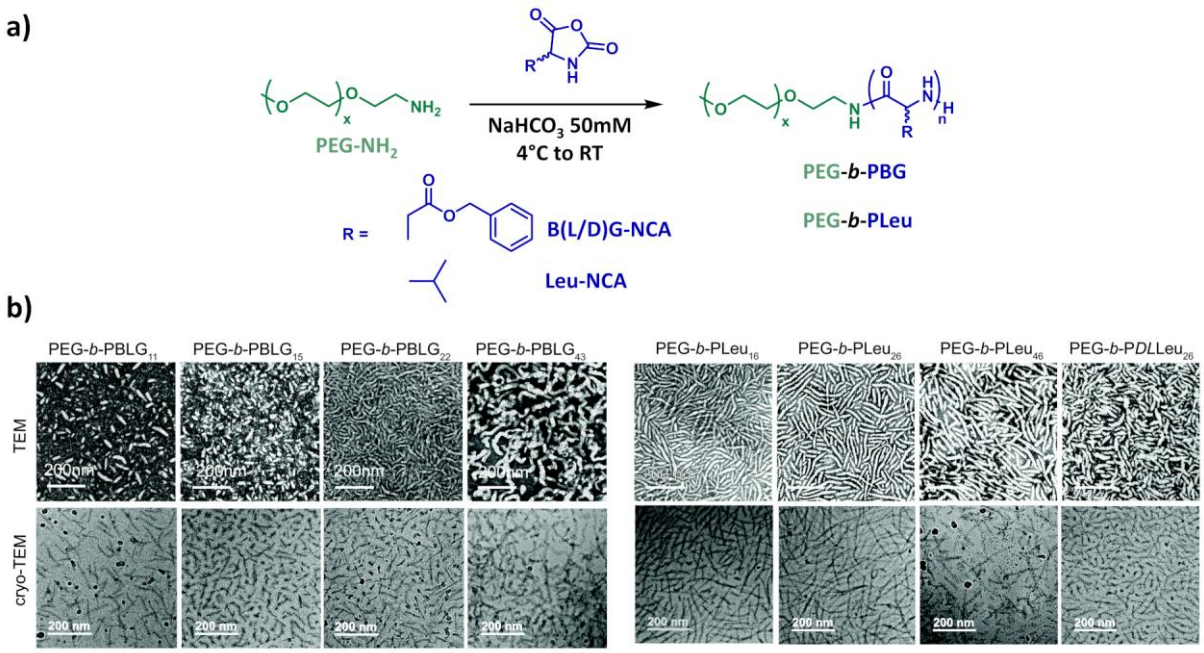

Figure I-50. (a) Ring-opening polymerization-induced self-assembly (ROPISA) of B(L/D)G-NCA or Leu-NCA bicarbonate solution. (b) Representative TEM (top) and cryo-TEM (bottom) images of the nanoparticle suspensions of PEG-*b*-PBLG and PEG-*b*-PLeu. Adapted from Bonduelle *et al.* [135]

Building on these findings, Chen and colleagues further explored the role of chirality in the aqueous ROPISA of ε-benzyloxycarbonyl-*D/L*-lysine *N*-carboxyanhydrides (*D/L*-Lys(Z)-NCA) (Figure I-51).[302] Using PEG-NH_2 as a macroinitiator and ultrasonication to accelerate polymerization kinetics, they obtained narrow-dispersity copolymers within minutes. Polymerization of the *L* and *D* enantiomers produced right- and left-handed superhelical assemblies, respectively, while a racemic mixture resulted in stereoselective polypeptide assemblies, again highlighting the importance of chirality in the ROPISA process.

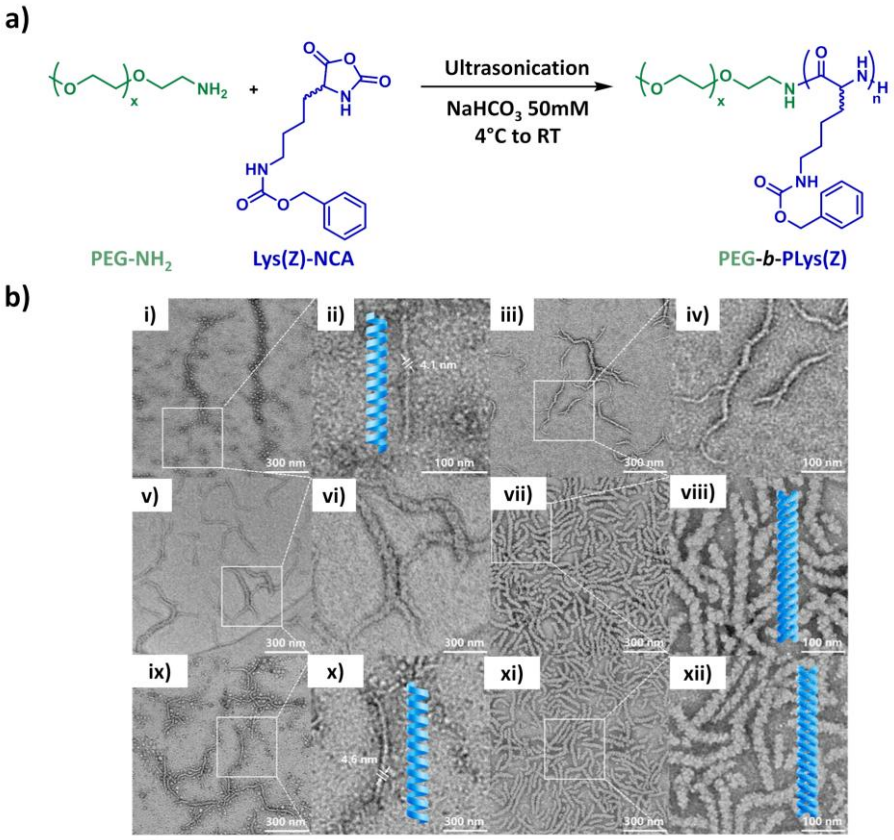

Figure I-51. (a) Ring-opening polymerization-induced self-assembly (ROPISA) of Lys(Z)-NCA in bicarbonate solution under ultrasonication. (b) Representative TEM images of the PEG-*b*-P(*L*-LysZ) nanoparticle suspensions at different polymerization times: (i) 30 s, (iii) 1 min, (v) 3 min, and (vii) 30 min and (ii, iv, vi, viii) corresponding enlarged TEM images of dashed boxes in (i, iii, v, vii). Representative TEM images of the PEG-*b*-P(*D*-LysZ) nanoparticle suspensions at different polymerization times: (ix) 30 s and (xi) 30 min and (x,xii) corresponding enlarged TEM images of dashed boxes in (ix,xi). Adapted from Chen *et al.*[302]

This ROPISA of NCA process has been further extended to the use of polysaccharide as stabilizer block with carboxymethyl chitosan, leading to hydrogel by micellar aggregation,[303] or with the chain extension of poly(proline)-based 8 arm initiator in ACN/water mixture.[304]

While this process is remarkably promising, enabling the one-step synthesis of polypeptide-based anisotropic nanoparticles in a fully aqueous system at high concentrations without the need for purification steps, several limitations remain. Only a limited range of monomers has been explored, the achievable degrees of polymerization are relatively low, and the use of macroinitiators has been predominantly limited to polyethylene glycol. In addition, there is currently no evidence of their use in drug delivery systems.

I.5. Conclusion

This chapter has outlined the potential of anisotropic nanocarriers as promising drug delivery systems in nanomedicine. These structures are typically obtained through the self-assembly of amphiphilic block copolymers, with polypeptides standing out as ideal candidates due to their biocompatibility, biodegradability, and intrinsic secondary structures. However, conventional self-assembly techniques often present significant limitations, including scalability challenges, multi-step processes, and difficulties in achieving precise morphological control under concentrated conditions.

In contrast, polymerization-induced self-assembly (PISA) has emerged as a powerful and scalable approach for designing nanocarriers with significant biomedical relevance. Notably, the group in which I achieved my PhD project previously demonstrated that aqueous ROPISA of *N*-carboxyanhydrides enables the simple and efficient preparation of anisotropic polypeptide micelles in a single step, at high concentrations, and under biofriendly conditions. Despite these advantages, this approach remains underexplored and poorly understood, primarily due to the inherent complexity of the process, which involves a heterogeneous reaction medium and a hydrophobic, moisture-sensitive monomer. Therefore, this PhD work aims to deepen the understanding and expand the potential of aqueous ROPISA of NCAs toward nanomedicine applications, particularly in oncology. By taking advantage of the one-pot nature of this process, this research seeks to develop biocompatible and biodegradable anisotropic nanoparticles at high concentrations, a feature that remains unexplored in the literature.

Chapter II will investigate the polymerization and self-assembly mechanisms occurring during aqueous ROPISA, using PEG-*b*-PBLG as a model system. Using advanced characterization techniques such as synchrotron small-angle and wide-angle X-rays scattering (SAXS/WAXS), size-exclusion chromatography (SEC), and transmission electron microscopy (TEM), we aim to elucidate why this process allows fast and controlled polymerization and self-assembly (Scheme I-5).

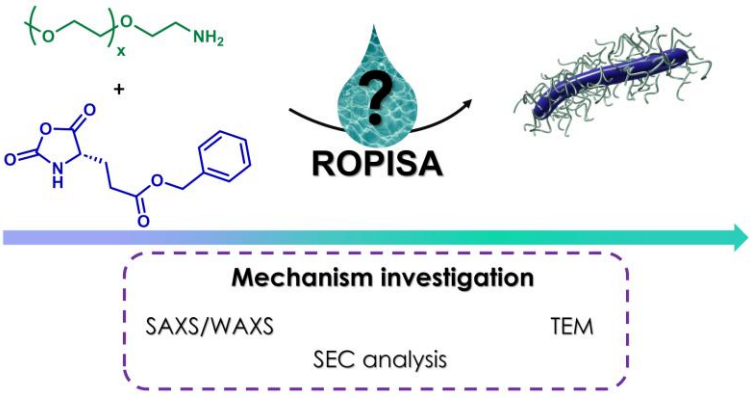

Scheme I-5. Mechanism investigation of aqueous ROPISA of BLG-NCA initiated by PEG_{5k}-NH_2.

Chapter III will extend this understanding by exploring the impact of monomer structure on the anisotropy of the resulting nanoparticles. By employing NCAs derived from various amino acids with

different hydrophobicities, π–π stacking abilities, and hydrogen-bonding interactions, we will assess their influence on nanoparticle shape and stability (Scheme I-6).

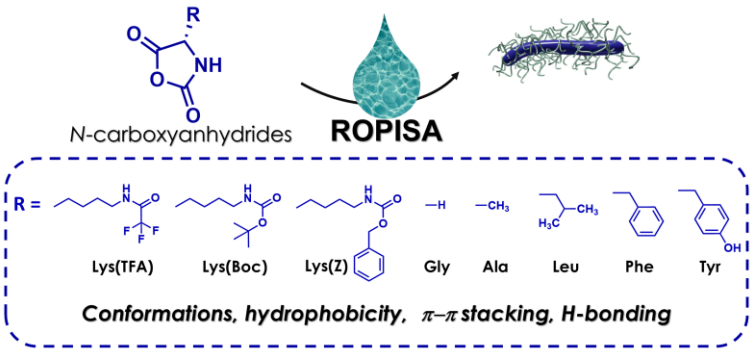

Scheme I-6. Influence of the nature of amino acid NCAs on aqueous ROPISA.

Chapter IV will explore the functionalization of the nanostructures by employing different (bio)degradable and functional macromolecules as macroinitiators for aqueous ROPISA. This step is crucial for expanding the versatility of the platform toward specific biomedical applications (Scheme I-7).

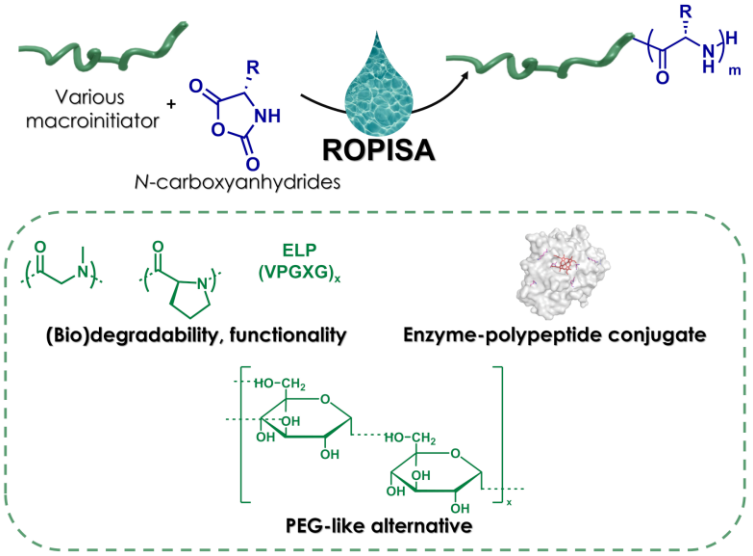

Scheme I-7. Diversifying the surface of nanoparticles obtained via queous ROPISA using various stabilizing blocks.

Chapter V will evaluate the biological behavior of worm-like nanoparticles in *in vitro* and *in vivo* models. A one-step approach for fluorescent labeling will be employed to track their cellular uptake and biodistribution. Their efficacy will be compared to spherical analogs, obtained via conventional self-assembly, in two tumor models with different vascularization and permeability (Scheme I-8).

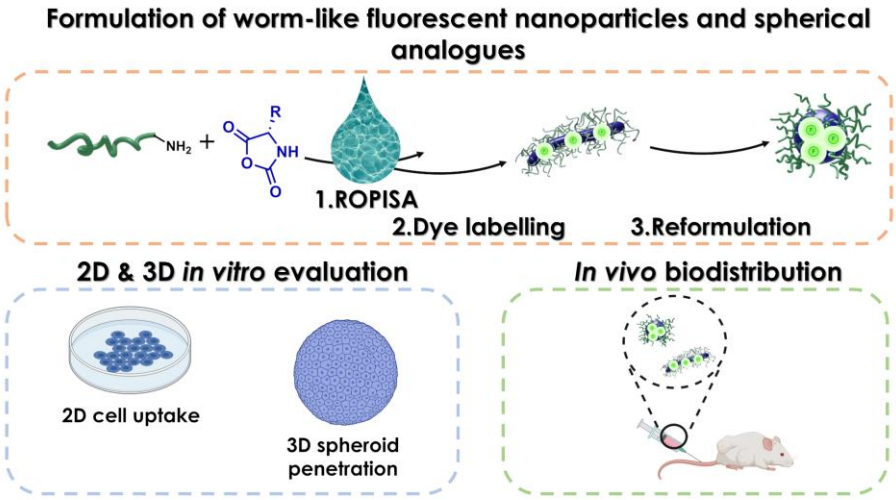

Scheme I-8. Comparative *in vitro* and *in vivo* evaluation of worm-like and spherical nanocarriers derived from aqueous ROPISA.

Chapter VI will explore the encapsulation of active ingredients such as anticancer drugs using a one-step approach, either *in situ* or post-ROPISA encapsulation. Depending on the nature of each drug, one technique or the other will be employed.

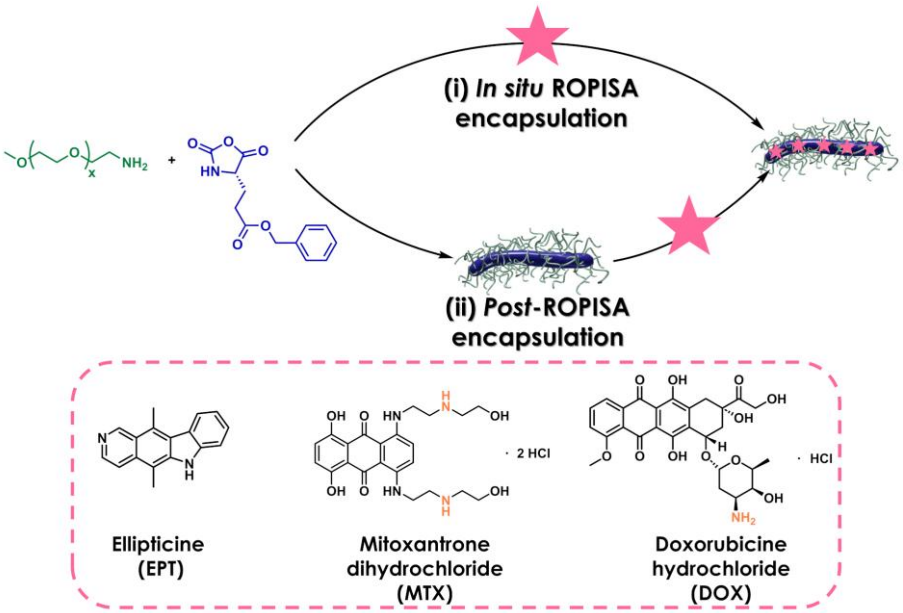

Scheme I-9. Development of anticancer drug-loaded nanocarriers via aqueous ROPISA.

Through these investigations, this PhD work contributes to broadening the scope of aqueous ROPISA of NCA in nanomedicine, offering a scalable and versatile strategy for the development of next-generation anisotropic polypeptide-based nanocarriers.

I.6. References

[1] M. May, *Nat. Med.* **2022**, *28*, 1100–1102.
[2] S. Kalepu, V. Nekkanti, *Acta Pharm. Sin. B* **2015**, *5*, 442–453.
[3] D. Peer, J. M. Karp, S. Hong, O. C. Farokhzad, R. Margalit, R. Langer, *Nat. Nanotechnol.* **2007**, *2*, 751–760.
[4] D. E. Large, R. G. Abdelmessih, E. A. Fink, D. T. Auguste, *Adv. Drug Deliv. Rev.* **2021**, *176*, 113851.
[5] V. Chandrakala, V. Aruna, G. Angajala, *Emergent Mater.* **2022**, *5*, 1593–1615.
[6] X. Hou, T. Zaks, R. Langer, Y. Dong, *Nat. Rev. Mater.* **2021**, *6*, 1078–1094.
[7] H. Cabral, K. Miyata, K. Osada, K. Kataoka, *Chem. Rev.* **2018**, *118*, 6844–6892.
[8] D. E. Discher, A. Eisenberg, *Science* **2002**, *297*, 967–973.
[9] R. J. Sarode, H. S. Mahajan, *J. Drug Deliv. Sci. Technol.* **2024**, *98*, 105896.
[10] M. Manzano, M. Vallet-Regí, *Adv. Funct. Mater.* **2020**, *30*, 1902634.
[11] H. Soo Choi, W. Liu, P. Misra, E. Tanaka, J. P. Zimmer, B. Itty Ipe, M. G. Bawendi, J. V. Frangioni, *Nat. Biotechnol.* **2007**, *25*, 1165–1170.
[12] J. Liu, H. Cabral, P. Mi, *Adv. Drug Deliv. Rev.* **2024**, *207*, 115239.
[13] M. Seleci, D. A. Seleci, R. Joncyzk, F. Stahl, C. Blume, T. Scheper, *BioNanoMaterials* **2016**, *17*, 33–41.
[14] Z. Pei, S. Chen, L. Ding, J. Liu, X. Cui, F. Li, F. Qiu, *J. Controlled Release* **2022**, *352*, 211–241.
[15] "Cancer," can be found under https://www.who.int/news-room/fact-sheets/detail/cancer, **n.d.**
[16] K. Strebhardt, A. Ullrich, *Nat. Rev. Cancer* **2008**, *8*, 473–480.
[17] Y. Matsumura, H. Maeda, *Cancer Res.* **1986**, *46*, 6387–6392.
[18] A. Ruddell, A. Croft, K. Kelly-Spratt, M. Furuya, C. J. Kemp, *BMC Cancer* **2014**, *14*, 354.
[19] H. Kobayashi, R. Watanabe, P. L. Choyke, *Theranostics* **2013**, *4*, 81–89.
[20] H. Pelicano, D. S. Martin, R.-H. Xu, P. Huang, *Oncogene* **2006**, *25*, 4633–4646.
[21] D. E. Owens, N. A. Peppas, *Int. J. Pharm.* **2006**, *307*, 93–102.
[22] X. Yan, G. L. Scherphof, J. A. A. M. Kamps, *J. Liposome Res.* **2005**, *15*, 109–139.
[23] F. Alexis, E. Pridgen, L. K. Molnar, O. C. Farokhzad, *Mol. Pharm.* **2008**, *5*, 505–515.
[24] N. Bertrand, J.-C. Leroux, *J. Controlled Release* **2012**, *161*, 152–163.
[25] C. Vauthier, C. Dubernet, E. Fattal, H. Pinto-Alphandary, P. Couvreur, *Adv. Drug Deliv. Rev.* **2003**, *55*, 519–548.
[26] N. Chiannilkulchai, Z. Driouich, J. P. Benoit, A. L. Parodi, P. Couvreur, *Sel. Cancer Ther.* **1989**, *5*, 1–11.
[27] J. Kattan, J.-P. Droz, P. Couvreur, J.-P. Marino, A. Boutan-Laroze, P. Rougier, P. Brault, H. Vranckx, J.-M. Grognet, X. Morge, H. Sancho-Garnier, *Invest. New Drugs* **1992**, *10*, 191–199.
[28] A. Abuchowski, J. R. McCoy, N. C. Palczuk, T. van Es, F. F. Davis, *J. Biol. Chem.* **1977**, *252*, 3582–3586.
[29] Y. Gao, M. Joshi, Z. Zhao, S. Mitragotri, *Bioeng. Transl. Med.* **2024**, *9*, e10600.
[30] M. Li, S. Jiang, J. Simon, D. Paßlick, M.-L. Frey, M. Wagner, V. Mailänder, D. Crespy, K. Landfester, *Nano Lett.* **2021**, *21*, 1591–1598.
[31] L. Shi, J. Zhang, M. Zhao, S. Tang, X. Cheng, W. Zhang, W. Li, X. Liu, H. Peng, Q. Wang, *Nanoscale* **2021**, *13*, 10748–10764.
[32] T. Verrecchia, G. Spenlehauer, D. V. Bazile, A. Murry-Brelier, Y. Archimbaud, M. Veillard, *J. Controlled Release* **1995**, *36*, 49–61.
[33] Y. Barenholz, A. Gabizon, *Liposome/Doxorubicin Composition and Method*, **1990**, US4898735A.
[34] D. W. Northfelt, B. J. Dezube, J. A. Thommes, B. J. Miller, M. A. Fischl, A. Friedman-Kien, L. D. Kaplan, C. Du Mond, R. D. Mamelok, D. H. Henry, *J. Clin. Oncol.* **1998**, *16*, 2445–2451.
[35] S. B. Bhowmick, A. B. Namdeo, J. Natarajan, P. Jain, *Process for the Preparation of Doxorubicin Liposomes*, **2010**, WO2010092590A2.
[36] Y. (Chezy) Barenholz, *J. Controlled Release* **2012**, *160*, 117–134.
[37] A. S. Abu Lila, H. Kiwada, T. Ishida, *J. Controlled Release* **2013**, *172*, 38–47.
[38] Q. Yang, S. K. Lai, *WIREs Nanomedicine Nanobiotechnology* **2015**, *7*, 655–677.
[39] S. Zalba, T. L. M. ten Hagen, C. Burgui, M. J. Garrido, *J. Controlled Release* **2022**, *351*, 22–36.

[40] P. H. Kierstead, H. Okochi, V. J. Venditto, T. C. Chuong, S. Kivimae, J. M. J. Fréchet, F. C. Szoka, *J. Controlled Release* **2015**, *213*, 1–9.
[41] T. Ishihara, T. Maeda, H. Sakamoto, N. Takasaki, M. Shigyo, T. Ishida, H. Kiwada, Y. Mizushima, T. Mizushima, *Biomacromolecules* **2010**, *11*, 2700–2706.
[42] M. Berger, F. Toussaint, S. B. Djemaa, J. Laloy, H. Pendeville, B. Evrard, C. Jerôme, A. Lechanteur, D. Mottet, A. Debuigne, G. Piel, *J. Controlled Release* **2023**, *361*, 87–101.
[43] M. Berger, F. Toussaint, S. Ben Djemaa, E. Maquoi, H. Pendeville, B. Evrard, C. Jerôme, J. Leblond Chain, A. Lechanteur, D. Mottet, A. Debuigne, G. Piel, *Adv. Healthc. Mater.* **2024**, *13*, 2302712.
[44] Z. Zhang, H. Vaisocherová, G. Cheng, W. Yang, H. Xue, S. Jiang, *Biomacromolecules* **2008**, *9*, 2686–2692.
[45] S. Colak, G. N. Tew, *Biomacromolecules* **2012**, *13*, 1233–1239.
[46] M. Bauer, C. Lautenschlaeger, K. Kempe, L. Tauhardt, U. S. Schubert, D. Fischer, *Macromol. Biosci.* **2012**, *12*, 986–998.
[47] E. Österberg, K. Bergström, K. Holmberg, J. A. Riggs, J. M. Van Alstine, T. P. Schuman, N. L. Burns, J. M. Harris, *Colloids Surf. Physicochem. Eng. Asp.* **1993**, *77*, 159–169.
[48] X. Li, H. Li, Y. Zhao, X. Tang, S. Ma, B. Gong, M. Li, *Polym. Chem.* **2015**, *6*, 6452–6456.
[49] B. Weber, A. Birke, K. Fischer, M. Schmidt, M. Barz, *Macromolecules* **2018**, *51*, 2653–2661.
[50] Y. Hu, Y. Hou, H. Wang, H. Lu, *Bioconjug. Chem.* **2018**, *29*, 2232–2238.
[51] S. Chen, P. Zhou, W. Yang, D. Hu, P. Chen, P. Sun, J. Ling, Q. Fan, *Biomater. Sci.* **2023**, *11*, 4644–4651.
[52] X. Yao, C. Sun, F. Xiong, W. Zhang, W. Yao, Y. Xu, W. Fan, F. Huo, *ACS Appl. Mater. Interfaces* **2024**, *16*, 19472–19479.
[53] H. He, L. Liu, E. E. Morin, M. Liu, A. Schwendeman, *Acc. Chem. Res.* **2019**, *52*, 2445–2461.
[54] S. Wilhelm, A. J. Tavares, Q. Dai, S. Ohta, J. Audet, H. F. Dvorak, W. C. W. Chan, *Nat. Rev. Mater.* **2016**, *1*, 1–12.
[55] Q. Dai, S. Wilhelm, D. Ding, A. M. Syed, S. Sindhwani, Y. Zhang, Y. Y. Chen, P. MacMillan, W. C. W. Chan, *ACS Nano* **2018**, *12*, 8423–8435.
[56] L. S. L. Price, S. T. Stern, A. M. Deal, A. V. Kabanov, W. C. Zamboni, *Sci. Adv.* **2020**, *6*, eaay9249.
[57] A. K. Pearce, R. K. O'Reilly, *Bioconjug. Chem.* **2019**, *30*, 2300–2311.
[58] C.-H. Heldin, K. Rubin, K. Pietras, A. Östman, *Nat. Rev. Cancer* **2004**, *4*, 806–813.
[59] B. R. Kingston, Z. P. Lin, B. Ouyang, P. MacMillan, J. Ngai, A. M. Syed, S. Sindhwani, W. C. W. Chan, *ACS Nano* **2021**, *15*, 14080–14094.
[60] N. Kamaly, Z. Xiao, P. M. Valencia, A. F. Radovic-Moreno, O. C. Farokhzad, *Chem. Soc. Rev.* **2012**, *41*, 2971–3010.
[61] S. Luo, Z. Lv, Q. Yang, R. Chang, J. Wu, *Pharmaceutics* **2023**, *15*, 1928.
[62] D. Fan, Y. Cao, M. Cao, Y. Wang, Y. Cao, T. Gong, *Signal Transduct. Target. Ther.* **2023**, *8*, 1–34.
[63] J. A. Champion, Y. K. Katare, S. Mitragotri, *J. Controlled Release* **2007**, *121*, 3–9.
[64] R. Toy, P. M. Peiris, K. B. Ghaghada, E. Karathanasis, *Nanomed.* **2014**, *9*, 121–134.
[65] R. Madathiparambil Visalakshan, L. E. González García, M. R. Benzigar, A. Ghazaryan, J. Simon, A. Mierczynska-Vasilev, T. D. Michl, A. Vinu, V. Mailänder, S. Morsbach, K. Landfester, K. Vasilev, *Small* **2020**, *16*, 2000285.
[66] Y. Geng, P. Dalhaimer, S. Cai, R. Tsai, M. Tewari, T. Minko, D. E. Discher, *Nat. Nanotechnol.* **2007**, *2*, 249–255.
[67] P. Dalhaimer, F. S. Bates, D. E. Discher, *Macromolecules* **2003**, *36*, 6873–6877.
[68] J. A. Champion, S. Mitragotri, *Pharm. Res.* **2009**, *26*, 244–249.
[69] G. Sharma, D. T. Valenta, Y. Altman, S. Harvey, H. Xie, S. Mitragotri, J. W. Smith, *J. Control. Release Off. J. Control. Release Soc.* **2010**, *147*, 408–412.
[70] J. T. Lovegrove, B. Kent, S. Förster, C. J. Garvey, M. H. Stenzel, *Exploration* **2023**, *3*, 20220075.
[71] M. Howard, B. J. Zern, A. C. Anselmo, V. V. Shuvaev, S. Mitragotri, V. Muzykantov, *ACS Nano* **2014**, *8*, 4100–4132.
[72] P. Kolhar, A. C. Anselmo, V. Gupta, K. Pant, B. Prabhakarpandian, E. Ruoslahti, S. Mitragotri, *Proc. Natl. Acad. Sci. U. S. A.* **2013**, *110*, 10753–10758.
[73] A. Zeeshan, H. Hadji, H. Khelifa, M. Bourge, K. Bouchemal, *Colloids Surf. Physicochem. Eng. Asp.* **2024**, *680*, 132680.
[74] K. G. Reuter, J. L. Perry, D. Kim, J. C. Luft, R. Liu, J. M. DeSimone, *Nano Lett.* **2015**, *15*, 6371–6378.

[75] N. P. Truong, M. R. Whittaker, C. W. Mak, T. P. Davis, *Expert Opin. Drug Deliv.* **2015**, *12*, 129–142.
[76] D. A. Christian, S. Cai, O. B. Garbuzenko, T. Harada, A. L. Zajac, T. Minko, D. E. Discher, *Mol. Pharm.* **2009**, *6*, 1343–1352.
[77] K. S. Chu, W. Hasan, S. Rawal, M. D. Walsh, E. M. Enlow, J. C. Luft, A. S. Bridges, J. L. Kuijer, M. E. Napier, W. C. Zamboni, J. M. DeSimone, *Nanomedicine Nanotechnol. Biol. Med.* **2013**, *9*, 686–693.
[78] K. L. Lee, L. C. Hubbard, S. Hern, I. Yildiz, M. Gratzl, N. F. Steinmetz, *Biomater. Sci.* **2013**, *1*, 581–588.
[79] Q. Yu, M. G. Roberts, L. Houdaihed, Y. Liu, K. Ho, G. Walker, C. Allen, R. M. Reilly, I. Manners, M. A. Winnik, *Nanoscale* **2021**, *13*, 280–291.
[80] V. P. Chauhan, Z. Popović, O. Chen, J. Cui, D. Fukumura, M. G. Bawendi, R. K. Jain, *Angew. Chem. Int. Ed.* **2011**, *50*, 11417–11420.
[81] P. Lagarrigue, F. Moncalvo, F. Cellesi, *Pharmaceutics* **2023**, *15*, 32.
[82] N. S. Oltra, J. Swift, A. Mahmud, K. Rajagopal, S. M. Loverde, D. E. Discher, *J. Mater. Chem. B* **2013**, *1*, 5177–5185.
[83] Y. Geng, D. E. Discher, *Polymer* **2006**, *47*, 2519–2525.
[84] N. S. Oltra, P. Nair, D. E. Discher, *Annu. Rev. Chem. Biomol. Eng.* **2014**, *5*, 281–299.
[85] M. A. Beach, U. Nayanathara, Y. Gao, C. Zhang, Y. Xiong, Y. Wang, G. K. Such, *Chem. Rev.* **2024**, *124*, 5505–5616.
[86] C. Zhu, J. Nicolas, *Biomacromolecules* **2022**, *23*, 3043–3080.
[87] M. K. Gordon, B. R. Olsen, *Curr. Opin. Cell Biol.* **1990**, *2*, 833–838.
[88] A. Gutteridge, J. M. Thornton, *Trends Biochem. Sci.* **2005**, *30*, 622–629.
[89] A. Ciechanover, A. Orian, A. L. Schwartz, *J. Cell. Biochem. Suppl.* **2000**, *34*, 40–51.
[90] K. A. Dill, *Biochemistry* **1990**, *29*, 7133–7155.
[91] In *Fennemas Food Chem.*, CRC Press, **2017**.
[92] T. Narancic, S. A. Almahboub, K. E. O'Connor, *World J. Microbiol. Biotechnol.* **2019**, *35*, 67.
[93] S. C. Lovell, I. W. Davis, W. B. Arendall III, P. I. W. de Bakker, J. M. Word, M. G. Prisant, J. S. Richardson, D. C. Richardson, *Proteins Struct. Funct. Bioinforma.* **2003**, *50*, 437–450.
[94] J. C. M. van Hest, D. A. Tirrell, *Chem. Commun.* **2001**, 1897–1904.
[95] R. B. Merrifield, *J. Am. Chem. Soc.* **1963**, *85*, 2149–2154.
[96] H. Leuchs, *Berichte Dtsch. Chem. Ges.* **1906**, *39*, 857–861.
[97] F. Fuchs, *Berichte Dtsch. Chem. Ges. B Ser.* **1922**, *55*, 2943–2943.
[98] A. C. Farthing, *J. Chem. Soc. Resumed* **1950**, 3213–3217.
[99] H. R. Kricheldorf, *Angew. Chem. Int. Ed.* **2006**, *45*, 5752–5784.
[100] Y. Wu, K. Chen, J. Wang, M. Chen, W. Dai, R. Liu, *J. Am. Chem. Soc.* **2024**, *146*, 24189–24208.
[101] A. Nagai, D. Sato, J. Ishikawa, B. Ochiai, H. Kudo, T. Endo, *Macromolecules* **2004**, *37*, 2332–2334.
[102] Y. Fujita, K. Koga, H.-K. Kim, X.-S. Wang, A. Sudo, H. Nishida, T. Endo, *J. Polym. Sci. Part Polym. Chem.* **2007**, *45*, 5365–5370.
[103] K. Koga, A. Sudo, T. Endo, *J. Polym. Sci. Part Polym. Chem.* **2010**, *48*, 4351–4355.
[104] G. Laconde, M. Amblard, J. Martinez, *Org. Lett.* **2021**, *23*, 6412–6416.
[105] H. Enomoto, B. Nottelet, S. A. Halifa, C. Enjalbal, M. Dupré, J. Tailhades, J. Coudane, G. Subra, J. Martinez, M. Amblard, *Chem. Commun.* **2012**, *49*, 409–411.
[106] J. R. Kramer, T. J. Deming, *Biomacromolecules* **2010**, *11*, 3668–3672.
[107] Z. Song, H. Fu, J. Wang, J. Hui, T. Xue, L. A. Pacheco, H. Yan, R. Baumgartner, Z. Wang, Y. Xia, X. Wang, L. Yin, C. Chen, J. Rodríguez-López, A. L. Ferguson, Y. Lin, J. Cheng, *Proc. Natl. Acad. Sci.* **2019**, *116*, 10658–10663.
[108] Y. Wu, K. Chen, X. Wu, L. Liu, W. Zhang, Y. Ding, S. Liu, M. Zhou, N. Shao, Z. Ji, J. Chen, M. Zhu, R. Liu, *Angew. Chem. Int. Ed.* **2021**, *60*, 26063–26071.
[109] Y. Kamei, A. Nagai, A. Sudo, H. Nishida, K. Kikukawa, T. Endo, *J. Polym. Sci. Part Polym. Chem.* **2008**, *46*, 2649–2657.
[110] L. Li, J. Cen, W. Pan, Y. Zhang, X. Leng, Z. Tan, H. Yin, S. Liu, *Research* **2021**, *2021*, DOI 10.34133/2021/9826046.
[111] J. Cheng, T. J. Deming, in *Pept.-Based Mater.* (Ed.: T. Deming), Springer, Berlin, Heidelberg, **2012**, pp. 1–26.
[112] T. J. Deming, *Nature* **1997**, *390*, 386–389.

[113] I. Dimitrov, H. Schlaad, *Chem. Commun.* **2003**, *0*, 2944–2945.
[114] M. Badreldin, P. Salas-Ambrosio, M. Ayala, S. Harrisson, C. Bonduelle, *Curr. Org. Chem.* **2024**, *28*, 1154–1163.
[115] T. Aliferis, H. Iatrou, N. Hadjichristidis, *Biomacromolecules* **2004**, *5*, 1653–1656.
[116] J. Zou, J. Fan, X. He, S. Zhang, H. Wang, K. L. Wooley, *Macromolecules* **2013**, *46*, 4223–4226.
[117] G. J. M. Habraken, M. Peeters, C. H. J. T. Dietz, C. E. Koning, A. Heise, *Polym. Chem.* **2010**, *1*, 514–524.
[118] X.-C. Li, C.-S. Hu, H.-J. Li, P.-Y. Li, A. Haleem, W.-D. He, *Polymer* **2018**, *151*, 1–5.
[119] P. D. Bartlett, H. Jones, **1957**, *79*, 7.
[120] P. D. Bartlett, D. C. Dittmer, *J. Am. Chem. Soc.* **1957**, *79*, 2159–2160.
[121] R. Plasson, J. Ph. Biron, H. Cottet, A. Commeyras, J. Taillades, *J. Chromatogr. A* **2002**, *952*, 239–248.
[122] N. Hadjichristidis, H. Iatrou, M. Pitsikalis, G. Sakellariou, *Chem. Rev.* **2009**, *109*, 5528–5578.
[123] Y. Wu, D. Zhang, P. Ma, R. Zhou, L. Hua, R. Liu, *Nat. Commun.* **2018**, *9*, 5297.
[124] Y. Wu, K. Chen, X. Wu, L. Liu, W. Zhang, Y. Ding, S. Liu, M. Zhou, N. Shao, Z. Ji, J. Chen, M. Zhu, R. Liu, *Angew. Chem. Int. Ed.* **2021**, *60*, 26063–26071.
[125] Y. Xia, Z. Song, Z. Tan, T. Xue, S. Wei, L. Zhu, Y. Yang, H. Fu, Y. Jiang, Y. Lin, Y. Lu, A. L. Ferguson, J. Cheng, *Nat. Commun.* **2021**, *12*, 732.
[126] R. Baumgartner, H. Fu, Z. Song, Y. Lin, J. Cheng, *Nat. Chem.* **2017**, *9*, 614–622.
[127] S. Lv, H. Kim, Z. Song, L. Feng, Y. Yang, R. Baumgartner, K.-Y. Tseng, S. J. Dillon, C. Leal, L. Yin, J. Cheng, *J. Am. Chem. Soc.* **2020**, *142*, 8570–8574.
[128] F. Yang, Z. Liu, W. Si, Z. Song, L. Yin, H. Tang, *ACS Macro Lett.* **2022**, *11*, 663–668.
[129] J. Zhu, Y. He, C. Ge, W. Si, Z. Song, L. Yin, *Chin. J. Chem.* **2023**, *41*, 2476–2482.
[130] Y. Liu, Z. Ren, N. Zhang, X. Yang, Q. Wu, Z. Cheng, H. Xing, Y. Bai, *Nat. Commun.* **2023**, *14*, 5598.
[131] Y. Wu, K. Chen, J. Wang, M. Chen, W. Dai, R. Liu, *J. Am. Chem. Soc.* **2024**, *146*, 24189–24208.
[132] Y. Hu, Z.-Y. Tian, W. Xiong, D. Wang, R. Zhao, Y. Xie, Y.-Q. Song, J. Zhu, H. Lu, *Natl. Sci. Rev.* **2022**, *9*, nwac033.
[133] J. Jacobs, D. Pavlović, H. Prydderch, M.-A. Moradi, E. Ibarboure, J. P. A. Heuts, S. Lecommandoux, A. Heise, *J. Am. Chem. Soc.* **2019**, *141*, 12522–12526.
[134] C. Grazon, P. Salas-Ambrosio, E. Ibarboure, A. Buol, E. Garanger, M. W. Grinstaff, S. Lecommandoux, C. Bonduelle, *Angew. Chem. Int. Ed.* **2020**, *59*, 622–626.
[135] C. Grazon, P. Salas-Ambrosio, S. Antoine, E. Ibarboure, O. Sandre, A. J. Clulow, B. J. Boyd, M. W. Grinstaff, S. Lecommandoux, C. Bonduelle, *Polym. Chem.* **2021**, *12*, 6242–6251.
[136] T. J. Deming, *Adv. Drug Deliv. Rev.* **2002**, *54*, 1145–1155.
[137] C. Schatz, S. Louguet, J.-F. Le Meins, S. Lecommandoux, *Angew. Chem. Int. Ed.* **2009**, *48*, 2572–2575.
[138] S. Lecommandoux, M. Lazzari, G. Liu, in *Block Copolym. Nanosci.*, John Wiley & Sons, Ltd, **2006**, pp. 1–7.
[139] J. Israelachvili, J. Sjösten, L. E. G. Eriksson, M. Ehrström, A. Gräslund, A. Ehrenberg, *Biochim. Biophys. Acta BBA - Biomembr.* **1975**, *382*, 125–141.
[140] I. A. Nyrkova, A. N. Semenov, *Faraday Discuss.* **2005**, *128*, 113–127.
[141] M. Dionzou, A. Morère, C. Roux, B. Lonetti, J.-D. Marty, C. Mingotaud, P. Joseph, D. Goudounèche, B. Payré, M. Léonetti, A.-F. Mingotaud, *Soft Matter* **2016**, *12*, 2166–2176.
[142] D. E. Discher, F. Ahmed, *Annu. Rev. Biomed. Eng.* **2006**, *8*, 323–341.
[143] Z. Deng, S. Liu, *Polymer* **2020**, *207*, 122914.
[144] A. Blanazs, S. P. Armes, A. J. Ryan, *Macromol. Rapid Commun.* **2009**, *30*, 267–277.
[145] J. Rodríguez-Hernández, F. Chécot, Y. Gnanou, S. Lecommandoux, *Prog. Polym. Sci.* **2005**, *30*, 691–724.
[146] E. G. Hochreiner, B. G. P. van Ravensteijn, *J. Polym. Sci.* **2023**, *61*, 3186–3210.
[147] R. C. Hayward, D. J. Pochan, *Macromolecules* **2010**, *43*, 3577–3584.
[148] H. Fessi, F. Puisieux, J. Ph. Devissaguet, N. Ammoury, S. Benita, *Int. J. Pharm.* **1989**, *55*, R1–R4.
[149] L. Zhang, A. Eisenberg, *Science* **1995**, *268*, 1728–1731.
[150] L. Zhang, K. Yu, A. Eisenberg, *Science* **1996**, *272*, 1777–1779.
[151] M. E. Allen, A. Golding, V. Rus, N. B. Karabin, S. Li, C. J. Lescott, S. Bobbala, E. A. Scott, G. L. Szeto, *ACS Biomater. Sci. Eng.* **2021**, *7*, 5666–5677.

[152] X. Shen, X. Liu, R. Li, P. Yun, C. Li, F. Su, S. Li, *J. Biomater. Sci. -- Polym. Ed.* **2017**, *28*, 1677–1694.
[153] S. Cai, K. Vijayan, D. Cheng, E. M. Lima, D. E. Discher, *Pharm. Res.* **2007**, *24*, 2099–2109.
[154] P. R. Nair, S. Karthick, K. R. Spinler, M. R. Vakili, A. Lavasanifar, D. E. Discher, *Nanomed.* **2016**, *11*, 1551–1569.
[155] X. Sun, X. Liu, C. Li, Y. Wang, L. Liu, F. Su, S. Li, *J. Appl. Polym. Sci.* **2018**, *135*, 45732.
[156] Y. Mai, A. Eisenberg, *Chem. Soc. Rev.* **2012**, *41*, 5969–5985.
[157] S. D. P. Fielden, *J. Am. Chem. Soc.* **2024**, *146*, 18781–18796.
[158] J. A. Massey, K. Temple, L. Cao, Y. Rharbi, J. Raez, M. A. Winnik, I. Manners, *J. Am. Chem. Soc.* **2000**, *122*, 11577–11584.
[159] X. Wang, G. Guerin, H. Wang, Y. Wang, I. Manners, M. A. Winnik, *Science* **2007**, *317*, 644–647.
[160] S. Ganda, M. H. Stenzel, *Prog. Polym. Sci.* **2020**, *101*, 101195.
[161] L. MacFarlane, C. Zhao, J. Cai, H. Qiu, I. Manners, *Chem. Sci.* **2021**, *12*, 4661–4682.
[162] J. Gou, S. Feng, H. Xu, G. Fang, Y. Chao, Y. Zhang, H. Xu, X. Tang, *Biomacromolecules* **2015**, *16*, 2920–2929.
[163] J. D. Garcia-Hernandez, S. T. G. Street, Y. Kang, Y. Zhang, I. Manners, *Macromolecules* **2021**, *54*, 5784–5796.
[164] H. C. Parkin, L. K. Shopperly, M. R. Perez, S. M. Willerth, I. Manners, *Biomater. Sci.* **2024**, *12*, 5283–5294.
[165] X. Zhang, G. Chen, B. Zheng, Z. Wan, L. Liu, L. Zhu, Y. Xie, Z. Tong, *Biomacromolecules* **2023**, *24*, 1032–1041.
[166] H. C. Parkin, S. T. G. Street, B. Gowen, L. H. Da-Silva-Correa, R. Hof, H. L. Buckley, I. Manners, *J. Am. Chem. Soc.* **2024**, *146*, 5128–5141.
[167] S. Ganda, C. K. Wong, M. H. Stenzel, *Macromolecules* **2021**, *54*, 6662–6669.
[168] N. M. Warne, C. J. Nowell, M. P. Tran, J. R. Finnegan, O. M. Feeney, K. Kempe, *Adv. Healthc. Mater.* **2024**, *13*, 2402029.
[169] C. Legros, M.-C. D. Pauw-Gillet, K. C. Tam, D. Taton, S. Lecommandoux, *Soft Matter* **2015**, *11*, 3354–3359.
[170] C. Autumn, S. Lecommandoux, *Curr. Opin. Colloid Interface Sci.* **2009**, *14*, 329–339.
[171] S. Lecommandoux, M.-F. Achard, J. F. Langenwalter, H.-A. Klok, *Macromolecules* **2001**, *34*, 9100–9111.
[172] P. Papadopoulos, G. Floudas, I. Schnell, T. Aliferis, H. Iatrou, N. Hadjichristidis, *Biomacromolecules* **2005**, *6*, 2352–2361.
[173] G. Floudas, H. W. Spiess, *Macromol. Rapid Commun.* **2009**, *30*, 278–298.
[174] E. A. Minich, A. P. Nowak, T. J. Deming, D. J. Pochan, *Polymer* **2004**, *45*, 1951–1957.
[175] G. Floudas, P. Papadopoulos, H.-A. Klok, G. W. M. Vandermeulen, J. Rodriguez-Hernandez, *Macromolecules* **2003**, *36*, 3673–3683.
[176] H.-A. Klok, J. F. Langenwalter, S. Lecommandoux, *Macromolecules* **2000**, *33*, 7819–7826.
[177] J. Nah, Y. Jeong, C. Cho, *J. Polym. Sci. Part B Polym. Phys.* **1998**, *36*, 415–423.
[178] Y.-I. Jeong, J.-B. Cheon, S.-H. Kim, J.-W. Nah, Y.-M. Lee, Y.-K. Sung, T. Akaike, C.-S. Cho, *J. Controlled Release* **1998**, *51*, 169–178.
[179] Y. Jeong, S. Seo, I. Park, H. Lee, I. Kang, T. Akaike, C. Cho, *Int. J. Pharm.* **2005**, *296*, 151–161.
[180] D. Kakkar, S. Mazzaferro, J. Thevenot, C. Schatz, A. Bhatt, B. S. Dwarakanath, H. Singh, A. K. Mishra, S. Lecommandoux, *Macromol. Biosci.* **2015**, *15*, 124–137.
[181] Z. Luo, Y. Yuan, L. Li, D. Xie, C. Liu, T. Li, Z. Guo, K. Hao, Y. Li, H. Tian, *Biomacromolecules* **2024**, *25*, 1096–1107.
[182] Z. Zhuang, C. Cai, T. Jiang, J. Lin, C. Yang, *Polymer* **2014**, *55*, 602–610.
[183] C. Bonduelle, S. Mazzaferro, J. Huang, O. Lambert, A. Heise, S. Lecommandoux, *Faraday Discuss.* **2013**, *166*, 137–150.
[184] X. Lin, X. He, C. Hu, Y. Chen, Y. Mai, S. Lin, *Polym. Chem.* **2016**, *7*, 2815–2820.
[185] C. Cai, L. Wang, J. Lin, X. Zhang, *Langmuir* **2012**, *28*, 4515–4524.
[186] A. M. Donald, A. H. Windle, S. Hanna, *Liquid Crystalline Polymers*, Cambridge University Press, Cambridge, **2006**.
[187] P. van der Asdonk, P. H. J. Kouwer, *Chem. Soc. Rev.* **2017**, *46*, 5935–5949.
[188] B. Jin, K. Sano, S. Aya, Y. Ishida, N. Gianneschi, Y. Luo, X. Li, *Nat. Commun.* **2019**, *10*, 2397.

[189] L. Gao, H. Gao, J. Lin, L. Wang, X.-S. Wang, C. Yang, S. Lin, *Macromolecules* **2020**, *53*, 8992–8999.
[190] X. Jin, C. Zhang, J. Lin, C. Cai, J. Chen, L. Gao, *Macromolecules* **2022**, *55*, 3831–3839.
[191] S. Xu, *J. Phys. Chem. B* **2009**, *113*, 12447–12455.
[192] G. Chen, T. Xu, Y. Yan, Y. Zhou, Y. Jiang, K. Melcher, H. E. Xu, *Acta Pharmacol. Sin.* **2017**, *38*, 1205–1235.
[193] V. Castelletto, I. W. Hamley, *Biophys. Chem.* **2009**, *141*, 169–174.
[194] H. Sun, X. Gu, Q. Zhang, H. Xu, Z. Zhong, C. Deng, *Biomacromolecules* **2019**, *20*, 4299–4311.
[195] A. Lalatsa, A. G. Schätzlein, M. Mazza, T. B. H. Le, I. F. Uchegbu, *J. Controlled Release* **2012**, *161*, 523–536.
[196] Y. Matsumura, T. Hamaguchi, T. Ura, K. Muro, Y. Yamada, Y. Shimada, K. Shirao, T. Okusaka, H. Ueno, M. Ikeda, N. Watanabe, *Br. J. Cancer* **2004**, *91*, 1775–1781.
[197] T. Nakanishi, S. Fukushima, K. Okamoto, M. Suzuki, Y. Matsumura, M. Yokoyama, T. Okano, Y. Sakurai, K. Kataoka, *J. Controlled Release* **2001**, *74*, 295–302.
[198] T. Hamaguchi, Y. Matsumura, M. Suzuki, K. Shimizu, R. Goda, I. Nakamura, I. Nakatomi, M. Yokoyama, K. Kataoka, T. Kakizoe, *Br. J. Cancer* **2005**, *92*, 1240–1246.
[199] B. C. Staff, "Nippon Kayaku's NK105 fails breast cancer Phase III," can be found under https://www.biocentury.com/article/269299/nippon-kayaku-s-nk105-fails-breast-cancer-phase-iii, **n.d.**
[200] "Search for: Other terms: NK012 | List Results | ClinicalTrials.gov," can be found under https://www.clinicaltrials.gov/search?term=NK012&viewType=Table.
[201] Y. Mochida, H. Cabral, K. Kataoka, *Expert Opin. Drug Deliv.* **2017**, *14*, 1423–1438.
[202] H. Mukai, T. Kogawa, N. Matsubara, Y. Naito, M. Sasaki, A. Hosono, *Invest. New Drugs* **2017**, *35*, 307–314.
[203] J. J. Arroyo-Crespo, A. Armiñán, D. Charbonnier, L. Balzano-Nogueira, F. Huertas-López, C. Martí, S. Tarazona, J. Forteza, A. Conesa, M. J. Vicent, *Biomaterials* **2018**, *186*, 8–21.
[204] J. J. Arroyo-Crespo, C. Deladriere, V. J. Nebot, D. Charbonnier, E. Masiá, A. Paul, C. James, A. Armiñán, M. J. Vicent, *Adv. Funct. Mater.* **2018**, *28*, 1800931.
[205] I. Dolz-Pérez, M. A. Sallam, E. Masiá, D. Morelló-Bolumar, M. D. Pérez del Caz, P. Graff, D. Abdelmonsif, S. Hedtrich, V. J. Nebot, M. J. Vicent, *J. Controlled Release* **2020**, *318*, 210–222.
[206] L. Pourtau, H. Oliveira, J. Thevenot, Y. Wan, A. R. Brisson, O. Sandre, S. Miraux, E. Thiaudiere, S. Lecommandoux, *Adv. Healthc. Mater.* **2013**, *2*, 1420–1424.
[207] C. Sanson, C. Schatz, J.-F. Le Meins, A. Soum, J. Thévenot, E. Garanger, S. Lecommandoux, *J. Controlled Release* **2010**, *147*, 428–435.
[208] K. K. Upadhyay, A. N. Bhatt, A. K. Mishra, B. S. Dwarakanath, S. Jain, C. Schatz, J.-F. Le Meins, A. Farooque, G. Chandraiah, A. K. Jain, A. Misra, S. Lecommandoux, *Biomaterials* **2010**, *31*, 2882–2892.
[209] K. K. Upadhyay, A. N. Bhatt, E. Castro, A. K. Mishra, K. Chuttani, B. S. Dwarakanath, C. Schatz, J.-F. Le Meins, A. Misra, S. Lecommandoux, *Macromol. Biosci.* **2010**, *10*, 503–512.
[210] K. K. Upadhyay, A. K. Mishra, K. Chuttani, A. Kaul, C. Schatz, J.-F. Le Meins, A. Misra, S. Lecommandoux, *Nanomedicine Nanotechnol. Biol. Med.* **2012**, *8*, 71–80.
[211] V. Jeannot, S. Mazzaferro, J. Lavaud, L. Vanwonterghem, M. Henry, M. Arboléas, J. Vollaire, V. Josserand, J.-L. Coll, S. Lecommandoux, C. Schatz, A. Hurbin, *Nanomedicine Nanotechnol. Biol. Med.* **2016**, *12*, 921–932.
[212] V. Jeannot, C. Gauche, S. Mazzaferro, M. Couvet, L. Vanwonterghem, M. Henry, C. Didier, J. Vollaire, V. Josserand, J.-L. Coll, C. Schatz, S. Lecommandoux, A. Hurbin, *J. Control. Release Off. J. Control. Release Soc.* **2018**, *275*, 117–128.
[213] "Starpharma | Home," can be found under https://starpharma.com/news/view/253/eu-marketing-approval-granted-for-vivagel-bv.
[214] C. F. Price, D. Tyssen, S. Sonza, A. Davie, S. Evans, G. R. Lewis, S. Xia, T. Spelman, P. Hodsman, T. R. Moench, A. Humberstone, J. R. A. Paull, G. Tachedjian, *PLOS ONE* **2011**, *6*, e24095.
[215] C. Bell, J. Anderson, T. Ganguly, J. Prescott, I. Capila, J. C. Lansing, R. Sachleben, M. Iyer, I. Fier, J. Roach, K. Storey, P. Miller, S. Hall, D. Kantor, B. M. Greenberg, K. Nair, J. Glajch, *J. Pharm. Pract.* **2018**, *31*, 481–488.
[216] S. Boissé, J. Rieger, K. Belal, A. Di-Cicco, P. Beaunier, M.-H. Li, B. Charleux, *Chem. Commun.* **2010**, *46*, 1950–1952.

[217] S. Boissé, J. Rieger, G. Pembouong, P. Beaunier, B. Charleux, *J. Polym. Sci. Part Polym. Chem.* **2011**, *49*, 3346–3354.
[218] S. Sugihara, A. Blanazs, S. P. Armes, A. J. Ryan, A. L. Lewis, *J. Am. Chem. Soc.* **2011**, *133*, 15707–15713.
[219] B. Charleux, G. Delaittre, J. Rieger, F. D'Agosto, *Macromolecules* **2012**, *45*, 6753–6765.
[220] N. J. Warren, O. O. Mykhaylyk, D. Mahmood, A. J. Ryan, S. P. Armes, *J. Am. Chem. Soc.* **2014**, *136*, 1023–1033.
[221] N. J. W. Penfold, J. Yeow, C. Boyer, S. P. Armes, *ACS Macro Lett.* **2019**, *8*, 1029–1054.
[222] J. Wan, B. Fan, S. H. Thang, *Chem. Sci.* **2022**, *13*, 4192–4224.
[223] D. Ikkene, J.-L. Six, K. Ferji, *Eur. Polym. J.* **2023**, *188*, 111848.
[224] C. Liu, C.-Y. Hong, C.-Y. Pan, *Polym. Chem.* **2020**, *11*, 3673–3689.
[225] E. J. Cornel, J. Jiang, S. Chen, J. Du, *CCS Chem.* **2021**, *3*, 2104–2125.
[226] M. J. Derry, L. A. Fielding, S. P. Armes, *Prog. Polym. Sci.* **2016**, *52*, 1–18.
[227] D. Zhou, S. Dong, R. P. Kuchel, S. Perrier, P. B. Zetterlund, *Polym. Chem.* **2017**, *8*, 3082–3089.
[228] G. Delaittre, J. Nicolas, C. Lefay, M. Save, B. Charleux, *Chem. Commun.* **2005**, 614.
[229] B. Charleux, J. Nicolas, *Polymer* **2007**, *48*, 5813–5833.
[230] G. Delaittre, J. Nicolas, C. Lefay, M. Save, B. Charleux, *Soft Matter* **2006**, *2*, 223.
[231] W.-M. Wan, C.-Y. Pan, *Macromolecules* **2007**, *40*, 8897–8905.
[232] K. Wang, Y. Wang, W. Zhang, *Polym. Chem.* **2017**, *8*, 6407–6415.
[233] Y. Wang, G. Han, W. Duan, W. Zhang, *Macromol. Rapid Commun.* **2019**, *40*, 1800140.
[234] D. B. Wright, M. P. Thompson, M. A. Touve, A. S. Carlini, N. C. Gianneschi, *Macromol. Rapid Commun.* **2019**, *40*, 1800467.
[235] L. Zhang, C. Song, J. Yu, D. Yang, M. Xie, *J. Polym. Sci. Part Polym. Chem.* **2010**, *48*, 5231–5238.
[236] J. C. Foster, S. Varlas, L. D. Blackman, L. A. Arkinstall, R. K. O'Reilly, *Angew. Chem. Int. Ed.* **2018**, *57*, 10672–10676.
[237] H. Tanaka, K. Yamauchi, H. Hasegawa, N. Miyamoto, S. Koizumi, T. Hashimoto, *Phys. B Condens. Matter* **2006**, *385–386*, 742–744.
[238] J. Wang, M. Cao, P. Zhou, G. Wang, *Macromolecules* **2020**, *53*, 3157–3165.
[239] Y. Kitayama, M. Okubo, *Polym. Chem.* **2014**, *5*, 2784–2792.
[240] A. Stiti, A. M. Cenacchi Pereira, S. Lecommandoux, D. Taton, *Angew. Chem. Int. Ed.* **2023**, *62*, e202305945.
[241] A. Stiti, A. M. Cenacchi Pereira, G. Fleury, S. Lecommandoux, D. Taton, *Macromolecules* **2024**, *57*, 1713–1724.
[242] P. J. Hurst, A. M. Rakowski, J. P. Patterson, *Nat. Commun.* **2020**, *11*, 1–12.
[243] Q. Shi, Y. Chen, J. Yang, J. Yang, *Chem. Commun.* **2021**, *57*, 11390–11393.
[244] J. Jiang, X. Zhang, Z. Fan, J. Du, *ACS Macro Lett.* **2019**, *8*, 1216–1221.
[245] D. Shen, B. Shi, P. Zhou, D. Li, G. Wang, *Macromolecules* **2023**, *56*, 4814–4822.
[246] D. Shen, B. Shi, P. Zhou, D. Li, W. Zhu, G. Wang, *Macromolecules* **2024**, *57*, 8970–8982.
[247] S. Varlas, P. G. Georgiou, P. Bilalis, J. R. Jones, N. Hadjichristidis, R. K. O'Reilly, *Biomacromolecules* **2018**, *19*, 4453–4462.
[248] A. P. Blum, J. K. Kammeyer, N. C. Gianneschi, *Chem. Sci.* **2016**, *7*, 989–994.
[249] H. Sun, W. Cao, N. Zang, T. D. Clemons, G. M. Scheutz, Z. Hu, M. P. Thompson, Y. Liang, M. Vratsanos, X. Zhou, W. Choi, B. S. Sumerlin, S. I. Stupp, N. C. Gianneschi, *Angew. Chem. Int. Ed.* **2020**, *59*, 19136–19142.
[250] G. Jutz, A. Böker, *Polymer* **2011**, *52*, 211–232.
[251] Y. H. Hui, F. Sherkat, *Handbook of Food Science, Technology, and Engineering - 4 Volume Set*, CRC Press, **2005**.
[252] C. Ma, X. Liu, G. Wu, P. Zhou, Y. Zhou, L. Wang, X. Huang, *ACS Macro Lett.* **2017**, *6*, 689–694.
[253] V. Kumar Kannaujiya, T. Zhang, M. Aquib, C. Boyer, *Eur. Polym. J.* **2024**, *221*, 113518.
[254] X. Liu, W. Gao, *ACS Appl. Mater. Interfaces* **2017**, *9*, 2023–2028.
[255] X. Liu, M. Sun, J. Sun, J. Hu, Z. Wang, J. Guo, W. Gao, *J. Am. Chem. Soc.* **2018**, *140*, 10435–10438.
[256] F. Jiao, Q. Su, X. Liu, *Polym. Chem.* **2024**, *15*, 1942–1946.
[257] D. J. Rucco, B. E. Barnes, J. B. Garrison, B. S. Sumerlin, D. A. Savin, *Biomacromolecules* **2020**, *21*, 5077–5085.
[258] C.-W. Chiang, X. Liu, J. Sun, J. Guo, L. Tao, W. Gao, *Nano Lett.* **2020**, *20*, 1383–1387.

[259] C. Bao, J. Chen, D. Li, A. Zhang, Q. Zhang, *Polym. Chem.* **2020**, *11*, 1386–1392.
[260] J. Li, L. Mo, C.-H. Lu, T. Fu, H.-H. Yang, W. Tan, *Chem. Soc. Rev.* **2016**, *45*, 1410–1431.
[261] L. Yang, M. Liang, C. Cui, X. Li, L. Li, X. Pan, H. S. Yazd, M. Hong, J. Lu, Y. C. Cao, W. Tan, *ChemBioChem* **2021**, *22*, 754–759.
[262] T. Lückerath, K. Koynov, S. Loescher, C. J. Whitfield, L. Nuhn, A. Walther, C. Barner-Kowollik, D. Y. W. Ng, T. Weil, *Angew. Chem. Int. Ed.* **2020**, *59*, 15474–15479.
[263] D. D. Chakraborty, P. Chakraborty, A. Mondal, *Int. J. Biol. Macromol.* **2024**, 138678.
[264] J. Bernard, M. Save, B. Arathoon, B. Charleux, *J. Polym. Sci. Part Polym. Chem.* **2008**, *46*, 2845–2857.
[265] V. Kapishon, R. A. Whitney, P. Champagne, M. F. Cunningham, R. J. Neufeld, *Biomacromolecules* **2015**, *16*, 2040–2048.
[266] I. Chaduc, E. Reynaud, L. Dumas, L. Albertin, F. D'Agosto, M. Lansalot, *Polymer* **2016**, *106*, 218–228.
[267] F. L. Hatton, M. Ruda, M. Lansalot, F. D'Agosto, E. Malmström, A. Carlmark, *Biomacromolecules* **2016**, *17*, 1414–1424.
[268] D. Ikkene, A. A. Arteni, M. Ouldali, G. Francius, A. Brûlet, J.-L. Six, K. Ferji, *Biomacromolecules* **2021**, *22*, 3128–3137.
[269] D. Ikkene, A. A. Arteni, C. Boulogne, J.-L. Six, K. Ferji, *Macromolecules* **2022**, *55*, 4268–4275.
[270] V. Delplace, J. Nicolas, *Nat. Chem.* **2015**, *7*, 771–784.
[271] T. Pesenti, J. Nicolas, *ACS Macro Lett.* **2020**, *9*, 1812–1835.
[272] S. Agarwal, *Polym. Chem.* **2010**, *1*, 953–964.
[273] M. R. Hill, E. Guégain, J. Tran, C. A. Figg, A. C. Turner, J. Nicolas, B. S. Sumerlin, *ACS Macro Lett.* **2017**, *6*, 1071–1077.
[274] A. Tardy, J. Nicolas, D. Gigmes, C. Lefay, Y. Guillaneuf, *Chem. Rev.* **2017**, *117*, 1319–1406.
[275] J. Folini, W. Murad, F. Mehner, W. Meier, J. Gaitzsch, *Eur. Polym. J.* **2020**, *134*, 109851.
[276] E. Guégain, C. Zhu, E. Giovanardi, J. Nicolas, *Macromolecules* **2019**, *52*, 3612–3624.
[277] C. Zhu, J. Nicolas, *Polym. Chem.* **2021**, *12*, 594–607.
[278] L. A. Fielding, M. J. Derry, V. Ladmiral, J. Rosselgong, A. M. Rodrigues, L. P. D. Ratcliffe, S. Sugihara, S. P. Armes, *Chem. Sci.* **2013**, *4*, 2081–2087.
[279] C. Zhu, S. Denis, J. Nicolas, *Chem. Mater.* **2022**, *34*, 1875–1888.
[280] C. Zhu, H. Beauseroy, J. Mougin, M. Lages, J. Nicolas, *Chem. Sci.* **2025**, *16*, 2619–2633.
[281] J. Liu, W.-J. Wu, X.-L. Sun, Q.-R. Qian, L.-R. Xiao, *Chem. Commun.* **2022**, *58*, 3182–3185.
[282] A. W. Jackson, *Polym. Chem.* **2020**, *11*, 3525–3545.
[283] R. A. Smith, G. Fu, O. McAteer, M. Xu, W. R. Gutekunst, *J. Am. Chem. Soc.* **2019**, *141*, 1446–1451.
[284] N. M. Bingham, P. J. Roth, *Chem. Commun.* **2018**, *55*, 55–58.
[285] M. Lages, N. Gil, P. Galanopoulo, J. Mougin, C. Lefay, Y. Guillaneuf, M. Lansalot, F. D'Agosto, J. Nicolas, *Macromolecules* **2022**, *55*, 9790–9801.
[286] P. Galanopoulo, N. Gil, D. Gigmes, C. Lefay, Y. Guillaneuf, M. Lages, J. Nicolas, F. D'Agosto, M. Lansalot, *Angew. Chem. Int. Ed.* **2023**, *62*, e202302093.
[287] L. P. D. Ratcliffe, C. Couchon, S. P. Armes, J. M. J. Paulusse, *Biomacromolecules* **2016**, *17*, 2277–2283.
[288] A. Tafech, A. Stéphanou, *Biology* **2024**, *13*, 225.
[289] S. Noack, D. Schanzenbach, J. Koetz, H. Schlaad, *Macromol. Rapid Commun.* **2019**, *40*, 1800639.
[290] C. E. Boott, J. Gwyther, R. L. Harniman, D. W. Hayward, I. Manners, *Nat. Chem.* **2017**, *9*, 785–792.
[291] Y. Sha, M. Anisur Rahman, T. Zhu, Y. Cha, C. Wayne McAlister, C. Tang, *Chem. Sci.* **2019**, *10*, 9782–9787.
[292] P. J. Hurst, A. A. Graham, J. P. Patterson, *ACS Polym. Au* **2022**, *2*, 501–509.
[293] P. Joshua Hurst, K. J. Gassaway, M. Faris Abouchaleh, N. S. Idris, C. R. Jones, C. A. Dicksion, J. S. Nowick, J. P. Patterson, *RSC Appl. Polym.* **2024**, *2*, 238–247.
[294] P. J. Hurst, J. Yoon, R. Singh, M. F. Abouchaleh, K. A. Stewart, B. S. Sumerlin, J. P. Patterson, *Macromol. Rapid Commun.* **2024**, *45*, 2400100.
[295] M. Inam, G. Cambridge, A. Pitto-Barry, Z. P. L. Laker, N. R. Wilson, R. T. Mathers, A. P. Dove, R. K. O'Reilly, *Chem. Sci.* **2017**, *8*, 4223–4230.
[296] W. Yu, M. Inam, J. R. Jones, A. P. Dove, R. K. O'Reilly, *Polym. Chem.* **2017**, *8*, 5504–5512.

[297] C. E. Ellis, J. D. Garcia-Hernandez, I. Manners, *J. Am. Chem. Soc.* **2022**, *144*, 20525–20538.
[298] H. Li, E. J. Cornel, Z. Fan, J. Du, *Chem. Sci.* **2022**, *13*, 14179–14190.
[299] A. Duro-Castano, L. Rodríguez-Arco, L. Ruiz-Pérez, C. De Pace, G. Marchello, C. Noble-Jesus, G. Battaglia, *Biomacromolecules* **2021**, *22*, 5052–5064.
[300] E. J. Dil, A. Ajji, A. Saffar, in *Polyest. Films*, John Wiley & Sons, Ltd, **2023**, pp. 306–342.
[301] S. Yao, J. Yang, J. Yang, *Polym. Chem.* **2023**, *14*, 3493–3500.
[302] B. Liu, R. Fang, W. Li, X. Wu, T. Liu, M. Lin, J. Sun, X. Chen, *J. Am. Chem. Soc.* **2024**, *146*, 16558–16566.
[303] X. Guo, B. Yang, J. Chen, *Biomacromolecules* **2024**, *25*, 3642–3650.
[304] E. Tinajero-Díaz, N. Judge, B. Li, T. Leigh, R. D. Murphy, P. D. Topham, M. J. Derry, A. Heise, *ACS Macro Lett.* **2024**, 1031–1036.

Chapter II. Elucidating the aqueous ROPISA of NCA mechanism

Table of Contents

Chapter II. Elucidating the aqueous ROPISA of NCA mechanism

II.2. Presentation of the study 79
II.2.1. Kinetics of polymerization 79
II.2.2. Presentation of the SAXS/WAXS experiment 82
II.3. Nucleation – a critical phase 86
II.3.1. SAXS/WAXS analysis 86
II.3.2. Pre-micellization hypothesis 87
II.4. Confinement-driven nucleophilicity 89
II.4.1. Acidification overtime 89
II.4.2. Initial pH effect 89
II.5. Monomer solubilization as the rate limiting factor 90
II.6. Nanoparticle growth via conformational maturation 93
II.6.1. β-sheet driven self-assembly 93
II.6.2. Conformational maturation 96
II.6.2.1. Radius estimation 96
II.6.2.2. WAXS analysis 98
II.6.3. Chain configuration evolution within nanoparticles 99
II.7. Overall Mechanism 101
II.8. Conclusion 102
II.9. Experimental section 104
II.9.1. Materials 104
II.9.2. Instruments and methods 104
II.9.2.1. Nuclear Magnetic Resonance (NMR) 104
II.9.2.2. Kinetics study 104
II.9.2.3. Size Exclusion Chromatography (SEC) 105
II.9.2.4. Fourier Transform Infrared spectroscopy (FTIR) 105
II.9.2.5. Dynamic Light Scattering (DLS) 105
II.9.2.6. Transmission Electron Microscopy (TEM) 105
II.9.2.7. Small and Wide-Angle X-ray Scattering (SAXS/WAXS) 106
II.9.2.8. CAC determination by fluorescence using Nile Red 106
II.9.3. Synthesis 106
II.9.4. SAXS models 107
II.9.5. Calculations details 107
II.10. References 109

II.1. Introduction

As discussed in **Chapter I**, polymerization-induced self-assembly (PISA) has emerged as a versatile and efficient method for synthesizing block copolymer nanoparticles with diverse morphologies at high concentrations.[1,2] Its potential applications cover various fields, including drug delivery systems, where it enables *in situ* or post encapsulation of active ingredients within highly concentrated nanoparticles.[3,4].

Several factors influence self-assembly in PISA, including the molar mass, chemical composition,[5] and architectural nature of the block copolymer,[6,7] as well as solvent polarity,[8] pH,[9] and ionic strength.[9,10] Kinetic parameters such as temperature,[11] solid content, monomer concentration,[10] and stirring conditions[10,12] also play a critical role in morphology evolution. The development of higher-order morphologies, particularly anisotropic structures such as worm-like or rod-like nanoparticles, remains challenging and is often confined to specific experimental conditions. Among the key parameters, the hydrophilic-to-hydrophobic balance is a primary determinant governing self-assembly and final nanoparticle architecture.[13] Understanding the mechanism of polymerization and self-assembly is crucial for achieving high-order morphologies in a controlled manner. The kinetic and mechanistic aspects of RAFT-mediated PISA have been widely investigated in this regard, both in dispersion and emulsion polymerization.[14–16] In this extend, X-ray scattering techniques[17] have provided valuable insights into heterogeneous processes such as emulsion PISA, elucidating the nucleation and growth of spherical nanoparticles,[18–20] as well as the morphological transitions occurring during dispersion PISA and the corresponding self-assembly and polymerization kinetics.[21–25]

On the other hand, ring-opening polymerization-induced self-assembly combined with crystallization-driven self-assembly (ROPI-CDSA) has emerged as a powerful strategy for efficiently generating both 2D and 3D anisotropic structures.[26,27] This approach harnesses the benefits of CDSA, such as access to micellar morphologies with low interfacial curvature,[28] while maintaining the scalability and practical feasibility of PISA. In this process, phase separation of crystalline-coil block copolymers is driven by a combination of solvophobic interactions and core crystallization, which collectively guide self-assembly and enable the formation of non-spherical nanoparticles. The proposed mechanism involves two competing growth pathways: (i) unimer addition and (ii) particle aggregation, which proceed via precursor particles with low corona densities, thereby facilitating 2D and 3D growth. Patterson's group has highlighted the critical role of polymerization kinetics in dictating self-assembly pathways and controlling the resulting morphologies.[29] Their findings suggest that the process operates under non-equilibrium conditions, where polymerization proceeds at a faster rate than self-assembly, leading to kinetically trapped nanoparticles.

More recently, the combination of ring-opening polymerization (ROP) of *N*-carboxyanhydrides (NCA) with PISA has been reported under both organic[30,31] and aqueous conditions.[32] This last approach has demonstrated the efficient formation of homogeneous polypeptide anisotropic nanostructures, such as

worm-like and rod-like nanoparticles, from an initially heterogeneous mixture. Furthermore, the anisotropy of the resulting nanostructures can be finely tuned through various molecular interactions, including secondary structure[38] and chirality,[39] within the polypeptide block.

Despite its promising potential, the underlying mechanism governing aqueous ROPISA remains poorly understood, limiting the ability to achieve higher degrees of polymerization or more complex morphologies. A major challenge arises from the nature of the NCA monomer, which is solid, poorly soluble, and highly susceptible to hydrolysis.[40,41] For successful and controlled polymerization, the kinetic balance must favor ROP over hydrolysis. Specific conditions, such as an initial pH of 8.5 maintained by a 50 mM sodium bicarbonate buffer and a solid content of 7 wt%, have been identified as key factors promoting aminolysis over hydrolysis, thereby enabling controlled polymerization.[32] We hypothesize that polymerization outpaces hydrolysis due to micellization and confinement effects, which locally enhance the concentration of reactive species. However, direct experimental evidence supporting this confinement-driven acceleration remains to be established.

In this chapter, we investigate the fundamental mechanisms underlying aqueous ROPISA through small-angle and wide-angle X-ray scattering (SAXS/WAXS) and complementary techniques like size-exclusion chromatography (SEC) and transmission electron microscopy (TEM), with the goal of elucidating the interplay between polymerization and self-assembly. We specifically focus on the ROPISA of γ-benzyl-*L*-glutamate *N*-carboxyanhydride (BLG-NCA), initiated by α-amino polyethylene glycol (PEG-NH_2) as the macroinitiator, leveraging our prior knowledge and experience with this system (Scheme II-1).

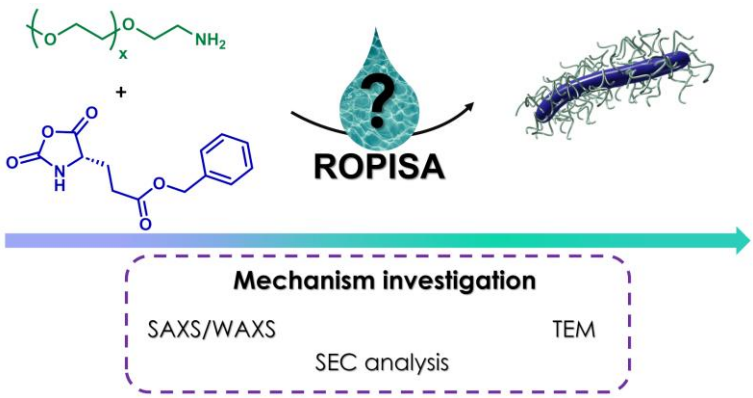

Scheme II-1. Mechanism investigation of aqueous ROPISA in the particular case of of γ-benzyl-*L*-glutamate *N*-carboxyanhydride polymerization by α-amino polyethylene glycol.

II.2. Presentation of the study

II.2.1. Kinetics of polymerization

The aqueous ROPISA of BLG-NCA initiated by PEG_{5k}-NH_2, already detailed in **Chapter I** and reported by Grazon *et al.*[32] involves the addition of a PEG_{5k}-NH_2 solution in 50 mM $NaHCO_3$ to BLG-

NCA powder under vigorous stirring, at a total solid content of 7 wt% (Scheme II-2). Starting from a heterogeneous mixture, the reaction proceeds overnight to yield a bluish opalescent dispersion.

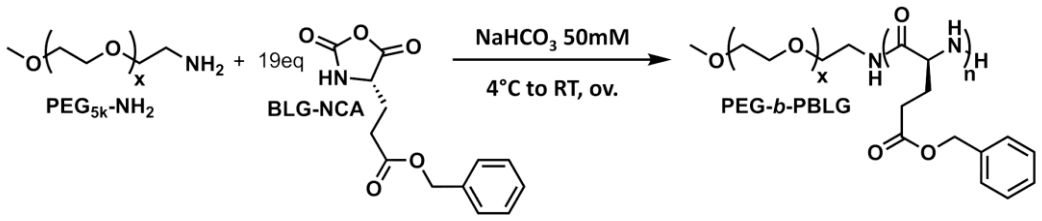

Scheme II-2. Aqueous ROPISA of γ-benzyl-*L*-glutamate *N*-carboxyanhydride initiated by α-amino polyethylene glycol.

Despite the successful application of this method, little is known about the underlying polymerization mechanism and kinetics. To gain further insight, we first investigated the kinetics of BLG-NCA polymerization using a quenching strategy. Earlier attempts in our group included monitoring by FTIR spectroscopy and quenching with fluorescein isothiocyanate (FITC).[32] However, FTIR in aqueous conditions proved difficult to optimize, and FITC may be too bulky and insufficiently reactive for effective quenching. We therefore turned to acid-based quenching, exploring two strategies: one using hydrochloric acid (HCl), based on previous studies indicating that HCl can hydrolyze NCA without interfering with ongoing polymer chains,[42] and another using acetic anhydride (Ac_2O). At selected time intervals, 0.4 mL aliquots of the reaction mixture were withdrawn and immediately quenched by the rapid addition of an excess of either HCl or Ac_2O. This step served to hydrolyze any remaining unreacted NCA into the corresponding amino acid. Additionally, Ac_2O acetylated the terminal amine group, effectively capping the growing polymer chains and halting further propagation. The quenched samples were then dialyzed against ultrapure water (MWCO 3.5 kDa), lyophilized, and analyzed by SEC to evaluate the efficiency of quenching and monitor polymer growth over time (Figure II-1).

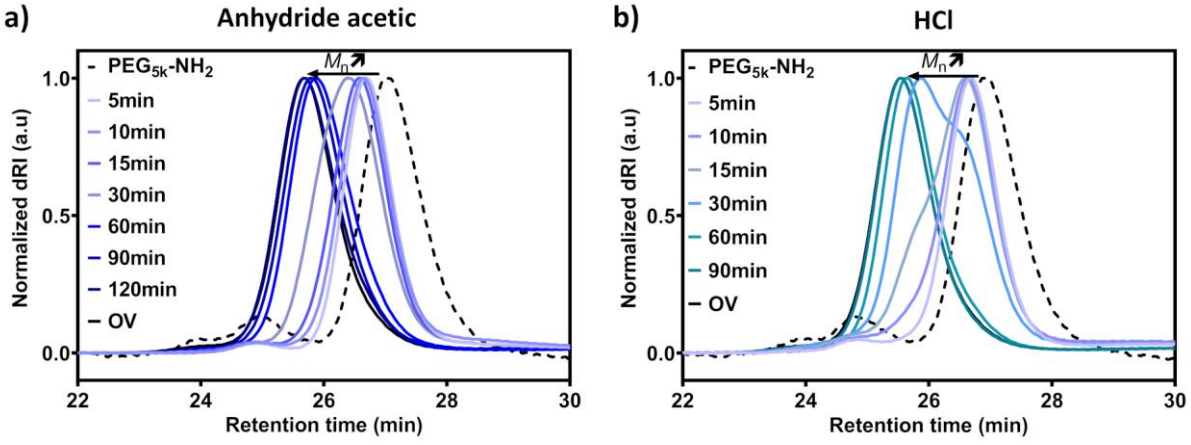

Figure II-1. (a) SEC chromatograms of quenched aliquots with acetic anhydride. (b) SEC chromatograms of quenched aliquots with hydrochloride acid in DMF (+ 1% LiBr, detection by differential refractive index).

SEC analysis indicated that HCl quenching was less effective, as shown by the presence of bimodal molecular weight distributions. As a result, acetic anhydride was selected as the preferred quenching agent.

Subsequently, the quenched aliquots were analyzed by ^{1}H NMR spectroscopy to indirectly determine the conversion of BLG-NCA by calculating the degree of polymerization (DP) over time (Figure II-2).

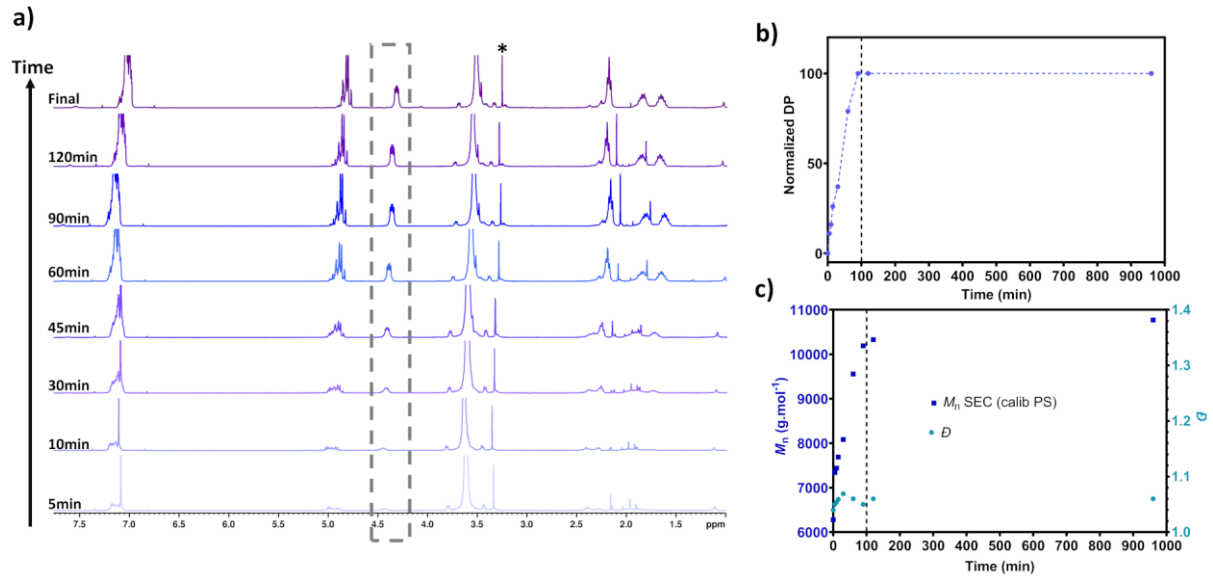

Figure II-2. (a) ^{1}H NMR spectra of quenched aliquots with acetic anhydride. In the red box, the C_α proton used for DP determination, as compared to the methyl protons for PEG (*). (b) Normalized evaluated DP overtime after quench with acetic anhydride and NMR measurements. (c) Corresponding number-average molar mass and dispersity determined by SEC using a polystyrene calibration (DMF + 1 % LiBR, dRI detection).

This analysis revealed that polymerization was completed within 100 minutes. This conclusion was further supported by the evolution of the molar mass over time, determined by size-exclusion chromatography (SEC) using polystyrene (PS) calibration, which plateaued accordingly. These results confirm the relatively fast kinetics of polymerization.

To investigate the kinetics of the self-assembly process, a synchrotron X-ray source was therefore required to achieve the high temporal resolution necessary for *in situ* SAXS studies of the aqueous ROPISA of BLG-NCA. The presence of large aggregates of crystalline, water-insoluble monomer in suspension during the reaction hindered turbidimetry or light scattering studies. However, a specific setup had to be used to ensure good stirring during the reaction.Indeed, stirring proved to be a critical parameter for efficient polymerization. SEC analysis showed that insufficient agitation, either no stirring (0 rpm) or low speed stirring (300 rpm), resulted in poor polymer growth from the macroinitiator, underscoring the importance of adequate mixing for properinitiation and propagation (Figure II-3a). Interestingly, despite ineffective initiation, nanoparticle formation still occurred, as shown in Figure II-3b, although with noticeable heterogeneity in the resulting assemblies.

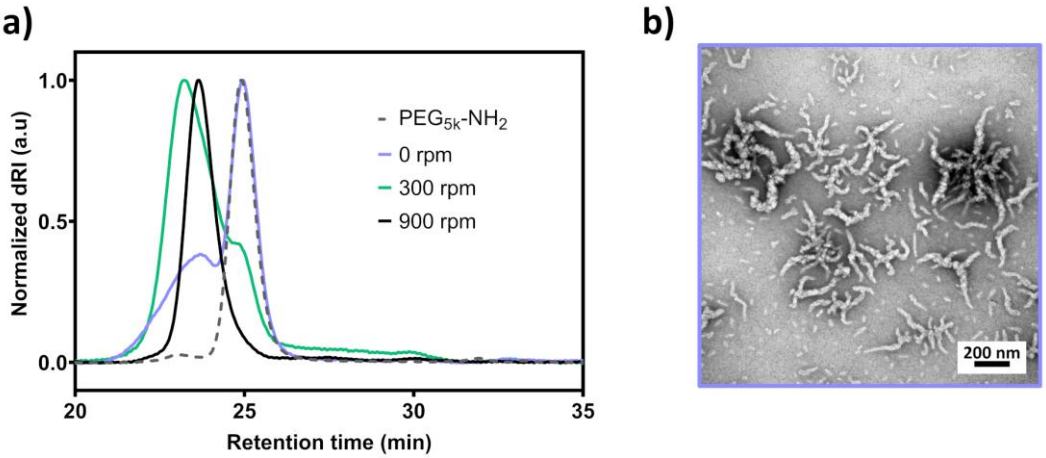

Figure II-3. (a) SEC chromatograms of PEG-*b*-PBLG copolymers obtained upon ROPISA at different stirring rate in DMF (+ 1% LiBr, detection by differential refractive index). (b) Representative TEM image for a PEG-*b*-PBLG nanoparticles dispersion obtained upon ROPISA with no stirring.

This feature is already well-known in PISA emulsion, where a sufficient stirring is needed to ensure adequate interfacial contact between the water-immiscible monomer and the water-soluble initiator in the continuous aqueous phase.[10,12,43]

II.2.2. Presentation of the SAXS/WAXS experiment

To address these constraints for the *in situ* SAXS experiments and enable a good mixing, the reaction was conducted in a vial immersed in an ice bath under vigorous stirring; with the quantities detailed in Table II-1. Comparison of experimental conditions and the results for the aqueous ROPISA of BLG-NCA initiated by PEG_{5k}-NH_2 for a targeted DP of 19, performed either in a conventional (lab conditions) or the *in situ* setup. The reactive medium was then transferred *via* a peristaltic pump to a capillary positioned within the X-ray beam within a closed flow setup (Figure II-4).

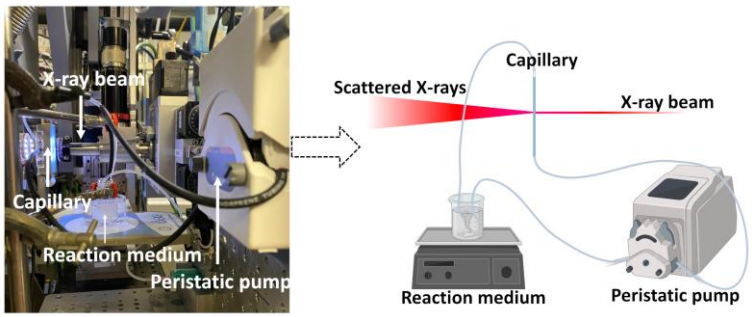

Figure II-4. Photograph of the setup used for *in situ* SAXS/WAXS experiments during the aqueous ROPISA of BLG-NCA, along with a schematic representation. For clarity, the capillary is depicted vertically but was positioned horizontally.

To prevent tubing clogging and minimize viscosity-related issues, the solid content was reduced from the usual 7 wt% to 6 wt%. At this concentration, the polymerization kinetics remained unaffected, as

confirmed by ^{1}H NMR analysis of quenched aliquots using the same procedure described previously (Figure II-5).

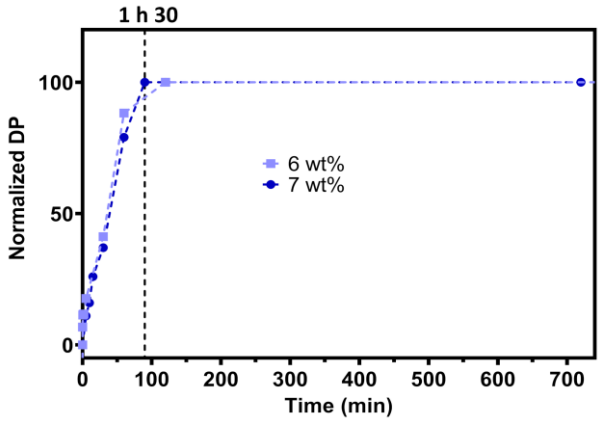

Figure II-5. Kinetic profiles of normalized DP *versus* time at an initial feed ratio [M]/[I] of 19, with solid contents of 6 or 7 wt%, as determined by ^{1}H NMR spectroscopy.

Data were collected in a q range between 0.0066 and 1 $Å^{-1}$ until no further change in the scattering pattern was observed, which indicated the end of the polymerization.

After the experiment, to ensure that the experimental setup did not affect the polymerization process, the mixture was collected, stirred overnight, and then purified by dialysis. ^{1}H NMR spectroscopy and SEC chromatography were performed to confirm the copolymer structure. The degree of polymerization calculated from ^{1}H NMR was 20, consistent with the targeted value of 19 (Figure II-6a). SEC analysis of PEG-*b*-PBLG diblock copolymer chains synthesized via the laboratory-based method indicated very similar molar mass data compared to that obtained after the *in situ* SAXS experiment (M_n = 10 900 and $Đ$ = 1.07 vs M_n = 10 500 g.mol^{-1} and $Đ$ = 1.05, respectively) (Figure II-6b).

Table II-1. Comparison of experimental conditions and the results for the aqueous ROPISA of BLG-NCA initiated by PEG_{5k}-NH_2 for a targeted DP of 19, performed either in a conventional (lab conditions) or the *in situ* setup.

	m (PEG_{5k}-NH_2) [mg]	m (BLG-NCA) [mg]	V ($NaHCO_3$ 50mM) [mL]	τ_s [wt%]	M_n ($Đ$) [a)] [kg.mol^{-1}]
In Situ	190	190	6	6	10.5 (1.05)
Lab conditions	300	300	8	7	10.9 (1.07)

[a)] Number average molar-mass (M_n) and molar-mass dispersity determined by SEC in DMF +1% LiBr using PS calibration.

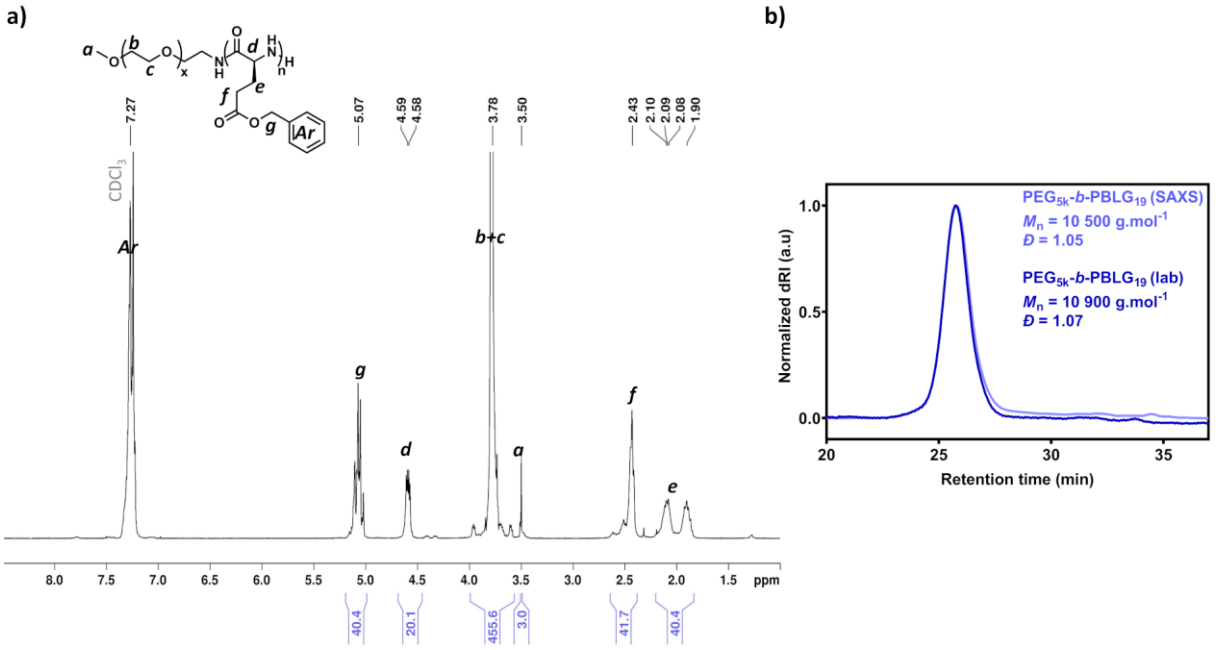

Figure II-6. (a) ^{1}H NMR spectrum in $CDCl_3$ + 15 % TFA. (b) SEC chromatogram of post-mortem PEG_{5k}-*b*-$PBLG_{19}$ compared to laboratory conditions in DMF (+ 1% LiBr, detection by differential refractive index).

The opalescent solution was further characterized by dynamic light scattering (DLS) and transmission electron microscopy (TEM). DLS studies revealed the presence of nanoparticles with Z-average diameter of 96 ± 5 nm with a polydispersity index of 0.27, in agreement with previous laboratory results (Figure II-7).[32,38]

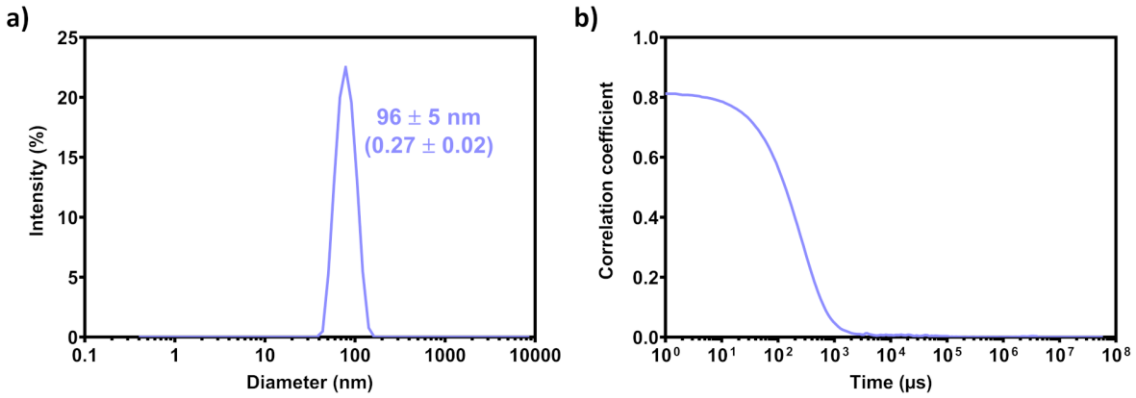

Figure II-7. (a) DLS profiles of *post-mortem* PEG_{5k}-*b*-$PBLG_{19}$ after dialysis and (b) associated correlogram.

TEM analysis further confirmed the presence of worm-like nanoparticles, with a mean width of 17 ± 2 nm and a mean length of 122 ± 40 nm (Figure II-8).

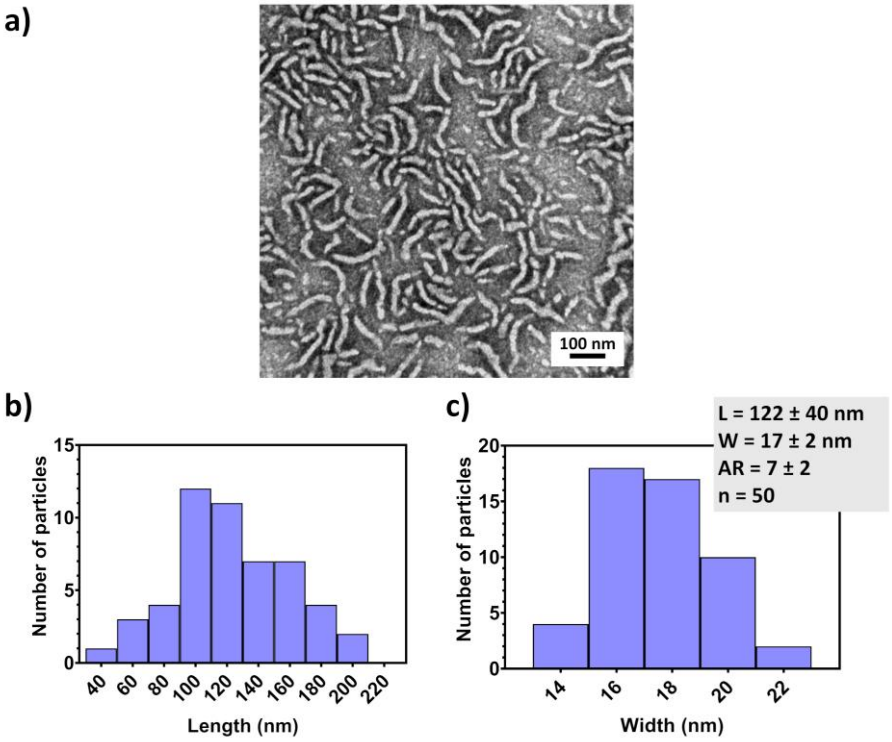

Figure II-8. (a) Representative TEM image of *post-mortem* PEG_{5k}-*b*-$PBLG_{19}$ nanoparticles. (b) Length and (c) diameter distribution of the *post-mortem* PEG_{5k}-*b*-$PBLG_{19}$ nanoparticles obtained by analysis of 50 nano-objects by ImageJ on a TEM image.

At the end of the experiment, SAXS was performed on nanoparticle dispersions in a static capillary (Figure II-9). The scattering intensity $I(q)$ as a function of the wave vector q, presented in a log-log plot, exhibited a characteristic q^{-1} power law in the low-q range, confirming the presence of cylindrical structures. A polydisperse cylinder model was used to extract the cylinder radius, though the applied q range did not allow for determining the cylinder length. The obtained radius of 6.5 nm aligns with previously reported laboratory results.[38]

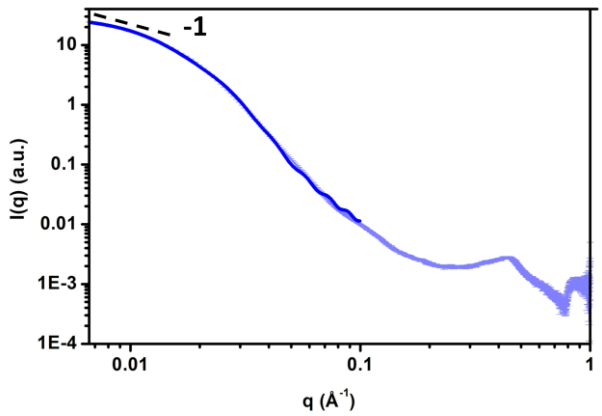

Figure II-9. *Post-mortem* SAXS pattern. Blue solid line shows the data fits obtained using a polydisperse cylinder model.

From all these experiments, we have been able to determine the different critical phases and features of the ROPISA process that will be described in the following parts.

II.3. Nucleation – a critical phase

II.3.1. SAXS/WAXS analysis

SAXS patterns were collected every 1.5 seconds for the first 5 minutes, and every 30 seconds for the remaining 45 minutes. For clarity, only the spectra collected every minute are shown, but the data were analyzed across all spectra (Figure II-10a). In order to determine the onset of micellization during the *in situ* SAXS experiment and to elucidate the kinetics of self-assembly, the scattering intensity, $I(q)$, was plotted as a function of time for the 50 minutes of reaction at an arbitrary q value of 0.015 Å^{-1} (Figure II-10b). Indeed, the volume of a scattering object is proportional to the scattering intensity in the low q regime, and an upturn in $I(q)$ could be assigned to the onset of nucleation.[18–20,22] The arbitrary q value was chosen to avoid the scattering signal from the larger crystalline aggregates of monomers, that should scatter at lower q values.

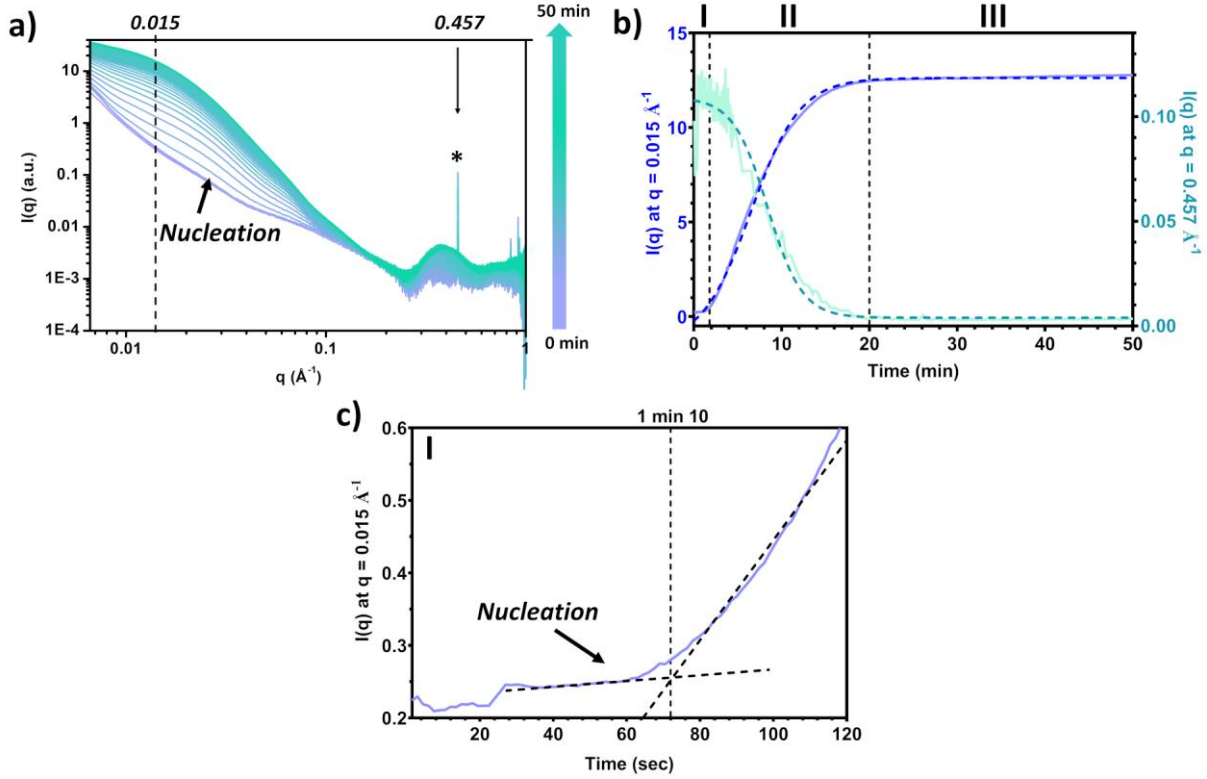

Figure II-10. SAXS patterns recorded during the aqueous ROPISA of BLG-NCA targeting PEG$_{5k}$-*b*-PBLG$_{19}$ at 6 wt% solid content. (a) Patterns every 1 minute from 0 to 50 minutes. (b) Plot of $I(q)$ at $q = 0.015$ Å^{-1} and $q^* = 0.457$ Å^{-1} *versus* time. (c) Plot of $I(q)$ at $q = 0.015$ Å^{-1} from 0 to 120 secondes *versus* time, exhibiting the onset of micellar nucleation, indicated by an arrow.

The scattering data appears to be sigmoidal, which has been observed in a variety of PISA processes.[22,29,44,45] Three distinct time intervals can be identified: (I) a lag phase before 1 min 10 s, where the scattering intensity remains low; (II), a growth-phase, during which the scattering intensity increases rapidly; and (III) a plateau phase after 20 minutes of reaction, where the scattering intensity stabilizes. The transition from the first to the second phase, occurring after approximately 1 minute, is marked by a sharp

increase in scattering intensity, indicating the formation of larger scattering objects, which corresponds to micelle formation or nucleation (Figure II-10c).

To better elucidate the self-assembly kinetics and compare it with polymerization kinetics, we monitored monomer consumption in its crystalline form. Indeed, BLG-NCA monomer used displayed a singular Bragg peak at $0.457\ Å^{-1}$ (Figure II-11).

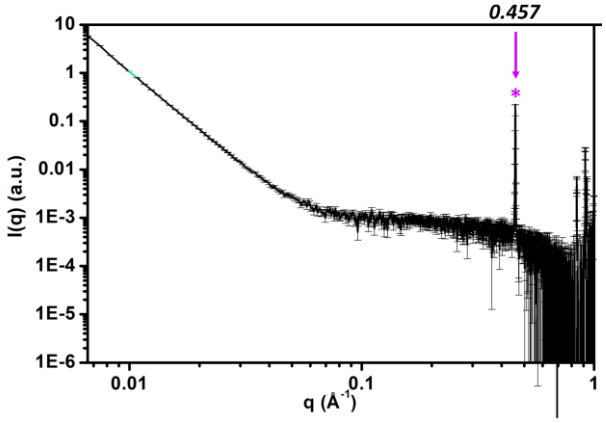

Figure II-11. SAXS patterns of BLG-NCA in bicarbonate buffer at initial time.

By plotting the scattering intensity at this value overtime, one can thus estimate the consumption rate and then, indirectly, the polymerization rate, assuming that the monomer is quickly transferred into micellar cores and polymerized (Figure II-10b). This analysis also revealed three times interval, corresponding to the ones determined by plotting the scattering intensity at $0.015\ Å^{-1}$. Similarly, before 1 minute, most of the monomers remained insoluble and thus not consumed in solutions as the scattering intensity remained stable. Then, ROPISA appears to allow very short growing chains to initiate nucleation.

II.3.2. Pre-micellization hypothesis

This rapid nucleation may result from a pre-micellization effect due to the high concentration of PEG_{5k}-NH_2 used as a macroinitiator. Indeed, referring to emulsion PISA, early nucleation is expected when a surfactant is present above its critical micelle concentration (CMC), as pre-formed micelles facilitate the entry of oligomeric growing chains once they reach a certain size. Conversely, when the surfactant concentration is below its CMC, oligomers must grow longer before undergoing phase separation and forming primary particles. In this case, homogeneous polymerization in the continuous aqueous phase is slower due to the limited solubility of the hydrophobic monomer.[19,46] In analogy, PEG_{5k}-NH_2 may act as a pseudo-surfactant due to its high concentration, potentially leading to the formation of pseudo-micelles because of its reduced solubility. To test this hypothesis, we determined the critical aggregation concentration (CAC) of PEG_{5k}-NH_2 under ROPISA conditions (50 mM $NaHCO_3$, 4 °C) (Figure II-12a). The CAC was determined to be around 30 $mg{\cdot}mL^{-1}$, while the *in situ* SAXS experiments, conducted at a solid content of 6 wt%, required a PEG_{5k}-NH_2 concentration of 32 $mg.mL^{-1}$, slightly above the CAC. When ROPISA was performed below this CAC, SEC analysis revealed a higher proportion of oligomers eluting

at higher retention times, which we attributed to water-initiated BLG oligomers (Figure II-12b). Once the CAC was exceeded, even largely, these oligomers were no longer detected, and the resulting nanoparticles exhibited the same worm-like morphology (Figure II-12c, d).

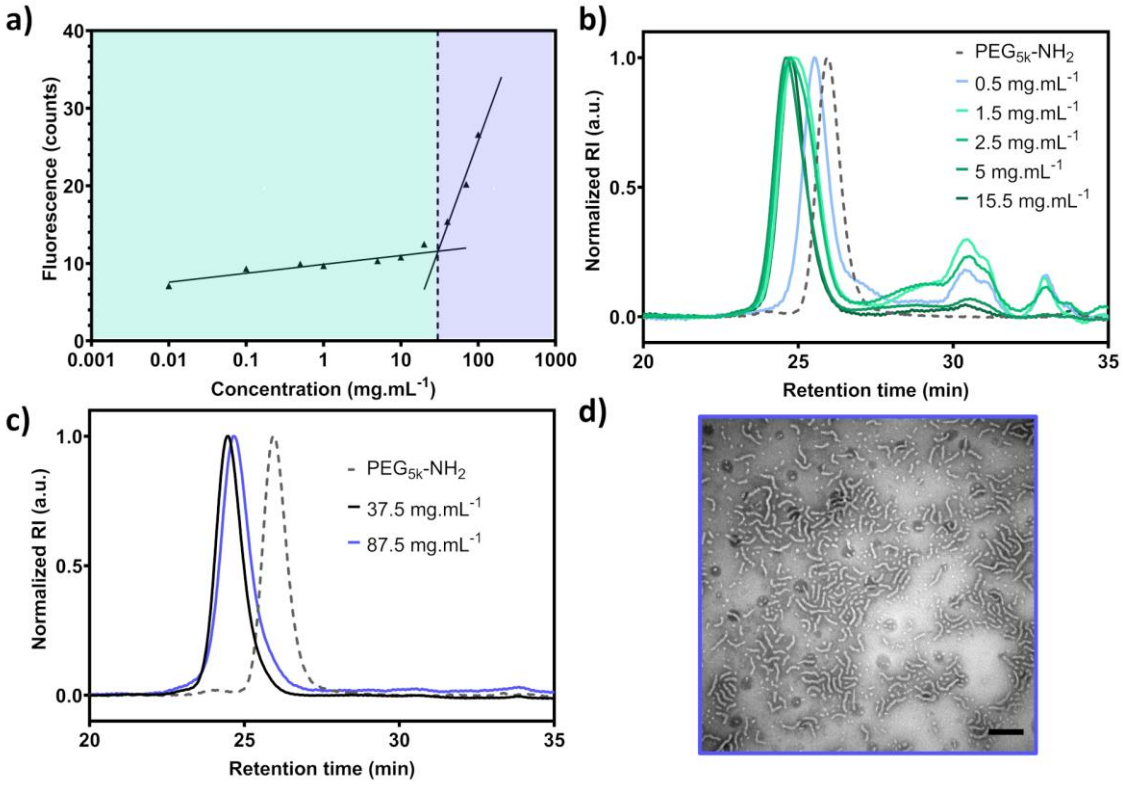

Figure II-12. (a) CAC determination of PEG_{5k}-NH_2 in $NaHCO_3$ 50mM at 4°C by using Nile Red and by measuring fluorescence at 650 nm. CAC is defined as the concentration at the intersection of the two logarithms regression $y = a - b \times \ln x$. (b) SEC chromatograms of PEG-*b*-PBLG copolymers obtained upon ROPISA at concentrations of PEG_{5k}-NH_2 below its CAC and above its CAC. (initial feeding ratio [M]/[I] = 19) in DMF (+ 1% LiBr, detection by differential refractive index). (d) Representative TEM image of PEG-*b*-PBLG suspension upon ROPISA using PEG_{5k}-NH_2 at 87.5 $mg.mL^{-1}$. Scale-bar : 200 nm.

These observations confirmed that PEG form pre-micelles, which facilitate early nucleation by sequestering soluble monomers in their core and protecting them from hydrolysis. Polymerization then occurs within these pre-micelles, leading to the formation of nascent micelles that are rapidly stabilized by short BLG oligomers which exhibit a strong propensity to adopt β-sheet conformations.[47,48] These β-sheets further self-assemble into highly stable fibers, reinforcing micelle stability.[49,50] Below the CAC, the limited solubility of BLG-NCA in the continuous aqueous phase slows polymerization, leading to greater hydrolysis, as evidenced by the larger proportion of water-initiated oligomers. This confined environment accelerates polymerization kinetics by increasing locally the monomer concentration and reducing diffusion. The reaction predominantly takes place within the self-assembled micelles, which act as individual nanoreactors. As the soluble monomer in the micelles is consumed, it is replenished *via* diffusion from the continuous phase.[44,51]

II.4. Confinement-driven nucleophilicity

II.4.1. Acidification overtime

Even if this is quite clear that fast nucleation and micellar confinement limit monomer hydrolysis, the amino group acting as the reactive site should theoretically undergo protonation during polymerization due to CO_2 release and the resulting acidification of the medium. This protonation of the chain-end amine would reduce its nucleophilicity, potentially leading to less efficient aminolysis and a slower polymerization rate. The acidification of the polymerization medium was confirmed by monitoring the pH value over time during a classical ROPISA of BLG-NCA (Figure II-13).

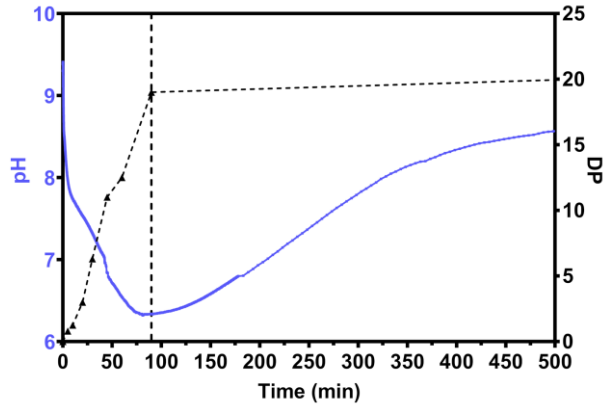

Figure II-13. Evolution of pH during the polymerization, correlated with the quenched DP.

Initially, the pH was 9.3, slightly higher than the expected value for the $NaHCO_3$ 50 mM buffer expected to be 8.5, attributed to the terminal amine of PEG_{5k}-NH_2 that contributed to the increase in pH. Then, a sharp pH decrease occurred within the first few minutes, followed by a more gradual decrease, reaching a pH 6.3 after 75 minutes. This value corresponds to the pKa of dissolved CO_2 in aqueous solution, indicating significant CO_2 release. Beyond this point, which marks the end of polymerization and CO_2 production, the pH gradually returned to its initial value, consistent with the buffering effect of the bicarbonate solution at 50mM. Despite this significant and rapid acidification, the polymerization kinetics did not seem affected. One can hypothesize that the initial buffered conditions are critical to induce rapid micelle formation and polymerization initiation. Then, once confined in the micellar core, the primary amine reactive site could remain more basic, maintaining a better nucleophilic character and enabling efficient propagation.[52–54]

II.4.2. Initial pH effect

To evaluate this hypothesis, we studied the effect of different initial pH values on polymerization. Specifically, we used $NaHCO_3$/Na_2CO_3 and NaH_2PO_4/Na_2HPO_4 at 0.05 M to adjust the initial pH between 4.6 and 11.4. The resulting copolymers were analyzed by SEC after typical ROPISA conditions, namely

overnight stirring at 7 wt% solid content for an initial feeding ratio of 19, followed by purification by dialysis (Figure II-14).

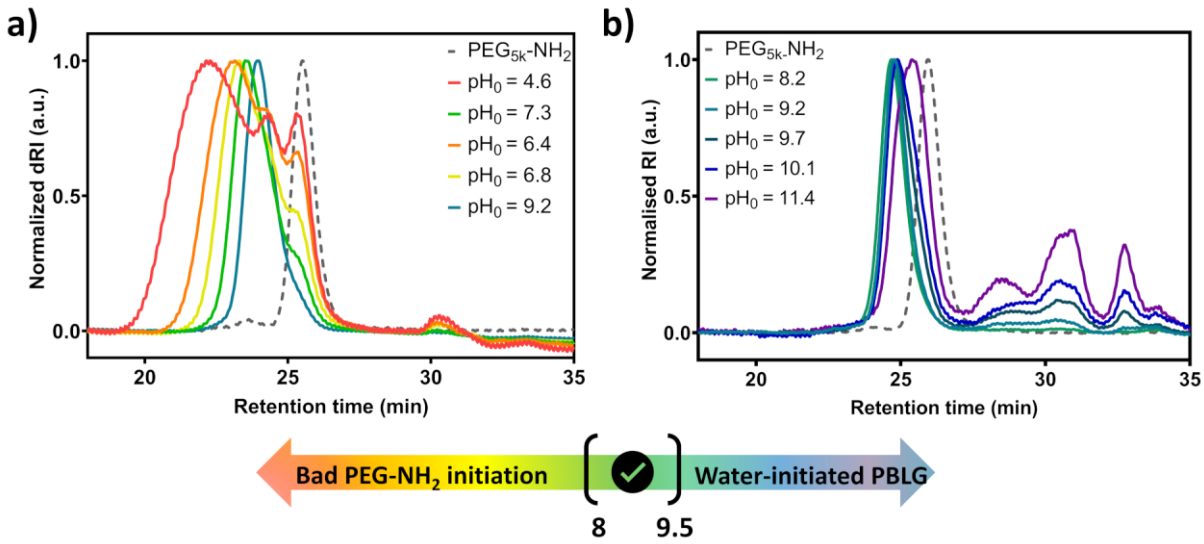

Figure II-14. (a) SEC chromatograms for ROPISA conducted in pH < 9 in phosphate buffer. (b) SEC chromatograms for ROPISA conducted in pH >9 in carbonate buffer in DMF (+ 1% LiBr, detection by differential refractive index).

At pH < 8, a second peak appeared in the chromatogram, overlapping with the macroinitiator peak, indicating unreacted PEG (Figure II-14a). This suggests that partial or complete protonation of the PEG amine hinders initiation. Conversely, at pH > 9.5, above the pKa of the PEG primary amine, polymerization is efficiently initiated, with no detectable unreacted PEG (Figure II-14b). However, additional peaks at higher retention times indicated the formation of low-molar mass species, likely resulting from BLG homopolymerization initiated by hydroxide ions.[55] Under highly basic conditions, NCA deprotonation may also lead to uncontrolled anionic polymerization through the activated monomer mechanism.[55,56]

Overall, for effective ROPISA, pH value should be initially maintained between 8 and 9.5, near the pKa of the PEG primary amine, to ensure the presence of the nucleophilic NH_2 form, allowing a fast polymerization initiation. Once micelles formed, even if the medium acidifies, the nucleophilic character of the amino propagation center is preserved due to the segregation effect. This confinement mechanism is similar to the ribosomal peptidyl transferase center (PTC), which isolates substrates to accelerate peptide bond formation, about 10^5 to 10^7 fold over the rate of comparable reactions in solution, by preventing protonation of the amino group and side reactions like unwanted hydrolysis.[57,58]

II.5. Monomer solubilization as the rate limiting factor

To further validate the hypothesis that confinement increases polymerization kinetics, we examined the monomer consumption rate and self-assembly dynamics in greater detail (Figure II-10). Our goal was to clarify the interplay between solubilization, polymerization, and self-assembly. Given previous observations, we hypothesize that polymerization within the confined micellar environment occurs at an

extremely fast rate. Consequently, the primary limiting factors should be the solubilization of the monomer and its diffusion into the micellar nanoreactors, rather than the polymerization itself.

As we have already determined that the scattering intensity data appears to be sigmoidal for both q values in the ROPISA case, we modeled the data as a logistic function:[29]

$$f(x) = \frac{L}{1 + e^{-k(x-x_0)}} + m$$

where L is the maximum value of the function, m is the intercept, x_0 is the x value of the steepness point of the curve and k quantifies the steepness of the sigmoidal curve. Herein, k can be used as a quantification of the rate of scattering intensity increase, which is an estimate for the rate of self-assembly (k_{SA}) at low q value (0.015 Å^{-1}) and for monomer consumption k_{BLG} at the q value of the Bragg peak (0.457 Å^{-1}). Using this model, the kinetic constants were found to be in the same order of magnitude, with k_{SA} estimated at 0.36 min^{-1} and k_{BLG} at 0.51 min^{-1}. The latter value, which accounts for both solubilization and polymerization kinetics, being slightly higher.

We also examined the consumption rate of BLG-NCA alone by performing *in situ* SAXS experiments under identical conditions without adding a macroinitiator. The scattering intensity at 0.457 Å^{-1} was monitored overtime (Figure II-15a, b). When crystalline BLG-NCA is introduced into a slightly basic environment, the monomer can undergo hydrolysis, leading to polymerization *via* a water-initiated process, as depicted in Figure II-15c. A mixture of amino acids, oligomers and polymers are then obtained, as it can be observed by SEC (Figure II-15d).By tracking the disappearance of the crystalline peak in the high q region, we can then compare the polymerization kinetics driven by water initiation and by ROP from the PEG macroinitiator The scattering intensity at 0.457 Å^{-1} decreased at a significantly slower rate, with a substantial proportion of unreacted monomer still present after 20 minutes, whereas in the ROPISA case, the monomer was fully consumed. A simple linear fit yielded an estimated kinetic rate of 0.002 min^{-1}, more than 500 times slower than in the ROPISA process.

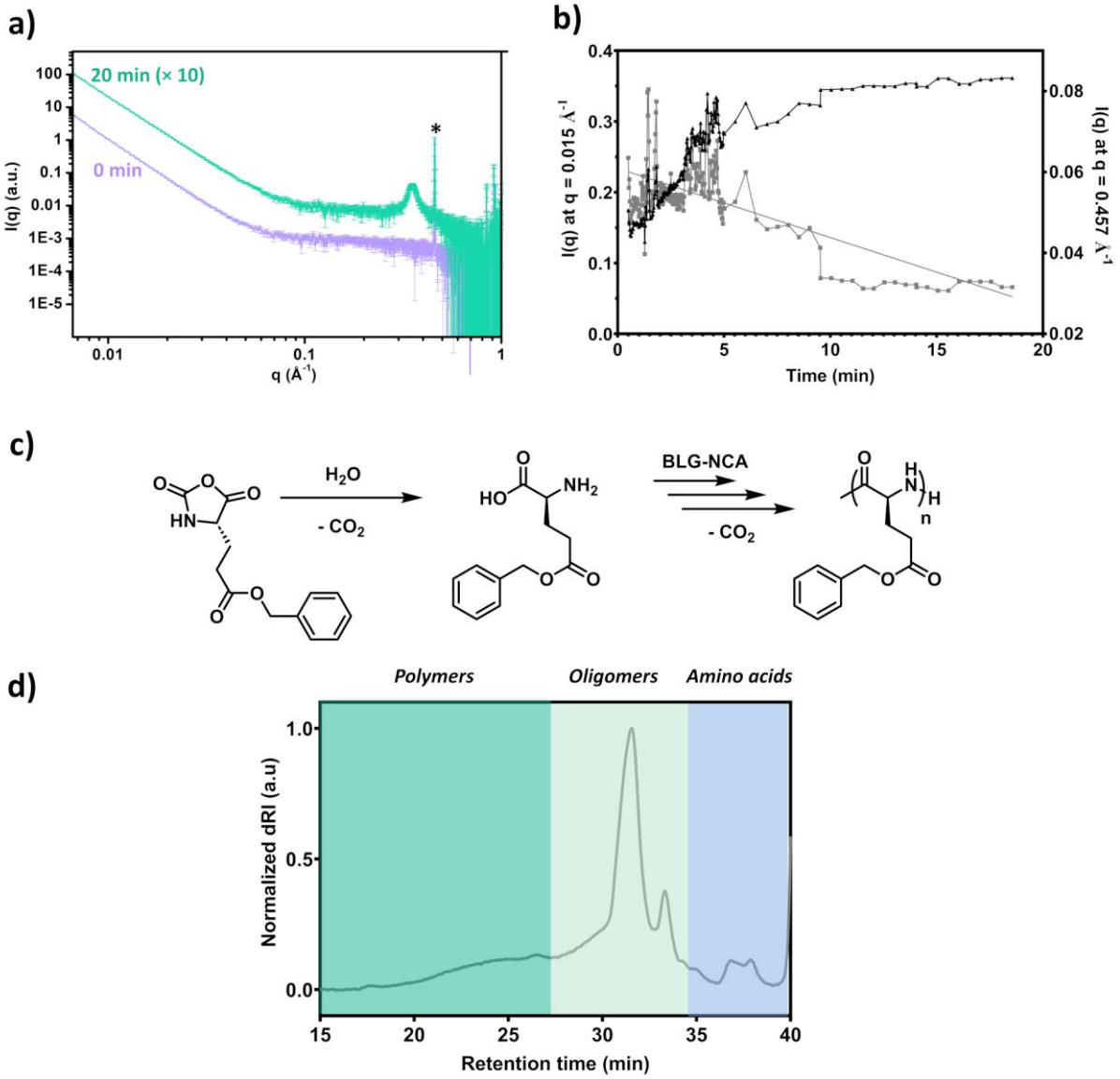

Figure II-15. (a) SAXS patterns of BLG-NCA in bicarbonate buffer at initial time and after 20 minutes of stirring (× 10). (b) Plot of $I(q)$ at $q = 0.015\,\text{Å}^{-1}$ and $q = 0.457\,\text{Å}^{-1}$ *vs* time. (c) Hydrolysis and water-initiated polymerization of BLG-NCA in aqueous solution. (d) Resulting SEC chromatograms of BLG-NCA in ROPISA conditions, without macroinitator, displaying broad populations of polymers, oligomers and amino acids (DMF + 1% LiBr, dRI detection).

These findings underscore the markedly faster polymerization kinetics of BLG-NCA in the ROPISA process compared to its hydrolysis or water-initiated polymerization. The slow consumption of BLG-NCA in bicarbonate buffer suggests that monomer solubility is the rate-limiting step. In contrast, within the micellar environment, confinement effects and the rapid polymerization of solubilized monomers shift the solubilization equilibrium, allowing for continuous monomer uptake and accelerated polymerization. This confinement effect, which accelerates the polymerization process, has already been explored by Cheng's group in the ROP of BLG-NCA in binary solvent mixtures.[59] In their study, the polymerization rate was enhanced by 100-fold compared to uncatalyzed polymerization in CH_2Cl_2, while effectively preventing unwanted NCA hydrolysis. This hypothesis is further supported by the influence of ultrasonication, which enhances monomer solubilization and diffusion, leading to an acceleration of

polymerization.[39] These results highlight the critical role of monomer solubility and diffusion in dictating the kinetics of ROPISA.

II.6. Nanoparticle growth via conformational maturation

II.6.1. β-sheet driven self-assembly

Having highlighted this crucial nucleation step, we next investigated nanoparticle growth to better understand the systematic formation of anisotropic morphologies, an outcome that is typically more challenging to achieve in conventional dispersion or emulsion PISA processes.[9,13] We then focused the analysis on intervals II and III determined previously to better understand nanoparticle evolution during the reaction (Figure II-10). To investigate morphological changes, we analyzed the characteristic slope of the scattering intensity in the mid q range ($0.006 \leq q \leq 0.010$ Å^{-1}) (Figure II-16). Indeed, this slope is characteristic of the shape of the scattered objects[60] where spheres, rigid rods and vesicles exhibit typical power-law slope of respectively zero, q^{-1} and q^{-2}. Initially, the slope was close to -4, reflecting the presence of large monomer crystals in dispersion, which correlates with the presence of the scattering peak at 0.457 Å^{-1} that is characteristic of the crystalline monomer (Figure II-11).

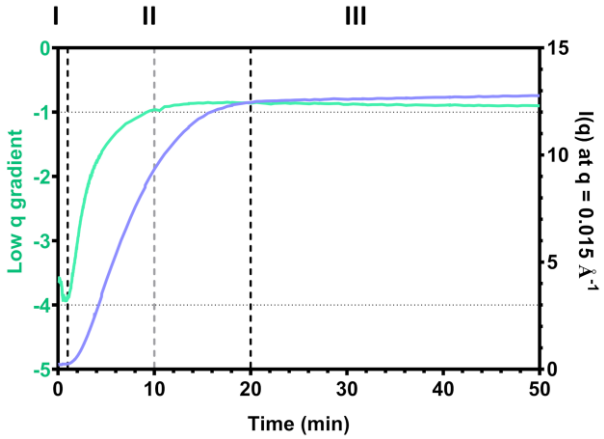

Figure II-16. Plot of $I(q)$ at $q = 0.015$ Å^{-1} and the gradient at low q ($0.006 \leq q \leq 0.010$ Å^{-1}) *vs* time.

Initially, the gradient was close to -4, reflecting the presence of large monomer crystals in dispersion, which correlates with the scattering intensity at 0.457 Å^{-1} exhibiting a large presence of crystalline monomer. After 10 minutes, it shifted to approximately q^{-1}, indicating the formation of linear cylinders. Subsequently, the slope remained constant, indicating that the morphology had stabilized in its cylindrical form. Unfortunately, the presence of monomer aggregates dominates the scattering signal, preventing the detection of the initial micelle formation associated with the nucleation phase However, based on previous PISA studies,[14,61,62] CDSA[26,63] and our understanding of PEG-*b*-PBLG at lower DP, we hypothesize that spherical micelles initially form when one or two BLG units are added, rapidly merging into fibers due to the β-sheet formation of oligo-BLG. This hypothesis was further supported by the ROPISA of BLG-NCA at a low initial feeding ratio ([M]/[I] = 5). After purification, ^{1}H NMR and SEC

analyses confirmed the formation of well-defined copolymers with a short BLG block (DP = 5) and narrow dispersity ($Đ$ = 1.04) (Figure II-17).

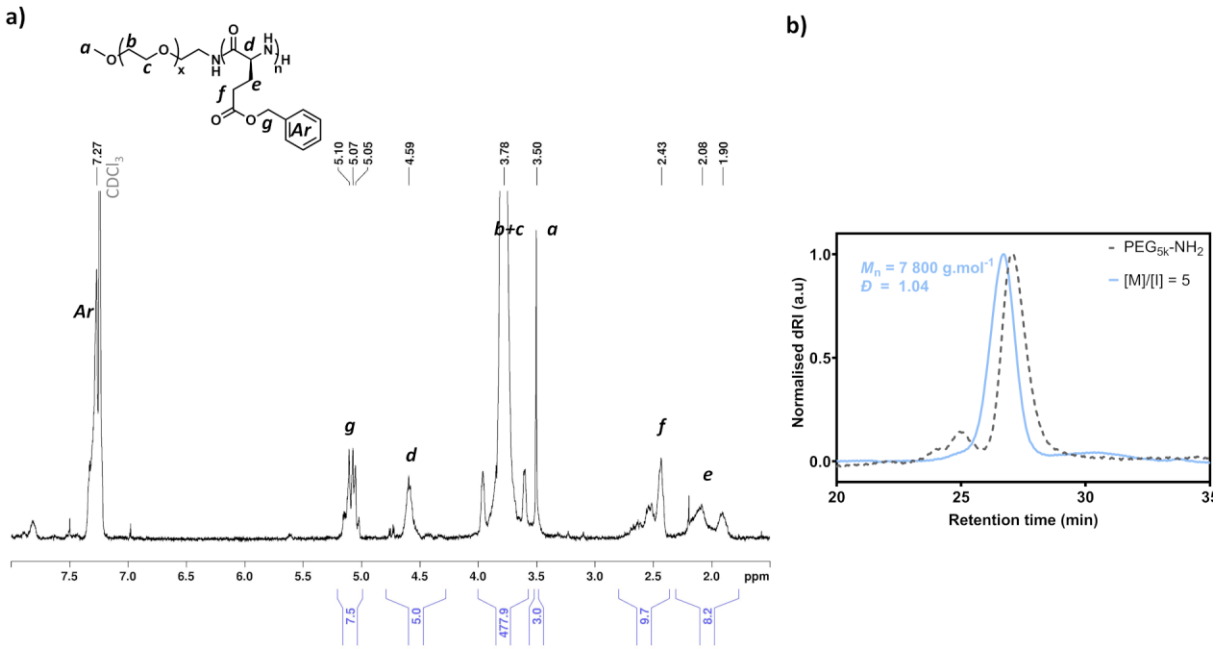

Figure II-17. (a) ^{1}H NMR spectrum PEG$_{5k}$-*b*-PBLG$_5$ in $CDCl_3$ + 15 % TFA. (b) SEC chromatogram of PEG$_{5k}$-*b*-PBLG$_5$ in DMF (+ 1% LiBr, detection by differential refractive index).

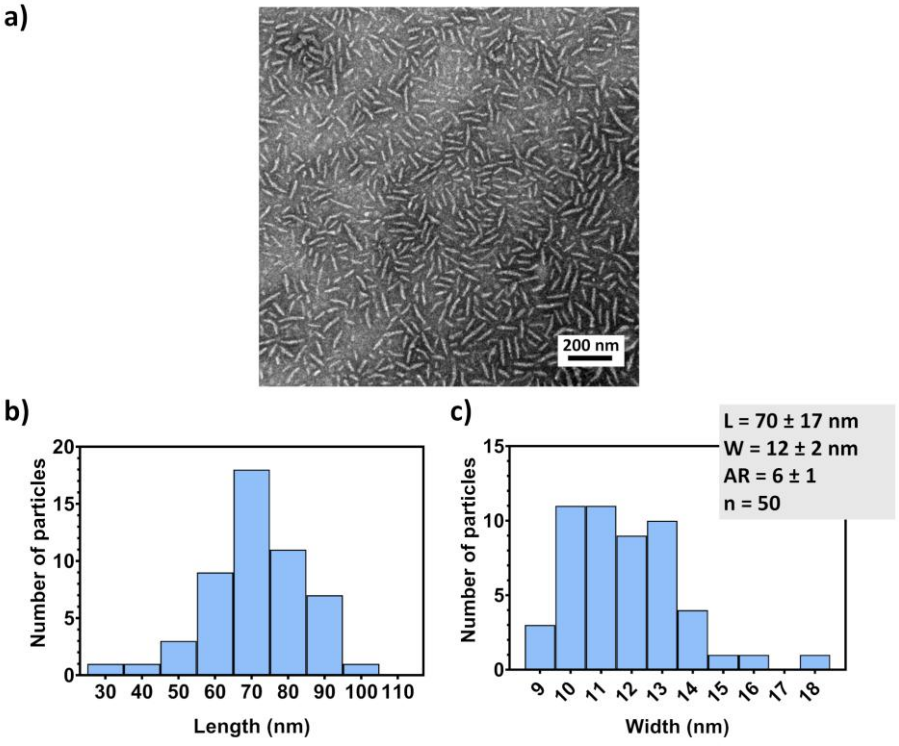

Figure II-18. (a) Representative TEM image of PEG$_{5k}$-*b*-PBLG$_5$ nanoparticle suspension. (b) Length and (c) width distribution of the PEG$_{5k}$-*b*-PBLG$_5$ nanoparticles obtained by analysis of 50 nano-objects by ImageJ on a TEM image.

TEM analysis revealed the presence of short fibers with an average width of 12 ± 2 nm and length of 70 ± 17 nm (Figure II-18). To elucidate the secondary structure, we analyzed the lyophilized powder using ATR-FTIR spectroscopy.

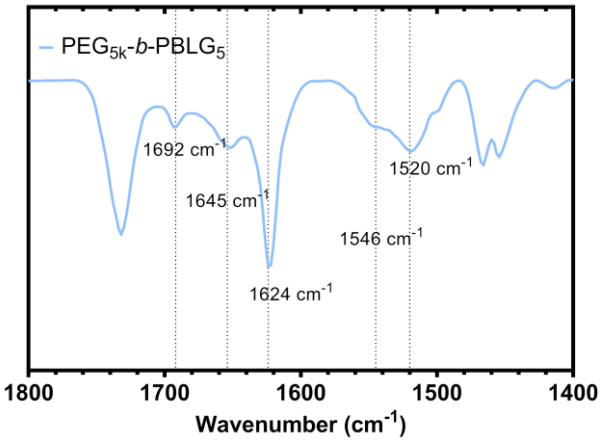

Figure II-19. FTIR of lyophilized powder of PEG_{5k}-*b*-$PBLG_5$.

The spectrum displayed a prominent band at 1624 cm^{-1} (amide I), associated with bands at 1526 cm^{-1} (amide II) and 1692 cm^{-1} (side-chain carbonyl), confirming the presence of an antiparallel β-sheet structure. A small band at 1645 cm^{-1} (amide I), coupled with one at 1546 cm^{-1} (amide II), was also detected, suggesting a minor proportion of α-helical structures, likely due to polymer dispersity.

These results were further validated by analyzing the WAXS region overtime at the beginning of the reaction (Figure II-20).

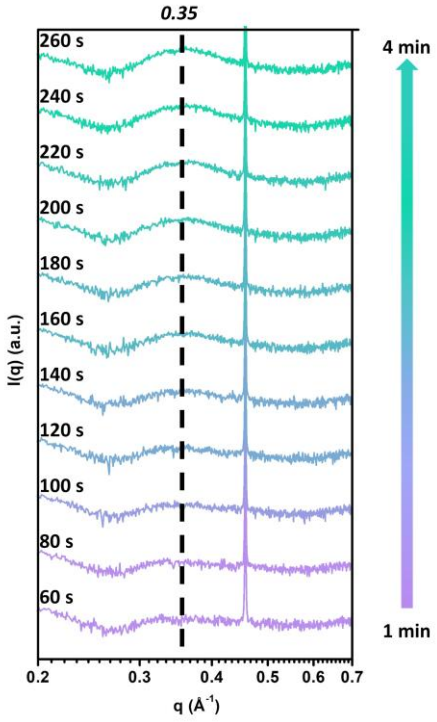

Figure II-20. β-sheet formation in the early stages of the ROPISA process evidenced by the appearance of the diffraction peak at 0.35 $Å^{-1}$ in the WAXS patterns recorded from 1 to 4 minutes.

WAXS patterns provide insights into the secondary peptide structure. In the high q range, during the first minutes of experiments (interval II), a broad diffraction peak emerged between 0.25 and 0.45 $Å^{-1}$, increasing in intensity and broadening overtime. In the first minutes, the peak maximum appeared at 0.35

Å^{-1}, which corresponds to a spacing of $d = \frac{2\pi}{q} = 17.8$ Å^{-1}. This distance aligns with the reported backbone spacing in the antiparallel β-pleated sheet structure, as previously observed for short PBLG oligomers in the literature.[48]

Although SAXS experiments did not directly capture the transition from micelles to cylindrical nanoparticles, our findings strongly support this morphological evolution. The rapid formation of β-sheet structures and the self-assembly of PEG_{5k}-*b*-$PBLG_5$ into fibers collectively suggest that the initial micelles formed during nucleation rapidly elongate into short fibers. These observations further validate our earlier hypothesis that β-sheet formation stabilizes the nucleation process. Thus, the ROPISA process exhibits strong similarity to ROPI-CDSA than to conventional PISA, as phase separation is governed not only by solvophobic interactions but also by intermolecular forces between the core-forming polypeptide chains. The early formation of β-sheet structures and hydrogen bonding likely stabilizes initial seeds, guiding self-assembly towards 2D anisotropic morphologies, in a manner analogous to CDSA.

II.6.2. Conformational maturation

II.6.2.1. Radius estimation

We further investigated the evolution of nanoparticle characteristics over time by fitting the SAXS patterns using a cylinder model (Figure II-21).

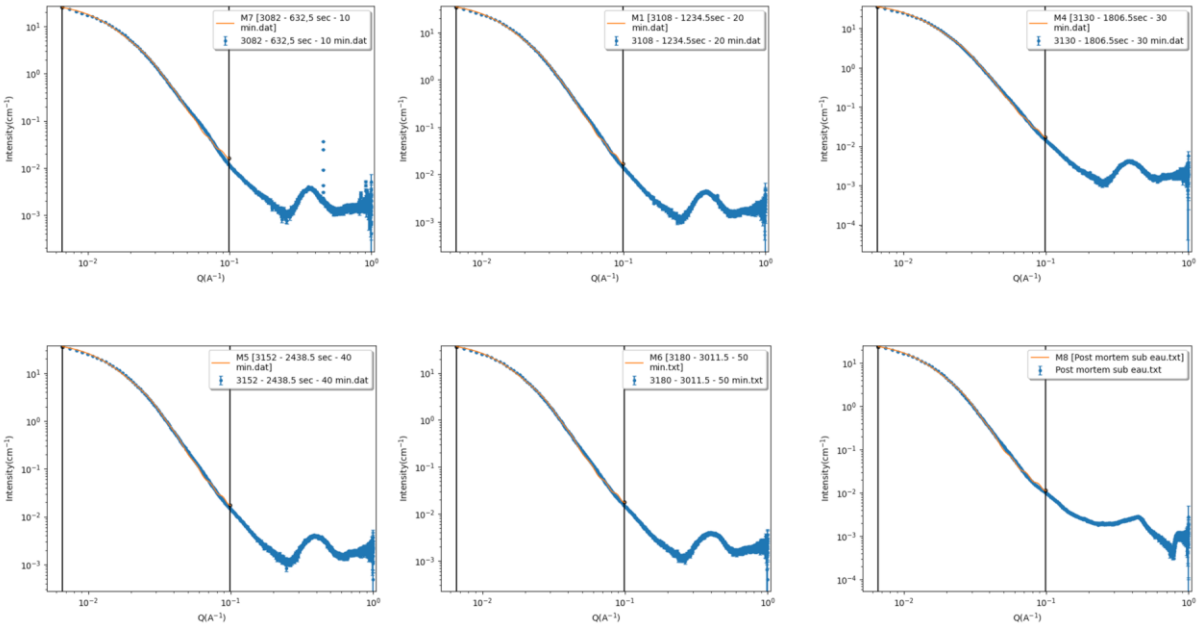

Figure II-21. SAXS patterns used for radius determination. In blue points, experimental data, in orange, fitted data with a polydisperse cylinder model.

However, given the nanoparticle lengths observed in TEM for DP 5 and DP 20, the accessible q range was not small enough to be in the Guinier regime and accurately determine cylindrical length values. To address this limitation, we fixed the length at an arbitrary 40 nm, as variations in this parameter had minimal impact on the fitted radius (Table II-2). The cylinder radius was found to be 5.1 nm at 10 minutes,

progressively increasing to 5.8 nm after 50 minutes of reaction. A post-mortem analysis of the sample, after overnight stirring in a static capillary, revealed a final radius of 6.5 nm. Using a first-order fit, which best described the data, we extracted a constant growth rate of $k_{rad} = 0.01$ min^{-1}, highlighting the slow yet continuous increase in radius over time (Figure II-22).

Table II-2. Parameters obtained from polydisperse cylinder fitting of signals recorded every 10 minutes, after 10 minutes of reaction in the flow device (except for overnight sample, in static capillary) for length fixed at 40 nm.

Time [min]	Scale	Background [cm^{-1}]	ρ_{BLG} [a)] [× 10^{-6} Å^2]	$\rho_{solvent}$ [a)] [× 10^{-6} Å^2]	Core radius (σ) [b)] [Å]	Length (σ') [c)] [Å]	χ^2 (fitting error)
10	0.0093	0.007	11.53 *	9.436 *	51.5 (0.39)	400	1847
	0.0092	0.0071			44.6 (0.55)	183.3 (0.53)	346
20	0.0126	0.005			54.3 (0.39)	400	1986
	0.0126	0.0028			52.3 (0.40)	326.3 (0.01)	929
30	0.0125	0.005			55.4 (0.37)	400	1850
	0.0127	0.0015			51.4 (0.45)	258.6 (0.37)	115
40	0.0124	0.006			55.5 (0.36)	400	1735
	0.0127	0.0016			54 (0.47)	190.2 (0.56)	86
50	0.0123	0.006			57.8 (0.36)	400	1651
	0.0126	0.0023			55.7 (0.46)	196.8 (0.56)	89
OV	0.0073	0.005			65.3 (0.32)	400	5063
	0.0076	0.0006			73.9 (0.41)	117.2 (0.94)	162

[a)] ρ_{BLG} : scattering length density of BLG, $\rho_{solvent}$: scattering length density of water. [b)] Core radius of cylinder with σ: radius polydispersity estimated with a lognormal distribution. [c)] Length of cylinder with σ': length polydispersity estimated with a lognormal distribution.

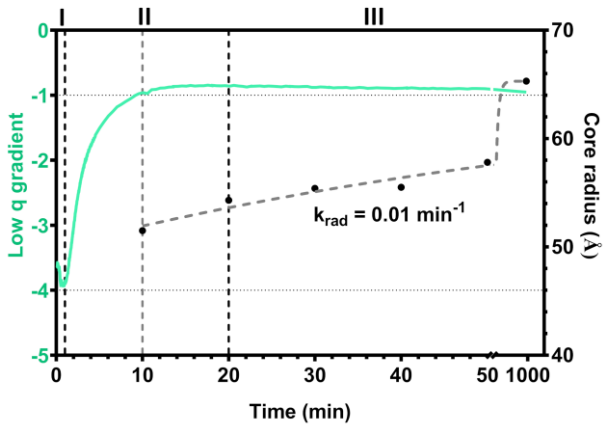

Figure II-22. Evolution of the PBLG core radius overtime, modeled using a polydisperse cylinder approximation, starting from 10 minutes into the reaction.

Even though polymerization was estimated to be complete after 20 minutes, as no remaining crystalline monomer was detected and no more CO_2 was generated, the nanoparticle radius continued to slightly increase. To better understand this evolution and gain further insight into the chain arrangement within the nanoparticles, we conducted a more detailed analysis of the WAXS patterns.

II.6.2.2. WAXS analysis

As previously mentioned, a diffraction peak around 0.35 Å^{-1} appeared within 2 minutes of reactions corresponding to spacing in the antiparallel β-pleated sheet structure, increasing in scattering intensity overtime (Figure II-20). However, the peak also broadens and shifts towards larger q values, indicating structural evolution. After 50 minutes of reaction, the peak remains broad, but after overnight stirring, a narrower peak around 0.45 Å^{-1} is observed, constituent with previous reports from our team (Figure II-23).

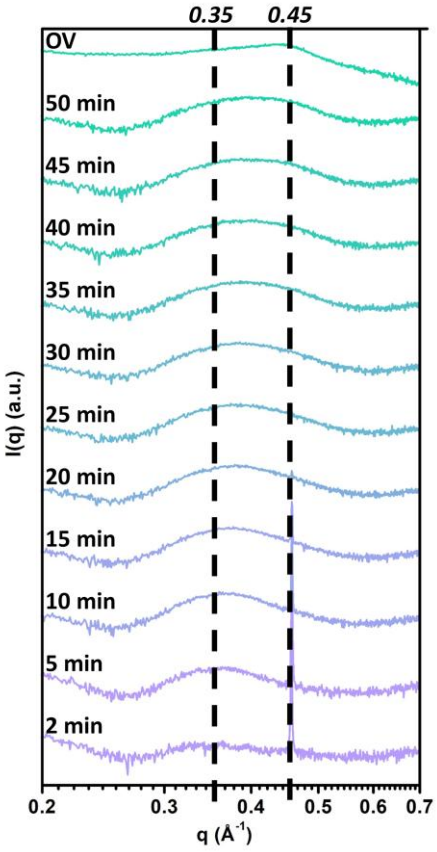

Figure II-23. WAXS patterns recorded throughout the reaction, from 2 minutes to overnight.

This corresponds to a spacing of $\frac{2\pi}{q} = 13.7$ Å, which is attributed to the repeating distance of hexagonal array formed by PBLG α-helices.[38,47,48,64] To quantify this transition from β-sheet towards the α-helix conformation, we plotted the peak maximum in the $0.25 - 0.45$ Å^{-1} range overtime (Figure II-24).

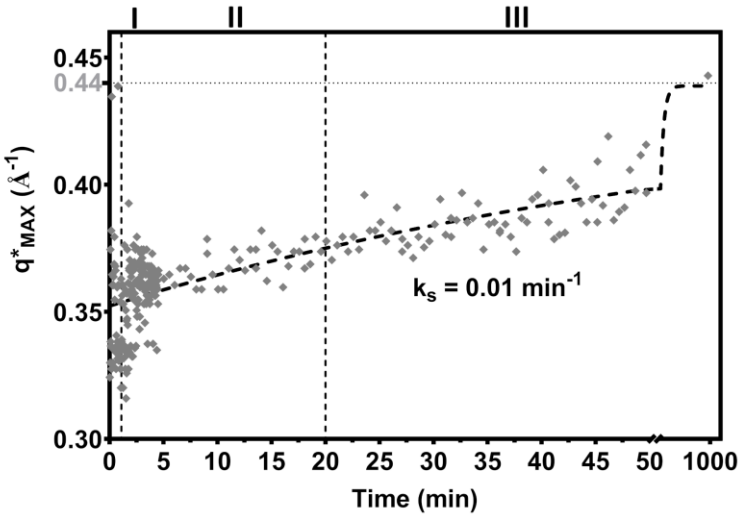

Figure II-24. Evolution of the diffraction peak (q) maximum within the $0.25 - 0.45$ Å^{-1} range overtime, from 0 minutes to overnight.

Using a first-order fit, we estimated a structural evolution rate k_s = 0.01 min^{-1}, approximately 40 times slower than self-assembly and polymerization, yet comparable to the rate of radius evolution after stabilization into cylindrical morphologies. Further investigations by Floudas' group using WAXS and ^{13}C NMR on the final lyophilized PEG$_{5k}$-*b*-PBLG$_{19}$ obtained via ROPISA confirmed 67–72% α-helix, 20–33% β-sheet, and 8% random coil, indicating an incomplete α-helix transition.[65]

Initially, the secondary structure is predominantly β-sheet, gradually transitioning to α-helices, as expected for PBLG at this DP. However, this transition is slow and remains incomplete. In contrast, PEG$_{5k}$-*b*-PBLG$_{19}$ synthesized via ROPISA and subsequently redissolved in an organic solvent exhibits a fully α-helical conformation, as demonstrated by Floudas *et al*, further demonstrating that this secondary structure transition is kinetically frozen.[65] This kinetics trapping can be attributed to geometric confinement which reduces conformational entropy, known to stabilize folded state. This phenomenon has been specifically studied in regard to protein stability and folding,[66] where living cells facilitate protein folding by entrapping them in chaperonins,[67,68] or where nascent peptides start folding within the ribosomal exit tunnel under confinement.[69] Similarly, in the ROPISA process, confinement within micelles hinders the transition from β-sheets to α-helices due to this reduces conformational entropy.

II.6.3. Chain configuration evolution within nanoparticles

This slow post-polymerization transition may explain the gradual increase in cylinder radius over time, as both processes exhibit similar kinetics. To gain further insight into conformation of the chains within the hydrophobic core, we can analyze both estimated radius and the observed secondary structure.

Considering the results obtained from the investigation on DP5 and the initial antiparallel β-sheets observed in the early stages of ROPISA by WAXS analysis, we can estimate the dimensions of PBLG chains and determine their likely conformation within the first cylindrical nanoparticles (detailed calculations can be found in experimental section). The ideal length of a PBLG chain in a β-sheet

conformation is given by $\xi_{sheet}^{ideal} = 0.35\ nm\ \times\ DP_{PBLG}$, which corresponds to $\xi_{sheet}^{ideal} = 2\ nm$ for a DP 5. The theoretical distance between two β-strands is $0.5\ nm$.[47] The distance d_{PEG} between the PEG chains can be then estimated at the double if we considered an antiparallel stacking: $d_{PEG} = 1\ nm.$. Additionally, based on scaling power laws,[70] the radius of gyration (R_g) of PEG with a molar mass of 5 000 g.mol^{-1} is estimated to be approximately 3 nm. Considering the grafting density Σ, PEG is then expected to be in the brush regime, with a layer thickness L ranging between 4 and 11 nm. The reported diameter of $12\ \pm\ 2\ nm$ in negative staining TEM includes the PEG corona, which is not accounted for in SAXS measurements. If we assume that the chains are stacked vertically in an antiparallel arrangement, as depicted in Scheme II-3, the theoretical total diameter ranges between 10 and 24 nm depending on the PEG layer thickness, which aligns well with our TEM observations, and further validates the predicted configuration.

By considering the measured dimensions of the final PEG$_{5k}$-*b*-PBLG$_{19}$ nanoparticles, we can predict the final chains configuration. Floudas *et al.* reported that the PEG$_{5k}$-*b*-PBLG$_{19}$ obtained via ROPISA exhibits a PBLG length of $3.0\ \pm\ 0.2\ nm$ and a radius of $0.87\ \pm\ 0.05\ nm$, which is consistent with the expected values for an ideal α-helix case ($\xi_{helix}^{ideal} = 0.15\ nm\ \times DP_{PBLG}$ which corresponds to 3 nm for DP 20).[47,65] Considering the obtained hydrophobic core radius with the SAXS (6.5 nm), and the fact that α-helical PBLG chains tend to adopt a hexagonal packing configuration, the chains are likely arranged as two stacked hexagonal units within the cylinder's cross-section. Based on this model, the excepted final radius for the hydrophobic core is $\xi_{helix}^{ideal}\ \times 2 \sim 6\ nm$, which aligns well with the SAXS-derived radius from the polydisperse cylinder model fitting. The post-mortem nanoparticles observed in TEM images had a measured diameter of approximately $17\ \pm\ 2\ nm$. In an ideal scenario where 100 % of the chains adopt an a-helix conformation, and given the theoretical inter-helix spacing of PBLG in a hexagonal array ($1.6\ nm$), which can also approximate the spacing between PEG chains, along with calculated radius of gyration (R_g) for PEG$_{5k}$, the PEG conformation is expected to be in the brush regime. Consequently, the PEG thickness corona is estimated to range between $5 - 18\ nm$. Overall, this leads to a final cylinder diameter ranging from 16 to 42 nm, which is in good agreement with the TEM measurements for PEG$_{5k}$-*b*-PBLG$_{19}$ nanoparticles width ($17\ \pm\ 2\ nm$).

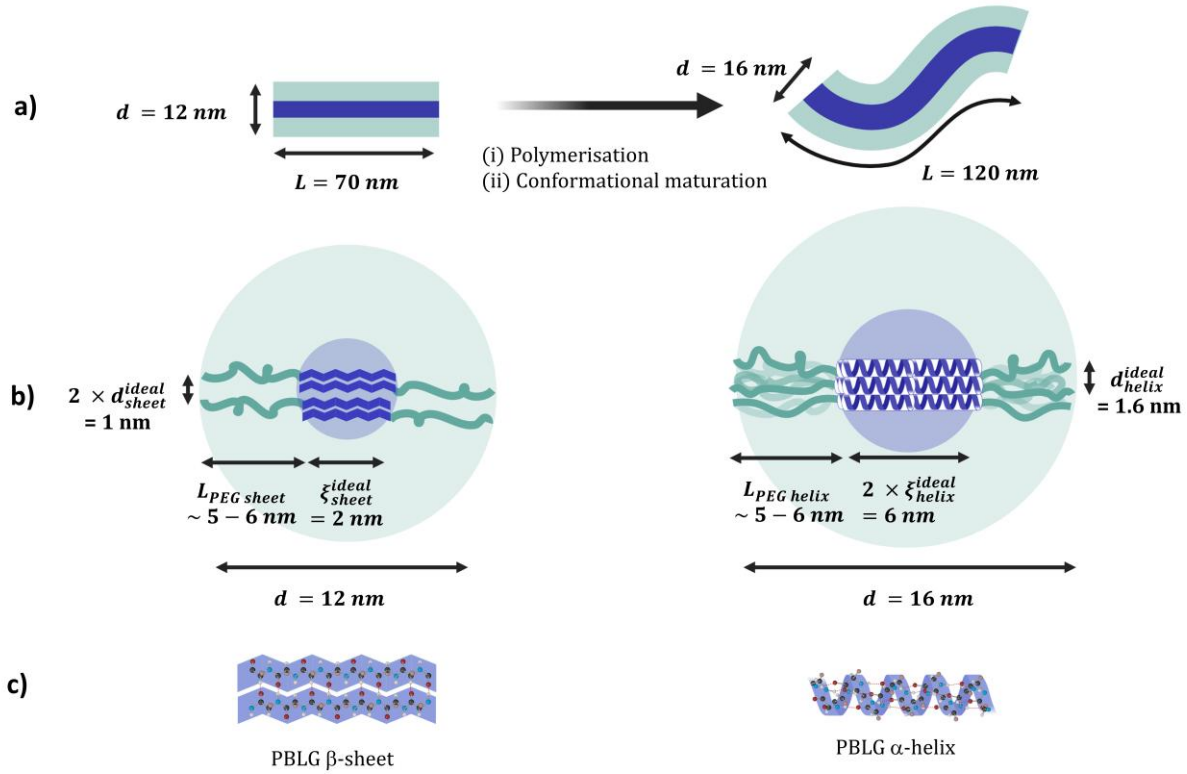

Scheme II-3. Conformational evolution in the PEG-*b*-PBLG nanoparticles during the ROPISA process. (a) Cylindrical nanoparticles growth in length and diameter through simultaneous polymerization and conformational maturation. (b) Zoom in the cylindrical cross-section, displaying the dimensions of the PBLG core and PEG corona. (c) Corresponding secondary structure of the PBLG, from β-sheet to α-helix.

II.7. Overall Mechanism

The *in situ* and time dependence SAXS/WAXS investigation of the ROPISA process of BLG-NCA initiated by PEG_{5k}-NH_2 allowed us to propose a mechanism that is schematically summarized in Scheme II-4. SAXS first revealed a rapid nucleation step, attributed to the formation of PEG-based pre-micelles. These initial micelles facilitate the diffusion of hydrophobic monomers in their soluble form, shielding them from hydrolysis and allowing polymerization to proceed via the terminal primary amine of PEG. This amine remains in its nucleophilic NH_2 form, as the initial pH in the bicarbonate buffer is close to its pKa. As polymerization progresses, the solubilization equilibrium shifts due to rapid confined polymerization, while global acidification occurs as CO_2 is released. Despite this acidification, the confined micellar environment maintains the nucleophilic character of the amino group, ensuring sustained polymerization by preserving a high local monomer concentration and limiting diffusion. Consequently, monomer solubilization and diffusion within the nanoreactors emerge as rate-limiting steps. Micelles are initially presumed to be spherical, but as polymer chains grow and β-sheets form, they quickly evolve into cylindrical fibers. These fibers act as templates for the final anisotropic nanoparticle morphology. Their elongation may occur via two possible pathways: (i) fusion of early fibers or (ii) progressive chain growth.

Meanwhile, a slower conformational transition from β-sheet to α-helix occurs, driven by reduced conformational entropy, further stabilizing the final worm-like structure.

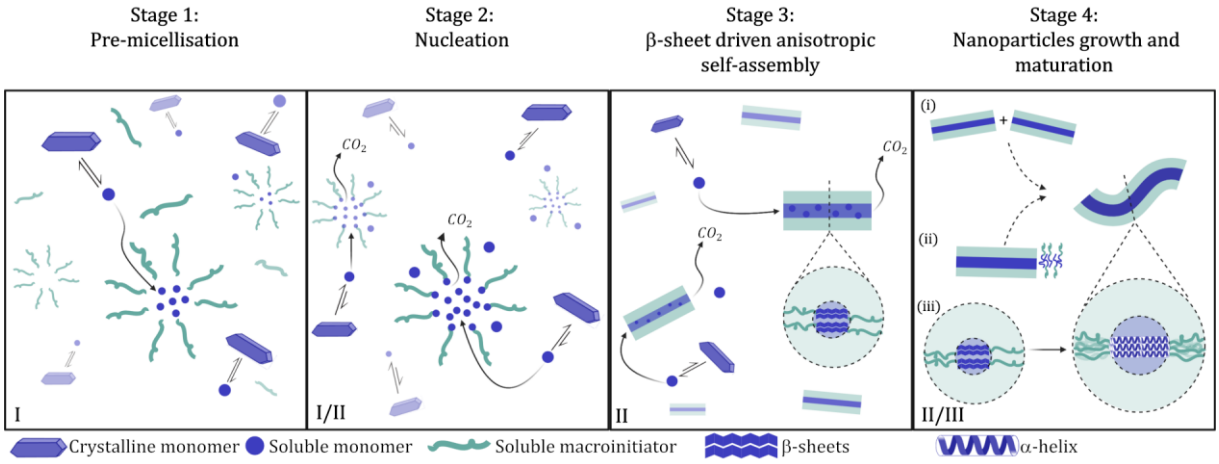

Scheme II-4. Schematic representation of the ROPISA mechanism. **Stage 1**: Initial heterogeneous reaction mixture, consisting of crystalline monomer (blue crystal) in equilibrium with soluble monomer (blue spheres) and a soluble macroinitiator (green cruves) forming pre-micelles. These pre-micelles facilitate polymerization initiation of soluble monomers diffusing into their core through aminolysis. (*Interval I*) **Stage 2**: Micelle nucleation occurs as the growing insoluble second block forms with a few repeating units. Soluble monomers diffuse and are sequestered within the micelle cores, shifting the solubilization equilibrium of the crystalline monomer. The ROP process releases CO_2 into the continuous aqueous phase, but the confined environment preserves the nucleophilicity of the reactive amino group site and limits water intrusion into the micelles. (*Interval I-II*) **Stage 3**: Nanoparticles elongate into fibers due to b-sheet formation in short peptides, further stabilizing the micelles. (*Interval II*) **Stage 4**: Nanoparticle continue to grow into longer anisotropic structures through (i) fusion of small fibers or (ii) progressive addition of growing chains. Simultaneously, (iii) a slow conformational transition from b-sheet to a-helix occurs, leading to an increase in the hydrophobic core radius.

II.8. Conclusion

In this chapter, we investigated the mechanistic aspects of aqueous ROPISA of BLG-NCA initiated by PEG_{5k}-NH_2 using time-resolved *in situ* SAXS/WAXS with synchrotron radiation. Our results demonstrate that polymerization in ROPISA proceeds significantly faster than hydrolysis or water-initiated polymerization, highlighting the crucial role of nucleation and confinement in locally increasing the concentration of soluble monomer and shifting the solubilization equilibrium. This confined microenvironment maintains the high nucleophilicity of the amino group despite medium acidification while also excluding water, thereby protecting the monomer from hydrolysis. Furthermore, the limited solubility of NCA monomers was identified as a key factor controlling polymerization kinetics, with ultrasonication accelerating the process. Our findings also provide strong evidence that ROPISA follows a self-assembly pathway more similar to ROPI-CDSA than conventional PISA. The early formation of β-sheet structures stabilizes nucleation and directs self-assembly toward anisotropic morphologies. The slower maturation of the secondary structure, due to reduced conformational entropy, leads to a progressive reorganization of the polypeptide chains within the PBLG core and an increase in core radius. While SAXS did not directly capture the spherical-to-worm-like transition, the rapid emergence of fiber-like structures, combined with existing literature, supports a mechanism involving either sequential copolymer chain

addition or fiber fusion. Future SAXS investigations at lower q-values could further elucidate the growth mechanism of these nanostructures.

Overall, these findings provide new insights into the aqueous ROPISA process, revealing its mechanistic parallels with both emulsion PISA and ROPI-CDSA. It appears clear that the polymerization kinetics is super-fast, as compared to bulk solution polymerization in organic solvent, the rate-limiting step being the monomer solubility but not directly the chemical reactivity. This deeper understanding paves the way for the rational design of polypeptide-based anisotropic nanomaterials for drug delivery applications. In particular, elucidating the relationship between polymerization, self-assembly, and conformational evolution offers a framework for optimizing *in situ* drug encapsulation by precisely controlling the timing of active ingredient addition.

Additionally, this study provides new hypotheses regarding the limitations in achieving larger degrees of polymerization and alternative morphologies. The solubility constraints of BLG-NCA appear to limit polymerization: when the initial monomer concentration is too high, the polymerization kinetics slow down significantly, preventing the formation of longer chains. Furthermore, the β-sheet-driven self-assembly inherently favors anisotropic morphologies, making the formation of polymersomes particularly challenging due to the rigidity of the polypeptide core.

II.9. Experimental section

II.9.1. Materials

Solvent for size-exclusion chromatography *N*,*N*-dimethylformamide (DMF) was bought from Sigma. γ-benzyl-*L*-glutamate *N*-carboxyanhydride (BLG-NCA) was supplied by PMC Isochem (Vert-le-Petit, France) and stored at -20 °C under argon atmosphere and weighed in a glove box. PEG_{5k}-NH_2 (M_p = 5000 $g.mol^{-1}$, $Đ$ = 1.02) was bought from RAPP Polymer Gmbh (Tübingen, Germany).

Ultra-pure water was obtained from a Milli Q system (Merck Millipore, France) with a resistivity of 18.2 MΩ. Deuterated solvent ($CDCl_3$) was purchased from Eurisotop. Dialysis membranes were purchased from SpectrumLabs.

II.9.2. Instruments and methods

II.9.2.1. Nuclear Magnetic Resonance (NMR)

^1H Nuclear Magnetic Resonance (NMR) spectra were recorded on a Bruker Avance III spectrometer equipped with a 5 mm BBFO (broad band fluorine observation) liquid probe, at 298 K. 1H data were acquired at 400.2 MHz observation frequency, with 16 scans and a recycle delay of 1 second. Signals were referred to the signal of residual protonated solvent signals.

II.9.2.2. Kinetics study

^1H NMR was chosen to follow the NCA polymerization initiated by PEG_{5k}-NH_2 in ice-cold aqueous $NaHCO_3$ solution. A typical kinetic procedure was conducted as follows: BLG-NCA (300 mg, 1.14 mmol) was placed in a Schlenk flask cooled in an ice bath, and 8 mL of ice-cold $NaHCO_3$ solution containing the PEG_{5k}-NH_2 initiator (300 mg, 0.06 mmol) was added. Two quenching protocols were implemented to monitor the reaction: one involving HCl, as previous studies indicated that HCl could hydrolyze NCA without impacting ongoing polymerization,[42] and one involving acetic anhydride (Ac_2O). At designated time intervals, 0.4 mL aliquots of the reaction mixture were withdrawn and quenched by rapid addition of an excess of HCl or Ac_2O. This step hydrolyzed any unreacted NCA into the corresponding amino acid, while Ac_2O also acetylated the chain end, effectively terminating polymerization. The samples were then dialyzed against ultrapure water (MWCO 3.5 kDa), lyophilized, and analyzed by ^1H NMR to indirectly determine BLG-NCA conversion through DP measurements. This purification step was necessary to eliminate interference from overlapping signals of hydrolyzed BLG-NCA and PBLG. SEC analysis revealed that HCl quenching was ineffective, as evidenced by the presence of double populations. Consequently, Ac_2O quenching was preferred. However, molar mass evolution over time, as assessed by SEC, indicated similar polymerization kinetics regardless of the quenching method.

II.9.2.3. Size Exclusion Chromatography (SEC)

Polymer molar masses were determined by SEC using *N,N*-dimethylformamide (DMF + LiBr 1 g.L^{-1}), hexafluoro-2-propanol (HFIP + 0.05% KTFA), dimethylsulfoxide (DMSO + LiBr 1 g.L^{-1}) or aqueous solvent as eluent. Measurements in DMF were performed on an Ultimate 3000 system from ThermoFischer Scientific (Ilkirch, France) equipped with a diode array detector (DAD). The system also includes a multiangle light scattering detector (MALS) and differential refractive index detector (dRI) from Wyatt technology (Santa Barbara CA, USA). Polymers were separated on three Shodex Asahipack gel columns [GF 310 (7.5 × 300 mm²), GF510 (7.5 × 300 mm²), exclusion limits from 500–300 000 Da] at a flowrate of 0.5 mL.min^{-1}. Columns temperature was held at 50 °C. Easivial™ kit of Polystyrene from Agilent (Santa Clara CA, USA) was used as calibration standard (M_n from 162 to 364 000 Da).

II.9.2.4. Fourier Transform Infrared spectroscopy (FTIR)

FTIR spectra were collected on a Bruker Vertex 70 spectrometer equipped with a diamond ATR tool in the spectral region of 900-2000 cm^{-1} from 32 scans with a resolution of 4 cm^{-1}. A background was recorded before loading the samples onto the ATR crystal for measurements. FTIR of copolymers dialyzed and lyophilized powders were measured using air as background.

II.9.2.5. Dynamic Light Scattering (DLS)

Hydrodynamic *Z*-average diameters (D_z) and the polydispersity index (σ) of the nanoparticles were determined by DLS with a Zetasizer Nano ZS from Malvern Instruments (Malvern, UK) operating with a He–Ne laser source (wavelength 633 nm, scattering angle 90°). The correlation functions were analysed using the cumulant method. The dispersions were analysed at 1 mg.mL^{-1} in water after filtration on a 0.45 µm CA filter.

II.9.2.6. Transmission Electron Microscopy (TEM)

The images were recorded on a Hitachi H7650 microscope working at 80 kV. Samples were prepared by deposing a drop of 0.1 mg.mL^{-1} NP dispersion onto a copper grid (200 mesh coated with carbon) that have been subjected to a glow discharge for 45 second and removing excess after 1 minute. Grids were negatively stained with 1.2% uranyl acetate.

The number-average lengths of nanoparticles were calculated with Eq 1; whereas the number-average diameters were calculated with Eq 2:

(1) $$L_n = \frac{\sum_{i=1}^{n} n_i L_i}{\sum_{i=1}^{n} n_i}$$

(2) $$w_n = \frac{\sum_{i=1}^{n} n_i w_i}{\sum_{i=1}^{n} n_i}$$

where n_i is the number of particles with length L_i and width w_i.

II.9.2.7. Small and Wide-Angle X-ray Scattering (SAXS/WAXS)

SAXS profiles were acquired on the SWING beamline at the Soleil synchrotron facility in Saint-Aubin (France) using a photon energy of 12 keV. The SAXS patterns were recorded in transmission mode as a function of the scattering vector, q, using an EIGERX 4M detector placed at 1100 mm from the sample, with q ranging from 0.0066 to 1 $Å^{-1}$. A flow-through capillary set-up was used as the sample holder, using a peristaltic pump (Heidolph Instruments, Germany) operating at 80 rpm and tubing (Saint-Gobain, France) with an inner diameter (ϕ_i) of 1.6 mm, an outer diameter (ϕ_e) of 4.8 mm, and a wall thickness of 1.6 mm, to ensure a high and continuous flow rate in the capillary. The NCA was weighed in a vial containing a magnetic stirrer inside a glove box and put under vigorous stirring. The ice-cold aqueous solution, with or without macroinitiator, was then rapidly injected into the vial using a syringe pump. SAXS patterns were collected every 1.5 s for the first 5 min, followed by measurements every 30 s until no further evolution in the scattering pattern was observed. The raw data were corrected for scattering due to background noise and the fluctuations of the intensity of the incident beam. Finally, the two-dimensional SAXS patterns were radially averaged in order to obtain the one-dimensional scattering profiles. The scattering profiles were analyzed using the SASView fitting software (http://www.sasview.org/) using the cylinder form factors. The X-ray scattering length densities (SLD) were set at their theoretical values calculated from the molecular formulas and mass densities. The particle volume fraction and the background intensity at high q were both let to vary by the fitting program.

II.9.2.8. CAC determination by fluorescence using Nile Red

PEG_{5k}-NH_2 solutions were prepared in ultrapure water at several concentrations by serial dilutions, ranging from 0.01 to 100 $mg.mL^{-1}$. A Nile Red solution in acetonitrile was prepared at 0.2 $mg.mL^{-1}$ and added in each solutions to target a final concentration of 0.002 $mg.mL^{-1}$. Measurements were made on a fluorescence spectrometer FP-8500 (Jasco) at 4°C. Emission fluorescence spectra were collected (λ_{ex} = 500 nm, λ_{em} = 550-750 nm) and fluorescence intensity was plotted at 650 nm. CAC is defined as the concentration at the intersection of the two logarithms regression $y = a - b \times \ln x$.

II.9.3. Synthesis

The typical procedure for the synthesis of PEG_{5k}-*b*-$PBLG_{19}$ is already reported and was employed similarly.[32] Briefly, BLG-NCA (300 mg, 1.14 mmol) was weighed in a Schlenk tube with a magnetic stirrer and 8mL of an ice-cooled solution of PEG_{5k}-NH_2 (300 mg, 0.06 mmol, [M]/[I] = 19) in $NaHCO_3$ 0.05 M was added under a strong agitation on the powder (τ_s = 7 wt%).The reaction was left to stir 1) first in an ice-cold water bath; 2) then at room temperature overnight. The opalescent dispersion obtained was then transferred to a 3.5 kDa dialysis membrane and dialyzed against deionized water for 2 days. An aliquot was kept for further microscopy imaging and dynamic light scattering and the remaining dispersion was lyophilized.

The protocol was then adjusted for experiments using other buffer solutions, at lower solid content, for SAXS/WAXS experiments and for experiments targeting a DP 5.

^{1}H NMR (400 MHz, $CDCl_3$ + 15 % TFA, d): 1.9-2.10 (br, 2H; -CH2-), 2.43 (br, 2H; -CH2-), 3.50 (s, 3H; ─CH3), 3.78 (br, 4H, -O–CH2-CH2-), 4.58 (br, 1H, -CH-), 5.07 (br, 2H, -CH2-Ar), 7.27 (br, 5H, ArH). PBLG degree of polymerization was calculated from the integration of the polymer backbone protons iH by ^{1}H NMR and gave a DP_{PBLG}= 20. SEC analysis using dRI detection and PS calibration gave M_n = 10.9 kg.mol^{-1} and $Đ$ = 1.07.

II.9.4. SAXS models

The scattering profiles were analyzed using the SASView fiiting software (Version 6.0.0) using the theoretical form factor of polydisperse cylinders, in the q region between 0.0066 and 0.1 Å^{-1}

II.9.5. Calculations details

To identify the type of PEG conformation, the distance between PEG chains (d_{PEG}) must be compared to the radius of gyration (R_g) of the chains.

First, R_g was determined using scaling laws determined in the literature:[70]

(3) $$R_g = 0.0215 \times M_w^{0.583}$$

For a $M_w = 5\,000$ g.mol^{-1}, it corresponds to R_g = 3 nm.

Then, d_{PEG} was estimated according to the conformation of the copolymer chains.

- For antiparallel β-sheet:

(4) $$d_{PEG,sheet} = 2 \times d_{sheet}^{ideal}$$

with d_{sheet}^{ideal} the theoretical distance between two β-strands, supposedly to be of $0.5\,nm$.[47] Then, $d_{PEG,sheet} = 1\,nm$.

- For α-helix:

(5) $$d_{PEG,helix} = d_{helix}^{ideal}$$

with d_{helix}^{ideal} the theoretical inter-helix spacing of PBLG in a hexagonal array, supposedly to be of $1.6\,nm$.

Then, the PEG surface density (σ), describing the number of PEG chains per nm² of the NP's surface, was estimated as follows:[72]

(6) $$\sigma = \frac{{d_{PEG}}^2}{4\pi}$$

- For antiparallel β-sheet, $\sigma_{sheet} = 0.08\,nm^2$
- For α-helix, $\sigma_{helix} = 0.2\,nm^2$.

Once R_g and d_{PEG} have been estimated in the two model conformations, the reduced grafting density (Σ) can be calculated using the equation and the conformational regime of the PEG chains can be determined:

(7) $$\Sigma = \frac{\pi {R_g}^2}{{d_{PEG}}^2}$$

A mushroom regime is obtained for $\Sigma < 1$, a dense brush regime for $\Sigma > 5$ and the intermediate regime for $1 < \Sigma < 5$.

For both conformations, a dense brush regime was determined, with:

- For antiparallel β-sheet, $\Sigma_{sheet} = 28$
- For α-helix, $\Sigma_{helix} = 11$.

Then, the thickness (L) of the layer for chains grafted on a spherical surface can be estimated using, the surface grafting density (σ), the number of repeating units in the polymer (N) and length of one repeating unit of the polymer (l_0), according to Dukes *et al.*:[73]

(8) $$L = \left[N(\sigma l_0^2)^{\frac{1}{2}}\right]^x, {}^3/_5 < x \leq 1$$

with $l_0 = 0.358\ nm$ for PEG.[74]

The thickness in the two conformations can be then determined:

- For antiparallel β-sheet, $4 < L_{sheet} \leq 11\ nm$
- For α-helix, $5 < L_{helix} \leq 18\ nm$.

II.10. References

[1] N. J. W. Penfold, J. Yeow, C. Boyer, S. P. Armes, *ACS Macro Lett.* **2019**, *8*, 1029–1054.
[2] Z. Zhao, S. Lei, M. Zeng, M. Huo, *Aggregate* **2024**, *5*, e418.
[3] M. Lages, J. Nicolas, *Prog. Polym. Sci.* **2023**, *137*, 101637.
[4] E. G. Hochreiner, B. G. P. van Ravensteijn, *J. Polym. Sci.* **2023**, *61*, 3186–3210.
[5] L. P. D. Ratcliffe, A. Blanazs, C. N. Williams, S. L. Brown, S. P. Armes, *Polym. Chem.* **2014**, *5*, 3643–3655.
[6] Z. Li, R. Wang, X. Luo, L. Zhang, J. Tan, *Polym. Chem.* **2024**, *15*, 1736–1747.
[7] C. Gao, S. Li, Q. Li, P. Shi, S. A. Shah, W. Zhang, *Polym. Chem.* **2014**, *5*, 6957–6966.
[8] X. Zhang, J. Rieger, B. Charleux, *Polym. Chem.* **2012**, *3*, 1502–1509.
[9] D. Zhou, S. Dong, R. P. Kuchel, S. Perrier, P. B. Zetterlund, *Polym. Chem.* **2017**, *8*, 3082–3089.
[10] S. Boissé, J. Rieger, G. Pembouong, P. Beaunier, B. Charleux, *J. Polym. Sci. A Polym. Chem.* **2011**, *49*, 3346–3354.
[11] S. J. Parkinson, S. D. P. Fielden, M. Thomas, A. J. Miller, P. D. Topham, M. J. Derry, R. K. O'Reilly, *Biomacromolecules* **2024**, *25*, 4905–4912.
[12] H. J. Kim, F. Ishizuka, J. Li, R. P. Kuchel, S. Chatani, H. Niino, P. B. Zetterlund, *Polym. Chem.* **2024**, *15*, 1102–1111.
[13] J. Rieger, *Macromol. Rapid Commun.s* **2015**, *36*, 1458–1471.
[14] A. Blanazs, J. Madsen, G. Battaglia, A. J. Ryan, S. P. Armes, *J. Am. Chem. Soc.* **2011**, *133*, 16581–16587.
[15] F. Brunel, J. Lesage de la Haye, M. Lansalot, F. D'Agosto, *J. Phys. Chem. B* **2019**, *123*, 6609–6617.
[16] J. Y. Rho, G. M. Scheutz, S. Häkkinen, J. B. Garrison, Q. Song, J. Yang, R. Richardson, S. Perrier, B. S. Sumerlin, *Polym. Chem.***2021**, *12*, 3947–3952.
[17] J. P. Patterson, M. P. Robin, C. Chassenieux, O. Colombani, R. K. O'Reilly, *Chem. Soc. Rev.* **2014**, *43*, 2412–2425.
[18] E. E. Brotherton, F. L. Hatton, A. A. Cockram, M. J. Derry, A. Czajka, E. J. Cornel, P. D. Topham, O. O. Mykhaylyk, S. P. Armes, *J. Am. Chem. Soc.* **2019**, *141*, 13664–13675.
[19] A. Czajka, P. A. Lovell, S. P. Armes, *Macromolecules* **2022**, *55*, 10188–10196
[20] F. Brunel, P. Galanopoulo, E. E. Rodriguez, M. Lansalot, F. D'Agosto, *Polym. Chem.* **2024**, 15, 979-990
[21] M. J. Derry, L. A. Fielding, N. J. Warren, C. J. Mable, A. J. Smith, O. O. Mykhaylyk, S. P. Armes, *Chem. Sci.* **2016**, *7*, 5078–5090.
[22] A. Czajka, S. P. Armes, *Chem. Sci.* **2020**, *11*, 11443–11454.
[23] M. J. Rymaruk, C. T. O'Brien, C. György, B. Darmau, J. Jennings, O. O. Mykhaylyk, S. P. Armes, *Angew. Chem. Int. Ed.* **2021**, *60*, 12955–12963.
[24] R. Takahashi, S. Miwa, F. H. Sobotta, J. H. Lee, S. Fujii, N. Ohta, J. C. Brendel, K. Sakurai, *Polym. Chem.* **2020**, *11*, 1514–1524.
[25] G. Liao, M. J. Derry, A. J. Smith, S. P. Armes, O. O. Mykhaylyk, *Angew. Chem. Int. Ed.* **2024**, *63*, e202312119.
[26] P. J. Hurst, A. M. Rakowski, J. P. Patterson, *Nat Commun* **2020**, *11*, 1–12.
[27] P. J. Hurst, J. Yoon, R. Singh, M. F. Abouchaleh, K. A. Stewart, B. S. Sumerlin, J. P. Patterson, *Macromol. Rapid Commun.* **2024**, *45*, 2400100.
[28] S. Ganda, M. H. Stenzel, *Prog. Polym. Sci.***2020**, *101*, 101195.
[29] P. J. Hurst, A. A. Graham, J. P. Patterson, *ACS Polym Au* **2022**, *2*, 501–509.
[30] J. Jiang, X. Zhang, Z. Fan, J. Du, *ACS Macro Lett.* **2019**, *8*, 1216–1221.
[31] A. Duro-Castano, L. Rodríguez-Arco, L. Ruiz-Pérez, C. De Pace, G. Marchello, C. Noble-Jesus, G. Battaglia, *Biomacromolecules* **2021**, *22*, 5052–5064.
[32] C. Grazon, P. Salas-Ambrosio, E. Ibarboure, A. Buol, E. Garanger, M. W. Grinstaff, S. Lecommandoux, C. Bonduelle, *Angew. Chem. Int. Ed.* **2020**, *59*, 622–626.
[33] H. Beauseroy, C. Grazon, S. Antoine, M. Badreldin, P. Salas-Ambrosio, S. Harrisson, E. Garanger, S. Lecommandoux, C. Bonduelle, *Macromol. Rapid Commun.s* **2024**, *45*, 2400079.
[34] A. H. Morrell, N. J. Warren, P. D. Thornton, *Macromol. Rapid Commun.s* **2024**, 2400103.
[35] E. Tinajero-Díaz, N. Judge, B. Li, T. Leigh, R. D. Murphy, P. D. Topham, M. J. Derry, A. Heise, *ACS Macro Lett.* **2024**, 1031–1036.

[36] X. Guo, B. Yang, J. Chen, *Biomacromolecules* **2024**, *25*, 3642–3650.
[37] A. F. Chinn, P. Farzeen, Z. Li, J. D. Mase, C. Vu, M. D. Schulz, S. Deshmukh, J. B. Matson, *Carbohydrate Polymers* **2025**, *352*, 123186.
[38] C. Grazon, P. Salas-Ambrosio, S. Antoine, E. Ibarboure, O. Sandre, A. J. Clulow, B. J. Boyd, M. W. Grinstaff, S. Lecommandoux, C. Bonduelle, *Polym. Chem.* **2021**, *12*, 6242–6251.
[39] B. Liu, R. Fang, W. Li, X. Wu, T. Liu, M. Lin, J. Sun, X. Chen, *J. Am. Chem. Soc.* **2024**, *146*, 16558–16566.
[40] P. D. Bartlett, R. H. Jones, *J. Am. Chem. Soc.* **1957**, *79*, 2153–2159.
[41] P. D. Bartlett, D. C. Dittmer, *J. Am. Chem. Soc.* **1957**, *79*, 2159–2160.
[42] Y. Hu, Z.-Y. Tian, W. Xiong, D. Wang, R. Zhao, Y. Xie, Y.-Q. Song, J. Zhu, H. Lu, *Natl Sci Rev* **2022**, *9*, nwac033.
[43] A. A. Cockram, R. D. Bradley, S. A. Lynch, P. C. D. Fleming, N. S. J. Williams, M. W. Murray, S. N. Emmett, S. P. Armes, *React. Chem. Eng.* **2018**, *3*, 645–657.
[44] S. L. Canning, G. N. Smith, S. P. Armes, *Macromolecules* **2016**, *49*, 1985–2001.
[45] X. Luo, S. Zhao, Y. Chen, L. Zhang, J. Tan, *Macromolecules* **2021**, *54*, 2948–2959.
[46] P. A. Lovell, F. J. Schork, *Biomacromolecules* **2020**, *21*, 4396–4441.
[47] H.-A. Klok, J. F. Langenwalter, S. Lecommandoux, *Macromolecules* **2000**, *33*, 7819–7826.
[48] P. Papadopoulos, G. Floudas, H.-A. Klok, I. Schnell, T. Pakula, *Biomacromolecules* **2004**, *5*, 81–91.
[49] S. Xu, *J. Phys. Chem. B* **2009**, *113*, 12447–12455.
[50] C. J. Bowerman, B. L. Nilsson, *Peptide Science* **2012**, *98*, 169–184.
[51] G. Liao, M. J. Derry, A. J. Smith, S. P. Armes, O. O. Mykhaylyk, *Angew. Chem. Int. Ed.* **2024**, *63*, e202312119.
[52] T. J. Deming, *Nature* **1997**, *390*, 386–389.
[53] A. R. Mazo, S. Allison-Logan, F. Karimi, N. J.-A. Chan, W. Qiu, W. Duan, N. M. O'Brien-Simpson, G. G. Qiao, *Chem. Soc. Rev.* **2020**, *49*, 4737–4834.
[54] Y. Wu, K. Chen, J. Wang, M. Chen, W. Dai, R. Liu, *J. Am. Chem. Soc.* **2024**, *146*, 24189–24208.
[55] H. R. Kricheldorf, *Angew. Chem. Int. Ed.* **2006**, *45*, 5752–5784.
[56] C. D. Vacogne, H. Schlaad, *Polymer* **2017**, *124*, 203–209.
[57] A. Sievers, M. Beringer, M. V. Rodnina, R. Wolfenden, *Proc. Natl. Acad. Sci. U.S.A.* **2004**, *101*, 7897–7901.
[58] D. A. Kingery, E. Pfund, R. M. Voorhees, K. Okuda, I. Wohlgemuth, D. E. Kitchen, M. V. Rodnina, S. A. Strobel, *Chem Biol* **2008**, *15*, 493–500.
[59] Z. Song, H. Fu, J. Wang, J. Hui, T. Xue, L. A. Pacheco, H. Yan, R. Baumgartner, Z. Wang, Y. Xia, X. Wang, L. Yin, C. Chen, J. Rodríguez-López, A. L. Ferguson, Y. Lin, J. Cheng, *Proc. Natl. Acad. Sci. U.S.A.* **2019**, *116*, 10658–10663.
[60] I. Pilz, O. Glatter, O. Kratky, in *Methods in Enzymology*, Academic Press, **1979**, pp. 148–249.
[61] N. J. Warren, O. O. Mykhaylyk, D. Mahmood, A. J. Ryan, S. P. Armes, *J. Am. Chem. Soc.* **2014**, *136*, 1023–1033.
[62] E. J. Cornel, J. Jiang, S. Chen, J. Du, *CCS Chemistry* **2021**, *3*, 2104–2125.
[63] A. Sahu, S. Mahapatra, P. Dey, G. Ghosh, *Macromol.Chem. Phys.* **2025**, 2400426.
[64] S. Lecommandoux, M.-F. Achard, J. F. Langenwalter, H.-A. Klok, *Macromolecules* **2001**, *34*, 9100–9111.
[65] M. Spyridakou, I. Tzourtzouklis, R. Graf, H. Beauseroy, C. Bonduelle, S. Lecommandoux, G. Floudas, *Biomacromolecules* **2025**, *26*, 1892-1903.
[66] H.-X. Zhou, K. A. Dill, *Biochemistry* **2001**, *40*, 11289–11293.
[67] R. J. Ellis, F. U. Hartl, *Current Opinion in Structural Biology* **1999**, *9*, 102–110.
[68] R. J. Ellis, *Current Biology* **2003**, *13*, R881–R883.
[69] P. Nissen, J. Hansen, N. Ban, P. B. Moore, T. A. Steitz, *Science* **2000**, *289*, 920–930.
[70] K. Devanand, J. C. Selser, *Macromolecules* **1991**, *24*, 5943–5947.
[71] C. Debrie, N. Coudert, J.-M. Guigner, T. Nicolai, F. Stoffelbach, O. Colombani, J. Rieger, *Angew. Chem. Int. Ed.* **2023**, *62*, e202215134.
[72] L. Adumeau, C. Genevois, L. Roudier, C. Schatz, F. Couillaud, S. Mornet, *Biochimica et Biophysica Acta (BBA) - General Subjects* **2017**, *1861*, 1587–1596.
[73] D. Dukes, Y. Li, S. Lewis, B. Benicewicz, L. Schadler, S. K. Kumar, *Macromolecules* **2010**, *43*, 1564–1570.
[74] M. A. Rixman, D. Dean, C. Ortiz, *Langmuir* **2003**, *19*, 9357–9372.

Chapter III. Tailoring anisotropic nanoparticles through NCA monomer selection in aqueous ROPISA

Table of Contents

Chapter III. Tailoring anisotropic nanoparticles through NCA monomers selection in aqueous ROPISA

III.1. Introduction 114

III.1.1. π–π interactions 114

III.1.2. H-bonding 116

III.1.3. Others driving forces 118

III.2. Influence of the chemical nature of protecting groups 120

III.2.1. [M]/[I] = 20 120

III.2.2. [M]/[I] from 10 to 40 124

III.3. Influence of the hydrophobicity of the amino-acid side chain 128

III.3.1. Aqueous ROPISA of Gly, Ala, Tyr, Leu and Phe-NCA 128

III.3.2. Kinetic studies 133

III.4. π-π interactions versus hydrophilic content: phenylalanine NCA 134

III.4.1. From low… 135

III.4.2. … to high hydrophilic fractions 138

III.5. Towards more functional π-π interactions: tyrosine NCA 141

III.6. Conclusion 147

III.7. Experimental Section 149

III.7.1. Materials 149

III.7.2. Instrumentation and methods 149

III.7.2.1. Nuclear Magnetic Resonance (NMR) 149

III.7.2.2. Kinetics study 149

III.7.2.3. Size Exclusion Chromatography (SEC) 150

III.7.2.4. Fourier Transform Infrared spectroscopy (FTIR) 150

III.7.2.5. Transmission Electron Microscopy (TEM) 150

III.7.2.6. Dynamic Light Scattering (DLS) 151

III.7.3. Synthesis 151

III.7.3.1. Synthesis procedure of poly(ethylene glycol)-*block*-poly(ε-benzyloxycarbonyl-*L*-lysine) PEG_{5k}-*b*-$PLys(Z)_n$ 151

III.7.3.2. Synthesis procedure of poly(ethylene glycol)-*block*-poly(ε-trifluoroacetyl-*L*-lysine) PEG_{5k}-*b*-$PLys(TFA)_n$ 151

III.7.3.3. Synthesis procedure of poly(ethylene glycol)-*block*-poly(ε-tert-butyloxycarbonyl-*L*-lysine) PEG_{5k}-*b*-$PLys(Boc)_n$ 152

III.7.3.4. Synthesis procedure of poly(ethylene glycol)-*block*-poly(glycine) PEG_{5k}-*b*-$PGly_{20}$ 152

III.7.3.5. Synthesis procedure of poly(ethylene glycol)-*block*-poly(*L*-alanine) PEG_{5k}-*b*-$PAla_{20}$ 152

III.7.3.5.1. Synthesis of Alanine *N*-Carboxyanhydride (Ala NCA) 152

III.7.3.5.2. Poly(ethylene glycol)-*block*-poly(*L*-alanine) PEG_{5k}-*b*-$PAla_{20}$ 152
III.7.3.6. Synthesis procedure of poly(ethylene glycol)-*block*-poly(-*L*-leucine) PEG_{5k}-*b*-$PLeu_{20}$ 153
III.7.3.7. Synthesis procedure of poly(ethylene glycol)-*block*-poly(*L*-phenylalanine) PEG_x-*b*-$PPhe_n$ 153
III.7.3.8. Synthesis procedure of poly(ethylene glycol)-*block*-poly(*L*-tyrosine) PEG_x-*b*-$PTyr_n$ 153

III.8. Supplementary Figures 155

III.9. References 167

III.1. Introduction

As previously mentioned in **Chapter I**, polymerization-induced self-assembly (PISA) has become as a highly versatile method in the field of dispersion polymerization. This method has enabled the synthesis of well-defined nano-objects in a single-step process and at high concentrations.[1,2] The PISA process results in the formation of amphiphilic block copolymers that self-assemble *in situ*, leading to the generation of self-stabilized nanoparticles with diverse morphologies (*e.g.* spheres, worms, vesicles) eliminating the need for additional surfactants.[3–6] The resulting morphology can be finely adjusted by modifying intrinsic parameters such as the chemical composition of the polymer segments,[7] the solvophilic/solvophobic ratio,[8,9] the architecture of the copolymer,[10,11] and the molar mass dispersity. Furthermore, it has been shown that other significant factors, such as the solvent,[12] pH, salt concentration,[13,14] monomer concentration,[15] temperature,[16] stirring rate,[14] and initiator concentration also played a crucial role in determining the morphology of the nanoparticles.[17]

Given the growing interest in anisotropic nanoparticles for nanomedical applications,[18–22] controlling their formation through PISA has become a key area of research. However, the scope of this control remains constrained, as it is currently applicable to a limited range of conditions that depend solely on the hydrophilic to hydrophobic balance and hydrophobic interactions.[23] To overcome these limitations, the PISA process has been extended to other supramolecular interactions, such as hydrogen bonding,[24] electrostatic interactions,[25] π-π interactions,[26] crystallization[27] and liquid crystal interactions.[28] The advent of these alternative driving forces has paved the way for the formation of anisotropic nanostructures characterized by elevated aspect ratios. These phenomena are discussed in more detail in the following sections.

III.1.1. π–π interactions

π-π interactions are non-covalent forces found in aromatic systems, arising from the electronic attraction between opposite quadrupole moments.[29] In this model, the central region of an aromatic ring carries a partial negative electrostatic potential, while the periphery is partially positive. As a result, aromatic rings tend to arrange in either an edge-to-face or parallel displaced configuration, with larger, substituted multiring systems favoring the latter (Figure III-1). The strength of these interactions depends on the size and degree of overlap of the aromatic rings, while solvent polarity has been shown to weaken them.[30]

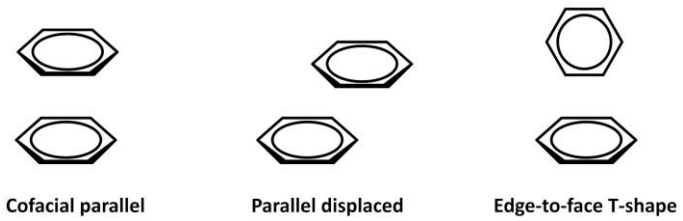

Figure III-1. Different stacked geometries of π-π interactions between aromatic systems.

Due to their rigidity and strong intermolecular interactions, π-conjugated polymers tend to assemble in an ordered manner, promoting the formation of anisotropic nanostructures.[31] These directional interactions have been successfully exploited in various studies to achieve elongated morphologies. In the following section, we will highlight key examples in which π-π interactions have driven the self-assembly of anisotropic nanoparticles.

In 2012, Choi *et al.* pioneered the PISA of poly(N-cyclohexyl-exo-norbornene-5,6-dicarboximide)-*b*-polyacetylene (PNB-*b*-PA) via sequential ROMP of norbornene (NB) and cyclooctatetraene (COT) in a one-pot approach.[32] Due to the strong π-π interactions between PA blocks, the resulting copolymer initially formed nanospheres at a low [COT]/[NB] ratio. As this ratio increased, the morphology underwent a transformation, evolving into undulated "nanocaterpillars" (Figure III-2). This PISA procedure was further simplified to a one-shot method, as the higher reactivity of NB over COT led to quasi-diblock copolymers.[33]

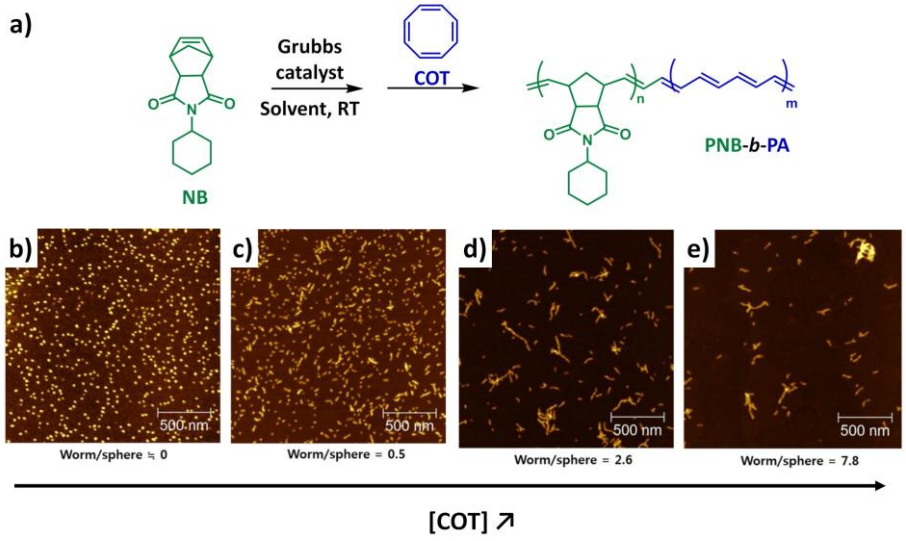

Figure III-2. (a) π-π interactions driven ROMPISA of COT. AFM images of the structures self-assembled from PNB-b-PA obtained using increasing [NB]/[COT] ratios of (a) 50:10, (b) 50:20, (c) 50:30 and (d) 50:50. Adapted from Choi *et al.* [32]

Alternatively, Hong *et al.* reported that the π-π interactions could be enhanced by incorporating 2-(methacryloyloxy)ethyl anthracene-9-carboxylate (MAEAC) in the RAFT-PISA of 2-(methacryloyloxy)ethyl benzoate (MAEB), which introduced a larger π-conjugated system.[34] This modification promoted directional self-assembly during PISA, leading to the formation of polymeric nanotubes with tunable lengths depending on the solid content of the formulation (Figure III-3).

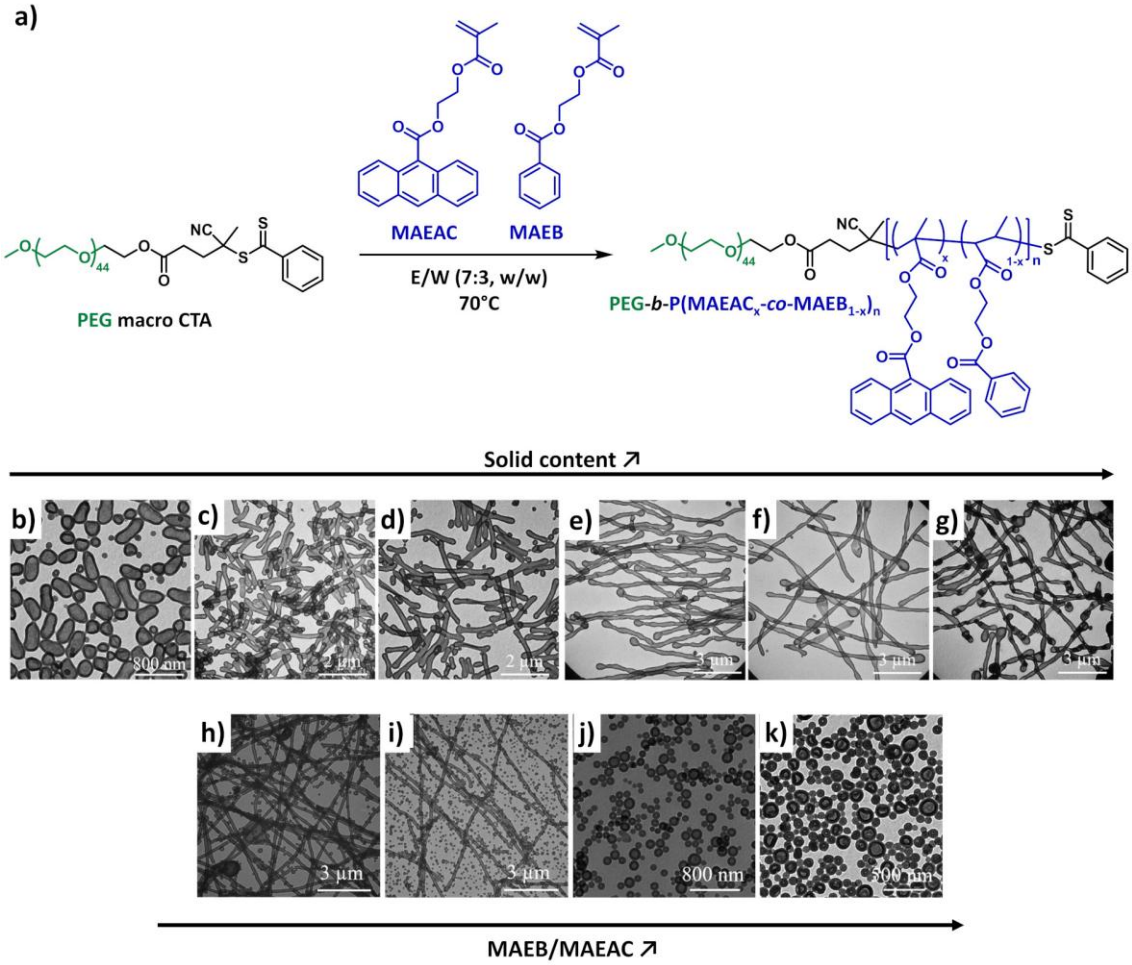

Figure III-3. (a) RAFT-PISA of MAEAC and MAEB. (b-g) TEM images of the PEG_{45}-*b*-P($MAEAC_{0.6}$-*co*-$MAEB_{0.4}$)$_{150}$ nano-objects obtained after PISA at different solid content. (b): 6.5%, (c) 8.5%, (d) 10.4%, (e) 10.7 %, (f) 11.5% and (g) 12.2%. (h-k) TEM images of the PEG_{45}-*b*-P($MAEAC_x$-*co*-$MAEB_{1-x}$)$_{150}$ nano-objects obtained after PISA at different fee molar ratio of MAEB/MAEAC. (h) 1:9, (i) 2:8, (j) 3:7 and (k) 4:6. Adapted from Hong *et al.*[34]

III.1.2. H-bonding

Hydrogen bonding plays a crucial role in biological systems, contributing to structural stabilization in molecules such as DNA, where it holds the double helix together,[35] and proteins, where it helps maintain their three-dimensional conformation.[36] In the context of synthetic polymers, hydrogen bonding emerges as a pivotal non-covalent interaction due to its strong directionality, which exerts a notable influence on the self-assembly processes. This property renders it particularly valuable in PISA, where it can drive the formation of nanofibers by promoting anisotropic growth and stabilizing elongated structures.[37]

Rieger *et al.* exploited hydrogen bonding by developing a bis-urea-functionalized chain transfer agent (CTA) and synthesizing a series of hydrophilic macro-CTAs via RAFT polymerization of common monomers such as *N,N*-dimethylacrylamide (DMAA), acrylic acid (AAc), acrylamide (AAm), and 2-(*N,N*-dimethylamino)ethyl acrylate (DMAEA). The strong hydrogen bonding interactions of the bis-urea groups facilitated the spontaneous self-assembly of these macro-CTAs into nanofibers in water.[38] Building on this property, they performed aqueous PISA of 2-methoxyethyl acrylate (MEA) using bis-urea-terminated

PDMAc as the macro-CTA, successfully generating nanofibers over a broad range of solid contents and chain lengths. In contrast, PISA with PDMAc-*b*-PMEA, which lacked the bis-urea motif, resulted in the formation of spherical or worm-like micelles. This observation highlights the pivotal role of hydrogen bonding in directing anisotropic morphologies (Figure III-4).[39]

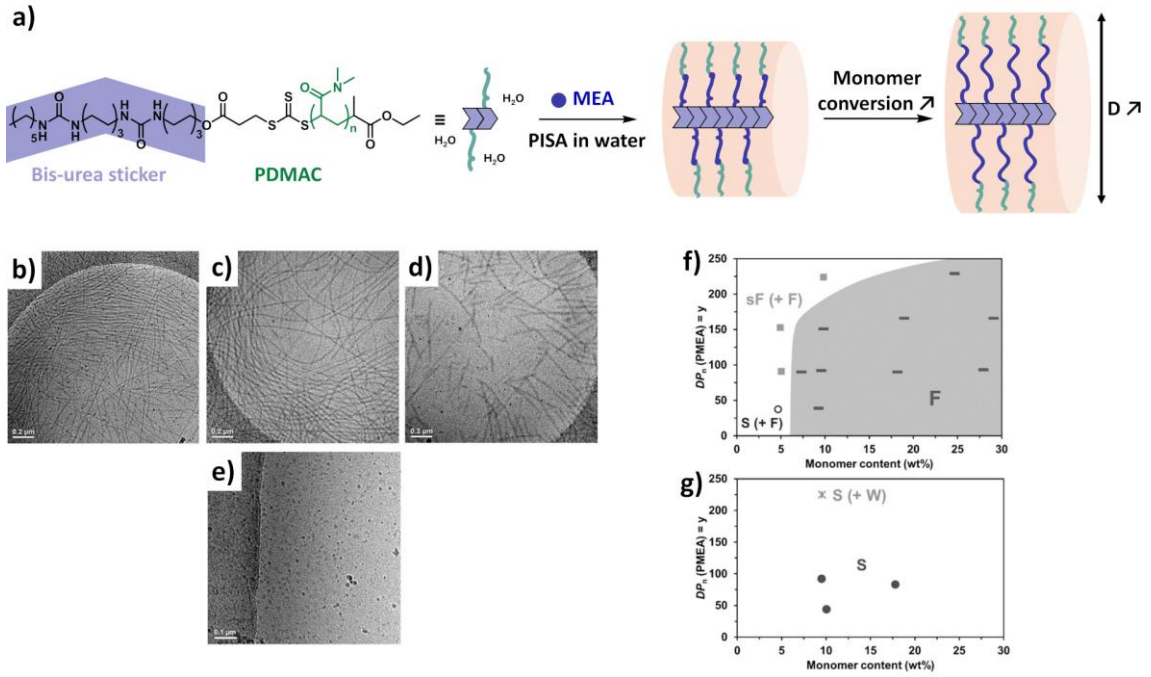

Figure III-4. (a) Proposed mechanism of bis-urea templated PISA in the particular case of MEA polymerization. (b-d) Cryo-TEM images of $PDMAC_{35}$-*b*-$PMEA_n$-TTC-U_2 diblock copolymers prepared by templated PISA at 10 wt% with increasing PMEA DP: (b) 39, (c) 92, (d) 151. (e) Cryo-TEM image of $PDMAC_{35}$-*b*-$PMEA_{92}$-TTC-C_{18}without bis-urea motif. (f-g) Pseudo-phase diagrams for $PDMAC_{35}$-*b*-$PMEA_n$-TTC-U_2 (f) and $PDMAC_{35}$-*b*-$PMEA_n$-TTC-C_{18} (g) deblock copolymers prepared at various monomer contents. The shaded area represents the pure long-fiber phase. Dash: fibers (F), full circle: spheres (S), empty circles: mainly spheres with few fibers, square: mainly short fibers (sF) with few fibers, cross: mainly spheres with few worms (W). Adapted from Rieger *et al.* [38]

Cai *et al.* also reported an example of PISA driven by hydrogen bonding, leading to the formation of diverse anisotropic nanostructures.[40] Their study revealed a unique morphological transition from film/silk-like structures to ribbons and eventually vesicles. Using RAFT dispersion copolymerization of diacetone acrylamide (which contains both hydrogen bond donors and acceptors) and *N*-2-aminoethylacrylamide hydrochloride (an ionized monomer), they successfully synthesized pore-switchable nanotubes. The formation of these distinctive nanostructures was attributed to electrostatic repulsion disrupting hydrogen bonding interactions within the tubular membranes.

More recently, Yang's team has achieved a notable milestone in the field by successfully synthesizing cubic nanostructures through a process known as emulsion-based PISA. This method involved the use of styrene (S) and 2-hydroxyethyl methacrylate (HEMA) as monomers, with a maleamic acid-alt-α-methyl styrene (MAA-*alt*-AMS) copolymer serving as the macroinitiator. [41] The formation of these cubic nanoparticles was driven by a combination of π-π interactions from styrene residues and hydrogen bonding between the carboxylic acid and amide functional groups in the MAA-alt-AMS polymer. Through

the strategic manipulation of the S-to-HEMA ratio and the ethanol-to-water solvent composition, a diverse array of morphologies was obtained, encompassing cubic nanoparticles, spherical micelles, and vesicles.

III.1.3. Others driving forces

Electrostatic interactions between complementary polyions have been shown to broaden the range of conditions conducive to forming anisotropic morphologies. For example, Shen and colleagues demonstrated that incorporating rigid siRNA during the RAFT-mediated PISA of the cationic monomer 3-acrylamidopropyl trimethylammonium chloride (APTAC) directs self-assembly toward non-spherical structures such as lamellae and nanotubes by effectively increasing the degree of polymerization of PAPTAC.[42] In addition, crystallization plays a critical role in driving PISA toward the formation of non-spherical and hierarchically complex assemblies. The advent of crystallization-driven self-assembly (CDSA), as discussed in **Chapter I**, further illustrates the manner in which directed crystallization can be leveraged in PISA to yield anisotropic nanostructures with enhanced functionality.[43–45] Similarly, liquid crystallization can also be integrated into PISA. Mesogens, defined as molecules that form liquid crystals and possess rod-like structures, exhibit specific orientations within the liquid crystalline phase, an organization stabilized by supramolecular interactions such as hydrogen bonding, π-π interactions, and dipole–dipole interactions.[46] As discussed in **Chapter I**, the self-assembly of amphiphilic block copolymers exhibiting liquid crystalline ordering facilitates the formation of anisotropic morphologies and nanofibers. Consequently, utilizing liquid crystallization as a driving force in PISA represents a powerful strategy for generating anisotropic nanostructures and has been successfully implemented in various systems. For example, Chen and colleagues demonstrated the formation of polymeric nanoparticles with diverse anisotropic morphologies, ranging from cuboids and short belts to lamellae and ellipsoidal vesicles, by employing poly(methacrylate) with azobenzene side-chain segments (PMAAz) as the core-forming block and poly(methylacrylic acid) (PMAA) as the stabilizing block.[47] This process, conducted via polymerization-induced hierarchical self-assembly in ethanol, effectively combined PISA with liquid crystalline ordering to achieve controlled anisotropic structures.

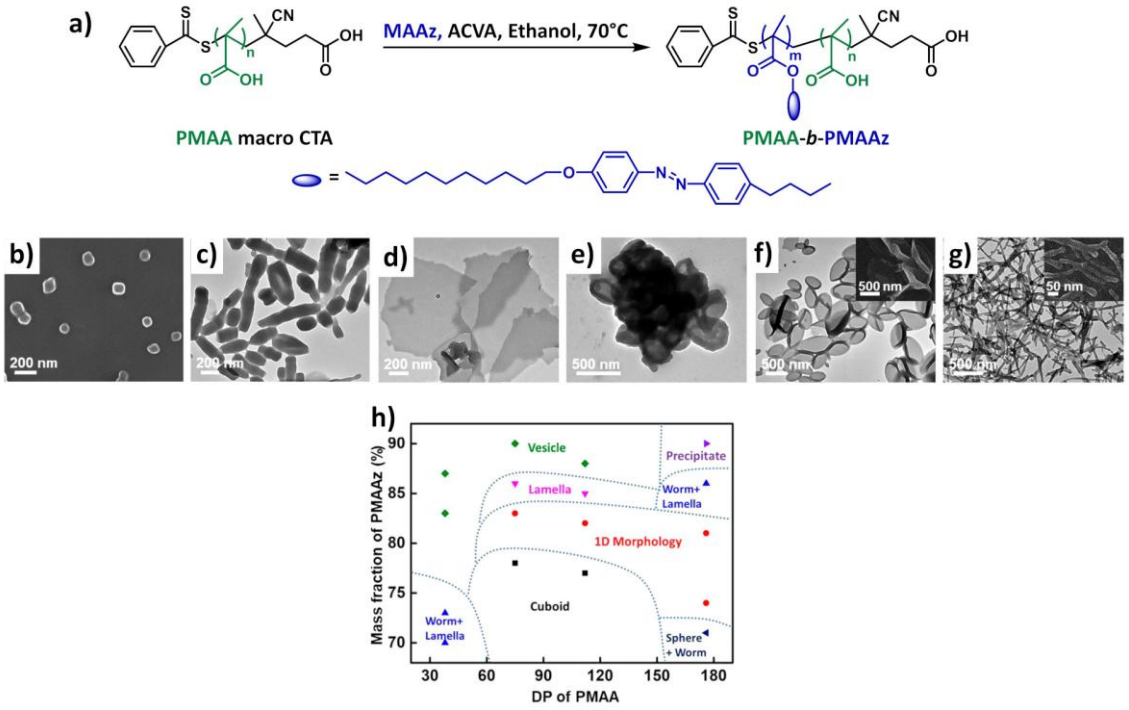

Figure III-5. (a) RAFT-PISA of MAAz by PMAA in ethanol. (b) SEM image of the $PMAA_{75}$-*b*-$PMAA_{48}$ nanoparticles. (c-g) TEM images of the (c) $PMAA_{75}$-*b*-$PMAA_{65}$, (d) $PMAA_{75}$-*b*-$PMAA_{84}$, (e) $PMAA_{75}$-*b*-$PMAA_{123}$, (f) $PMAA_{38}$-*b*-$PMAA_{44}$, (g) $PMAA_{176}$-*b*-$PMAAz_{87}$ NPs. (h) Phase diagram on the morphology with different DP_{PMAA} and mass fraction of PMAAz. Adapted from Chen *et al.* [47]

This chapter aims to expand the scope of aqueous ROPISA by exploring the influence of monomer structure on nanoparticle anisotropy, building on our previous findings and considering the literature context. Common amino acids possess side chains with diverse properties, ranging from varying hydrophobicity to aromatic groups capable of π-π stacking and hydrogen bonding, which can be exploited to generate a broad spectrum of anisotropic nanostructures. In **Chapter II**, the issue of monomer hydrolysis and subsequent uncontrolled polymerization was addressed.[48,49] Adjusting the reaction conditions (pH and solids content) is crucial to enable the ring opening by the amine propagating species to occur at a rate that surpasses the rate of hydrolysis. Although the aqueous ROPISA of NCAs has been shown to yield anisotropic nanoparticles, with morphology modulated by monomer chirality and polypeptide secondary structure, only a limited number of monomers have been systematically investigated,[50–52] and the conventional principles of PISA, such as varying the hydrophilic/hydrophobic block ratio or concentration to achieve diverse morphologies, seem not applicable in this context.

Therefore, in this chapter, we comprehensively investigate a range of NCA monomers, starting with lysine derivatives bearing different protecting groups (benzyloxycarbonyl, Z; trifluoroacetyl, TFA; and tert-butyloxycarbonyl, Boc), followed by NCAs derived from glycine, alanine, leucine, and phenylalanine to probe side-chain hydrophobicity, and finally focusing on phenylalanine and tyrosine NCAs, both emerging amino acid to design drug delivery systems,[53] to elucidate the role of π-π stacking and hydrogen bonding interactions (Scheme III-1). This systematic study will provide deeper insights into how these molecular

interactions govern the formation of anisotropic nanoparticles, thereby broadening the monomer library for aqueous ROPISA and enhancing its potential for nanomedicine applications.

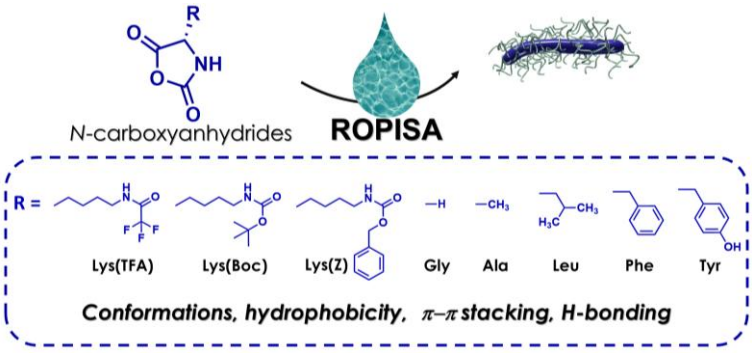

Scheme III-1. Influence of the nature of amino acid NCAs on aqueous ROPISA.

III.2. Influence of the chemical nature of protecting groups

Although recent advances in ROP has allowed the rapid generation of polypeptides with predictable molar masses (M_n), low dispersity ($Đ$), and well-defined reactive end group, the synthesis of NCA monomers and their polymerization usually requires the use of organic solvents and therefore, amino acids units with protected side chains.[54] We initially examined the impact of such protecting groups exhibiting varying degrees of steric hindrance and solubility in water on the aqueous ROPISA of three NCA monomers derived from lysine and known to stabilize similar conformations: ε-trifluoroacetyl-*L*-lysine-NCA (Lys(TFA)-NCA) , ε-tert-butyloxycarbonyl-*L*-lysine-NCA (Lys(Boc)-NCA)) and ε-benzyloxycarbonyl-*L*-lysine-NCA (Lys(Z)-NCA) (Scheme III-2).[55]

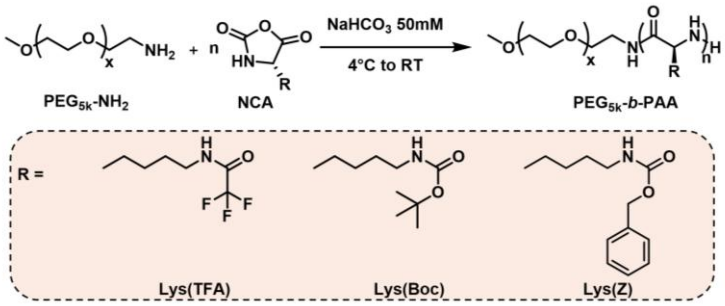

Scheme III-2. Aqueous ROPISA of lysine-derived *N*-Carboxyanhydrides, with different protective groups: Lys(TFA), Lys(Boc) and Lys(Z).

III.2.1. [M]/[I] = 20

The aqueous ROPISA was conducted for each monomer using α-amino-poly(ethylene glycol) (PEG_{5k}-NH_2) as the macro-initiator in an ice-cold aqueous sodium bicarbonate solution (pH 8.5, 50 mM) with 20 equivalents of NCA monomer, under vigorous stirring conditions, as described in **Chapter II**. In all three cases, the NCA monomers were fully converted in a few hours, as evidenced by ^{1}H NMR spectroscopy and SEC chromatography. The resulting SEC chromatograms exhibited a monomodal distribution with narrow molar mass dispersity values, and the retention times shifted to lower values

compared to the PEG macroinitiator, confirming effective block extension. Moreover, ^{1}H NMR spectra indicated that block copolymers exhibited similar degree of polymerization (DP) values ranging from 22 to 24 (see Table III-1, Figure III-6).

Table III-1. Macromolecular characteristics of lysine-based diblock copolymers obtained by aqueous ROPISA using a-amino polyethylene glycol as macroinitiator, at a feeding ratio of 20.

Copolymer	Monomer	Theory	SEC		^{1}H NMR		Yield (%)	DLS
		M_n [g.mol^{-1}]	M_n [g.mol^{-1}] [a]	$Đ$ [a]	M_n [g.mol^{-1}] [b]	DP [b]		D_Z [nm] (σ) [c]
PEG$_{5k}$-*b*-PLys(TFA)$_{20}$	*L-NTFA*Lys	9 200	13 100	1.06	10 400	24	77	114 ± 2 (0.21 ± 0.01)
PEG$_{5k}$-*b*-PLys(Boc)$_{20}$	*L-NBoc*Lys	9 400	12 100	1.05	10 000	22	82	92 ± 3 (0.38 ± 0.04)
PEG$_{5k}$-*b*-PLys(Z)$_{20}$	*L-NZ*Lys	9 900	13 900	1.12	10 800	22	92	101 ± 2 (0.15 ± 0.02)

[a] Number average molar-mass (M_n) and molar-mass dispersity determined by SEC in DMF +1% LiBr using PS calibration, [c] Number average molar-mass (M_n) and degree of polymerization (DP) determined by ^{1}H NMR in DMSO-d$_6$, [c] Hydrodynamic Z-average diameter (D_Z) and polydispersity (σ) determined by DLS at 90°.

Following dialysis against water to remove salts, the nanomaterial suspensions were characterized using microscopy and light scattering techniques. Dynamic light scattering (DLS) analyses revealed the presence of nanoparticles with Z-average diameters of 101 nm for PEG$_{5k}$-*b*-PLys(Z)$_{20}$, 92 nm for PEG$_{5k}$-*b*-PLys(Boc)$_{20}$ and 114 nm for PEG$_{5k}$-*b*-PLys(TFA)$_{20}$, with polydispersity index values of 0.15, 0.38 and 0.21 respectively (Table III-1, Figure III-7). In the case of nanomaterials with anisotropic shape, the Z-average diameter provided by DLS is only equivalent to that of a sphere, which can be misleading for particles that are not spherical. This anisotropic shape was indeed revealed by imaging the opalescent solutions obtained upon ROPISA using transmission electron microscopy (TEM). For the three NCA monomers, the microscopy images established the presence of flexible, worm-like nanoparticles (Figure III-7b) and approximately fifty nanoparticles were randomly selected and compared to statistically analyze the length and width of the nanomaterials (Figure III-7c).

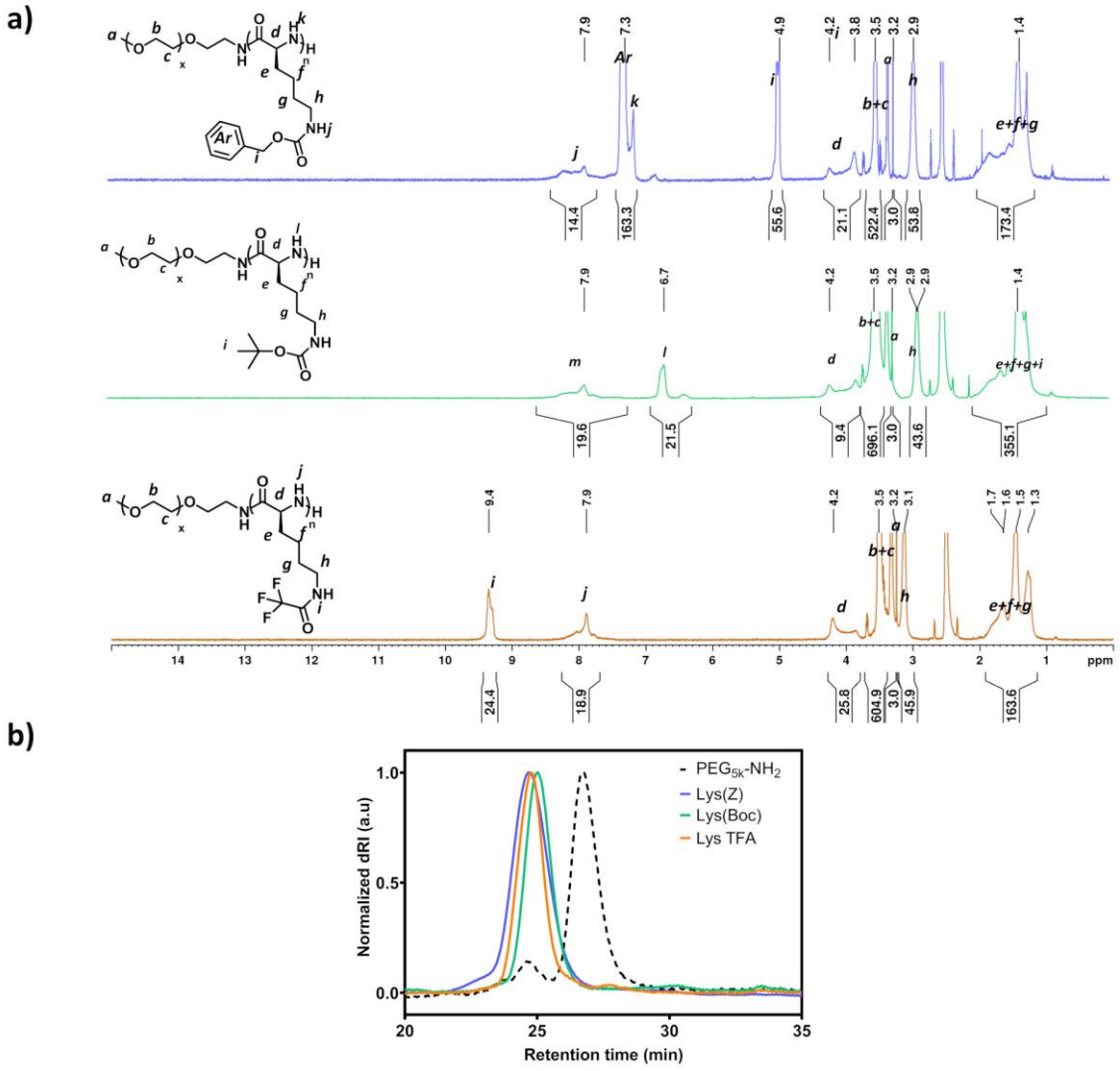

Figure III-6. (a) ^{1}H NMR spectra of PEG_{5k}-*b*-$PLys(Z)_{20}$, PEG_{5k}-*b*-$PLys(Boc)_{20}$ and PEG_{5k}-*b*-$PLys(TFA)_{20}$ in DMSO-d_6 with targeted DP of 20. (b) SEC chromatograms of PEG_{5k}-*b*-$PLys(Z)_{20}$, PEG_{5k}-*b*-$PLys(Boc)_{20}$ and PEG_{5k}-*b*-$PLys(TFA)_{20}$ in DMF (+1% LiBr, detection by differential refractive index).

Remarkably, anisotropic nanoparticles were obtained with all 3 monomers. TEM imaging with PEG_{5k}-*b*-$PLys(TFA)_{20}$ exhibited a coexistence of spherical micelles and necklace-type nanoparticles with a total mean length of 59 ± 37 nm, and a width of 21 ± 4 nm, while in TEM imaging of PEG_{5k}-*b*-$PLys(Boc)_{20}$ suspensions, long and thick worm-like nanoparticles were observed, with a mean length of 116 ± 43 nm, and a width of 30 ± 5 nm. As already reported by Liu *et al.*,[52] TEM imaging of PEG_{5k}-*b*-$PLys(Z)_{20}$, displayed homogeneous superhelix type nanoparticles of 173 ± 80 nm length and 38 ± 7 nm width. Overall, the DLS results and TEM imaging indicated that nanoparticles formed with the benzyloxycarbonyl (Z) protecting group are longer and thicker than those with the tert-butyl carbamate (Boc) protecting group, and more homogeneous than those with the trifluoroacetyl (TFA) one.

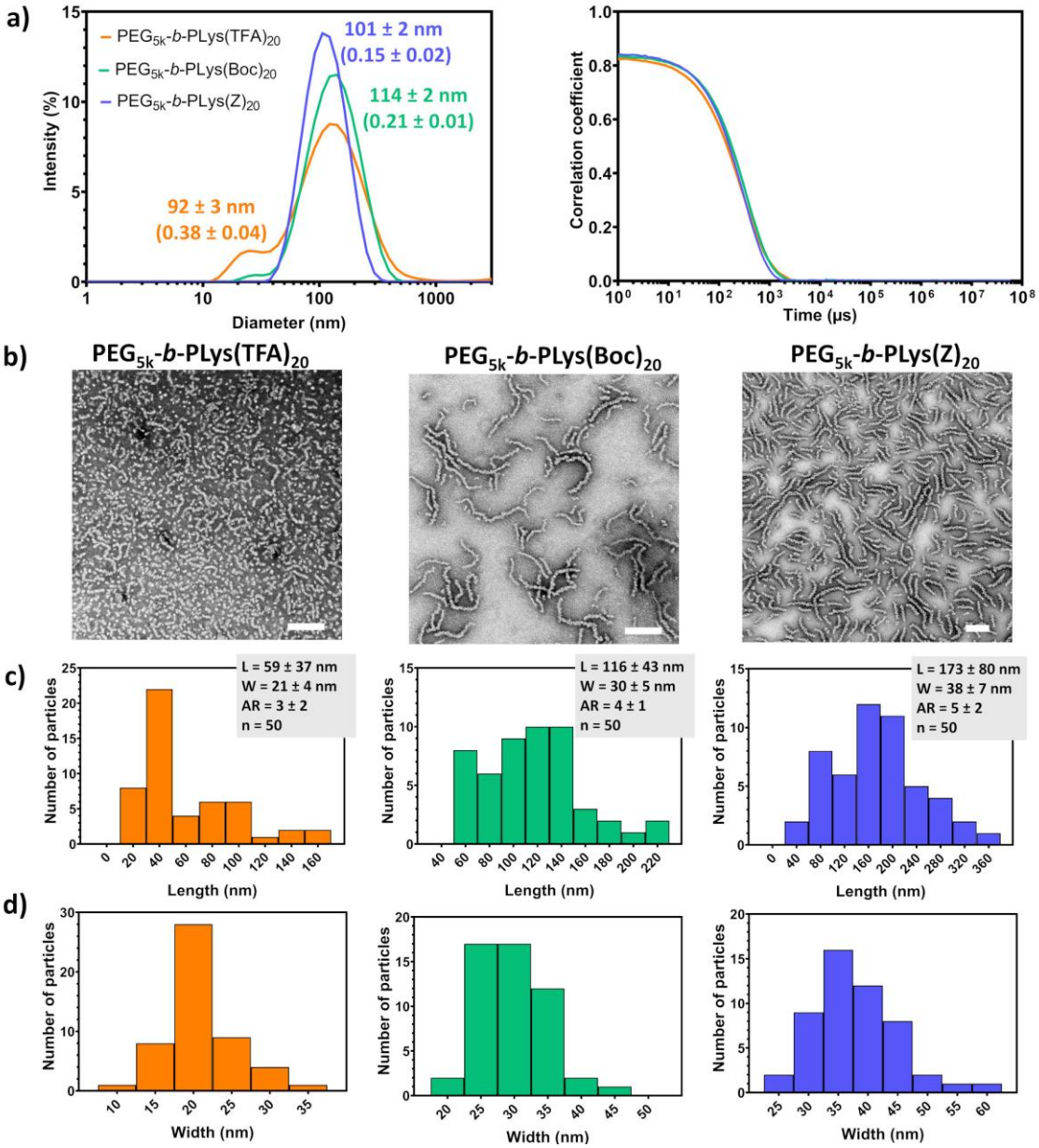

Figure III-7. Nanoparticles characterization after aqueous ROPISA of lysine-derivatives NCAs for a targeted DP of 20. (a) DLS profiles (left) of PEG_{5k}-*b*-$PLys(Boc)_{20}$, PEG_{5k}-*b*-$PLys(Z)_{20}$, and PEG_{5k}-*b*-$PLys(TFA)_{20}$ nanoparticles suspensions and (right) associated correlograms. (b) Representative TEM images of the different copolymer nanoparticles PEG_{5k}-*b*-$PLys(TFA)_{20}$, PEG_{5k}-*b*-$PLys(Boc)_{20}$, and PEG_{5k}-*b*-$PLys(Z)_{20}$. (c) Length and (d) width distribution of the PEG_{5k}-*b*-$PLys(TFA)_{20}$, PEG_{5k}-*b*-$PLys(Boc)_{20}$, and PEG_{5k}-*b*-$PLys(Z)_{20}$ nanoparticles obtained by analysis of 50 nano-objects by ImageJ on a TEM image.

As has been previously established, the influence of the secondary structure is an important factor that may guide the anisotropy upon ROPISA,[56] and to further elucidate this influence, we analyzed the lyophilized powder obtained with the 3 different monomer units using ATR-FTIR spectroscopy (Figure III-8).

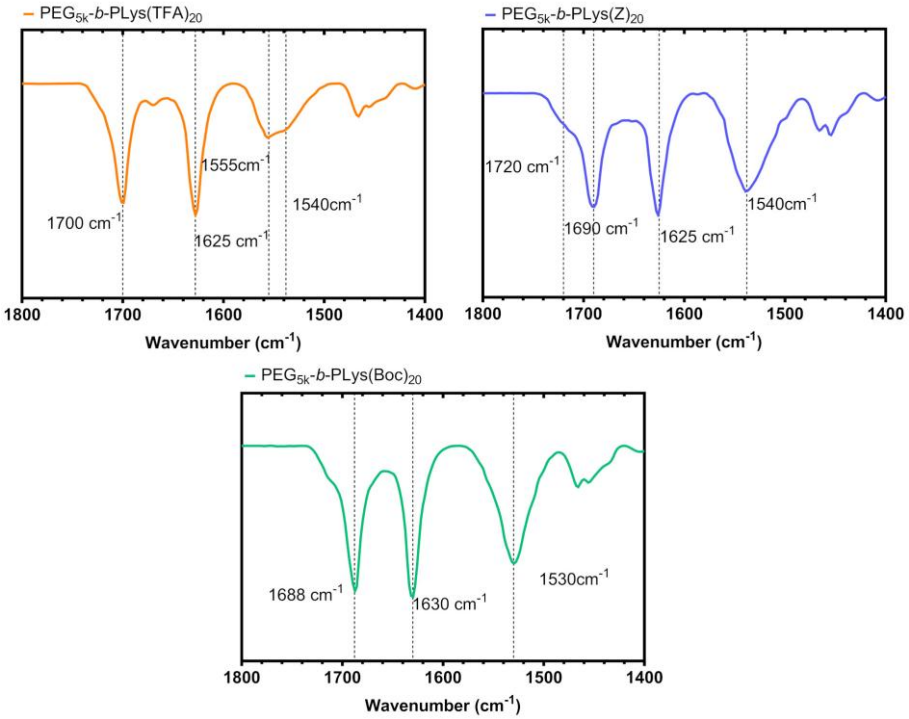

Figure III-8. ATR-FTIR spectra of lyophilized powders of PEG_{5k}-*b*-PLys(TFA)$_{20}$, PEG_{5k}-*b*-PLys(Z)$_{20}$, and PEG_{5k}-*b*-PLys(Boc)$_{20}$.

With both Boc and Z protecting groups, the spectra demonstrated the presence of a prominent peak at 1630 cm^{-1}, which was attributed to the amide I and associated to a peak at 1530 cm^{-1} (the amide II region), along with a peak at 1690 cm^{-1} (side chain carbonyl). These stretching corroborated the presence of an antiparallel β-sheet structure, a conformation that was previously associated to the formation of ribbon-like nanostructures.[52] In our ROPISA conditions, no notable differences in conformation were observed between the Boc and Z protecting groups. However, the anisotropic shapes of the nanomaterial exhibited significant variation (116 nm *versus* 173 nm) that we attributed to the π-π stacking introduced with Z. With TFA protecting groups, the ATR-FTIR spectra revealed that the amide I region exhibited a prominent peak at 1625 cm^{-1}, while the amide II region displayed peaks at 1555 cm^{-1} and 1540 cm^{-1}. These findings suggest that this last β-sheet structure was more constrained (*i.e.,* parallel β-sheet), which resulted in less pronounced anisotropy. Overall, the present study demonstrated that besides the secondary structure, the dimension (parallel/antiparallel) and the chemical nature of the protecting group (π-π stacking) were also key parameters modulating the anisotropy.

III.2.2. [M]/[I] from 10 to 40

To further investigate the influence of the overall hydrophilic/hydrophobic ratio with the 3 lysine derivatives, various aqueous ROPISA were implemented using different feeding ratios (*e.g.*, initial [M]/[I] from 10 to 40) and α-amino-poly(ethylene glycol) (PEG_{5k}-NH_2) as the macro-initiator.

The results of the ^{1}H NMR spectroscopy performed upon ROPISA indicated that the PEG$_{5k}$-*b*-PLys(Z) block copolymers exhibited degree of polymerization values ranging from 15 to 44, which were in close agreement with the targeted values (Table III-2, Figure SIII-1).

Table III-2. Characterization of lysine based-diblock copolymers PEG$_{5k}$-*b*-PLys(Boc)$_n$, PEG$_{5k}$-*b*-PLys(Z)$_n$, and PEG$_{5k}$-*b*-PLys(TFA)$_n$ for initial feeding ratio ([M]/[I]) of 10, 30 and 40.

Copolymer	Monomer	Theory		SEC		^{1}H NMR	
		[M]/[I]	M_n [g.mol^{-1}]	M_n [g.mol^{-1}] [a)]	$Đ$ [a)]	M_n [g.mol^{-1}] [b)]	DP [b)]
PEG$_{5k}$-*b*-PLys(TFA)$_{10}$	*L-NTFA*Lys	10	7 300	11 800	1.05	7 700	12
PEG$_{5k}$-*b*-PLys(TFA)$_{30}$		30	11 700	15 100	1.08	12 200	32
PEG$_{5k}$-*b*-PLys(TFA)$_{40}$		40	13 900	16 100	1.11	13 300	37
PEG$_{5k}$-*b*-PLys(Boc)$_{10}$	*L-NBoc*Lys	10	7 300	11 000	1.06	8 000	13
PEG$_{5k}$-*b*-PLys(Boc)$_{30}$		30	11 900	11 700	1.08	12 100	31
PEG$_{5k}$-*b*-PLys(Boc)$_{40}$		40	14 100	12 200	1.11	13 700	38
PEG$_{5k}$-*b*-PLys(Z)$_{10}$	*L-NZ*Lys	10	7 600	11 800	1.08	8 900	15
PEG$_{5k}$-*b*-PLys(Z)$_{30}$		30	12 900	15 800	1.15	14 400	36
PEG$_{5k}$-*b*-PLys(Z)$_{40}$		40	15 300	16 400	1.26	16 500	44

[a)] Number average molar-mass (M_n) and molar-mass dispersity determined by SEC in DMF +1% LiBr using PS calibration, [c)] Number average molar-mass (M_n) and degree of polymerization (DP) determined by ^{1}H NMR in DMSO-d$_6$, [c)] Hydrodynamic Z-average diameter (D_Z) and polydispersity (σ) determined by DLS at 90°.

The corresponding SEC chromatograms exhibited a monomodal distribution with narrow molar mass dispersity values, and the retention times shifted to lower values compared to the PEG macroinitiator, confirming effective block extension (Figure III-9).

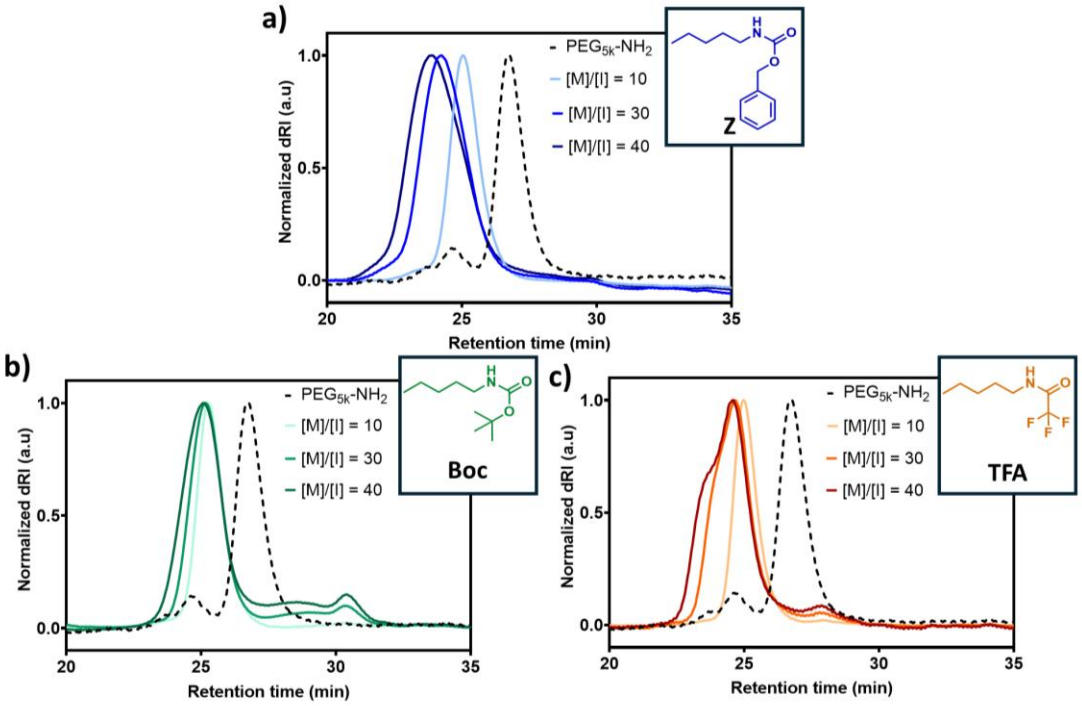

Figure III-9. SEC chromatograms of (a) PEG_{5k}-*b*-$PLys(Z)_n$, (b) PEG_{5k}-*b*-$PLys(Boc)_n$ and (c) PEG_{5k}-*b*-$PLys(TFA)_n$ with targeted DP of 10, 30 and 40 in DMF (+1% LiBr, detection by differential refractive index). The peaks observed at lower mass, below the macroinitiator, were attributed to water-initiated ROP.

DLS analysis revealed a progressive increase in the size of the nanoparticles (Figure III-10) while TEM imaging showed the formation of heterogeneous helical ribbons for PEG_{5k}-*b*-$PLysZ_{10}$. However, with increasing Lys(Z) block length, larger aggregates were observed. Overall, anisotropic morphologies were obtained at specific hydrophilic/hydrophobic ratios, but increasing the length of the hydrophobic block resulted in uncontrolled aggregation. This highlights the critical balance needed in tuning block copolymer composition to achieve well-defined self-assembled structures with the ROPISA of Lys(Z)-NCA.

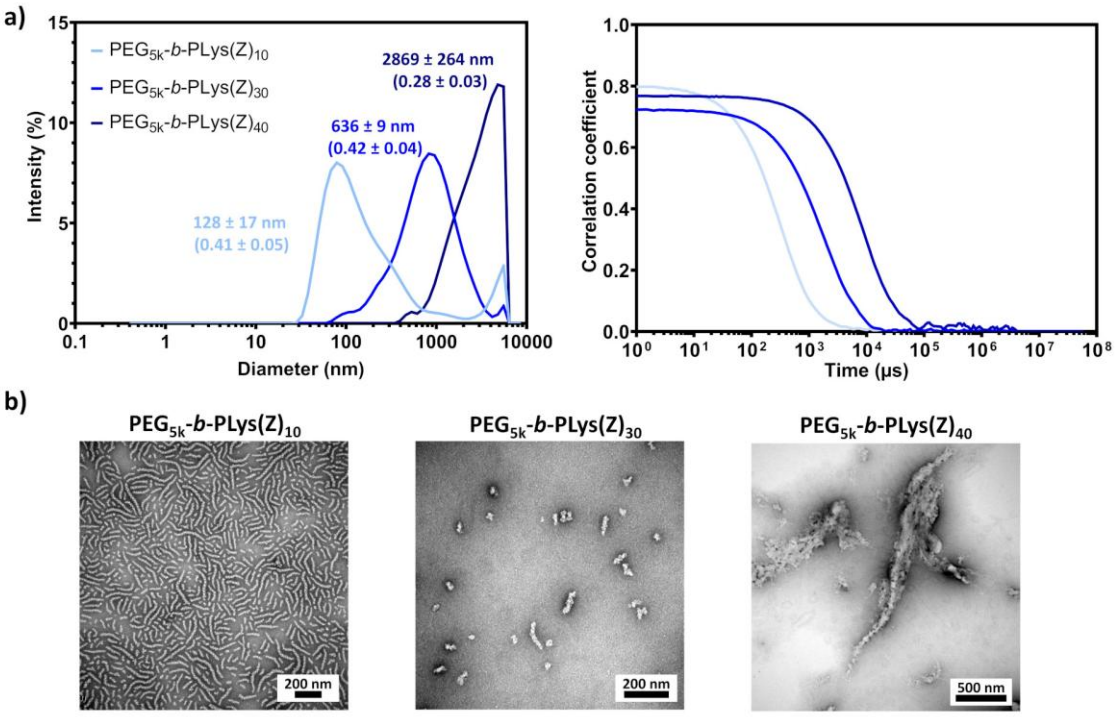

Figure III-10. (a) DLS profiles (left) of the PEG_{5k}-*b*-$PLys(Z)_n$ with targeted DP of 10, 30 and 40 suspensions, with associated correlograms (right). (b) Representative TEM images of the corresponding nanoparticles.

In the absence of π-π stacking stabilization, the aqueous ROPISA of Lys(TFA)-NCA also led to the formation of copolymers whose degree of polymerization (DP) as determined by ^{1}H NMR was found to be in agreement with the theoretical values (see Table III-2, Figure SIII-2). However, beyond M/I = 20, SEC profiles (Figure III-9) exhibited peak splitting, which correlated with increasing molar mass and the emergence of a peak at lower molar masses. This phenomenon suggested the formation of an oligomeric population generated through residual hydrolysis of NCA monomers ("water-initiated"). This was attributed to less efficient dispersion of the NCA monomer in the aqueous phase that could originate from the strong hydrophobic nature of TFA.

Finally, the aqueous ROPISA of Lys(Boc)-NCA, displaying more steric hindrance than the two other lysine derivatives, led to the formation of copolymers whose degree of polymerization (DP) calculated by ^{1}H NMR indicated that the molar masses remained unchanged at increasing feeding ratio (Table III-2, Figure SIII-3). Moreover, the SEC profiles exhibited an increased number of oligomers formed through water initiation, suggesting that the polypeptide chains were unable to maintain an optimal propagation rate during ROPISA.

Overall, comparing the aqueous ROPISA of Lys(TFA)-NCA, Lys(Boc)-NCA, and Lys(Z)-NCA, demonstrated that the hydrophobicity of the different protecting groups significantly influenced the polymerization process and the anisotropy. At higher [M]/[I], water initiation was observed with Lys(TFA)-NCA and Lys(Boc)-NCA. Moreover, we found that the benzyl group facilitated a superior dispersion of the monomer powder in the aqueous medium and favored a more pronounced anisotropic shape through π-π stacking. All these factors, in turn, enable a more regulated aqueous polymerization and self-assembly

for Lys(Z)-NCA, which results in a more uniform distribution of nanoparticles than that observed with Boc- and TFA-protected groups.

III.3. Influence of the hydrophobicity of the amino-acid side chain

III.3.1. Aqueous ROPISA of Gly, Ala, Tyr, Leu and Phe-NCA

The study of the lysine derivatives with different protecting groups clearly showed that the hydrophobicity of the side chain can play an important role in the ROPISA process and modulate the anisotropy of the nanoparticles that are obtained. To better evaluate this influence, we selected a series of 5 NCA monomers, Glycine-NCA, Alanine-NCA, Tyrosine-NCA, Leucine-NCA, and Phenylalanine-NCA, arranged in order of increasing hydrophobicity, with calculated Log P_{oct} values of -0.31, 0.02, 1, 1.33 and 1.48 respectively (Scheme III-3).[57–59]

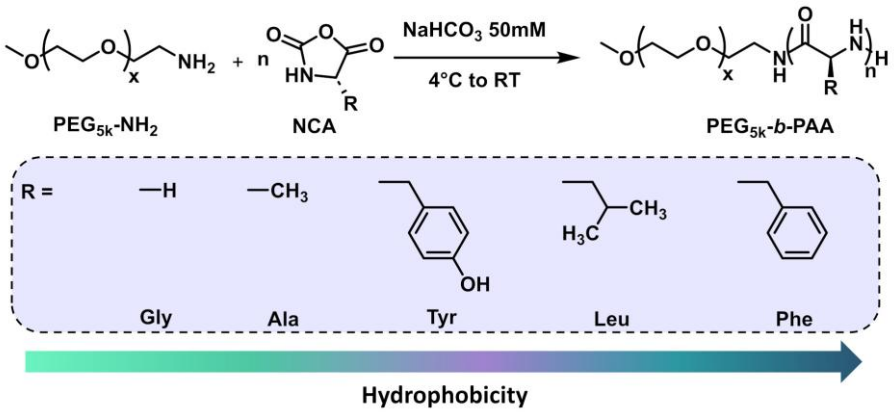

Scheme III-3. Aqueous ROPISA with a range of NCAs to study the influence of hydrophobicity.

Alanine NCA (Ala-NCA) was synthesized by the Leuchs method (Figure SIII-4), while the others were commercially available. The aqueous polymerization was carried out under the same conditions as those previously used with lysine derivatives, with an initial feed ratio [M]/[I] of 20. According to ^{1}H NMR spectroscopy, the different ROPISA afforded copolymers with DP values similar to the targeted ones (Table III-3, Figure SIII-5**,** Figure SIII-9). SEC analyses demonstrated that well-defined amphiphilic block copolymers with a narrow dispersity ($Đ < 1.2$) were consistently produced, confirming the effectiveness of the aqueous ROPISA at low [M]/[I] for all hydrophobic monomers and surprisingly, even for the non-hydrophobic monomer Glycine-NCA (Table III-3, Figure III-11).

Table III-3. Macromolecular characteristics of diblock copolymers obtained by aqueous ROPISA with different monomers, using a-amino polyethylene glycol as macroinitiator, at a feeding ratio of 20.

Copolymer	Monomer	Theory	SEC		^{1}H NMR		Yield (%)	DLS
		M_n [g.mol^{-1}]	M_n [g.mol^{-1}]	$Đ$	M_n [g.mol^{-1}]	DP		D_Z [nm] (σ) [e]
PEG$_{5k}$-*b*-PGly$_{20}$	Gly	6 100	49 100 [a]	1.07 [a]	6 400 [c]	25 [c]	56	265 ± 8 (0.53 ± 0.02)
PEG$_{5k}$-*b*-PAla$_{20}$	*L*-Ala	6 400	33 600 [a]	1.07 [a]	6 500 [c]	21 [c]	73	149 ± 1 (0.41 ± 0.03)
PEG$_{5k}$-*b*-PLeu$_{20}$	*L*-Leu	7 200	9 200 [b]	1.03 [b]	7 400 [c]	21 [c]	90	101 ± 2 (0.34 ± 0.05)
PEG$_{5k}$-*b*-PPhe$_{20}$	*L*-Phe	7 900	9 000 [b]	1.03 [b]	8 200 [c]	22 [c]	79	85 ± 1 (0.27 ± 0.02)
PEG$_{5k}$-*b*-PTyr$_{20}$	*L*-Tyr	8 200	9 400 [b]	1.07 [b]	7 600 [d]	16 [d]	89	77 ± 4 (0.23 ± 0.01)

[a] Number average molar-mass (M_n) and molar-mass dispersity determined by SEC in HFIP+0.05% KTFA using PMMA calibration [b] in DMF+1%LiBr using PS calibration. [c] Number average molar-mass (M_n) and degree of polymerization (DP) determined by ^{1}H NMR in TFA-*d*, [d] DMSO-d$_6$. [e] Hydrodynamic Z-average diameter (D_Z) and polydispersity (σ) determined by DLS at 90°.

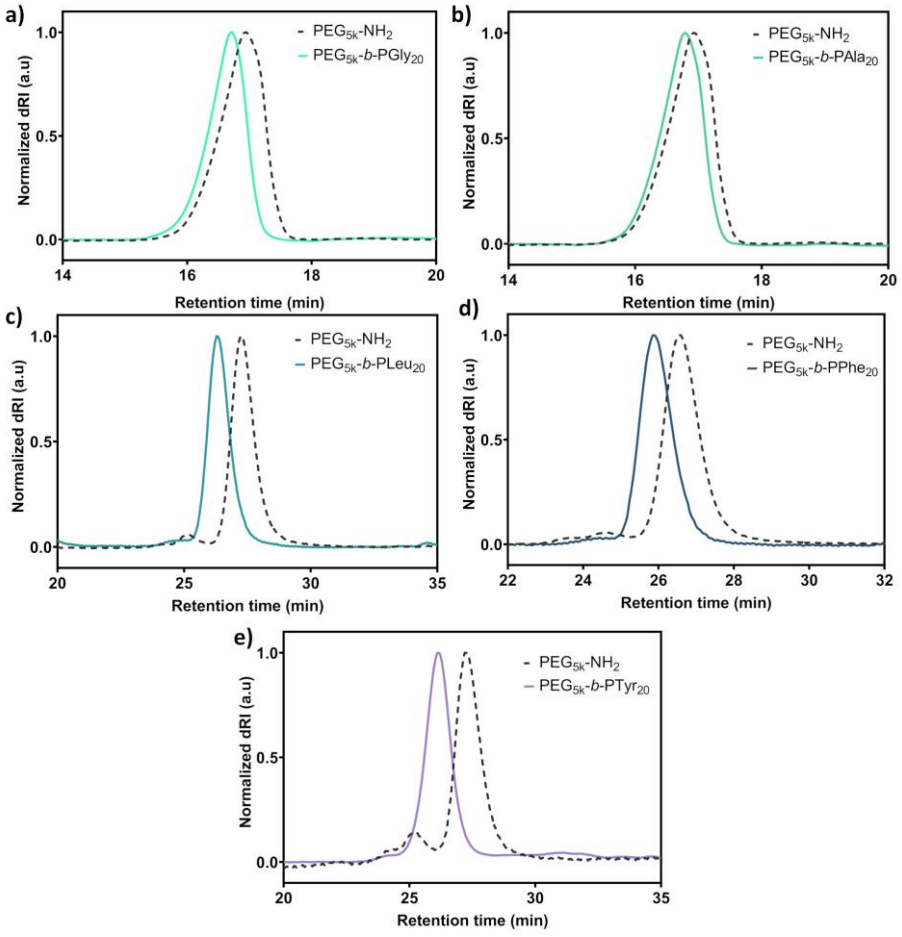

Figure III-11. SEC chromatograms of (a) PEG$_{5k}$-*b*-PGly$_{20}$, (b) PEG$_{5k}$-*b*-PAla$_{20}$, (c) PEG$_{5k}$-*b*-PLeu$_{20}$, (d) PEG$_{5k}$-*b*-PPhe$_{20}$ and (e) PEG$_{5k}$-*b*-PTyr$_{20}$. (a-b): HFIP +0.05% KTFA; (c-e): DMF + 1% LiBr. Detection by differential refractive index.

Following dialysis to remove salts, the suspensions of nanoparticles were analyzed by DLS and imaged by TEM. For PEG$_{5k}$-*b*-PGly$_{20}$, DLS showed sizes with high dispersity (σ ≈ 0.5) (Figure III-12a),

likely due to the nanoparticles' morphology. Indeed, TEM images revealed the presence of flexible fibrils, both simple and branched, with an average diameter of 13 ± 2 nm (Figure III-13). The length of these fibrils could not be determined because of the variability in branching. It is important to note that the glycine monomer was fully soluble at the initial stage of the ROPISA process and that the aggregation of the polypeptide is attributable to its ability to form intermolecular hydrogen bond and other dipolar interactions such as CO–CO interactions.[60]

Interestingly, the sphere-equivalent Z-average diameter of the nanoparticles suspensions was found to be larger for PEG_{5k}-*b*-$PAla_{20}$ than for PEG_{5k}-*b*-$PLeu_{20}$, although the dispersity was high ($\sigma > 0.2$) in both cases (Table III-3, Figure III-12b,c, Figure III-13). For both NCA monomers, TEM revealed the presence of long, thin, and rigid rod-like nanoparticles with homogeneous diameters (151 ± 58 nm in length and 11 ± 2 nm diameter for PEG_{5k}-*b*-$PAla_{20}$; 102 ± 42 nm in length, 11 ± 2 nm diameter for PEG_{5k}-*b*-$PLeu_{20}$, Figure III-13). PEG_{5k}-*b*-$PAla_{20}$ nanoparticles had a higher aspect ratio than PEG_{5k}-*b*-$PLeu_{20}$ nanoparticles. Nanoparticles suspensions prepared from PEG_{5k}-*b*-$PPhe_{20}$ exhibited a sphere-equivalent z-average diameter distribution that was more homogenous, with a mean diameter of 85 ± 1 nm and a polydispersity index (σ) of 0.27 ± 0.02 (Table III-3, Figure III-12d). However, in marked contrast to the findings reported by Morrel *et al.* using a poly(sarcosine) macroinitiator,[50] we observed by TEM a heterogeneous mixture of long, thick and rigid nanorods with spherical micelles. The distribution of nanoparticles was rather heterogenous in length (105 ± 82 nm), but the dispersion of diameters was narrow (26 ± 4 nm) (Figure III-13). Finally, DLS analyses of PEG_{5k}-*b*-$PTyr_{20}$, indicated a Z-average hydrodynamic diameter of 77 ± 4 nm (Table III-3, Figure III-12e). In comparison to PEG_{5k}-*b*-$PPhe_{20}$, this ROPISA yielded nanoparticles with a smaller diameter and a significantly lower proportion of spherical micelles as shown by TEM (Figure III-13).

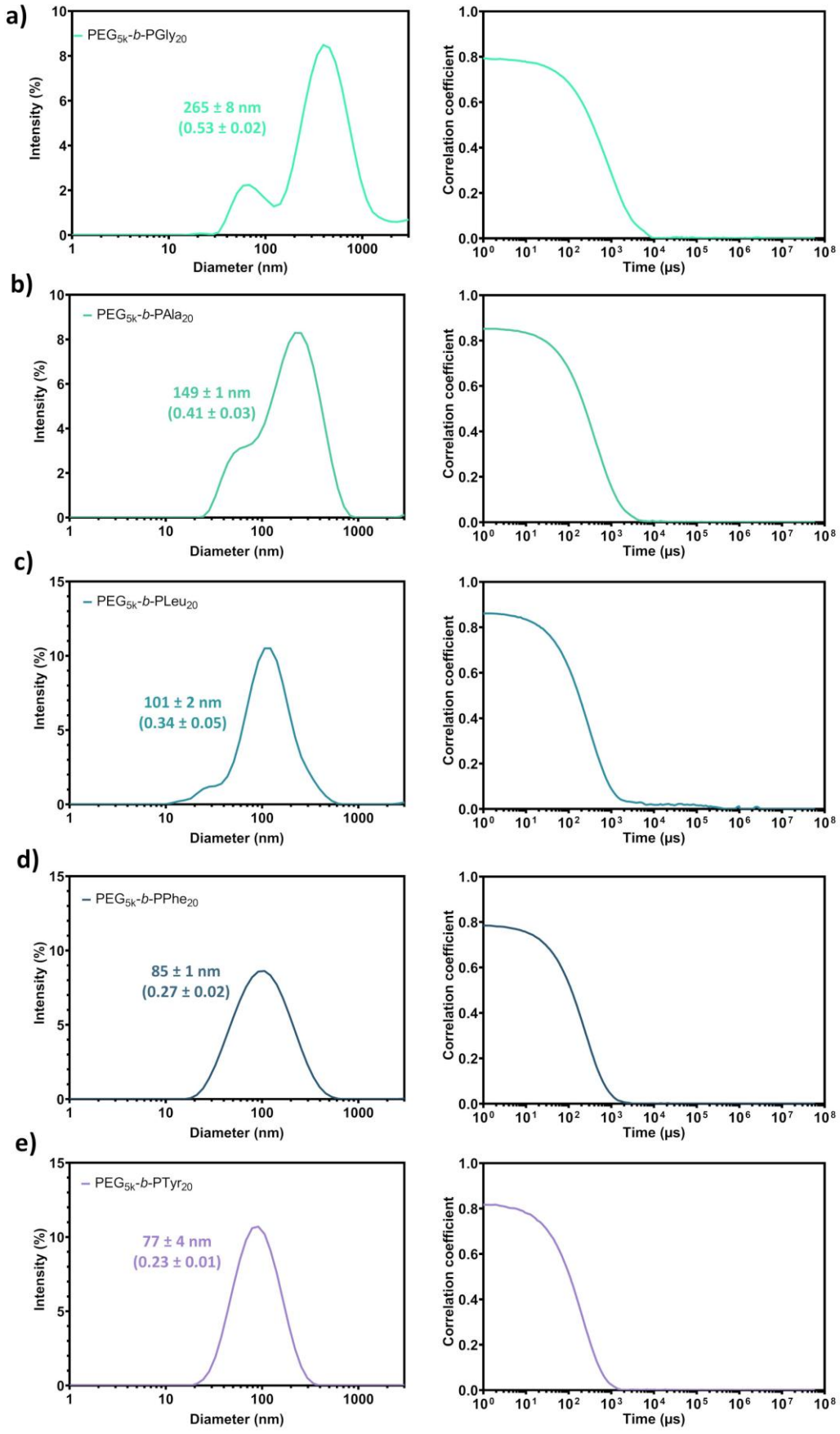

Figure III-12. DLS profiles (left) and associated correlograms (right) of (a) PEG_{5k}-*b*-$PGly_{20}$, (b) PEG_{5k}-*b*-$PAla_{20}$, (c) PEG_{5k}-*b*-$PLeu_{20}$, (d) PEG_{5k}-*b*-$PPhe_{20}$ and (e) PEG_{5k}-*b*-$PTyr_{20}$ nanoparticle suspensions.

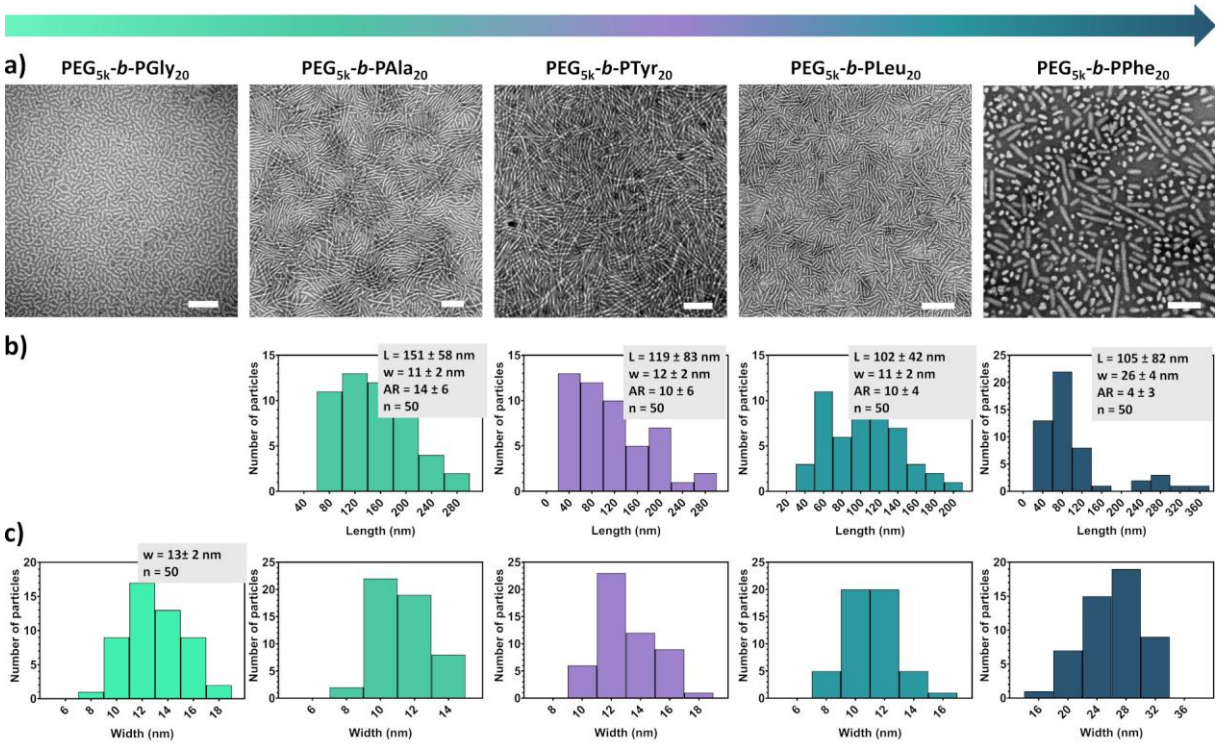

Figure III-13. (a) Representative TEM images of the different copolymer nanoparticles obtained with Gly, Ala, Tyr, Leu, and Phe at an initial [M]/[I] ratio of 20, initiated by PEG_{5k}-NH_2, with increasing hydrophobicity. Scale-bar: 200 nm. (b) Length and (c) width distribution of the nanoparticles obtained by analysis of 50 nano-objects by ImageJ on a TEM image.

Beyond hydrophobicity, the influence of the secondary structure is an important factor that may also guide the anisotropy of the proposed 5 monomers. To further elucidate this influence, we also analyzed the lyophilized powder obtained upon ROPISA using ATR-FTIR spectroscopy. First, glycine, the simplest and achiral amino acid, lacks the classic structural features of typical polypeptides affording secondary structure. However, glycine's specific conformational structures involving hydrogen bonding have already been reported and found similar to β-sheets.[61,62]

The spectrum displayed a prominent peak in the amide I region at 1644 cm^{-1} and another in the amide II region at 1560 cm^{-1}, which are characteristic of the poly(glycine II) (PGII) conformation—an extended helical structure commonly found in solution (Figure III-14).[61,63] In comparison, the FTIR spectrum of PEG_{5k}-*b*-$PAla_{20}$ showed a peak at 1625 cm^{-1} in the amide I region and at 1538 cm^{-1} in the amide II region, indicating a β-sheet conformation. For PEG_{5k}-*b*-$PLeu_{20}$, a prominent peak at 1627 cm^{-1} and a smaller one at 1653 cm^{-1} in the amide I region, along with a peak at 1544 cm^{-1} in the amide II region, suggest a mix of β-sheet and α-helical structures, as also reported by Floudas *et al*.[64] For all 3 monomers, the "β-sheet" conformation was likely responsible for the increased rigidity observed particularly comparing alanine and leucine. FTIR analyses were also conducted on dried powders of PEG_{5k}-*b*-$PPhe_{20}$ and PEG_{5k}-*b*-$PTyr_{20}$. The phenylalanine-based copolymer displayed a peak at 1632 cm^{-1} in the amide I region and at 1545 cm^{-1} in the amide II region, indicative of β-sheet structures.

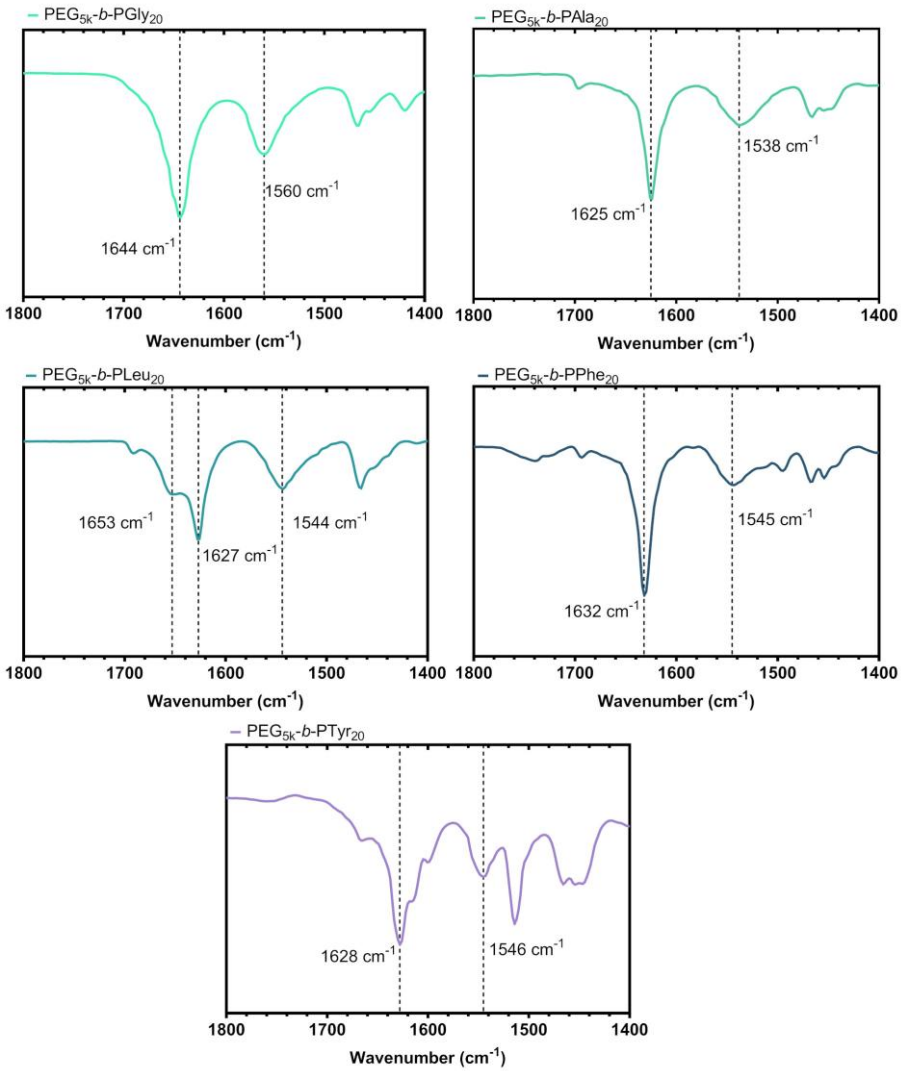

Figure III-14. ATR-FTIR spectra of lyophilized powders of PEG_{5k}-*b*-$PLysGly_{20}$, PEG_{5k}-*b*-$PAla_{20}$, PEG_{5k}-*b*-$PLeu_{20}$, PEG_{5k}-*b*-$PPhe_{20}$ and PEG_{5k}-*b*-$PTyr_{20}$.

Similarly, the tyrosine-based copolymer exhibited characteristic peaks in both the amide I and amide II regions, also confirming the presence of β-sheet conformations. The observed anisotropic structures likely arise from the combined effects of hydrophobic interactions and the intrinsic β-sheet secondary structure of the polypeptides. The β-sheet conformation provides a rigid and directional framework, while the degree of hydrophobicity modulates the overall rigidity and prominence of the anisotropy.

III.3.2. Kinetic studies

Recent studies carried out in organic solvents and with lactide suggested that the ROPISA process may be strongly influenced by ROP kinetics and that the speed of these kinetics, compared with self-assembly kinetics involving a CDSA process, may explain the formation of more anisotropic morphologies.[65] To better understand such influence, aqueous ROPISA kinetics were studied by monitoring the different monomer conversion using ^{1}H NMR at a feed-ratio of 20 and initiated by PEG_{5k}-

NH_2. HCl was used to quench polymerization at different timepoints (Figure SIII-10,Figure SIII-14). Remarkably, in the case of glycine and alanine, the aqueous ROP was "superfast" and achieved in less than 5 minutes. Plots of ln ($[M]_0/[M]_t$) versus time indicated a first-order dependence on the monomer concentration (Figure III-15). A detailed investigation of polymerization kinetics yielded an apparent kinetics rate constant (k) value of 1.52 min^{-1} and 1.535 min^{-1} respectively. The k values with the use of leucine, phenylalanine and tyrosine NCAs were found slightly higher with values of 0.286 min^{-1}, 0.152 min^{-1} and 0.004 min^{-1} respectively. This kinetic study indicates that the aqueous ROP kinetics are directly influenced by the hydrophobicity of the NCA monomer. Hypothetically, the more hydrophobic the monomer, such as phenylalanine-NCA, the slower the dispersion and diffusion of the solid-state. This finding further reinforces the hypothesis raised in **Chapter II**, suggesting that monomer solubility is a key limiting factor in the reaction rate. In addition, consistent with previous studies on the ROPI-CDSA of lactide, slower ROP kinetics observed with phenylalanine-NCA and tyrosine-NCA may lead to reduced anisotropy. This could explain the coexistence of spherical and rod-like nanoparticles for these monomers.

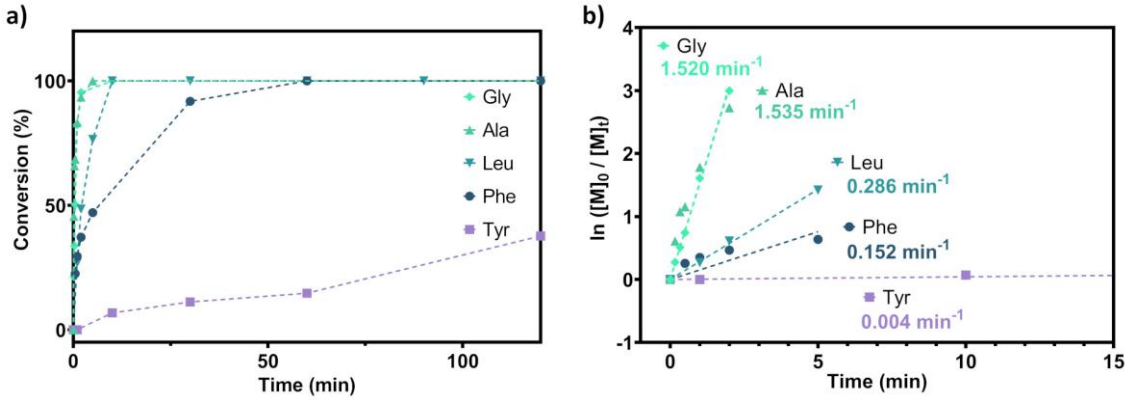

Figure III-15. Kinetic profiles of (a) conversion vs time and (b) ln($[M]_0/[M]_t$) vs time at an initial [M]/[I] ratio of 20 determined by ^{1}H NMR spectra.

In summary, aqueous ROPISA enables the polymerization of diverse NCA monomers with varying hydrophobicity. The hydrophobicity, chemical structure, and steric hindrance of these monomers significantly influence polymerization kinetics and self-assembly behavior. In contrast to classical dispersion methods, such as RAFT-PISA in water, which impose limitations on the available monomers, ROPISA appears to exhibit a wider range of monomer options. In RAFT-PISA, the hydrophobicity of core-forming monomers and their corresponding oligomers requires careful control.[66] In contrast, aqueous ROPISA accommodates a wider range of hydrophobic monomers, as long as they are sufficiently dispersed to diffuse into the polymerization locus.

III.4. π-π interactions versus hydrophilic content: phenylalanine NCA

Our previous studies[67,68] and the current investigation indicate that the majority of our ROPISA attempts result in the formation of anisotropic nanomaterials, in marked contrast to other PISA processes.

Nevertheless, nanoparticles solutions comprising PEG_{5k}-*b*-$PPhe_{20}$ and PEG_{5k}-*b*-$PTyr_{20}$ also exhibited the simultaneous formation of spherical micelles during ROP. This difference can be attributed to slower ROP kinetics, which are not amenable to a CDSA process, as shown by recent studies on lactide.[65] Indeed, the presence of spherical shapes suggests that self-assembly is closer to an equilibrium in which the amphiphilic character may have more influence. To determine whether morphology could be influenced by the hydrophilic/hydrophobic ratio, we further investigated the ROPISA of Phe-NCA by varying the M/I ratio. The objective was also to decipher how the aromatic ring of the side chain of phenylalanine could arrange stabilizing π-π interactions that are especially relevant in drug delivery applications.[69,70] So far, the traditional ring-opening polymerization performed in organic solvent still presents significant challenges when used to polymerize Phe-NCA and this monomer has been mainly studied in copolymerization systems.[71–73] In a non-aqueous ROPISA approach, Du *et al.* investigated the fate of Phe-NCA in THF, initiated by PEG_{2k}-NH_2, and achieved the formation of polymersomes with a block ratio of 1:20 and a solid content of 20%.[74] Subsequently, Morrel *et al*. employed aqueous ROP to extend poly(sarcosine) with Phe-NCA, with the objective of synthesizing a polymer with DP ranging from 8 to 33. In this second case, the process also resulted in nanomaterials exhibiting anisotropic characteristics.[50]

III.4.1. From low…

We first performed the aqueous ROPISA of Phe-NCA, utilizing a 2kDa PEG amine macroinitiator, with the aim of targeting lower hydrophilic fractions than the one already studied. The monomer powder was combined with the initiator using extensive stirring at 4°C and in sodium bicarbonate aqueous buffer (pH 8.5, 50 mM) at a monomer-to-initiator ratio of 2 (f_{PEG} of 0.6, PEG_{2k}-*b*-$PPhe_2$), 5 (f_{PEG} of 0.5, PEG_{2k}-*b*-$PPhe_5$), 10 (f_{PEG} of 0.4, PEG_{2k}-*b*-$PPhe_{10}$) and 20 (f_{PEG} of 0.3, PEG_{2k}-*b*-$PPhe_{20}$) and at a solid content of 7 wt%. Upon ROPISA, the solutions were dialyzed against ultra-pure water (RC cut-off 1kDa) for 2 days, with regular changes of water.

^{1}H NMR analyses confirmed the expected chemical structures and enabled the estimation of number-averaged molar mass M_n values that were slightly higher than the targeted values (Table III-4**,** Figure SIII-15). Furthermore, the chain extension proceeded effectively, as demonstrated by the SEC chromatograms and corroborated by the low molar mass dispersity values between 1.05 and 1.07 (Figure III-16a).

Table III-4. Macromolecular characteristics of diblock copolymers obtained by aqueous ROPISA with Phe-NCA.

Copolymer	Theory	SEC		^{1}H NMR			Yield (%)	DLS
	M_n [g.mol^{-1}]	M_n [a)] [g.mol^{-1}]	$Đ$ [a)]	M_n [c)] [g.mol^{-1}]	DP [c)]	f_{PEG} [d)]		D_Z [nm] (σ) [e)]
PEG$_{2k}$-*b*-PPhe$_2$	2 300	3 900	1.07	3 200	8	0.62	9	-
PEG$_{2k}$-*b*-PPhe$_5$	2 800	3 900	1.05	3 600	11	0.55	50	113 ± 1 (0.27 ± 0.01)
PEG$_{2k}$-*b*-PPhe$_{10}$	3 500	4 100	1.05	4 200	15	0.48	86	102 ± 1 (0.26 ± 0.02)
PEG$_{2k}$-*b*-PPhe$_{20}$	4 900	ns [b)]	ns [b)]	5 100	21	0.39	81	715 ± 55 (0.21 ± 0.16)
PEG$_{5k}$-*b*-PPhe$_2$	5 300	7 000	1.07	5 300	2	0.94	58	135 ± 5 (0.27 ± 0.01)
PEG$_{5k}$-*b*-PPhe$_5$	5 700	7 400	1.07	5 800	5	0.87	65	82 ± 2 (0.25 ± 0.01)
PEG$_{5k}$-*b*-PPhe$_{10}$	6 400	7 900	1.07	6 500	10	0.77	74	87 ± 1 (0.2 ± 0.01)
PEG$_{5k}$-*b*-PPhe$_{20}$	7 900	9 000	1.03	8 200	22	0.61	79	85 ± 1 (0.27 ± 0.02)
PEG$_{10k}$-*b*-PPhe$_2$	10 300	18 400	1.02	10 400	3	0.96	82	253 ± 4 (0.48 ± 0.06)
PEG$_{10k}$-*b*-PPhe$_5$	10 800	19 900	1.03	11 000	7	0.91	95	66 ± 2 (0.38 ± 0.04)
PEG$_{10k}$-*b*-PPhe$_{10}$	11 500	19 900	1.03	11 500	10	0.87	76	80 ± 1 (0.37 ± 0.02)
PEG$_{10k}$-*b*-PPhe$_{20}$	12 900	ns [b)]	ns [b)]	13 700	25	0.73	84	118 ± 1 (0.23 ± 0.04)

[a)] Number average molar-mass (M_n) and molar-mass dispersity determined by SEC in DMF + 1% LiBr using PS calibration, [b)] not soluble in common SEC solvents, [c)] Number average molar-mass (M_n) and degree of polymerization (DP) determined by ^{1}H NMR in in TFA-*d*, [d)] Hydrophilic fraction or PEG fraction determined by this equation $\frac{M_n \text{ PEG}}{M_n \text{ copolymer}}$ with M_n from ^{1}H NMR. [e)] Hydrodynamic Z-average diameter (D_Z) and polydispersity (σ) determined by DLS at 90°.

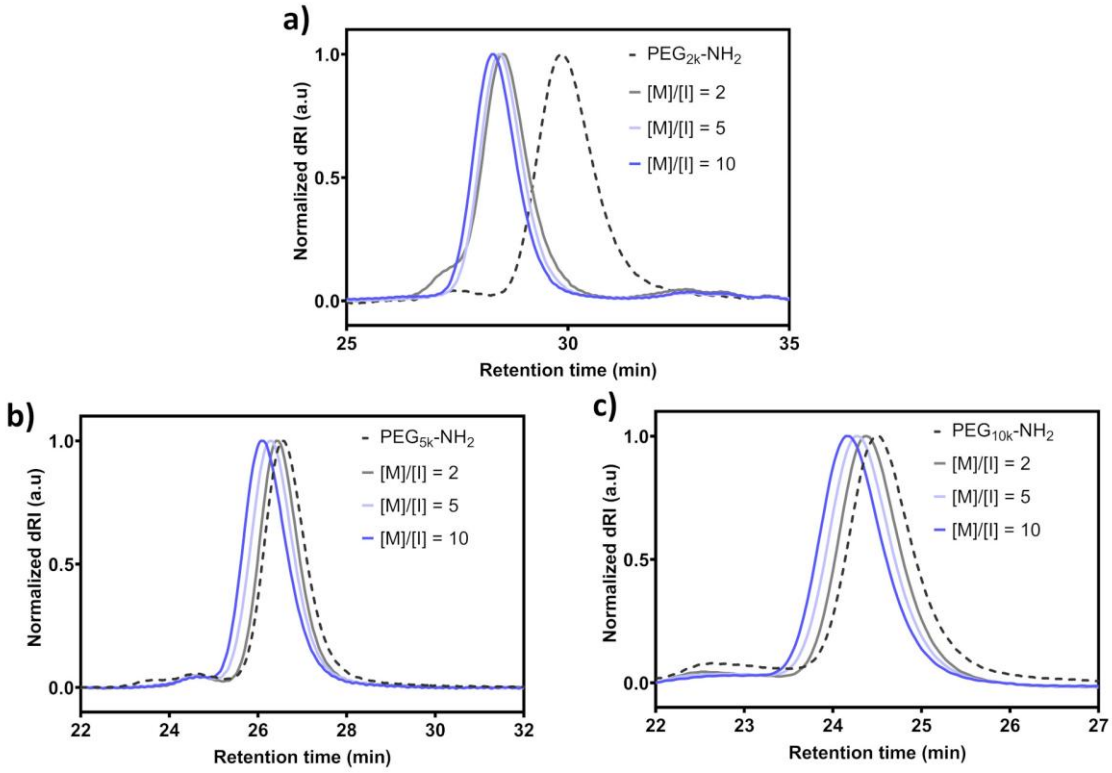

Figure III-16. SEC chromatograms of (a) PEG_{2k}-*b*-$PPhe_n$, (b) PEG_{5k}-*b*-$PPhe_n$ and (c) PEG_{10k}-*b*-$PPhe_n$ with targeted DP of 2, 5 and 10 in DMF (+ 1% LiBr, detection by differential refractive index).

Following dialysis, nanoparticle formation was confirmed by DLS and TEM analyses, even at a DP of 8, with a mixture of short rod and aggregate structures (Table III-4, Figure III-17, Figure III-18). As the length of the polypeptide block increased, the nanoparticles developed into progressively longer and more elongated structures at DP of 11. At a DP of 15, the nanoparticles exhibited enhanced rigidity, and at a DP of 20, they formed aggregates (Figure III-18).

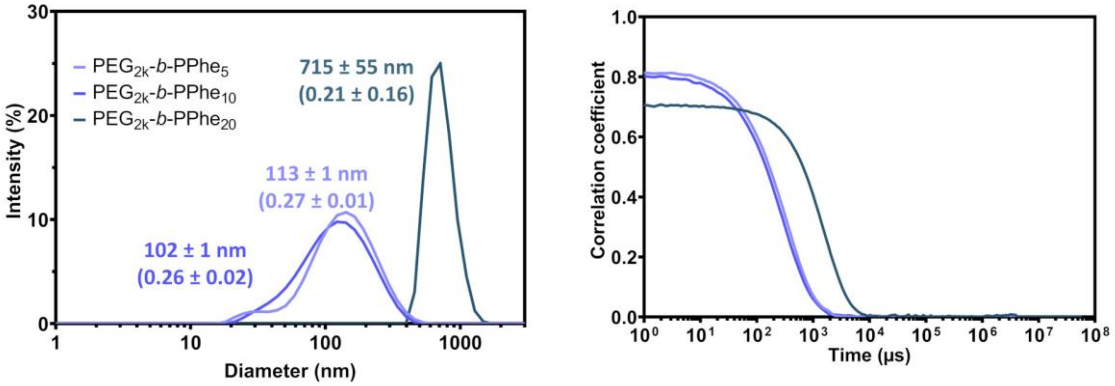

Figure III-17. DLS profiles (left) and associated correlograms (right) of PEG_{2k}-*b*-$PPhe_n$ with targeted DP of 5, 10 and 20 nanoparticle suspensions.

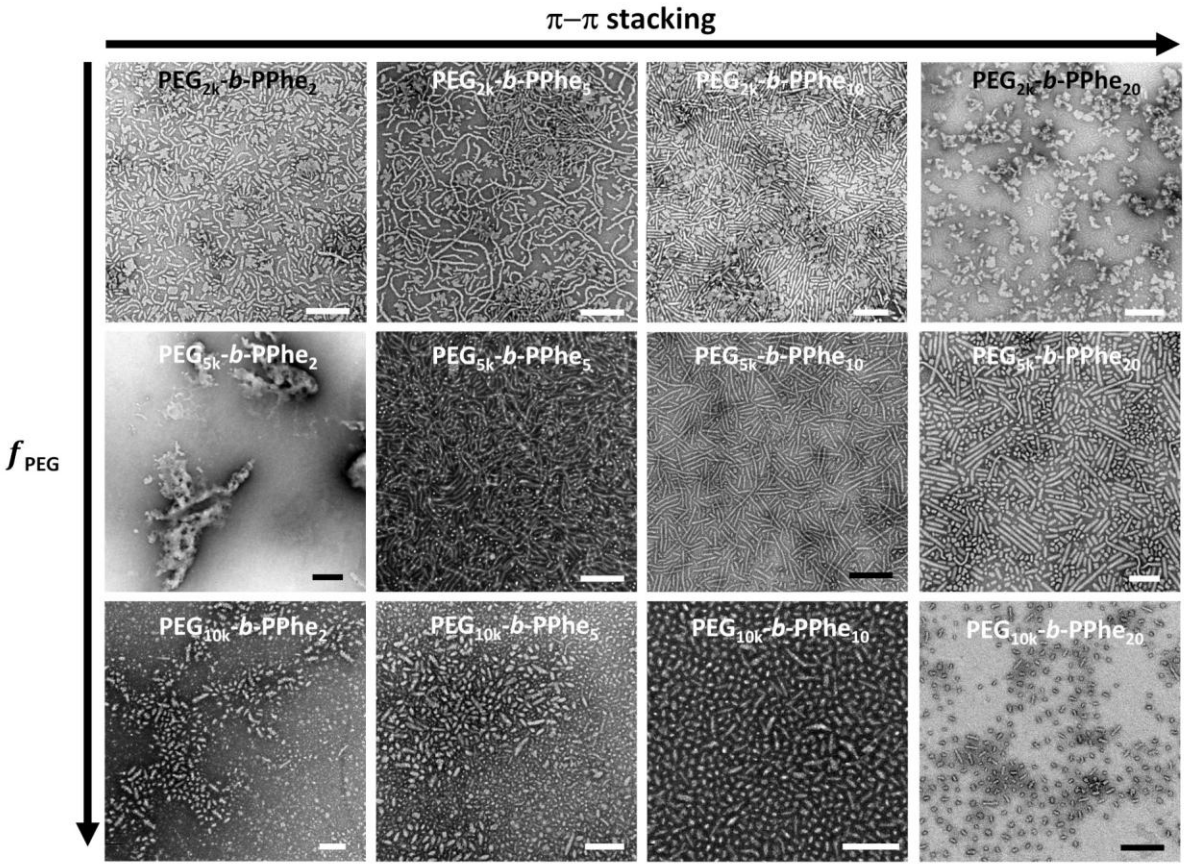

Figure III-18. Representative TEM images of the different copolymer nanoparticles obtained with Phe, with different hydrophilic/hydrophobic block ratio and degree of π–π stacking. Scale-bar: 200 nm.

III.4.2. … to high hydrophilic fractions

To enhance the hydrophilic/hydrophobic ratio and examine its influence on the resulting nanoparticle morphology, we proceeded to conduct the aqueous ROPISA of Phe-NCA with the incorporation of 5 kDa or 10 kDa PEG amine (f_{PEG} between 0.6 and 0.9,Table III-4). The macroinitiator was combined with the monomer powder through extensive stirring at 4°C and in a sodium bicarbonate aqueous buffer (pH 8.5, 50 mM) at a monomer-to-initiator ratio ranging from 2 to 20. In all instances, the NCA monomers underwent complete conversion, as substantiated by ^{1}H NMR spectroscopy. Additionally, ^{1}H NMR spectroscopy and SEC chromatograms demonstrated effective control over the polymerization process. The calculated DP values by ^{1}H NMR exhibited a high degree of correlation with the targeted values, as evidenced by the data presented in Figure SIII-16 and Figure SIII-17.

SEC analysis confirmed the effective extension of the PEG chains and the attainment of a low molar mass dispersity (ranging from 1.03 to 1.07) (Figure III-16b, c). To further distinguish the influence of the polypeptide molar mass from any influence of the secondary structure, we also analyzed the lyophilized powder obtained upon ROPISA using ATR-FTIR spectroscopy. The IR spectra of all copolymers, regardless of the size of the PEG component, exhibited β-sheet conformation, as evidenced by the presence of amide I and II peaks at 1630 cm^{-1} and at 1540 cm^{-1} (Figure III-14e,Figure III-19).

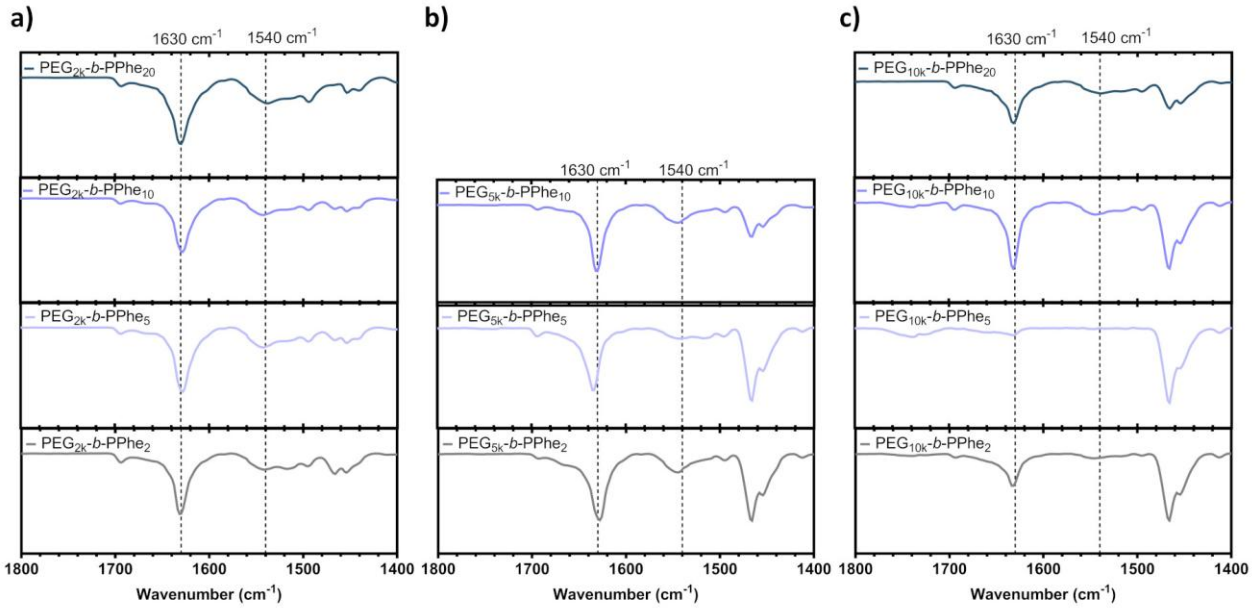

Figure III-19. ATR-FTIR spectra of lyophilized powders of (a) PEG_{2k}-*b*-$PPhe_n$, (b) PEG_{5k}-*b*-$PPhe_n$ and PEG_{10k}-*b*-$PPhe_n$ with targeted DP of 2, 5, 10 and 20.

Overall, good control over the polymerization was achieved when initiated with PEG5k and PEG10k, demonstrating effective chain extension, no water initiation, and high yield. In contrast, the initiation with PEG2k showed less control, resulting in lower yields and higher average DPs than targeted. This suggests the potential hydrolysis of Phe-NCA into its corresponding amino acid, which was subsequently removed by dialysis. Notably, no evidence of water initiation was observed in this case.

Following dialysis against water to remove salts, the nanomaterial suspensions were also characterized by microscopy and light scattering techniques. DLS analysis confirmed the presence of nanoparticles with Z-average diameter ranging between 82 and 715 nm, with a relatively narrow size dispersity in the case of PEG_{5k} (Table III-4, Figure III-11, Figure III-20). Overall, TEM observations of the different suspensions indicated that the PEG fraction exerted a significant influence on the morphology of the nanoparticles. Representative TEM imaging is depicted in Figure III-18 as a function of PEG content or π– π stacking ability.

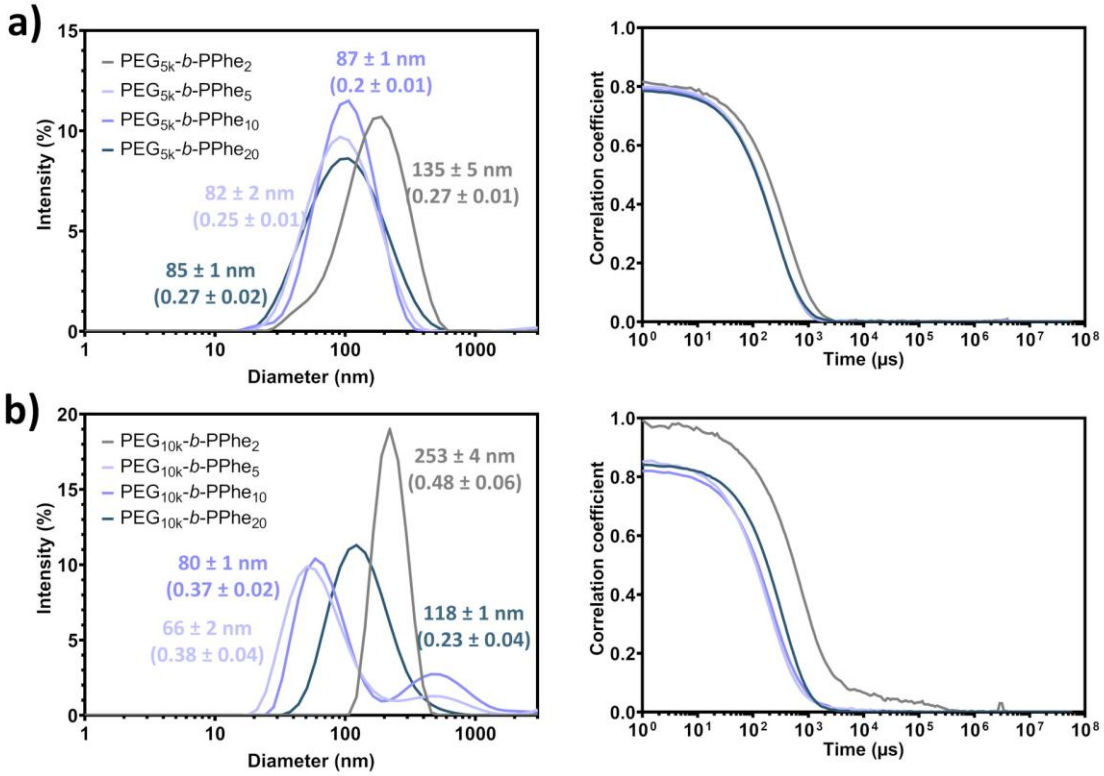

Figure III-20. DLS profiles (left) and associated correlograms (right) of (a) PEG_{5k}-*b*-$PPhe_n$ and PEG_{10k}-*b*-$PPhe_n$ with targeted DP of 2, 5, 10 and 20 nanoparticle suspensions.

First, the addition of a longer polypeptide block and subsequent reduction of the hydrophilic fraction from 0.94 to 0.61 resulted in the formation of more rigid and thicker nanoparticles when PEG_{5k} was used (second line Figure III-18). The PEG_{5k}-*b*-$PPhe_5$ nanoparticles were characterized by a long, thin and flexible morphology. The PEG_{5k}-*b*-$PPhe_{10}$ nanoparticles were thicker and more rigid, yet they were also mixed with shorter nanoparticles. With a lower PEG fraction value of 0.61, PEG_{5k}-*b*-$PPhe_{20}$ exhibited thick and rigid structures but also mixed with spherical micelles. In comparison, when PEG_{10k} was used to increase the PEG fraction, the nanoparticles were of a shorter length and exhibited a markedly reduced degree of anisotropy. This phenomenon was attributable to the increased curvature that results from the larger hydrophilic PEG block and the higher hydrophilic fraction (0.73-0.96). Indeed, an increase in the hydrophilic block size enhances the surface area in contact with the aqueous environment, thereby facilitating the formation of more spherical or less elongated structures. In marked contrast, when the hydrophilic ratio was lower, as observed in the case of PEG_{2k}-*b*-$PPhe_{20}$ (f_{PEG} = 0.48), resulting nanoparticles exhibited reduced anisotropy and aggregates morphology. Additionally, despite having a similar hydrophilic fraction close to 0.75, PEG_{10k}-*b*-$PPhe_{20}$ and PEG_{5k}-*b*-$PPhe_{10}$ displayed distinct aspect ratio with more anisotropy arising from lower PEG molar mass.

The ROPISA of phenylalanine, using poly(ethylene glycol) initiators of different molar masses, demonstrated that controlled polymerization could be achieved, leading to the formation of nanoparticles with different aspect ratios. In this context, the tuning of anisotropy is not solely dependent on the secondary structure (as beta-sheets are formed in all cases) or the monomer's hydrophobicity. It is also influenced by

the hydrophilic/hydrophobic ratio and the π-π stacking interactions of phenylalanine. These findings highlight the potential of ROPISA as a powerful tool for generating anisotropic nanoparticles whose morphologies are tailored by various non-covalent interactions, including the use of monomers such as Phe-NCA, which are usually challenging to polymerize.

III.5. Towards more functional π-π interactions: tyrosine NCA

In the field of nanomedicine, another NCA monomer of interest is derived from tyrosine, which shares similarities with phenylalanine. In contrast to phenylalanine, tyrosine possesses a polar side chain that undergoes a change in solubility when the pH of the solution exceeds the pKa of its phenol group. In drug-delivery, this specific feature enables the formation of strong π-π stacking and H-bonding interactions with drug molecules.[75,76] Aiming to design anisotropic nanomaterials made of this amino acid, a goal not yet achieved in literature, an in-depth study was conducted on the aqueous ROPISA of tyrosine NCA and compared to phenylalanine. A series of block copolymers were synthesized by implementing the aqueous ROPISA using PEG_{5k}-NH_2 as the macroinitiator in an ice-cold aqueous sodium bicarbonate solution (pH 8.5, 50 mM) with 10, 20, 30, and 50 equivalents of Tyr-NCA monomer, while stirring vigorously. These stoichiometries were chosen to best cover the different PEG fractions, from 10 to 80% (Table III-5). It was noteworthy that for targeted DPs of 30 and 50, the aqueous medium exhibited a gradual gelation over time. The gelation ability of tyrosine in aqueous media has been previously investigated for its potential applications in biomedical fields, including drug delivery.[77–79] This encompasses the research conducted by Huang *et al*., who synthesized amphiphilic block copolymers based on PEG-*b*-(oligo)Tyr.[80] The previous research indicated that gelation properties were a result of the interaction between the polar phenolic side chains and the hydrophobic Tyr block.

Following purification, either from the gel or from the aqueous solution, the copolymers presented in Table III-5 were subjected to analysis by ^{1}H NMR and SEC. The results of the ^{1}H NMR spectroscopy revealed that the average number molar mass (M_n) values were in agreement with the initial [M]/[I] ratio (Table III-5, Figure SIII-18). However, the SEC chromatograms indicated that as the [M]/[I] ratio increases, there was a corresponding rise in the proportion of population observed at higher retention times (Figure III-21). We attributed this residual oligomer populations to water initiated polytyrosine that may have been produced by the gelation of the medium during ROPISA, which likely reduced the efficiency of monomer dispersion when stirring was ceased. We also conducted ATR-FTIR spectroscopy on the lyophilized powder obtained after ROPISA. All copolymers exhibited β-sheet conformation, an expected result, as evidenced by the presence of amide I and II peaks in their IR spectra (Figure III-14c, Figure III-22).

Table III-5. Macromolecular characteristics of diblock copolymers obtained by aqueous ROPISA with Tyr-NCA.

Copolymer	Theory	SEC		^{1}H NMR			Yield (%)	DLS
	M_n [g.mol^{-1}]	M_n [a)] [g.mol^{-1}]	$Đ$ [a)]	M_n [c)] [g.mol^{-1}]	DP [c)]	f_{PEG} [d)]		D_Z [nm] (σ) [e)]
PEG$_{5k}$-*b*-PTyr$_{10}$	6 600	9 300	1.05	6 300	8	0.79	67	73 ± 3 (0.21 ± 0.01)
PEG$_{5k}$-*b*-PTyr$_{20}$	8 200	9 900	1.07	7 500	15	0.67	85	77 ± 4 (0.23 ± 0.1)
PEG$_{5k}$-*b*-PTyr$_{30}$	10 100	11 100	1.15	9 900	30	0.50	91	Gel
PEG$_{5k}$-*b*-PTyr$_{50}$	13 300	12 000	1.13	12 300	45	0.40	81	Gel
PEG$_{750}$-*b*-PTyr$_{20}$	3 900	3 300	1.46	4 300	22	0.14	85	Aggregates
PEG$_{2k}$-*b*-PTyr$_{20}$	5 200	5 500	1.13	5 300	20	0.46	84	560 ± 16 (0.21 ± 0.05)
PEG$_{10k}$-*b*-PTyr$_{20}$	13 300	22 200	1.06	17 700	47	0.56	46	441 ± 56 (0.75 ± 0.06)

[a)] Number average molar-mass (M_n) and molar-mass dispersity determined by SEC in DMF + 1% LiBr using PS calibration, [b)] Number average molar-mass (M_n) and degree of polymerization (DP) determined by ^{1}H NMR in DMSO-d_6, [c)] Hydrophilic fraction or PEG fraction determined by this equation $\frac{M_n \text{ PEG}}{M_n \text{ copolymer}}$ with M_n from ^{1}H NMR. [d)] Hydrodynamic Z-average diameter (D_Z) and polydispersity (σ) determined by DLS at 90°.

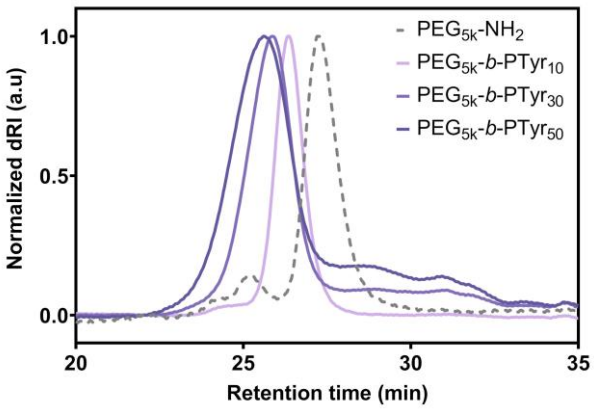

Figure III-21. SEC chromatograms of PEG$_{5k}$-*b*-PTyr$_n$ with targeted DP of 10, 30 and 50 in DMF (+ 1% LiBr, detection by differential refractive index).

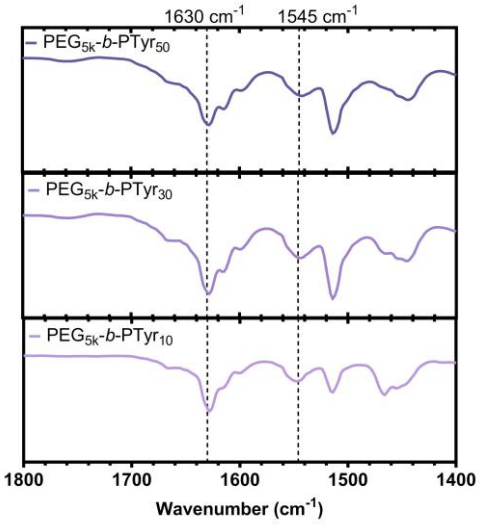

Figure III-22. ATR-FTIR spectra of lyophilized powders of PEG_{5k}-*b*-$PTyr_n$ with targeted DP of 10, 30 and 50 using a 5kDa PEG-NH_2.

Dynamic light scattering analysis of PEG_{5k}-*b*-$PTyr_{10}$ and PEG_{5k}-*b*-$PTyr_{20}$ revealed a close size distribution around 70 nm with a dispersity index of about 0.2 (Figure III-23). However, TEM revealed that PEG_{5k}-*b*-$PTyr_{10}$ formed spherical aggregates with an average diameter of 38 ± 8 nm and PEG_{5k}-*b*-$PTyr_{20}$ long and thin nanoparticles mixed with spherical micelles with an average length of 119 ± 83 nm and 12 ± 2 of diameter as shown in Figure III-24 and Figure III-25. PEG_{5k}-*b*-$PTyr_{30}$ and PEG_{5k}-*b*-$PTyr_{50}$ could not be analyzed by DLS due to gel formation. However, TEM analysis revealed the presence of non-homogeneous anisotropic nanoparticles, whose entanglement likely contributed to gel formation. These nanoparticles exhibited dimensions of 113 ± 71 nm in length for the targeted DP of 30 and 61 ± 33 nm for the targeted DP of 50, with widths of 11 ± 2 nm and 17 ± 7 nm, respectively (Figure III-24, Figure III-25).

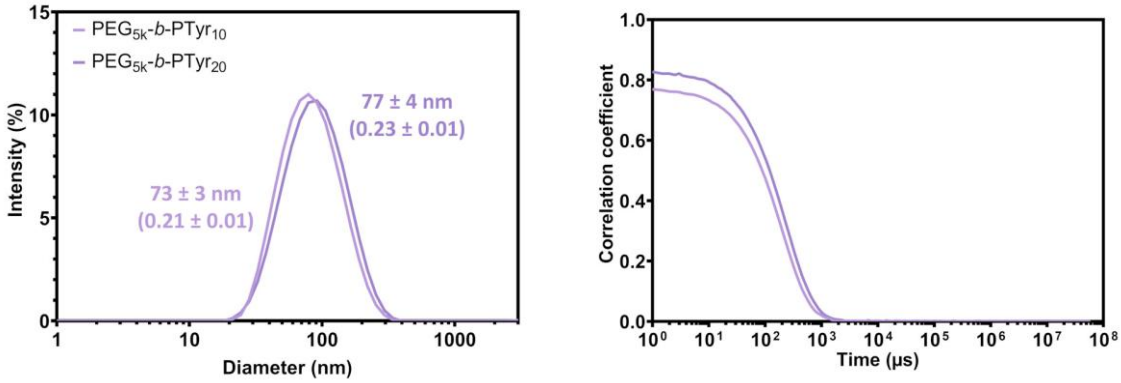

Figure III-23. DLS profiles (left) and associated correlograms (right) of the PEG_{5k}-*b*-$PTyr_n$ suspensions with targeted DP of 10 and 20.

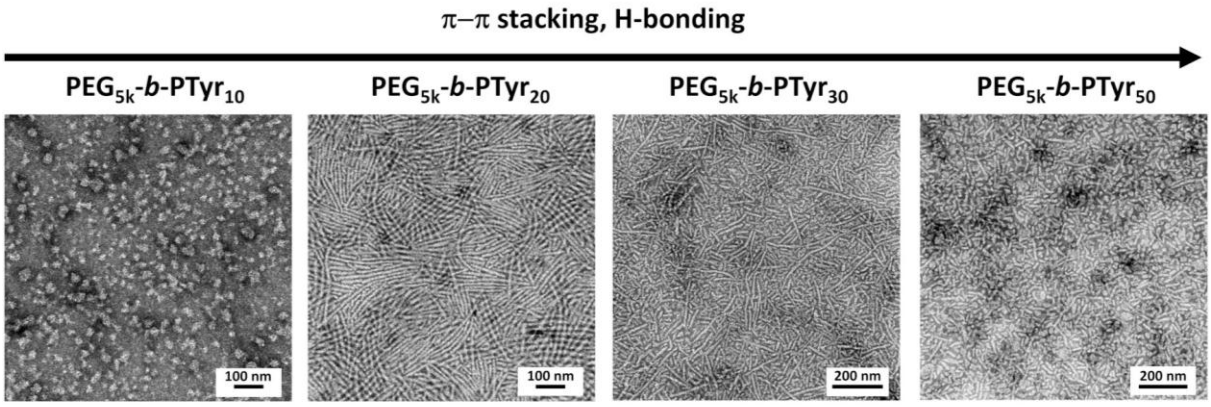

Figure III-24. Representative TEM images of the different copolymer nanoparticles obtained with Tyr, with different hydrophilic/hydrophobic block ratio and degree of π–π stacking and H-bonding.

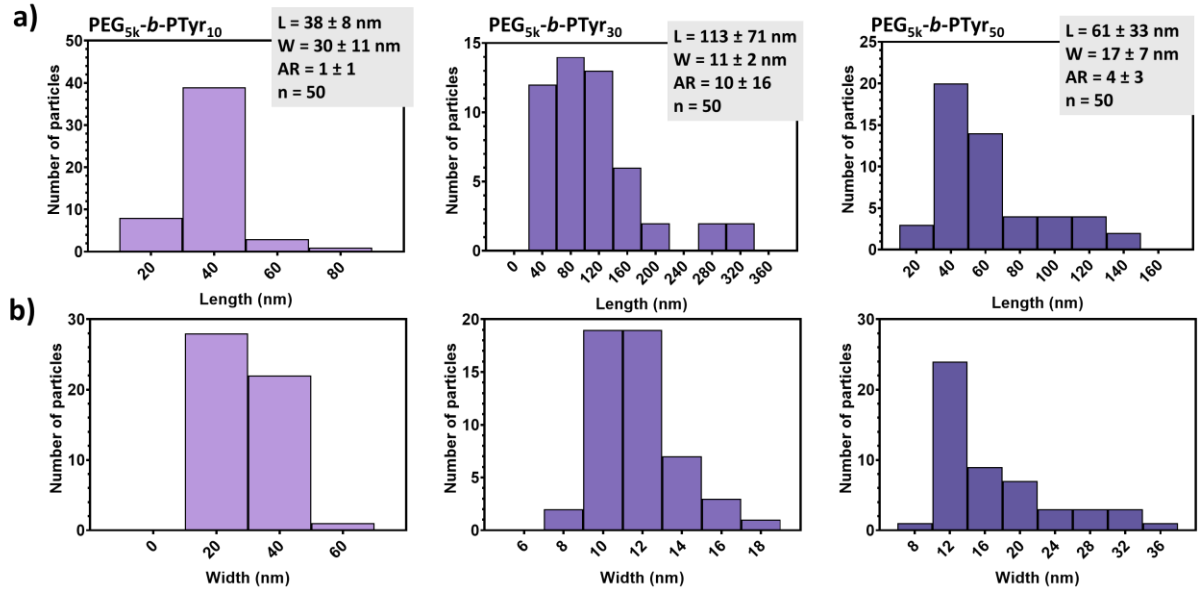

Figure III-25. (a) Length and (b) width distribution of the PEG_{5k}-*b*-$PTyr_n$ nanoparticles with targeted DP 10, 30 and 50 obtained by analysis of 50 nano-objects by ImageJ on a TEM image.

Achieving anisotropy control and modulation with tyrosine proves to be challenging. Adjusting the feeding ratio during polymerization introduces additional complexities, including gel formation, which promotes water initiation and reduces control over polymerization. These factors result in less homogeneous self-assembled structures, highlighting the need for further optimization.

To better assess the influence of the PEG fraction, aqueous ROPISA was also attempted using $PEG\text{-}NH_2$ of different sizes, specifically 750 Da, 2 kDa, and 10 kDa, to vary the hydrophilic fraction as well as the number of tyrosine units (hydrophilic/hydrophobic ratio). ROPISA experiments were performed using ice-cold aqueous bicarbonate sodium buffer, with a feeding ratio of 20. Following the purification, ^{1}H NMR analysis was conducted, revealing that the DP values were close to the targeted one, with the exception of PEG_{10k} which exhibited a higher molar mass than the theoretical one (Table III-5, Figure SIII-19). In the SEC chromatograms, a shift to lower retention times confirmed the successful chain extension from the macroinitiator (Figure III-26). PEG_{750}-*b*-$PTyr_{20}$ displayed a rather high molar mass

dispersity ($Đ$ = 1.46) as compared to the other copolymers but this result was attributed to the high dispersity of the commercial PEG_{750}-NH_2 used in this experiment ($Đ$ = 1.38). For PEG_{10k}-*b*-$PTyr_{20}$, the presence of tyrosine oligomers was observed, likely due to water-initiated polymerization of Tyr-NCA. At higher DP, NMR analyses indicated a loss in the control over the polymerization, confirming the SEC analyses.

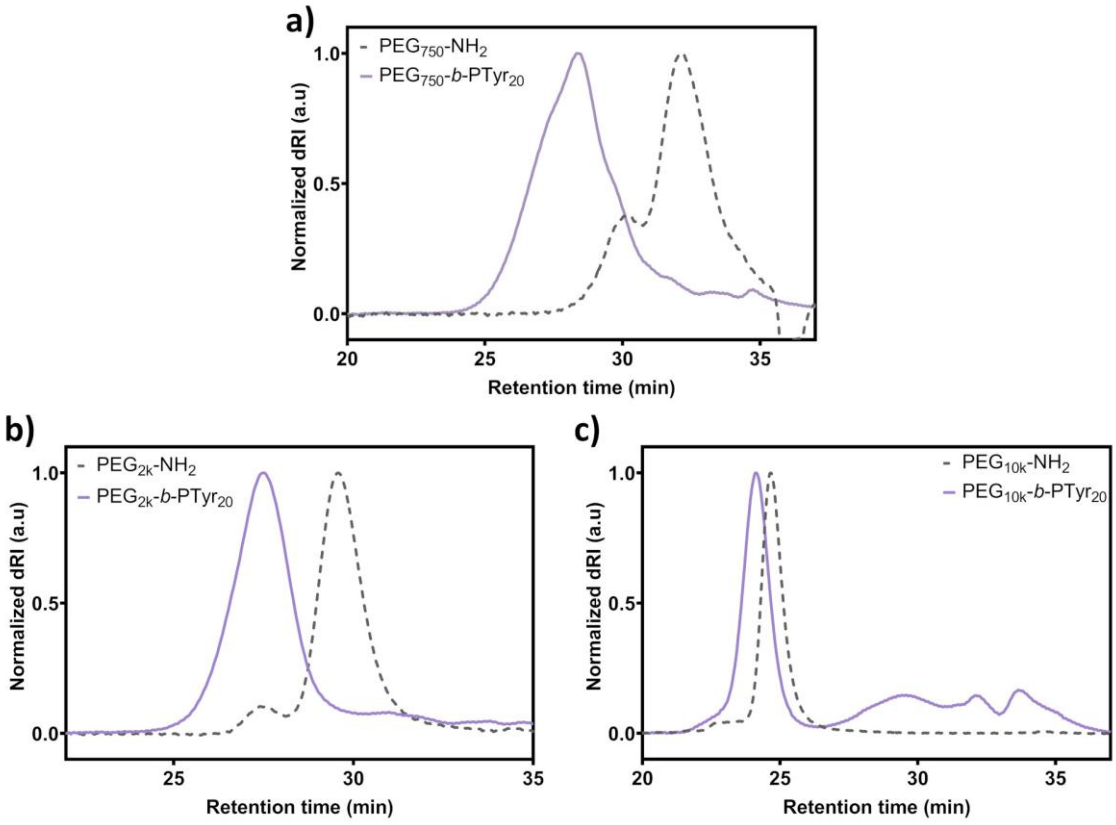

Figure III-26. SEC chromatograms of PEG_{750}-*b*-$PTyr_{20}$, PEG_{2k}-*b*-$PTyr_{20}$, and PEG_{10k}-*b*-$PTyr_{20}$ with targeted DP of 20 using a 750Da, 2kDa and 10kDa PEG-NH_2 in DMF (+ 1% LiBr, detection by differential refractive index).

FTIR spectra revealed the presence β-sheet amide I and II bands for all the copolymers (Figure III-27).

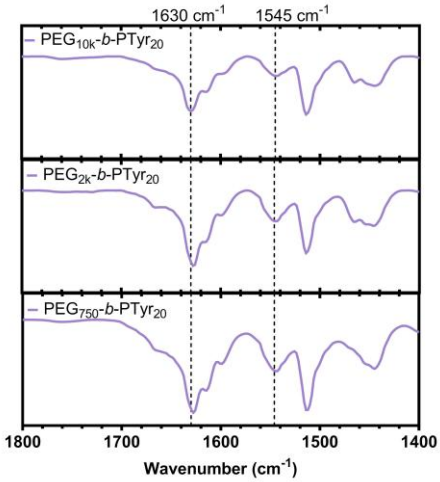

Figure III-27. ATR-FTIR spectra of lyophilized powders of PEG_{750}-*b*-$PTyr_{20}$, PEG_{2k}-*b*-$PTyr_{20}$ PEG_{10k}-*b*-$PTyr_{20}$ with targeted DP of 20 using a 750Da, 2kDa and 10kDa PEG-NH_2.

Following dialysis against water to remove salts, the nanomaterial suspensions were characterized using microscopy and light scattering techniques to assess the formation of anisotropic nanomaterials. PEG_{750}-*b*-$PTyr_{20}$, which has the lowest PEG fraction (f_{PEG} value of 0.14), displayed aggregates with a lamellar morphology in TEM (Figure III-28).

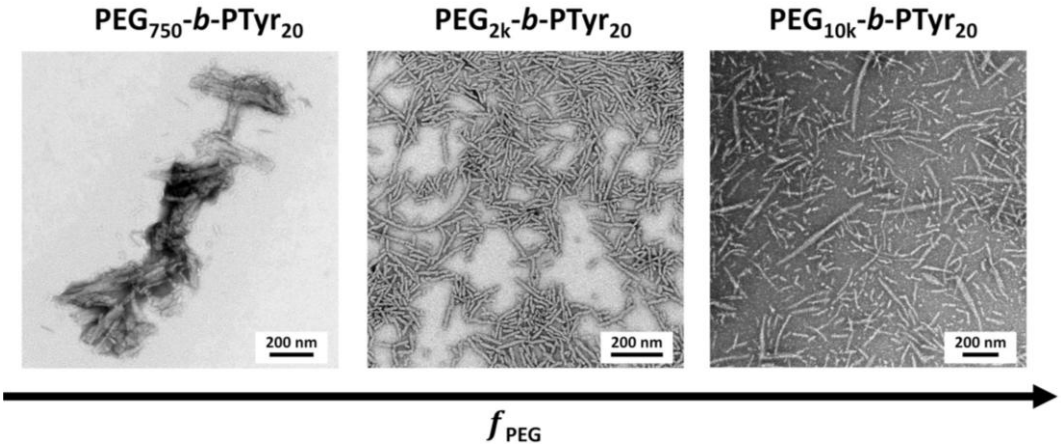

Figure III-28. Representative TEM images of the copolymer nanoparticles obtained with Tyr with different hydrophilic/hydrophobic block ratio.

This morphology has already been reported by Jiang *et al.* with PEG_{2k}-*b*-$PTyr_{10}$ and upon nanoprecipitation.[81] Increasing the hydrophilic fraction while keeping the same targeted number of Tyr units appeared to stabilize the formation of elongated, heterogeneous nanoparticles, as observed by TEM and DLS. PEG_{2k}-*b*-$PTyr_{20}$ nanoparticles (101 ± 51 nm, 15 ± 2 nm) were a bit thicker than PEG_{5k}-*b*-$PTyr_{20}$ (12 ± 2 nm) (Figure III-28**,** Figure III-29). For PEG_{10k}-*b*-$PTyr_{20}$, the nanoparticles were long and rigid but exhibited significant heterogeneity in length with a nanosheet morphology (Figure III-28**,** Figure III-29). The rigidity observed in the PEG_{10k}-*b*-$PTyr_{20}$ nanoparticles could be due to strong π-π interactions among the tyrosine residues, but the variation in their lengths suggests that the assembly process was not entirely uniform, possibly due to the lack of control during the ROPISA process.

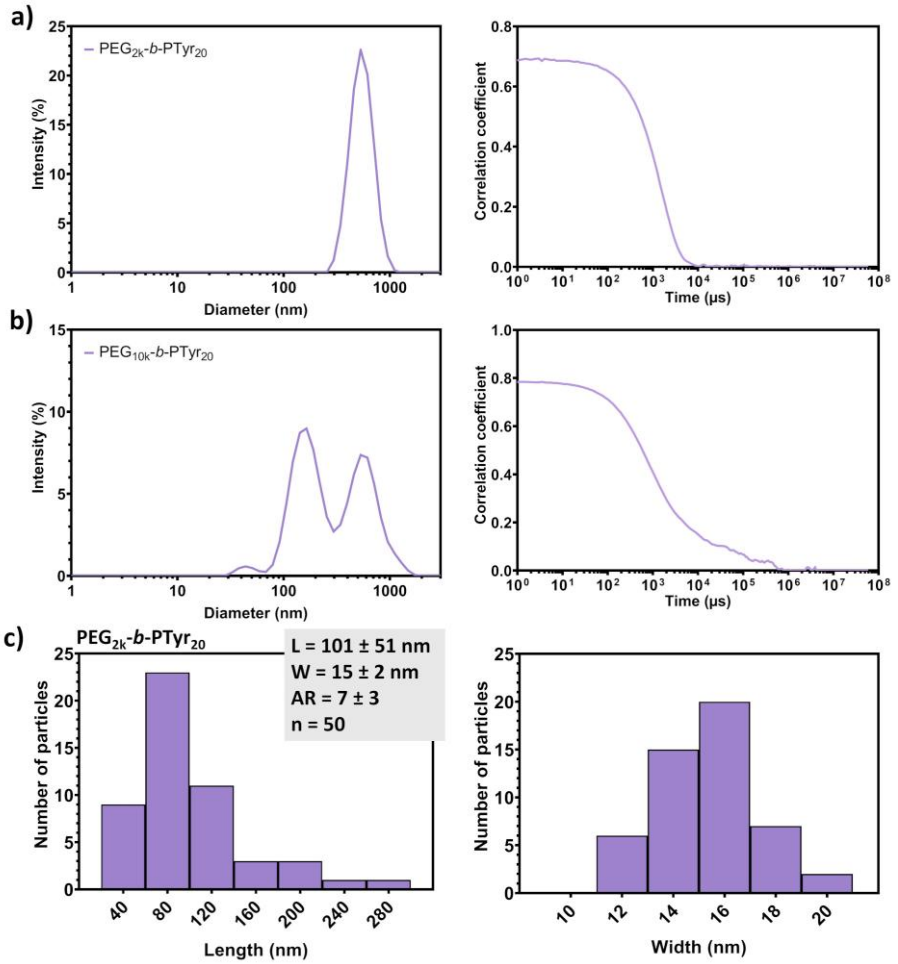

Figure III-29. DLS profiles (left) and associated correlograms (right) of (a) PEG_{2k}-*b*-$PTyr_{20}$ and (b) PEG_{10k}-*b*-$PTyr_{20}$ nanoparticle suspensions. (c) Length (left) and width (right) particles distribution of the PEG_{2k}-*b*-$PTyr_{20}$ nanoparticles by analysis of 50 nano-objects by ImageJ on a TEM image.

Overall, the aqueous ROPISA of tyrosine-NCA demonstrated that both the PEG fraction and the π–π stacking influenced the polymerization process and the anisotropy. Indeed, aqueous ROPISA performed with tyrosine-NCA afforded anisotropic nanomaterials with a complex influence of various factors, beyond the secondary structure, hydrophobicity, π-π stacking, and the hydrophilic/hydrophobic ratio. At higher M/I, water initiation and gel formation were observed but we found conditions in which a more pronounced anisotropic shape could be induced. Eventually, additional factors, such as hydrogen bonding ability and the amount of water-initiated polymerization could have also played a pivotal role in determining the final morphology, but these parameters were not studied in this work.

III.6. Conclusion

The synthesis of anisotropic nanoparticles by polymerization-induced self-assembly (PISA) remains a challenging process, yet it holds great promise to design drug-delivery systems. In this regard, the emerging use of aqueous ring-opening polymerization induced self-assembly (ROPISA) of *N*-carboxyanhydrides (NCAs) offers a promising strategy, enabling straightforward access to peptide-based nanomaterials. After elucidating the self-assembly and polymerization mechanism using the BLG-NCA

monomer, demonstrating that both processes occur ultra-fast due to confinement effects and that anisotropy arises from the early formation of β-sheet structures, this chapter explores the versatility of aqueous ROPISA with a variety of NCAs, highlighting how their hydrophobicity and the chemical nature of their side chains influence the formation of anisotropic nanoparticles.

In the initial phase of the study, lysine NCAs with Z, Boc, and TFA protecting groups were subjected to ROPISA. A more regulated aqueous polymerization and self-assembly was found for Lys(Z)-NCA, which results in a more uniform distribution of nanoparticles than that observed with Boc- and TFA-protected groups. Subsequently, to gain insight into the influence of side chain hydrophobicity, glycine, alanine, leucine and phenylalanine NCAs were subjected to further investigation. Interestingly, all these monomers produced anisotropic nanomaterials and we clearly observed that varying hydrophobicity but also π-π stacking or H-bonding ability impacted the kinetic of the ROP and the aspect ratio of the resulting nanomaterials. The incorporation of glycine, a hydrophilic monomer that polymerizes into a via hydrogen bonding, results in flexible fibrils due to its specific conformation. Nanoparticles derived from alanine exhibited greater anisotropy, which was attributed to a reduction in steric hindrance and a lower degree of hydrophobicity. The complexity of the system was increased by introducing phenylalanine, a more hydrophobic amino acid that promotes π-π stacking, which is of great interest in drug delivery. A comprehensive analysis was conducted by varying the size of both the hydrophilic poly(ethylene glycol) block and the hydrophobic polypeptide block, demonstrated that the hydrophilic/hydrophobic ratio and the number of phenylalanine units, which affect the extent of π-π stacking, had a significant impact on nanoparticle anisotropy. Similarly, the ability of tyrosine to influence nanoparticle morphology was examined, following the same approach used for phenylalanine. Tyrosine, with its phenol side chain, participates in π-π stacking and introduces hydrogen bonding, which is influenced by the pH of the medium. This property is advantageous in drug delivery applications as it potentially improves the drug loading contents due to these dual interactions. These interactions, in conjunction with the hydrophilic/hydrophobic equilibrium, were demonstrated to influence both the polymerization and self-assembly processes.

In summary, in this chapter, we demonstrate the versatility and the robustness of aqueous ROPISA, a process that can be applied with almost all NCA monomers and its capacity to afford a wide range of tailored anisotropic nanoparticles. Most notably, it elucidates that factor such as hydrophobicity and steric hindrance, by influencing the polymerization kinetics, as well as π-π stacking, hydrophilic/hydrophobic ratio, and hydrogen bonding serve as pivotal driving forces in regulating anisotropic self-assembly, in conjunction with secondary structure and monomer chirality.

III.7. Experimental Section

III.7.1. Materials

Solvents for size-exclusion chromatography *N*,*N*-dimethylformamide (DMF) and hexafluoropropan-2-ol (HFIP) were bought from Sigma. Tetrahydrofuran was obtained from a solvent system purifier (PureSolv, Innovative Technology), kept under an argon atmosphere, and freshly used. All *N*-carboxyanhydrides (NCAs), except for alanine *N*-carboxyanhydride (Ala-NCA), were supplied by PMC Isochem (Vert-le-Petit, France) and stored at -20 °C under argon atmosphere and weighed in the glove box Jacomex GP13 no. 2675. PEG_{750}-NH_2 (M_n = 750 g.mol^{-1}, $Đ$ = 1.39), PEG_{2k}-NH_2 (M_n = 2000 g.mol^{-1}, $Đ$ = 1.08), PEG_{5k}-NH_2 (M_p = 5000 g.mol^{-1}, $Đ$ = 1.02) and PEG_{10k}-NH_2 (M_p = 10 000 g.mol^{-1}, $Đ$ = 1.06) were bought from RAPP Polymer Gmbh (Tübingen, Germany). Milli-Q water was obtained from a Purelab Prima purification system (ELGA) with a resistivity of 18.2 MΩ.cm^{-1}. Deuterated solvent (DMSO-d_6, TFA-*d*) were purchased from Eurisotop. Dialysis membranes were purchased from SpectrumLabs.

III.7.2. Instrumentation and methods

III.7.2.1. Nuclear Magnetic Resonance (NMR)

^{1}H Nuclear Magnetic Resonance (NMR) spectra were recorded on a Bruker Avance III spectrometer equipped with a 5 mm BBFO (broad band fluorine observation) liquid probe, at 298 K. ^{1}H data were acquired at 400.2 MHz observation frequency, with 16 scans and a recycle delay of 1 second. Signals were referred to the signal of residual protonated solvent signals.

III.7.2.2. Kinetics study

^{1}H NMR was chosen to follow the NCA polymerization initiated by PEG_{5k}-NH_2 in ice-cold aqueous $NaHCO_3$ solution. A typical kinetic procedure was conducted as follows: Gly-NCA (100 mg, 1 mmol) was placed in a Schlenk flask cooled in an ice bath, and 4.7 mL of ice-cold NaHCO3 solution containing the PEG_{5k}-NH_2 initiator (250 mg, 0.05 mmol) was added. The reaction was performed under vigorous stirring in an ice-cold bath. Previous studies indicated that HCl could hydrolyze NCA without impacting ongoing polymerization.[82] Therefore, an HCl-quenching protocol was implemented to monitor the reaction progress. In contrast to the ROPISA of BLG-NCA, this quenching approach proved effective in this context. Moreover, dialysis was not required, as the NMR signals of the hydrolyzed monomers were clearly distinguishable from those of the polymer backbone. At designated time intervals, 0.4 mL aliquots of the reaction mixture were withdrawn and quenched with 51 µL of 15 wt% HCl. This rapid addition hydrolyzed any unreacted NCA into the corresponding amino acid. The samples were then lyophilized and analyzed using ^{1}H NMR to determine the conversion rates of Gly-NCA. The conversions of Gly-NCA were calculated based on the following formula:

Conv. = $I_{4.36ppm}$ / ($I_{4.3ppm}$ + $I_{4.36ppm}$), where $I_{4.36ppm}$ and $I_{4.3ppm}$ were the integrations of the peak at 4.36 ppm (PGly) and 4.3 ppm (Gly), respectively.

For the other monomers, this procedure was adapted considering the corresponding polymer and amino acid NMR peaks.

III.7.2.3. Size Exclusion Chromatography (SEC)

Polymer molar masses were determined by SEC using dimethylformamide (DMF + LiBr 1 g.L^{-1}) or hexafluoro-2-propanol (HFIP + 0.05% KTFA) as eluent. Measurements in DMF were performed on an Ultimate 3000 system from ThermoFischer Scientific (Ilkirch, France) equipped with a diode array detector (DAD). The system also includes a multiangle light scattering detector (MALS) and differential refractive index detector dRI from Wyatt technology (Santa Barbara CA, USA). Polymers were separated on three Shodex Asahipack gel columns [GF 310 (7.5 × 300 mm²), GF510 (7.5 × 300 mm²), exclusion limits from 500–300 000 Da] at a flowrate of 0.5 mL.min^{-1}. Columns temperature was held at 50 °C. Easivial™ kit of Polystyrene from Agilent (Santa Clara CA, USA) was used as calibration standard (M_n from 162 to 364 000 Da). Measurements in HFIP were performed on similar equipment as DMF analyses with the same components: DAD, MALS dRI. Polymers were separated on a PL HFIP gel column (300 × 7.5 mm²), exclusion limits from 100 Da to 150 000 Da at a flowrate of 0.8 mL.min^{-1}. Columns temperature was held at 40 °C. Easivial™ kit of PMMA from Agilent (Santa Clara CA, USA) was used as calibration standard (M_n from 1 800 to 256 000 Da). Molar masses and dispersities were calculated based on the main polymer peak (excluding oligomers) for clarity and comparison purposes.

III.7.2.4. Fourier Transform Infrared spectroscopy (FTIR)

FTIR spectra were collected on a Bruker Vertex 70 spectrometer equipped with a diamond ATR tool in the spectral region of 900-2000 cm^{-1} from 32 scans with a resolution of 4 cm^{-1}. A background was recorded before loading the samples onto the ATR crystal for measurements. FTIR of copolymers dialyzed and lyophilized powders were measured using air as background.

III.7.2.5. Transmission Electron Microscopy (TEM)

The images were recorded on a Hitachi H7650 microscope working at 80 kV. Samples were prepared by deposing a drop of 0.1 mg.mL^{-1} NP dispersion onto a copper grid (200 mesh coated with carbon) that have been subjected to a glow discharge for 45 second and removing excess after 1 minute. Grids were negatively stained with 1.2% uranyl acetate.

The number-average lengths of nanoparticles were calculated with Eq 1; whereas the number-average widths were calculated with Eq 2:

(1) $$L_n = \frac{\sum_{i=1}^{n} n_i L_i}{\sum_{i=1}^{n} n_i}$$

(2) $$w_n = \frac{\sum_{i=1}^{n} n_i w_i}{\sum_{i=1}^{n} n_i}$$

where n_i is the number of particles with length L_i and width w_i.

III.7.2.6. Dynamic Light Scattering (DLS)

Z-average hydrodynamic diameters (D_Z) and the polydispersity index (σ) of the nanoparticles were determined by DLS with a Zetasizer Nano ZS from Malvern Instruments (Malvern, UK) operating with a He–Ne laser source (wavelength 633 nm, scattering angle 90°). The correlation functions were analysed using the cumulant method. The dispersions were analysed at 1 mg.mL^{-1} in water after filtration on a 0.45 µm CA filter.

III.7.3. Synthesis

III.7.3.1. Synthesis procedure of poly(ethylene glycol)-*block*-poly(ε-benzyloxycarbonyl-*L*-lysine) PEG_{5k}-*b*-$PLys(Z)_n$

A typical procedure for the synthesis of PEG_{5k}-*b*-$PLys(Z)_{20}$ is as follows: Lys(Z)-NCA (100 mg, 0.37 mmol) was weighted in a Schlenk tube with a magnetic stirrer and a 2.9 mL of an ice-cooled solution of PEG_{5k}-NH_2 (100 mg, 0.02 mmol, [M]/[I] = 20) in $NaHCO_3$ 0.05 M was added under a strong agitation on the powder (τ_s = 7 wt%).The reaction was left to stir 1) first in an ice-cold water bath; 2) then at room temperature overnight. The opalescent dispersion obtained was then transferred to a 3.5 kDa dialysis membrane and dialyzed against deionized water for 2 days. An aliquot was kept for further microscopy imaging and dynamic light scattering and the remaining dispersion was lyophilized. ^{1}H NMR (400 MHz, DMSO-d_6, d): 1.24-2.15 (br, 6H; ─CH2-CH2-CH2-), 2.94 (br, 2H; ─CH2─NH-), 3.25 (s, 3H; ─CH3), 3.51 (br, 4H, -O–CH2-CH2-), 3.82-3.20 (br, 1H, -CH-), 4.95(br, 2H, -CH2-Ar), 7.25(br, 1H, -NH), 7.32 (br, 5H, ArH), 7.87 (br, 1H, -NH). PLys(Z) degree of polymerization was calculated from the integration of the polymer backbone protons iH by ^{1}H NMR and gave a $DP_{Lys(Z)}$ = 22. SEC analysis using dRI detection and PS calibration gave M_n = 13.9 kg.mol^{-1} and $Đ$ = 1.12. The same procedure was adapted for the other targeted DP.

III.7.3.2. Synthesis procedure of poly(ethylene glycol)-*block*-poly(ε-trifluoroacetyl-*L*-lysine) PEG_{5k}-*b*-$PLys(TFA)_n$

The same method was used as described before by using Lys(TFA)-NCA as a monomer. For the synthesis of PEG_{5k}-*b*-$PLys(TFA)_{20}$, Lys(TFA)-NCA (100 mg, 0.37 mmol) was weighted in a Schlenk tube containing a magnetic stirring bar. 2.7 mL of an ice-cooled solution of $NaHCO_3$ 0.05 M containing the initiator PEG_{5k}-NH_2 (100 mg, 0.02 mmol, [M]/[I] = 20) was added to the Lys(TFA)–NCA powder under a strong agitation (τ_s = 7 wt%). ^{1}H NMR (400 MHz, DMSO-d_6, d): 1.24-1.64 (br, 6H; ─CH2-CH2-CH2-), 3.13 (br, 2H; ─CH2─NH-), 3.13 (s, 3H; ─CH3), 3.51 (br, 4H, -O–CH2-CH2-), 4.21 (br, 1H, -CH-), 7.89 (br, 1H, -NH), 9.35-9.37 (br, 1H, -NH). PLys(TFA) degree of polymerization was calculated from the integration of the C_α proton (*d*) by ^{1}H NMR and gave a $DP_{Lys(TFA)}$ = 24. SEC analysis using dRI detection and PS calibration gave M_n = 13.1 kg.mol^{-1} and $Đ$ = 1.06. The same procedure was adapted for the other targeted DP.

III.7.3.3. Synthesis procedure of poly(ethylene glycol)-*block*-poly(ε-tert-butyloxycarbonyl-*L*-lysine) PEG_{5k}-*b*-$PLys(Boc)_n$

The same method was employed as described before using Lys(Boc)-NCA as a monomer. For the synthesis of PEG_{5k}-*b*-$PLys(Boc)_{20}$, Lys(Boc)-NCA (100 mg, 0.37 mmol) was weighted in a Schlenk tube with a magnetic stirrer and a 2.7 mL of an ice-cooled solution of PEG_{5k}-NH_2 (100 mg, 0.02 mmol, [M]/[I] = 20) in $NaHCO_3$ 0.05 M was added under a strong agitation on the powder (τ_s = 7 wt%). ^{1}H NMR (400 MHz, DMSO-d_6, d): 1.24-1.64 (br, 15H; ─CH2-CH2-CH2-, -C-(CH3)3), 2.86-2.88 (br, 2H; ─CH2─NH-), 3.25 (s, 3H; ─CH3), 3.51 (br, 4H, -O–CH2-CH2-), 3.77-4.21 (br, 1H, -CH-), 6.38-6.70 (br, 1H, -NH), 6.66 (br, 1H, -NH), 7.85 (br, 1H, -NH). PLys(Boc) degree of polymerization was calculated from the integration of *h* protons by ^{1}H NMR and gave a $DP_{Lys(Boc)}$ = 22. SEC analysis using dRI detection and PS calibration gave M_n = 12.1 kg.mol^{-1} and $Đ$ = 1.05. The same procedure was adapted for the other targeted DP.

III.7.3.4. Synthesis procedure of poly(ethylene glycol)-*block*-poly(glycine) PEG_{5k}-*b*-$PGly_{20}$

The same method was used as described before by using Gly-NCA as a monomer. For the synthesis of PEG_{5k}-*b*-$PGly_{20}$, Gly-NCA (20 mg, 0.2 mmol) was weighted in a Schlenk tube with a magnetic stirrer and a 0.9 mL of an ice-cooled solution of PEG_{5k}-NH_2 (50 mg, 0.01 mmol, [M]/[I] = 20) in $NaHCO_3$ 0.05 M was added under a strong agitation on the powder (τ_s = 7 wt%). ^{1}H NMR (400 MHz, TFA-*d*, d): 3.66 (s, 3H; ─CH3), 4.00 (br, 4H, -O–CH2-CH2-), 4.37 (br, 2H, -CH2-). PGly) degree of polymerization was calculated from the integration of the C_α proton (*d*) by ^{1}H NMR and gave a DP_{Gly} = 25. SEC analysis using dRI detection and PMMA calibration gave M_n = 49.1 kg.mol^{-1} and $Đ$ = 1.07.

III.7.3.5. Synthesis procedure of poly(ethylene glycol)-*block*-poly(*L*-alanine) PEG_{5k}-*b*-$PAla_{20}$

III.7.3.5.1. Synthesis of Alanine N-Carboxyanhydride (Ala NCA)

L-Ala NCA was synthesized using Leuch's method. In a clean and dried Schlenk flask, *N*-Boc-*L*-Alanine (2 g, 10.5 mmol, 1 equiv) was dried for 15 minutes on the Schlenk line. Subsequently, 50 mL of anhydrous THF was added, followed by thionyl chloride (0.806 mL, 11.1 mmol, 1.05 equiv). After 4 hours of stirring at RT, the solvent was evaporated under vacuum. The dry residue was dissolved in 100 mL of THF and the solution filtered through dry Celite. The NCAs were recrystallized in a mixture of THF/Pentane and the resulting crystals washed with pentane. This recrystallization step may be repeated if necessary. Finally, the crystals were collected by vacuum filtration and placed in a vacuum oven at RT for two days. Yield: 882 mg, 73%. ^{1}H NMR (400 MHz, DMSO-d_6, d): 1.33-1.35 (d, 3H; ─CH3), 4.46-4.51 (q, 1H; ─CH─), 9 (s, 1H; ─NH─).

III.7.3.5.2. Poly(ethylene glycol)-block-poly(L-alanine) PEG_{5k}-b-$PAla_{20}$

The same method was used as described before using Ala-NCA as a monomer: 90 mg (0.78 mmol) of Ala-NCA was weighted in a Schlenk tube containing a magnetic bar. 3.8 mL of an ice-cooled solution of PEG_{5k}-

NH_2 (200 mg, 0.04 mmol, [M]/[I] = 20) was added to the Ala-NCA powder under a strong agitation (τ_s = 7 wt%). ^{1}H NMR (400 MHz, TFA-*d*, d): 1.45 (br, 3H; ─CH3) 3.51 (s, 3H; ─CH3), 3.85 (br, 4H, -O–CH2-CH2-), 4.60 (br, 1H, -CH-). PAla degree of polymerization was calculated from the integration of the C_α proton (*d*) by ^{1}H NMR ^{1}H NMR and gave a DP_{Ala} = 21. SEC analysis using dRI detection and PMMA calibration gave M_n = 33.6 kg.mol^{-1} and $Đ$ = 1.07.

III.7.3.6. Synthesis procedure of poly(ethylene glycol)-*block*-poly(-*L*-leucine) PEG_{5k}-*b*-$PLeu_{20}$

The same method was used as described before, using Leu-NCA as a monomer: 62 mg (0.39 mmol) of Leu-NCA was weighted in a Schlenk tube containing a magnetic bar. 2.2 mL of an ice-cooled solution of PEG_{5k}-NH_2 (100 mg, 0.02 mmol, [M]/[I] = 20) was added to the Leu-NCA powder under a strong agitation (τ_s = 7 wt%).^{1}H NMR (400 MHz, TFA-*d*, *δ*): 1-1.04 (br, 6H; ─(CH3)2), 1.58-2 (br, 2H, -CH2-), 3.64 (s, 3H; ─CH3), 3.98 (br, 4H, -O–CH2-CH2-), 4.47-4.78 (br, 1H, -CH-). PLeu degree of polymerization was calculated from the integration of the C_α proton (*d*) by ^{1}H NMR and gave a DP_{Leu} = 21. SEC analysis using dRI detection and PS calibration gave M_n = 9.1 kg.mol^{-1} and $Đ$ = 1.03.

III.7.3.7. Synthesis procedure of poly(ethylene glycol)-*block*-poly(*L*-phenylalanine) PEG_x-*b*-$PPhe_n$

The same method was used as described before by using Phe-NCA as a monomer. Different molar masses of polyethylene glycol were also used. Briefly, the typical procedure for the synthesis of PEG_{5k}-*b*-$PPhe_{20}$ is as follows: 60 mg (0.31 mmol) of Phe-NCA was weighted in a Schlenk tube containing a magnetic bar. 1.9 mL of an ice-cooled solution of PEG_{5k}-NH_2 (100 mg, 0.02 mmol, [M]/[I] = 20) was added to the Leu-NCA powder under a strong agitation (τ_s = 7 wt%). ^{1}H NMR (400 MHz, TFA-*d*, *δ*): 2.95 (br, 2H; ─CH2-), 3.52 (s, 3H; ─CH3), 3.91 (br, 4H, -O–CH2-CH2-), 4.77-4.78 (br, 1H, -CH-), 7.06-7.26 (m br, 5H, Ar). PPhe degree of polymerization was calculated from the integrations of the aromatic protons (*Ar*) by ^{1}H NMR and gave a DP_{Phe} = 22. SEC analysis using dRI detection and PS calibration gave M_n = 9.0 kg.mol^{-1} and $Đ$ = 1.03. The same procedure was adapted for the other targeted DP and PEG chain length.

III.7.3.8. Synthesis procedure of poly(ethylene glycol)-*block*-poly(*L*-tyrosine) PEG_x-*b*-$PTyr_n$

The same method was used as described before by using Tyr-NCA as a monomer. Different molar masses of polyethylene glycol were also used. Briefly, the typical procedure for the synthesis of PEG_{5k}-*b*-$PTyr_{20}$ is as follows: 80 mg (0.39 mmol) of Tyr-NCA was weighted in a Schlenk tube containing a magnetic bar. 2.4 mL of an ice-cooled solution of PEG_{5k}-NH_2 (100 mg, 0.02 mmol, [M]/[I] = 20) was added to the Tyr-NCA powder under a strong agitation (τ_s = 7 wt%). ^{1}H NMR (400 MHz, DMSO-d_6, *δ*): 2.68-2.83 (br, 2H; -CH2-), 3.24 (s, 3H; -CH3), 3.61-3.69 (br, 4H, -O–CH2-CH2-), 4.42 (br, 1H, -CH-), 6.60-6.97 (m br, 5H, Ar), 7.96 (br, 1H, -OH), 9.11 (br, 1H, -NH-). PTyr degree of polymerization was calculated from the integration of the polymer backbone protons iH by ^{1}H NMR ^{1}H NMR and gave a DP_{Tyr} = 16. SEC analysis using dRI

detection and PS calibration gave M_n = 9.4 kg.mol^{-1} and $Đ$ = 1.07. The same procedure was adapted for the other targeted DP and PEG chain length.

III.8. Supplementary Figures

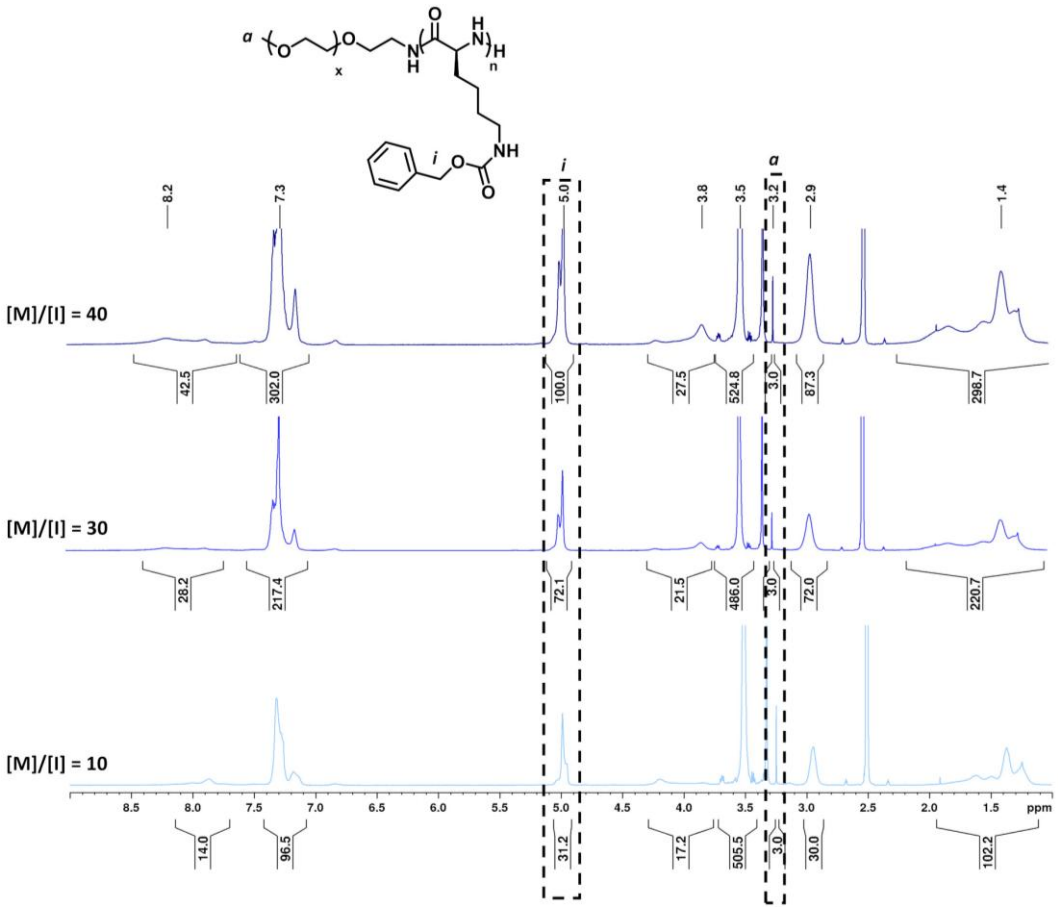

Figure SIII-1. ^{1}H NMR spectra of PEG_{5k}-*b*-$PLys(Z)_n$ in DMSO-d_6 with targeted DP of 10, 30 and 40. The CH3 signals (a) from the PEG end-chain were used as a reference to determine the DP of the PLys(Z) block, with the integration of the -CH2-Ar protons (i).

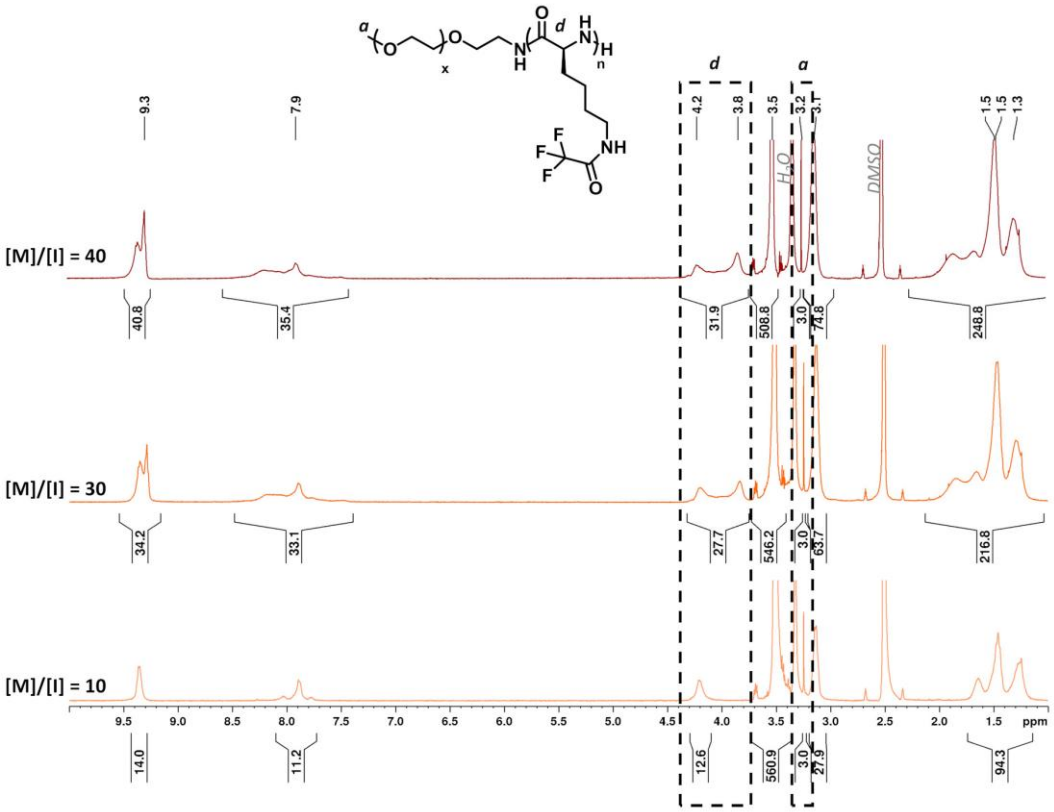

Figure SIII-2. ^{1}H NMR spectra of PEG_{5k}-*b*-$PLys(TFA)_n$ in DMSO-d_6 with targeted DP of 10, 30 and 40. The CH3 signals (a) from the PEG end-chain were used as a reference to determine the DP of the PLys(TFA) block, with the integration of the C_α proton (d).

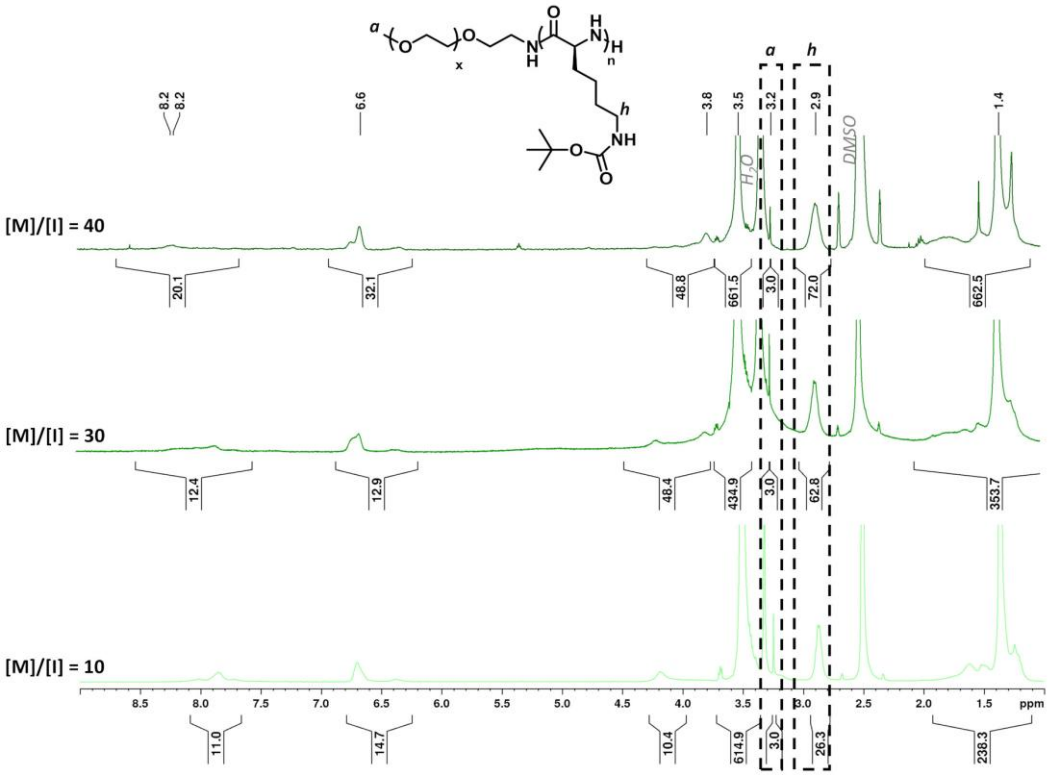

Figure SIII-3. ^{1}H NMR spectra of PEG_{5k}-*b*-$PLys(Boc)_n$ in DMSO-d_6 with targeted DP of 10, 30 and 40. The CH3 signals (a) from the PEG end-chain were used as a reference to determine the DP of the PLys(Boc) block, with the integration of the -CH2-NH- protons (h).

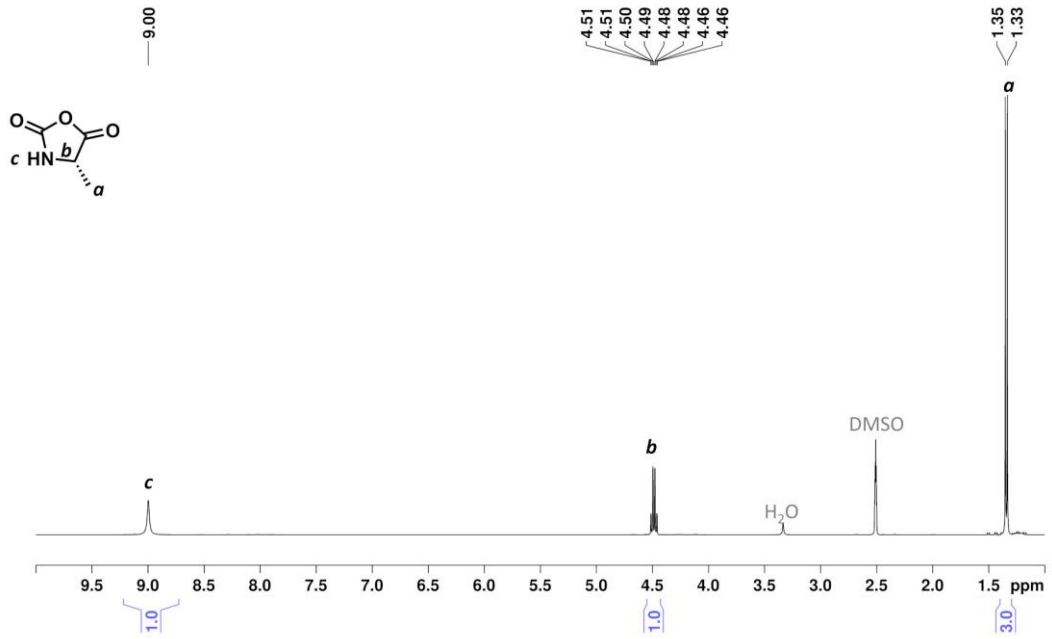

Figure SIII-4.^{1}H NMR spectrum of Alanine *N*-Carboxyanhydride (Ala-NCA) in DMSO-d_6.

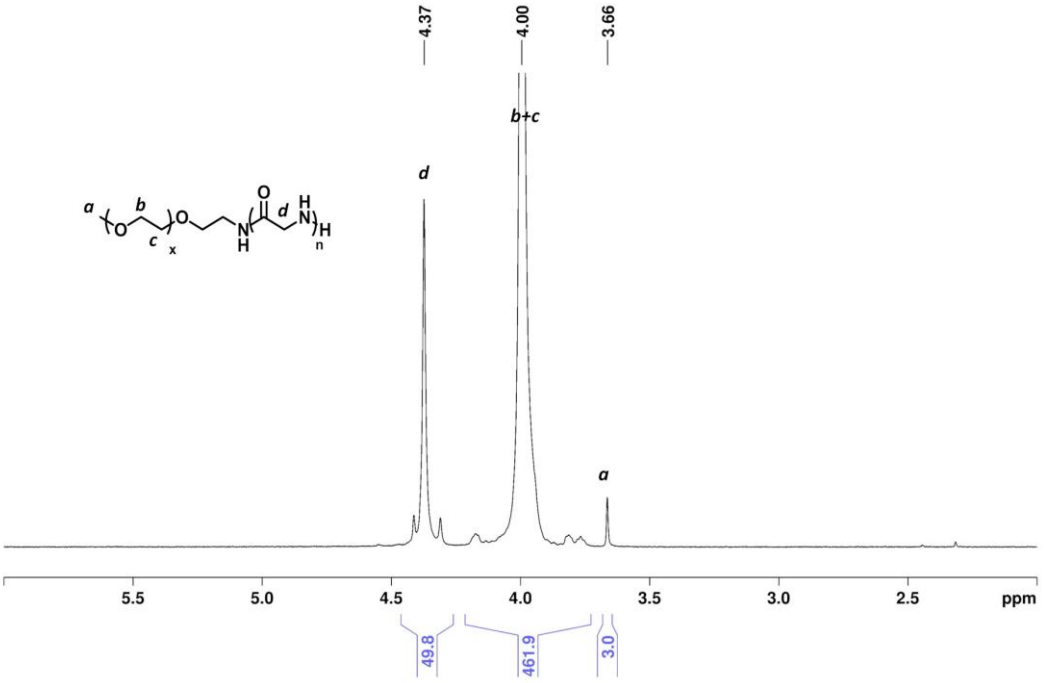

Figure SIII-5. ^{1}H NMR spectrum of PEG_{5k}-*b*-$PGly_{20}$ in TFA-d with targeted DP of 20.

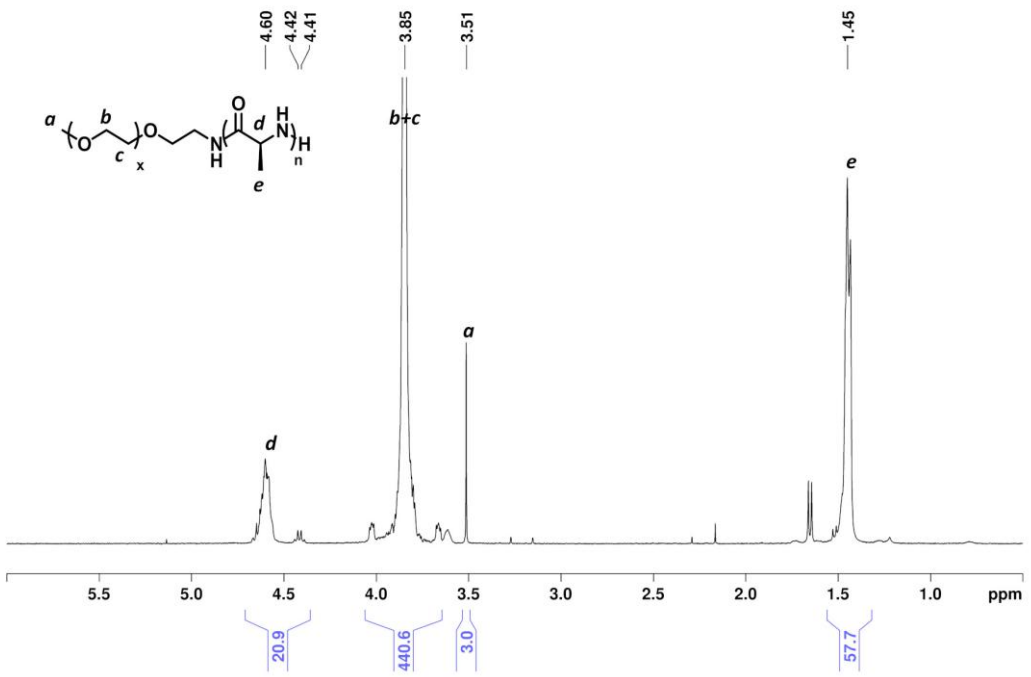

Figure SIII-6. ^{1}H NMR spectrum of PEG_{5k}-*b*-$PAla_{20}$ in TFA-d with targeted DP of 20.

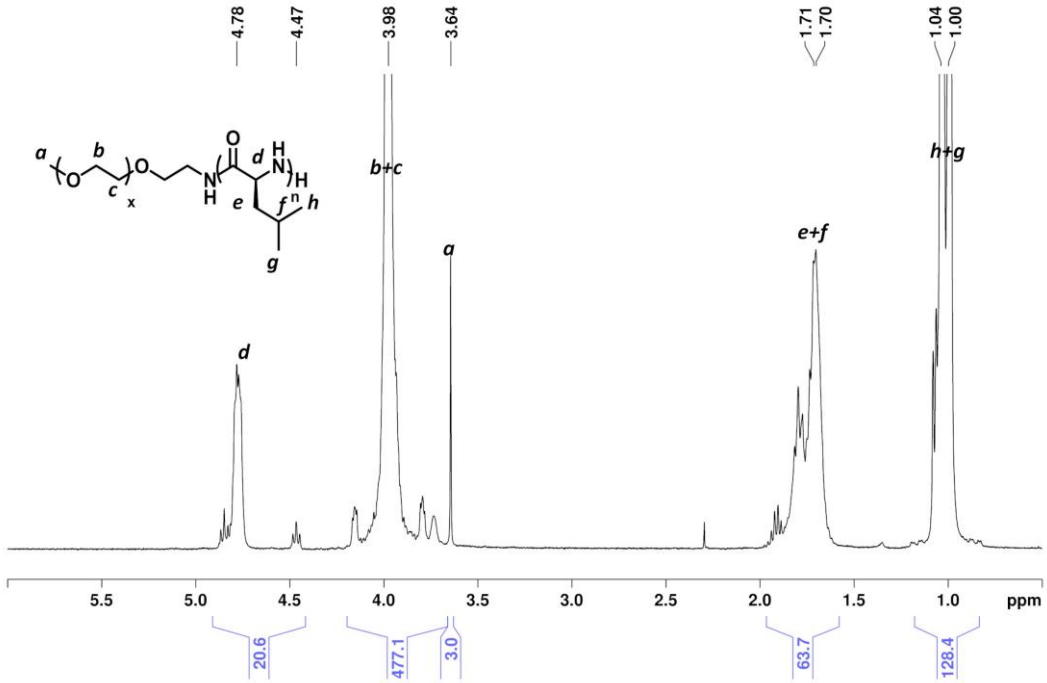

Figure SIII-7. ^{1}H NMR spectrum of PEG_{5k}-*b*-$PLeu_{20}$ in TFA-d with targeted DP of 20.

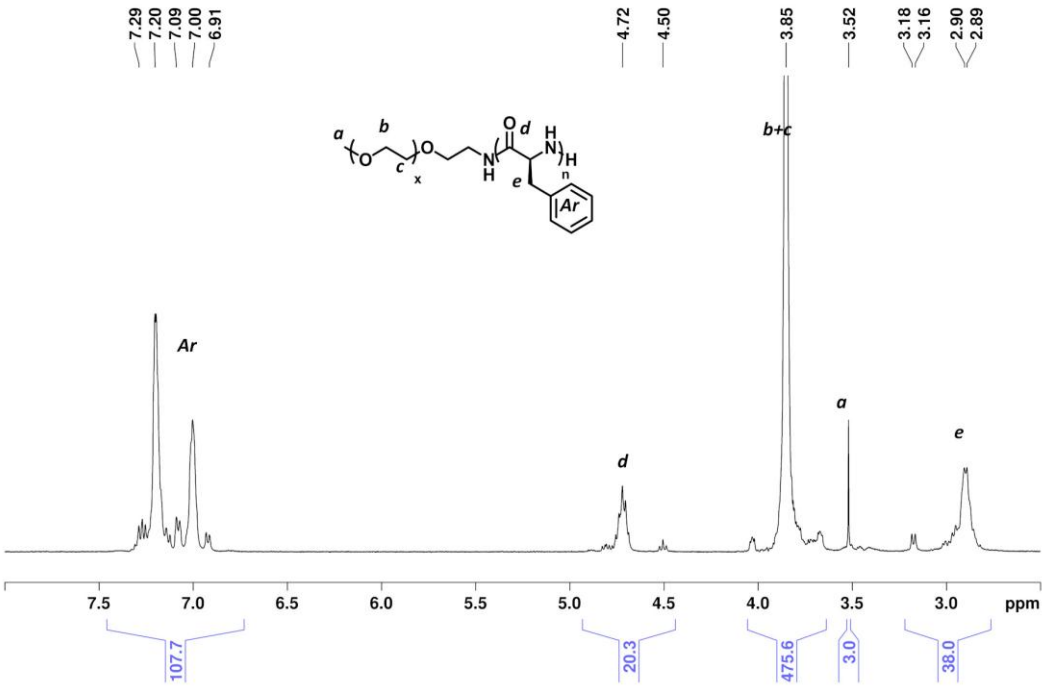

Figure SIII-8. ^{1}H NMR spectrum of PEG_{5k}-*b*-$PPhe_{20}$ in TFA-d with targeted DP of 20.

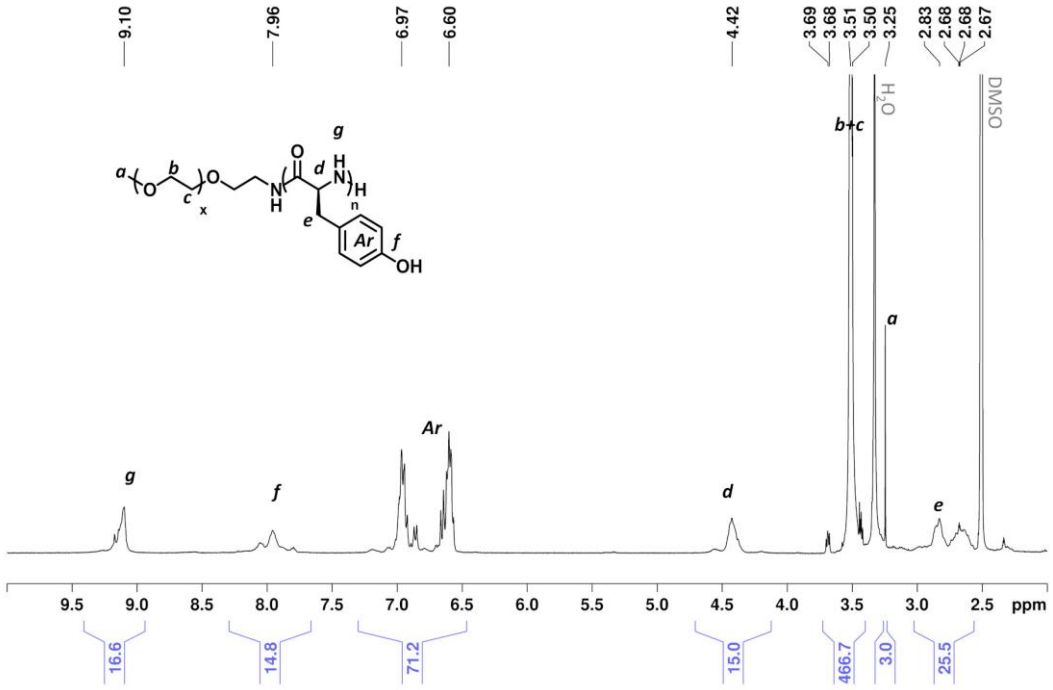

Figure SIII-9. ^{1}H NMR spectrum of PEG_{5k}-*b*-$PTyr_{20}$ in DMSO-d_6 with targeted DP of 20.

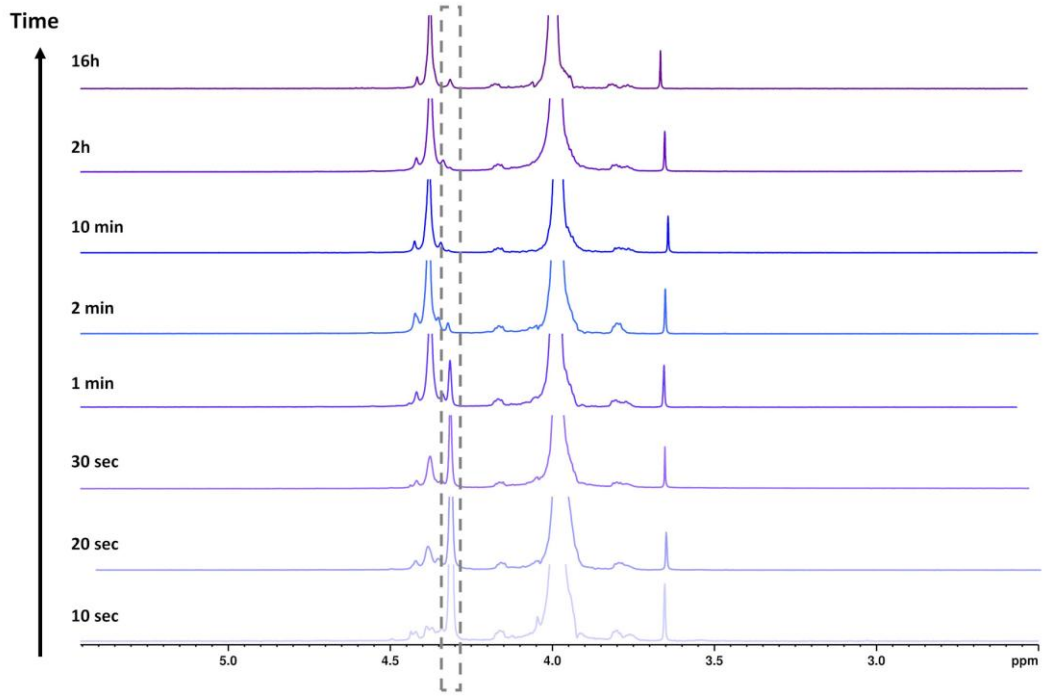

Figure SIII-10. Overlay of the original ^{1}H NMR spectra for the kinetic studies of the PEG_{5k}-NH_2 initiated aqueous ROPISA of Gly-NCA at an initial feeding ratio [M]/[I] of 20. The spectra were taken from ROPISA reactions quenched at specific time points. Note that the peaks in grey box (4.3 ppm) were glycine (hydrolyzed monomer).

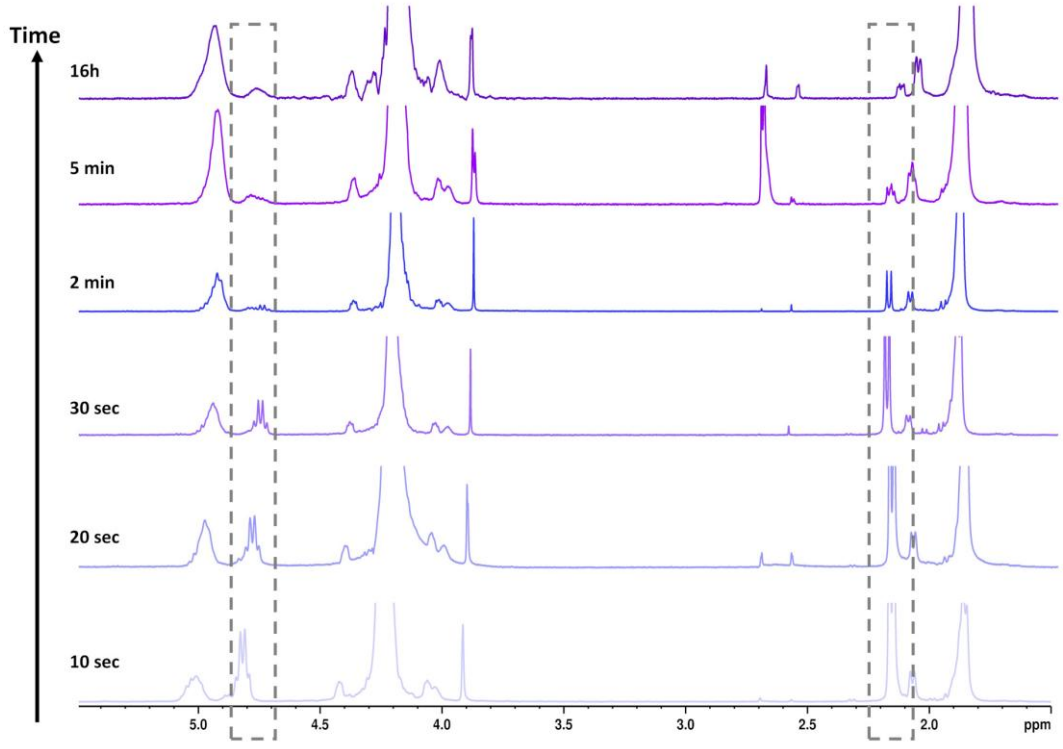

Figure SIII-11. Overlay of the original ^{1}H NMR spectra for the kinetic studies of the PEG_{5k}-NH_2 initiated aqueous ROPISA of Ala-NCA at an initial feeding ratio [M]/[I] of 20. The spectra were taken from ROPISA reactions quenched at specific time points. Note that the peaks in grey box (2.2 ppm and 4.8 ppm) were alanine (hydrolyzed monomer).

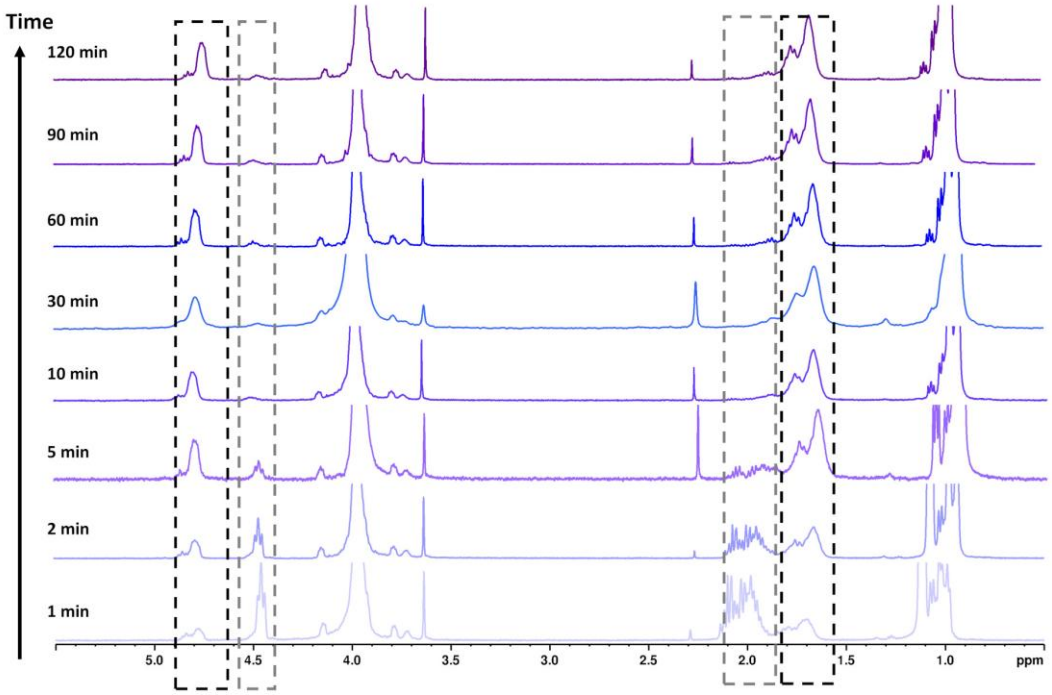

Figure SIII-12. Overlay of the original ^{1}H NMR spectra for the kinetic studies of the PEG_{5k}-NH_2 initiated aqueous ROPISA of Leu-NCA at an initial feeding ratio [M]/[I] of 20. The spectra were taken from ROPISA reactions quenched at specific time points. Note that the peaks in grey box (2.0 ppm and 4.5 ppm) were leucine (hydrolyzed monomer) and in black box (1.7 ppm and 4.8 ppm) PLeu.

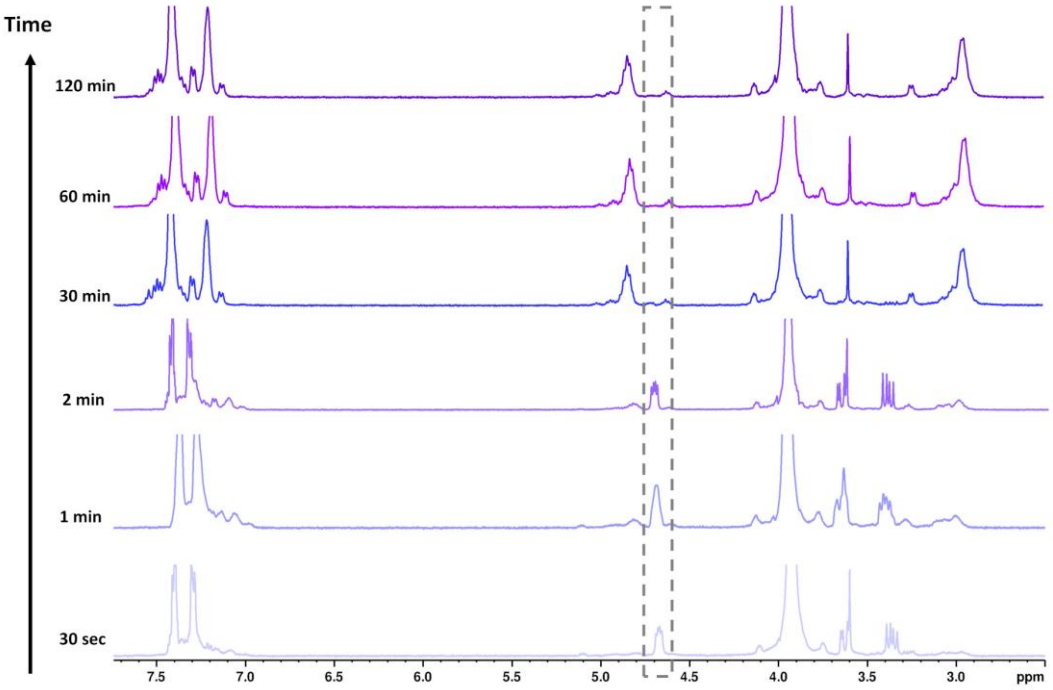

Figure SIII-13. Overlay of the original ^{1}H NMR spectra for the kinetic studies of the PEG_{5k}-NH_2 initiated aqueous ROPISA of Phe-NCA at an initial feeding ratio [M]/[I] of 20. The spectra were taken from ROP reactions quenched at specific time points. Note that the peaks in grey box (4.8 ppm) were phenylalanine (hydrolyzed monomer).

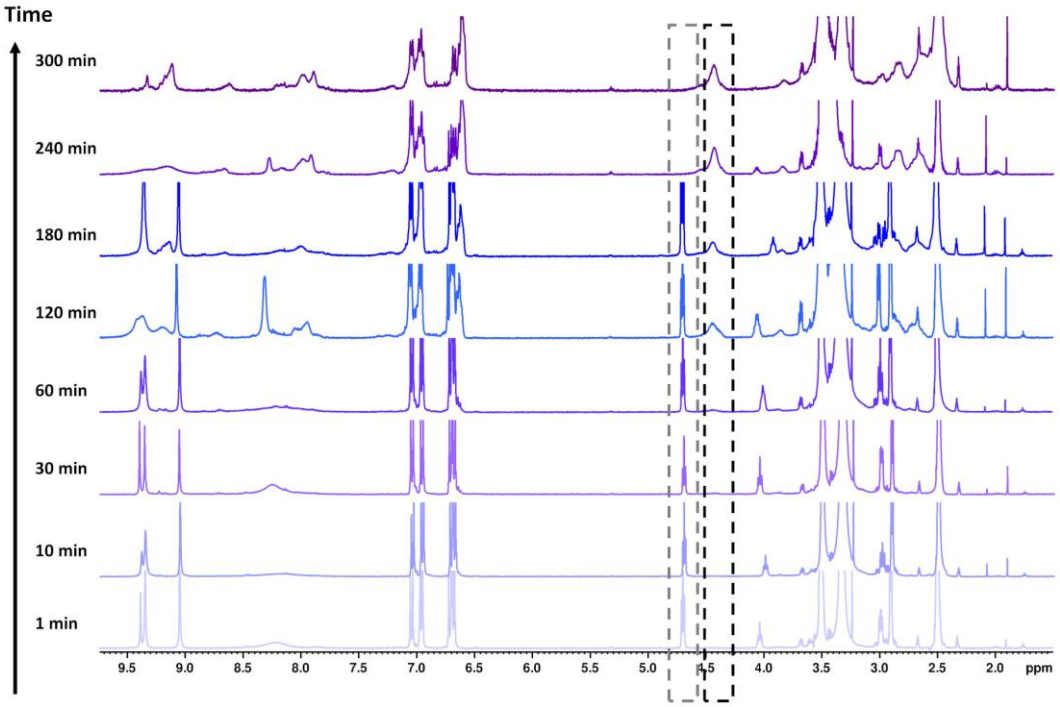

Figure SIII-14. Overlay of the original ^{1}H NMR spectra for the kinetic studies of the PEG_{5k}-NH_2 initiated aqueous ROPISA of Tyr-NCA at an initial feeding ratio [M]/[I] of 20. The spectra were taken from ROPISA reactions quenched at specific time points. Note that the peaks in gray box (4.8 ppm) were tyrosine (hydrolyzed monomer) and in black box (4.3 ppm) PTyr.

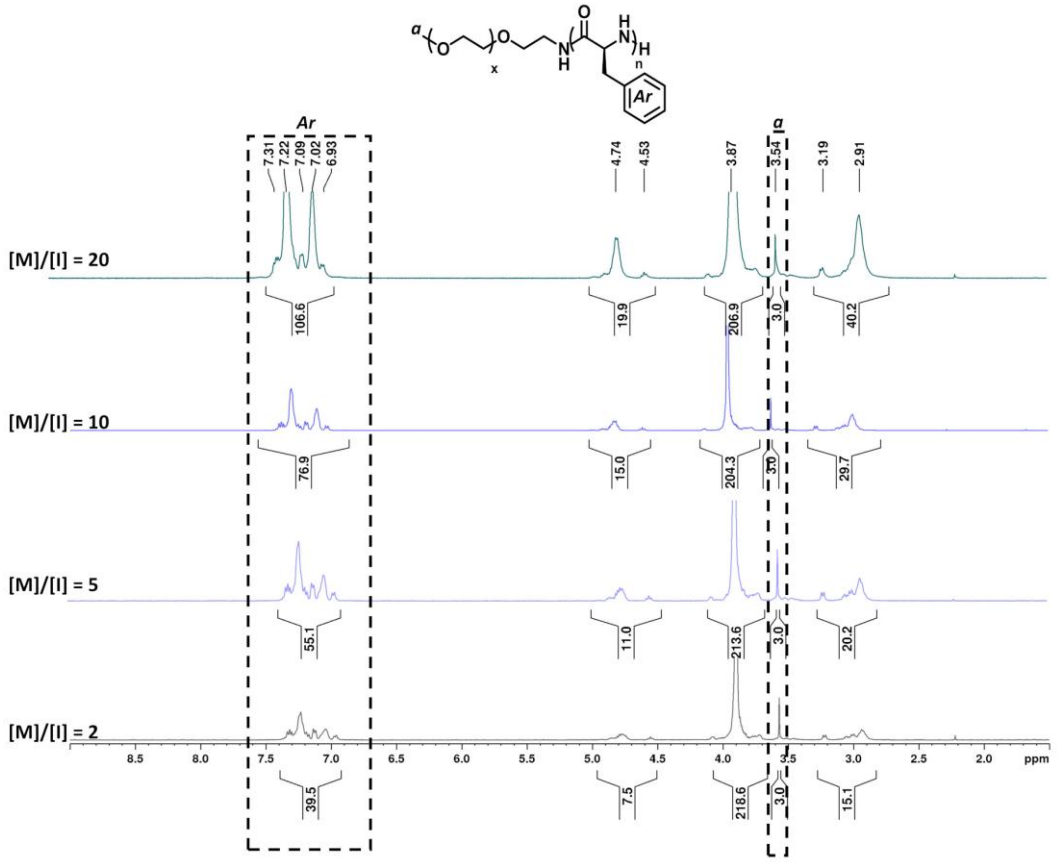

Figure SIII-15. ^{1}H NMR spectra of PEG_{2k}-*b*-$PPhe_n$ in TFA-*d* with targeted DP of 2, 5, 10 and 20. The CH3 signals (a) from the PEG end-chain were used as a reference to determine the DP of the PPhe block, with the integration of the aromatic protons (Ar).

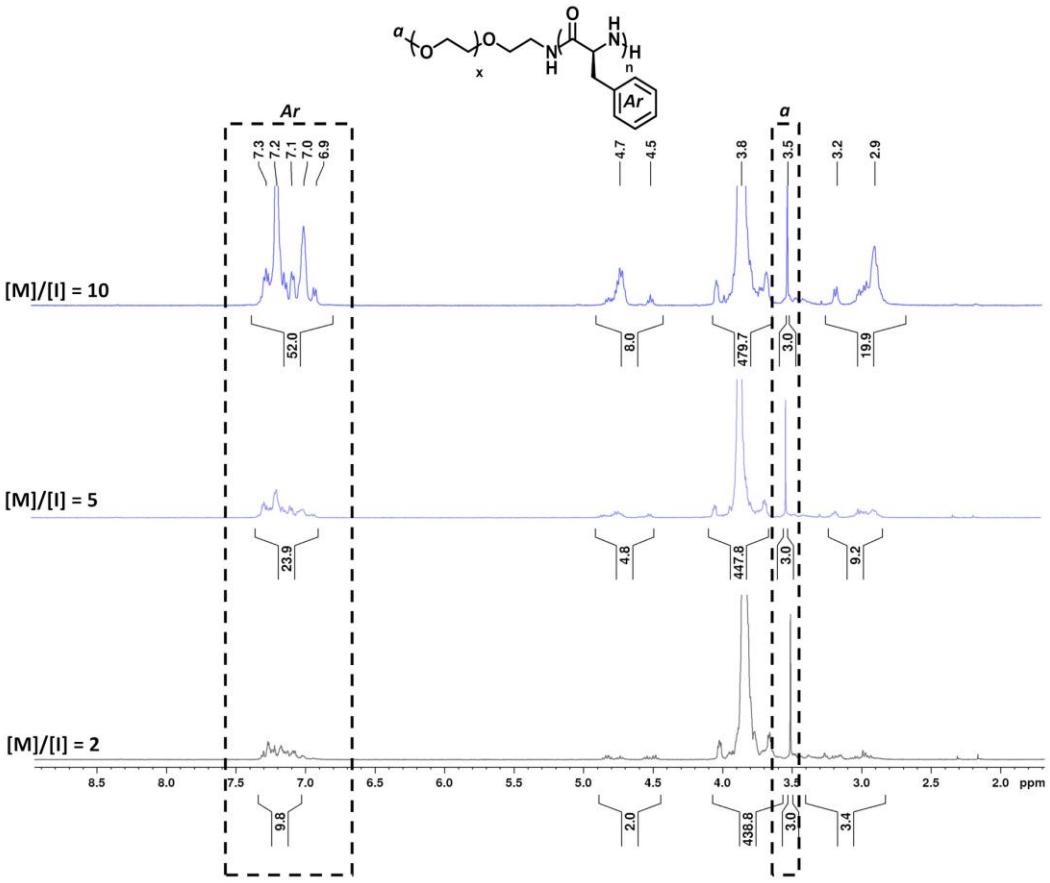

Figure SIII-16. ^{1}H NMR spectra of PEG_{5k}-*b*-$PPhe_n$ in TFA-*d* with targeted DP of 2, 5, and 10. The CH3 signals (a) from the PEG end-chain were used as a reference to determine the DP of the PPhe block, with the integration of the aromatic protons (Ar).

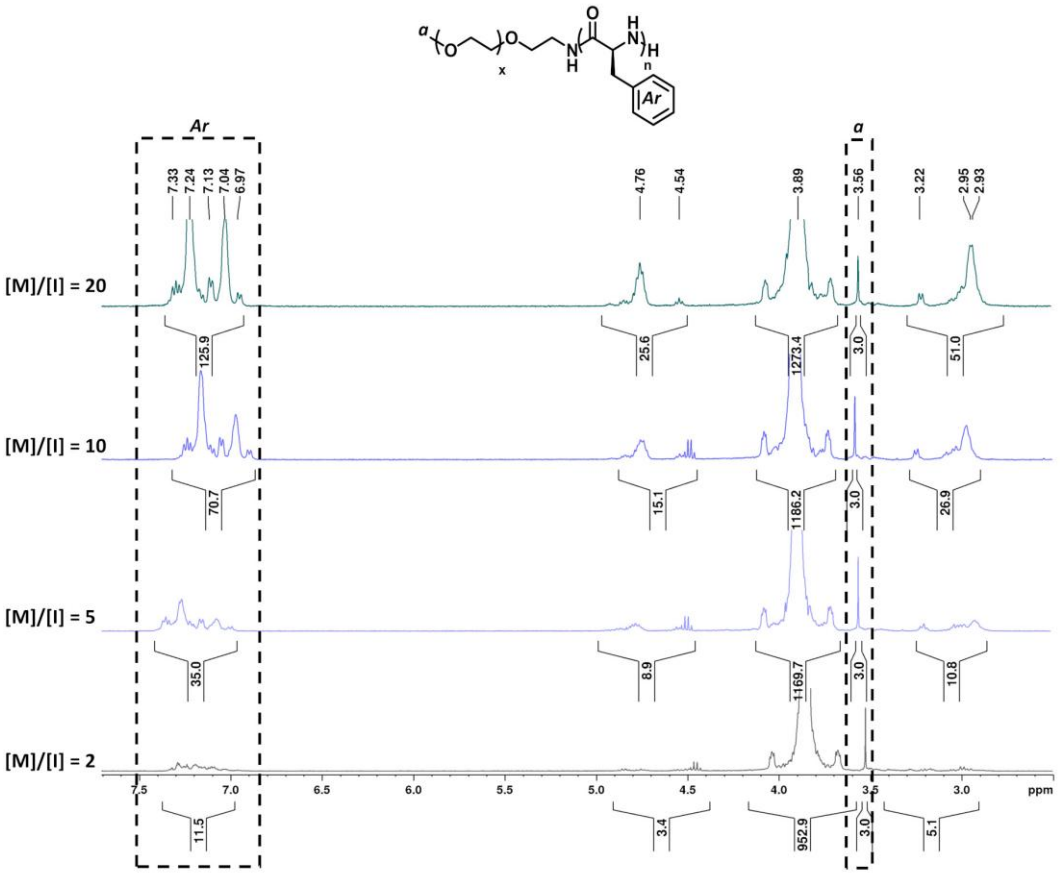

Figure SIII-17. ^{1}H NMR spectra of PEG_{10k}-*b*-$PPhe_n$ in TFA-*d* with targeted DP of 2, 5, 10 and 20. The CH3 signals (a) from the PEG end-chain were used as a reference to determine the DP of the PPhe block, with the integration of the aromatic protons (Ar).

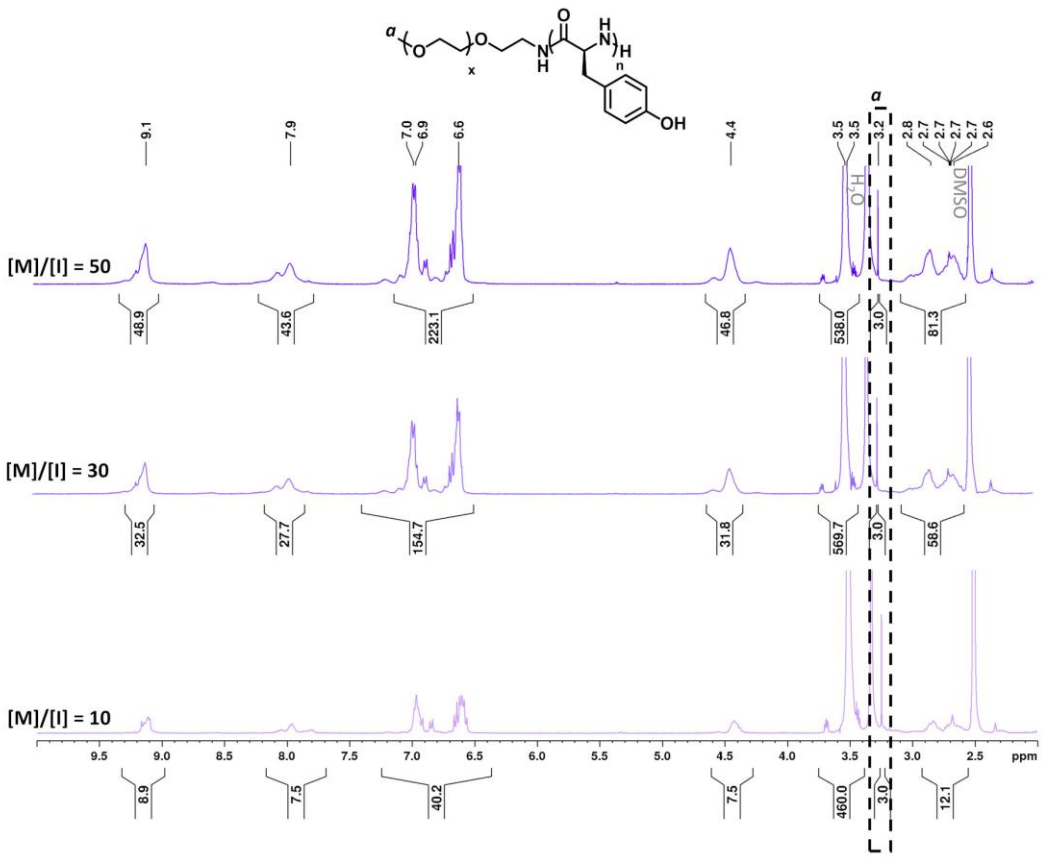

Figure SIII-18. ^{1}H NMR spectra of PEG_{5k}-*b*-$PTyr_n$ in DMSO-d_6 with targeted DP of 10, 30 and 50. The CH3 signals (a) from the PEG end-chain were used as a reference to determine the DP of the PPhe block, with the average integration of the protons from Tyr unit.

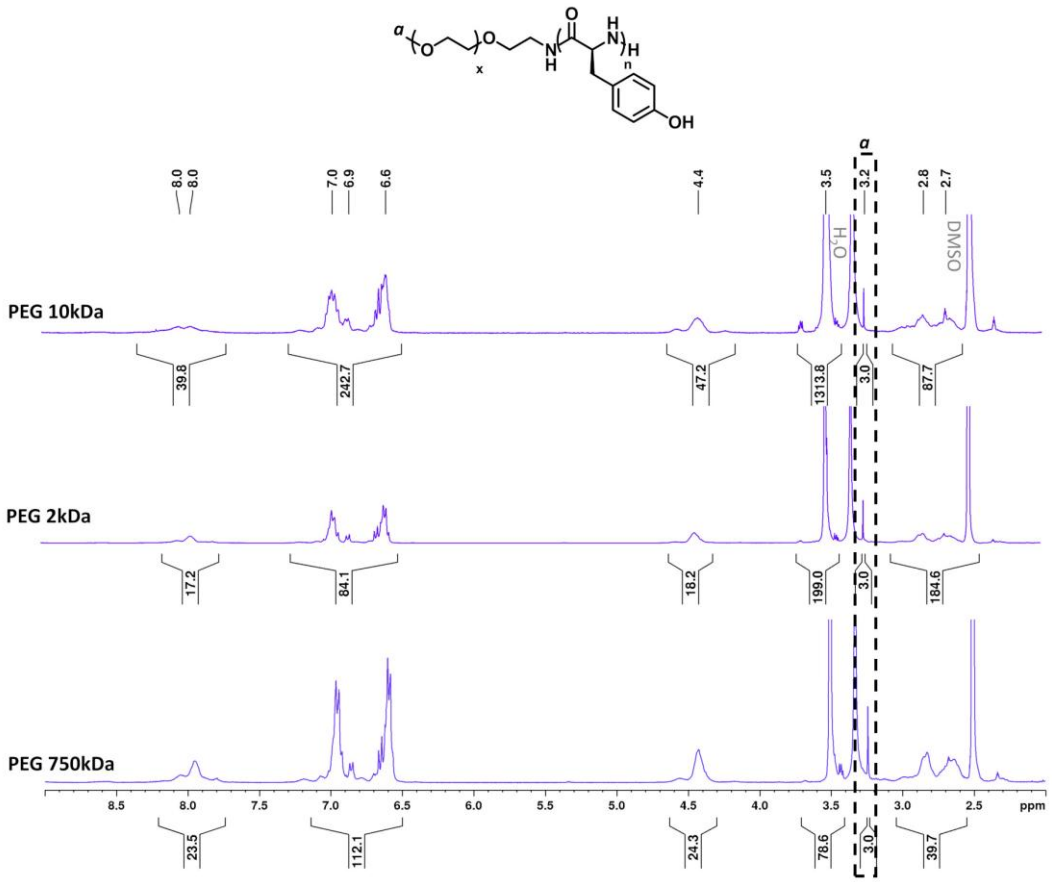

Figure SIII-19. ^{1}H NMR spectra of PEG_{750}-*b*-$PTyr_{20}$, PEG_{2k}-*b*-$PTyr_{20}$ and PEG_{10k}-*b*-$PTyr_{20}$ in DMSO-d_6 with targeted DP of 20 using a 750Da, 2kDa and 10kDa PEG-NH_2. The CH3 signals (a) from the PEG end-chain were used as a reference to determine the DP of the PPhe block, with the average integration of the protons from Tyr unit.

III.9. References

[1] N. J. W. Penfold, J. Yeow, C. Boyer, S. P. Armes, *ACS Macro Lett.* **2019**, *8*, 1029–1054.
[2] Z. Zhao, S. Lei, M. Zeng, M. Huo, *Aggregate* **2024**, *5*, e418.
[3] R. Takahashi, S. Miwa, F. H. Sobotta, J. H. Lee, S. Fujii, N. Ohta, J. C. Brendel, K. Sakurai, *Polym. Chem.* **2020**, *11*, 1514–1524.
[4] A. Czajka, S. P. Armes, *Chem. Sci.* **2020**, *11*, 11443–11454.
[5] M. J. Derry, L. A. Fielding, S. P. Armes, *Prog. Polym. Sci.* **2016**, *52*, 1–18.
[6] N. J. Warren, O. O. Mykhaylyk, D. Mahmood, A. J. Ryan, S. P. Armes, *J. Am. Chem. Soc.* **2014**, *136*, 1023–1033.
[7] L. P. D. Ratcliffe, A. Blanazs, C. N. Williams, S. L. Brown, S. P. Armes, *Polym. Chem.* **2014**, *5*, 3643–3655.
[8] A. Blanazs, A. J. Ryan, S. P. Armes, *Macromolecules* **2012**, *45*, 5099–5107.
[9] J. D. Guild, S. T. Knox, S. B. Burholt, Eleanor. M. Hilton, N. J. Terrill, S. L. M. Schroeder, N. J. Warren, *Macromolecules* **2023**, *56*, 6426–6435.
[10] Z. Li, R. Wang, X. Luo, L. Zhang, J. Tan, *Polym. Chem.* **2024**, *15*, 1736–1747.
[11] C. Gao, S. Li, Q. Li, P. Shi, S. A. Shah, W. Zhang, *Polym. Chem.* **2014**, *5*, 6957–6966.
[12] X. Zhang, J. Rieger, B. Charleux, *Polym. Chem.* **2012**, *3*, 1502–1509.
[13] D. Zhou, S. Dong, R. P. Kuchel, S. Perrier, P. B. Zetterlund, *Polym. Chem.* **2017**, *8*, 3082–3089.
[14] S. Boissé, J. Rieger, G. Pembouong, P. Beaunier, B. Charleux, *J. Polym. Sci. A Polym. Chem.* **2011**, *49*, 3346–3354.
[15] Z. Ding, C. Gao, S. Wang, H. Liu, W. Zhang, *Polym. Chem.* **2015**, *6*, 8003–8011.
[16] S. J. Parkinson, S. D. P. Fielden, M. Thomas, A. J. Miller, P. D. Topham, M. J. Derry, R. K. O'Reilly, *Biomacromolecules* **2024**, *25*, 4905–4912.
[17] W.-M. Wan, C.-Y. Pan, *Macromolecules* **2010**, *43*, 2672–2675.
[18] A. K. Pearce, T. R. Wilks, M. C. Arno, R. K. O'Reilly, *Nat Rev Chem* **2021**, *5*, 21–45.
[19] N. P. Truong, J. F. Quinn, M. R. Whittaker, T. P. Davis, *Polym. Chem.* **2016**, *7*, 4295–4312.
[20] Y. Geng, P. Dalhaimer, S. Cai, R. Tsai, M. Tewari, T. Minko, D. E. Discher, *Nature Nanotech* **2007**, *2*, 249–255.
[21] H. Hadji, K. Bouchemal, *J. Control. Release.* **2022**, *342*, 93–110.
[22] A. Zeeshan, H. Hadji, H. Khelifa, M. Bourge, K. Bouchemal, *Colloids Surf. A Physicochem. Eng. Asp.* **2024**, *680*, 132680.
[23] J. Rieger, *Macromol. Rapid Commun.***2015**, *36*, 1458–1471.
[24] Y. Kang, A. Pitto-Barry, H. Willcock, W.-D. Quan, N. Kirby, A. M. Sanchez, R. K. O'Reilly, *Polym. Chem.* **2014**, *6*, 106–117.
[25] Q. Yu, Y. Ding, H. Cao, X. Lu, Y. Cai, *ACS Macro Lett.* **2015**, *4*, 1293–1296.
[26] K.-Y. Yoon, I.-H. Lee, K. O. Kim, J. Jang, E. Lee, T.-L. Choi, *J. Am. Chem. Soc.* **2012**, *134*, 14291–14294.
[27] C. E. Boott, J. Gwyther, R. L. Harniman, D. W. Hayward, I. Manners, *Nature Chem* **2017**, *9*, 785–792.
[28] M. Huo, G. Song, J. Zhang, Y. Wei, J. Yuan, *ACS Macro Lett.* **2018**, *7*, 956–961.
[29] R. Thakuria, N. K. Nath, B. K. Saha, *Crystal Growth & Design* **2019**, *19*, 523–528.
[30] D. Yang, S. Gao, Y. Fang, X. Lin, X. Jin, X. Wang, L. Ke, K. Shi, *Nanomedicine (Lond.)* **2018**, *13*, 3159–3177.
[31] Z. Yu, K. Lu, Z. Wei, *Sci. China Chem.* **2012**, *55*, 2283–2291.
[32] K.-Y. Yoon, I.-H. Lee, K. O. Kim, J. Jang, E. Lee, T.-L. Choi, *J. Am. Chem. Soc.* **2012**, *134*, 14291–14294.
[33] S. Shin, K.-Y. Yoon, T.-L. Choi, *Macromolecules* **2015**, *48*, 1390–1397.
[34] R.-M. Zhu, Z.-X. Chang, W.-J. Zhang, C.-Y. Hong, *Macromolecules* **2023**, *56*, 3296–3303.
[35] E. T. Kool, J. C. Morales, K. M. Guckian, *Angew. Chem. Int. Ed.* **2000**, *39*, 990–1009.
[36] J. U. Bowie, *Curr Opin Struct Biol* **2011**, *21*, 42–49.
[37] S. E. Paramonov, H.-W. Jun, J. D. Hartgerink, *J. Am. Chem. Soc.* **2006**, *128*, 7291–7298.
[38] G. Mellot, J.-M. Guigner, J. Jestin, L. Bouteiller, F. Stoffelbach, J. Rieger, *Macromolecules* **2018**, *51*, 10214–10222.

[39] G. Mellot, J.-M. Guigner, L. Bouteiller, F. Stoffelbach, J. Rieger, *Angew. Chem. Int. Ed.* **2019**, *58*, 3173–3177.
[40] P. Gao, H. Cao, Y. Ding, M. Cai, Z. Cui, X. Lu, Y. Cai, *ACS Macro Lett.* **2016**, *5*, 1327–1331.
[41] X. Qi, C. Chen, C. Fei, J. Zhou, K. Liu, Y. Wu, C. Zhao, W. Yang, *J. Colloid Sci.* **2025**, *688*, 582–590.
[42] L. Shen, Y. Li, Q. Lu, X. Qi, X. Wu, Z. Zhou, J. Shen, *Chem. Commun.* **2020**, *56*, 2411–2414.
[43] A. M. Oliver, J. Gwyther, C. E. Boott, S. Davis, S. Pearce, I. Manners, *J. Am. Chem. Soc.* **2018**, *140*, 18104–18114.
[44] Y. Sha, M. Anisur Rahman, T. Zhu, Y. Cha, C. Wayne McAlister, C. Tang, *Chem. Sci.***2019**, *10*, 9782–9787.
[45] R. A. Scanga, A. Shahrokhinia, J. Borges, S. H. Sarault, M. B. Ross, J. F. Reuther, *J Am Chem Soc* **2023**, *145*, 6319–6329.
[46] J. W. Steed, J. L. Atwood, *Supramolecular Chemistry*, John Wiley & Sons, **2022**.
[47] S. Guan, C. Zhang, W. Wen, T. Qu, X. Zheng, Y. Zhao, A. Chen, *ACS Macro Lett.* **2018**, *7*, 358–363.
[48] P. D. Bartlett, R. H. Jones, *J. Am. Chem. Soc.* **1957**, *79*, 2153–2159.
[49] P. D. Bartlett, D. C. Dittmer, *J. Am. Chem. Soc.* **1957**, *79*, 2159–2160.
[50] A. H. Morrell, N. J. Warren, P. D. Thornton, *Macromol. Rapid Commun.* **2024**, 2400103.
[51] S. Xi Huang, Z. Hao Wang, M. Lin, X. Hui Fu, J. Sun, *Polym. Chem.***2023**, *14*, 1801–1808.
[52] B. Liu, R. Fang, W. Li, X. Wu, T. Liu, M. Lin, J. Sun, X. Chen, *J. Am. Chem. Soc.* **2024**, *146*, 16558–16566.
[53] L. Tian, C. Cao, J. Ho, M. H. Stenzel, *J. Am. Chem. Soc.* **2024**, *146*, 8120–8130.
[54] A. Isidro-Llobet, M. Álvarez, F. Albericio, *Chem. Rev.* **2009**, *109*, 2455–2504.
[55] J. Rodríguez-Hernández, M. Gatti, H.-A. Klok, *Biomacromolecules* **2003**, *4*, 249–258.
[56] C. Grazon, P. Salas-Ambrosio, S. Antoine, E. Ibarboure, O. Sandre, A. J. Clulow, B. J. Boyd, M. W. Grinstaff, S. Lecommandoux, C. Bonduelle, *Polym. Chem.* **2021**, *12*, 6242–6251.
[57] V. Gavva, O. Al Musaimi, C. Bent, D. R. Williams, *Separations* **2023**, *10*, 456.
[58] V. V. Mozhaev, I. V. Berezin, K. Martinek, Y. Nosoh, *Critical Reviews in Biochemistry* **1988**, *23*, 235–281.
[59] "Calculation of molecular properties and bioactivity score," can be found under https://www.molinspiration.com/cgi/properties
[60] D. Karandur, K.-Y. Wong, B. M. Pettitt, *J. Phys. Chem. B* **2014**, *118*, 9565–9572.
[61] S. Bykov, S. Asher, *J. Phys. Chem. B* **2010**, *114*, 6636–6641.
[62] B. Lotz, *ChemBioChem* **2022**, *23*, e202100658.
[63] K. Taga, M. G. Sowa, J. Wang, H. Etori, T. Yoshida, H. Okabayashi, H. H. Mantsch, *Vibrational Spectroscopy* **1997**, *14*, 143–146.
[64] M. Spyridakou, I. Tzourtzouklis, R. Graf, H. Beauseroy, C. Bonduelle, S. Lecommandoux, G. Floudas, *Biomacromolecules* **2025**, *26* ; 1892-1903.
[65] P. J. Hurst, A. A. Graham, J. P. Patterson, *ACS Polym Au* **2022**, *2*, 501–509.
[66] J. C. Foster, S. Varlas, B. Couturaud, J. R. Jones, R. Keogh, R. T. Mathers, R. K. O'Reilly, *Angew. Chem. Int. Ed.* **2018**, *57*, 15733–15737.
[67] C. Grazon, P. Salas-Ambrosio, E. Ibarboure, A. Buol, E. Garanger, M. W. Grinstaff, S. Lecommandoux, C. Bonduelle, *Angew. Chem. Int. Ed.* **2020**, *59*, 622–626.
[68] H. Beauseroy, C. Grazon, S. Antoine, M. Badreldin, P. Salas-Ambrosio, S. Harrisson, E. Garanger, S. Lecommandoux, C. Bonduelle, *Macromol. Rapid Commun.* **2024**, *45*, 2400079.
[69] N. Y. Palermo, J. Csontos, R. F. Murphy, S. Lovas, *Int J Quantum Chem* **2008**, *108*, 814–819.
[70] E. Lanzarotti, R. R. Biekofsky, D. A. Estrin, M. A. Marti, A. G. Turjanski, *J Chem Inf Model* **2011**, *51*, 1623–1633.
[71] X. Liu, R. Fan, B. Lu, Y. Le, *Pharmaceutics* **2018**, *10*, 230.
[72] A. Bossion, J. Nicolas, *European Polymer Journal* **2020**, *140*, 110033.
[73] E. Aydinlioglu, M. Abdelghani, G. Le Fer, J. C. M. van Hest, O. Sandre, S. Lecommandoux, *Macromol.Chem. Phys.***2023**, *224*, 2200306.
[74] J. Jiang, X. Zhang, Z. Fan, J. Du, *ACS Macro Lett.* **2019**, *8*, 1216–1221.
[75] X. Gu, M. Qiu, H. Sun, J. Zhang, L. Cheng, C. Deng, Z. Zhong, *Biomater. Sci.* **2018**, *6*, 1526–1534.
[76] X. Gu, Y. Wei, Q. Fan, H. Sun, R. Cheng, Z. Zhong, C. Deng, *J. Control. Release.* **2019**, *301*, 110–118.

[77] G. Bastiat, F. Plourde, A. Motulsky, A. Furtos, Y. Dumont, R. Quirion, G. Fuhrmann, J.-C. Leroux, *Biomaterials* **2010**, *31*, 6031–6038.
[78] M. C. Costache, A. D. Vaughan, H. Qu, P. Ducheyne, D. I. Devore, *Acta Biomater* **2013**, *9*, 6544–6552.
[79] P. Tiwari, A. Basu, S. Sahu, S. Gound, R. M. Christman, A. K. Tiwari, P. Trivedi, A. DuttKonar, *New J. Chem.* **2018**, *42*, 4915–4922.
[80] J. Huang, C. L. Hastings, G. P. Duffy, H. M. Kelly, J. Raeburn, D. J. Adams, A. Heise, *Biomacromolecules* **2013**, *14*, 200–206.
[81] C. Jiang, C. Zhao, P. Xu, Q. Song, X. Tao, S. Lin, *Biomacromolecules* **2024**, DOI 10.1021/acs.biomac.4c00437.
[82] Y. Hu, Z.-Y. Tian, W. Xiong, H. Lu, **2022**, *National Science Review*, **9**, nwac033

.

Chapter IV. Modulation of stabilizing blocks in aqueous ROPISA to diversify nanoparticle surfaces

Table of Contents

Chapter IV. Modulation of stabilizing blocks in aqueous ROPISA to diversify nanoparticle surfaces

IV.1. Introduction 173

IV.2. Aqueous ROPISA initiated by poly(sarcosine) 174

IV.2.1. Poly(sarcosine)-glycine synthesis 174

IV.2.2. Aqueous ROPISA initiated by poly(sarcosine) of BLG-NCA 176

IV.3. Aqueous ROPISA initiated by poly(*L*-proline) 177

IV.3.1. Poly(*L*-proline) synthesis 179

IV.3.2. Aqueous ROPISA initiated by poly(*L*-proline) of various NCAs 179

IV.3.3. Thermoresponsive properties 184

IV.4. Aqueous ROPISA initiated by elastin-like polypeptide 186

IV.4.1. Aqueous ROPISA initiated by elastin-like polypeptide of various chain length 187

IV.4.2. Thermoresponsive properties 190

IV.5. Enzyme-polypeptide conjugates via aqueous ROPISA 191

IV.5.1. Presentation of the enzymes 192

IV.5.2. Aqueous ROPISA initiated by metalloenzymes of Gly-NCA and BLG-NCA 193

IV.5.2.1. HRP 193

IV.5.2.2. Versatile Peroxidase (VP) 196

IV.5.2.3. Laccase (Lac) 196

IV.6. Perspectives: other macroinitiators of interest 197

IV.6.1. Poly(ethylene glycol)-cyclic peptide conjugate (PEG-CP) 197

IV.6.2. Self-Immolative Polymers (SIP) 201

IV.6.3. Polysaccharides 204

IV.7. Conclusion 210

IV.8. Experimental section 212

IV.8.1. Materials 212

IV.8.2. Instrumentation and methods 212

IV.8.2.1. Nuclear Magnetic Resonance (NMR) 212

IV.8.2.2. Size Exclusion Chromatography (SEC) 212

IV.8.2.3. Atomic Force Microscopy (AFM) 213

IV.8.2.4. Transmission Electron Microscopy (TEM) 214

IV.8.2.5. Cryo-Transmission Electron Microscopy (cryo-TEM) 214

IV.8.2.6. Dynamic Light Scattering (DLS) 214

IV.8.2.7. UV-Vis spectroscopy 214

IV.8.2.8. CAC determination by fluorescence using Nile Red 215

IV.8.2.9. SDS-PAGE 215

IV.8.2.10. Native PAGE 215
IV.8.2.11. Enzyme concentration 215
IV.8.2.12. Enzymatic assays 215
IV.8.3. Synthesis 216
IV.8.3.1. Synthesis of PSar-*b*-PBLG block copolymers 216
IV.8.3.1.1. Ring-opening polymerization of Sar-NCA 216
IV.8.3.1.2. Coupling with Boc-Glycine-OH 216
IV.8.3.1.3. Poly(sarcosine)-*block*-poly(γ-benzyl-*L*-glutamate) PSar-*b*-PBLG 217
IV.8.3.2. Synthesis of PLP-based diblock copolymers 217
IV.8.3.2.1. Synthesis of poly(*L*-proline) macroinitiator 217
IV.8.3.2.2. Poly(*L*-proline)-*block*-poly(amino acids) 217
IV.8.3.3. Synthesis of ELP-*b*-PBLG 217
IV.8.3.3.1. Synthesis of elastin-like polypeptide by recombinant production 217
IV.8.3.3.2. Elastin like polypeptide-*block*-poly(γ-benzyl-*L*-glutamate) ELP-*b*-PBLG 218
IV.8.3.4. Synthesis of PEG-CP-PBLG 218
IV.8.3.4.1. Synthesis of Poly(ethylene glycol)-cyclic peptide conjugate 218
IV.8.3.4.2. Poly(ethylene glycol)-cyclic peptide-*block*-poly(γ-benzyl-*L*-glutamate) 218
IV.8.3.5. Synthesis of SIP-*b*-PBLG 218
IV.8.3.6. Enzyme-polypeptide conjugates 218
IV.8.3.7. Synthesis of Dex-*g*-PBLG and Dex-*b*-PBLG 219

IV.9. Supplementary figures 220

IV.10. References 230

IV.1. Introduction

As previously mentioned in **Chapter I**, the production of degradable nanoparticles is a key feature of safe nanocarriers in the context of drug delivery. Another primary concern is enhancing the functionality of these systems to improve their therapeutic efficacy. A thorough review of the literature reveals pioneering reports involving polymerization-induced self-assembly (PISA) with degradable or functional macroinitiators including biomolecules.[1,2]

After demonstrating that ROPISA is a versatile technique using various monomers, which directly influence the self-assembly into nanostructures with different aspect ratios, this chapter explores the use of a wide range of macroinitiators for the ring-opening polymerization-induced self-assembly (ROPISA) of *N*-carboxyanhydrides (NCAs), including polypeptides, enzymes, and other functional macromolecules. In a first part, synthetic polypeptides such as poly(sarcosine) (PSar) and poly(*L*-proline) (PLP), as well as biologically derived elastin-like polypeptides (ELPs), have been used as macroinitiators. This approach enables their direct use in PISA without the necessity for preliminary chemical modification, thereby preserving their native structure under non-denaturing conditions and allowing access to fully peptide-based block copolymers with potential applications in nanomedicine and biomaterials.[3]

In the second part of the chapter, in addition to the afore mentioned polypeptides, 3 different metalloenzymes, horseradish peroxidase (HRP), versatile peroxidase (VP) and laccase (Lac), were also investigated as macroinitiators in ROPISA. This approach offers a promising avenue for the development of enzyme-polypeptide conjugates, paving the way to new possibilities in biocatalysis and therapeutic applications by implementing stabilization and immobilization of enzymes in nanomaterials while maintaining their activity.

In the final section of the chapter, beyond the use of protein or polypeptides as macroinitiators, alternative stabilizers with unique properties were also explored (Scheme IV-1). In the framework of a collaborative effort with the group of S. Perrier, peptide-cyclic conjugates, known for their ability to self-assemble into nanotubes, were studied for their potential in drug delivery. In a parallel effort with the group of E. Gillies, self-immolative polymers (SIPs) were also considered due to their ability to undergo triggered depolymerization, providing a fully degradable system ideal for controlled drug release. Finally, polysaccharides such as dextran were investigated as macroinitiators, leveraging their PEG-like hydrophilicity and their capacity to target tumors via interactions with overexpressed receptors on cancer cell surfaces.

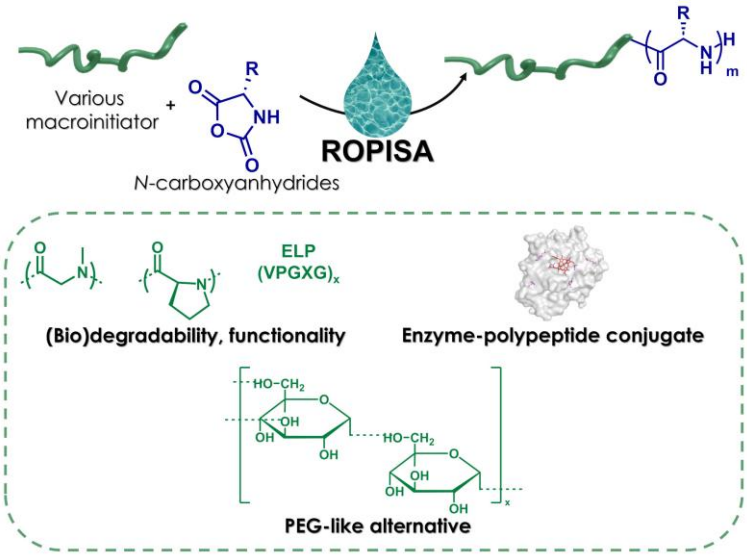

Scheme IV-1. Diversifying the surface of nanoparticles obtained via queous ROPISA using various stabilizing blocks.

IV.2. Aqueous ROPISA initiated by poly(sarcosine)

Poly(sarcosine) has emerged as a promising alternative to poly(ethylene glycol) (PEG),[4,5] with several studies focusing on the development of amphiphilic diblock copolypeptides using PSar as a macroinitiator for the ROP of NCA.[6–9] Given its solution properties that are comparable to those of PEG,[10] we initiated our investigation with this polypeptide. However, it is important to note that poly(sarcosine) is composed of amino acids with an *N*-methyl substitution, a class of polymer called polypeptoid, which results in a secondary amine at the end extremity. This structural feature could impart different reactivity compared to primary amines, and this factor was carefully considered in this part of the study.

IV.2.1. Poly(sarcosine)-glycine synthesis

The initial step in the synthesis process involved the preparation of poly(sarcosine), which was to be used as macroinitiator. Conventional ROP of Sarcosine-NCA in dimethylformamide (DMF) was initially conducted, using hexylamine as the initiator ($[M]_0$ = 0.6 mol.L^{-1}, initial feeding ratio [M]/[I] = 70) (Scheme IV-2a). After purification by precipitation in diethyl ether, the resulting polymer was characterized by by ^{1}H NMR spectroscopy and SEC chromatography. These analyses indicated that the process yielded a well-defined polymer with a degree of polymerization (DP) of 75 and narrow molar mas dispersity ($Đ$ = 1.05).

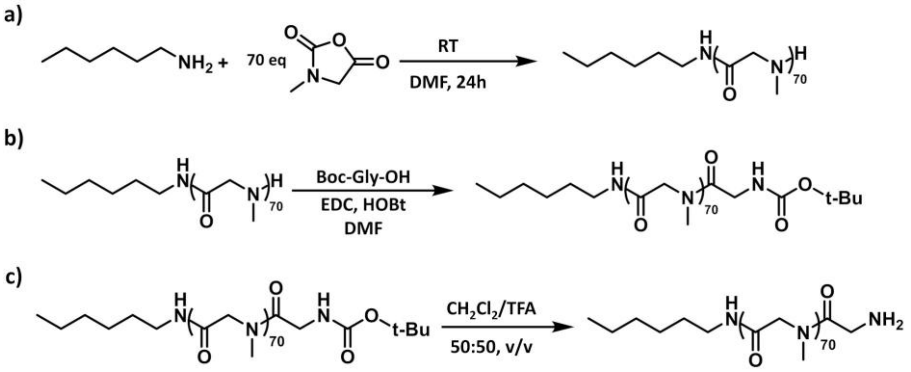

Scheme IV-2. PSar-NH_2 synthesis. (a) ROP of Sar-NCA initiated by hexylamine. (b) Peptide coupling with Boc-Gly-OH. (c) Boc deprotection.

To display a primary terminal group analogous to that of PEG-NH_2 previously used in **Chapter II** and **III**, this PSar was functionalized with glycine through a peptide coupling with a Boc-protected glycine (Scheme IV-2b). After deprotection in a mixture of dichloromethane (CH_2Cl_2) / trifluoroacetic acid (TFA) for a duration of one night and subsequent to dialysis following neutralization with a saturated bicarbonate solution (Scheme IV-2c), the PSar-NH_2 was characterized by ^{1}H NMR analysis to verify the disappearance of the Boc protecting group, and by SEC analysis to compare the evolution of the molar mass with the initial PSar (Figure IV-1). The results of these analyses indicated the absence of Boc signals and a slight shift in the SEC chromatogram towards a higher retention time. This shift can be attributed to an increase in molar mass following glycine coupling, or potentially due to interactions with the column, possibly from the primary amine group.

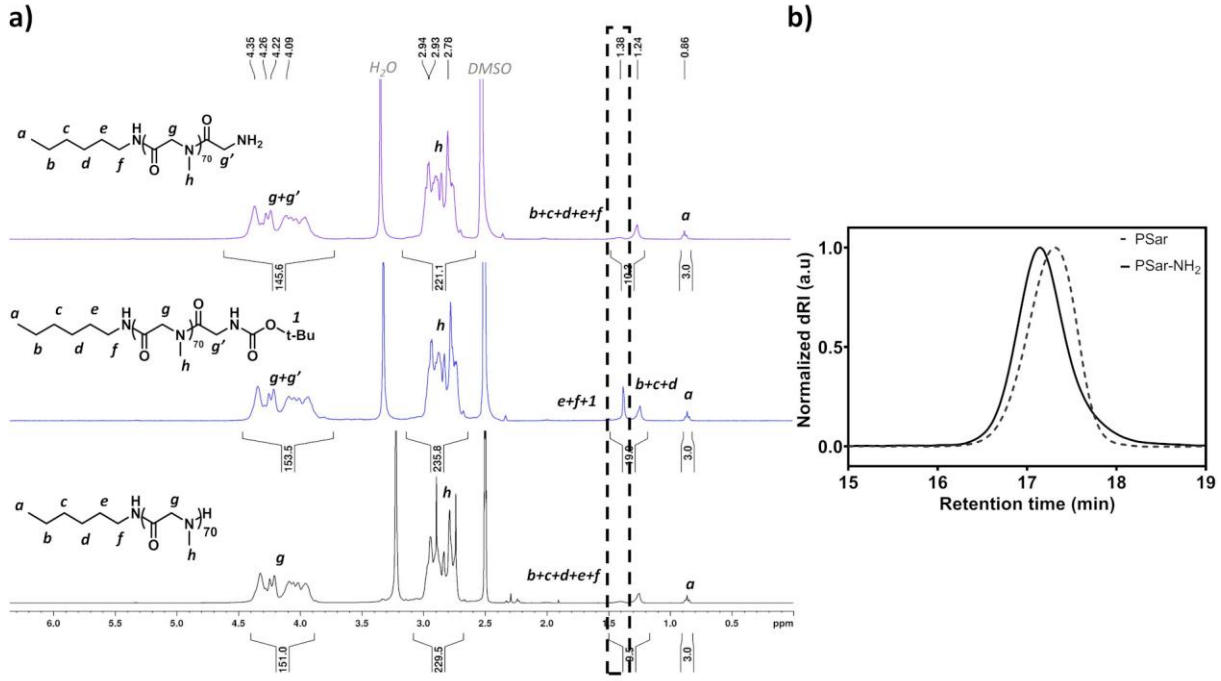

Figure IV-1. (a) ^{1}H NMR spectra of native PSar (bottom), PSar-Gly(*N*Boc) (middle) and PSar-NH_2 (top). (b) SEC chromatograms of native PSar and PSar-NH_2 in HFIP (+0.05% KTFA, detection by differential refractive index).

IV.2.2. Aqueous ROPISA initiated by poly(sarcosine) of BLG-NCA

The ROPISA experiment was conducted under identical conditions to those of the PEG-NH_2 experiment (cf. **Chapter II**) and was compared with the use of PSar-NH_2 and native PSar in the same conditions. The resulting copolymers were analyzed using ^{1}H NMR and SEC. The DP values were in agreement with the targeted ones according to ^{1}H NMR (Figure SIV-2). However, SEC displayed a bigger population at higher retention times for PSar compared to PSar-NH_2, which can be attributed to oligomers of BLG produced through water-initiation. This suggests that initiation with a secondary amine is moderately less efficient. The use of PSar remains a viable option, as evidence by Thornton and coworkers who employed PSar to initiate ROPISA of Phe-NCA and Ala-NCA.[11] However, in our experimental setting, the use of PSar-NH_2 led to a reduction in oligomer population, as indicated by SEC, suggesting that initiation by a primary amine is more effective than that by a native secondary amine. Consequently, we opted for the use of PSar-NH_2.

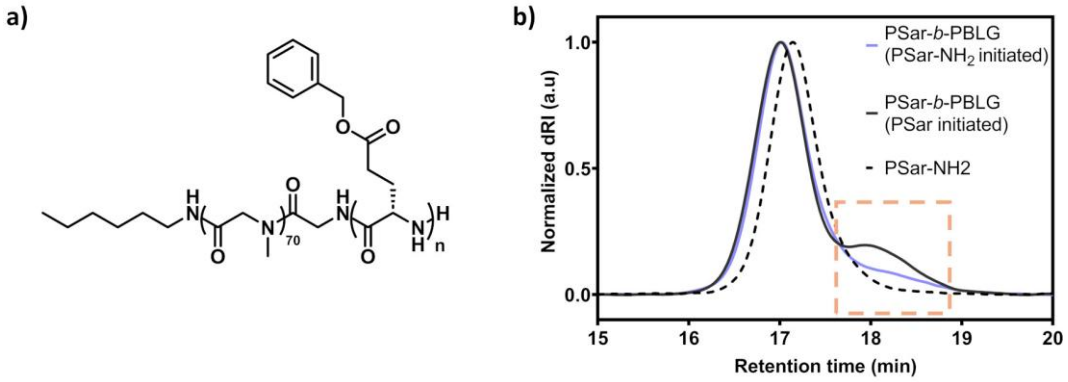

Figure IV-2. (a) Chemical structure of PSar-*b*-PBLG by using PSar-NH_2 as macroinitiator. (b) SEC chromatograms of the diblock copolymers obtained by using either PSar or PSar-NH_2 as macroinitiator, compared to PSar-NH_2 homopolymer in HFIP (+0.05% KTFA, detection by differential refractive index). In orange box, population which can be assimilated to water-initiated oligomers of BLG.

Following ROPISA with PSar-NH_2, the nanoparticles were analyzed after dialysis by dynamic light scattering (DLS) and transmission electron microscopy (TEM) imaging. This revealed a nanoparticle size that was bigger than for PEG-initiated copolymer (cf **Chapter II**), with a hydrodynamic Z-average diameter of 170 ± 2 nm, also the dispersity was high ($\sigma > 0.2$; Figure SIV-1). Furthermore, the nanoparticles displayed different morphologies by TEM and cryo-TEM, with a coiled ribbon morphology, as shown in Figure IV-3.

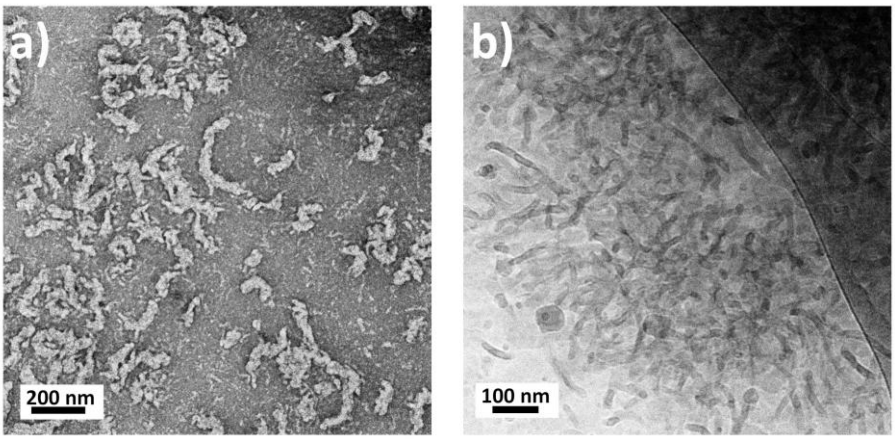

Figure IV-3. Representative TEM (a) and Cryo-TEM (b) of PSar-*b*-PBLG nanoparticles suspensions.

Overall, the use of PSar in ROPISA demonstrated that fully peptidic nanoparticles with a poly(sarcosine) shell and anisotropic morphologies can be obtained, which hold promise for nanomedicine applications in a context where PEG is under increasing criticism and scrutinity. This serves as proof of concept for the further production of fully peptidic nanoparticles. Indeed, this successful ROPISA from PSar-NH_2 encouraged us to extend this approach to other functional polypeptide or protein macroinitiators.

IV.3. Aqueous ROPISA initiated by poly(*L*-proline)

The initial success of the ROPISA from PSar-NH_2 prompted the extension of this approach to polypeptide macroinitiators exhibiting lower critical solution temperature (LCST) behavior: poly(*L*-proline) (PLP) and elastin-like polypeptide (ELP).

PLP is a distinctive polypeptide derived from *L*-Proline (Pro), the only amino acid featuring a secondary amine structure, formed via a cyclic aliphatic side chain linking the α-carbon and the amino group. This unique side chain enables PLP to adopt two distinct secondary structures: the right-handed, hydrophobic PLP I helix with cis-peptide bonds[12], and the left-handed, hydrophilic PLP II helix with trans-peptide bonds. The latter is favored in aqueous conditions and is particularly abundant in globular, water-dispersible proteins.[13,14] In recent studies, our research group investigated the thermoresponsive behavior of PLP,[15] leveraging the well-controlled polymerization of *L*-proline NCA in binary aqueous mixtures developed by Lu's group.[14] A lower critical solution temperature (LCST)-like behavior was observed, characterized by a significant hysteresis, as shown in Figure IV-4a. In this context, the cloud point temperature (T_{CP}) corresponds to the temperature at which the polymer undergoes phase separation, while the clear point temperature (T_{CL}) represents the temperature at which the polymer re-dissolves. The large gap between these two temperatures indicates a strong hysteresis resulting from a transition between the highly soluble PLP II conformation and an intermediate insoluble state characterized by a mixture of cis and trans amide conformations. These findings highlight temperature-induced changes in the secondary structure of PLP. PLP is therefore a synthetic polymer that exhibits temperature-driven aggregation in water with hysteresis, thereby serving as a simple model of functional protein.

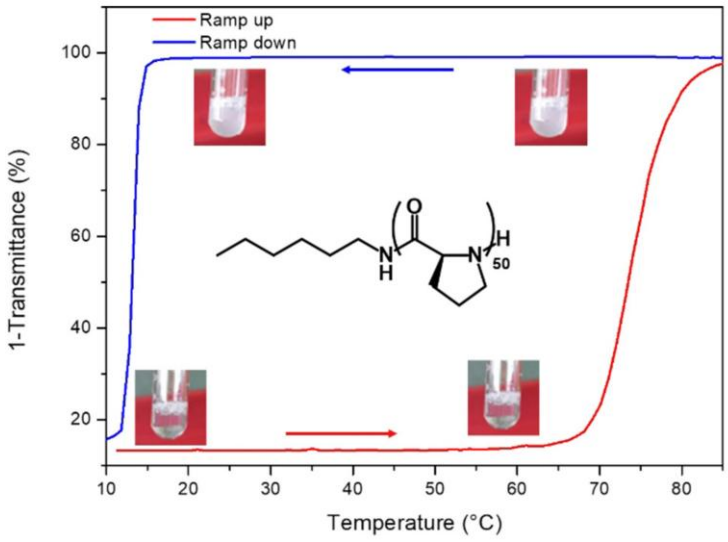

Figure IV-4. UV-vis turbidimetry curves for PLP as function of the temperature, which displays a LCST-like behavior with strong hysteresis. Adapted from Bonduelle *et al.*[15]

Heise and coworkers have also contributed to this field by successfully synthesizing nanoparticles via a one-pot method that employs poly(*L*-proline) as the macroinitiator.[16] Their approach involved the initial preparation of branched poly(*L*-proline), which was subsequently chain-extended with BLG-NCA and ε-benzyloxycarbonyl -*L*-lysine-NCA (Lys(Z)-NCA) in a single pot to yield a range of morphologies, thereby demonstrating poly(proline)'s capacity to stabilize self-assembly (Figure IV-5). In contrast, our approach differs by synthesizing the macroinitiator separately, followed by chain extension in pure aqueous conditions using a two-step process rather than a one-pot reaction.

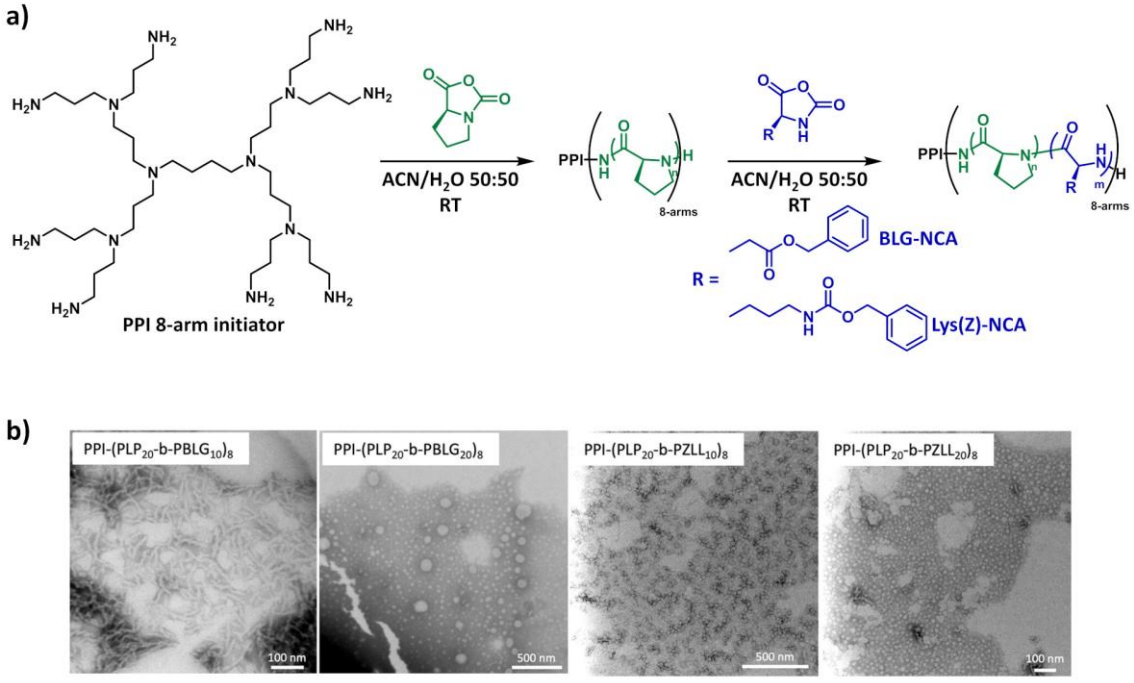

Figure IV-5. (a) One-pot synthetic approach to obtain PLP-based nanoparticles with sequential ROP of NCA in ACN/water (1:1, v/v) at RT. (b) Representative TEM images of PLP-based nanostructures using BLG-NCA or Lys(Z)-NCA as core-forming monomer. Adapted from Heise *et al.*[16]

IV.3.1. Poly(*L*-proline) synthesis

The water-enhanced ROP of *L*-proline NCA was used to prepare poly(*L*-proline), in agreement with the published procedure, targeting a DP 50 (Scheme IV-3).[15]. The synthesis of this polymer was carried out by Mostafa Badreldin, a former PhD student of the team.

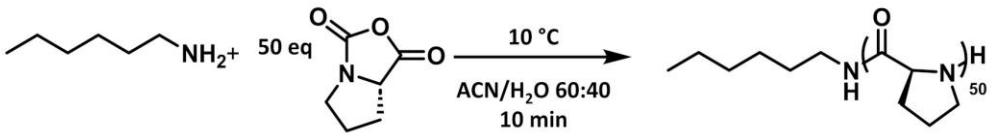

Scheme IV-3. PLP synthesis via ROP of *L*-Pro-NCA in ACN/H_2O.

The resulting polymer was characterized by ^{1}H NMR, which indicated a DP of 55, while SEC analysis revealed a number-average molar mass (M_n) of 5.4 kg·mol^{-1} with a narrow dispersity ($Đ$ = 1.03), as shown in Figure IV-6.

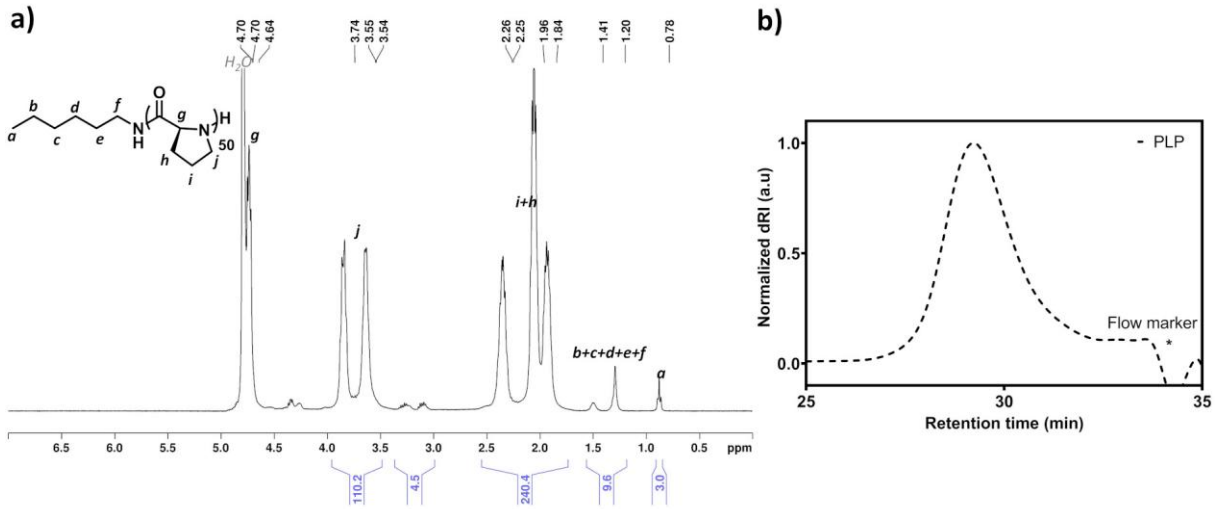

Figure IV-6. (a) ^{1}H NMR spectrum of PLP in D_2O for a targeted DP of 50. (b) SEC chromatogram of PLP in ACN/AcOH buffer (detection by differential refractive index).

IV.3.2. Aqueous ROPISA initiated by poly(*L*-proline) of various NCAs

Subsequently, the PLP was used as a macroinitiator of aqueous ROPISA following the same experimental conditions as the one used with PSar-NH_2 and with 20 equivalents of BLG-NCA (Section IV.2.2). After stirring for one night, a milky solution was obtained. Following dialysis and freeze-drying, the obtained copolymer was first analyzed by ^{1}H NMR. The result indicated that the block copolymer exhibited a molar mass that was similar to the targeted value (M_n = 10 900 g.mol^{-1}, DP_{PBLG} = 25; Table IV-1, Figure SIV-3).

Table IV-1. Macromolecular characteristics of diblock copolymers obtained by ROPISA with poly(proline) as macroinitiator.

Copolymer	Monomer	Theory		^{1}H NMR			Yield (%)	DLS
		M_n [g.mol^{-1}]	τs [wt%]	M_n [g.mol^{-1}] [a]	DP [a]	$D \times 10^{-10}$ [m².s^{-1}] [b]		D_Z [nm] (σ) [c]
PLP		5 000				1.05 ± 0.01		
PLP-*b*-PBLG	BLG	9 900	7	10 900	25	0.97 ± 0.04	89	402 ± 7 (0.25 ± 0.03)
PLP-*b*-PLys(Boc)	*L-NBoc*Lys	9 600	7	9 400	19	0.89 ± 0.04	78	129 ± 1 (0.21 ± 0.01)
PLP-*b*-PGly	Gly	6 200	7	6 000	17	0.98 ± 0.17	85	90 ± 1 (0.18 ± 0.01)

[a] Number average molar-mass (M_n) and degree of polymerization (DP) determined by ^{1}H NMR in TFA-*d*. [b] Diffusion coefficient (D) determined by DOSY ^{1}H NMR in TFA-*d* using a monoexponential fit. [c] Hydrodynamic Z-average diameter (D_Z) and polydispersity (s) determined by DLS at 90°.

Given the diblock copolymer's insolubility in conventional SEC solvents, DOSY-NMR spectroscopy was performed. This technique serves as an alternative to the SEC, providing insights into chain extension occurrence.[17] The DOSY technique enables the determination of the diffusion coefficient (D), which is directly related to the hydrodynamic radius (r_h) of a species via the Stokes-Einstein relation, with T the temperature, k_B the Boltzmann constant and η the solvent bulk viscosity:

$$D = \frac{k_B T}{6\pi\eta r_h} \quad (1)$$

r_h can be correlated to the average molecular weight of the polymer via the empirical Rouse-Zimm model,[18]

$$r_h \sim bM^{-\nu} \quad (2)$$

where b and ν are arbitrary parameters, and M the molecular weight.

It should be noted that the objective was not to determine the precise molar mass. Rather comparisons of diffusion coefficients were used to infer chain extension. A decrease in diffusion coefficient would indicate an increase in molecular weight, suggesting successful chain extension. The diffusion coefficient of PLP was measured at (1.05 ± 0.01) × 10^{-10} m².s^{-1}, which decreased to (0.97 ± 0.04) × 10^{-10} m².s^{-1} after ROPISA, consistent with an increase in molecular weight (Table IV-1, Figure IV-7). Moreover, the absence of residual PLP macroinitiator signals in the PLP-*b*-PBLG spectrum supports the conclusion of quantitative side chain extension.

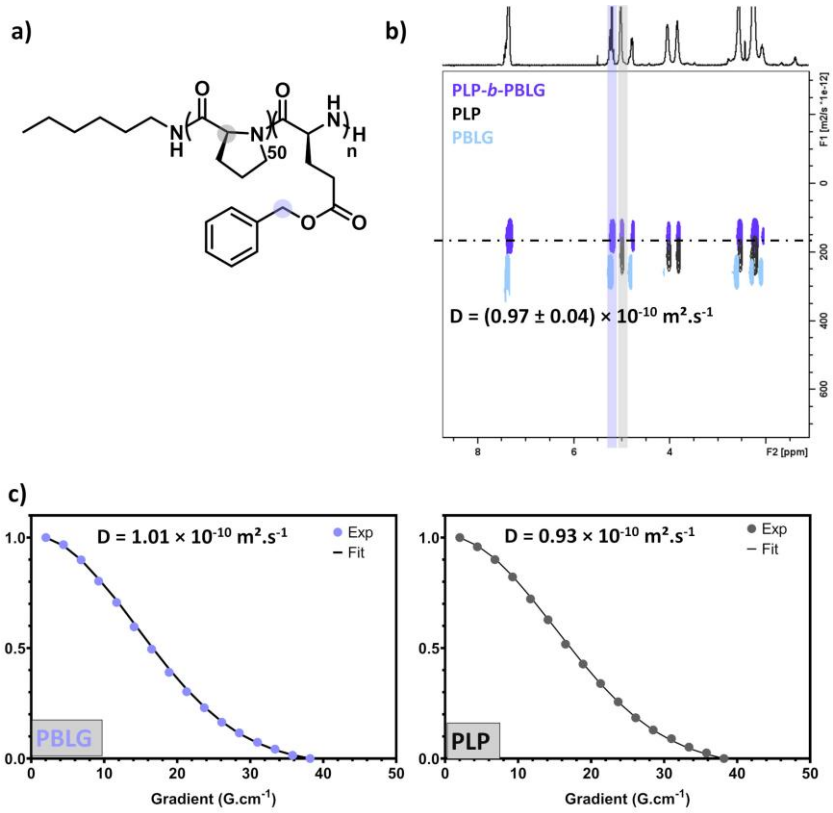

Figure IV-7. (a) Chemical structure of PLP-*b*-PBLG. (b) ^{1}H diffusion ordered NMR spectroscopy (DOSY) spectra of PLP (black), PLP-b-PBLG (purple) and PBLG (blue) in TFA-*d*. (c) Determination of diffusion coefficient for PBLG ester protons (5.2 ppm) and for PLP backbone protons (4.9 ppm) in PLP-*b*-PBLG using monoexponential function fitting.

Subsequently, the milky solution was subjected to investigation through the means of light scattering (Figure SIV-6a,b) and electronic microscopy (Figure IV-8a,b). DLS analyses revealed the presence of nanoparticles with Z-average diameters of 402 ± 7 nm with polydispersity index values of 0.25 ± 0.03. TEM and cryo-TEM images revealed the presence of elongated, branched nanoparticles. These results highlight that the nature of the hydrophilic macroinitiator significantly influences the final nanoparticle morphology. This effect is likely attributable to the unique conformation of PLP II, in contrast to random coil polymers such as PEG or PSar, which lack a defined structure. The versatility of PLP as a macroinitiator in ROPISA was then investigated by varying the NCA monomers. ε-tert-butyloxycarbonyl-*L*-lysine NCA (Lys(Boc)-NCA) and glycine NCA (Gly-NCA) were consequently used at 20 equivalents of monomer, employing the conditions that had been previously established with BLG-NCA. After stirring vigorously for one night and purification by dialysis against ultra-pure water, the resulting copolymers were analyzed using ^{1}H NMR (Figure SIV-4, Figure SIV-5) and DOSY-NMR (Figure IV-9, Figure IV-10). Indeed, the insolubility of PLP-*b*-PLys(Boc) and PLP-*b*-PGly in conventional SEC solvent precluded the use of SEC analysis. It is noteworthy that ^{1}H NMR measurements were conducted in TFA-*d*, the only solvent in which the copolymers were soluble. This also resulted in the deprotection of the Boc protecting group. Consistent with the results obtained in the BLG case, ^{1}H NMR analysis indicated that the molar masses closely matched the targeted values. DOSY spectroscopy provided additional evidence for successful chain extension in the case of PLP-*b*-PLys(Boc), as indicated by a diffusion coefficient of (0.89

± 0.04) × 10^{-10} $m^2.s^{-1}$ that was found smaller than those of the initial PLP, and the absence of residual PLP signals (Table IV-1, Figure IV-9).

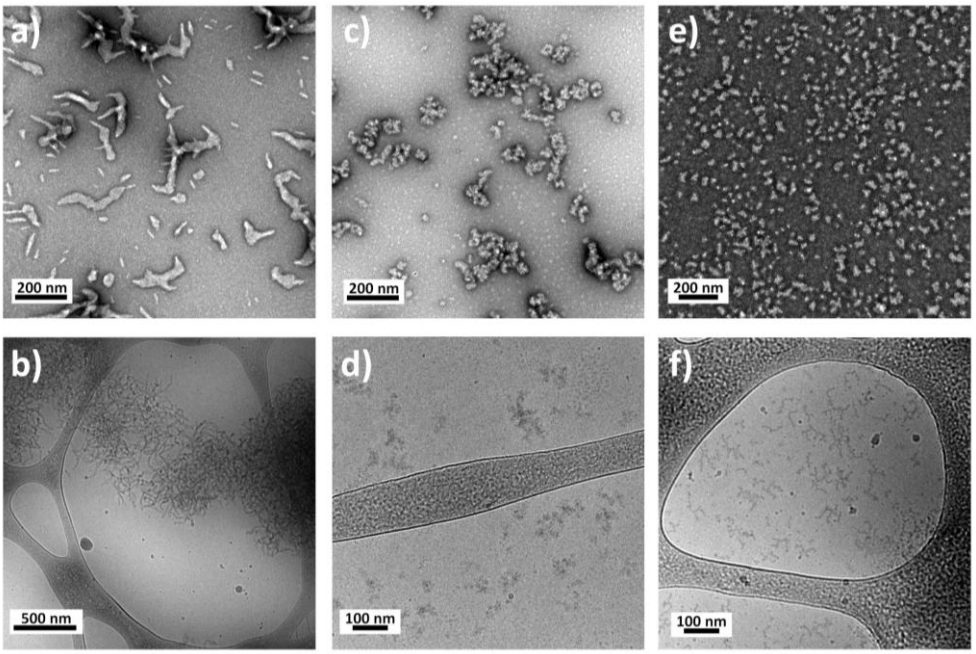

Figure IV-8. Representative TEM (top) and Cryo-TEM (right) images of (a-b) PLP-*b*-PBLG, (c-d) PLP-*b*-PLys(Boc) and (e-f) PLP-*b*-PGly suspensions.

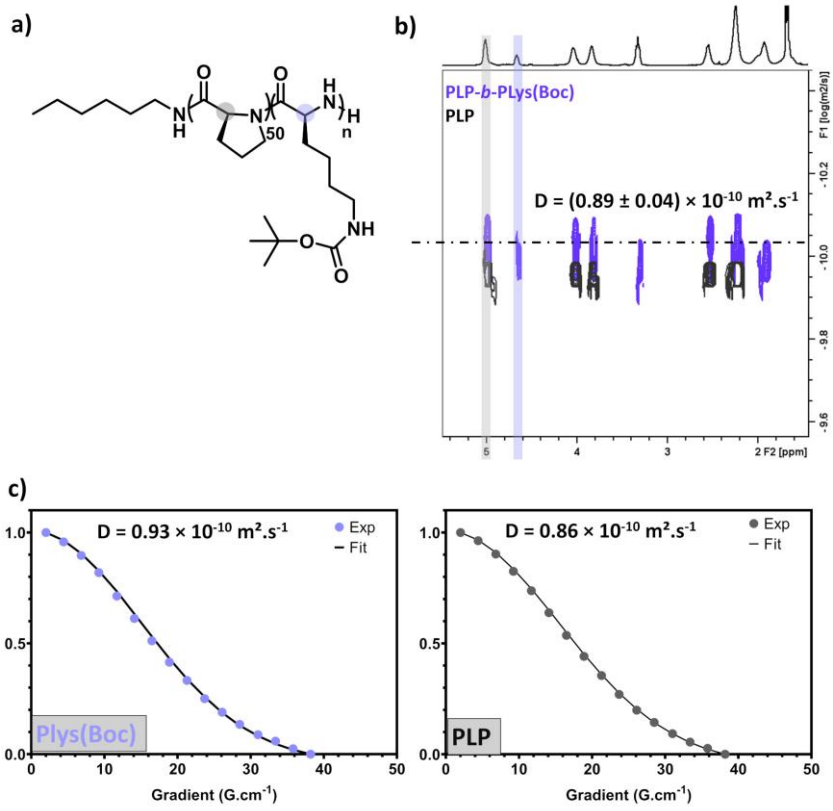

Figure IV-9. (a) Chemical structure of PLP-*b*-PLys(Boc). (b) ^{1}H diffusion ordered NMR spectroscopy (DOSY) spectra of PLP (black) and PLP-*b*-Lys(Boc) (purple) in TFA-*d*. (c) Determination of diffusion coefficient for PLys(Boc) backbone protons (4.6 ppm) and for PLP backbone protons (5 ppm) in PLP-*b*-Lys(Boc) using monoexponential function fitting.

However, for PLP-*b*-PGly, despite the smaller average diffusion coefficient observed (0.99×10^{-10} $m^2.s^{-1}$;Table IV-1, Figure IV-10), the signal from the PGly backbone exhibited faster diffusion than the PLP macroinitiator. This result suggests the presence of PGly oligomers mixed with the copolymers, likely resulting from water-initiated polymerization of Gly-NCA. The secondary amine in PLP is inherently less reactive than primary amines, which could lead to slower aminolysis compared to hydrolysis for certain monomers. This effect appears to be particularly pronounced for Gly-NCA, which is more hydrophilic than BLG and Lys(Boc),[19] further facilitating hydrolysis over chain extension.

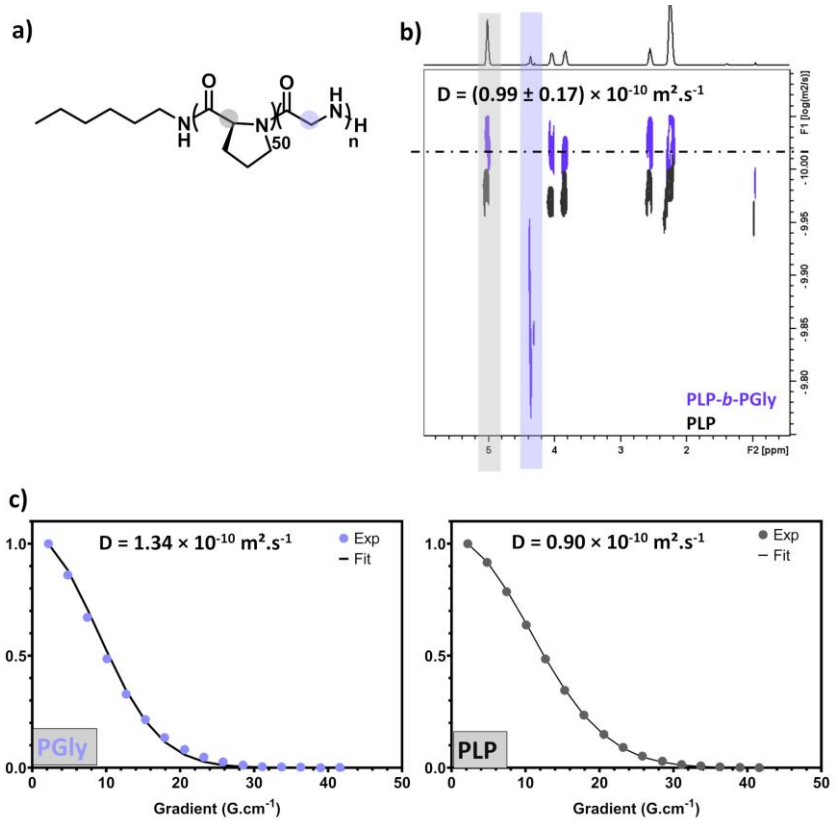

Figure IV-10. (a) Chemical structure of PLP-*b*-PGly. (b) ^{1}H diffusion ordered NMR spectroscopy (DOSY) spectra of PLP (black) and PLP-*b*-PGly (purple) in TFA-*d*. (c) Determination of diffusion coefficient for PGly backbone protons (4.35 ppm) and for PLP backbone protons (5 ppm) in PLP-*b*-PGly using monoexponential function fitting.

In conclusion, the study demonstrates that PLP can serve as a macroinitiator for the ROPISA of BLG-NCA and Lys(Boc)-NCA, as confirmed by ^{1}H NMR and DOSY-NMR analyses. However, the polymerization of Gly-NCA exhibited uncertain control, as indicated by the DOSY-NMR results. The absence of additional analytical methods capable of fully characterizing the copolymer structure hinders the determination of the success of the chain extension. Optimizing polymerization conditions, such as increasing the solid content, can enhance the efficiency of the process, as discussed in **Chapter II**.

In both suspensions, a bluish opalescence was still present, indicating the presence of nanoparticles. Investigations on nanoparticle suspensions after dialysis by DLS revealed smaller Z-average diameters compared to PLP-*b*-PBLG nanostructures, with 129 ± 1 nm for PLP-*b*-PLys(Boc) and 90 ± 1 nm for PLP-*b*-PGly, with polydispersity index of 0.21 ± 0.01 and 0.18 ± 0.01 respectively (Table IV-1, Figure SIV-6).

Notably TEM and cryo-TEM imaging (Figure IV-8) revealed different nanoparticles morphologies: "popcorn-like" structures with Lys(Boc) and small fibrils with Gly, resembling those obtained with PEG initiation as discussed in **Chapter III**. These findings highlight the significant influence of the monomer on self-assembly when PLP was used as a macroinitiator.

IV.3.3. Thermoresponsive properties

Given that PLP is a thermoresponsive polymer, the subsequent step of the study was to monitor the thermally induced phase transition behavior of the nanomaterials. To this end, the first objective was to monitor the change in absorbance (at 550 nm) of the PLP-*b*-PBLG dispersion while increasing the temperature at a rate of 1 °C.min^{-1} (Figure IV-11). A clear cloud point was observed at 76 °C confirming the LCST aggregation properties of the PLP at the surface of the nanomaterial. After a 10 minutes isotherm at 85 °C, the solution was cooled down by 1 °C.min^{-1} and a clearing point temperature was found at a much lower temperature of 4 °C. This revealed a hysteresis width of over 50 °C provided by the polypeptide shell, in agreement with the thermoresponsiveness of the PLP alone. The local aggregation of the PLP shell was further confirmed by Cryo-TEM analysis performed before and after heating as shown in Figure IV-11.

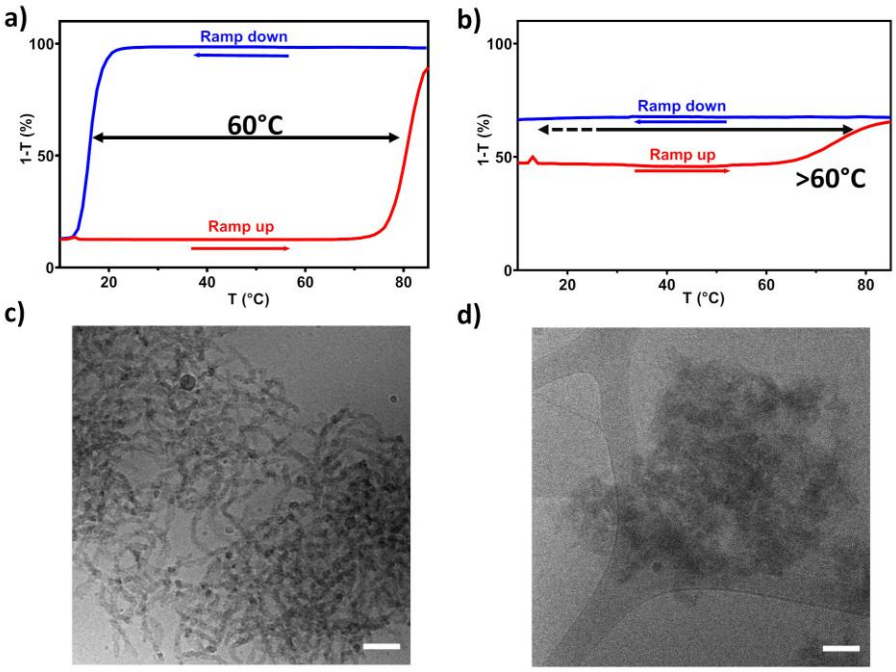

Figure IV-11. (a-b) Transmission- normalised (λ_{abs}= 550 nm) turbidimetry curves for PLP (a) and PLP-*b*-PBLG solution (b) as function of temperature in pure water at 0.4 mg.mL^{-1}. (c-d): PLP-*b*-PBLG suspension observed before heating (c) and after heating up to 80°C and cooling down at RT (d) by cryo-TEM. Scale-bar: 100 nm.

We then conducted the same measurement of absorbance as a function of temperature with the PLP-*b*-PLys(Boc) and PLP-*b*-PGly suspensions (Figure IV-12). The analysis revealed a cloud point at 73 °C for PLP-*b*-PLys(Boc) with a clearing point at 15 °C, exhibiting hysteresis over 50 °C. Unfortunately, no Cryo-TEM has been conducted on this system after heating. For PLP-*b*-PGly, the analysis was less conclusive, indicating two potential aggregation steps at approximately 63 °C and 78 °C (Figure IV-12b).

This behavior could be attributed to the presence of glycine oligomers and/or unreacted free PLP. Further investigation using DLS revealed hysteresis values that diverged from those obtained via turbidimetry, although similar cloud points were observed around 64 °C and 74 °C. Notably, the clear point was observed to be considerably higher in DLS (≈ 35 °C) compared to turbidimetry (≈ 14 °C). This discrepancy may be attributed to the reduced volume used in DLS. Additionally, elevated temperatures, which could concentrate the sample, may also affect the clear point. Further analyses are necessary to elucidate these observations and their potential implications.

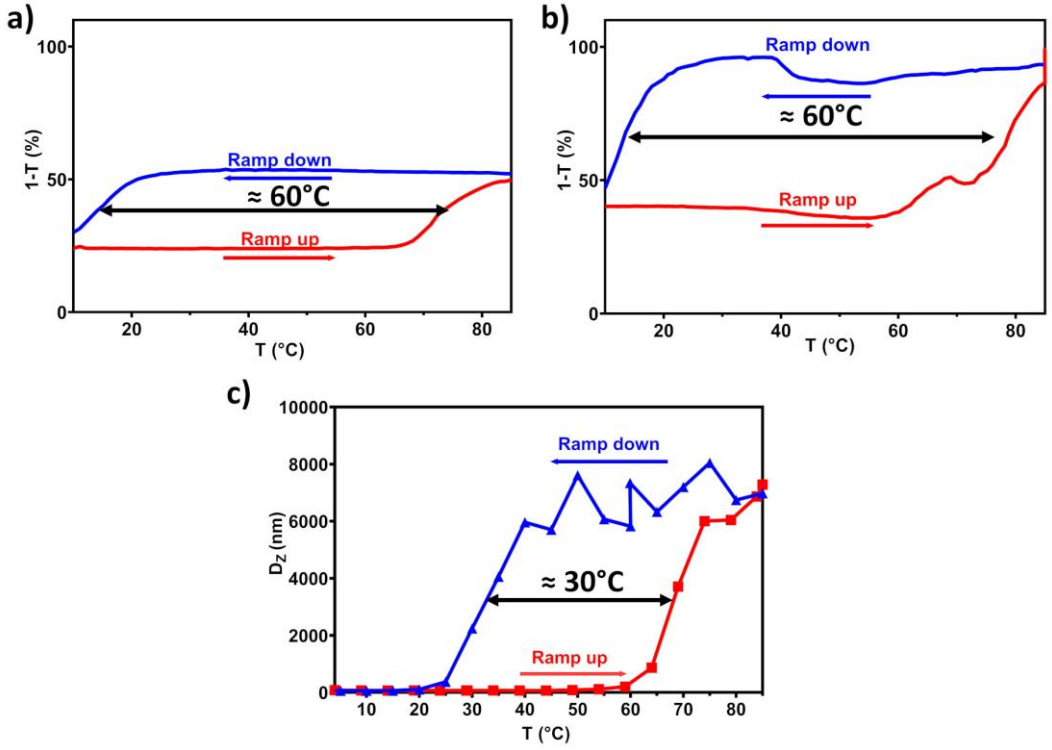

Figure IV-12. (a) Transmission-normalized (λ_{abs}=550 nm) turbidimetry curves for PLP-*b*-PLys(Boc) (a) and PLP-*b*-PGly solution (b) as function of temperature in pure water at 0.4 mg.mL^{-1}. (c) Evolution of the scattered light intensity with temperature of a PLP-*b*-PGly solution of in pure water at 0.4 mg.mL^{-1}.

In summary, the results demonstrate the efficacy of poly(*L*-proline) as a functional polypeptide macroinitiator, which successfully stabilized the ROPISA of BLG-NCA. The initiation process was confirmed through DOSY analysis, with diffusion coefficients indicating effective chain extension. The polymerization process exhibited high yields, thereby validating the versatility of PLP as a macroinitiator for diverse NCAs, including Lys(Boc) and Gly. The resulting copolymers were found to form distinct nanoparticles, as characterized by DLS and transmission electron microscopy. The influence of PLP on the self-assembly behaviors resulted in morphologies that were dependent on the monomer used. With Lys(Boc), "popcorn-like" particles were obtained, while fibrils formed with Gly, mirroring observations from PEG macroinitiators. These findings highlight the role of PLP in influencing nanoparticle structure. The thermoresponsive behavior of PLP was retained in the nanoparticles, resulting in local aggregation of PLP in the nanoparticle shell. Despite its potential advantages, PLP poses significant challenges in the context of controlling the polymerization of hydrophilic monomers like Gly-NCA. DOSY NMR indicated

the presence of glycine oligomers, likely due to faster hydrolysis of the NCA compared to aminolysis of PLP's secondary amine. The optimization of reaction conditions, such as the reaction medium as discussed in **Chapter II**, holds potential in addressing these challenges and improve polymerization outcomes.

IV.4. Aqueous ROPISA initiated by elastin-like polypeptide

In a further step toward protein–polymer conjugates, sequence-controlled recombinant elastin-like polypeptide (ELP) presenting a protein-like thermoresponsive character that preferentially results in the formation of coacervates[20] was also employed as macroinitiator. ELP primary structure consists of repeating [-Val-Pro-Gly-Xaa-Gly-] pentapeptide sequences, where Xaa represents any amino acid except proline. ELPs exhibit structural similarities to intrinsically disordered proteins naturally present in the body, such as tropoelastin.[21] The repeat sequences within the biopolymer, along with the monomer composition and chain length, define the unique structure of each ELP and significantly influence its LCST, commonly referred to as the transition temperature (T_t). ELPs have emerged as a class of protein-like polymers with considerable promise for biomedical applications due to their advantageous properties, including precise and reproducible chemical structure, high production yields, and scalability. They are also known to be nonimmunogenic, non-pyrogenic and biocompatible.[22] Their stimuli-responsive properties further enable non-chromatographic purification and self-assembly in the absence of organic solvents. Consequently, the development of amphiphilic block copolymers incorporating ELP as the hydrophilic segment and a synthetic polymer as the hydrophobic counterpart has gained increasing interest. Several studies have reported the conjugation of ELP with various polymer segments, including poly(γ-benzyl-*L*-glutamate),[23] poly(*L*-glutamic acid),[24] poly(aspartic acid),[25] poly(ethylene glycol),[26] polyelectrolytes,[27] and polysaccharides.[28] We then aimed to utilize aqueous ROPISA to initiate polymerization on the *N*-terminal of ELP, enabling the *in situ* formation of protein-polypeptide conjugate self-assembling into nanoparticles. The ELP used in this study were recombinantly prepared using *Escherichia coli* as an expression system,[29] as illustrated in Figure IV-13.

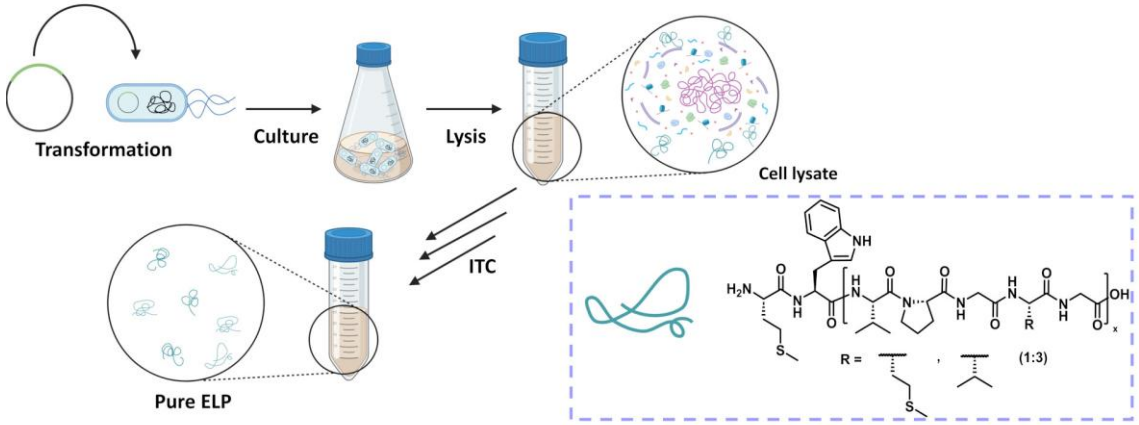

Figure IV-13. Schematic representation of elastin-like polypeptide (ELP) recombinant production. ELP gene is first designed by genetic engineering and transfer in a plasmid, which is introduced in *E. coli*. Bacterial clones are cultured, and recombinant protein production is triggered. ELP is extracted by bacterial lysis and purified by Inverse Transition Cycling (ITC). In the purple box, the chemical structure of ELPM. Adapted from Lecommandoux *et al.*[29]

IV.4.1. Aqueous ROPISA initiated by elastin-like polypeptide of various chain length

The initial ELP used as a macroinitiator was designated as ELPM40 (M_n = 17,035 g.mol^{-1}, Figure SIV-7). This ELP had previously been used as a macroinitiator for the ROP of BLG-NCA under anhydrous conditions, thereby ensuring effective control over polymerization with low dispersity in the resulting copolymers.[23] Moreover, the amphiphilic diblock copolymers obtained could self-assemble into various nanostructures, including spherical and worm-like micelles, as well as vesicles, using solvent displacement techniques such as dialysis and microfluidics. To maintain controlled polymerization and prevent excessive aggregation, the reaction was conducted at 4 °C with a solid content of 0.5 wt%. The critical aggregation concentration (CAC) was determined to be 2.7 mg.mL^{-1} through fluorescence analysis using Nile Red (Figure IV-14a). At 0.5 wt%, the initial ELP concentration (3.7 mg.mL^{-1}) slightly exceeded the CAC, thereby ensuring solubility while limiting premature aggregation. In contrast, increasing the solid content to 7 % would raise the ELP concentration to 37 mg.mL^{-1}, inducing substantial aggregation and reduced accessibility of free amines, ultimately impeding the desired controlled polymerization process. A study of the aqueous ROPISA of BLG-NCA with 20 equivalents under these conditions yielded solutions of well-defined copolymers in high yield (approximately 90%), as confirmed by ^{1}H NMR, with a DP consistent with the monomer feed ratio (DP_{PBLG} = 22), and narrow molar mass dispersity ($Đ$ = 1.03) as revealed by SEC (Table IV-2, Figure III-13, Figure SIV-8,).

Table IV-2. Macromolecular characteristics of diblock copolymers obtained by ROPISA with elastin-like polypeptides as macroinitiators.

Macro-initiator	Copolymer	Theory		SEC		^{1}H NMR		Yield (%)	DLS
		M_n [g.mol^{-1}]	τs [wt%]	M_n [g.mol^{-1}] [a]	$Đ$ [a]	M_n [g.mol^{-1}] [b]	DP [b]		D_Z [nm] (σ) [c]
ELPM20		8 697	-	12 900	1.02	-	-	-	-
	ELP20-*b*-PBLG	3 100	0.5	14 600	1.02	14 600	27	85	133 ± 3 (0.38 ± 0.01)
ELPM40	-	17 035	-	25 600	1.02	-	-	-	-
	ELP40-*b*-PBLG	21 400	0.5	27 700	1.03	21 900	22	93	83 ± 1 (0.15 ± 0.01)
ELPM80	-	3 735	-	48 200	1.06	-	-	-	-
	ELP80-*b*-PBLG	8 100	0.5	49 100	1.06	36 800	14	72	253 ± 10 (0.25 ± 0.02)

[a] Number average molar-mass (M_n) and molar-mass dispersity determined by SEC in DMF +1% LiBr using PS calibration, [b] Number average molar-mass (M_n) and degree of polymerization (DP) determined by ^{1}H NMR in in DMSO-d_6. [c] Hydrodynamic Z-average diameter (D_Z) and polydispersity (σ) determined by DLS at 90°.

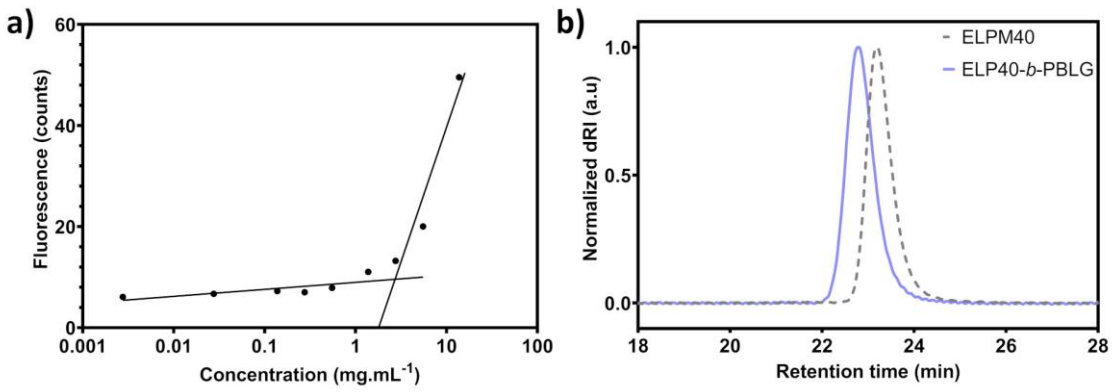

Figure IV-14. (a) CAC determination of ELPM40 in pure water at 4 °C by using Nile Red and by measuring fluorescence at 650 nm. CAC is defined as the concentration at the intersection of the two logarithms regression $y = a - b \times \ln x$. (b) SEC chromatograms of ELP40-*b*-PBLG compared to ELPM40 homopolymer in DMF (+1% LiBr, detection by differential refractive index).

In a similar manner, ELPM20 and ELPM80 were used as macroinitiators under the same conditions as ELPM40. The efficacy of chain extension of ELPs of varying sizes was substantiated by the presence of well-defined copolymers, as evidenced by ^{1}H NMR analysis, which indicated DPs of 27 and 14 for ELP20-*b*-PBLG and ELP80-*b*-PBLG, respectively (Figure SIV-8), and by SEC, which showed dispersity values below 1.1 (Figure IV-15). However, for ELP80-*b*-PBLG, the DP of PBLG was slightly lower than the targeted value, which may be attributed to steric hindrance or reduced accessibility of the initiating sites in the larger ELP macroinitiator.

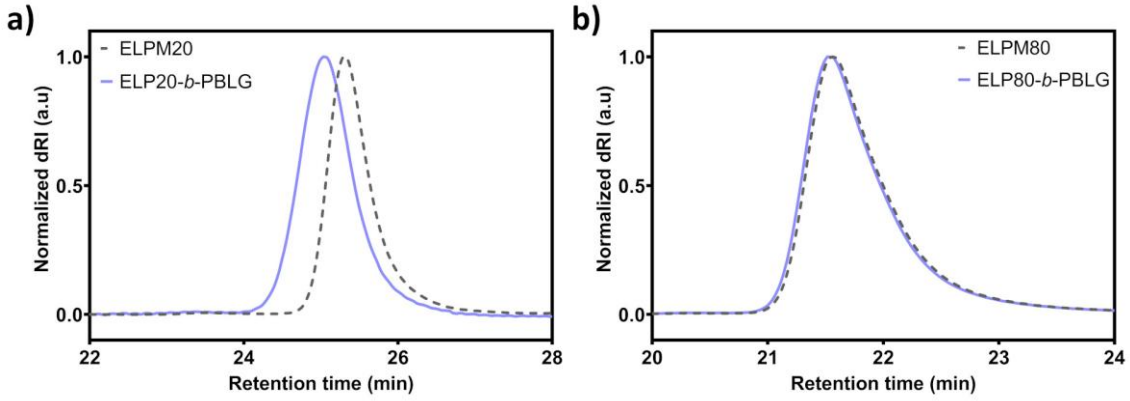

Figure IV-15. SEC chromatograms of (a) ELP20-*b*-PBLG compared to ELPM20 homopolymer and (b) ELP80-*b*-PBLG compared to ELPM80 homopolymer in DMF (+1% LiBr, detection by differential refractive index).

Next, we studied the resulting nanomaterial suspensions by light scattering and microscopy. Initiating ROPISA with the recombinantly synthetized ELPM40 yielded homogeneous cocoon-like nano-objects with a Z-average diameter of 83 ± 1 nm with low dispersity (σ = 0.15 ± 0.01), displaying much less anisotropy than in the case of PSar and PLP initiation (Table IV-2, Figure SIV-9a,b, Figure IV-16).

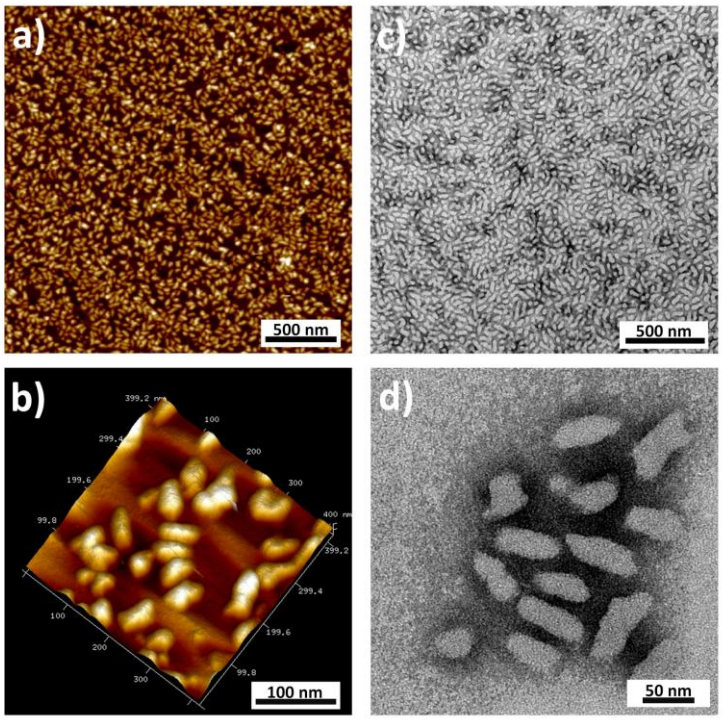

Figure IV-16. Nanoparticles obtained upon aqueous ROPISA initiated by ELPM40. (a-b): Observed by AFM. (c-d): Observed by TEM.

For ELPM20 and ELPM80, the Z-average diameters of the nanoparticles were larger compared to those of ELPM40, with values of 133 ± 3 nm and 253 ± 10 nm, respectively (Table IV-2, Figure SIV-9c,f). In addition, the polydispersity indices were higher ($\sigma > 2$), reflecting increased size heterogeneity within the nanoparticle populations formed with these macroinitiators. TEM microscopy confirmed these findings, showing the same cocoon-like morphology in all samples, but with varying degrees of size heterogeneity (Figure IV-17). In particular, ELP20-*b*-PBLG showed greater anisotropy in nanoparticle structures, while ELP80-*b*-PBLG revealed two distinct populations: smaller cocoon-like particles and larger aggregates. This suggests that the size of the ELP macroinitiator significantly impacts both the morphology and the uniformity of the resulting nanoparticle assemblies.

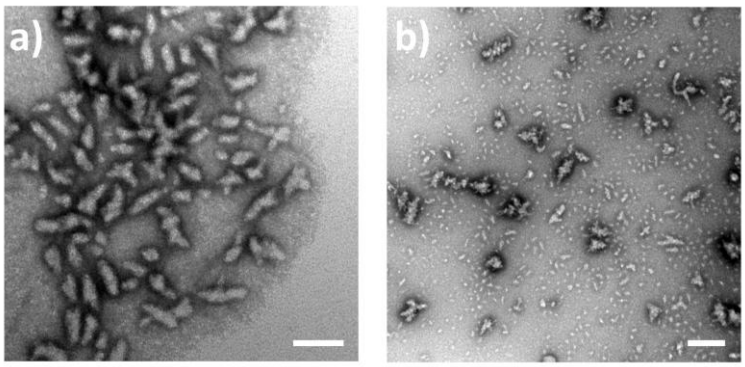

Figure IV-17. Representative TEM images of (a) ELP20-*b*-PBLG and (b) ELP80-*b*-PBLG nanoparticle suspensions. Scale-bar: 200 nm.

IV.4.2. Thermoresponsive properties

We then monitored the nanoparticle suspension of ELP40-*b*-PBLG by light scattering analysis while increasing the temperature at a rate of 2 °C.min^{-1}. Interestingly, the scattered light intensity (measured as the derived count rate (DCR); Figure IV-8a) was found to increase below the cloud point temperature of the pure ELP (*i.e.*, 32 °C at 1 mg.mL^{-1}; Figure IV-8b) as expected from the covalent fusion of a hydrophobic peptide (PBLG) to the ELP. The decrease in DCR is correlated with an increase in nanoparticle density due to the dehydration of the ELP on the surface of the nano-objects.[30–32] It is accompanied by a decrease in the diameter of the object of about 20% due to this dehydration, which leads to a shrinking of the ELP shell. However, no aggregation of the nanomaterial was observed, in contrast to the analysis performed with the ELP alone in solution (Figure IV-8b), showing that the nanoparticles remained colloidally stable.

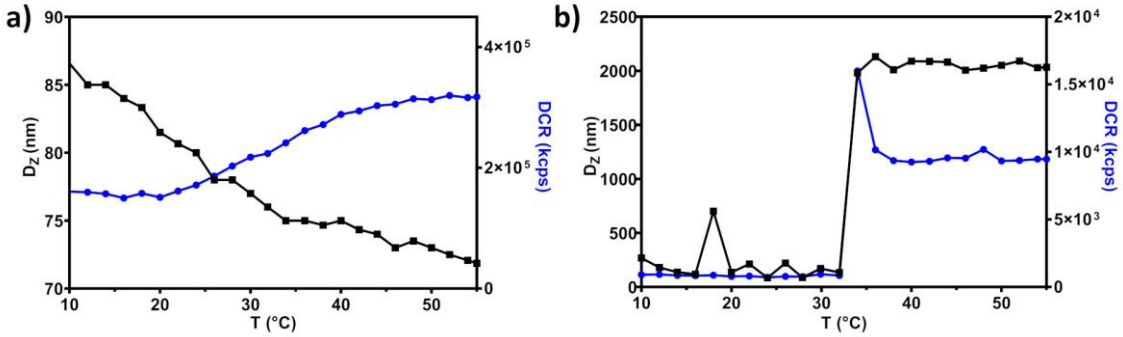

Figure IV-18. Evolution of the scattered light intensity with temperature of a solution of (a) ELP40-*b*-PBLG and (b) ELPM40 in pure water at 1 mg.mL^{-1}.

The same study was performed with ELPM20 and ELPM80-based nanoparticles. No transition was observed for ELP20-*b*-PBLG nanoparticles (Figure IV-19a). However, it is worth noting that the chain length of ELP with identical sequence and concentration has an effect on the cloud point temperature.[33] The transition temperature for ELPM20 at 1 mg.mL^{-1} is approximately 50 °C, while measurements were only made up to 55 °C (Figure IV-19b). This suggests that the transition temperature for the nanoparticles may exceed the applied temperature range. In contrast, a transition was observed for ELP80-*b*-PBLG nanoparticles, as indicated by an increase in Z-average diameter and a decrease in derived count rates around 30 °C (Figure IV-19c), which corresponds to the transition temperature of ELPM80 at 1 mg.mL^{-1} (Figure IV-19d). This behavior was different from that of ELP40-*b*-PBLG nanoparticles. The observed increase in hydrodynamic size is consistent with the hydrophobic transition of ELPs, which favors aggregation. However, the concomitant decrease in scattering intensity suggests that these aggregates become less detectable, either due to the partial sedimentation, changes in optical contrast, or increased polydispersity. To confirm this hypothesis, complementary techniques such as turbidity measurements, static light scattering (SLS), or microscopy (Cryo-TEM) would be valuable to further elucidate the structural organization of the nanoparticles at elevated temperatures.

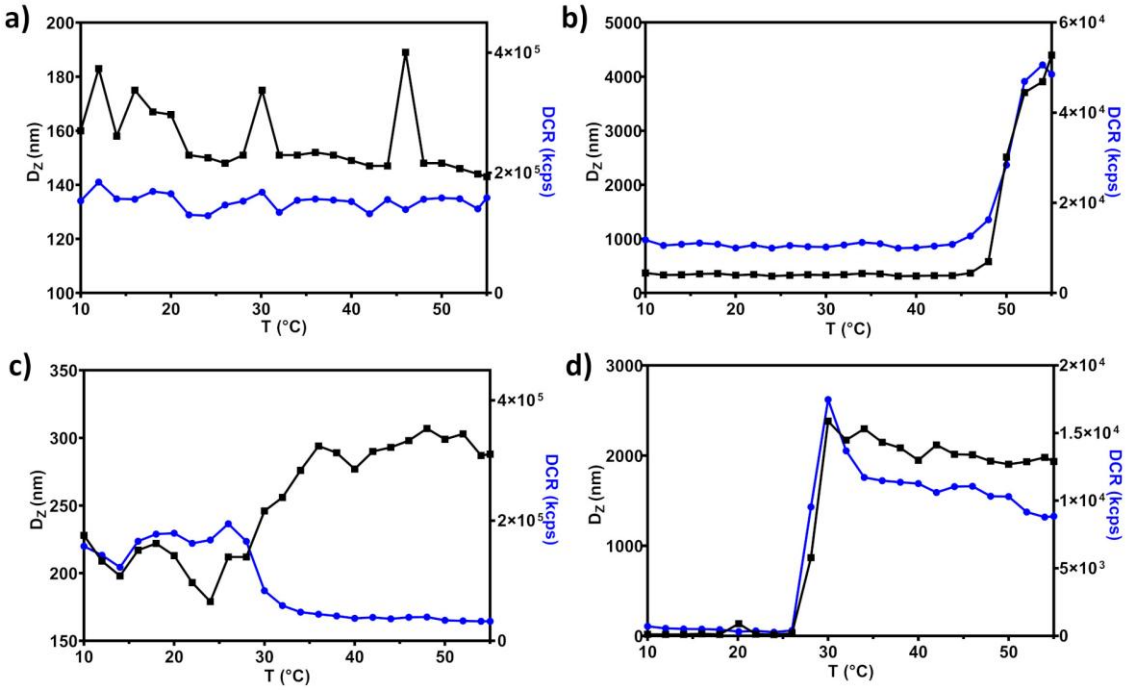

Figure IV-19. Evolution of the scattered light intensity with temperature of a solution of (a) ELP20-*b*-PBLG, (b) ELPM20, (c) ELP80-*b*-PBLG and (d) ELPM80 in pure water at 1 mg.mL^{-1}.

Overall, the use of elastin-like polypeptides as macroinitiators for the ROPISA of BLG-NCA successfully led to the formation of well-defined block copolymers and self-assembled anisotropic nanoparticles with a characteristic cocoon-like morphology. These nanoparticles exhibited thermoresponsive behavior, with a transition temperature dependent on the ELP block length. However, establishing a clear trend between ELP chain length and thermoresponsive properties proved difficult, possibly due to variations in nanoparticle definition and stability. The significant influence of the macroinitiator suggests that factors such as intermolecular interactions and hydration differences may play a key role in both self-assembly and thermal responsiveness.

In conclusion, using aqueous ROPISA of NCA monomers, we present an efficient process to obtain protein–polymer conjugates and polymeric nanomaterials that are entirely composed of amino acid residues, in high yield and with high purity. This ROPISA method is easy to implement, can involve the native amines of any polypeptide structures, and is time efficient. To the best of our knowledge, this work also demonstrates for the first time the feasibility of synthesizing fully biodegradable nanoparticles in aqueous media using a PISA approach.[34] Moreover, as proved with thermoresponsiveness in this work, the use of polypeptides or proteins opens the field to many possible functional nanomaterials that take advantage of the great chemical diversity of amino acids.

IV.5. Enzyme-polypeptide conjugates via aqueous ROPISA

Encouraged by these results, where protein-polymer conjugates were obtained and the intrinsic properties of the protein were retained, we believed that ROPISA could also be used to create enzyme-

polymer conjugates. Enzymes are highly sensitive to their environment, with factors such as extreme pH, temperature, and exposure to polar solvents leading to denaturation and loss of function. In addition, enzymes are susceptible to inactivation due to their own activity, particularly when radicals generated during catalysis interact with the enzyme, resulting in oxidative self-inactivation.[35] To overcome these challenges and prolong enzyme stability, various strategies have been employed. One common approach is the covalent immobilization of enzymes, which can prevent denaturation and increase their stability.[36] Alternatively, enzymes can be conjugated, either covalently or noncovalently, with protective stabilizing polymers, to provide a protective shield that helps maintain their activity under harsh conditions.[37] Most commonly, PEGylation, the conjugation of poly(ethylene glycol) to enzymes, is used to improve their stability and circulation time *in vivo*.[38] However, PEGylation has recently raised concerns, particularly due to the "PEG dilemma" discussed in **Chapter I**. As a result, alternative strategies have been explored, one of which is PEPylation, the conjugation of polypeptides to enzymes.[39] This approach offers a promising alternative that may address some of the limitations associated with PEGylation. However, PEPylation is mainly achieved by a "grafting-to" strategy, in which preformed polypeptides are conjugated to the enzyme. Alternatively, PISA has been explored to synthesize enzyme-polymer conjugates via a "grafting-from" approach, using enzymes as macroinitiators in RAFT-PISA reactions.[40,41] While this method has shown promising results, preserving enzymatic activity and site-selectivity, the resulting polymers are not degradable, which may limit their biomedical applications.

In this section, we propose the implementation of ROPISA in the development of fully amino acid-based enzyme-polymer conjugates. This approach aimed at using enzymes as macroinitiators, eliminating prior chemical modification. This approach could therefore entail the direct initiation of polymerization through naturally occurring amines, such as lysine residues. Moreover, this method aimed at preserving the native structure and activity of the enzyme. ROPISA offers a unique advantage by enabling polymerization under mild, non-denaturing conditions, allowing for the formation of biocompatible and biodegradable protective polymer coatings on enzymes. This strategy also constitutes a potential alternative to PEGylation, aligning more closely with PEPylation principles while offering degradability and improved biomimetic properties. The main objective of this study was to examine the impact of this conjugation on the catalytic behavior of 3 different metalloenzymes. This research was conducted in collaboration with Alina Elizabeth Torres Aguirre, a PhD student under the supervision of Marcela Ayala at the Instituto de Biotecnología, UNAM. Within the context of a CONACYT project, Alina was responsible for conducting enzymatic characterizations, including electrophoresis gel and enzymatic activity determination.

IV.5.1. Presentation of the enzymes

The three enzymes used in this study are unspecific redox enzymes, including horseradish peroxidase (HRP), laccases (Lac) and versatile peroxidases (VP). Laccases are copper-containing enzymes that utilize oxygen as an electron acceptor,[42] while HRP and VP are heme-containing enzymes that rely on peroxides as electron acceptors.[43]

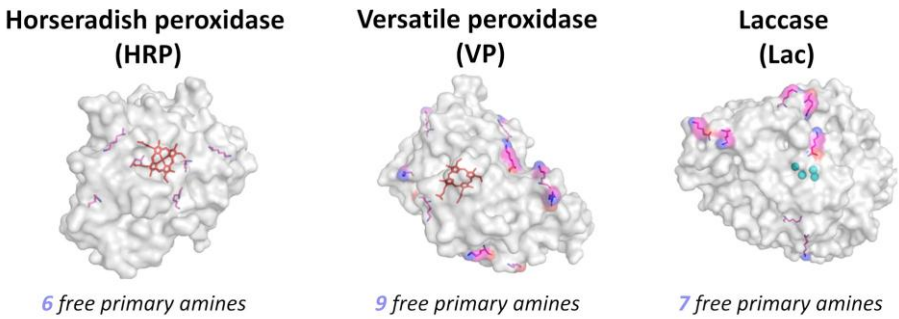

Figure IV-20. Horseradish peroxidase (HRP), Versatile peroxidase (VP) and Laccase (Lac) 3D structures with the free primary amines from the lysine residues highlighted.

IV.5.2. Aqueous ROPISA initiated by metalloenzymes of Gly-NCA and BLG-NCA

IV.5.2.1. HRP

HRP was used as a macroinitiator in the ROPISA of BLG-NCA and Gly-NCA at varying monomer equivalents in 100 µL of 50 mM $NaHCO_3$, conducted in Eppendorf tubes under high stirring for a duration of one night (Table IV-3). Subsequent to dialysis, the samples were initially analyzed by DLS. In all cases, significant light scattering and the presence of large nanoparticles (Z-average diameter ranging from 402 to 528 nm, with polydispersity index σ >2) in suspension were observed, suggesting successful chain extension on the enzyme surface. This assertion is further substantiated by the observation that free enzymes alone do not exhibit substantial light scattering (Table IV-3, Figure SIV-10) verifying that the observed DLS signal is not induced solely by the scattering of the enzyme alone.

Table IV-3. Macromolecular characteristics of enzyme-polypeptide conjugates

Enzyme	Ref	Monomer	Eq/NH_2	τs [wt%]	D_Z [nm] (σ) [a]	DCR [kcps] [a]	Residual activity (%) [b]
HRP	-	-	-	-	9 ± 1 (0.31 ± 0.03)	10 ± 1	-
	HRP-PGly (17 eq)	Gly-NCA	17	1.6	419 ± 27 (0.25 ± 0.02)	1270 ± 30	-
	HRP-PGly (84eq)		84	1.2	470 ± 9 (0.24 ± 0.04)	2130 ± 10	-
	HRP-PBLG (17 eq)	BLG-NCA	17	3.8	402 ± 5 (0.31 ± 0.04)	5170 ± 140	-
	HRP-PBLG (83 eq)		83	2.1	528 ± 6 (0.30 ± 0.06)	1250 ± 40	10
VP	-	-	-	-	135 ± 33 (0.87 ± 0.17)	120 ± 10	-
	VP-PGly	Gly-NCA	100	8.2	448 ± 15 (0.21 ± 0.05)	4210 ± 20	60
	VP-PBLG	BLG-NCA	99	3.8	698 ± 14 (0.36 ± 0.06)	7750 ± 130	27
Laccase	-	-	-	-	51 ± 6 (0.84 ± 0.08)	150 ± 10	-
	Lac-PGly	Gly-NCA	100	3.9	363 ± 11 (0.28 ± 0.05)	970 ± 60	100
	Lac-PBLG	BLG-NCA	100	2.2	675 ± 33 (0.29 ± 0.03)	4790 ± 220	2

[a] Hydrodynamic Z-average diameter (D_Z), polydispersity (σ) and derived count rates (DCR) determined by DLS at 90°. [b] Residual enzymatic activity determined by ABTS assays and relativized based on free enzyme activity.

In addition, SDS-PAGE was performed to verify the chain extension. In the case of HRP-PBLG (84 eq), no residual band corresponding to free HRP was detected, indicating that the enzyme was fully conjugated to the polypeptide (Figure IV-21).

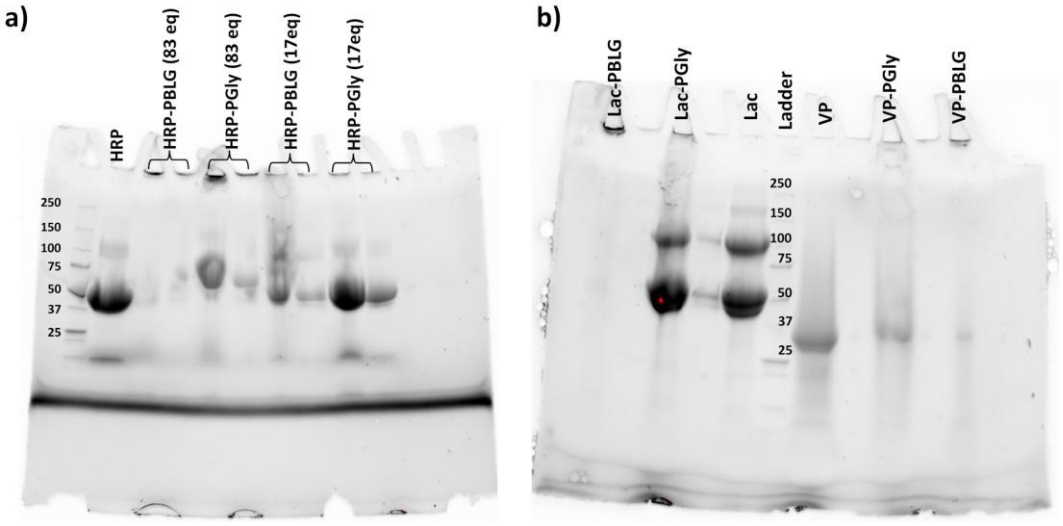

Figure IV-21. SDS-PAGE of (a) HRP and HRP conjugates and (b) Laccase and VP with their conjugates.

Further confirmation was provided by TEM analysis, which revealed the presence of irregular nanoaggregates. This result indicates that the chain extension on the enzyme surface successfully led to

nanoparticle formation in solution. For HRP-PBLG (17 eq), the presence of both free HRP and conjugated material was detected, with the free HRP band remaining visible, indicating incomplete conjugation. TEM images revealed very few nanoaggregates for the glycine-based conjugates (HRP-PGly), and no clear discernible particles were observed for the BLG conjugates under these experimental conditions. Consequently, these experimental conditions were not investigated further.

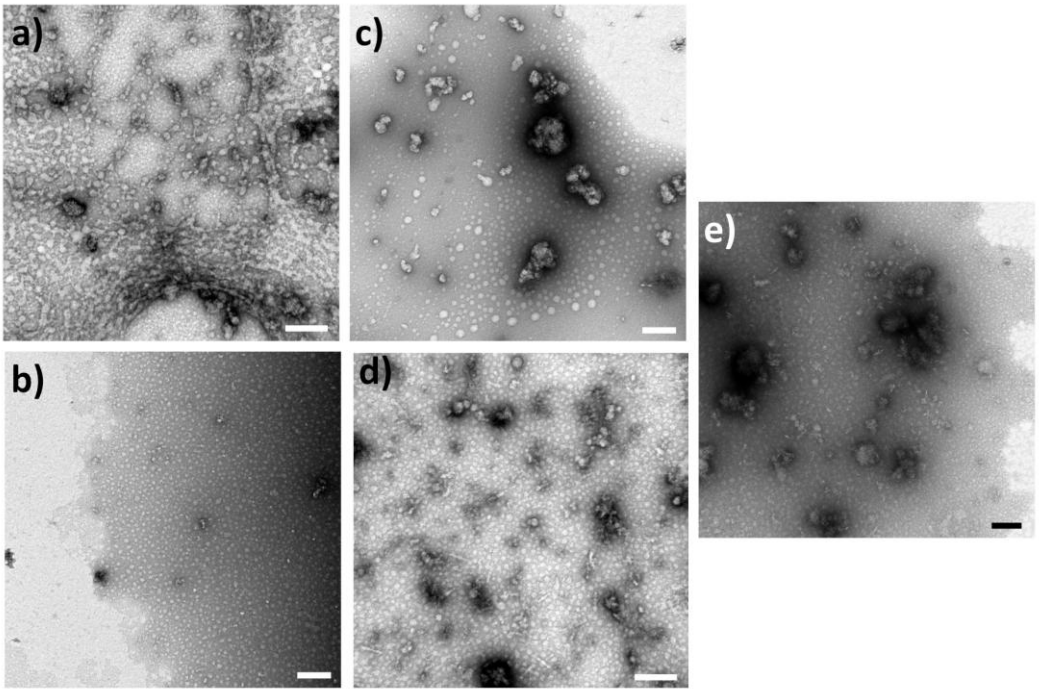

Figure IV-22. Representative TEM images of (a) HRP-PBLG (84 eq), (b) HRP-PBLG (17 eq), (c) VP-PBLG, (d) VP-PGly; (e) Lac-PGly suspensions. Scale bar: 200 nm.

To assess the retention of enzymatic activity following conjugation, we performed enzymatic assays using ABTS as a substrate. The study included the examination of both free HRP and HRP-PBLG (84 eq). The results indicated that HRP-PBLG (84 eq) retained approximately 10% of the activity compared to free HRP (Table IV-3). This decline in activity may be attributable to two factors: first, the pH conditions during the reaction may have altered the enzyme's activity, and second, the steric hindrance introduced by the PBLG polymer could have obstructed substrate diffusion and impaired proper binding within the enzyme's catalytic pocket. To further confirm that the activity detected by UV-vis spectroscopy was indeed from the conjugate, a native gel electrophoresis was performed with HRP-PBLG (84 eq). The gel was submerged in a reaction mixture containing ABTS, and oxidation of ABTS was observed at the top of the gel (Figure IV-23). The absence of free enzyme bands indicated that the enzyme in question has undergone full conjugation, thereby confirming that the activity measured in the UV-vis assay originates from the conjugate.

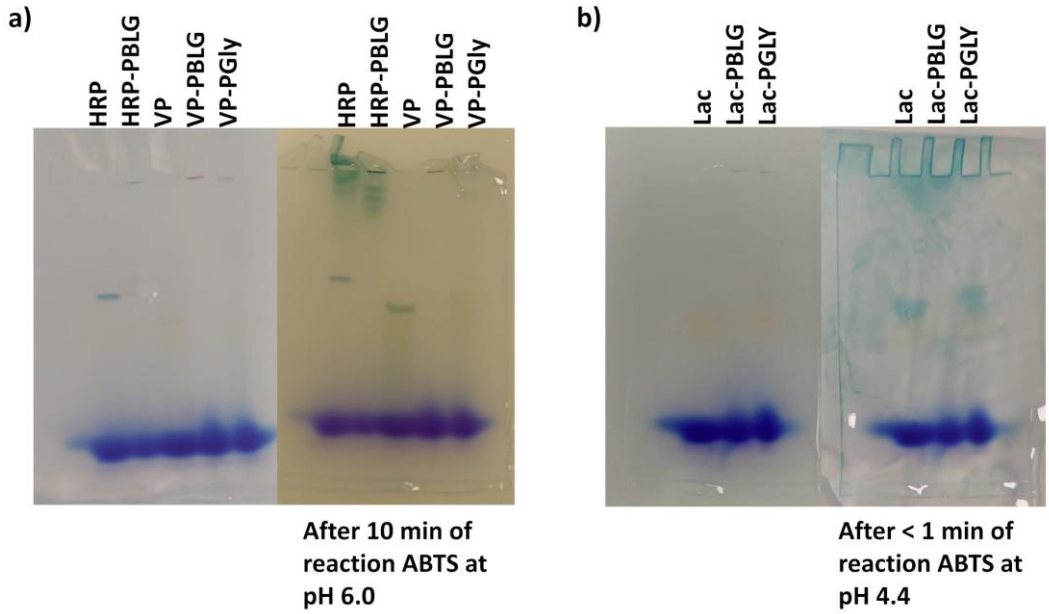

Figure IV-23. Native gel of (a) HRP and VP conjugates compared to the native enzyme, just after reaction with ABTS (left) and after 10 min of reaction (right), (b) Lac conjugates compared to the native enzyme, just after reaction with ABTS (left) and after less than 1 min.

IV.5.2.2. Versatile Peroxidase (VP)

In light of these encouraging initial results, we conducted the same ROPISA experiment using 100 equivalents of BLG-NCA or Gly-NCA with versatile peroxidase (VP). DLS analysis confirmed the presence of nanoparticles, while SDS-PAGE indicated successful conjugation, although free enzyme was still detected, particularly in the case of VP-PGly. Despite this observation, TEM analysis revealed the formation of nanoaggregates for both VP-PBLG and VP-PGly. Subsequently, the enzymatic activity was assessed using the ABTS assay and UV-vis spectroscopy. The results demonstrated that VP-PGly maintained 100% of its activity, while VP-PBLG exhibited a reduced activity of 27%. However, further analysis via native gel electrophoresis, followed by incubation with ABTS, provided additional insights: ABTS oxidation was barely visible for VP-PGly. However, no visual VP free band was observed. In contrast, for VP-PBLG, oxidation was distinctly observed at the top of the gel, thereby confirming that the enzymatic activity was associated with the conjugated enzyme.

IV.5.2.3. Laccase (Lac)

The same procedure was applied using laccase (Lac) as a macroinitiator. The DLS analysis confirmed the formation of nano-objects, with a Z-average diameter larger than that of the free enzyme and higher scattered intensity as depicted by derived count rates (DCR) values (Table IV-3, Figure SIV-12). SDS-PAGE revealed no detectable free enzyme for Lac-PBLG, with all conjugates retained at the top of the gel (Figure IV-21b). In contrast, for Lac-PGly, a significant band indicative of free Lac was discerned, with a minimal amount of material retained at the top of the gel. However, TEM analysis still revealed the presence of nanoaggregates, which may correspond to the fraction of enzyme-conjugate. These observations are consistent with the enzymatic activity measurements. Lac-PGly exhibited complete

enzymatic activity retention, indicating negligible conjugation (Table IV-3). Native gel analysis further corroborated this observation, as ABTS oxidation occurred at the same molecular weight as free Lac, indicating that the activity originated from unmodified enzyme in solution rather than the conjugate (Figure IV-23b). For Lac-PBLG, conjugation appeared to be more effective, as no free enzyme was detected by SDS-PAGE. However, the study noted a significant reduction in enzymatic activity, with only 2% remaining. Attempts to perform TEM analysis were unsuccessful, thus preventing further characterization of the formed nanoaggregates.

In conclusion, a comprehensive study encompassing advanced characterizations such as TEM, DLS, and electrophoresis gels was conducted yielding findings that indicate the conjugation to enzyme occurred at varying levels. Notably, the most favorable outcome was achieved when employing BLG NCA as the monomer. In addition, a decrease in enzymatic activity was observed in all samples, a phenomenon that may be ascribed to the degree of polymerization, which could affect the diffusion between ABTS and the enzyme, thereby impeding the reaction. Future research endeavors will center on the optimization of the ROPISA reactions, as well as the subsequent purification and characterization of the enzyme polymer complex.

IV.6. Perspectives: other macroinitiators of interest

IV.6.1. Poly(ethylene glycol)-cyclic peptide conjugate (PEG-CP)

A recently developed class of self-assembled materials that is the focus of extensive study is represented by supramolecular polymers formed from cyclic peptide–polymer conjugates.[44] Due to their alternating *D*- and *L*-amino acid configuration, cyclic peptides adopt a flat ring-like structure, which drives their self-assembly into nanotubes through strong multiple hydrogen bonds.[45] The design of a water-soluble polymer with predominantly hydrophobic properties is essential for the stabilization of the obtained nanoaggregates within an aqueous solution.[46] These conjugates hold many promises in the field of drug delivery, owing to their cylindrical assemblies with high aspect ratios.[47–49] Several strategies have been investigated to obtain these conjugates, employing grafting-to and grafting-from methods.[50] However, to the best of our knowledge, no degradable or polypeptide moieties have been grafted to this cyclic peptide. Given the ease with which anisotropic nanoparticles can be obtained via ROPISA, and the degradability of the polypeptide, a collaboration was initiated with Sébastien Perrier, an expert of cyclic peptide-polymer conjugates and with one of his post-doctoral researcher, Min Zheng. Initially, the cyclic peptide was synthesized by Min Zheng according to their own procedure (Scheme IV-4a).[51] To enhance the solubility of the cyclic peptide in water, polyethylene glycol (PEG) was grafted onto the peptide according to the following procedure (Scheme IV-4b). The cyclic peptide was initially dissolved in DMF, followed by the addition of EDC, HOBt, and PEG-COOH. The reaction mixture was stirred overnight at room temperature. The coupling reaction was confirmed through the use of DOSY-NMR, as shown in Figure SIV-13. The mean diffusion coefficient was found to be less than that of PEG-COOH and CP, with no residual signals

of free PEG-COOH or CP detected. Subsequently, the Dde protecting group was removed by treating the conjugate with 2% (v/v) hydrazine in DMF overnight to recover the primary amine from the lysine residue. The resulting deprotecting conjugate was characterized by ^{1}H NMR, where signals from the PEG and the peptide were observed, without the signals from the Dde protecting group (Figure IV-24a).

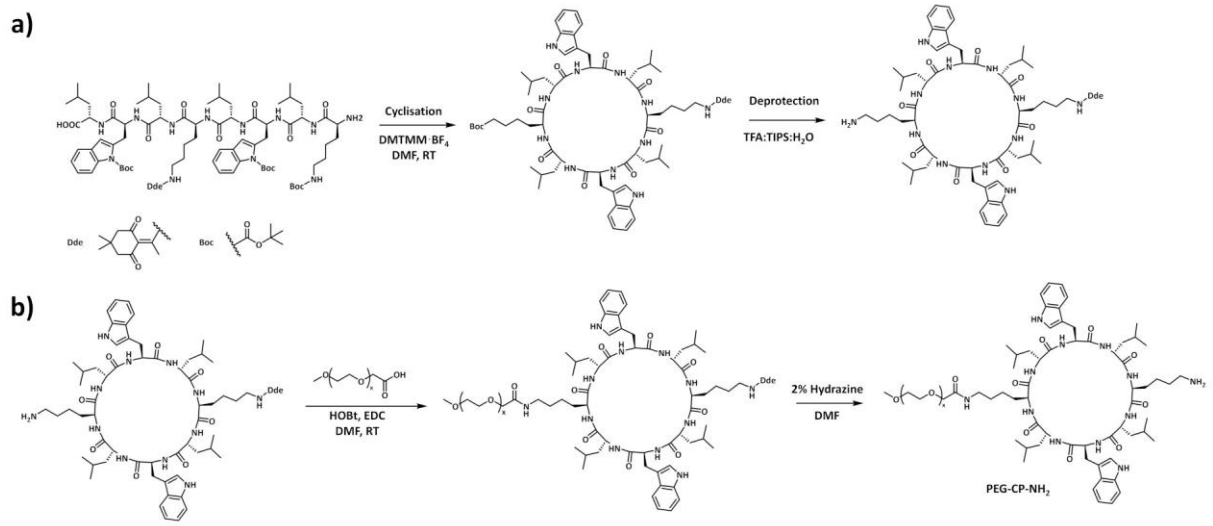

Scheme IV-4. (a) Schematic route of cyclic peptide synthesis. (b) PEG-CP conjugate obtention via a peptide coupling.

Then, aqueous ROPISA of BLG-NCA ([M]/[I] = 19, τ_s = 7 wt%) was implemented following the same conditions as the reference (PEG-NH_2) using the PEG-CP-NH_2 (Scheme IV-5).

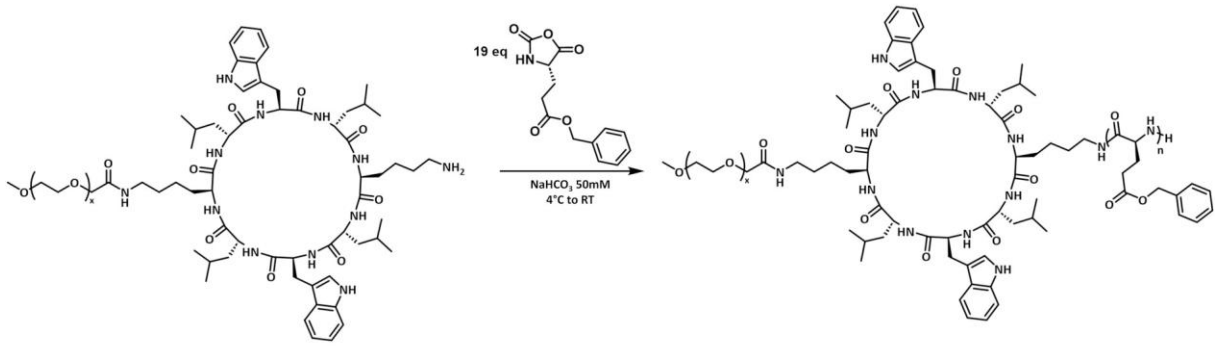

Scheme IV-5. Aqueous ROPISA of BLG-NCA ([M]/[I] = 19) initiated by PEG-CP-NH_2.

After dialysis, the final product PEG-CP-PBLG was recovered by freeze-drying with a high yield of 89%. In addition, ^{1}H NMR analysis confirmed the presence of PBLG signals, with an apparent DP_{PBLG} of 25, which was close to the targeted value (Figure IV-24a).

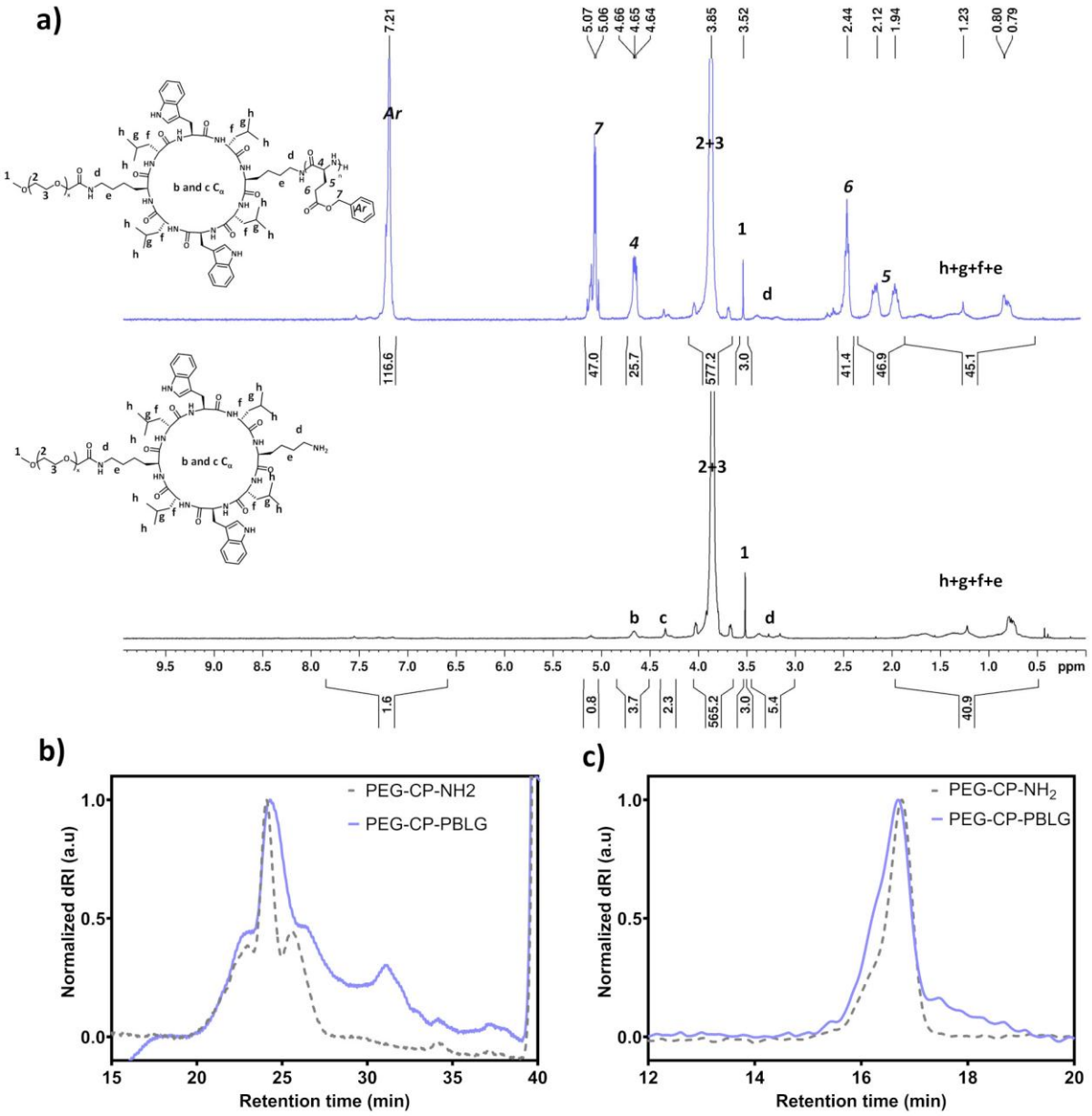

Figure IV-24. (a) ^{1}H NMR spectra of PEG-CP-NH_2 conjugate (bottom) and PEG-CP-PBLG (top) in TFA-*d*. (b) SEC chromatograms of PEG-CP-PBLG in DMF (+1% LiBr, differential refractive index detection) compared to PEG-CP-NH_2. (c) SEC chromatograms of PEG-CP-PBLG in HFIP (+0.05% KTFA, differential refractive index detection) compared to PEG-CP-NH_2.

However, SEC analysis in DMF did not provide conclusive evidence of chain extension, as no shift was observed between the macroinitiator and the copolymer (Figure IV-24b). The estimated M_n was 8 200 g.mol^{-1} based on polystyrene calibration, with a broad dispersity ($Đ > 2$). This raises the question of whether the SEC conditions were appropriate for this particular type of polymer. It is noteworthy that the SEC traces of the macroinitiators exhibited multimodal distributions (Figure SIV-14a), despite the monomodal profile exhibited by PEG-COOH and the well-defined molecular weight of the cyclic peptide, suggesting potential interactions with the stationary phase. Indeed, the retention time of the cyclic peptide was higher than that of PEG-COOH, despite its theoretically lower molar mass. Moreover, the SEC analysis conducted under the conditions employed in Perrier's laboratory did not manifest this behavior, showing consistent

monomodal peaks for conjugates and cyclic peptides (Figure SIV-14). In contrast, SEC analysis in hexafluoropropan-2-ol (HFIP) yielded more reassuring results for PEG-CP-NH_2, displaying a monomodal peak with a slight shoulder (Figure IV-24c). The SEC profile in HFIP of PEG-CP-PBLG exhibited reduced dispersity, accompanied by a modest shift toward higher retention times compared to the initial conjugate. However, a shoulder at lower retention times was still present, likely corresponding to water-initiated BLG oligomers. According to PMMA calibration, the estimated M_n was 37 500 g.mol^{-1} for a dispersity $Đ$ of 1.36. This observed average molar mass is smaller than the one estimated for PEG-CP-NH_2, which was 48 600 g.mol^{-1} ($Đ$ = 1.07).

Despite the inconclusive nature of.these results, the solution obtained after one night of stirring was opalescent, indicating the presence of nanoparticles. After dialysis, the solution was subjected to DLS analysis, which revealed a Z-average diameter of 67 ± 1 nm with a narrow polydispersity index (0.23 ± 0.01) (Figure IV-25). These findings were further confirmed by TEM analysis, which revealed the presence of spherical nanoaggregates with a mean width of 25 ± 3 nm were observed (Figure IV-25c, d). To confirm that self-assembly was not driven by PEG-CP-NH_2 alone, DLS analysis was performed on a macroinitiator solution at the same concentration as the PEG-CP-PBLG suspension (1 mg·mL^{-1}) (Figure S15). The scattered signal exhibited a notably low intensity, suggesting that PEG-CP-NH_2 did not undergo self-assembly under these specific conditions.

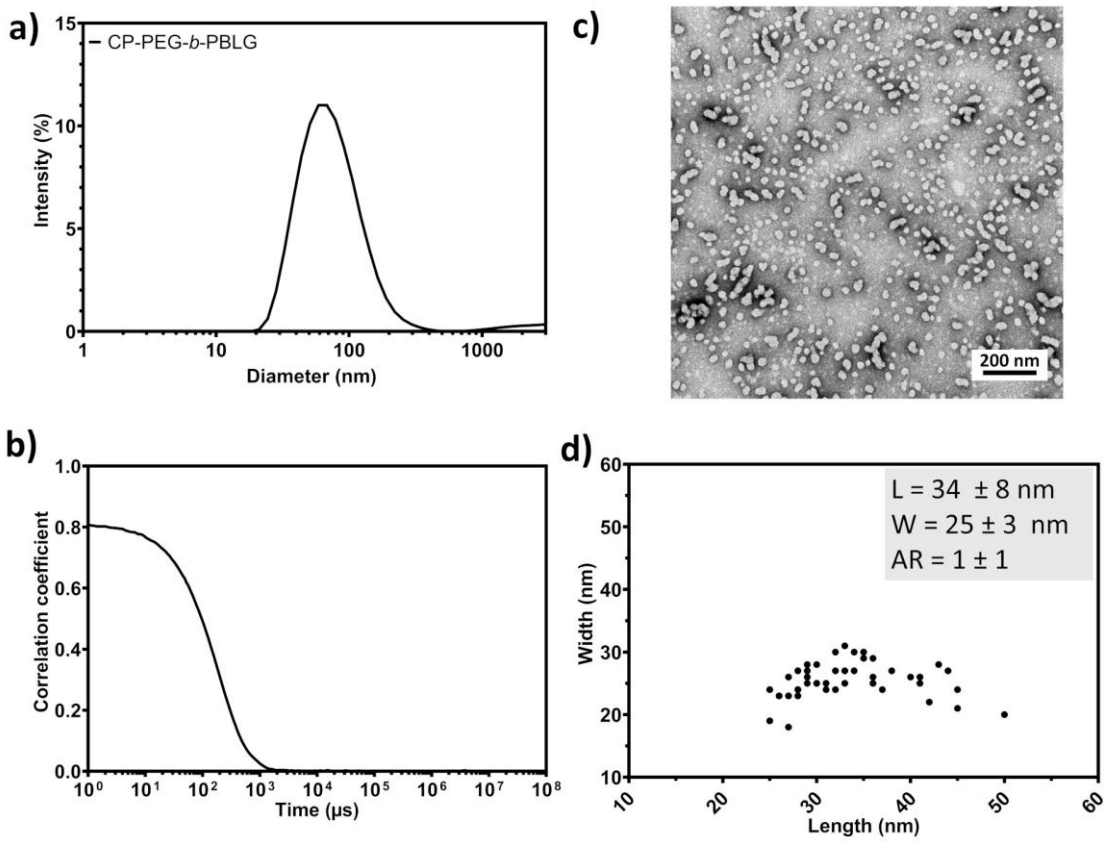

Figure IV-25. (a) DLS profile of PEG-CP-PBLG suspension and (b) associated correlogram. (c) Representative TEM image of PEG-CP-PBLG suspension. (d) Length and width distribution of PEG-CP-PBLG nanoparticles obtained by analysis of 50 nanoparticles by Image J on a TEM image.

In summary, despite the absence of definitive evidence for chain extension, the nanoparticles obtained were well-defined, thereby substantiating the successful formation of nanostructures via ROPISA using cyclic peptide conjugated to poly(ethylene glycol). Notably, this is the first instance in which spherical nanoparticles have been obtained using this approach, which is unexpected given that cyclic peptides typically drive supramolecular self-assembly into nanotubes, while PEG-*b*-PBLG copolymer usually leads to worm-like micelles. This unexpected outcome requires further investigation focusing on the behavior of the secondary structure and of the self-assembly of these systems, as well as deeper chemical analyses. The exploration of alternative monomers, such as alanine, could potentially yield a more diverse array of anisotropic nanostructures.

IV.6.2. Self-Immolative Polymers (SIP)

Self-immolative polymers (SIPs) constitute a growing class of degradable polymers that undergo end-to-end depolymerization upon stimulus-responsive cleavage of either an end-cap or the backbone.[52] When incorporated into amphiphilic block copolymers, they can impart unique functionalities, such as the triggered disintegration of copolymer nanoassemblies upon depolymerization.[53] The incorporation of SIP into block copolymers is a subject of considerable interest in the field of polymer science. This includes polycarbamates,[54] polyglyoxylates,[55] and polyglyoxylamides[56] as hydrophobic blocks, combined with poly(ethylene glycol) or polyacrylamide as hydrophilic blocks. The application of SIPs as hydrophilic blocks offers a promising alternative to PEG. When combined with polypeptides as hydrophobic blocks, they could enable the formation of nanoassemblies capable of controlled disassembly in response to specific stimuli. This property is particularly advantageous for drug delivery, allowing for precise release while ensuring biocompatibility and biodegradability.

In this regard, we engaged in a collaborative effort with the team led by Elizabeth Gillies, a leading authority in the field of SIPs, to explore the potential of polyglyoxylamide bearing a primary amine as a SIP of interest to initiate the ROPISA of BLG-NCA. The provided SIP, which is pH-responsive and undergoes cleavage in acidic conditions,[56] was used in aqueous ROPISA following the conditions used with the PEG and feeding the polymerization with BLG-NCA ([M]/[I] = 20, τ_s = 7 wt%; Scheme IV-6).

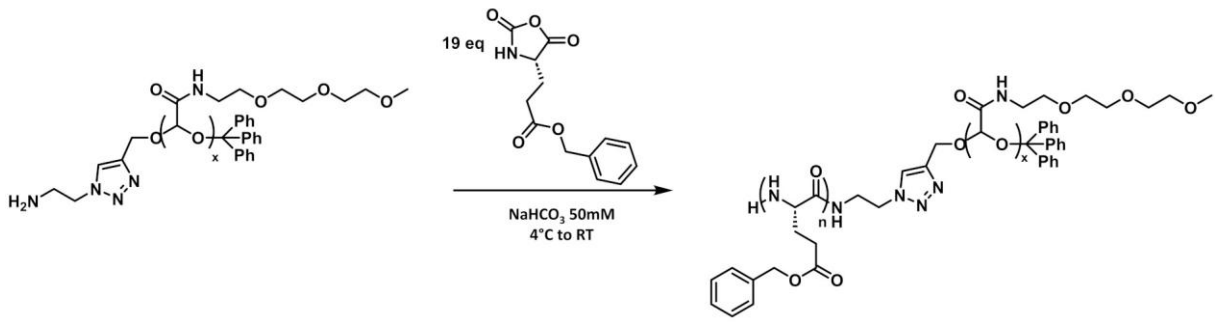

Scheme IV-6. Aqueous ROPISA of BLG-NCA ([M]/[I] = 20) initiated by SIP.

After dialysis, the product was recovered with a relatively low yield of 30% that was attributed to the unsuccessful initiation by the SIP and the hydrolysis of BLG-NCA into its corresponding amino acids. However, it is worth noting that the quantities used for the synthesis were modest, which might also contribute to the observed low yield. In addition, ^{1}H NMR analysis indicated the presence of PBLG signals, with an estimated DP_{PBLG} of 22, which was in agreement with the targeted value (Figure IV-26a). This finding supported the hypothesis that the low yield was due to synthesis scale rather than inefficient polymerization.

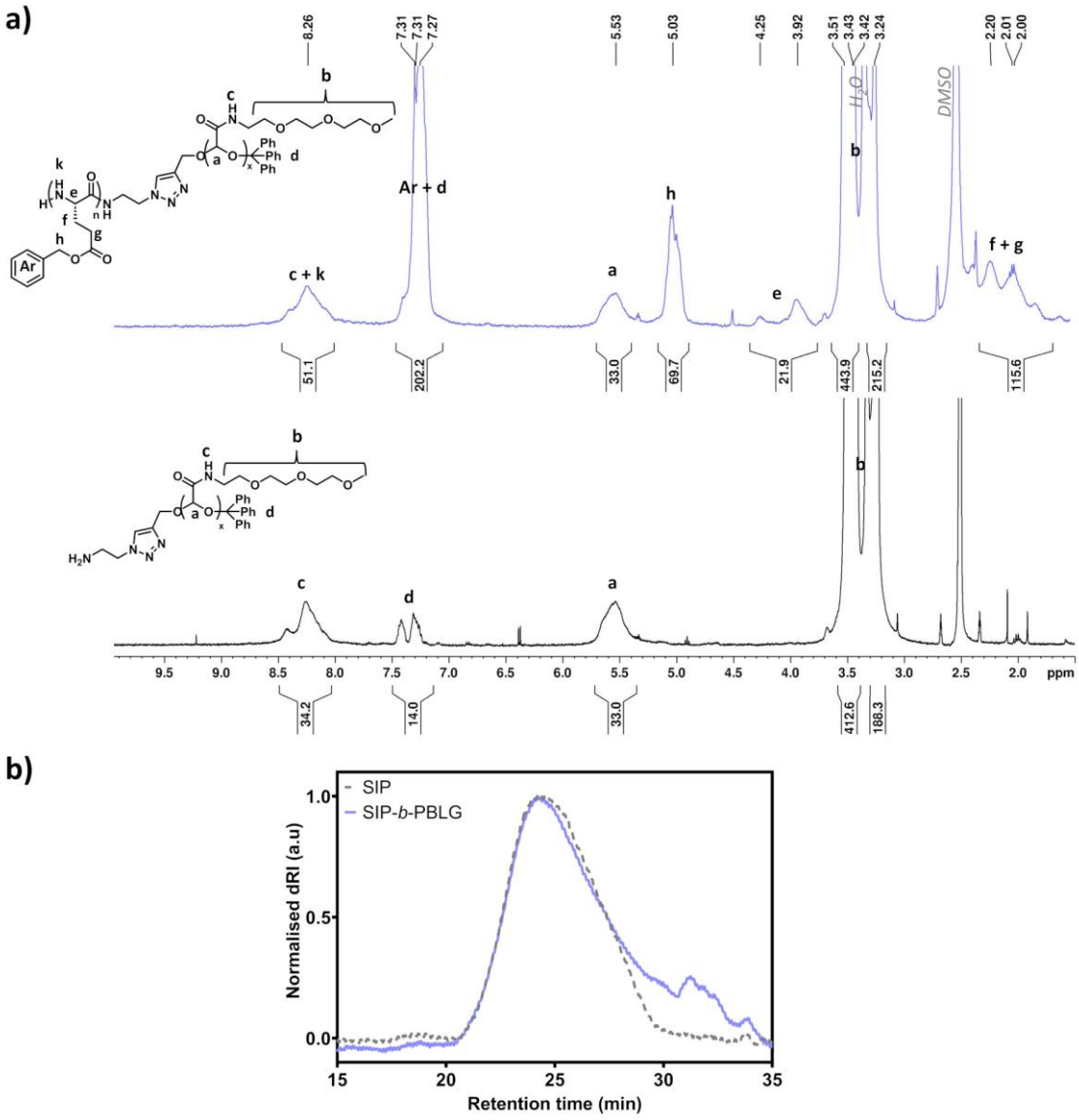

Figure IV-26. (a) ^{1}H NMR spectra of SIP (bottom) and SIP-*b*-PBLG (top) in DMSO-d_6. (b) SEC chromatogram of SIP-*b*-PBLG in DMF (+1% LiBr, differential refractive index detection) compared to SIP homopolymer.

With respect to the SEC analysis, no discernible shift towards a higher retention time was observed. The estimated number-average molar mass, calculated using PS calibration, was found to be approximately 10 100 g.mol^{-1} with a dispersity of 1.89 (Figure IV-26b). In comparison, the SIP precursor exhibited an M_n of 11 500 g.mol^{-1} and a dispersity of 1.69. These results do not provide definitive evidence of successful

chain extension. It is plausible that the solubility issues and interactions between the polymer and the SEC column may have influenced the analysis. Despite these uncertainties, the reaction mixture appeared opalescent upon ROPISA, which was indicative of nanoparticle formation. This was further confirmed by DLS and TEM (Figure IV-27). The Z-average diameter was found to be 826 ± 29 nm, with a polydispersity index of 0.5 ± 0.1. Furthermore, TEM imaging revealed the presence of anisotropic, worm-like nanoparticles.

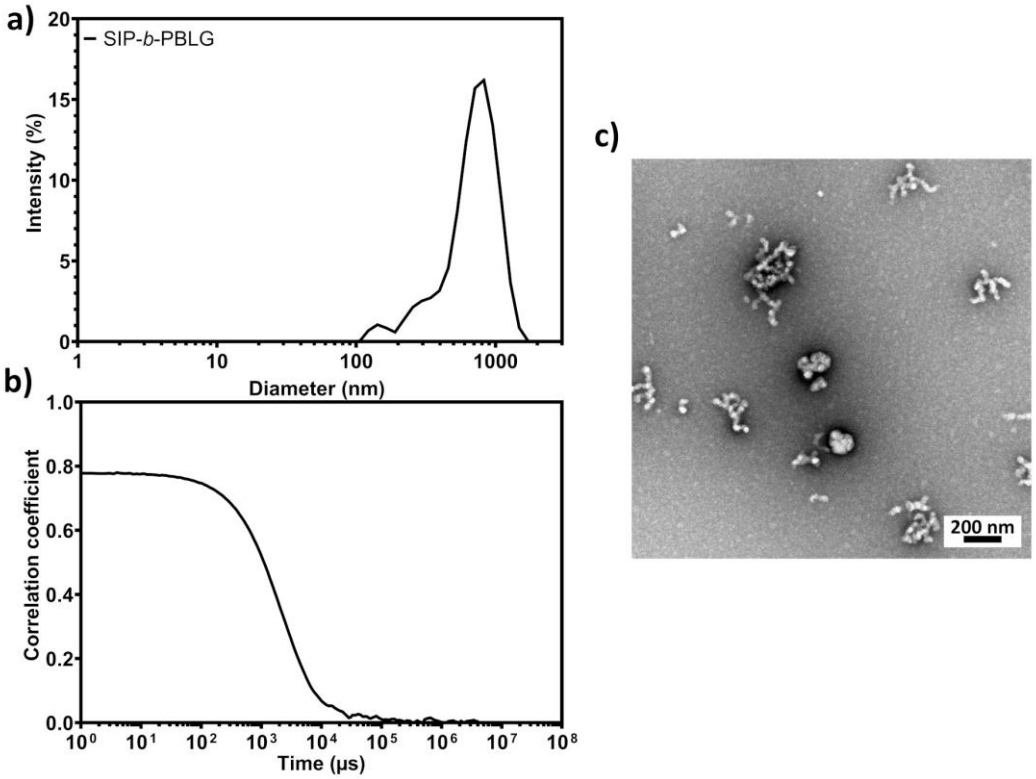

Figure IV-27. (a) DLS profile of SIP-*b*-PBLG suspension and (b) associated correlogram. (c) Representative TEM image of SIP-*b*-PBLG suspension.

In summary, the successful formation of nanoparticles with worm-like morphologies strongly suggests that an amphiphilic diblock copolymer was obtained and underwent spontaneous self-assembly in situ. This finding indicates that chain extensions of SIP have likely occurred to some extent, resulting in nanostructure formation. However, the precise extent of PBLG polymer chain growth remains unclear, possibly due to the limitations of the characterization techniques employed, particularly SEC, which may not be well-suited for this type of copolymer. Further investigation is necessary to ascertain the efficiency of the chain extension and to better understand the structural features of the resulting assemblies. Future studies should focus on refining analytical methods, particularly by evaluating the critical aggregation concentration (CAC) of the SIP block, investigating its primary amine pKa, and assessing the influence of different buffer systems on polymerization and self-assembly. Moreover, given the potential interest of SIP-based materials in biomedical applications, exploring their depolymerization behavior will be essential to assess their biodegradability and long-term stability.

IV.6.3. Polysaccharides

Polysaccharides have emerged as a promising alternative to PEG in the development of biocompatible and tumor-targeting nanocarriers.[57] Beyond their hydrophilic and stealth-like properties, certain polysaccharides have been shown to actively target tumor cells by interacting with overexpressed receptors. Among these polysaccharides, hyaluronan has received significant attention due to its ability to interact with CD44 receptors, which are overexpressed in various cancer types.[58] Previous studies in our group have demonstrated the potential of hyaluronan-based block copolymers for drug delivery. For instance, hyaluronan-*block*-PBLG polymersomes obtained *via* copper-catalyzed click chemistry successfully encapsulated doxorubicin, achieving efficient intracellular drug delivery and antitumor activity both *in vitro* and *in vivo*.[59–61] However, as a polyanion, hyaluronan introduces a degree of complexity that remains to be thoroughly explored in the PISA context.[62,63] In order to establish a more controlled approach, it was decided to first investigate dextran as a macroinitiator for ROPISA. Dextran, a neutral, PEG-like polysaccharide, offers several advantages over hyaluronan, including high-water solubility and biocompatibility.[64] The formation of polymersomes using Dextran-*block*-PBLG, synthesized via click chemistry, has also been previously reported in our group, further highlighting the potential of dextran-based block copolymers for self-assembled nanostructures.[65]

This research was conducted in collaboration with Khalid Ferji, who recently reported the efficient use of RAFT-PISA in aqueous solutions using dextran modified with grafted side chains as chain transfer agents (CTAs). This approach enabled the formation of high-order morphologies, highlighting the potential of dextran-based PISA systems for advanced self-assembled nanostructures.[66,67] In this study, we seek to investigate its potential as a direct macroinitiator for ROPISA to engineer polysaccharide-based nanocarriers. The initial series of experiments was conducted with a Dextran that had been functionalized with 15 primary amine per chain. This macroinitiator was synthetized by the research team led by Khalid Ferji. The second step was to explore the use of aqueous ROPISA from this functionalized Dextran (Scheme IV-7). The experiment sought to assess various DP for graft chains under previously used ROPISA conditions: 50 mM $NaHCO_3$ buffer, low temperature, and a 7 wt% solid content (Table IV-4). The experiments were conducted within Eppendorf tubes, which were subjected to agitation overnight at 10°C using a temperature-controlled thermomixer.

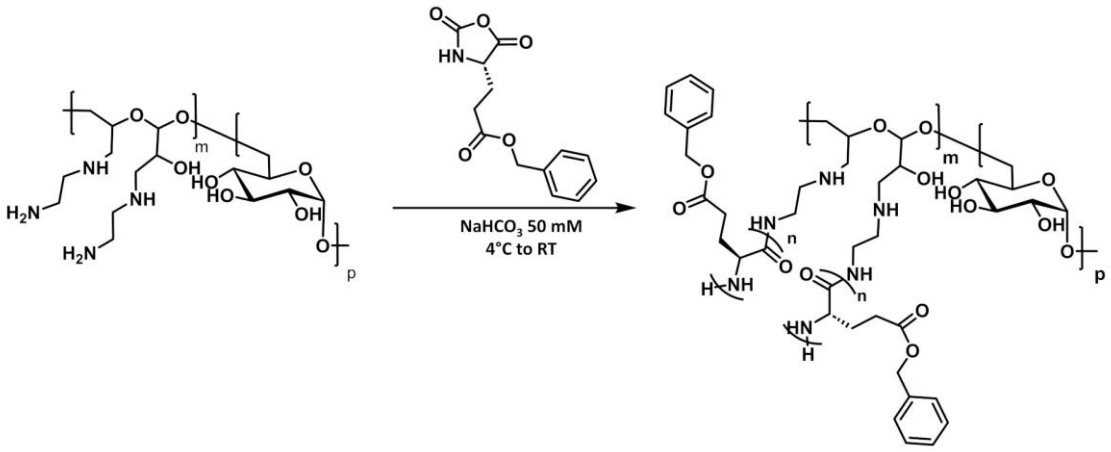

Scheme IV-7. Aqueous ROPISA with various equivalents of BLG-NCA initiated by DexN7.5.

Following a one-night stirring period, the samples exhibited turbidity, accompanied by the formation of a solid precipitate at the bottom of the Eppendorf. Subsequently, a series of analytical procedures were performed, including SEC chromatography following centrifugation with the objective of characterizing the nature of the aggregate (Figure IV-28). No significant differences were observed between the dextran trace and the supernatants of the three precipitates. However, a population eluting around 28 minutes was detected, which was likely to correspond to water-initiated PBLG.

Table IV-4. Macromolecular characteristics of diblock copolymers obtained by ROPISA with Dextran as macroinitiators.

Macroinitiator	$NaHCO_3$ concentation [mM]	Theory			SEC		^{1}H NMR		Yield (%)
		[M]/[I]	Eq/NH_2	M_n [g.mol^{-1}]	M_n [g.mol^{-1}] [a)]	$Đ$ [a)]	M_n [g.mol^{-1}] [b)]	DP [b)]	
DexN7.5	-	-	-	-	6 200	1.82	-	-	-
	50	304	16	106 600	2 100	5.38			73
		152	8	73 300	2 700	4.01			68
		76	4	56 700	2 700	3.94			54
Dex-NH_2	-	-	-	5 000	3 600	1.76	-	-	-
	0	27	27	10 900	2 400	2.21	7 600	12	25
	50				2 300	2.18	8 100	14	33
	100				2 300	2.22	10 000	23	41
Dex-ADH	-	-	-	5 000	3 600	1.38	-	-	-
	0	19	19	9 200	4 400	1.46	9 200	19	76
	50				2 700	1.93	10 300	24	76
	100				2 200	2.13	7 600	12	78

[a)] Number average molar-mass (M_n) and molar-mass dispersity ($Đ$) determined by SEC in DMSO +1% LiBr using Dextran calibration, [b)] Number average molar-mass (M_n) and degree of polymerization (DP) determined by ^{1}H NMR in in DMSO-d_6.

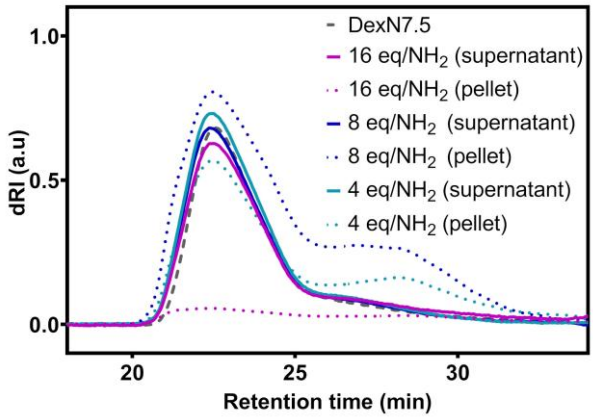

Figure IV-28. SEC chromatograms of DexN7.5-*g*-PBLG compared to DexN7.5 homopolymer in DMSO (+1% LiBr, detection by differential refractive index).

TEM images were obtained from solutions derived from the "supernatants", yet clear observations were challenging (Figure IV-29). It is important to note that the images are not highly representative of the samples, as they may depict artifacts, PBLG fibers, or aggregates.

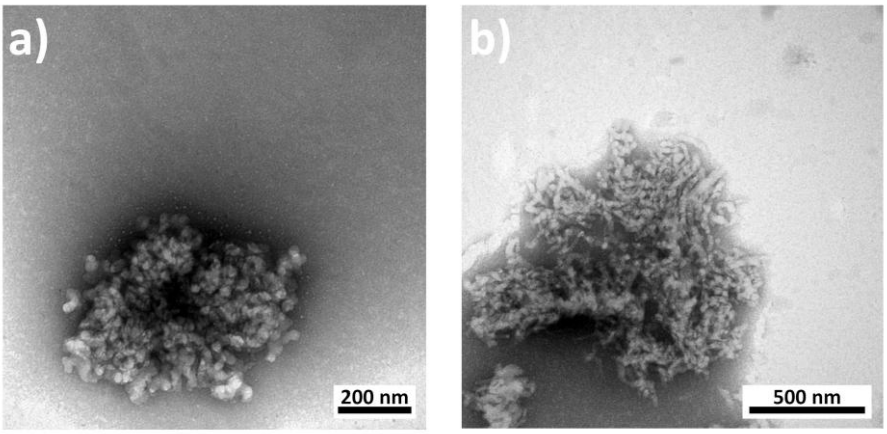

Figure IV-29. Representative TEM images of samples after ROPISA with DexN7.5: (a) For 8eq/NH_2 and (b) 4eq/NH_2 of BLG-NCA.

Considering the macroscopic appearance, the SEC profiles, and the TEM results, it was determined that no additional analyses were necessary. Given the complexity of forming a graft copolymer under these conditions, a comparison was made with a linear dextran bearing a single primary amine. Two distinct linkers were used in this study: a shorter one with a primary amine and a longer one featuring a adipic acid dihydrazide (ADH) function. ADH possesses a lower pKa (approximately 3.1) in comparison to the primary amine of dextran (approximately 9), rendering it more nucleophilic. This increased nucleophilicity can promote aminolysis over hydrolysis, facilitating a more efficient reaction. Dextran bearing an ADH end-chain function (Dex-ADH) was kindly prepared by Elise Courtecuisse according to a published procedure,[68] while dextran with a primary amine (Dex-NH_2) was provided by Khalid Ferji, synthetized according to another published procedure.[69] Both Dextran has a M_n of 5 000 g.mol^{-1}. The same ROPISA conditions were implemented, with the objective of targeting a single DP (27 for Dex-NH_2 and 19 for Dex-

ADH). However, the buffer was modified to assess whether ionic strength could influence the success of the polymerization (Scheme IV-8).

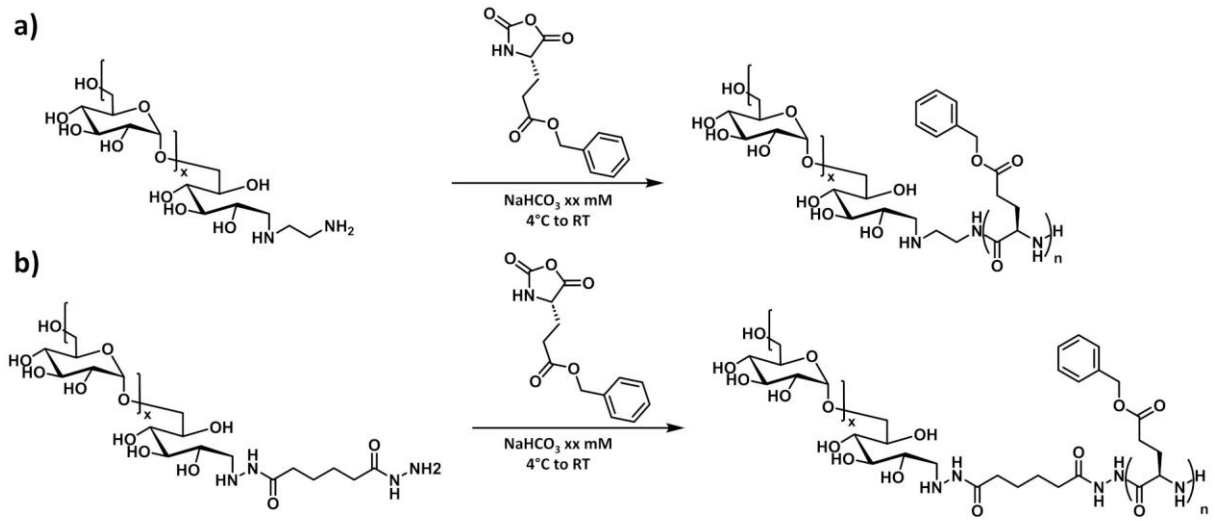

Scheme IV-8. Aqueous ROPISA of BLG-NCA initiated by (a) Dex-NH_2 and (b) Dex-ADH.

Following a one-night reaction, milky solutions were obtained. After dialysis, SEC chromatography and ^{1}H NMR analysis were conducted. ^{1}H NMR spectra confirmed the presence of PBLG (Table IV-4, Figure SIV-16, Figure SIV-17). However, the DP exhibited variation depending on the nature of the dextran end-group and the buffer conditions. For Dex-NH_2, an increase in ionic strength resulted in a DP_{PBLG} closer to the targeted feed ratio (DP_{PBLG}=23 for buffer $NaHCO_3$ 100mM) and an improvement in polymerization yield, suggesting enhanced polymerization control under these conditions. Conversely, for Dex-ADH, an increase in ionic strength led to a decrease in DP, highlighting a distinct influence of buffer composition on polymerization efficiency depending on the nucleophilicity of the initiator group. SEC was employed to assess chain-extension and potential water-initiated polymerization, which could introduce bias in NMR-based DP estimations (Figure IV-30). In the case of Dex-NH_2, significant amount of water-initiated polymerization was observed, as evidenced by the presence of high-retention-time populations corresponding to low-molecular-weight BLG oligomers and the absence of a clear shift compared to the dextran peak. In contrast, Dex-ADH exhibited a diminished propensity for water-initiated polymerization, exhibiting no discernible oligomeric shoulder when the reaction was carried out in pure water.

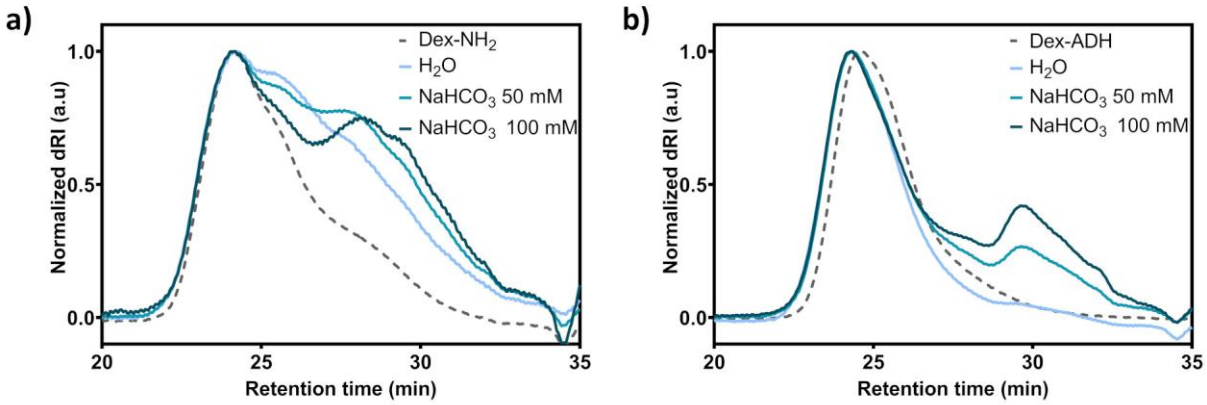

Figure IV-30. SEC chromatograms of Dex-*b*-PBLG compared to homopolymer in DMSO (+1% LiBr, detection by differential refractive index) using (a) Dex-NH_2 as macroinitiator and (b) Dex-ADH as macroinitiator.

Among the conditions that were tested, ROPISA initiated by Dex-ADH in pure water yielded the most promising outcome, supporting further structural characterization via DLS and TEM. This structural characterization aimed to assess the morphology and self-assembly behavior of the resulting nanostructures. The DLS analysis confirmed the presence of homogeneous nanoparticles in all three conditions (Figure IV-31a,b). In the water condition, the Z-average diameter was measured to be 171 ± 3 nm with a polydispersity index of approximately 0.2. The Z-average diameters in the other conditions were slightly larger, while the polydispersity index remained around 0.2, indicating relatively well-defined size distributions. However, no clear correlation was found between the nanoparticle size and the ionic strength. TEM imaging of the water conditions also revealed the presence of homogenous anisotropic and wrapped nanostructures, exhibiting a morphology that was not seen before (Figure IV-31c). In contrast, under bicarbonate conditions, the nanoparticles appeared less homogenous, with a mixture of fibers and larger aggregates. This observation was attributed to the presence of BLG oligomers and shorter copolymer blocks (Figure IV-31d, e). The results obtained from this study provide substantial evidence to support the hypothesis that ROPISA initiated by Dex-ADH in pure water enables the formation of well-defined copolymers and homogeneous nanoparticles with an outstanding morphology.

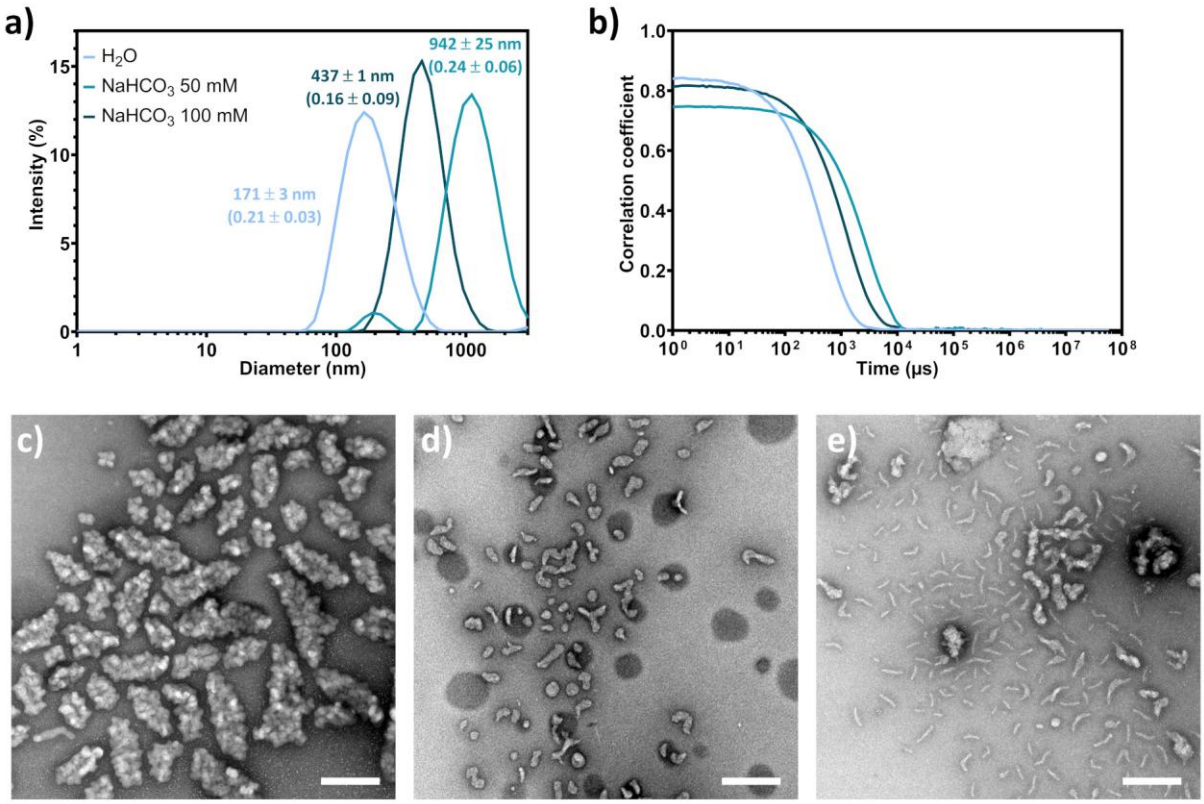

Figure IV-31. Nanoparticle characterizations upon ROPISA of BLG-NCA using Dex-ADH as macroinitiator. Top: (a) DLS profiles of Dex-*b*-PBLG suspensions and (b) associated correlograms. Bottom: Representative TEM images of Dex-*b*-PBLG nanoparticles upon ROPISA in (c) pure water, (d) $NaHCO_3$ 50mM and (e) $NaHCO_3$ 100 mM.. Scale-bar: 200 nm.

Despite the absence of direct evidence for efficient initiation by Dex-NH_2, the results highlight the pivotal role of nucleophilicity of the initiator and the buffer composition on the polymerization process. Further investigations, particularly those focused on the effect of pH and the determination of the critical aggregation concentration (CAC) of the macroinitiators, could provide deeper insight into their polymerization behavior and self-assembly potential. The dihydrazide functionality appears to be particularly suitable for conducting ROPISA under mild conditions, with Dex-ADH demonstrating the best performance in ultra-pure water. However, due to temporal limitations, further analyses and experiments were not pursued. Nonetheless, recent studies have demonstrated the feasibility of obtaining polysaccharide-based block copolymers via aqueous ROPISA of NCA. Notably, Dextran-NH_2, which possesses a longer linker than the one used in this study (six carbons *vs.* two), has been used as a macroinitiator for the ROPISA of BLG-*N*-thiocarboxyanhydride (NTA).[70] NTAs demonstrate a lower activation of the ROP in comparison to NCAs, resulting in enhanced stability within aqueous media but a slower rate of polymerization. The polymerization was performed at a pH 6.5, because a higher pH (8.5), typically used for NCA-based ROPISA, resulted in uncontrolled polymerization. Interestingly, globular nanostructures were obtained with NCA using Dextran, whereas PEG-initiated ROPISA of BLG-NTA produced anisotropic nanostructures, albeit with a smaller aspect ratio compared to NCA-based ROPISA from PEG. Molecular simulations revealed that Dextran has a lower solvent-accessible surface area than

PEG, adopting a more compact conformation in water. Coarse-grained models previously showed that Dextran-based nanostructures are stabilized by strong Dextran-Dextran interactions and their affinity for water, whereas PEG chains remain mostly independent, with a denser hydration shell but weaker interchain interactions.[70] These previous findings may explain the challenges encountered when using Dextran as a macroinitiator, but also the morphology obtained when ROPISA was initiated by Dex-ADH. Interestingly, carboxymethyl chitosan, which is water-soluble polysaccharide under alkaline conditions (unlike native chitosan), was also used to polymerize various NCAs by aqueous ROPISA, leading to the formation of hydrogels with gelation properties influenced by NCA type, NCA equivalents and intermolecular interactions of the resulting polypeptides.[71] However, the presence of nanostructures was not clearly evidenced.

To enhance the efficiency of Dextran as a macroinitiator in ROPISA, ADH but also alternative functions and reaction conditions could be explored. For instance, Dextran tetraalkylammonium carboxylate has been shown to efficiently initiate the ROP of BLG-NCA, Ala-NCA, Lys(TFA)-NCA, and Leu-NCA in anhydrous DMSO, leading to self-assembled structures such as worm-like nanoparticles and spherical nanoparticles.[72] The extension of this approach to aqueous ROPISA has the potential to yield enhanced control over self-assembly and stability. With regard to the use of hyaluronan, Amin El Jarroudi Hamou's PhD project, which focuses on polyelectrolytes as initiators in ROPISA will provide valuable insights into the optimization of polymerization conditions. On another hand, building on this work, Maura Martinez Morales, a PhD student who is continuing my PhD project, will develop hyaluronan-coated nanoparticles through ROPISA for active targeting in cancer therapy.

IV.7. Conclusion

In summary, the present study explored the use of various (bio)degradable and functional macromolecules as macroinitiators for aqueous ROPISA of NCA. In the initial phase of the study, we investigated peptide-based macroinitiators, like poly(sarcosine), poly(*L*-proline) and elastin-like polypeptides for the ROPISA of NCA monomers. This investigation resulted in well-defined polymers and anisotropic nanostructures while preserving the intrinsic properties of the macroinitiator. Notably, poly(proline)-based nanostructures exhibited the hysteretic thermoresponse of the parent macroinitiator, with the polypeptide hydrophobic block influencing the extent of hysteresis. In a similar manner, elastin-like polypeptides of varying chain lengths resulted in the formation of peculiar cocoon-like nanostructures, which also exhibited thermoresponsive behavior dependent on the ELP sequence. These results validate the use of aqueous ROPISA as a promising approach for the synthesis of fully peptidic nanoparticles and protein-conjugate in native conditions, which holds significant potential for drug delivery and protein conjugation applications.

Based on this study, we also explored the synthesis of enzyme-polypeptide conjugate via ROPISA. Preliminary results revealed the formation of nanoaggregates, with effective polymerization of BLG-NCA

onto the enzyme surface. However, the introduction of the polypeptide block on the enzyme led to reduced enzymatic activity, likely due to steric hindrance impeding substrate access to the catalytic pocket. These optimized results will lead to a more complete work by Maura Martinez Morales and Alina Elizabeth Torres Aguirre.

Additionally, other macroinitiators of interest, studied in collaboration with Elizabeth Gillies, Sébastien Perrier and Khalid Ferji, were evaluated. An important result was that cyclic peptide conjugates induced the formation of spherical nanoparticles through ROPISA, although the underlying mechanism remains ambiguous and should be better characterized. Self-immolative polymers (SIPs) also induced nanoparticle formation, but chain extension could not be demonstrated. In addition, dextran was employed as a macroinitiator, revealing that the nature of the end-chain functionality impacts ROP efficiency: differences in nucleophilicity between dextran derivatives influenced the polymerization process.

The results presented in this chapter highlight, on one hand, the remarkable versatility of the aqueous ROPISA process, which enables the formation of diverse nanoparticle morphologies through careful monomer selection (**Chapter III**), and on the other hand, the critical role of the stabilizing block in determining final morphology. This is evidenced by the wide range of structures obtained using the same PBLG block while maintaining a constant hydrophilic fraction Additional interactions involving the hydrophilic block, both with water and between chains, likely contribute to these structural variations.

Various surface properties can thus be achieved by using functional and/or (bio)degradable stabilizing blocks. Future studies should aim to further elucidate the underlying interactions and improve characterization techniques to refine our understanding of the polymerization mechanisms and nanostructure formation. In particular, other stabilizing blocks with specific relevance to oncology, such as hyaluronan, will be explored.

IV.8. Experimental section

IV.8.1. Materials

Solvents for size-exclusion chromatography *N,N*-dimethylformamide (DMF), dimethylsulfoxide (DMSO), acetonitrile (ACN) and hexafluoropropan-2-ol (HFIP) were bought from Sigma. DMF and ACN for macroinitiators synthesis were obtained from a solvent system purifier (PureSolv, Innovative Technology), kept under argon atmosphere and freshly used. Dichloromethane was bought from Sigma and trifluoroacetic acid from TCI. *N*-carboxyanhydrides were supplied by PMC Isochem (Vert-le-Petit, France) and stored at -20 °C under argon atmosphere and weighed in the glove box Jacomex GP13 no. 2675. *N*-(tert-Butoxycarbonyl)glycine (Boc-Gly-OH), 1-ethyl-3-carbodiimide hydrochloride (EDC), 1-Hydroxybenzotriazole hydrate (HOBt) and hexylamine were bought from Sigma and were used without any purification, except for hexylamine which was freeze-thawed and cryo-distilled on the Schlenk line prior to use.

Ultra-pure water was obtained from a Milli Q system (Merck Millipore, France) with a resistivity of 18.2 MΩ. Deuterated solvent ($CDCl_3$, DMSO-d_6, TFA-*d*) were purchased from Eurisotop. Dialysis membranes were purchased from SpectrumLabs. Amicon Ultra centrifugal filters were purchased from Merck.

IV.8.2. Instrumentation and methods

IV.8.2.1. Nuclear Magnetic Resonance (NMR)

^{1}H Nuclear Magnetic Resonance (NMR) spectra were recorded on a Bruker Avance III spectrometer equipped with a 5 mm BBFO (broad band fluorine observation) liquid probe, at 298 K. ^{1}H data were acquired at 400.2 MHz observation frequency, with 16 scans and a recycle delay of 1 second. Signals were referred to the signal of residual protonated solvent signals. DOSY-NMR was performed at 296 K on a Bruker Avance NEO 400 MHz NMR spectrometer, equipped with a 5 mm BBO Bruker Cryoprobe Prodigy, capable of producing gradients in the z direction with strength 50 G.cm^{-1}. The DOSY spectra were acquired with the dstebpgp3s pulse program. All spectra were recorded with 16K time domain data points in the t2 dimension and 16 t1 increments. The gradient strength was linearly incremented in 16 steps from 5% up to 95% of the maximum gradient strength. All measurements were performed with a compromise diffusion Δ of 100 ms. The gradient pulse length δ was 2.3 ms.

IV.8.2.2. Size Exclusion Chromatography (SEC)

Polymer molar masses were determined by SEC using *N,N*-dimethylformamide (DMF + LiBr 1 g.L^{-1}), hexafluoro-2-propanol (HFIP + 0.05% KTFA), dimethylsulfoxide (DMSO + LiBr 1 g.L^{-1}) or aqueous solvent as eluent. Measurements in DMF were performed on an Ultimate 3000 system from ThermoFischer Scientific (Ilkirch, France) equipped with a diode array detector (DAD). The system also includes a multiangle light scattering detector (MALS) and differential refractive index detector (dRI) from Wyatt technology (Santa Barbara CA, USA). Polymers were separated on three Shodex Asahipack gel columns

[GF 310 (7.5 × 300 mm²), GF510 (7.5 × 300 mm²), exclusion limits from 500–300 000 Da] at a flowrate of 0.5 mL.min^{-1}. Columns temperature was held at 50 °C. Easivial™ kit of Polystyrene from Agilent (Santa Clara CA, USA) was used as calibration standard (M_n from 162 to 364 000 Da). Measurements in HFIP were performed on an Ultimate 3000 system from Thermoscientific equipped with UV detector. The system also includes differential refractive index detector dRI from Wyatt technology. Polymers were separated on PSS PFG 100Å and PFG 1000Å columns (300 × 8 mm², 2 µm) (exclusion limits from 100 Da to 12 000 000 Da) at a flowrate of 1 mL.min^{-1}. Columns temperature was held at 30°C. Easivial™ kit of PMMA from Agilent was used as the standard.

Poly(*L*-proline) samples were analyzed using two TOSOH TSK Gel G4000PWXL and G3000PWXL columns (300 × 7.8 mm²) (exclusion limits from 200 Da to 300 000 Da) at a flowrate of 0.6 mL.min^{-1}. Aqueous solvent composed of acetic acid (AcOH) 0.3 M, ammonium acetate 0.2 M and ACN (H_2O/ACN: 6.5/3.5, v/v) was used as the eluent. Column temperature was held at 25°C. d*n*/d*c* measurements were performed on the differential refractive index detector dRI from Wyatt technology by injecting 500 µL of each sample dissolved in the aqueous phosphate buffer at 0.5-5 mg.mL^{-1}. The chromatograms were recorded with Chromeleon 7.2 software and Astra 7.1.0 software and analyzed using the latter d*n*/d*c* values calculated were of 0.1616 mg.mL^{-1} for *L*-Proline homopolymers.

Measurements in DMSO were performed on an Ultimate 3000 system from ThermoFischer Scientific (Ilkirch, France) equipped with a diode array detector (DAD). The system also includes a multiangle light scattering detector (MALS) and differential refractive index detector (dRI) from Wyatt technology. Polymers were separated on two Tosoh gel columns, with a TSK guard column HHR-L, [G3000 HHR (7.8 × 300 mm²), G2000HHR (7.8 × 300 mm²), exclusion limits from 200–60 000 Da] at a flowrate of 0.5 mL.min^{-1}. Columns temperature was held at 80 °C. Easivial™ kit of Dextran from Agilent (Santa Clara CA, USA) was used as calibration standard (M_n from 504 to 43 500 Da).

IV.8.2.3. Atomic Force Microscopy (AFM)

Atomic Force Microscopy (AFM) measurements were performed at room temperature in a dry state using a Multimode 8™ microscope (Veeco Instruments Inc., Bruker, Santa Barbara CA, USA). Both topographic and phase images of needle-like nanoparticles were obtained in Tapping Mode™ using rectangular silicon cantilever (AC 160-TS, Atomic Force Microscopy probes Asylum, Wiesbaden, Germany) with a spring constant of 26 N.m^{-1}, a resonance frequency lying in the 270–320 kHz range and a radius of curvature of less than 10 nm. Samples were prepared by solvent casting at ambient temperature from a stock solution (70 mg.mL^{-1}). A 5 µL drop of suspension was deposited onto freshly cleaved mica, and after 10 minutes the excess of solution was removed with blotting paper. Subsequently, the substrate was dried under nitrogen flow for several minutes.

IV.8.2.4. Transmission Electron Microscopy (TEM)

The images were recorded on a Hitachi H7650 microscope working at 80 kV. Samples were prepared by spraying a 0.1 $g.L^{-1}$ solution of the block copolymer onto a copper grid (200 mesh coated with carbon) using a homemade spray tool or by deposing a drop of NP dispersion grid and removing excess after 1 minute. Both types of grids were negatively stained with 1.2% uranyl acetate or Uranyless.

IV.8.2.5. Cryo-Transmission Electron Microscopy (cryo-TEM)

Cryo-Transmission Electron Microscopy (cryo-TEM) micrographs were obtained by deposing 4 µL of samples on an EM grid coated with a perforated carbon film. After draining the excess liquid with a filter paper, grids were plunge-frozen into liquid ethane cooled by liquid nitrogen using a Leica EMCPC cryo-chamber (Leica Microsystems, Wetzlar, Germany). For cryo-TEM observation, grids were mounted onto a Gatan 626 cryoholder and transferred to a Tecnai F20 microscope (Thermo Fisher Scientific) operated at 200 kV. Images were recorded with an Eagle 2k CCD camera (FEI, USA).

IV.8.2.6. Dynamic Light Scattering (DLS)

Hydrodynamic *Z*-average diameters (D_z) and the polydispersity index (σ) of the nanoparticles were determined by DLS with a Zetasizer Nano ZS from Malvern Instruments (Malvern, UK) operating with a He–Ne laser source (wavelength 633 nm, scattering angle 90° or 173°). The correlation functions were analysed using the cumulant method. The dispersions were analyzed at 0.1 wt% in water. Cloud point temperatures (T_{CP}) were determined by DLS between 10 and 55 °C at a 2 °C·min^{-1} scan rate in water for ELPM and ELP-*b*-PBLG nanoparticles (1 $mg.mL^{-1}$). Z-average hydrodynamic diameters (D_z) and derived count rates (kcps) were plotted as a function of temperature. For PLP-*b*-PGly nanoparticles, a range between 4 and 85 °C was applied at a 5 °C·min^{-1} scan rate.

IV.8.2.7. UV-Vis spectroscopy

The cloud point temperature (T_{CP}) and the clearing point temperature (T_{CL}) of PLP and PLP-based diblock copolymer suspensions in pure water were determined by measuring the turbidity at 550 nm between 10 °C and 85 °C at a 1 °C.min^{-1} scan rate according to Baldreldin et al.[73] Data were collected on a Cary 100 UV−Vis spectrophotometer equipped with a multicell thermoelectric temperature controller from Agilent Technologies. T_{CP} was defined as the temperature at the inflection point of the transmittance-temperature curves during heating ramps and concordantly for T_{CL} during the cooling ramps. A typical experiment followed the following heating program:

1. 10 min isotherm at 10 °C
2. 1 °C.min^{-1} ramp to 85 °C
3. 10 min isotherm at 85 °C
4. 1 °C.min^{-1} ramp to 10 °C

Transmittance was plotted as a function of temperature, with isotherm data not collected. The y-axis in the results is displayed as 1-Transmittance (%) to help the reader relate the soluble and the aggregated forms to low and high values respectively.

IV.8.2.8. CAC determination by fluorescence using Nile Red

ELPM40 solutions were prepared in ultrapure water at several concentrations by serial dilutions, ranging from 0.0028 to 16 mg.mL^{-1}. A Nile Red solution in acetonitrile was prepared at 0.2 mg.mL^{-1} and added in each solution to target a final concentration of 0.002 mg.mL^{-1}. Measurements were made on a fluorescence spectrometer FP-8500 (Jasco) at 4°C. Emission fluorescence spectra were collected (λ_{ex} = 500 nm, λ_{em} = 550-750 nm) and fluorescence intensity was plotted at 650 nm. CAC is defined as the concentration at the intersection of the two logarithms regression $y = a - b \times \ln x$.

IV.8.2.9. SDS-PAGE

SDS-PAGE was performed using Mini-PROTEAN® TGX™ precast gels (4 – 20%, 12 wells). Samples were prepared by mixing with Laemmli buffer and heating at 90°C for 10 minutes. A total sample volume of 10 or 20 µL was loaded per well. Electrophoresis was carried out in Tris-Glycine-SDS (TGS) running buffer at 80, 85 or 100 V for 1 hour and 30 minutes. The gel was imaged using a Bio-Rad Gel Doc system under label-free detection mode to ensure optimal resolution.

IV.8.2.10. Native PAGE

Native PAGE was performed using Mini-PROTEAN® TGX™ precast gels (4–20%, 12 wells). Samples were prepared in a lysis solution without SDS or β-mercaptoethanol to preserve the native state of the proteins. A total volume of 10 or 20 µL per well was loaded. Electrophoresis was conducted at 90 V for 1 hour and 30 minutes using a custom-prepared Tris-Glycine (TG) running buffer without SDS.

After elution, the gel was incubated in the following mixtures for enzyme activity detection:

- HRP and VP: 2 mM ABTS, 1 mM H_2O_2 and PBS (pH 6.0) for 10 minutes.
- Laccase: 2 mM ABTS in citrate-phosphate buffer (pH 4.4) for less than 1 minute.

The gel was visualized using a Bio-Rad Gel Doc system under label-free detection mode to assess enzyme migration and activity while maintaining their native conformation.

IV.8.2.11. Enzyme concentration

Nanodrop ND1000 was used to determine enzyme concentration.

IV.8.2.12. Enzymatic assays

Enzymatic activity was determined using the ABTS assay, with absorbance measured at 420 nm every 3 seconds for 2 minutes in a 500 µL reaction mixture. The reaction mixtures for each enzymatic solution were prepared as follows:

- HRP: 100 µL ABTS (20 mM), 5 µL H_2O_2 (200 mM) in phosphate buffer (50 mM, pH 6.0)
- VP: 100 µL ABTS (20 mM), 5 µL H_2O_2 (200 mM) in citrate-phosphate buffer (50 mM, pH 4.0)

- Lac: 100 µL ABTS (20 mM) in citrate-phosphate buffer (50 mM, pH 4.4)

IV.8.3. Synthesis

All the diblock copolymers were synthesized by ring-opening polymerization induced self-assembly (ROPISA) in aqueous buffer, as described previously in **Chapter II** and **III.**

IV.8.3.1. Synthesis of PSar-*b*-PBLG block copolymers

IV.8.3.1.1. Ring-opening polymerization of Sar-NCA

Sar-NCA (3 g, 2.6×10^{-2} mol, 70 eq) was introduced to a flame-dried Schlenk equipped with a stirrer and dissolved in 44 mL of dry DMF. While stirring, hexylamine (50 µL, 1.4×10^{-2} mmol, 1eq) was added to the solution to initiate the ROP. The consumption of Sar-NCA was monitored by FTIR spectroscopy by checking the disappearance of the bands at 1859 cm^{-1} and 1787 cm^{-1} characteristic of the C=O stretching of NCAs. Upon completion of the polymerization reaction the final PSar homopolymer was precipitated in diethyl ether and dried under vacuum overnight. The powder was then solubilized in water and dialyzed against deionized water in a 1 kDa dialysis membrane before being lyophilized. Yield = 50%, white powder. ^{1}H NMR (400 MHz, DMSO-d_6, 50°C): δ=0.86 (t, 3H; -CH_3, hexylamine), 1.24 (6H; -CH_2-CH_2-CH_2, hexylamine), 1.38 (m, 4H; -CH_2-CH_2-NH-, hexylamine), 2.73-2.94 (br m 3H; CH_3 of PSar side chain), 3.93−4.34 (br m, CH_2 of PSar backbone). M_n^{NMR} = 5 300 g.mol^{-1} (DP^{NMR} = 73). SEC (1% KTFA in HFIP) $M_{n,\,SEC\ RI}$ = 33 600 g. mol^{-1}, $Đ$ = 1.06.

IV.8.3.1.2. Coupling with Boc-Glycine-OH

PSar (500 mg, 1×10^{-1} mmol, 1eq) and EDC (90 µL, 5×10^{-1} mmol, 5eq) were solubilized in 10 mL DMF in a round-bottom flask. BOC-Gly-OH (88 mg, 5×10^{-1} mmol, 5eq) and HOBT (68 mg, 5×10^{-1} mmol, 5eq) were solubilized in a second flask in 10 mL DMF. After 1 hour, the solution containing Boc-Gly-OH was added to the PSar solution. The mixture was left to stir for 16 hours. The product was then precipitated in diethyl ether and dried under vacuum overnight. The powder was then solubilized in water and dialyzed against deionized water in a 1 kDa dialysis membrane before being lyophilized. Yield = 50%, white powder. ^{1}H NMR (400 MHz, DMSO-d_6, 50°C): δ=0.86 (t, 3H; -CH_3, hexylamine), 1.24 (6H; -CH_2-CH_2-CH_2,hexylamine), 1.38 (m, 13H; -CH_2-CH_2-NH-,hexylamine and $(CH_3)_3$ - , Boc-Gly-), 2.73-2.94 (br m 3H; CH_3 of PSar side chain), 3.93−4.34 (br m, CH_2 of PSar backbone**)**.

Then, PSar-Gly(NBoc) (260 mg, 5×10^{-2} mmol, 1eq) was solubilized in a 6mL mixture of CH_2Cl_2/TFA (50:50) and left to stir for 2 hours. The final product was precipitated in diethyl ether, neutralized in saturated $NaHCO_3$ solution, and then dialyzed against deionized water in a 1 kDa dialysis membrane and lyophilized. Yield = 80%, white powder. ^{1}H NMR (400 MHz, DMSO-d_6): δ=0.86 (t, 3H; -CH_3, hexylamine), 1.24 (6H; -CH_2-CH_2-CH_2, hexylamine), 1.38 (m, 4H; -CH_2-CH_2-NH-,hexylamine), 2.73-2.94 (br m 3H; CH_3 of PSar side chain), 3.93−4.34 (br m, CH_2 of PSar backbone and of Gly chain-end**)**. M_n^{NMR} = 5 400 g.mol^{-1} (DP^{NMR} = 73). SEC (1% KTFA in HFIP) $M_{n,\,SEC\ RI}$ = 35 600 g. mol^{-1}, $Đ$ = 1.06.

IV.8.3.1.3. Poly(sarcosine)-block-poly(γ-benzyl-L-glutamate) PSar-b-PBLG

In a glove box, the NCA monomer of γ-benzyl-*L*-glutamate (40 mg, 0.142 mmol) was weighed in a Schlenk tube containing a magnetic stirring bar. The Schlenk is removed from the glove box and cooled on ice. 1mL of an ice-cooled solution of $NaHCO_3$ 0.05M containing the initiator PSar-NH_2 (40 mg, 0.0071 mmol, [M]/[I] = 20) is added to the BLG-NCA powder under a strong agitation (τ_s = 7 wt%). The reaction is left to stir 1) first in an ice-cold water bath; 2) then at room temperature overnight. The opalescent dispersion obtained is then transferred to a 3.5 kDa dialysis membrane and dialyzed against deionized water for 2 days. An aliquot is kept for further microscopy imaging and dynamic light scattering and the remaining dispersion is lyophilized. A white powder is obtained with a yield of 79%.

IV.8.3.2. Synthesis of PLP-based diblock copolymers

IV.8.3.2.1. Synthesis of poly(L-proline) macroinitiator

PLP was synthesized as reported previously by Baldredin et al.[73] *L*-Pro-NCA (1 g, 71 $\times 10^{-1}$ mmol, 50 eq) was introduced in a flame-dried Schlenk equipped with a stirrer and suspended in 0.5 mL of dry ACN. Hexylamine (10.43 mg, 1.4×10^{-1} mmol, 1eq) dissolved in 10.5 mL H_2O:ACN (1:1) at 10°C was added to the first solution to start the ROP under vigorous stirring. The solution quickly became clear, and bubbling was observed. FTIR confirmed the reaction completion after 10 minutes by monitoring the disappearance of the bands at 1859 cm^{-1} and 1787 cm^{-1} characteristic of the C=O stretching of NCAs. The reaction mixture was dialyzed against deionized water in a 100-500 Da dialysis membrane to remove all unreacted monomers and solvent before being lyophilized. Yield: 90%, white powder. ^{1}H NMR (400 MHz, D_2O): δ=0.85 (t, 3H; -CH_3, hexylamine), 1.26 (6H; -CH_2-CH_2-CH_2-, hexylamine), 1.45-1.48 (m, 4H; -CH_2-CH_2-NH-,hexylamine), 2.03 (t, 2H; -CH_2-CH_2-CH_2-, polymer backbone), 1.80-2.40 (m, 2H; -CH_2CH_2-CH_2-, polymer backbone), 3.55-3.90 (m, 2H; -CH_2-CH_2-N-, polymer backbone), 4.71 ppm (t, 1H; OC-CH-N, polymer backbone). M_n, ^{NMR} = 5 400 g.mol^{-1} (DP^{NMR} = 55). SEC (Acetate/ACN) M_n $^{SEC\ LS}$ = 5 800 g.mol^{-1}, $Đ$ = 1.03.

IV.8.3.2.2. Poly(L-proline)-block-poly(amino acids)

PLP was also used as an initiator using the same ROPISA protocol as described for PSar-NH_2, using BLG-NCA, Lys(Boc)-NCA and Gly-NCA as monomers, for an initial feeding ratio [M]/[I] of 20. In this case, the buffer used was $NaHCO_3$ 0.1M.

IV.8.3.3. Synthesis of ELP-*b*-PBLG

IV.8.3.3.1. Synthesis of elastin-like polypeptide by recombinant production

ELP[M_1V_3-(20,40,80)] – ELP – used for this study was produced using *Escherichia coli* as an expression system, purified by inverse transition cycling and characterized as previously described.[29] They were synthesized by Pauline Coutand and Alice Delhaes. The amino acid sequence is MW[(VPGVG)(VPGMG)$(VPGVG)_2]_{5,10,20}$, the molecular weight is precisely 8 687, 17 035 and 33 735 g.mol^{-1} respectively.

IV.8.3.3.2. Elastin like polypeptide-block-poly(γ-benzyl-L-glutamate) ELP-b-PBLG

ELPM20, ELPM40 and ELPM80 were used as an initiator for the ROPISA of BLG-NCA. The protocol as described for PSar-*b*-PBLG was slightly modified to decrease the solid content of the reaction to 0.5 wt% and temperature was maintained at 4°C for the whole duration of the reaction.

IV.8.3.4. Synthesis of PEG-CP-PBLG

IV.8.3.4.1. Synthesis of Poly(ethylene glycol)-cyclic peptide conjugate

The cyclic peptide was first synthesized by Min Zheng, according to a published procedure.[50] Then, peptide coupling on PEG-COOH have been realized according to the following procedure:

PEG-COOH (416 mg, 8.3×10^{-5} mol, 1 eq), dried previously by azeotropic evaporation with toluene, was solubilized with anhydrous DMF (20 mL). HOBt (35 mg, 2.5×10^{-4} mol, 3 eq) was first added, followed by the cyclic peptide (105 mg, 8.4×10^{-5} mol, 1 eq) and EDC (36 µL, 2×10^{-4} mol, 2.4 eq). The mixture was left to stir for 16 hours. Conjugate was then purified by dialysis against ultra-pure water using a 1 kDa cut-off membrane. Yield: 429 mg, 82%.

Then, the protected conjugate (333 mg, 5.3×10^{-5} mol, 1 eq) was dissolved in 8 mL of 2% hydrazine in DMF. The mixture was left to stir for 16 hours. The deprotected PEG-CP-NH_2 was purified by dialysis against ultra-pure water using a 3.5 kDa cut-off membrane. The isolated conjugate was freeze-dried. Yield: 219 mg, 85%.

IV.8.3.4.2. Poly(ethylene glycol)-cyclic peptide-block-poly(γ-benzyl-L-glutamate)

ROPISA of BLG-NCA was carried out using the PEG-CP as macroinitiator in the same conditions as PSar-NH2, with an initial feeding ratio [M]/[I] of 20.

IV.8.3.5. Synthesis of SIP-*b*-PBLG

The Self-Immolative Polymer was furnished by Elizabeth Gillies team.

ROPISA of BLG-NCA was carried out using the SIP as macroinitiator in the same conditions as PSar-NH_2, with an initial feeding ratio [M]/[I] of 20.

IV.8.3.6. Enzyme-polypeptide conjugates

HRP, Lac, or VP were first transferred from PBS buffer to 50 mM $NaHCO_3$ using Amicon Ultra Centrifugal filters, adjusting the concentration to 10 mg·mL^{-1}. Each enzyme was then mixed with varying equivalents of Gly-NCA or BLG-NCA, targeting lysine residues as initiation sites. The solid content ranged from 1.2% to 8.2%, depending on the feed ratio. Polymerization was carried out overnight in Eppendorf tubes submerged in an ice bath, with a final reaction volume of 0.1 mL.

Samples were then analyzed without purification (DLS, TEM) and after transferred to citrate-phosphate buffer (pH 4.4) for Lac-based conjugates or phosphate buffer (pH 6.0) for HRP and VP-conjugates, for SDS PAGE, native PAGE and enzymatic assays.

IV.8.3.7. Synthesis of Dex-*g*-PBLG and Dex-*b*-PBLG

DexN7.5 and Dex-NH_2 were provided by Khalid Ferji's team, synthetized following published protocols[69,74] (detailed Dextran characterizations are available in the referenced articles). Dex-ADH was synthesized by Elise Courtecuisse.[68]

ROPISA of BLG-NCA was carried out using the Dex as macroinitiator with a feeding ratio of 27 (Dex-NH_2) or 19 (DexADH), using three types of buffers: ultra-pure water, $NaHCO_3$ 50mM and $NaHCO_3$ 100mM. Samples were then purified and analyzed according to previous procedures.

IV.9. Supplementary figures

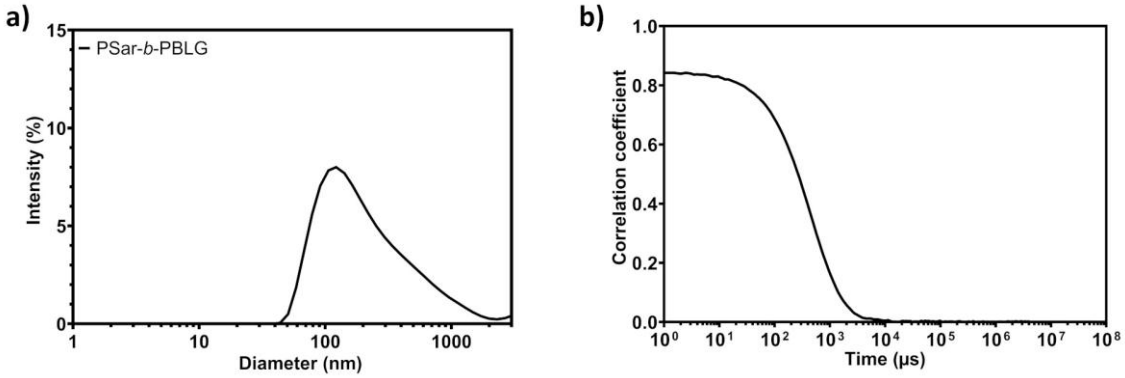

Figure SIV-1. (a) DLS profile of PSar-*b*-PBLG initiated by PSar-NH_2 and (b) corresponding correlogram.

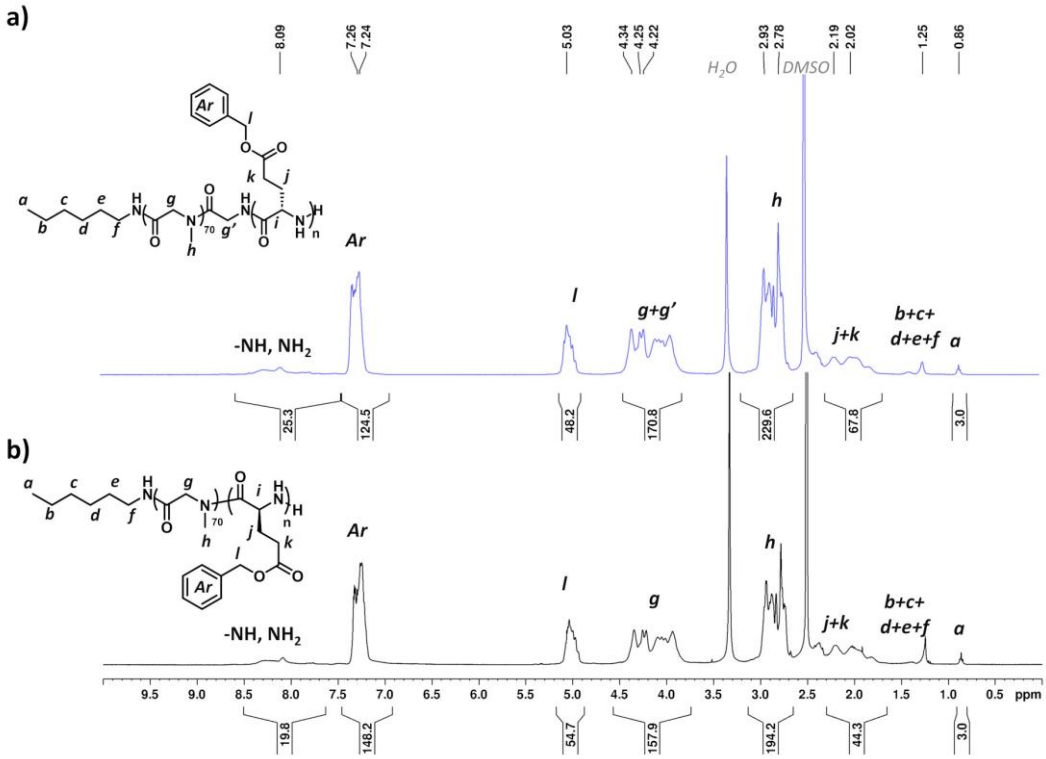

Figure SIV-2. ^{1}H NMR spectra of (a) PSar-*b*-PBLG initiated by PSar-NH_2 and (b) initiated by PSar in DMSO-d_6 for a targeted DP of 20.

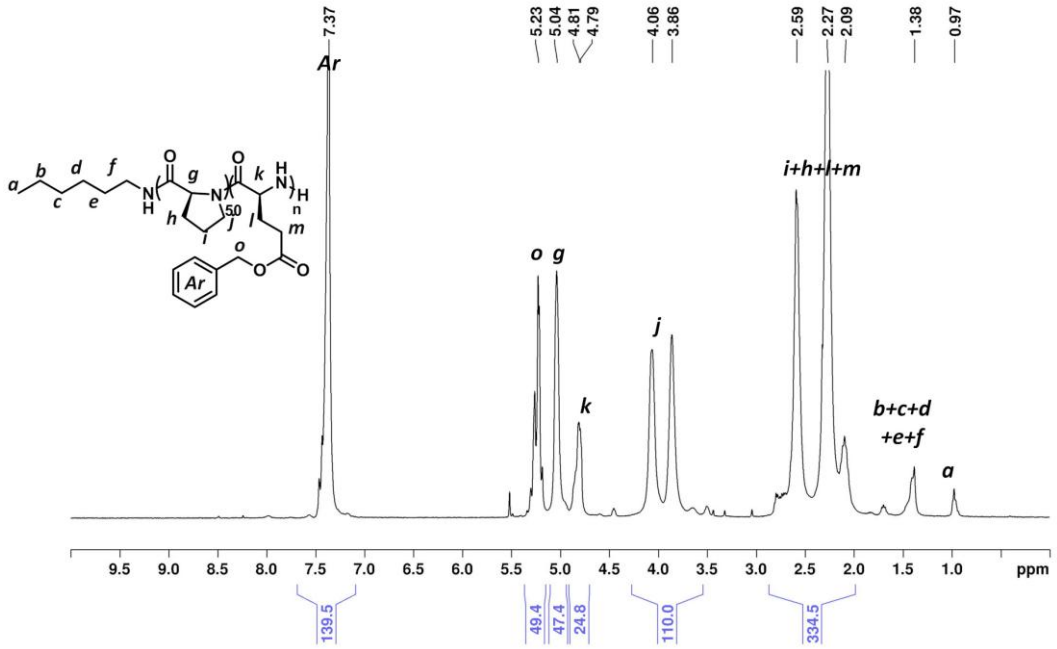

Figure SIV-3. ^{1}H NMR spectrum of PLP-*b*-PBLG in TFA-*d*.

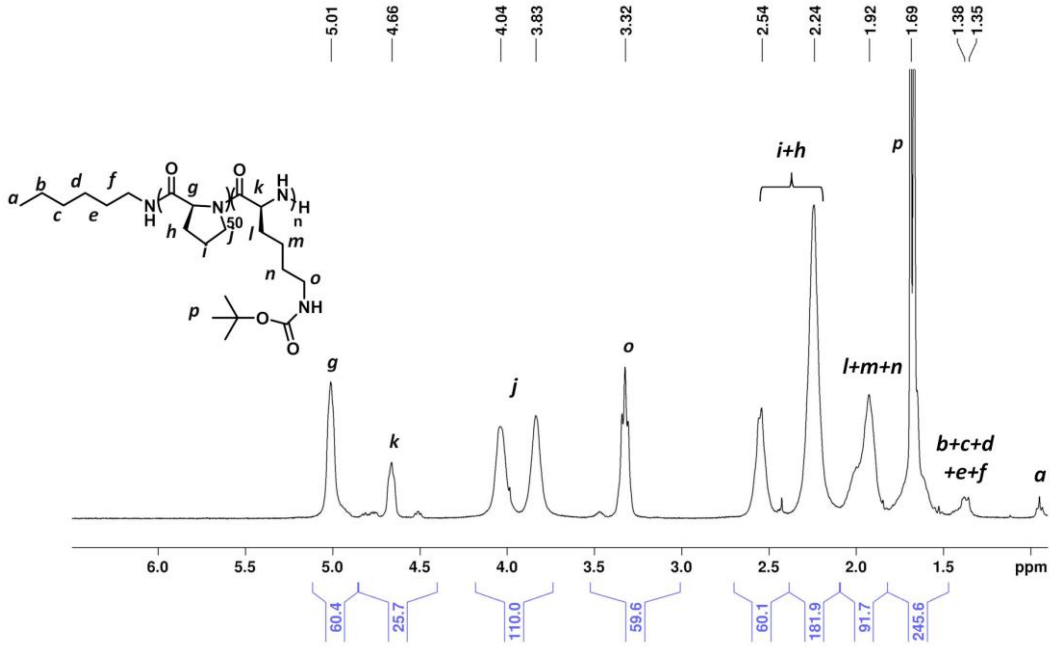

Figure SIV-4. ^{1}H NMR spectrum of PLP-*b*-PLys(Boc) in TFA-*d*.

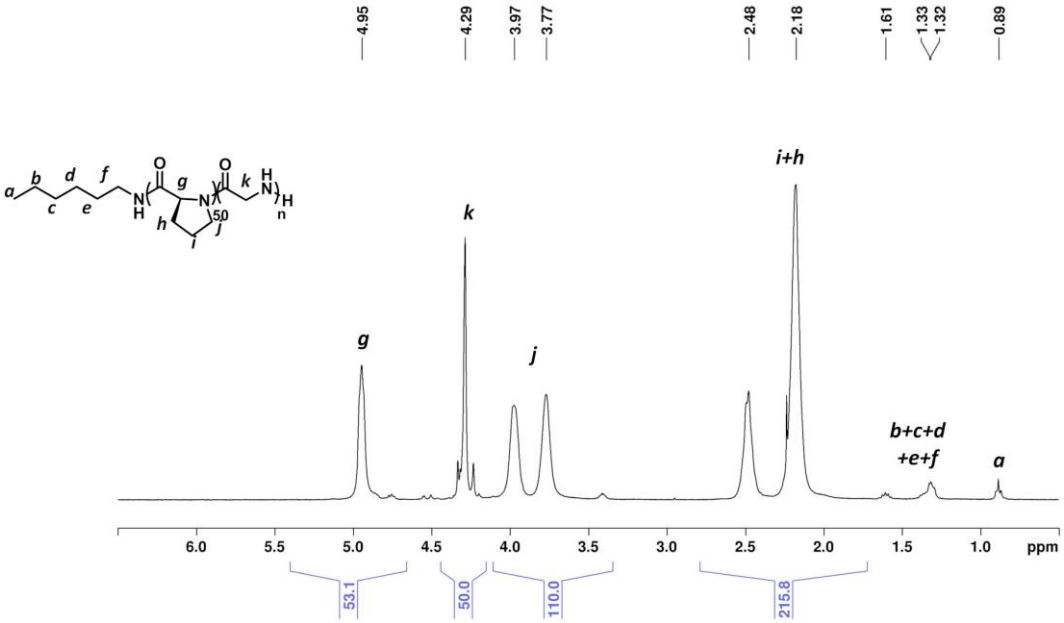

Figure SIV-5. ^{1}H NMR spectrum of PLP-*b*-PGly in TFA-*d*.

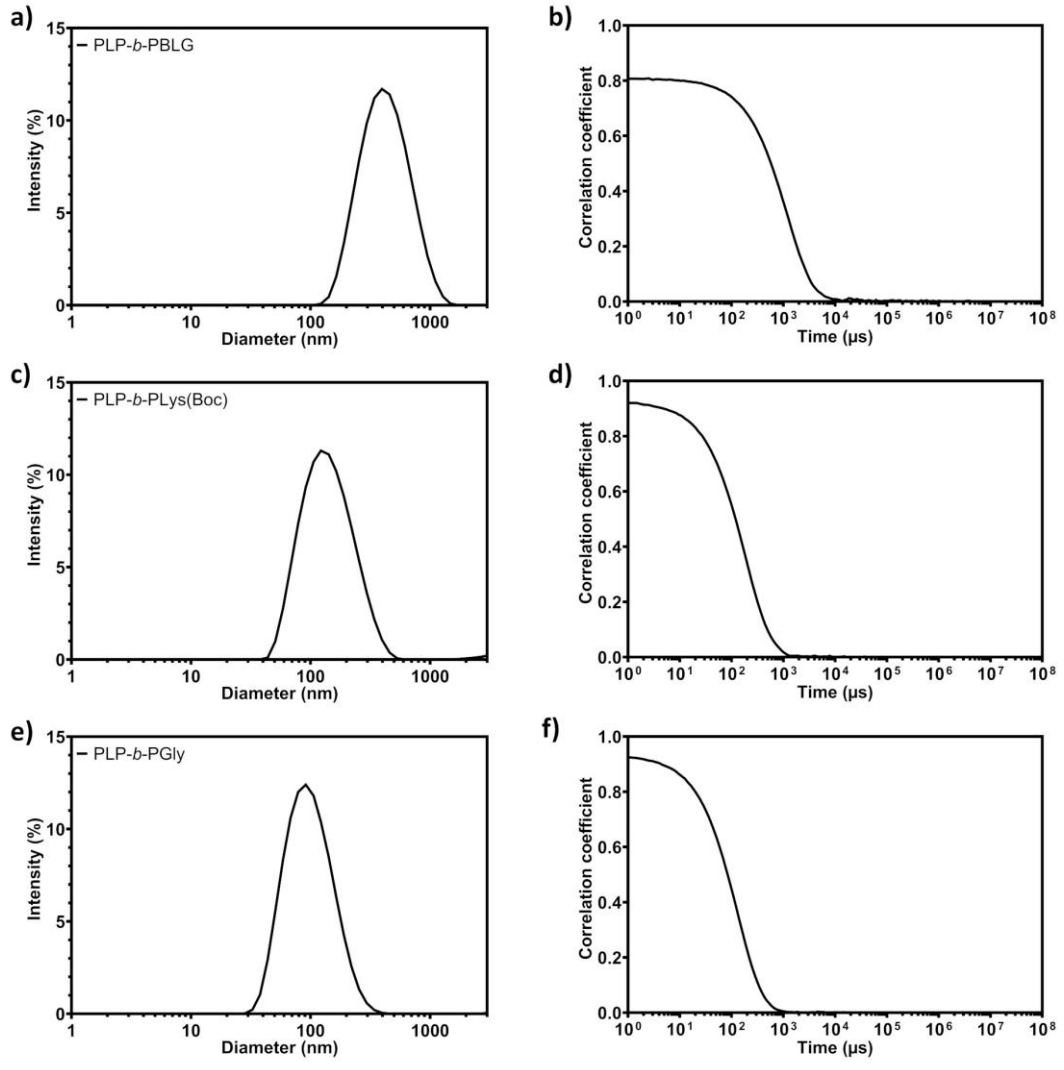

Figure SIV-6. DLS profiles (left) and associated correlograms (right) at 25 °C of (a-b): PLP-*b*-PBLG, (c-d): PLP-*b*-PLys(Boc), (e-f): PLP-*b*-PGly.

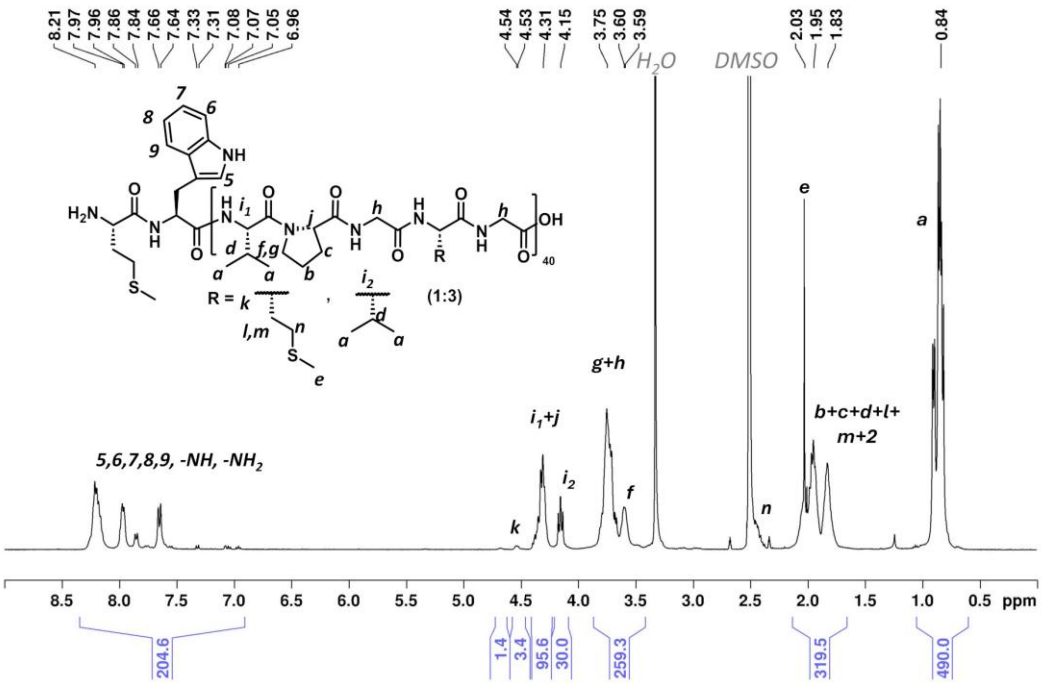

Figure SIV-7. ^{1}H NMR spectrum of ELPM40 in DMSO-d_6.

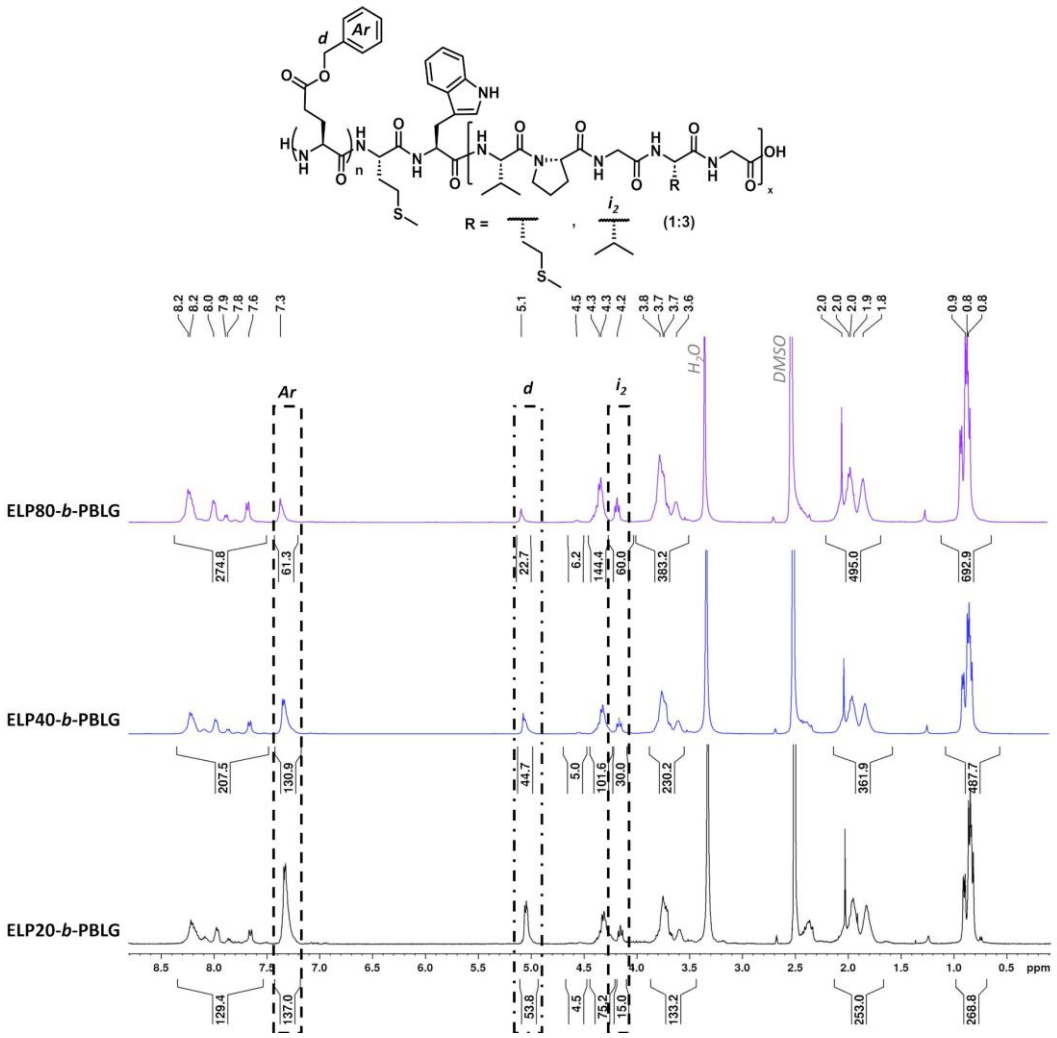

Figure SIV-8. ^{1}H NMR spectra of ELPx-*b*-PBLG in DMSO-d_6 initiated by ELPM20 (bottom), ELPM40 (middle) and ELPM80 (top).

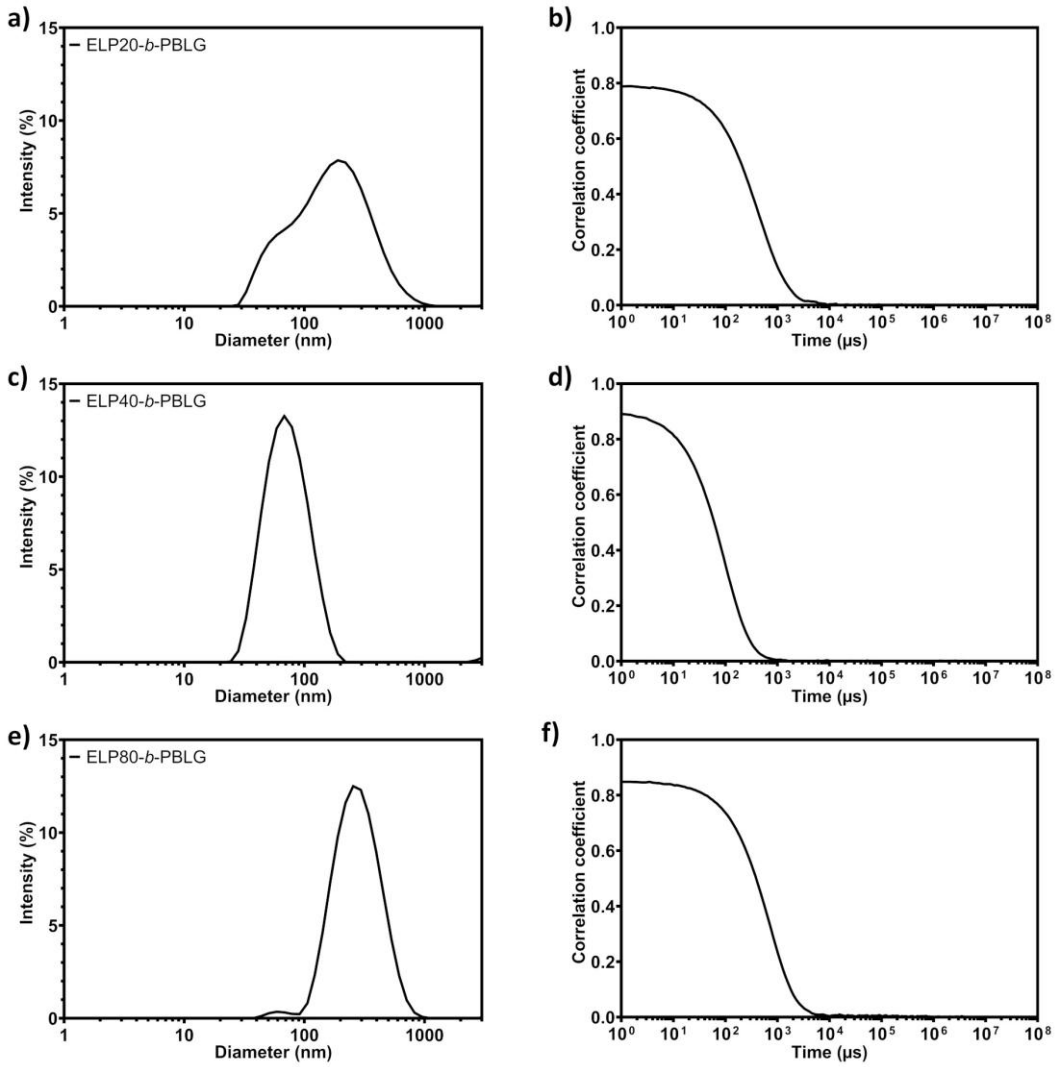

Figure SIV-9. DLS profiles (left) and associated correlograms (right) at 25 °C. (a-b): ELP20-*b*-PBLG. (c-d): ELP40-*b*-PBLG. (e-f): ELP80-*b*-PBLG.

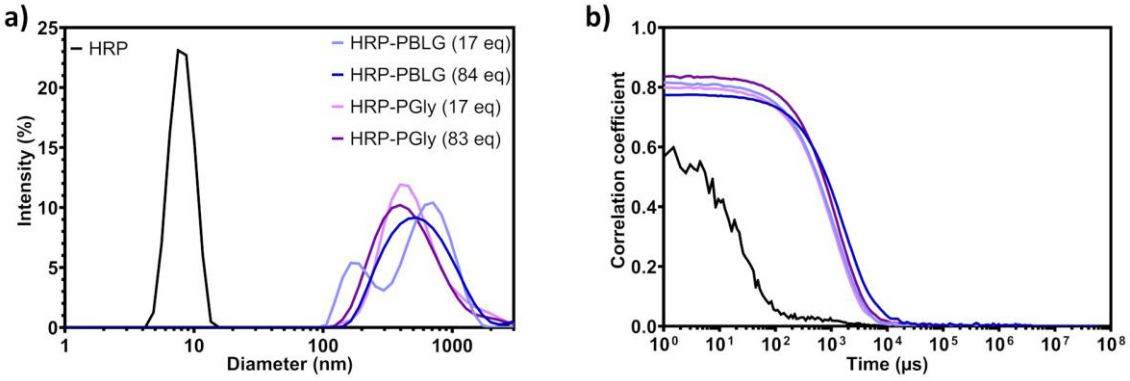

Figure SIV-10. (a) DLS profiles of free HRP and HRP-conjugates obtained by ROPISA and (b) corresponding correlograms.

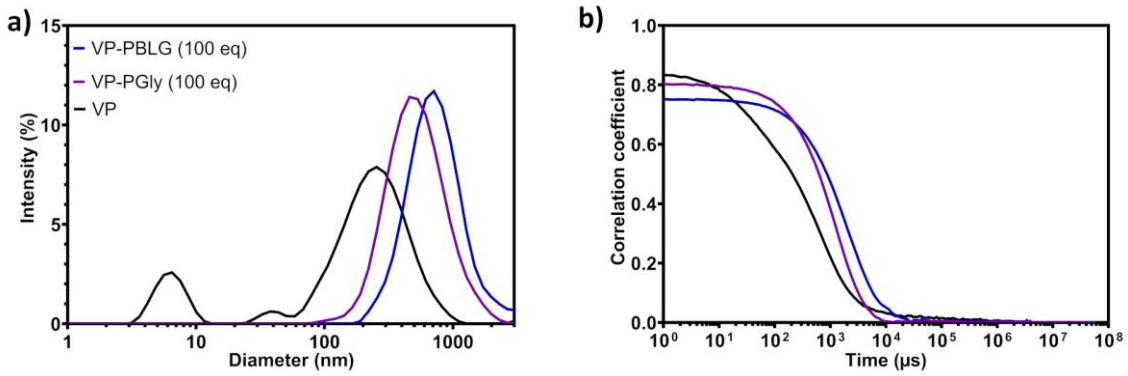

Figure SIV-11. (a) DLS profiles of free VP and VP-conjugates obtained by ROPISA and (b) corresponding correlograms.

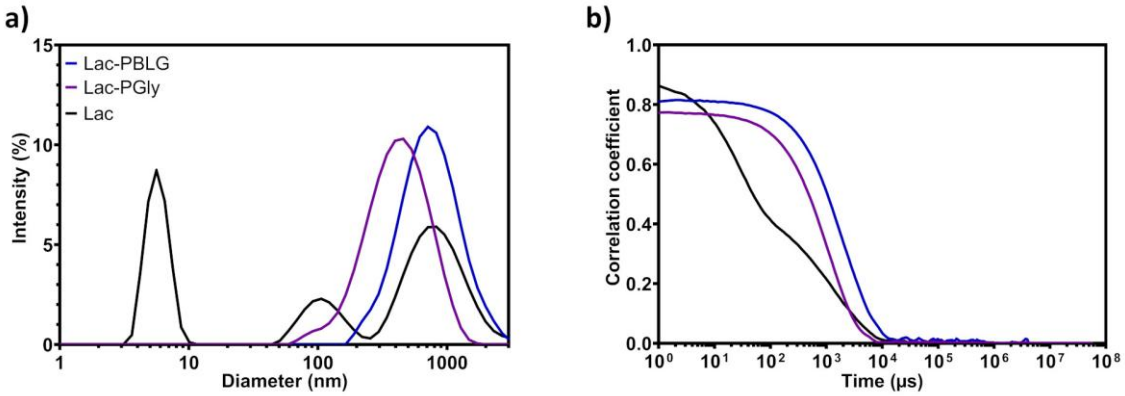

Figure SIV-12. (a) DLS profiles of free Lac and Lac-conjugates obtained by ROPISA and (b) corresponding correlograms.

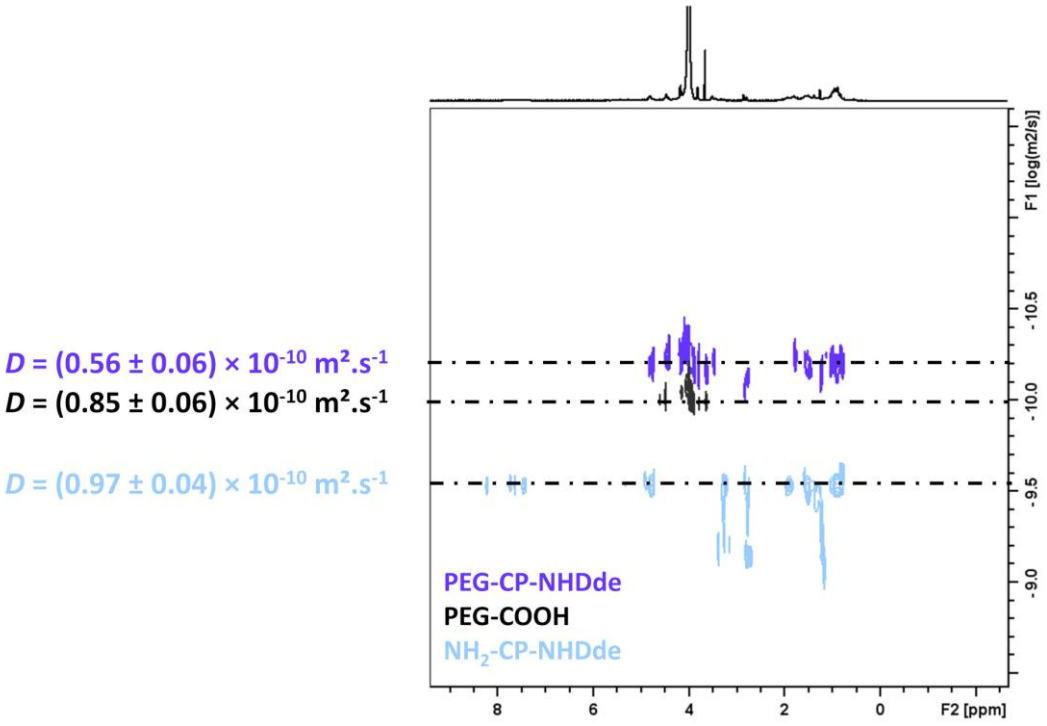

Figure SIV-13. ^{1}H diffusion ordered NMR spectroscopy (DOSY) spectra of PEG-CP-NHDde conjugate (purple), PEG-COOH (black) and NH_2-CP-NHDde (blue) in TFA-*d*.

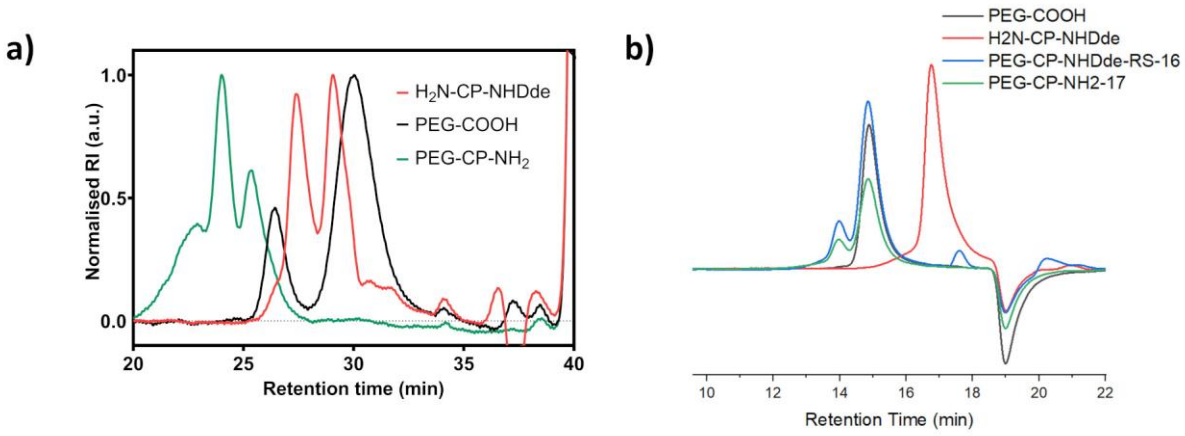

Figure SIV-14. (a) SEC chromatograms of PEG-CP-NH_2 conjugate compared to PEG-COOH and initial peptide cyclic (+1% LiBr, detection by differential refractive index, LCPO conditions). (b) SEC chromatograms of PEG-CP-NHDde and PEG-CP NH_2 conjugates compared to PEG-COOH initial peptide cyclic (+1% LiBr, detection by differential refractive index, Perrier's lab conditions).

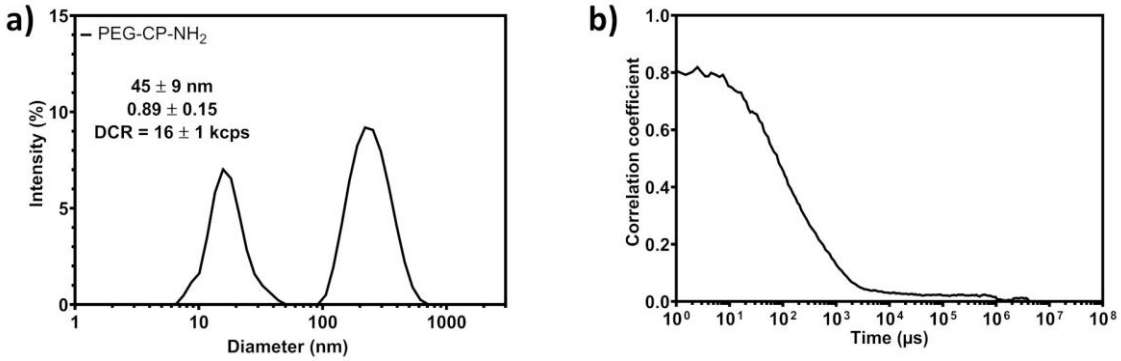

Figure S15. (a) DLS profile of PEG-CP-NH_2 in water at 1 mg.mL^{-1} and (b) corresponding correlogram.

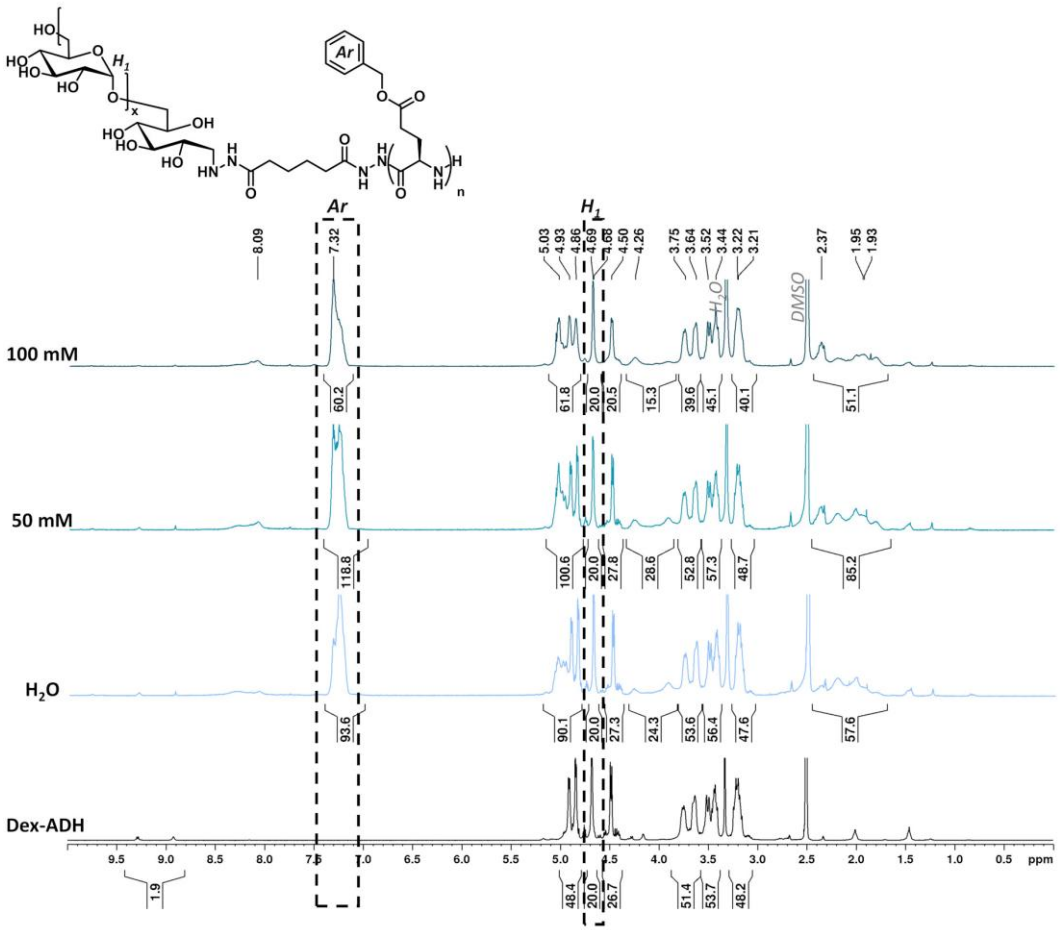

Figure SIV-16. ^{1}H NMR spectra of Dex-*b*-PBLG in DMSO-d_6 initiated by DexADH for ROPISA in various buffer concentrations. The H_1 signals from the Dextran backbone were used as a reference to determine the DP of the PBLG block, with the integration of the aromatic protons (Ar).

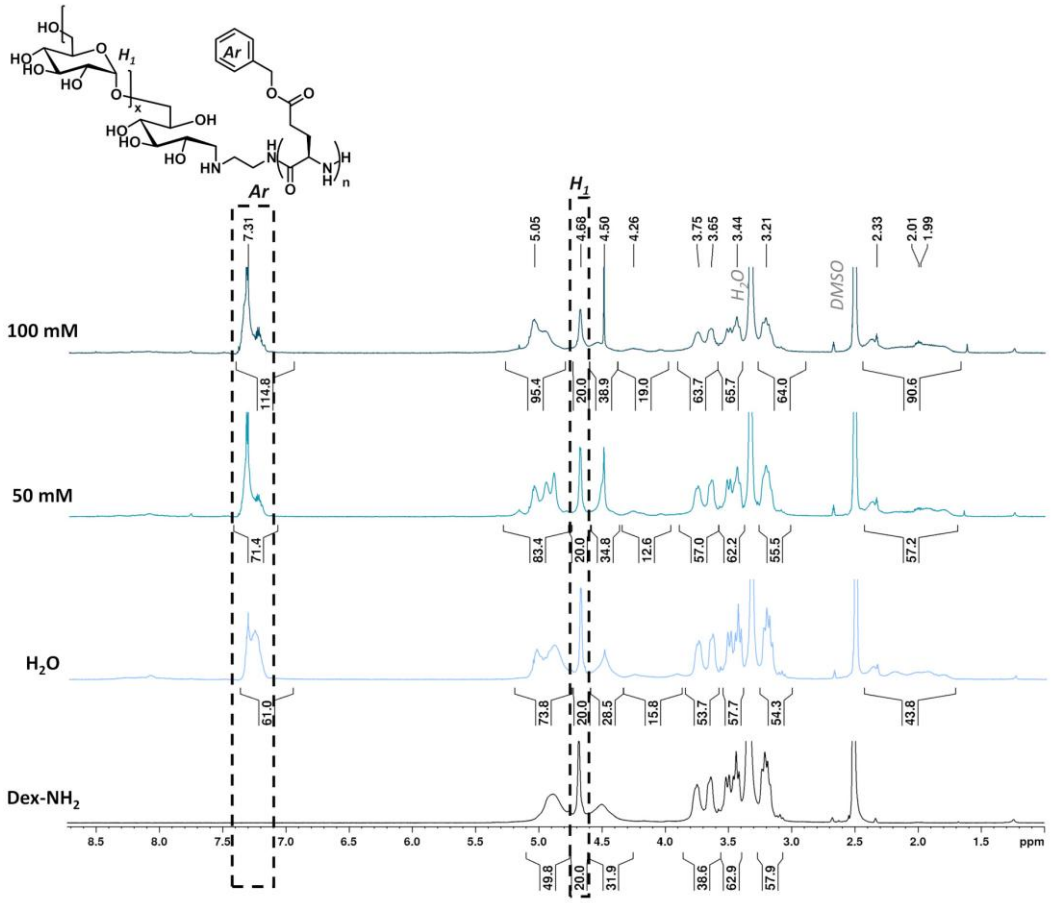

Figure SIV-17. ^{1}H NMR spectra of Dex-*b*-PBLG in DMSO-d_6 initiated by DexNH_2 for ROPISA in various buffer concentrations. The H_1 signals from the Dextran backbone were used as a reference to determine the DP of the PBLG block, with the integration of the aromatic protons (Ar).

IV.10. References

[1] C. Zhu, J. Nicolas, *Biomacromolecules* **2022**, *23*, 3043–3080.
[2] F. Shirinichi, T. Ibrahim, M. Rodriguez, H. Sun, *Journal of Polymer Science* **2023**, *61*, 631–645.
[3] H. Beauseroy, C. Grazon, S. Antoine, M. Badreldin, P. Salas-Ambrosio, S. Harrisson, E. Garanger, S. Lecommandoux, C. Bonduelle, *Macromol. Rapid Commun.***2024**, *45*, 2400079.
[4] S. Chen, P. Zhou, W. Yang, D. Hu, P. Chen, P. Sun, J. Ling, Q. Fan, *Biomater. Sci.* **2023**, *11*, 4644–4651.
[5] X. Yao, C. Sun, F. Xiong, W. Zhang, W. Yao, Y. Xu, W. Fan, F. Huo, *ACS Appl. Mater. Interfaces* **2024**, *16*, 19472–19479.
[6] P. Heller, A. Birke, D. Huesmann, B. Weber, K. Fischer, A. Reske-Kunz, M. Bros, M. Barz, *Macromolecular Bioscience* **2014**, *14*, 1380–1395.
[7] A. Birke, D. Huesmann, A. Kelsch, M. Weilbächer, J. Xie, M. Bros, T. Bopp, C. Becker, K. Landfester, M. Barz, *Biomacromolecules* **2014**, *15*, 548–557.
[8] A. Birke, J. Ling, M. Barz, *Prog. Polym. Sci.***2018**, *81*, 163–208.
[9] C. Lebleu, L. Plet, F. Moussy, G. Gitton, R. Da Costa Moreira, L. Guduff, B. Burlot, R. Godiveau, A. Merry, S. Lecommandoux, G. Errasti, C. Philippe, T. Delacroix, R. Chakrabarti, *Int. J. Pharm.***2023**, *631*, 122501.
[10] B. Weber, A. Birke, K. Fischer, M. Schmidt, M. Barz, *Macromolecules* **2018**, *51*, 2653–2661.
[11] A. H. Morrell, N. J. Warren, P. D. Thornton, *Macromol. Rapid Commun.***2024**, 2400103.
[12] R. K. Dukor, T. A. Keiderling, *Biospectroscopy* **1998**, *2*, 83–100.
[13] L. Shi, A. E. Holliday, H. Shi, F. Zhu, M. A. Ewing, D. H. Russell, D. E. Clemmer, *J. Am. Chem. Soc.* **2014**, *136*, 12702–12711.
[14] Y. Hu, Z.-Y. Tian, W. Xiong, D. Wang, R. Zhao, Y. Xie, Y.-Q. Song, J. Zhu, H. Lu, *National Science Review* **2022**, *9*, nwac033.
[15] M. Badreldin, R. Le Scouarnec, S. Lecommandoux, S. Harrisson, C. Bonduelle, *Angew. Chem. Int. Ed.* **2022**, *134*, e202209530.
[16] E. Tinajero-Díaz, N. Judge, B. Li, T. Leigh, R. D. Murphy, P. D. Topham, M. J. Derry, A. Heise, *ACS Macro Lett.* **2024**, 1031–1036.
[17] P.-J. Voorter, A. McKay, J. Dai, O. Paravagna, N. R. Cameron, T. Junkers, *Angew. Chem. Int. Ed.* **2022**, *61*, e202114536.
[18] M. Rubinstein, R. H. Colby, M. Rubinstein, R. H. Colby, *Polymer Physics*, Oxford University Press, Oxford, New York, **2003**.
[19] M. C. J. Wilce, M.-Isabel. Aguilar, M. T. W. Hearn, *Anal. Chem.* **1995**, *67*, 1210–1219.
[20] K. Widder, S. R. MacEwan, E. Garanger, V. Núñez, S. Lecommandoux, A. Chilkoti, D. Hinderberger, *Soft Matter* **2017**, *13*, 1816–1822.
[21] J. A. Foster, E. Bruenger, W. R. Gray, L. B. Sandberg, *J Biol Chem* **1973**, *248*, 2876–2879.
[22] M. F. Shamji, H. Betre, V. B. Kraus, J. Chen, A. Chilkoti, R. Pichika, K. Masuda, L. A. Setton, *Arthritis & Rheumatism* **2007**, *56*, 3650–3661.
[23] G. L. Fer, D. Portes, G. Goudounet, J.-M. Guigner, E. Garanger, S. Lecommandoux, *Org. Biomol. Chem.* **2017**, *15*, 10095–10104.
[24] G. Le Fer, A.-L. Wirotius, A. Brûlet, E. Garanger, S. Lecommandoux, *Biomacromolecules* **2019**, *20*, 254–272.
[25] Y. Fujita, M. Mie, E. Kobatake, *Biomaterials* **2009**, *30*, 3450–3457.
[26] H. Wang, L. Cai, A. Paul, A. Enejder, S. C. Heilshorn, *Biomacromolecules* **2014**, *15*, 3421–3428.
[27] A. V. Janorkar, P. Rajagopalan, M. L. Yarmush, Z. Megeed, *Biomaterials* **2008**, *29*, 625–632.
[28] Y. Xiao, Z. S. Chinoy, G. Pecastaings, K. Bathany, E. Garanger, S. Lecommandoux, *Biomacromolecules* **2020**, *21*, 114–125.
[29] R. Petitdemange, E. Garanger, L. Bataille, W. Dieryck, K. Bathany, B. Garbay, T. J. Deming, S. Lecommandoux, *Biomacromolecules* **2017**, *18*, 544–550.
[30] N. K. Li, F. G. Quiroz, C. K. Hall, A. Chilkoti, Y. G. Yingling, *Biomacromolecules* **2014**, *15*, 3522–3530.
[31] E. Garanger, S. R. MacEwan, O. Sandre, A. Brûlet, L. Bataille, A. Chilkoti, S. Lecommandoux, *Macromolecules* **2015**, *48*, 6617–6627.

[32] V. Ibrahimova, H. Zhao, E. Ibarboure, E. Garanger, S. Lecommandoux, *Angew. Chem. Int. Ed.* **2021**, *60*, 15036–15040.
[33] A. Chilkoti, M. R. Dreher, D. E. Meyer, *Adv. Drug Deliv. Rev.***2002**, *54*, 1093–1111.
[34] S. Zhang, R. Li, Z. An, *Angew. Chem. Int. Ed.* **2024**, *63*, e202315849.
[35] B. Valderrama, M. Ayala, R. Vazquez-Duhalt, *Chemistry & Biology* **2002**, *9*, 555–565.
[36] Y. R. Maghraby, R. M. El-Shabasy, A. H. Ibrahim, H. M. E.-S. Azzazy, *ACS Omega* **2023**, *8*, 5184–5196.
[37] J. D. Schulz, M. Patt, S. Basler, H. Kries, D. Hilvert, M. A. Gauthier, J. Leroux, *Advanced Materials* **2016**, *28*, 1455–1460.
[38] S. Moreno-Pérez, A. H. Orrego, M. Romero-Fernández, L. Trobo-Maseda, S. Martins-DeOliveira, R. Munilla, G. Fernández-Lorente, J. M. Guisan, in *Methods in Enzymology*, Elsevier, **2016**, pp. 55–72.
[39] Y. Hou, H. Lu, *Bioconjugate Chem.* **2019**, *30*, 1604–1616.
[40] C. Bao, J. Chen, D. Li, A. Zhang, Q. Zhang, *Polym. Chem.* **2020**, *11*, 1386–1392.
[41] C.-W. Chiang, X. Liu, J. Sun, J. Guo, L. Tao, W. Gao, *Nano Lett.* **2020**, *20*, 1383–1387.
[42] S. H. Khatami, O. Vakili, A. Movahedpour, Z. Ghesmati, H. Ghasemi, M. Taheri-Anganeh, *Biotechnology and Applied Biochemistry* **2022**, *69*, 2658–2672.
[43] N. C. Veitch, *Phytochemistry* **2004**, *65*, 249–259.
[44] Q. Song, Z. Cheng, M. Kariuki, S. C. L. Hall, S. K. Hill, J. Y. Rho, S. Perrier, *Chem. Rev.* **2021**, *121*, 13936–13995.
[45] M. L. Koh, P. A. FitzGerald, G. G. Warr, K. A. Jolliffe, S. Perrier, *Chemistry A European J* **2016**, *22*, 18419–18428.
[46] S. Catrouillet, J. C. Brendel, S. Larnaudie, T. Barlow, K. A. Jolliffe, S. Perrier, *ACS Macro Lett.* **2016**, *5*, 1119–1123.
[47] B. M. Blunden, R. Chapman, M. Danial, H. Lu, K. A. Jolliffe, S. Perrier, M. H. Stenzel, *Chemistry – A European Journal* **2014**, *20*, 12745–12749.
[48] S. C. Larnaudie, J. C. Brendel, I. Romero-Canelón, C. Sanchez-Cano, S. Catrouillet, J. Sanchis, J. P. C. Coverdale, J.-I. Song, A. Habtemariam, P. J. Sadler, K. A. Jolliffe, S. Perrier, *Biomacromolecules* **2018**, *19*, 239–247.
[49] S. K. Hill, R. M. England, S. Perrier, *J. Control. Release.***2024**, *367*, 687–696.
[50] S. C. Larnaudie, J. C. Brendel, K. A. Jolliffe, S. Perrier, *J. Polym. Sci. Part A: Polym. Chem.* **2016**, *54*, 1003–1011.
[51] Z. Cheng, Q. Song, S. C. L. Hall, S. Perrier, *Chem. Sci.***2025**, *16*, 1894–1906.
[52] O. Shelef, S. Gnaim, D. Shabat, *J. Am. Chem. Soc.* **2021**, *143*, 21177–21188.
[53] X. Liang, E. R. Gillies, *ACS Polym. Au* **2022**, *2*, 313–323.
[54] M. A. DeWit, E. R. Gillies, *J. Am. Chem. Soc.* **2009**, *131*, 18327–18334.
[55] B. Fan, E. R. Gillies, *Mol. Pharmaceutics* **2017**, *14*, 2548–2559.
[56] Q. E. A. Sirianni, X. Liang, G. K. Such, E. R. Gillies, *Macromolecules* **2021**, *54*, 10547–10556.
[57] Y. Jiang, C. Yan, M. Li, S. Chen, Z. Chen, L. Yang, K. Luo, *International Journal of Biological Macromolecules* **2024**, *278*, 135072.
[58] V. M. Platt, F. C. Jr. Szoka, *Mol. Pharmaceutics* **2008**, *5*, 474–486.
[59] K. K. Upadhyay, J.-F. L. Meins, A. Misra, P. Voisin, V. Bouchaud, E. Ibarboure, C. Schatz, S. Lecommandoux, *Biomacromolecules* **2009**, *10*, 2802–2808.
[60] K. K. Upadhyay, A. N. Bhatt, A. K. Mishra, B. S. Dwarakanath, S. Jain, C. Schatz, J.-F. Le Meins, A. Farooque, G. Chandraiah, A. K. Jain, A. Misra, S. Lecommandoux, *Biomaterials* **2010**, *31*, 2882–2892.
[61] K. K. Upadhyay, A. K. Mishra, K. Chuttani, A. Kaul, C. Schatz, J.-F. Le Meins, A. Misra, S. Lecommandoux, *Nanomedicine: Nanotechnology, Biology and Medicine* **2012**, *8*, 71–80.
[62] S. M. North, S. P. Armes, *Polymer Chemistry* **2020**, *11*, 2147–2156.
[63] V. Ladmiral, A. Charlot, M. Semsarilar, S. P. Armes, *Polymer Chemistry* **2015**, *6*, 1805–1816.
[64] C. Lemarchand, R. Gref, C. Passirani, E. Garcion, B. Petri, R. Müller, D. Costantini, P. Couvreur, *Biomaterials* **2006**, *27*, 108–118.
[65] C. Schatz, S. Louguet, J.-F. Le Meins, S. Lecommandoux, *Angew. Chem. Int. Ed.* **2009**, *48*, 2572–2575.
[66] D. Ikkene, A. A. Arteni, M. Ouldali, G. Francius, A. Brûlet, J.-L. Six, K. Ferji, *Biomacromolecules* **2021**, *22*, 3128–3137.

[67] D. Ikkene, A. A. Arteni, C. Boulogne, J.-L. Six, K. Ferji, *Macromolecules* **2022**, *55*, 4268–4275.
[68] E. Courtecuisse, S. Bourasseau, B. E. Christensen, C. Schatz, *Carbohydrate Polymers* **2024**, *345*, 122576.
[69] V. L. Romero Castro, B. Nomeir, A. A. Arteni, M. Ouldali, J.-L. Six, K. Ferji, *Polymers* **2021**, *13*, 4064.
[70] A. F. Chinn, P. Farzeen, Z. Li, J. D. Mase, C. Vu, M. D. Schulz, S. Deshmukh, J. B. Matson, *Carbohydrate Polymers* **2025**, *352*, 123186.
[71] X. Guo, B. Yang, J. Chen, *Biomacromolecules* **2024**, *25*, 3642–3650.
[72] S. Wang, Y. Tang, X. Kou, J. Chen, K. J. Edgar, *Biomacromolecules* **2024**, *25*, 3122–3130.
[73] M. Badreldin, R. Le Scouarnec, S. Lecommandoux, S. Harrisson, C. Bonduelle, *Angew. Chem. Int. Ed.* **2022**, *61*, e202209530.
[74] D. Ikkene, A. A. Arteni, H. Song, H. Laroui, J.-L. Six, K. Ferji, *Carbohydrate Polymers* **2020**, *234*, 115943.

Chapter V. *In vitro* and *in vivo* evaluation of nanoparticles obtained by aqueous ROPISA

Table of Contents

Chapter V. *In vitro* and *in vivo* evaluation of nanoparticles obtained by aqueous ROPISA

V.1. Introduction 236

V.2. Nanoparticles preparation 238

V.2.1. Worm-like micelles preparation with covalent attachment of cyanine 238

V.2.2. Spherical nanoparticles obtention via solvent displacement 242

V.3. Cell internalization in 2D monolayer cell cultures 245

V.3.1. Cell viability in HUVEC 245

V.3.2. Cell association study in monolayer CT26 and 4T1 cells 245

V.3.2.1. CT26 245

V.3.2.1.1. Real-time confocal laser scanning microscopy 246

V.3.2.1.2. Flow cytometry 247

V.3.2.2. 4T1 249

V.3.2.2.1. Real-time confocal laser scanning microscopy 249

V.3.2.2.2. Flow cytometry 250

V.4. Spheroids penetration 251

V.4.1. Preparation of multicellular tumor spheroids (MCTS) 251

V.4.2. CLSM 253

V.4.2.1. CT26 MCTS 254

V.4.2.2. 4T1 MCTS 255

V.4.3. Flow cytometry 256

V.4.3.1. CT26 MCTS 257

V.4.3.2. 4T1 MCTS 258

V.5. Biodistribution 259

V.5.1. Circulation time in healthy BALB/c nude mice 259

V.5.2. Accumulation of fluorescent NPs in CT26 and 4T1 tumors 260

V.6. Conclusion 263

V.7. Experimental section 265

V.7.1. Materials 265

V.7.2. Instrumentation and methods 265

V.7.2.1. Nuclear Magnetic Resonance (NMR) 265

V.7.2.2. Size Exclusion Chromatography (SEC) 265

V.7.2.3. Cell viability 266

V.7.2.4. Dynamic Light Scattering (DLS) 266

V.7.2.5. Transmission Electron Microscopy (TEM) 266

V.7.2.6. Cryo-Transmission Electron Microscopy (cryo-TEM) 266

V.7.2.7. Fluorescence measurements 266

V.7.2.8. *In vitro* cytotoxicity of nanoparticles on HUVEC cells 266
V.7.2.9. Cell culture 267
V.7.2.10. Confocal Laser Scanning Microscopy (CLSM) 267
V.7.2.11. Flow cytometry measurements 268
V.7.2.12. In Vivo Laser Scanning Microscopy 269
V.7.2.13. Biodistribution and tumor accumulation of Cy7 nanoparticles in CT26-tumor bearing mice 269
V.7.2.14. Biodistribution and tumor accumulation of Cy7 nanoparticles in 4T1-tumor bearing mice 270
V.7.2.15. Animals and animal Care 270
V.7.2.16. Data analysis 270
V.7.3. Synthesis 270
V.7.3.1. Synthesis procedure of poly(ethylene glycol)-*block*-poly(γ-benzyl- *L*-glutamate) PEG_{5k}-*b*-$PBLG_{31}$ 270
V.7.3.2. Grafting of cyanine 5.5: poly(ethylene glycol)-*block*-poly(γ-benzyl-*L*-glutamate) PEG_{5k}-*b*-$PBLG_{31}$-Cy5.5 270
V.7.3.3. Grafting of cyanine 7: poly(ethylene glycol)-*block*-poly(γ-benzyl-*L*-glutamate) PEG_{5k}-*b*-$PBLG_{31}$-Cy7 271
V.7.3.4. Reformulation into spherical analogue nanoparticles 271

V.8. References 272

V.1. Introduction

As mentioned in **Chapter I**, polymeric nanoparticles have gained significant attention in nanomedicine due to their versatile properties and the potential applications they offer in the field of drug delivery.[1,2] Their synthesis *via* controlled polymerization processes, followed by self-assembly, enables the formation of nanoparticles with tunable morphologies and surface properties.[3,4] This structural versatility is particularly advantageous in cancer therapy, where nanoparticles can serve as carriers for hydrophobic drugs,[5] nucleic acids,[6] or metal complexes,[7,8] improving their solubility, stability, and targeted delivery.[9] However, the use of nanoparticles and by extension, polymers, in medical applications depends on their biocompatibility and (bio)degradability, which significantly restricts the available polymer options.[10] In this context, we evidenced in **Chapter I** that polypeptides stand out as particularly attractive for their ability to mimic key protein properties, such as biocompatibility, biodegradability and hierarchical organization.[11–13] They can be obtained easily through ring-opening polymerization (ROP) of amino acid *N*-carboxyanhydrides (NCA), enabling the design of well-controlled polymers with narrow dispersity.[14] In the literature, many examples of amphiphilic polypeptides have been investigated for drug delivery, owing to their versatility for entrapping hydrophobic drugs through different interactions (*e.g.* electrostatic interactions,[15,16] π–π stacking,[17] and hydrophobic associations[18–20]). Some of these polypeptide systems have reached clinical trials, demonstrating significant clinical potential.[21–23] More specifically, nanoparticles resulting from the self-assembly of amphiphilic block copolymers composed of poly(γ-benzyl-*L*-glutamate) (PBLG) and poly(ethylene glycol) (PEG) have been extensively studied for biomedical applications. These nanocarriers offer a hydrophobic core with aromatic benzyl groups capable of inducing π-π stacking, facilitating the encapsulation of various hydrophobic compounds, such as clonazepam,[24,25] paclitaxel[19] or doxorubicin.[26]

A thorough examination of the current existing nanomedicine reveals that majority of these particles exhibit a spherical morphology and require at least a two-step formulation process involving separate synthesis and self-assembly steps. This approach often results in low nanoparticle concentrations, limiting scalability and industrial applications. Taking advantage of the ease of the procedure and our understanding of the process, this chapter aims to evaluate the viability of the worm-like nanoparticles obtained *via* ROPISA of BLG-NCA for nanomedicine applications by investigating the biocompatibility, and the *in vitro* and *in vivo* behavior. Those worm-like nanoparticles, as our literature review have evidenced, should extravasate easily through leaky vascular networks *via* the well-known enhanced permeability and retention (EPR) effect,[27] without the need of deformation.[28] This property facilitates their deep penetration and high accumulation in solid tumors, making them highly promising candidates for drug delivery applications, particularly in cancer therapy.[29,30] Regarding PEG-*b*-PBLG nanoparticles, cellular internalization studies comparing different morphologies, including helical rods, striped spheres, and smooth spheres, have revealed that, for similar hydrodynamic radii, helical rods exhibit the highest uptake efficiency. [31]

In the first part of this chapter, to evaluate the viability of the nanoparticles by directly comparing their performance with traditional spherical nanoparticles composed of the same materials, a one-pot synthesis procedure have been set up in order to synthetized fluorescent worm-like micelles *via* ROPISA of BLG-NCA initiated by PEG, where a cyanine dye (Cy5.5 or Cy7) was covalently conjugated to the amino group at the omega end in the hydrophobic core. For comparison, spherical nanoparticles were prepared by reformulating the same fluorescent diblock copolymer using a conventional solvent-displacement method (Scheme V-1).

In a second part, we investigated the interaction of PEG-*b*-PBLG worm-like micelles and their spherical analogues with two distinct cancer cell lines, CT26 and 4T1, which are commonly used syngeneic tumor models with contrasting EPR effects influencing the passive accumulation of nanocarriers in solid tumors.[32,33] CT26, derived from undifferentiated colorectal carcinoma, exhibits high vascularity and permeability, while 4T1, a breast cancer model, is considered to be stroma rich and less leaky tumor.[34] These differences contribute to a more pronounced EPR effect for CT26 and potentially greater nanoparticle accumulation in the tumor. We used laser confocal fluorescence microscopy and flow cytometry to assess cell uptake in two-dimensional (2D) cultures and penetration into three-dimensional (3D) Multi-Cellular Tumor Spheroids (MCTS) derived from both cell lines.

Finally, circulation times of both nanoparticles were evaluated using intravital laser scanning confocal microscopy, and biodistribution studies in tumor-bearing mice were conducted to assess their therapeutic potential (Scheme V-1).

This study was carried out in close collaboration with the Innovation Center of Nanomedicine (iCONM) in Kawasaki, Japan, under the guidance of Pr. Kazunori Kataoka and Dr. Sabina Quader. During a three-month research stay from April 1 to June 27, 2024, I had the opportunity to conduct biological experimental work with the help of Dr. Sabina Quader and Dr. Xueying Liu.

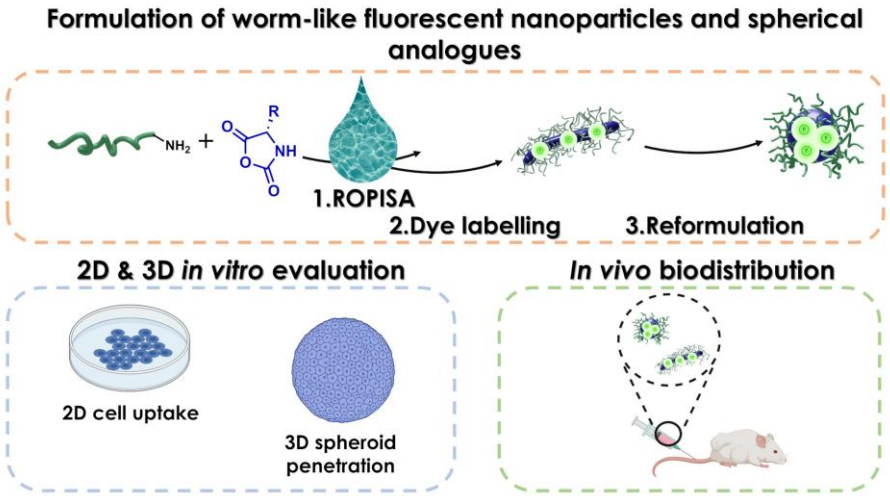

Scheme V-1. *In vitro* and *in vivo* evaluation of worm-like nanocarriers and their spherical counterparts.

V.2. Nanoparticles preparation

V.2.1. Worm-like micelles preparation with covalent attachment of cyanine

To assess cellular uptake in 2D monolayers, penetration into Multi-Cellular Tumor Spheroids (MCTS) in two cancer cell lines, as well as biodistribution and tumor accumulation, nanoparticles were labeled with fluorescent probes. A one-pot reaction was developed to graft cyanine dye (Cy5.5 for confocal and flow cytometry analysis, Cy7 for IVIS imaging), as depicted in Scheme V-2. The aqueous ROPISA reaction was initiated with α-amino-poly(ethylene glycol) (PEG_{5k}-NH_2) in an ice-cold 50 mM aqueous sodium bicarbonate solution (pH 8.5) containing 31 equivalents of γ-benzyl-*L*-glutamate NCA monomer under vigorous stirring, based on previous established protocol already described in **Chapter II**. After an overnight reaction, an aliquot was sampled for analysis. Then, cyanine 5.5 or cyanine 7, with an *N*-hydroxysuccinimide ester as an activated carboxyl group, was dissolved in DMSO and added to the opalescent solution (0.1 eq, DMSO/H_2O 10:90).

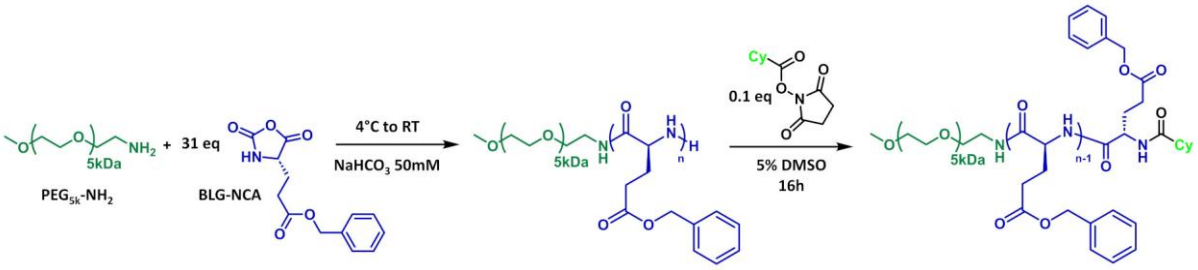

Scheme V-2. Grafting of cyanine dye through NHS ester coupling onto the chain-end omega primary amine of PEG-*b*-PBLG copolymer obtained after the ROPISA process.

The resulting blue solutions were purified by dialysis against ultrapure water for 5 days, after which the copolymer was recovered by freeze-drying, and a portion of the solution containing the nanoparticles was transferred to PBS. The copolymer pre-grafting was analyzed by ^{1}H NMR spectroscopy and size exclusion chromatography (SEC) to confirm controlled chain extension, resulting in a well-defined amphiphilic block copolymer with a PBLG degree of polymerization (DP) of 30 with narrow dispersity ($Đ$ = 1.05) (Figure V-1). The labeling of the copolymer was confirmed by SEC analysis using differential refractive index (dRI) detection and absorbance detection at specific wavelengths: 683 nm for cyanine 5.5 and 750 nm for cyanine 7 (Figure V-2). The dRI detection indicated that the labeling did not result in any alterations to the copolymer's mass distribution, while the absorbance detection revealed a narrow peak that exhibited a slight shift to a later retention time, closely resembling the dRI detection results. This shift indicates the successful labeling of a portion of the copolymer with cyanine as targeted, potentially due to increased retention on the column resulting from interactions with the stationary phase.

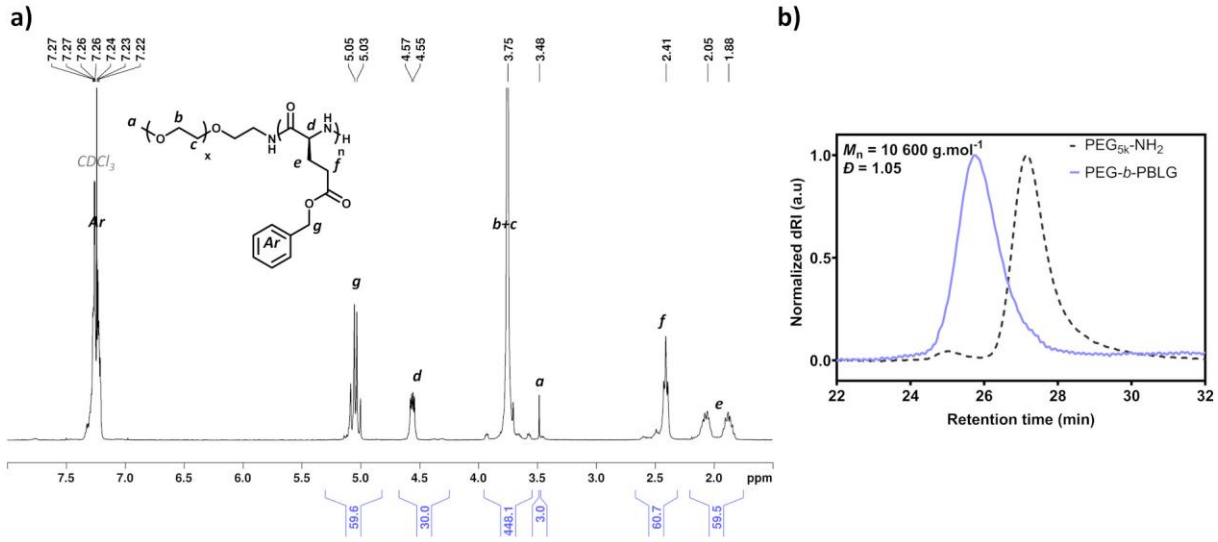

Figure V-1. (a) ^{1}H NMR spectrum of PEG-*b*-PBLG copolymer in $CDCl_3$ + 15% TFA. (b) SEC chromatograms of PEG-*b*-PBLG copolymer in DMF (+1% LiBr, detection by differential refractive index), compared to PEG_{5k}-NH_2 homopolymer.

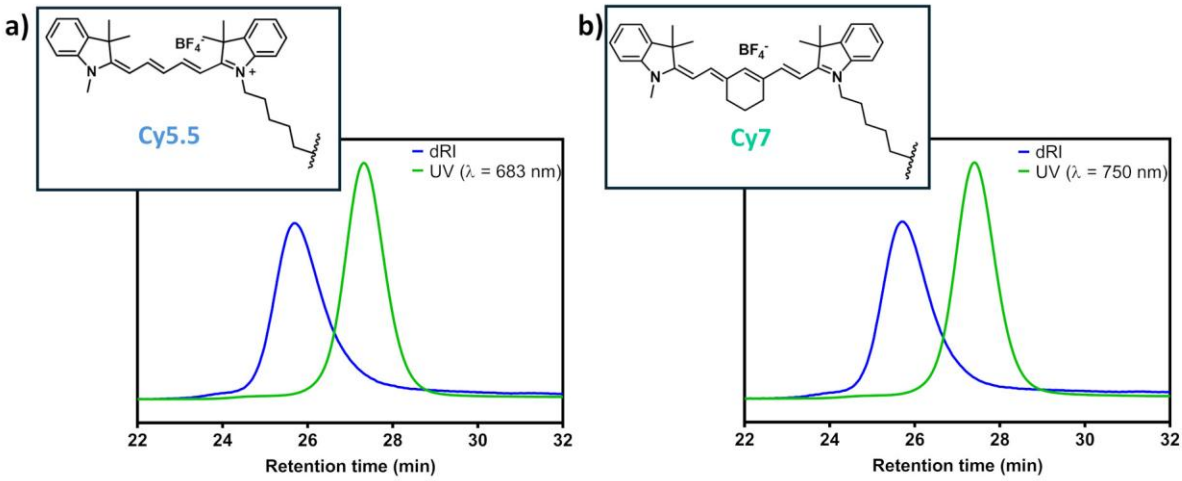

Figure V-2. SEC chromatograms of (a) Cy5.5-PEG-*b*-PBLG copolymer (detection by differential refractive index in blue, by absorbance at Cy5.5 maximum absorption wavelength, 683 nm, in green) and (b) Cy7-PEG-*b*-PBLG copolymer (detection by differential refractive index in blue, by absorbance at Cy5.5 maximum absorption wavelength, 750 nm, in green).

UV-vis spectroscopy in DMF, compared with cyanine in DMF, estimated a grafting efficiency of 10 cyanine molecules per 100 copolymer chains (Figure V-3).

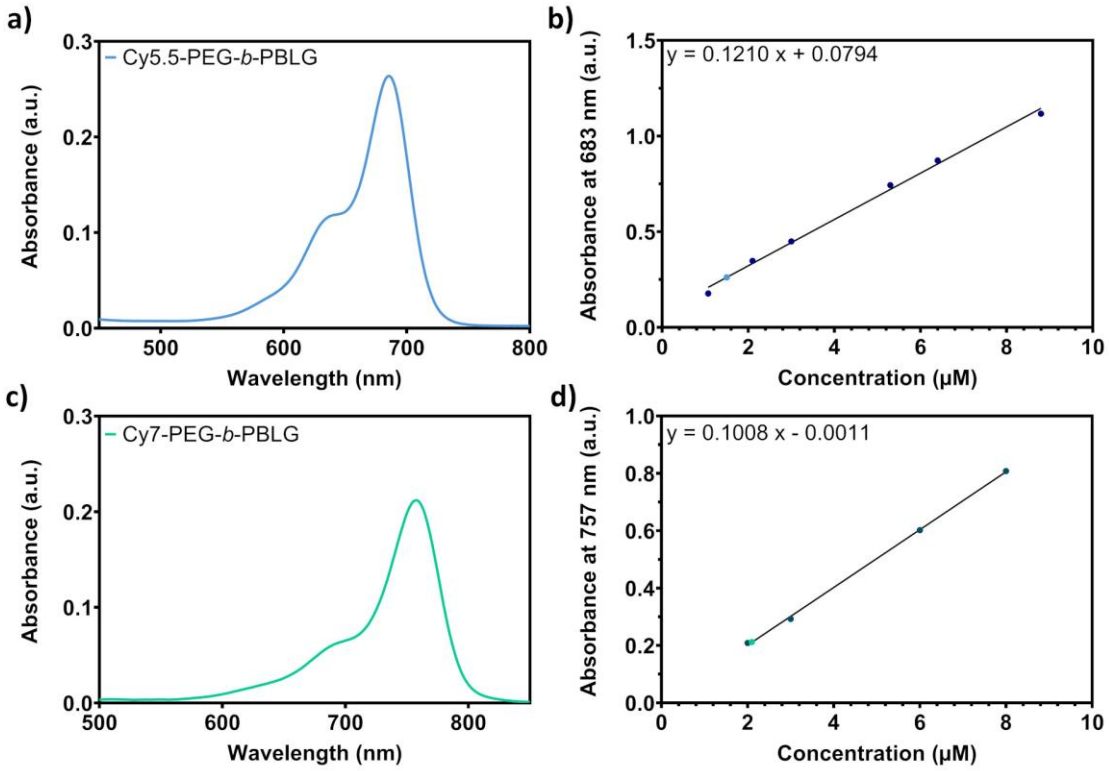

Figure V-3. (a,c) UV-vis spectra of grafted PEG-*b*-PBLG copolymer with (a) Cyanine 5.5 and (b) corresponding calibration curve of cyanine 5.5 in DMF; (c) with cyanine 7 and (d) corresponding calibration curve of cyanine 7 in DMF.

Following the thorough evaluation of the labelling process, the fluorescent nanoparticles were subjected to meticulous analysis using dynamic light scattering (DLS) and electronic microscopy (TEM and cryo-TEM). The sphere-equivalent Z-average diameter of the nanoparticle suspensions, following dialysis against PBS and filtration through a 0.22 µm membrane filter, was found to be similar for both Cy5.5- and Cy7-labeled worms, displaying a moderate dispersity (~91 nm, σ = 0.16; Table V-1, Figure V-4).

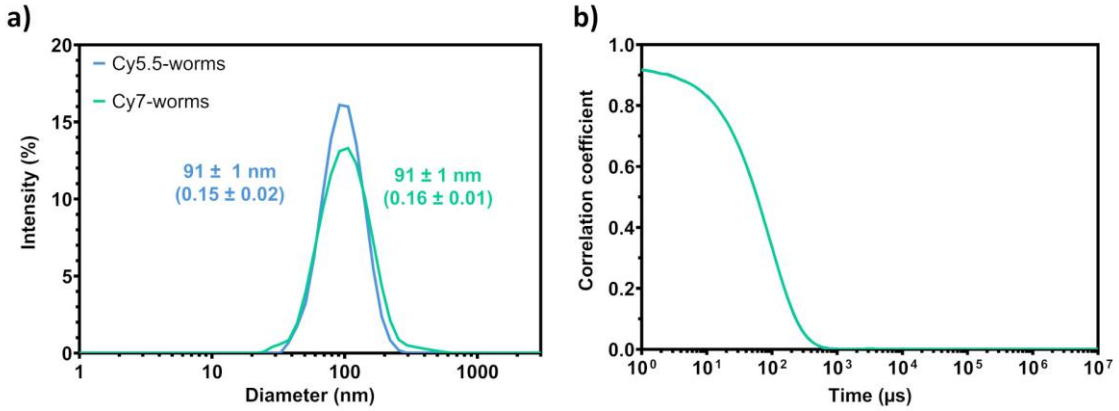

Figure V-4. DLS profiles of (a) Cy5.5 and Cy7-worm-like micelles in PBS and (b) associated correlograms

TEM images revealed long, flexible worm-like nanoparticles with comparable dimensions: the length and diameter of the Cy5.5 worms were measured to be approximately 168 ± 55 nm and 23 ± 4 nm

respectively, while the diameter and length of the Cy7 worms were estimated to be around 182 ± 65 nm and 27 ± 5 nm respectively (Table V-1, Figure V-5). Using a cylindrical model, the estimated surface area was 12 000 nm² for Cy5.5 and 15 000 nm² for Cy7 with number-average length and width determined by TEM analysis. These findings highlight the influence of the dye on nanoparticle dimensions, despite both values remaining within the same range.

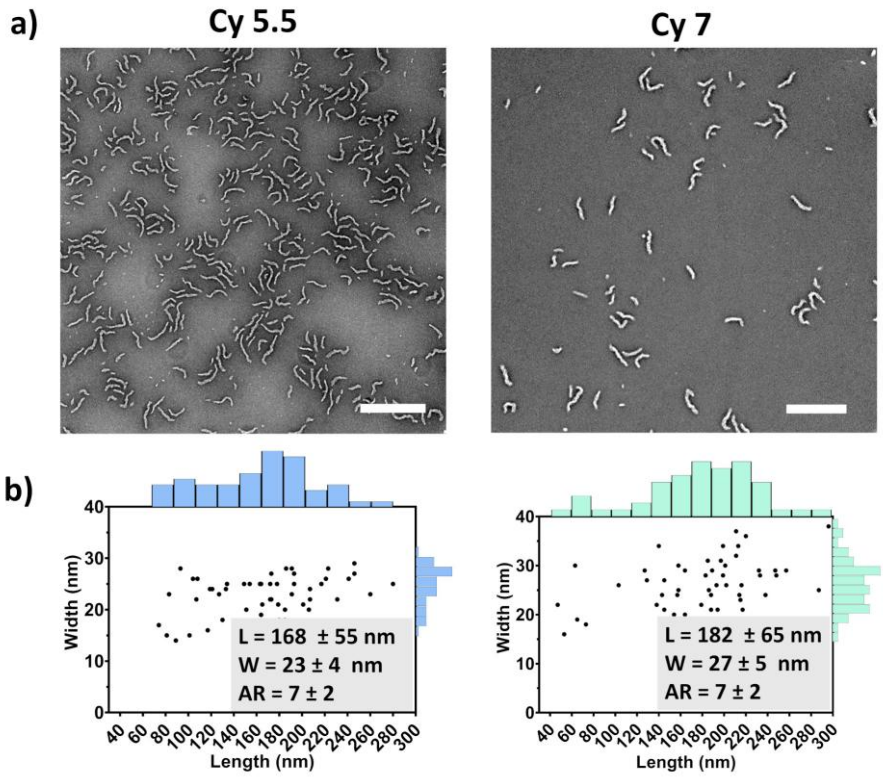

Figure V-5. (a) Representative TEM image of Cy5.5-worms (left) and Cy7-worms (right). (b) Length and width distribution of Cy5.5-worms (left) and Cy7-worms (right) obtained by analysis of 50 nanoparticles by Image J on a TEM image. Scale-bar: 500 µm.

Cryo-TEM analysis corroborated these observations, demonstrating comparable lengths but narrower diameters, likely due to the invisibility of the hydrophilic polyethylene glycol segment under hydrated conditions (Figure V-6). Consequently, surface areas obtained from image analysis were smaller, approximately 5 000 nm² (Table V-1).

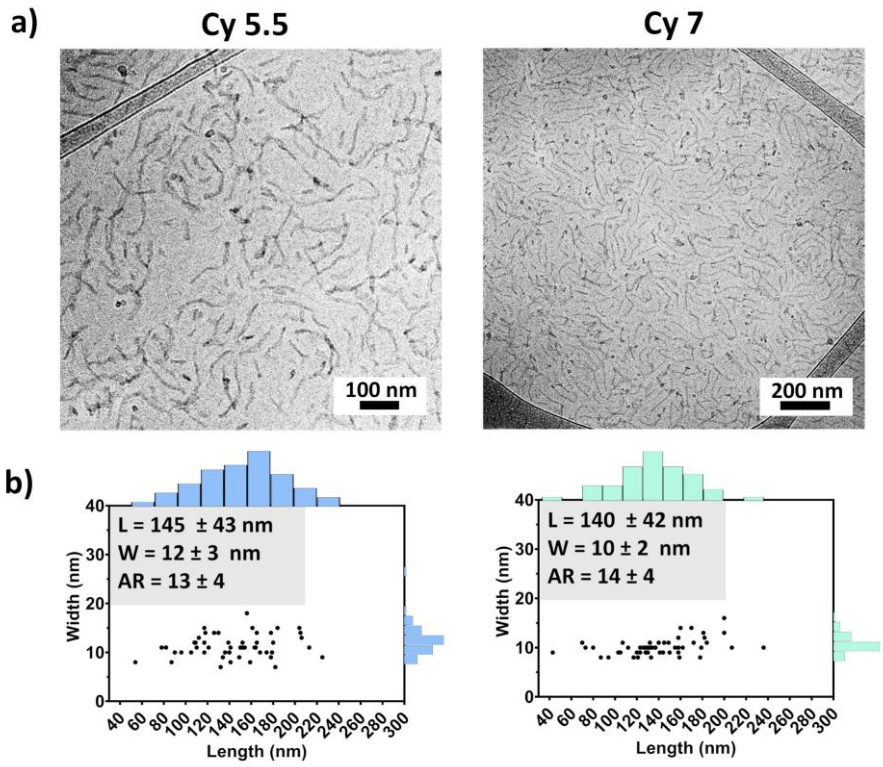

Figure V-6. (a) Representative cryo-TEM image of Cy5.5-worms (left) and Cy7-worms (right). (b) Length and width distribution of Cy5.5-worms (left) and Cy7-worms (right) obtained by analysis of 50 nanoparticles by Image J on a cryo-TEM image.

Table V-1. Characteristics of cyanine 5.5 and cyanine 7-grafted PEG-*b*-PBLG nanoparticles.

Nanoparticles	D_Z [a)] [nm]	σ [a)]	L_n TEM [b)] [nm]	L_n cryo-TEM [c)] [nm]	A TEM [d)] [nm²]	A cryo-TEM [e)] [nm²]
Cy5.5-Worms	91 ± 1	0.16 ± 0.06	168 ± 55	145 ± 43	12 100	5 300
Cy5.5-Spheres	67 ± 1	0.06 ± 0.01	63 ± 17	40 ± 10	8 100	3 500
Cy7-Worms	91 ± 1	0.16 ± 0.01	182 ± 65	140 ± 42	15 500	4 500
Cy7-Spheres	66 ± 1	0.05 ± 0.01	70 ± 17	41 ± 9	9 500	4 200

[a)] Hydrodynamic Z-average diameter (D_Z) and polydispersity (σ) determined by DLS at 173°, 532 nm, after filtration with 0.22 µm membrane filter. [b)] Number-average length obtained by TEM image analysis ± one standard deviation ($n = 50$). [c)] Number-average length obtained by cryo-TEM image analysis ± one standard deviation ($n = 50$). Surface area : $A^{worms} = 2\pi \times L_n \times {}^{w_i}/_2 + 2\pi({}^{w_i}/_2)^2$; $A^{spheres} = 4\pi \times L_n \times ({}^{w_i}/_2)^2$ [d)] L_n and w_n determined with TEM, [e)] with cryo-TEM.

V.2.2. Spherical nanoparticles obtention *via* solvent displacement

The self-assembly of labeled block copolymers into spherical nanoparticles was achieved through a solvent displacement method, whereby a transition was made from a good solvent for both blocks (DMSO) to a selective solvent (water), as outlined schematically in Scheme V-3. The initiation of this process involved the rapid addition of water to a preheated polymer solution (30°C for 2 hours) until a 9:1 volume ratio of water to DMSO was achieved. The final step involved removing the DMSO through dialysis against PBS.

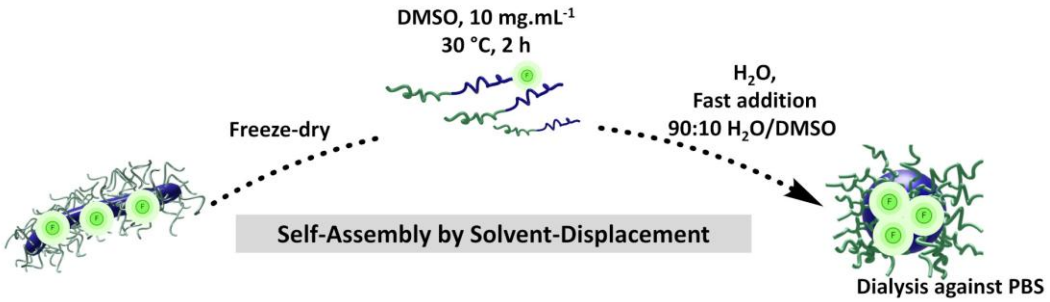

Scheme V-3. Schematic representation of the reformulation process by solvent-displacement.

The suspension was subsequently analyzed using DLS, TEM, and cryo-TEM following filtration through a 0.22 µm membrane filter. The Z-average diameter was found to be similar for both Cy5.5-spheres and Cy7-spheres (67 ± 1 nm and 66 ± 1 nm, respectively ;Table V-1, Figure V-7), with low dispersity ($\sigma < 0.1$).

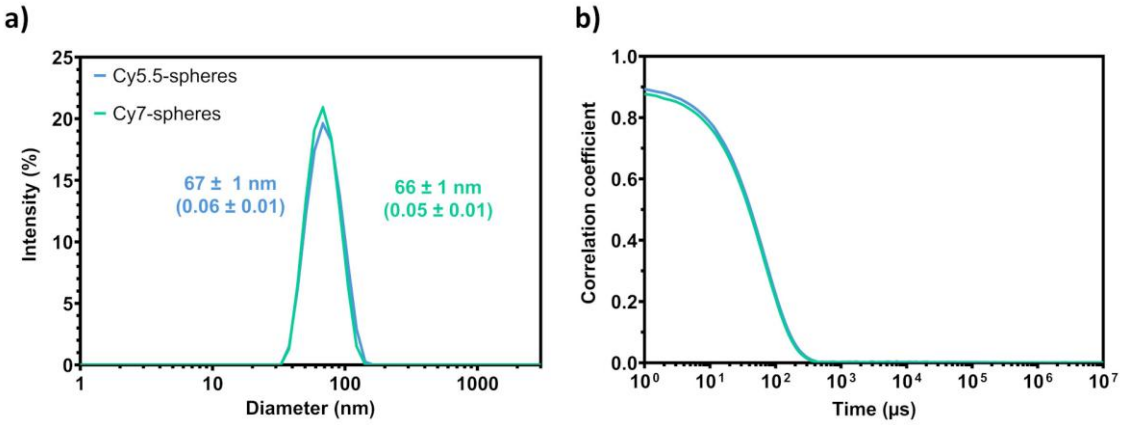

Figure V-7. DLS profiles of (a) Cy5.5 and Cy7-spheres in PBS and (b) associated correlograms

To ascertain the morphology and size of the nanoparticles, TEM and cryo-TEM analyses were conducted. The resulting images revealed spherical structures, with an average diameter of 60 nm as measured by TEM (Figure V-8) and 40 nm by cryo-TEM (Figure V-9). Next, the surface area was estimated using a spherical model, yielding slightly lower values than those of the worm-like micelles but still within the same range (≈ 8 000 nm² for Cy5.5 and 9 500 nm² for Cy7-spheres by TEM estimation, and ≈ 4 000 nm² by cryo-TEM estimation for both, Table V-1).

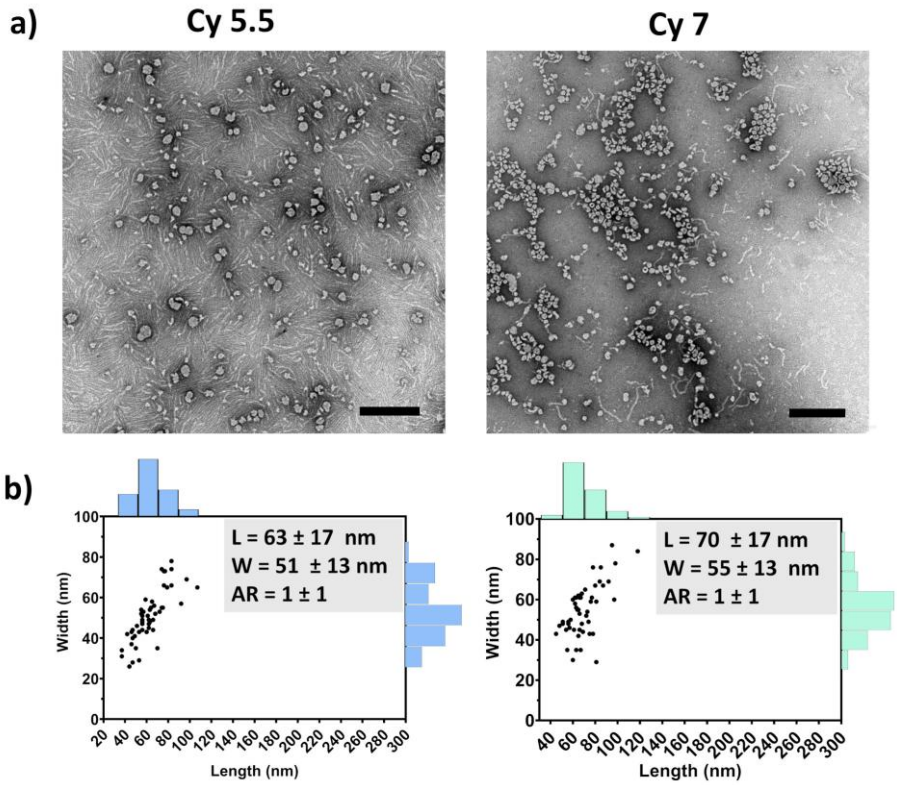

Figure V-8. (a) Representative TEM image of Cy5.5-spheres (left) and Cy7-spheres(right). (b) Length and width distribution of Cy5.5-spheres (left) and Cy7-spheres (right) obtained by analysis of 50 nanoparticles by Image J on a TEM image. Scale-bar: 500 µm.

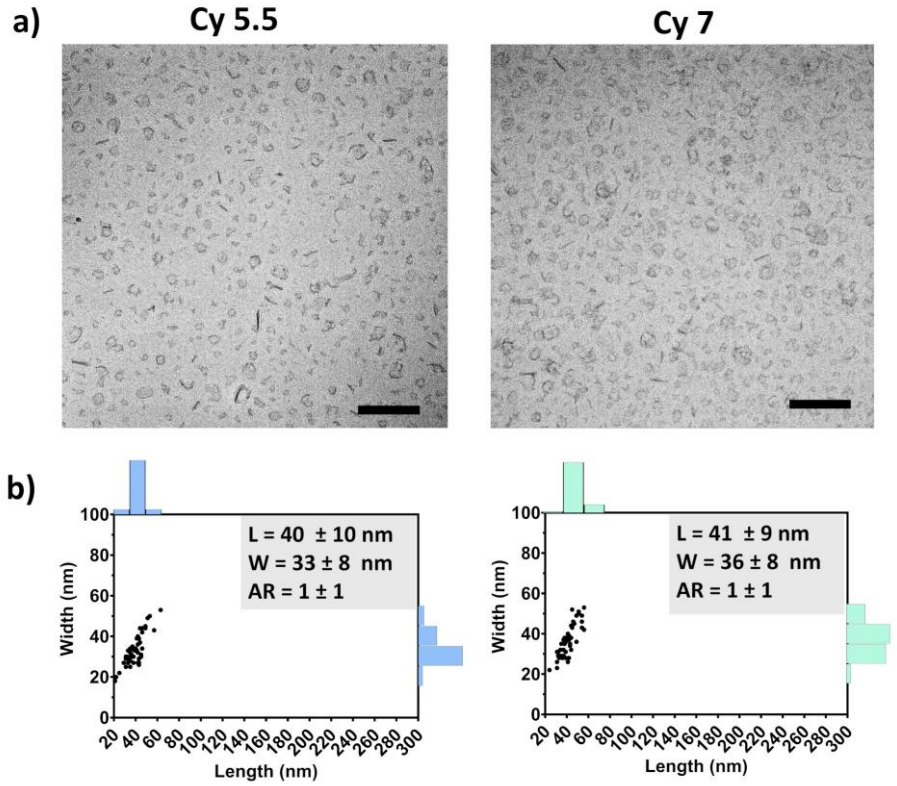

Figure V-9. (a) Representative cryo-TEM image of Cy5.5-spheres (left) and Cy7-spheres(right). (b) Length and width distribution of Cy5.5-spheres (left) and Cy7-spheres (right) obtained by analysis of 50 nanoparticles by Image J on a cryo-TEM image. Scale-bar: 200 nm.

V.3. Cell internalization in 2D monolayer cell cultures

V.3.1. Cell viability in HUVEC

In order to assess the potential toxicity of the nanoparticles in the context of their intended applications, which include cellular uptake, penetration of tumor spheroid, and *in vivo* biodistribution, the CCK-8 assay was employed on HUVEC cells. These cells, which are a representative model of human endothelial cells, exhibit heightened sensitivity to toxicity in comparison to tumor cell lines.[35] Given that the nanoparticles are administered intravenously, this assay ensures their biocompatibility by assessing the toxicity of both worm-like and spherical morphologies.[36] The cells were incubated at 37 °C for 24 hours after being exposed to varying concentrations of the nanoparticles. The results, presented in Figure V-10, indicate that the nanoparticles exhibited no significant cytotoxicity up to a concentration of 1.6 mg.mL^{-1}.

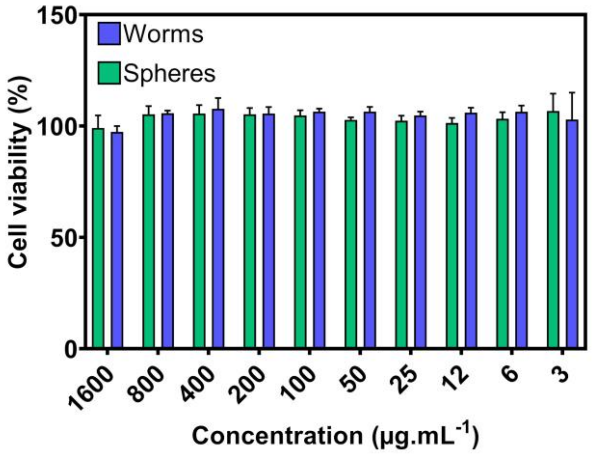

Figure V-10. Viability tested by CCK-8 assay after incubating the HUVEC cell monolayer with worm-like micelles and spherical nanoparticles at various concentrations for 24 hours.

V.3.2. Cell association study in monolayer CT26 and 4T1 cells

V.3.2.1. CT26

The initial incubation of 2D CT26 cell cultures with nanoparticles entailed the incorporation of a Cy5.5-labeled nanoparticle solution into the culture medium, with a final concentration of 0.5 mg.mL^{-1} for worm-like micelles and 0.2 mg.mL^{-1} for spherical nanoparticles. These concentrations were selected based on the same fluorescence intensity (Figure V-11).

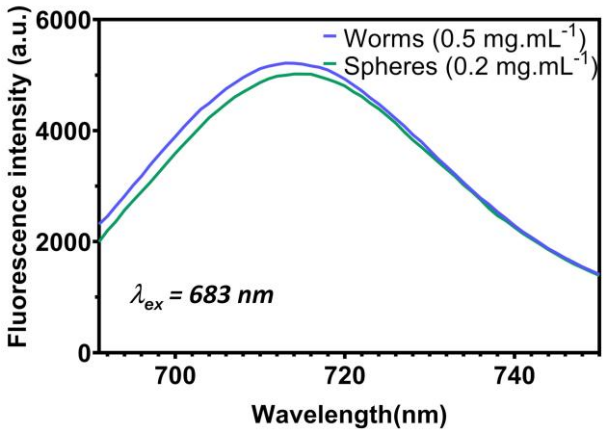

Figure V-11. Fluorescence spectra of Cy5.5-labelled nanoparticles in PBS buffer after filtration, using non-labelled nanoparticles as blank.

V.3.2.1.1. Real-time confocal laser scanning microscopy

Fluorescence was continuously monitored for 15 hours, with an interval of 15 minutes, by confocal laser scanning microscopy without any washing step (Figure V-12). The quantification of Cy5.5 fluorescence intensities from the confocal images was performed by selecting three regions of interest (ROI) that included at least 10 cells each (Figure V-12a). The resulting data were then normalized based on the maximum fluorescence for each sample, thereby facilitating the comparison of association kinetics (Figure V-12b). The analysis employed a one-phase exponential association model, which did not differentiate between adsorption, desorption and internalization processes from the cell membrane. This methodological framework enabled a straightforward comparison of the total association kinetics using the observed rate constant (k_{obs}). Indeed, the fate of nanoparticles devoid of specific ligands when exposed to cells is governed by an adsorption/desorption equilibrium before ultimately being internalized.[37] This aspect cannot be fully assessed in our study, as we did not observe the cells at high resolution or investigate potential alterations in cell functioning to distinguish between nanoparticle internalization and surface adsorption.

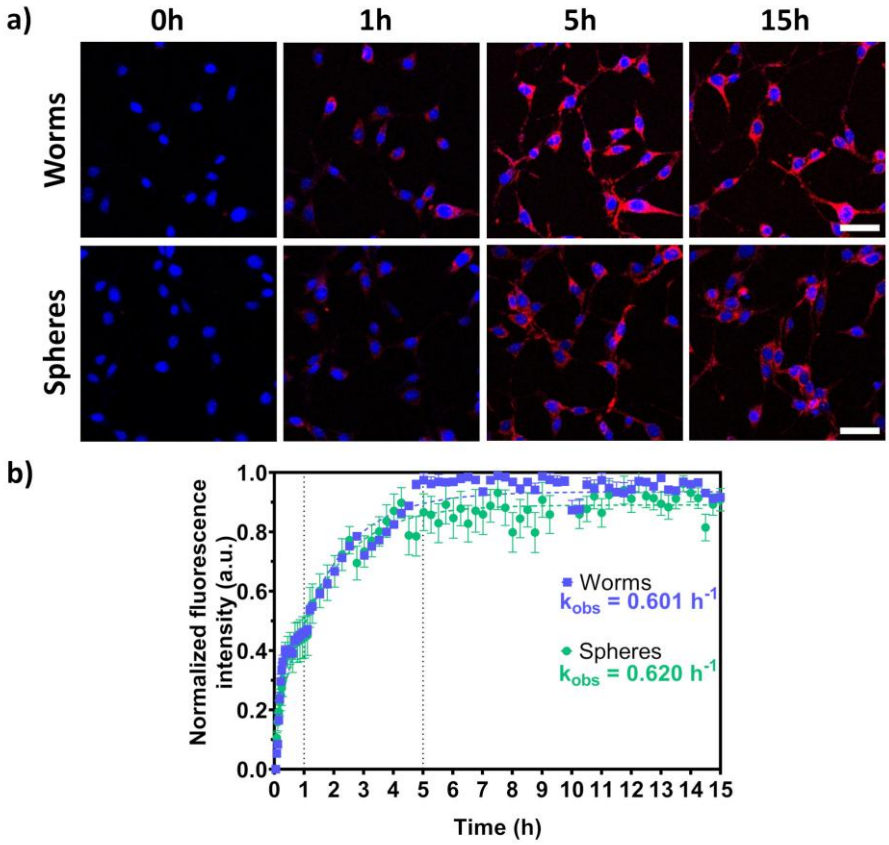

Figure V-12. Cell association of the spherical (spheres) and worm-like (worms) nanoparticles in CT26 2D cell cultures. (a) Real-time *in vitro* CLSM images of CT26 cells after incubation with Cy5.5 fluorescent nanoparticles (red). Cells were staining with Hoescht (blue). Scale-bar: 200 µm. (b) Normalized fluorescence intensity of red fluorescence from worms and spheres association in cells, measured for a 15-hour time frame.

In the CT26 cell line, a phenomenon of fluorescence saturation was observed after 5 hours for both the spheres and the worms. This finding suggests that the cell uptake process was complete by that time as depicted in Figure V-12b. No significant difference in k_{obs} was observed between the two types of nanoparticles ($k_{obs} \approx 0.6$ h^{-1}), suggesting similar fast association kinetics in CT26 cells.

V.3.2.1.2. Flow cytometry

CT26 cells were then exposed to fluorescent nanoparticles at final concentrations of 0.25 mg.mL^{-1} for worm-like micelles and 0.1 mg.mL^{-1} for spherical nanoparticles for various timespans, for flow cytometry analysis. Flow cytometry quantifies the total fluorescence intensity of all cell-associated nanoparticles on a single-cell basis, including both internalized nanoparticles and those adsorbed onto the outer cell membrane. However, given the rigorous washing procedures employed during sample preparation, it was assumed that the number of membrane-bound nanoparticles is negligible. This hypothesis was supported by CLSM imaging after 15 minutes of incubation and subsequent washing, which revealed fluorescence signals precisely localized to the cell structure (Figure V-13).

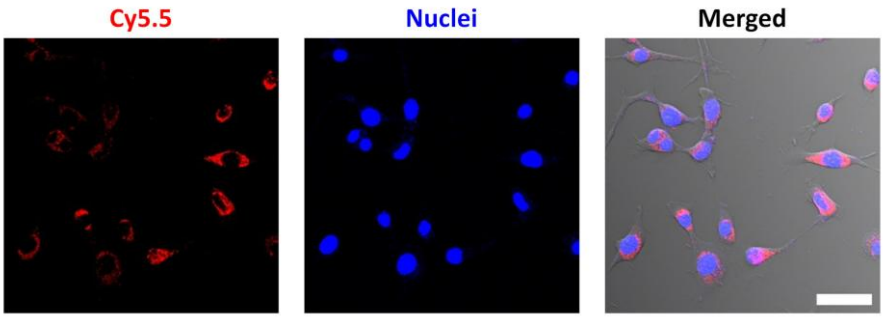

Figure V-13. CLSM images of CT26 cells after 15 minutes of incubation with worm-like nanoparticles, followed by two washing steps. Cell nuclei are stained with Hoechst (blue), while Cy5.5-labeled block copolymers exhibit red fluorescence. Scale bar: 50 µm.

Therefore, the fluorescence measured by flow cytometry rationally corresponds to internalized nanoparticles (Figure V-14a, b). This approach enabled a comparison of the internalization kinetics observed in CLSM and a semi-quantification of the nanoparticles taken up by the cells, using the same one-phase exponential model. Indeed, the results of the flow cytometry analysis of CT26 cells demonstrated a rapid association process with comparable observed rate constant values (k_{obs}') than CLSM observation (Figure V-14c), with nearly all cells containing nanoparticles within 1 hour, as indicated by the mean fluorescence intensity (MFI) and the percentage of fluorescent cells (Figure V-14a, b, d). However, after 6 hours, the mean fluorescence intensity was observed to be equivalent for both morphologies.

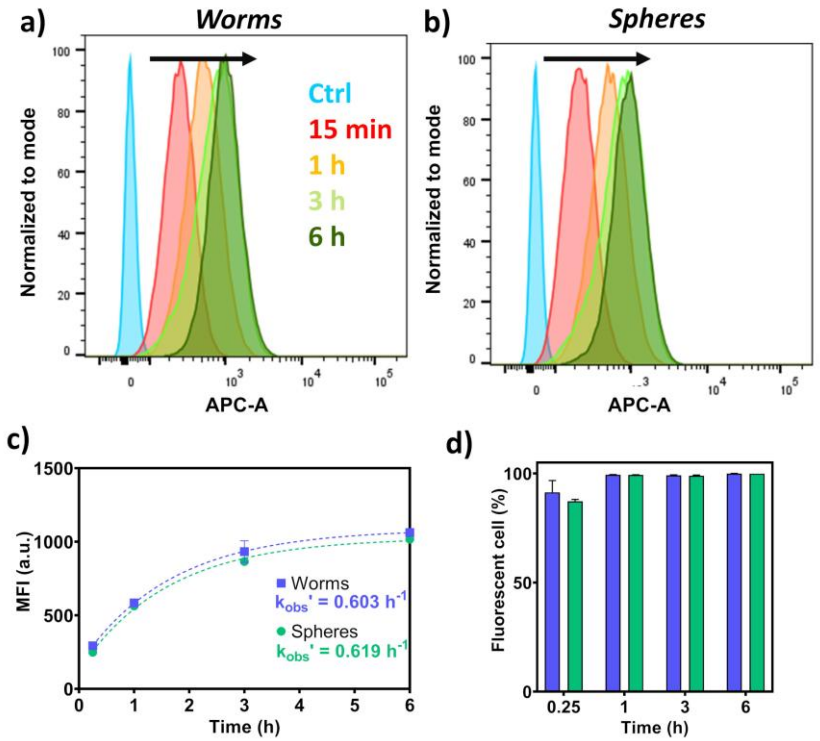

Figure V-14. Flow cytometry histogram plots illustrating cellular uptake in CT26 cells of (a) worm-like and (b) spherical nanoparticles after incubation for 15 minutes, 1, 3 and 6 hours. The plots were generated with the FlowJo software. (c) Cell association of worms and spheres in CT26 at different time points, determined *via* flow cell cytometry. The line graph represents the total mean fluorescence intensity of the samples. (d) Percentage of fluorescence cells determined *via* flow cell cytometry after incubation with fluorescent nanoparticles, at different time points.

In any case, the results of the flow cytometry analysis indicated that a significant quantity of nanoparticles were internalized by the cells, as all of them exhibited fluorescence after one hour, with a high MFI.

V.3.2.2. 4T1

V.3.2.2.1. Real-time confocal laser scanning microscopy

The same experiment was repeated with 4T1 breast cancer cells. The cells were incubated with fluorescent nanoparticles by adding samples to achieve the same final concentration as for CT26. Real-time confocal laser scanning microscopy (CLSM) was conducted over a 15-hour period, and fluorescence intensity was measured from three defined regions of interest (ROIs) (Figure V-15a). The observed rate constant (k_{obs}), derived using a simple one-phase exponential association model, indicated that the association kinetics for both worm-like and spherical nanoparticles were slightly slower compared to CT26 cells ($k_{obs} \approx 0.6$ h^{-1} for both worms and spheres in CT26 case; k_{obs} for worms = 0.418 h^{-1}, k_{obs} for spheres = 0.284 h^{-1} for 4T1) (Figure V-15b). Additionally, the data indicated that spherical nanoparticles were associated with the cells at a slightly slower rate than worm-like micelles.

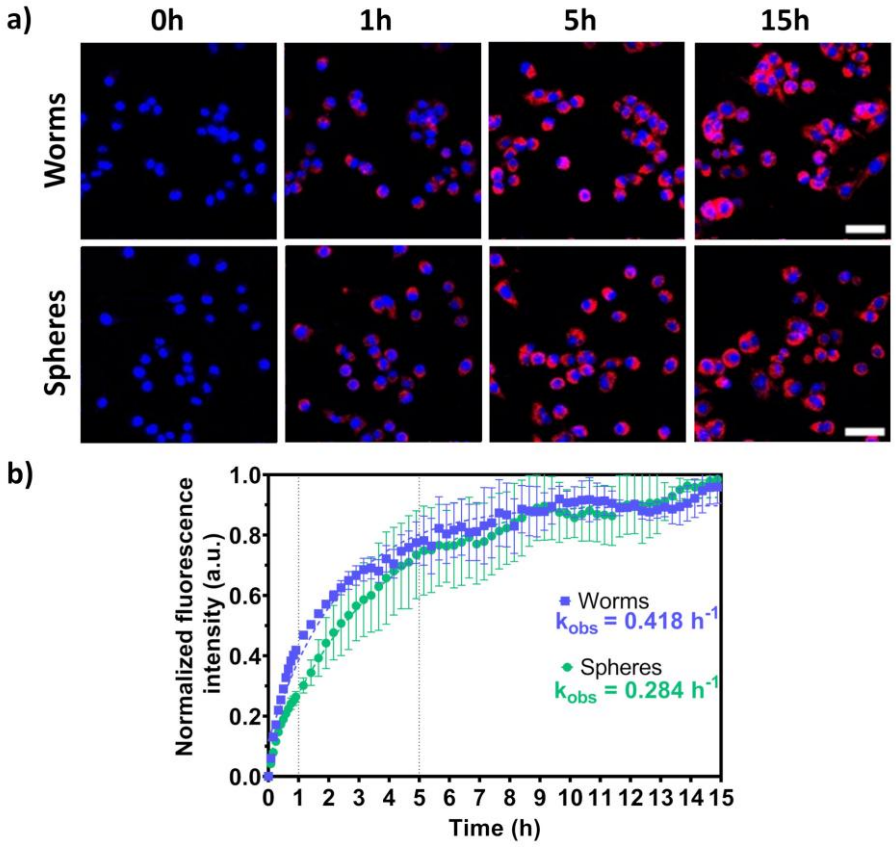

Figure V-15. Cell association of the spherical (spheres) and worm-like (worms) nanoparticles in 4T1 2D cell cultures. (a) Real-time *in vitro* CLSM images of 4T1 cells after incubation with Cy5.5 fluorescent nanoparticles (red). Cells were staining with Hoescht (blue). Scale-bar: 50 µm. (b) Normalized fluorescence intensity of red fluorescence from worms and spheres association in cells, measured for a 15-hour time frame.

V.3.2.2.2. Flow cytometry

Flow cytometry analysis was also performed after incubation at different time points, confirming these observations by revealing a diminished MFI for spheres in comparison to worms (Figure V-16a-c). It was observed that all cells exhibited fluorescence within 15 minutes of incubation, suggesting rapid initial internalization, which may be attributed to the high concentration of nanoparticles used during the experiments (Figure V-16d). After 6 hours, it was observed that the MFI in 4T1 cells surpassed that in CT26 cells. However, it was noted that the saturation was not reached, and the apparent kinetic constants obtained from this experiment exceeded those derived from CLSM measurements. This discrepancy can be attributed to two factors: the limited experimental timeframe, which impacts the fitting process, and the influence of varying concentration conditions between experiments.[38]

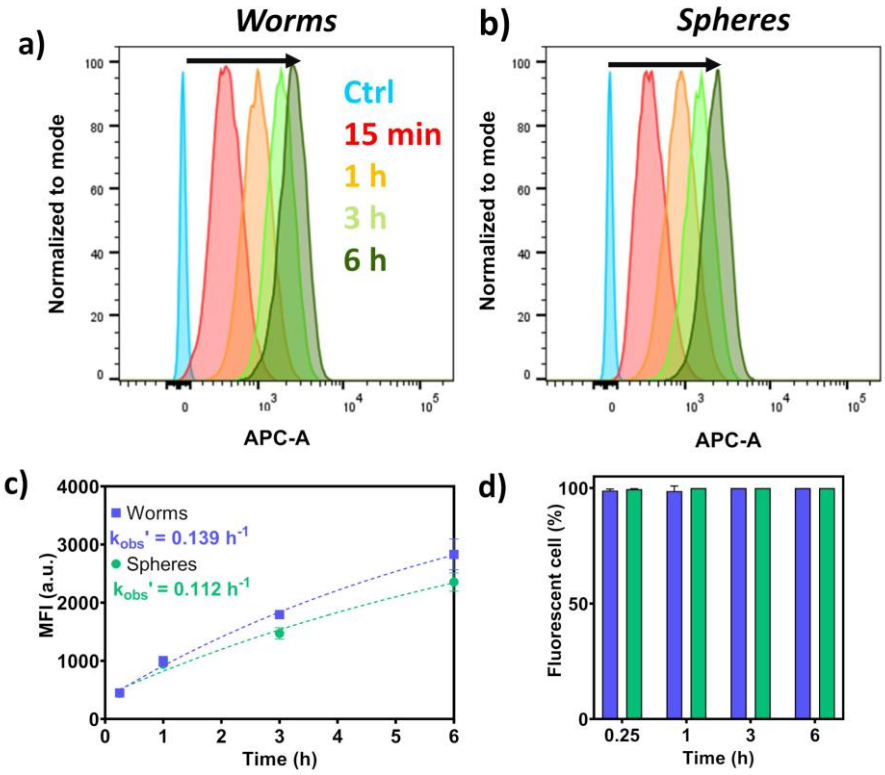

Figure V-16. Flow cytometry histogram plots illustrating cellular uptake in 4T1 cells of (a) worm-like and (b) spherical nanoparticles after incubation for 15 minutes, 1, 3 and 6 hours. The plots were generated with the FlowJo software. (c) Cell association of worms and spheres in 4T1 at different time points, determined *via* flow cell cytometry. The line graph represents the total mean fluorescence intensity of the samples. (d) Percentage of fluorescence cells determined *via* flow cell cytometry after incubation with fluorescent nanoparticles, at different time points.

In conclusion, these results indicate that worm-like micelles formed *via* ROPISA are rapidly associated with two distinct tumor cell lines in 2D monolayer culture, which can be interpreted as accelerated internalization, as observed by flow cytometry. The efficiency of worm-like micelles in this regard is comparable to that of traditional spherical nanoparticles prepared through the solvent displacement method, and they may even exhibit enhanced internalization in 4T1 cells. In the existing literature, comparisons of 2D cellular uptake between anisotropic and spherical nanoparticles frequently focus on rod-like nanoparticles, which possess rigid structures and high persistence lengths. Representative studies in

this area include those conducted by Liu *et al.* [39] with gold nanoparticles and those conducted by Xue *et al.* [31] with PEG-*b*-PBLG-based nanoparticles. They both show that rigid rod-like particles typically exhibit higher uptake than spheres due to their reduced surface curvature, which facilitates faster membrane wrapping. These findings also emphasize the notion that the enhanced internalization of rod-like particles is predominantly influenced by their rigidity and aspect ratio, rather than being solely dictated by their morphology. In the context of worm-like nanoparticles analogous to those examined in this study, Ke *et al.* conducted a comparative analysis of short (180 nm) and long (2.5 µm) filomicelles to spherical micelles (40 nm).[40] The investigation revealed that short, positively charged filomicelles exhibited higher internalization than long filomicelles, a phenomenon that is attributable to steric hindrance. However, despite the hypothesis that short filomicelles would exhibit improved uptake due to the limited contact area of spherical micelles, no statistically significant difference was observed.

V.4. Spheroids penetration

V.4.1. Preparation of multicellular tumor spheroids (MCTS)

In light of the limitations inherent to 2D cultures in replicating the complexity of the tumor microenvironment, our objective was to further investigate their behavior in a 3D model. The 3D model more closely mimics the structural and physiological characteristics of solid tumors. Indeed, in a 3D context, disparities in nanoparticle morphology may have a more pronounced effect on penetration and internalization.[41–43] To further investigate this aspect, a more relevant model was used: multicellular tumor spheroids (MCTSs). MCTSs, also known as 3D spheroids, have been shown to replicate key physiological characteristics of *in vivo* tumors. These characteristics include, but are not limited to, extracellular matrix (ECM) deposition, mass transport barriers (such as limited diffusion of nutrients and oxygen), and abnormal structural features, such as enhanced cell-cell and cell-matrix interactions.[44] These properties make MCTSs a relevant model for studying nanoparticle penetration and internalization in a tumor-like microenvironment.

MCTSs were prepared using spontaneous spheroid formation *via* the use of a low attachment plate with the two cancer cell lines, 4T1 and CT26. The formation of spheroid with a diameter of approximately 300 µm, a size frequently used in penetration studies,[45] was optimized by testing different seeding density, days of formation and centrifugation effect (Figure V-17).

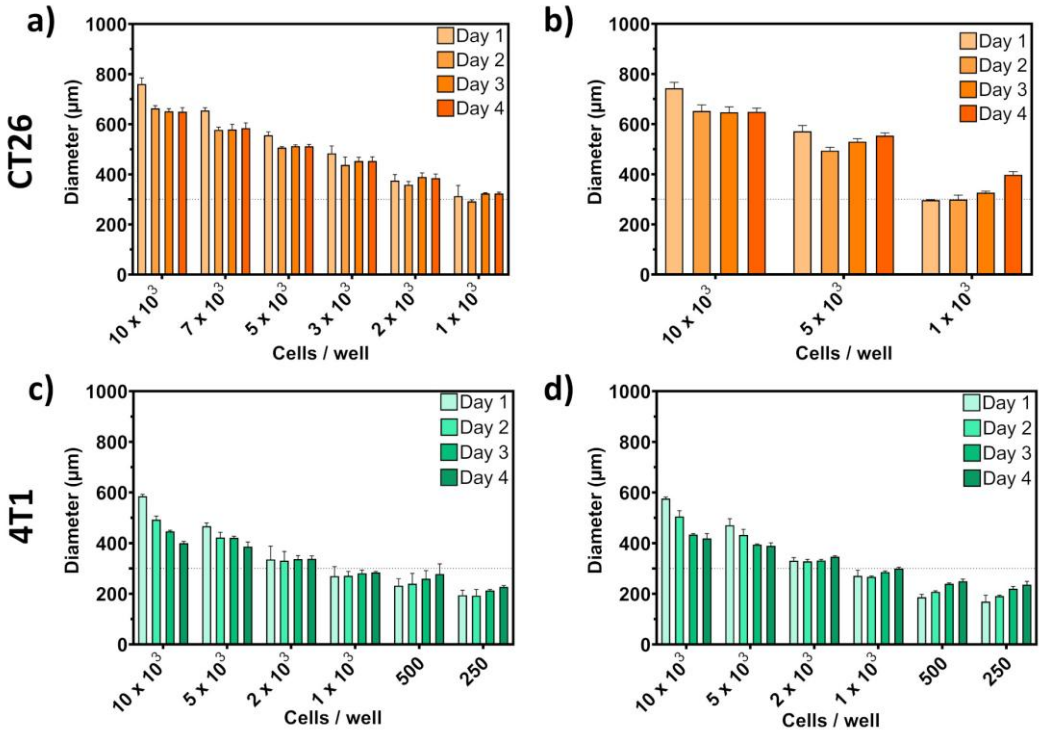

Figure V-17. Growth profile of MCTSs formation with different cells density of (a) CT26, (b) CT26 after centrifugation at 500 rpm for 5 minutes, (c) 4T1, (d) 4T1 after centrifugation at 500 rpm for 5 minutes.

Then, the MCTS were prepared with a seeding density of 1000 cells per well for both cell lines, with centrifugation at 500 rpm for 5 minutes. The growth profiles for CT26 and 4T1 MCTSs are shown in Figure V-18. The cells were provided with sufficient growth time to facilitate the development of tight, compact spheroids rather than loosely packed aggregates, as monitored by optical microscopy. For CT26, attaining the desired size and compactness required a growth period of 4 days, whereas for 4T1, 2 days were sufficient to achieve the desired spheroid structure.

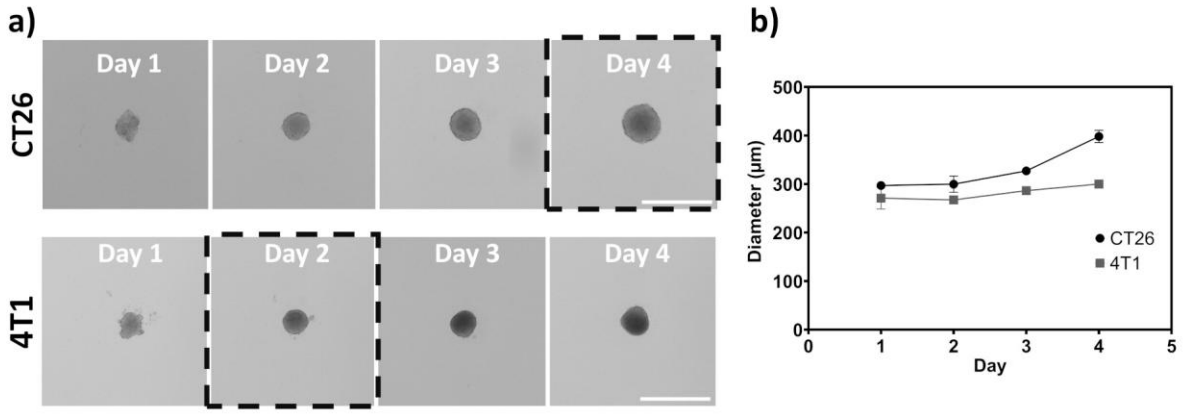

Figure V-18. Growth profile showing (a) light microscope images of CT26 and 4T1 MCTSs from day 1 to 4. Scale bar: 500 µm. (b) Size measurements of CT26 and 4T1 spheroids at different days. On day 4 the tumor spheroids reached an average diameter of 398 ± 12 µm for CT26 and at day 2, 267 ± 3 µm for 4T1.

V.4.2. CLSM

CT26 and 4T1 MCTS were cultivated in black 96-well plates with clear u-bottom in order to investigate nanoparticles penetration and facilitate real-time fluorescence monitoring. Fluorescent worm-like micelles and spherical nanoparticles were separately incubated with the MCTSs at concentrations of 0.5 $mg.mL^{-1}$ and 0.2 $mg.mL^{-1}$, respectively. The initial examination of spheroid penetration was conducted through the use of confocal fluorescence microscopy, which captured optical sections at 20, 40, and 70 µm from the bottom of the spheroid at various time points post-incubation (Figure V-19).

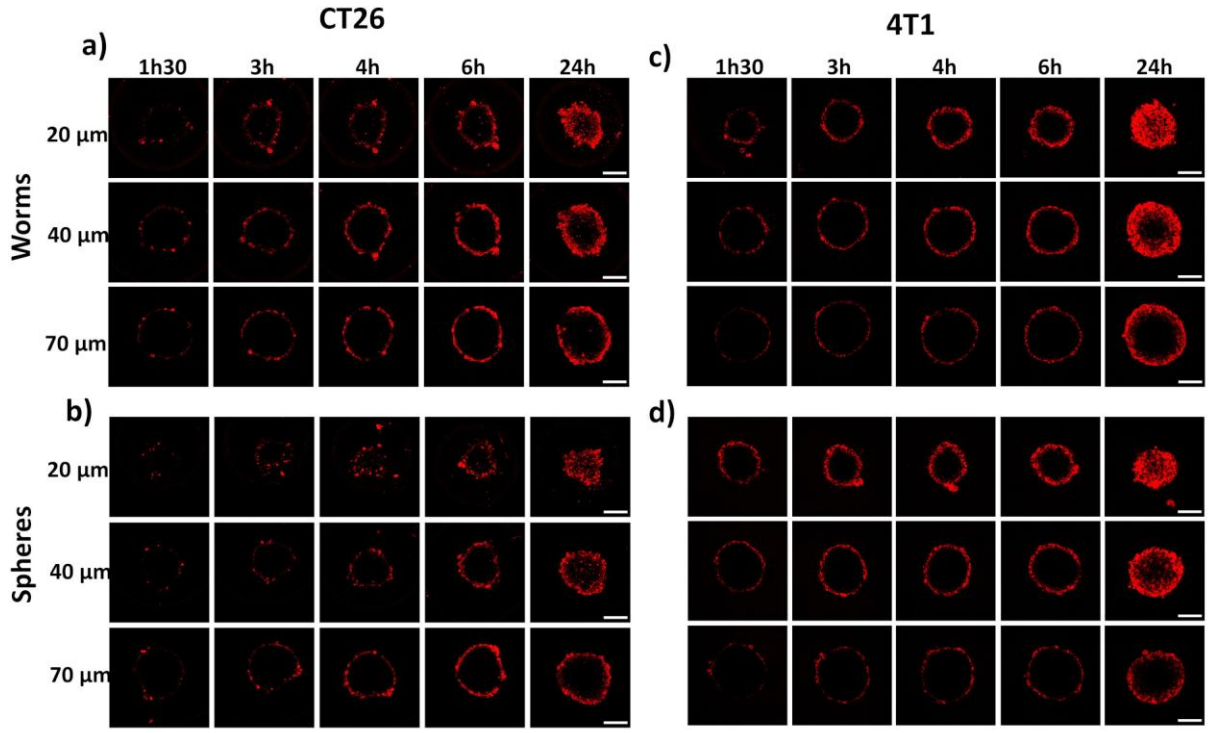

Figure V-19. Assessment of micelle accumulation in MCTSs. CLSM images taken at 20, 40 or 70 µm depth from the spheroid surface spheroids incubated with (a) worm-like micelles (worms) or (b) spherical nanoparticles (spheres) in CT26, and (c) worm-like micelles (worms) and (d) spherical micelles (spheres) in 4T1 at different time points. Scale-bar: 100 µm.

Because of the high cell density of the spheroids, sufficient laser diffusion for quantitative investigation of penetration depth of the nanoparticles into the spheroid at different times could not be achieved. Consequently, we used two distinct methods to estimate the kinetics of penetration and penetration depth. First, Cy5.5 fluorescence was tracked over time and normalized to the maximum fluorescence to ensure consistency. The penetration kinetics were evaluated based on the increase in fluorescence intensity, and the data were best modeled using a simple one-phase exponential association model. To better elucidate nanoparticles penetration inside the spheroids, after 24 hours, MCTS cross-sections was further analyzed according to Allen's group procedure,[46,47] which was also used by Yu *et al.* [45] to compare block copolymer micelle length on penetration in MCTS. Briefly, fluorescence intensity per unit area was determined for periphery (P), intermediate (I) and center (C) regions of each optical slice (Figure V-20).

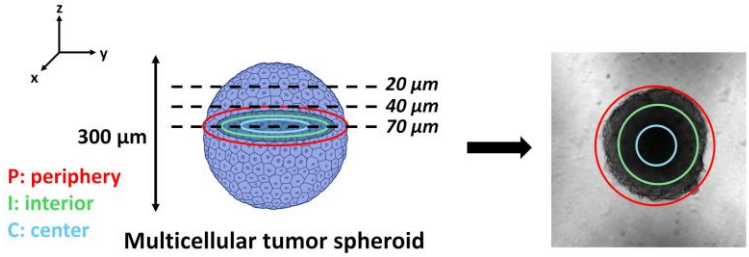

Figure V-20. Workflow for evaluating nanoparticles penetration in MCTSs. Three MCTSs per group were imaged using confocal microscopy. Images were taken at 20, 40 and 70 µm from the MCTS surface. For each slice, three concentric regions were determined (P: periphery, I: interior, C: center). For each of the three defined regions, the average signal intensity within the three optical slices was calculated. This value was finally reported as mean ± SD for $n = 3$ MCTS.

V.4.2.1. CT26 MCTS

The corresponding rate constants for CT26 penetration kinetics k_{obs} were extracted to allow for comparative analysis. For worms, k_{obs} ranged between 0.158 h^{-1} and 0.2 h^{-1} depending on the cross-section studied. As concern spheres, measured k_{obs} was between 0.149 h^{-1} and 0.221 h^{-1}. These results suggest that nanoparticle morphology does not significantly influence the penetration kinetics under these conditions.

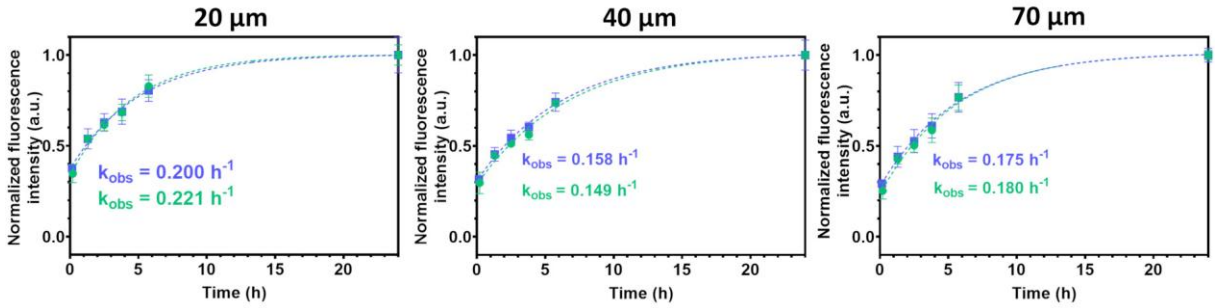

Figure V-21. Normalized fluorescence intensity from CT26 MCTSs CLSM images after micelles incubation overtime at 20, 40 or 70 µm depth (in green: spheres, in blue: worms).

For CLSM images after 24 hours of incubation, fluorescence signals from each region (P, I and C) were averaged for each MCTS, and these values were then averaged for the three MCTS within each treatment group. Fluorescence intensity values for each region are reported as mean ± standard deviation (SD) for $n = 3$ MCTS and normalized (Figure V-22). This method provides semi-quantitative data on micelle penetration at specific spheroid depths, as described above in Figure V-20. As shown in Figure V-22, the distribution of nanoparticles following incubation with worm-like or spherical nanoparticles varied significantly depending on the spheroid region. In the peripheral region, fluorescence intensity was comparable between the two nanoparticle types, except at depths of 40 µm and 70 µm, where spheroids incubated with worms exhibited higher fluorescence levels. In contrast, within the intermediate and central regions, no significant differences in fluorescence intensity were observed between the two groups. However, for both worm- and sphere-treated spheroids, a gradual decrease in nanoparticle penetration was evident from the periphery toward the core of CT26 MCTSs. This trend was statistically significant across the three regions, particularly at 70 µm depth, highlighting the diffusion limitations of nanoparticles in the dense 3D tumor microenvironment.

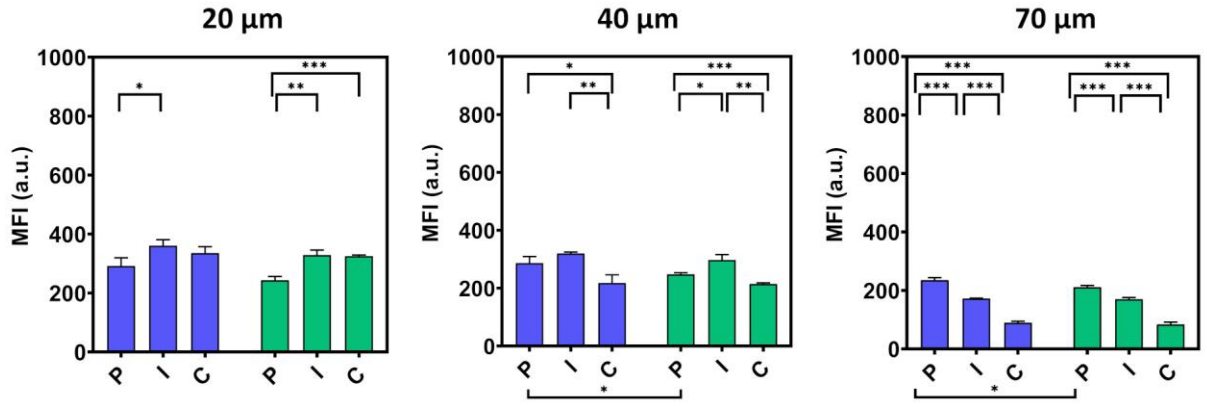

Figure V-22. Penetration of worms and spheres in CT26 MCTS in periphery, intermediate and core regions at 20, 40 and 70 µm depth. In green: spheres, in blue: worms. Data points represent mean ± standard deviation in each area, $n = 3$ MCTSs. Statistically significant differences between p region is denoted by (*), $p < 0.05$, (**), $p < 0.01$ and (***), $p < 0.001$.

V.4.2.2. 4T1 MCTS

The investigation of nanoparticle penetration kinetics was expanded to include 4T1 MCTSs, which offer a more compact model than CT26 spheroids.[34] The objective of this study was to ascertain whether nanoparticle morphology influences the depth and efficiency of penetration into more densely packed tumor spheroids. Following incubation under the same conditions as those employed for CT26 spheroids, the nanoparticles analysis was first conducted using CLSM (Figure V-19c,d). The fluorescence tracking on CLSM images allowed for the estimation of penetration kinetics, revealing apparent rate constants (k_{obs}) for worms and spheres at various depths within the spheroids (Figure V-23). For worms, k_{obs} values were 0.098 h^{-1}, 0.048 h^{-1}, and 0.028 h^{-1} at depths of 20 µm, 40 µm, and 70 µm, respectively. In contrast, the rate constants for spherical nanoparticles were slightly higher, with values of 0.119 h^{-1}, 0.070 h^{-1}, and 0.047 h^{-1} at the same depths. This finding indicates that spherical nanoparticles exhibit enhanced penetration capability into 4T1 spheroids in comparison to worm-like nanoparticles. It is noteworthy that while penetration kinetics decrease with depth for both types of nanoparticles, the difference in penetration rates across the spheroid regions was more pronounced in 4T1 spheroids than in CT26, where no significant differences in kinetics were observed.

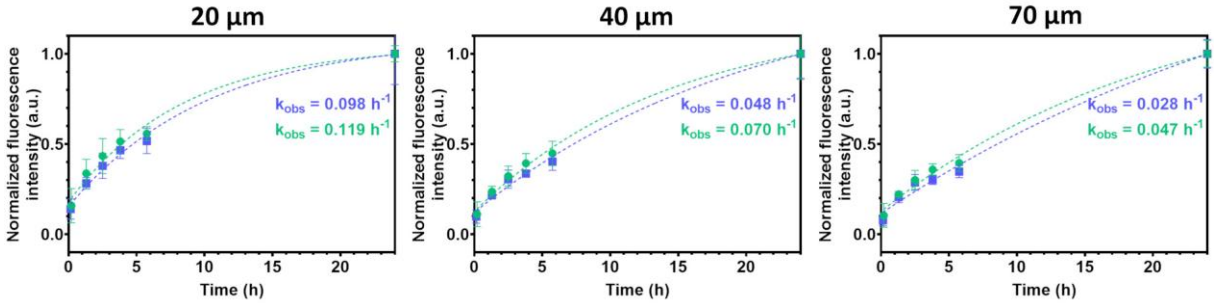

Figure V-23. Normalized fluorescence intensity from 4T1 MCTSs CLSM images after micelles incubation overtime at 20, 40 or 70 µm depth. In green: spheres, in blue: worms.

After a 24-hour incubation period, the distribution of nanoparticles within the spheroids was analyzed across the defined peripheral, intermediate, and core regions (Figure V-24). Significant differences in fluorescence intensity were observed between the regions. Fluorescence in the peripheral region was consistently higher than in the intermediate and core regions, with the exception of the 20 µm depth, where the intermediate region exhibited higher fluorescence for both types of nanoparticles This result suggests that both nanoparticle types encounter difficulties in penetrating deeper into the 4T1 MCTS, resulting in a notable accumulation at the surface of the nanoparticles at the 20 µm depth. However, at 70 µm, worms exhibited higher fluorescence in the periphery compared to spheres, indicating higher accumulation in this region. Additionally, the mean fluorescence intensity for 4T1 spheroids was consistently higher than that of CT26 across all optical slices and regions, suggesting more effective nanoparticle uptake in 4T1 spheroid cells. This observation is consistent with the results obtained from 2D monolayer cell uptake studies.

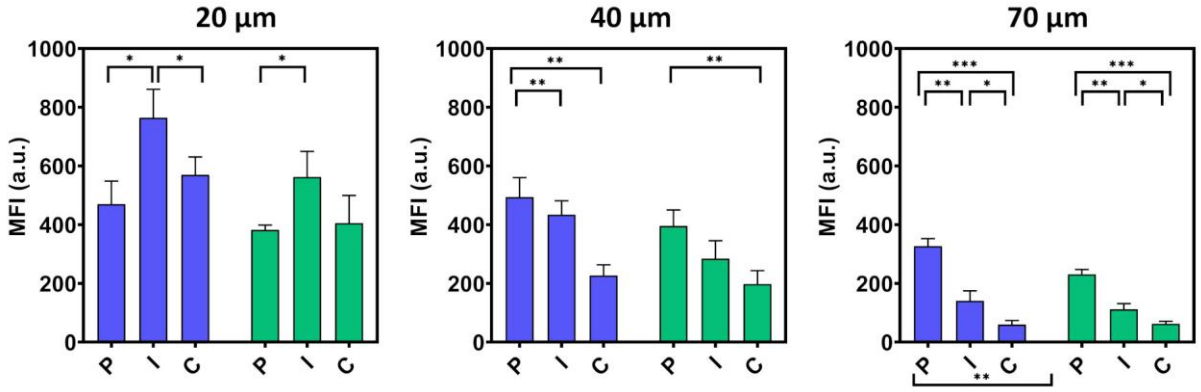

Figure V-24. Penetration of worms and spheres in 4T1 MCTS in periphery, intermediate and core regions at 20, 40 and 70 µm depth. In green: spheres, in blue: worms. Data points represent mean ± standard deviation in each area, $n = 3$ MCTSs. Statistically significant differences between p region is denoted by (*), $p < 0.05$, (**), $p < 0.01$ and (***), $p < 0.001$.

V.4.3. Flow cytometry

This approach involves incubating spheroids with nanoparticles for a defined period without washing steps, allowing continuous observation and assessment of penetration kinetics, including potential micelle adsorption on the spheroid surface. To validate the penetration kinetics and quantify micelle uptake, we conducted flow cytometry analysis for both types of spheroids. Following incubation with worm-like and spherical nanoparticles, the spheroids were detached, dissociated into single cells, and washed to remove any non-internalized nanoparticles, under the assumption that surface-adsorbed nanoparticles are eliminated during this process. The uptake within the spheroid's cells over time was assessed by analyzing fluorescence intensity distribution, as shown in the histogram. In this analysis, APC-A indicates fluorescence intensity resulting from 633 nm laser excitation, corresponding to Cy5.5 fluorescence.

V.4.3.1. CT26 MCTS

For CT26, the histogram exhibited a slight shoulder after 6 and 24 hours of incubation, indicating incomplete penetration into the deeper layers of the spheroids (Figure V-25a, b). This observation was corroborated by the percentage of fluorescent cells, which demonstrated that while not all cells were fluorescent after 24 hours, effective uptake was nonetheless achieved following penetration into the spheroids (Figure V-25c). It is important to acknowledge a limitation of this approach: it does not provide spatial information on the micelle distribution within the spheroid, making it challenging to accurately assess penetration depth. As shown in Figure V-25d, the mean fluorescence intensity over time was plotted to confirm the CLSM findings, revealing rapid initial penetration and saturation of uptake within 6 hours of incubation. Using a simple one-phase association model fitting, comparable k_{obs}' can be observed around 0.2 h^{-1} between the two treated groups. These results are consistent with those obtained by CLSM measurements.

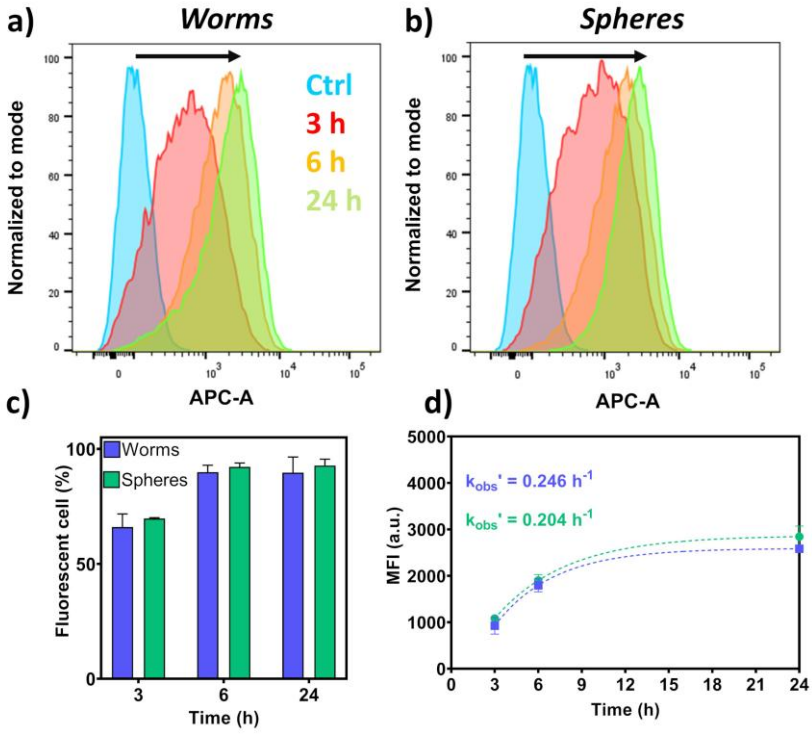

Figure V-25. Histogram obtained from flow cytometry after CT26 MCTSs incubation for 3, 6 or 24 hours with (a) worms and (b) spheres. The plots were generated with the FlowJo software. (c) Percentage of fluorescence cells determined *via* flow cell cytometry after incubation with fluorescent nanoparticles, at different time points. (d) Cell association of worms and spheres in CT26 at different time points, determined *via* flow cell cytometry. The line graph represents the total mean fluorescence intensity of the samples.

To conclude on micelle penetration in CT26 spheroids, both CLSM measurements and flow cytometry demonstrated high and rapid uptake kinetics for both worm-like and spherical nanoparticles, thereby demonstrating their efficient internalization into the CT26 spheroids. Worm-like micelles exhibited slightly higher fluorescence at the 40 µm and 70 µm depths compared to spherical nanoparticles, suggesting a minor advantage in the periphery. However, this advantage was not observed in the deeper regions of the spheroid. Both micelle populations appeared to encounter difficulties in penetrating the core, as indicated

by the gradual decrease in fluorescence from the periphery to the center. Subsequent flow cytometry analysis revealed that not all cells exhibited equivalent levels of fluorescent intensity, thereby suggesting less efficient uptake in the deeper layers of the spheroids.

V.4.3.2. 4T1 MCTS

Similarly, to further substantiate CLSM findings, flow cytometry analysis was performed after detaching and washing the cells from the 4T1 spheroids. The results presented in Figure V-26 indicate a slower uptake of nanoparticles by spheroid cells compared to CT26. After a 3-hour incubation period, 62% of cells exhibited fluorescent properties for worms and 44% for spheres, increasing to 64% and 69% respectively after a 6-hour incubation period. However, following a 24-hour period, the vast majority of cells exhibited fluorescence, thereby confirming the efficacy of penetration and internalization processes. The MFI results corroborated these findings, showing that saturation was not attained even after 24 hours, with diminished penetration kinetics observed in 4T1 spheroids compared to CT26 (Figure V-26d). To elucidate these observations, flow cytometry histograms at 3 and 6 hours revealed two discrete fluorescence populations, likely corresponding to the outer and core cell layers of the spheroid (Figure V-26a,b). The outer layer exhibited higher fluorescence, while deeper cells showed lower uptake efficiency, suggesting that nanoparticles face challenges in penetrating the spheroid core. This reduced penetration kinetics could be attributed to the elevated cellular density present in 4T1 spheroids. After 24 hours, a monomodal distribution was observed. The majority of cells had internalized nanoparticles, even in the deeper core (Figure V-26c). This observation indicates that, over time, nanoparticle penetration occurs predominantly through cell-to-cell transfer rather than solely by direct uptake from the surrounding medium. An alternative hypothesis is that the association number or shape of the micelles undergoes a transformation upon interaction with cells in the spheroid, a process that could facilitate their transportation to the center. However, the present study does not provide enough evidence to validate either hypothesis, and further investigations are needed.

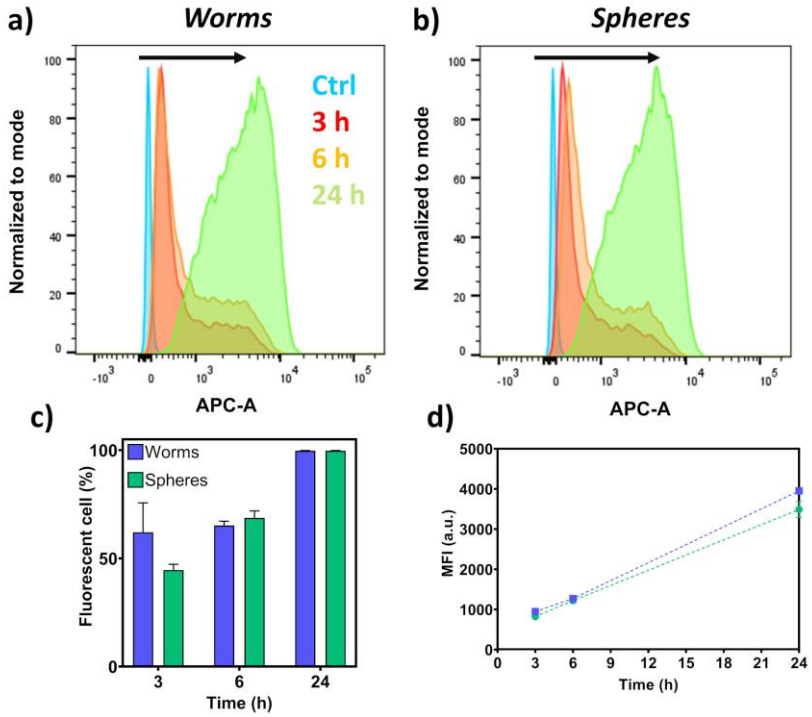

Figure V-26. Histogram obtained from flow cytometry after 4T1 MCTSs incubation for 3, 6 or 24 hours with (a) worms and (b) spheres. The plots were generated with the FlowJo software. (c) Percentage of fluorescence cells determined *via* flow cell cytometry after incubation with fluorescent nanoparticles, at different time points. (d) Cell association of worms and spheres in CT26 at different time points, determined *via* flow cell cytometry. The line graph represents the total mean fluorescence intensity of the samples.

In conclusion, while nanoparticle penetration is reduced in 4T1 spheroids relative to CT26 spheroids, probably due to their higher cell density, their overall uptake is greater, consistent with observations from 2D monolayer studies.

V.5. Biodistribution

V.5.1. Circulation time in healthy BALB/c nude mice

The blood circulation profiles of both spherical and worm-like nanoparticles were determined using intravital confocal micro-videography. Specifically, nanoparticle solutions in PBS were injected into the tail vein of an anesthetized mouse. Then the Cy5.5 fluorescence was monitored inside the blood vessels within the earlobe area over time using confocal microscopy (Figure V-27a, b). To facilitate comparison between the two samples, fluorescence in the vein was monitored for 12 hours and normalized to its peak intensity. Immediately following intravenous injection, both Cy5.5-labeled worms and spheres were visible in the experimental mouse's earlobe blood vessels, and they were still detectable in circulation 12 hours later (Figure V-27c). Of particular interest was the observation that the larger fluorescence intensity of worms after 12 hours, retaining 50% of the nanoparticles compared to spheres with less than 40%, suggested that worm-like nanoparticles exhibit prolonged circulation in the mouse organism. For spherical nanoparticles, the half-life was estimated to be approximately 4 hours. Although the measurement

timeframe for worm-like nanoparticles was insufficient to determine their half-life with precision. Nonetheless, the decay curve indicates that their half-life was longer than 4 hours.

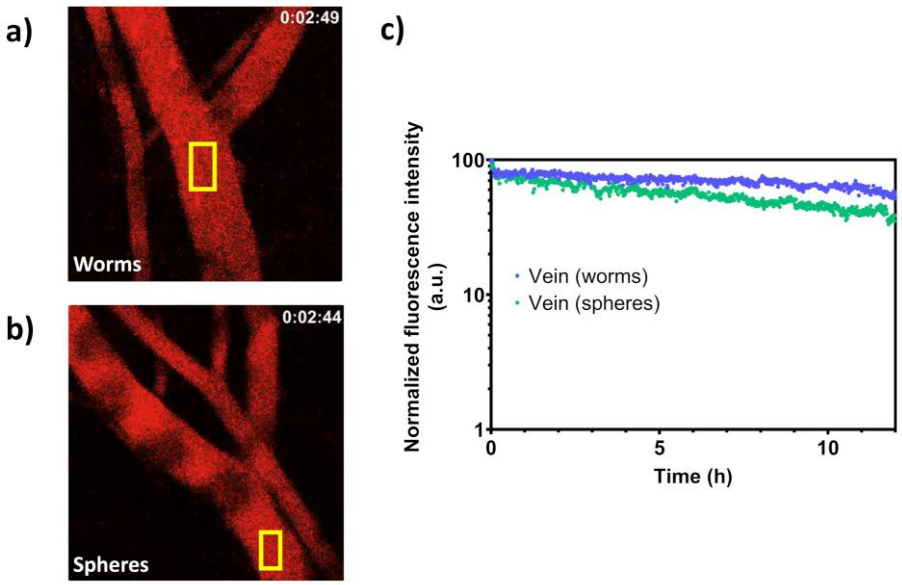

Figure V-27. *In vivo* CLSM observation of Cy7-worms and spheres in blood vessels. A region of interest (ROI) is selected as an vein (yellow) for mouse inoculated with (a) worms and (b) spheres. (c) Normalized fluorescence intensity in the vein ROIs plotted against time (Y-axis is in logarithmic scale).

V.5.2. Accumulation of fluorescent NPs in CT26 and 4T1 tumors

Subsequently, the tumor accumulation ability of the nanoparticles was investigated both in hyperpermeable CT26 tumor and in stroma rich 4T1 tumor. IVIS images were obtained at 1, 6, 9 and 24 hours, post-injection. For the 4T1 model, images were taken at 3, 6, 9, and 24 hours post-injection. The concentration of Cy7-labeled worms and spheres was adjusted to ensure equivalent fluorescence levels by IVIS. Then, the *in vivo* distribution of Cy7-labeled worms and spheres within the two mouse populations was assessed by means of fluorescence imaging. For CT26, selective accumulation was confirmed by a strong fluorescence signal at the tumor site, even just after 1 hour post tail injection (Figure V-28).

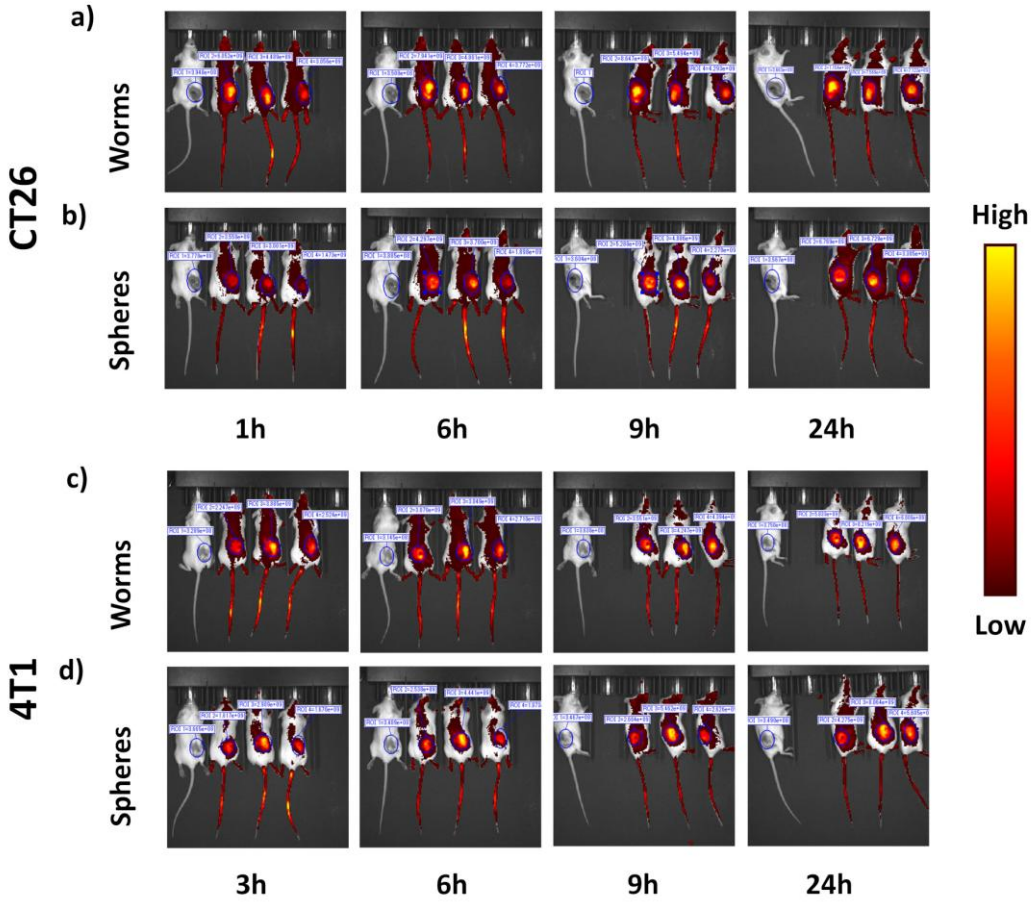

Figure V-28. Biodistribution of worms and spheres. (a-b) Whole body fluorescent image of subcutaneous CT26 tumor bearing mice, at different time points after the injection of (a) worms and (b) spheres. Nanoparticles are detected specifically at the tumor site. (c-d) Whole body fluorescent image of subcutaneous 4T1 tumor bearing mice, at different time points after the injection of (c) worms and (d) spheres.

To compare the kinetics of accumulation, the fluorescence on the tumor site was measured and plotted versus time (Figure V-29).

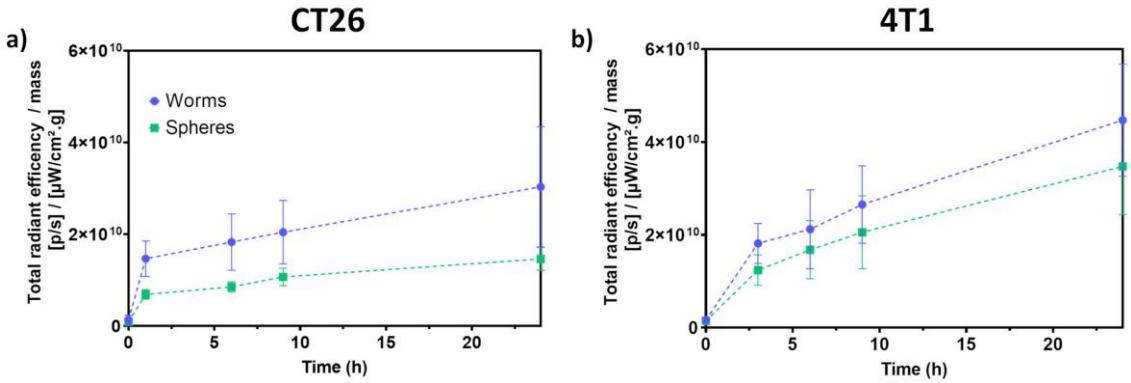

Figure V-29. Nanoparticles biodistribution and tumor accumulation in tumor-bearing mice. *In vivo* fluorescence intensity of tumors in (a) CT26 bearing mice, (b) 4T1 bearing mice.

This analysis revealed a discrepancy in fluorescence intensity, with tumors subsequent to spheres injection showing a weaker signal intensity compared to worms. The saturation was not reached after 24 hours. However, when the kinetics are compared using a 1st order model, the same apparent constant rate

of 0.11 h^{-1} is obtained. Furthermore, for 4T1, selective accumulation at the tumor site can also be observed. By plotting the fluorescence intensity *vs* time, and using a 1st order model, it is observed that the constant rate is slightly smaller for 4T1 than for CT26, approximately 0.08 h^{-1}. However, the final fluorescence intensity at the tumor site is higher for both populations of nanoparticles in this case. These findings are consistent with the results obtained *in vitro*, which demonstrate a slower accumulation but higher levels of fluorescence in the 4T1 tumor.

To corroborate the biodistribution and accumulation of nanoparticles in tumors and other organs, the mice were sacrificed after 24h. At that point, the main organs were collected, weighed, and analyzed by fluorescence with the IVIS (Figure V-30). The nanoparticle organ accumulation is displayed as a percentage of the recovered fluorescence per gram of tissue. This percentage was determined by dividing the collected fluorescence from each tissue by the total sum fluorescence of all excised tissues for each individual mouse. This approach allows for meaningful comparisons of tissue accumulation between worms and spherical nanoparticles.

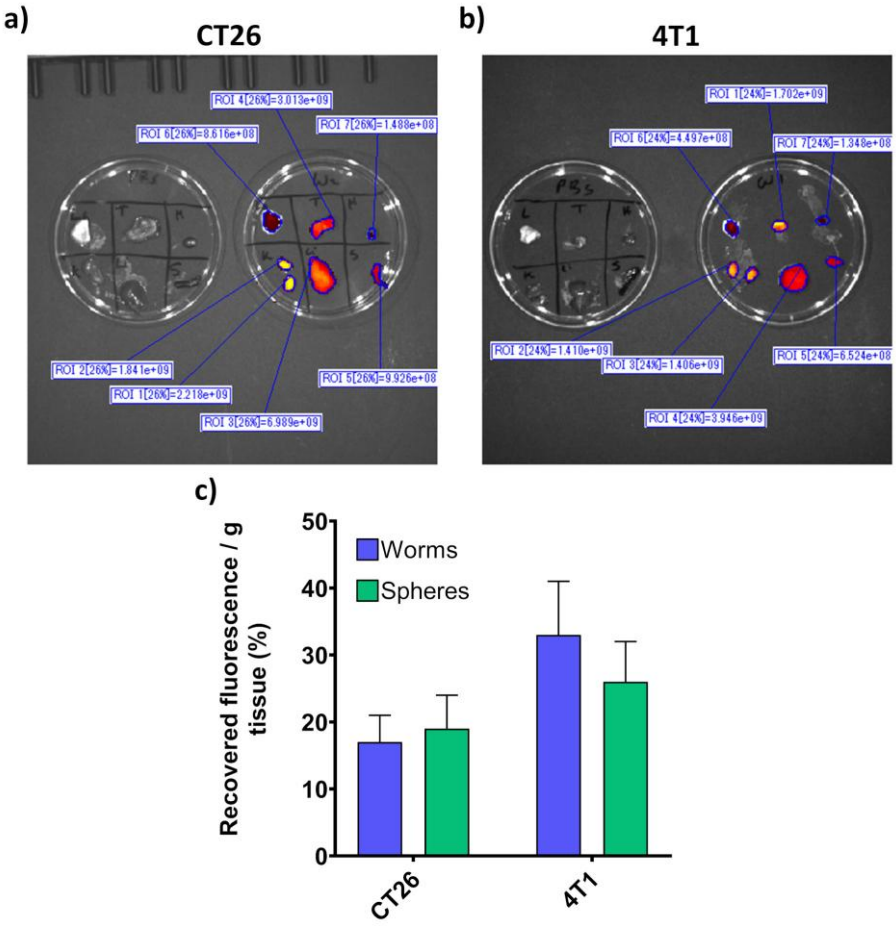

Figure V-30. *Ex vivo* fluorescent imaging of tumor part and the other vital organs from (a) CT26 and (b) 4T1 tumor bearing mouse. (c) Comparison between *ex vivo* quantification of fluorescence signals in tumor at 24 hours for worms and spheres in CT26 and 4T1 tumor. The percentage of recovered fluorescence per gram of tissue for each organ was calculated by dividing collected fluorescence from each tissue by the total sum fluorescence of all excised tissues for each individual mouse.

With respect to tumor accumulation, nanoparticles were detected in both tumor types. However, a surprising finding was the significantly higher worms' accumulation in 4T1 tumors compared to CT26 tumors and other organs (Figure V-31c). This outcome aligns with the *in vitro* findings from both 2D and 3D models. However, *in vivo*, the tumor microenvironment is more complex, and 4T1 tumors are known to be stroma-rich, which typically hinders nanoparticle accumulation.[34,48] Additionally, it is important to note that in this study, tumors were implanted subcutaneously, meaning they lack the native breast tumor microenvironment. This may have implications for angiogenesis and the structure of tumor stroma.[49] This difference may offer a partial explanation for the observed accumulation pattern. With regard to the biodistribution in the organs, the results showed also accumulation in the liver, kidneys and spleen in both CT26 and 4T1 tumor-bearing mice, with no discernable trend related to morphology (Figure V-31).

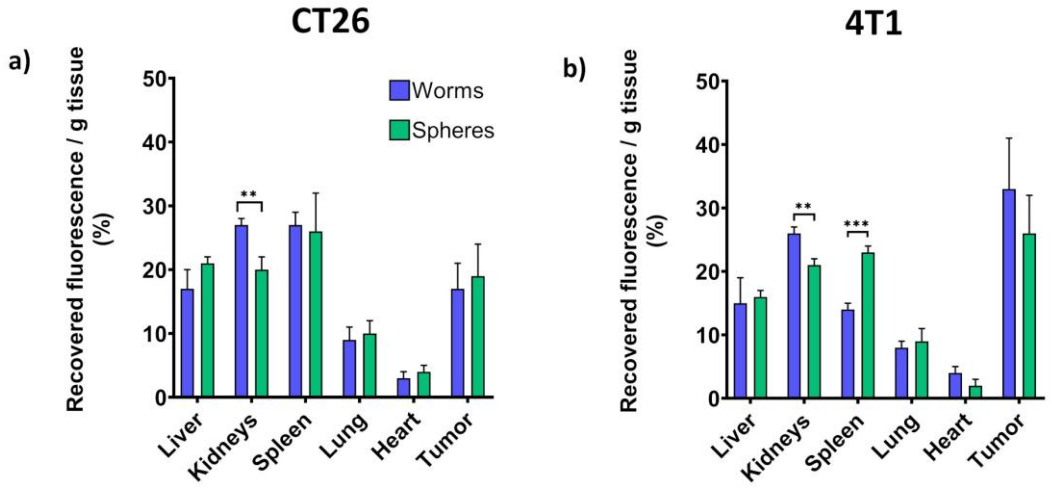

Figure V-31. *Ex vivo* quantification of fluorescence signals per organ at 24 hours for (a) CT26 bearing mice, (b) 4T1 bearing mice.

V.6. Conclusion

In this chapter, we successfully synthesized fluorescent polypeptide-based worm-like nanoparticles via a straightforward, one-step aqueous ROPISA of BLG-NCA, incorporating an optimized fluorescent labeling strategy within the same reaction. To assess their performance in comparison with conventional polypeptide-based nanocarriers, we also prepared analogous spherical nanoparticles using a solvent-displacement method. Their cellular uptake and *in vivo* biodistribution were evaluated in two tumor cell models, CT26 (colorectal carcinoma) and 4T1 (breast cancer), which present distinct vascular architectures and permeability, thereby influencing the EPR effect and passive nanoparticle accumulation.

Both worm-like and spherical nanoparticles exhibited efficient internalization in 2D cell cultures, with CT26 cells demonstrating a faster uptake, while 4T1 cells showed higher overall nanoparticle accumulation. Notably, no significant difference was observed between the two morphologies, emphasizing the robust potential of ROPISA-derived nanocarriers for tumor targeting. These results were further supported by studies in 3D spheroid models, where both nanoparticle types demonstrated deep penetration.

However, penetration kinetics differed, with slower diffusion in 4T1 spheroids yet leading to a greater final accumulation.

Most importantly, *in vivo* studies in healthy mice revealed prolonged circulation times, confirming the stability of these nanocarriers in physiological conditions. Additionally, both CT26 and 4T1 tumor-bearing mice exhibited efficient tumor accumulation, further validating the suitability of ROPISA-derived nanoparticles for drug delivery applications. The particularly strong tumor accumulation observed in 4T1 models highlights the promise of worm-like nanoparticles in addressing challenging tumor environments with high intratumoral pressure.

These findings provide the first compelling evidence of the potential of aqueous ROPISA of NCA in nanomedicine. This work establishes a foundation for developing next-generation drug-loaded nanocarriers via covalent drug conjugation and/or in situ encapsulation, as explored in **Chapter VI**.

V.7. Experimental section

V.7.1. Materials

γ-benzyl-*L*-glutamate was purchased from PMC Isochem (Vert-le-Petit, France) and stored at -20°C under argon atmosphere and weighed in the glove box Jacomex GP13 no. 2675. α-methoxy-ω-amino poly(ethylene glycol) PEG_{5k}-NH_2 (M_p = 5000 g.mol^{-1}, $Đ$ = 1.02) was bought from RAPP Polymer Gmbh (Tübingen, Germany). Cyanine 5.5 *N*-hydroxysuccidimide ester (Cy5.5 NHS ester) and cyanine 7 *N*-hydroxysuccidimide ester (Cy7 NHS ester) were bought from Lumiprobe (Hannover, Germany). Dimethyl sulfoxide (DMSO) and *N*-*N*-dimethylformamide (DMF) were purchased from Sigma. Milli-Q water was obtained from a Purelab Prima purification system (ELGA) with a resistivity of 18.2 MΩ.cm^{-1}. Deuterated solvent ($CDCl_3$) was purchased from Eurisotop. Dialysis membranes (SpectraPor®) were purchased from different providers, like SpectrumLabs, Fujifilm or Funakoshi. Dulbecco's modified Eagle's medium (DMEM), Roswell Park Memorial Institute medium (RPMI-1640), Phosphate-buffered saline (PBS) for *in vitro* and *in vivo* samples dilution were purchased from Fujifilm Wako Pure Chemical Industries, Ltd., penicillin/streptomycin (P/S) and Trypsin/Ethylenediamine tetraacetate (EDTA) were obtained from Gibco *via* ThermoFisher. Phosphate-buffered saline (PBS) was purchased from Takara and UGAP for nanoparticles dialysis. Fetal bovine serum (FBS) was purchased from (Gibco™, Fisher Scientific). Endothelial Basal Medium-2 (EBM-2) and the EGM-2 Bullet Kit were obtained from Lonza. 4′,6-diamidino-2-phenylindole (DAPI) was obtained from Invitrogen. Cell counting kit-8 (CCK-8) and Hoescht 33342 were obtained from Dojindo Laboratories (Kumamoto, Japan).

V.7.2. Instrumentation and methods

V.7.2.1. Nuclear Magnetic Resonance (NMR)

^{1}H Nuclear Magnetic Resonance (NMR) spectra were recorded on a Bruker Avance III spectrometer equipped with a 5 mm BBFO (broad band fluorine observation) liquid probe, at 298 K. ^{1}H data were acquired at 400.2 MHz observation frequency, with 16 scans and a recycle delay of 1 second. Signals were referred to the signal of residual protonated solvent signals.

V.7.2.2. Size Exclusion Chromatography (SEC)

Polymer molar masses were determined by SEC using dimethylformamide (DMF + LiBr 1 g.L^{-1}) as eluent. Measurements were performed on an Ultimate 3000 system from ThermoFischer Scientific (Ilkirch, France) equipped with a diode array detector (DAD). The system also includes a multiangle light scattering detector (MALS) and differential refractive index detector dRI from Wyatt technology (Santa Barbara CA, USA). Polymers were separated on three Shodex Asahipack gel columns [GF 310 (7.5 × 300 mm²), GF510 (7.5 × 300 mm²), exclusion limits from 500–300 000 Da] at a flowrate of 0.5 mL.min^{-1}. Columns temperature was held at 50 °C. Easivial™ kit of Polystyrene from Agilent (Santa Clara CA, USA) was used as calibration standard (Mn from 162 to 364 000 Da).

V.7.2.3. Cell viability

Cell viability was measured by using a Tecan infinite M1000Pro microplate reader.

V.7.2.4. Dynamic Light Scattering (DLS)

For DLS measurements, the nanoparticles were diluted to a concentration of 1 mg.mL^{-1} and filtered before being used in biological experiments, a Zetasizer nano ZS (Malvern Instruments, UK) instrument with a detection angle of 173° and a green laser (532 nm) as the incident beam was used. Measurements were carried out at 25 °C in triplicate.

V.7.2.5. Transmission Electron Microscopy (TEM)

The images were recorded on a Hitachi H7650 microscope operating at 80 kV. Samples were prepared following dialysis against PBS and filtration with a 0.22 µm CA filter. A 0.1 mg.mL^{-1} nanoparticles dispersion was deposited onto a copper grid (200 mesh coated with carbon) previously treated with a 45 second glow discharge treatment. The remaining drop was removed after 1 minute and the resulting grids were negatively stained twice with 1.2% uranyl acetate for two consecutive 1-minute periods.

The number-average lengths of nanoparticles were calculated with Eq 1; whereas the number-average widths were calculated with Eq 2,

(1) $$L_n = \frac{\sum_{i=1}^{n} n_i L_i}{\sum_{i=1}^{n} n_i}$$

(2) $$w_n = \frac{\sum_{i=1}^{n} n_i w_i}{\sum_{i=1}^{n} n_i}$$

where n_i is the number of particles with length L_i and width w_i.

V.7.2.6. Cryo-Transmission Electron Microscopy (cryo-TEM)

Cryo-TEM images were obtained by deposing 4 µL of samples after dialysis against PBS and filtration with a 0.22 µm CA filter on an EM grid coated with a perforated carbon film. After draining the excess liquid with a filter paper, grids were plunge-frozen into liquid ethane cooled by liquid nitrogen using a Leica EMCPC cryo-chamber (Leica Microsystems, Wetzlar, Germany). For cryo-TEM observation, grids were mounted onto a Gatan 626 cryoholder and transferred to a Tecnai F20 microscope (Thermo Fisher Scientific) operated at 200 kV. Images were recorded with an Eagle 2k CCD camera (FEI, USA).

V.7.2.7. Fluorescence measurements

Fluorescence measurements were carried out on a JASCO FP-8600 NIR spectrofluorometer at an excitation wavelength of 683 nm. For Cy7-labelled nanoparticles, fluorescence was directly measured by IVIS.

V.7.2.8. *In vitro* cytotoxicity of nanoparticles on HUVEC cells

In vitro cell viability of nanoparticles was investigated on HUVEC cultured in EBM-2 with growth supplements (EGM-2 Bullet Kit). 96 well flat-bottom plates were prepared with 6000 cells per well. Micelle solutions in PBS were diluted in cell medium to obtain final concentrations in the range of 1575 − 2.5

μg.mL^{-1}. Subsequent to incubation for 24 hours, the cells were exposed to micelle solutions of different concentrations. After an additional 20 hours of incubation, the viability of the cells was determined by coloring with CCK-8, incubating for an additional 4 hours, and measuring the formazan absorbance at 450 nm.

V.7.2.9. Cell culture

Cell culture was carried out as follows: hyperpermeable CT26 colon adenocarcinoma cells and 4T1 breast tumor cells were used from stocks.

CT26 2D cell cultures were grown in DMEM containing 10 vol % FBS and 1 vol % P/S in PBS. Cells were incubated in a humidified atmosphere containing 5% CO_2 at 37 °C. After reaching confluence, cells were detached using Trypsin/EDTA and the cell suspension was collected for further experiments.

CT26 3D cell cultures (spheroids) were generated as follows: after the CT26 cells were collected from a 2D cell culture, they were dispersed in cell culture medium at a density of 10 000 cells/ mL. 100 μL of the cell suspension were seeded into each well (1 000 cells/well) of a low cell adhesion Prime Surface 96-well U-bottom plate (Sumitomo Bakelite Co., Japan), centrifuged at 500 rpm for 5 min and incubated in a humidified atmosphere containing 5% CO_2 at 37 °C for 4 days. After approximately 2 days, the spontaneous formation of spheroids was observed. After 4 days, the spheroids had a diameter of 398 ± 12 μm as determined from microscopic images.

4T1 2D cell cultures were grown in the RPMI-1640 medium containing 10 vol % FBS and 1 vol % P/S. Cells were incubated in a humidified atmosphere containing 5% CO_2 at 37 °C. After reaching confluence, cells were detached using Trypsin/EDTA and the cell suspension was collected for further experiments. After reaching confluence, cells were detached using trypsin/EDTA, and the cell suspension was collected for further experiments**.**

4T1 3D cell cultures (spheroids) were generated as follows: after the 4T1 cells were collected from a 2D cell culture, they were dispersed in cell culture medium at a density of 10 000 cells/ mL. 100 μL of the cell suspension were seeded into each well (1 000 cells/well) of a low cell adhesion Prime Surface 96-well U-bottom plate (Sumitomo Bakelite Co., Japan), centrifuged at 500 rpm for 5 min and incubated in a humidified atmosphere containing 5% CO_2 at 37 °C for 4 days. After 2 days, the spheroids had a diameter of 267 ± 3 μm as determined from microscopic images using a Keyence all-in-one fluorescence microscope BZ-X710.

Cell vitality and the cell number were controlled after detachment using an Invitrogen Countess II FL automated cell counter in all cases.

V.7.2.10. Confocal Laser Scanning Microscopy (CLSM)

Confocal laser scanning microscopy (CLSM) measurements were carried out on a Carl Zeiss CLSM 880 confocal microscope (Carl Zeiss, Oberkochen, Germany) using of 10× or 20× objective lenses and white

light as well as a UV (405 nm) and a red (633 nm) laser for fluorophore excitation. Incubation studies were carried out as described in the following paragraphs.

For CLSM measurements of 2D cell cultures, the cells were seeded onto µ-slide 8-well high glass bottom plates (ibidi) at a cell density of 15 000 cells per well in 200 µL of the cell culture medium for CT26, and 10 000 cells for 4T1, respectively, and incubated in a humidified atmosphere containing 5% CO2 at 37 °C for 24 hours before usage. Hoescht at 1 $\mu L.mL^{-1}$ was added for nucleus staining 5 minutes before observation.

Cy5.5-labeled nanoparticles in a medium/PBS mixture (less than ¼ of PBS to avoid cell death) were added to the well plates to yield a concentration of 0.5 mg per mL for worms and 0.2 mg per mL for spheres of the cell culture medium to have same fluorescence intensity. Real-time confocal imaging was performed by the incubation system for microscopes with acquisition every 2 min for 1 hour, and then every 30 min, for a total of 15 hours.

For CLSM measurements of 3D cell culture, spheroids were generated as described above but were seeded into each well (1 000 cells/well) of ultra-low attachment 96-wells plate with clear round bottom (Corning, New York). Hoescht at 1 $\mu L.mL^{-1}$ was added for nucleus staining 30 minutes before observation. Cy5.5-labeled nanoparticles in a medium/PBS mixture (less than ¼ of PBS to avoid cell death) was added to the well plates to yield a concentration of 0.5 mg per mL for worms and 0.2 mg per mL for spheres of the cell culture medium to have same fluorescence intensity. The spheroids were incubated in a humidified atmosphere containing 5% CO_2 at 37 °C for the given time and observed by CLSM (no real-time confocal imaging is possible with 96-well plates).

V.7.2.11. Flow cytometry measurements

Flow cytometry measurements were performed on a BD LSRFortessa X-20 cell analyzer using FSC and SSC detection, and a UV laser (355 nm) and a red laser (640 nm) for detection of the used fluorophores. Incubation studies were carried out as described in the following paragraphs. Cells for 2D cell culture incubation were seeded in 6-well polystyrene plates (Corning, New York) at a cell density of ca. 200 000 cells per well in 3 mL of cell culture medium and incubated in a humidified atmosphere containing 5% CO_2 at 37 °C for 24 hours before usage. The medium was then replaced with 3 mL of the fresh medium and the Cy5.5-labeled micelle solution in PBS was added to the well plates to yield a concentration of 0.25 mg per mL for worms and 0.1 mg per mL for spheres of the cell culture medium to reach same fluorescence intensity. The cells were incubated under the same conditions for the given time. After that, the cells were washed with PBS, detached with trypsin/EDTA, washed with 2 vol% FBS/PBS, and finally dispersed in a solution of 1 $\mu g.mL^{-1}$ DAPI in 2 vol% FBS/PBS. The cell suspension was then measured using a flow cytometer.

The spheroids for 3D cell culture incubation were prepared as described. For incubation, the micellar solution of Cy5.5-labelled nanoparticles was added to the cell culture medium of the spheroids after 4 days

of cultivation time for CT26 and 2 days for 4T1 to yield a concentration of 1 mg per mL of the cell culture medium for worms and 0.4 mg per mL for spheres (based on same fluorescence intensity after filtration). The spheroids were incubated in a humidified atmosphere containing 5% CO_2 at 37 °C for the given time. They were then carefully collected in a falcon tube, the medium was removed *via* centrifugation, and the spheroids were washed with PBS. Afterward, they were detached to yield single cells by treatment with Accutase, followed by dispersion and washing in 2 vol% FBS/PBS. The cells were then dispersed in a solution of 1 $\mu g.mL^{-1}$ DAPI in 2 vol% FBS/ PBS and measured using the flow cytometer.

V.7.2.12. In Vivo Laser Scanning Microscopy

In vivo laser scanning microscopy was conducted using Nikon A1R confocal laser scanning microscope system attached to an upright ECLIPSE FN1 equipped with a CFI Plan Apo λ 20× objective (Nikon Corp., Tokyo, Japan). The pinhole diameter was adjusted to 10 μm. The ear lobe dermis was fixed beneath a coverslip with immersion oil to determine the longevity. Blood vessels in the ear lobe dermis were focused using a 488 nm laser with a 525/50 nm band-pass emission filter. Ten seconds after recording Cy5.5 fluorescence (using a 640 nm laser with a 700/75 nm band-pass emission filter), 200 μL Cy5.5-labeled nanoparticles at a concentration of 1 $mg.mL^{-1}$ were intravenously administered into BALB/c mice (female, 7 weeks old). Acquired data were processed using Nikon NIS Elements (ver. 4.00.06). Relative fluorescence intensity (%) was calculated for the regions of interest (ROIs) defined over the vein as follows.

Fluorescence intensity (%) $= \frac{I}{I_{max}} \times 100\%$, where I and I_{max} represent background-subtracted intensity and background-subtracted maximum intensity of ROIs at indicated time points, respectively.

V.7.2.13. Biodistribution and tumor accumulation of Cy7 nanoparticles in CT26-tumor bearing mice

BALB/c mice (female) were inoculated subcutaneously with CT26 cells (5×10^5 cells/per mouse, V = 50 μL in DMEM cell culture). Tumors were allowed to grow for 13 days (average tumor size was 580 mm^3). Cy7-labeled worm-like and spherical nanoparticles were prepared to investigate the accumulation in a CT26 subcutaneous tumor. Cy7-labeled nanoparticles were intravenously injected into tumor-bearing mice and the mice were imaged during 24 hours to track the accumulation of nanoparticles in the whole body by using IVIS imaging system (excitation: 710 nm; emission: 760 nm). Then, the mice were sacrificed, and the organs (liver, kidney, heart, lung and spleen) and the tumor were imaged ex vivo to evaluate the accumulation of nanoparticles

V.7.2.14. Biodistribution and tumor accumulation of Cy7 nanoparticles in 4T1-tumor bearing mice

In the same way, BALB/c mice (female) were inoculated subcutaneously with 4T1 cells (1×10^6 cells/per mouse, V = 50 µL in DMEM cell culture). Tumors were allowed to grow for 11 days (average tumor size was 380 mm^3).

V.7.2.15. Animals and animal Care

BALB/c mice (6 weeks old females weighing around 18-20 g) were procured from Charles River Japan (Kanagawa, Japan). These animals were maintained in a controlled environment that met specific pathogen-free standards, adhering to a strict 12-hour light/dark cycle. All animal experiments were executed in compliance with the guidelines for the care and use of laboratory animals as mandated by the ethics committee of the Innovation Center of NanoMedicine (Kawasaki, Japan).

V.7.2.16. Data analysis

Bar graphs indicate mean ± standard error of the mean. The p value was assessed by the Student T-test. * indicates $p < 0.05$, ** indicates $p < 0.01$ and *** indicates $p < 0.001$.

All data that require linear and non-linear regression analysis were processed using GraphPad Prism (version 7, GraphPad Software, San Diego, CA).

V.7.3. Synthesis

V.7.3.1. Synthesis procedure of poly(ethylene glycol)-*block*-poly(γ-benzyl- *L*-glutamate) PEG_{5k}-*b*-$PBLG_{31}$

The same protocol as described in **Chapter II** was adapted for a targeted DP of 31: γ-benzyl-*L*-glutamate (675 mg, 2.56 mmol), 15 mL of an ice-cooled solution of $NaHCO_3$ 0.05M containing the initiator PEG_{5k}-NH_2 (420 mg, 0.08 mmol, [M]/[I] = 31).

PBLG degree of polymerization was calculated from ^{1}H NMR (DP_{PBLG} = 30).

SEC provided a number-average molecular weight $M_n^{SEC\ RI}$ of 10 600 g·mol^{-1} (RI, PS calibration) and $Đ$ = 1.05.

^{1}H NMR (400 MHz, $CDCl_3$ + 15% TFA, δ, ppm): 7.85 (b, 1H, NH), 7.28 (b, 5H, Ar), 5.08 (q, 2H, CH2), 4.60 (b, 1H, CH), 3.70 (s, 4H, O–CH2CH2), 3.52 (s, 3H, CH3), 2.44 (b, 2H, CH2), 2.11–1.91 (b, 2H, CH2).

V.7.3.2. Grafting of cyanine 5.5: poly(ethylene glycol)-*block*-poly(γ-benzyl-*L*-glutamate) PEG_{5k}-*b*-$PBLG_{31}$-Cy5.5

In 6 mL of the solution of PEG_{5k}-*b*-$PBLG_{31}$, 0.26 mL at 10 mg.mL^{-1} of cyanine 5.5 *N*-hydroxysuccimide ester DMSO solution (3.36×10^{-3} mmol, 0.1 eq) was added and the mixture was stirred one day in the dark. The blue solution obtained was then transferred to a 50 kDa dialysis membrane and dialyzed against

deionized water for 5 days. An aliquot was freeze-dried for further analysis. The Cy5.5 grafting ratio was determined by UV-vis spectroscopy of the obtained powder in DMF, revealing 10 Cy5.5 for 100 polymer chains.

SEC then provided a number-average molecular weight $M_n^{SEC\ RI}$ of 10 800 g·mol^{-1} (RI, PS calibration) and $Đ$ = 1.05.

V.7.3.3. Grafting of cyanine 7: poly(ethylene glycol)-*block*-poly(γ-benzyl-*L*-glutamate) PEG_{5k}-*b*-$PBLG_{31}$-Cy7

In 6 mL of the solution of PEG_{5k}-*b*-$PBLG_{31}$, 0.25 mL at 10 mg.mL^{-1} of cyanine 7 *N*-hydroxysuccimide ester DMSO solution (3.36×10^{-3} mmol, 0.1 eq) is added and the mixture is stirred one day in the dark. The blue solution obtained is then transferred to a 50 kDa dialysis membrane and dialyzed against deionized water for 5 days. An aliquot is freeze-dried for further analysis. Cy7 grafting ratio was determined by UV-Vis spectroscopy of the obtained powder in DMF and revealed 10 Cy7 for 100 polymer chains.

SEC then provided a number-average molecular weight $M_n^{SEC\ RI}$ of 10 300 g·mol^{-1} (RI, PS calibration) and $Đ$ = 1.07.

V.7.3.4. Reformulation into spherical analogue nanoparticles

In a specific procedure, half of the Cy5.5-PEG_{5k}-*b*-$PBLG_{31}$ and Cy7-PEG_{5k}-*b*-$PBLG_{31}$ solutions were subjected to freeze-drying and nanoprecipitation, a process that results in the formation of spherical nanoparticles. The copolymer was dissolved in DMSO for a duration of one night to reach a concentration of 10 mg.mL^{-1}. Then, the solution was heated up at 30°C for 2h, and MilliQ water was added rapidly to the organic solution at a high stirring rate (90:10 H_2O/DMSO). The mixture was then allowed to equilibrate for several minutes, after which dialysis against PBS was achieved.

V.8. References

[1] H. Cabral, K. Miyata, K. Osada, K. Kataoka, *Chem. Rev.* **2018**, *118*, 6844–6892.
[2] M. A. Beach, U. Nayanathara, Y. Gao, C. Zhang, Y. Xiong, Y. Wang, G. K. Such, *Chem. Rev.* **2024**, *124*, 5505–5616.
[3] Y. Mai, A. Eisenberg, *Chem. Soc. Rev.***2012**, *41*, 5969–5985.
[4] A. Ahmed, S. Sarwar, Y. Hu, M. U. Munir, M. F. Nisar, F. Ikram, A. Asif, S. U. Rahman, A. A. Chaudhry, I. U. Rehman, *Expert Opin. Drug Deliv.* **2021**, *18*, 1–24.
[5] Y. Shi, T. Lammers, G. Storm, W. E. Hennink, *Macromolecular Bioscience* **2017**, *17*, 1600160.
[6] I. Jarak, M. Pereira-Silva, A. C. Santos, F. Veiga, H. Cabral, A. Figueiras, *Appl. Mater. Today* **2021**, *25*, 101217.
[7] M. Callari, J. R. Aldrich-Wright, P. L. de Souza, M. H. Stenzel, *Prog. Polym. Sci.***2014**, *39*, 1614–1643.
[8] Y. Han, P. Wen, J. Li, K. Kataoka, *J. Control. Release.***2022**, *345*, 709–720.
[9] S. Quader, K. Kataoka, *Mol Ther* **2017**, *25*, 1501–1513.
[10] C. Zhu, J. Nicolas, *Biomacromolecules* **2022**, *23*, 3043–3080.
[11] A. R. Mazo, S. Allison-Logan, F. Karimi, N. J.-A. Chan, W. Qiu, W. Duan, N. M. O'Brien-Simpson, G. G. Qiao, *Chem. Soc. Rev.* **2020**, *49*, 4737–4834.
[12] Li Z, Zheng Y, Yan J, Yan Y, Peng C, Wang Z, Liu H, Liu Y, Zhou Y, Ding M, *Chembiochem* **2023**, *24*, e202300132.
[13] C. Cai, J. Lin, Y. Lu, Q. Zhang, L. Wang, *Chem. Soc. Rev.* **2016**, *45*, 5985–6012.
[14] Y. Wu, K. Chen, J. Wang, M. Chen, W. Dai, R. Liu, *J. Am. Chem. Soc.* **2024**, *146*, 24189–24208.
[15] A. Harada, K. Kataoka, *Macromolecules* **1998**, *31*, 288–294.
[16] P. Heller, A. Birke, D. Huesmann, B. Weber, K. Fischer, A. Reske-Kunz, M. Bros, M. Barz, *Macromol Biosci* **2014**, *14*, 1380–1395.
[17] X. Gu, M. Qiu, H. Sun, J. Zhang, L. Cheng, C. Deng, Z. Zhong, *Biomater. Sci.* **2018**, *6*, 1526–1534.
[18] K. Kataoka, T. Matsumoto, M. Yokoyama, T. Okano, Y. Sakurai, S. Fukushima, K. Okamoto, G. S. Kwon, *J. Control. Release.***2000**, *64*, 143–153.
[19] Y. Jeong, S. Seo, I. Park, H. Lee, I. Kang, T. Akaike, C. Cho, *Int. J. Pharm.***2005**, *296*, 151–161.
[20] S. Hua, Y. Li, Y. Liu, W. Xiao, C. Li, F. Huang, X. Zhang, R. Zhuo, *Macromol. Rapid Commun.* **2010**, *31*, 81–86.
[21] H. Mukai, T. Kogawa, N. Matsubara, Y. Naito, M. Sasaki, A. Hosono, *Invest New Drugs* **2017**, *35*, 307–314.
[22] T. Hamaguchi, A. Tsuji, K. Yamaguchi, K. Takeda, H. Uetake, T. Esaki, K. Amagai, D. Sakai, H. Baba, M. Kimura, Y. Matsumura, T. Tsukamoto, *Cancer Chemother Pharmacol* **2018**, *82*, 1021–1029.
[23] Y. Kosaka, T. Saeki, T. Takano, T. Aruga, T. Yamashita, N. Masuda, Y. Koibuchi, A. Osaki, J. Watanabe, R. Suzuki, *Int J Nanomedicine* **2022**, *17*, 4567–4578.
[24] J. Nah, Y. Jeong, C. Cho, *J. Polym. Sci. B Polym. Phys.* **1998**, *36*, 415–423.
[25] Y.-I. Jeong, J.-B. Cheon, S.-H. Kim, J.-W. Nah, Y.-M. Lee, Y.-K. Sung, T. Akaike, C.-S. Cho, *J. Control. Release.***1998**, *51*, 169–178.
[26] D. Kakkar, S. Mazzaferro, J. Thevenot, C. Schatz, A. Bhatt, B. S. Dwarakanath, H. Singh, A. K. Mishra, S. Lecommandoux, *Macromolecular Bioscience* **2015**, *15*, 124–137.
[27] Y. Matsumura, H. Maeda, *Cancer Research* **1986**, *46*, 6387–6392.
[28] N. P. Truong, M. R. Whittaker, C. W. Mak, T. P. Davis, *Expert Opin. Drug Deliv.***2015**, *12*, 129–142.
[29] P. Lagarrigue, F. Moncalvo, F. Cellesi, *Pharmaceutics* **2023**, *15*, 32.
[30] J. Mougin, C. Bourgaux, P. Couvreur, *Adv. Drug Deliv. Rev.* **2021**, *172*, 127–147.
[31] J. Xue, Z. Guan, X. Zhu, J. Lin, C. Cai, X. Jin, Y. Li, Z. Ye, W. Zhang, X. Jiang, *Biomater. Sci.* **2018**, *6*, 3251–3261.
[32] K. J. Harrington, S. Mohammadtaghi, P. S. Uster, D. Glass, A. M. Peters, R. G. Vile, J. S. W. Stewart, *Clinical Cancer Research* **2001**, *7*, 243–254.
[33] N. Schleich, C. Po, D. Jacobs, B. Ucakar, B. Gallez, F. Danhier, V. Préat, *J. Control. Release.***2014**, *194*, 82–91.
[34] K.-C. Mei, J. Bai, S. Lorrio, J. T.-W. Wang, K. T. Al-Jamal, *Biomaterials* **2016**, *106*, 276–285.
[35] K. Itaka, T. Ishii, Y. Hasegawa, K. Kataoka, *Biomaterials* **2010**, *31*, 3707–3714.

[36] Y. Cao, Y. Gong, L. Liu, Y. Zhou, X. Fang, C. Zhang, Y. Li, J. Li, *J. Appl. Toxicol.* **2017**, *37*, 1359–1369.
[37] C. J. Richards, T. C. Q. Burgers, R. Vlijm, W. H. Roos, C. Åberg, *ACS Nano* **2023**, *17*, 16517–16529.
[38] R. Ferrari, M. Lupi, C. Colombo, M. Morbidelli, M. D'Incalci, D. Moscatelli, *Colloids Surf. B Biointerfaces* **2014**, *123*, 639–647.
[39] M. Liu, F. Wang, T. Zhu, Z. Jiang, *Colloid Interface Sci. Commun.* **2023**, *54*, 100712.
[40] W. Ke, N. Lu, A. A.-W. M. M. Japir, Q. Zhou, L. Xi, Y. Wang, D. Dutta, M. Zhou, Y. Pan, Z. Ge, *J. Control. Release.***2020**, *318*, 67–77.
[41] Q. Yu, M. G. Roberts, L. Houdaihed, Y. Liu, K. Ho, G. Walker, C. Allen, R. M. Reilly, I. Manners, M. A. Winnik, *Nanoscale* **2021**, *13*, 280–291.
[42] K. L. Lee, L. C. Hubbard, S. Hern, I. Yildiz, M. Gratzl, N. F. Steinmetz, *Biomater. Sci.* **2013**, *1*, 581–588.
[43] L. Zhang, Y. Wang, D. Yang, W. Huang, P. Hao, S. Feng, D. Appelhans, T. Zhang, X. Zan, *Mol. Pharmaceutics* **2019**, *16*, 2902–2911.
[44] R. M. Sutherland, *Science* **1988**, *240*, 177–184.
[45] Q. Yu, M. G. Roberts, L. Houdaihed, Y. Liu, K. Ho, G. Walker, C. Allen, R. M. Reilly, I. Manners, M. A. Winnik, *Nanoscale* **2021**, *13*, 280–291.
[46] A. S. Mikhail, S. Eetezadi, S. N. Ekdawi, J. Stewart, C. Allen, *Int. J. Pharm.***2014**, *464*, 168–177.
[47] S. Eetezadi, R. De Souza, M. Vythilingam, R. Lessa Cataldi, C. Allen, *Mol. Pharmaceutics* **2015**, *12*, 3973–3985.
[48] A. S. Postovalova, Y. A. Tishchenko, M. S. Istomina, T. E. Karpov, S. A. Shipilovskikh, D. Akhmetova, A. Rogova, N. V. Gavrilova, A. S. Timin, *Nanomedicine: Nanotechnology, Biology and Medicine* **2024**, *59*, 102753.
[49] Y. Zhang, G.-L. Zhang, X. Sun, K.-X. Cao, C. Ma, N. Nan, G.-W. Yang, M.-W. Yu, X.-M. Wang, *Oncology Letters* **2018**, *15*, 6233–6240.
[50] C. Grazon, P. Salas-Ambrosio, E. Ibarboure, A. Buol, E. Garanger, M. W. Grinstaff, S. Lecommandoux, C. Bonduelle, *Angew. Chem. Int. Ed.* **2020**, *59*, 622–626.

Chapter VI. Aqueous ROPISA for drug delivery: encapsulation strategies

Table of Contents

Chapter VI. Aqueous ROPISA for drug delivery: encapsulation strategies

VI.1. Introduction 276
VI.1.1. *In situ* encapsulation 276
VI.1.1.1. Physical encapsulation 276
VI.1.1.1.1. Small active ingredients 276
VI.1.1.1.2. More complex cargo 278
VI.1.1.2. Chemical encapsulation 280
VI.1.1.2.1. Chemical encapsulation in the core 280
VI.1.1.2.2. Chemical encapsulation at the surface 282
VI.1.2. *Post*-PISA encapsulation 283
VI.1.2.1. Physical encapsulation 283
VI.1.2.2. Chemical encapsulation 285
VI.1.2.2.1. Chemical encapsulation in the core 285
VI.1.2.2.2. Chemical encapsulation at the surface 285
VI.2. *In-situ* ROPISA encapsulation 287
VI.2.1. Ellipticine 287
VI.2.2. Mitoxantrone 290
VI.2.3. Doxorubicin 293
VI.3. Post-ROPISA encapsulation 298
VI.4. Conclusion 303
VI.5. Experimental section 304
VI.5.1. Materials 304
VI.5.2. Instrumentation and methods 304
VI.5.2.1. Nuclear Magnetic Resonance (NMR) 304
VI.5.2.2. Size Exclusion Chromatography (SEC) 304
VI.5.2.3. Transmission Electron Microscopy (TEM) 305
VI.5.2.4. Dynamic Light Scattering (DLS) 305
VI.5.2.5. Drug Loading Content (DLC) and Encapsulation Efficiency (EE) Determination 305
VI.5.3. Encapsulation procedures 306
VI.5.3.1. *In-situ* encapsulation of ellipticine (EPT) 306
VI.5.3.2. *In-situ* encapsulation of mitoxantrone (MTX) 306
VI.5.3.3. *In-situ* encapsulation of doxorubicin (DOX) 306
VI.5.3.4. *Post-PISA* encapsulation of doxorubicin (DOX) 307
VI.6. References 308

VI.1. Introduction

After demonstrating in **Chapter V** that worm-like nanoparticles obtained via aqueous ROPISA of γ-benzyl-*L*-glutamate *N*-carboxyanhydrides (BLG-NCA) show strong potential for tumor accumulation, the next step is to develop drug-loaded nanocarriers based on these structures. Given our investigation into nanoparticle formation mechanisms in **Chapter II**, it is conceivable to incorporate a drug into the hydrophobic core during the self-assembly process. Similar strategies have been successfully implemented in various PISA systems. This introduction will discuss different approaches, from simultaneous encapsulation during self-assembly (*in situ* encapsulation) to post-polymerization loading (*post*-PISA encapsulation), highlighting key examples of therapeutic cargo incorporation via the PISA process.

VI.1.1. *In situ* encapsulation

Using PISA-derived nanoparticles for drug delivery presents significant challenges, as drugs must either be incorporated during polymerization or introduced post-assembly. *In situ* encapsulation involves the simultaneous synthesis of the polymer, self-assembly into nanocarriers, and cargo entrapment. This process can occur via non-covalent interactions (physical encapsulation) or through covalent bonding (chemical encapsulation).

VI.1.1.1. Physical encapsulation

For physical encapsulation, the cargo is incorporated during the formation of the nanoparticles during the PISA, where the encapsulation efficiency is influenced by the affinity of the cargo with the hydrophobic core related on the solvophilicity (Scheme VI-1).

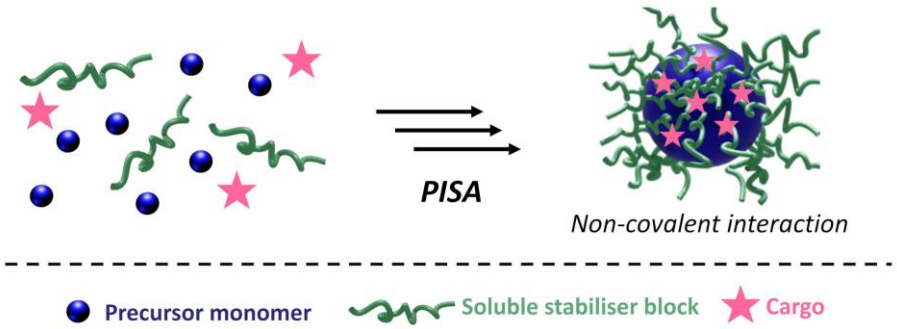

Scheme VI-1. *In situ* physical encapsulation of cargo during PISA through spontaneous incorporation into the self-assembling nanostructures.

VI.1.1.1.1. Small active ingredients

Davis and colleagues reported the first example of Nile Red (NR) encapsulation during RAFT-mediated PISA of styrene (S) using poly(oligoethylene glycol methacrylate) (POEGMA) as macroinitiator in methanol.[1] The dye was simply dissolved in the same solution as the POEGMA macro-initiator. However, since Nile Red is known to act as a radical scavenger, the polymerization feed ratio was adjusted by increasing the amount of initiator to mitigate its inhibitory effect. After purification by dialysis against methanol, transmission electron microscopy (TEM) analysis confirmed that the resulting POEGMA-*b*-PS

nanoparticles maintained the same morphology as their unloaded counterparts, although the vesicle structures appeared slightly less homogeneous (Figure VI-1).

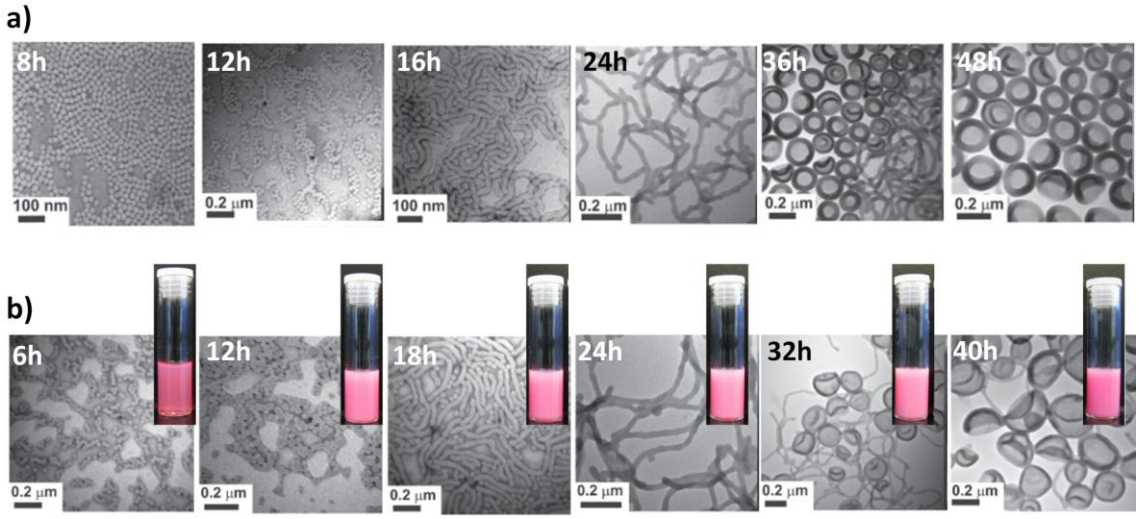

Figure VI-1. (a) Representative TEM images of empty POEGMA-*b*-PS nanoparticles at different polymerization times. (b) Representative TEM images of Nile Red-loaded POEGMA-*b*-PS nanoparticles at different polymerization times, after dialysis against methanol, along with corresponding images of the reactive media. Adapted from Davis *et al.*[1]

Malmström's group later investigated the encapsulation of Nile Red (NR) during aqueous RAFT-mediated emulsion PISA of methyl methacrylate (MMA), using poly(*N*-[3-(dimethylamino)propyl] methacrylamide) (PDMAPMA) as a macroinitiator.[2] To achieve this, NR was dissolved in MMA, allowing its confinement within monomer droplets during emulsion polymerization. Following nucleation and PISA, the dye was encapsulated within the hydrophobic core. The resulting nanoparticles exhibited similar colloidal properties to empty ones, suggesting that encapsulation had no adverse effects. However, drug loading content (DLC) and encapsulation efficiency (EE) were not evaluated. More notably, in the same study, the group reported the first encapsulation of the anticancer agent doxorubicin (DOX) using RAFT-mediated emulsion PISA.[2] DOX, initially in its charged hydrochloride form (DOX·HCl), was neutralized to increase its hydrophobicity before following the same encapsulation procedure as NR. After purification (dialysis for 2 hours), an encapsulation efficiency of 30% was achieved for a targeted DLC of 15 wt%. *In vitro* studies revealed that loaded nanoparticles exhibited higher toxicity than free DOX in RAW 264.7 cells, likely due to the cationic corona from PDMAPMA chains promoting enhanced cellular uptake. In contrast, a slight increase in toxicity was observed in MCF-7 breast cancer cells. In the same line, Couturaud and colleagues demonstrated that the encapsulation efficiency of DOX could be increased to 70% by neutralizing doxorubicin with a strong base.[3] This approach enhanced its hydrophobicity, improving its solubility in water-miscible HPMA monomers and facilitating higher drug loading.

Stenzel's group investigated the encapsulation of the antioxidant curcumin during RAFT-PISA of MMA using poly(2-(methacryloyloxy)ethylphosphorylcholine) (PMPC) as a macro-initiator. Curcumin modified nanoparticle morphology, shifting micelle-to-worm transitions to shorter PMMA block lengths

and favoring polymersome formation by expanding the hydrophobic domain (Figure VI-2). Despite satisfying encapsulation efficiency (20–30%) for drug loading content ranging from 0.17 wt% to 1.5 wt%, structural changes influenced cellular uptake: higher drug-loading enhanced uptake for micelles and worms but reduced it for polymersomes. Small-angle X-ray and neutron scattering (SAXS and SANS) analyses revealed that curcumin altered shell hydration and polymer arrangement, directly affecting nanoparticle-cell interactions. These findings emphasize how hydrophobic drug loading influences both self-assembly and biological behavior in PISA systems.[4]

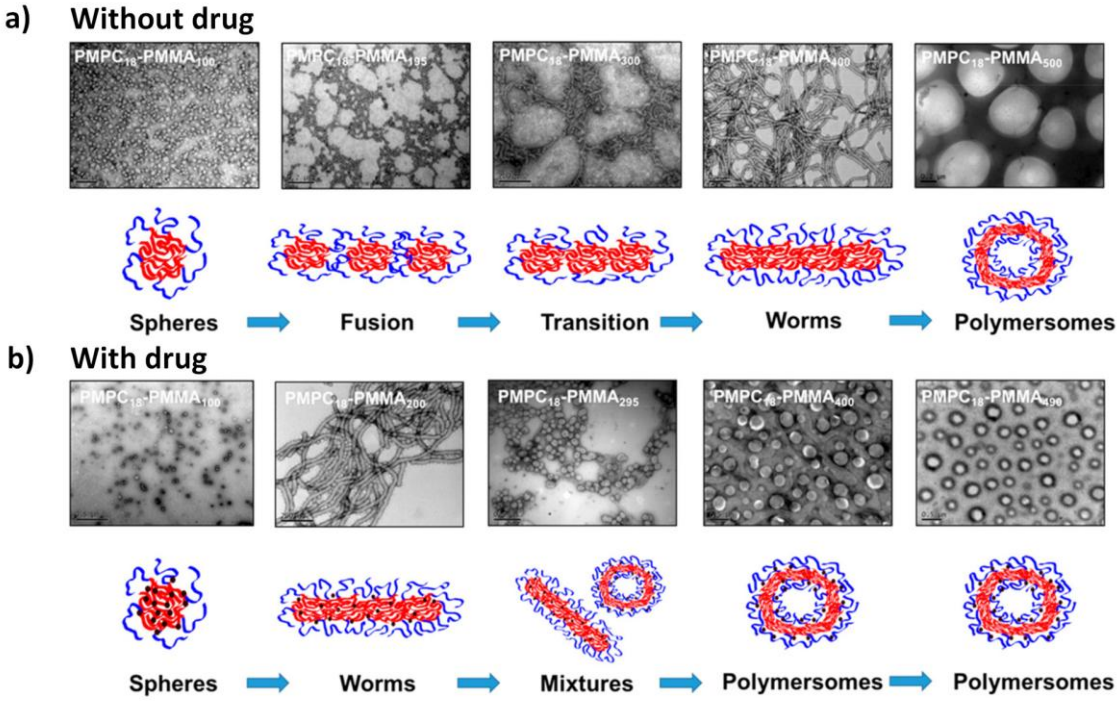

Figure VI-2. Representative TEM images showing the morphological evolution of self-assemblies during the PISA of MMA using PMPC over time: (a) without curcumin and (b) in the presence of curcumin. Adapted from Stenzel *et al.*[4]

A similar observation was reported by Ricarte and coworkers, who studied the *in situ* encapsulation of phenylacetic acid (PA) in poly(glycerol monomethacrylate)-*block*-poly(2-hydroxypropyl methacrylate) (PGMA-*b*-PHPMA) nanoparticles during PISA. Increasing PA loading induced a morphological transition from spherical micelles to cylindrical micelles and eventually to vesicles.[5] The study also emphasized the crucial role of the hydrophilic corona in determining encapsulation efficiency. Favorable interactions between the corona's repeating units and the drug molecules significantly enhanced encapsulation, even when using simple physical entrapment methods.

VI.1.1.1.2. More complex cargo

Loading more complex cargo, like nanoparticles, proteins and enzymes have also been investigated. The Armes group has explored the encapsulation of silica nanoparticles within PGMA-*b*-PHPMA diblock copolymer vesicles via aqueous RAFT-mediated PISA.[6] Silica nanoparticles, chosen both as a model cargo and for their potential biomedical applications,[7] were simply introduced into the

aqueous solution during vesicle formation. Purification was performed by centrifugation followed by redispersion in water, with TEM analysis confirming the successful retention of silica nanoparticles within the vesicle lumen (Figure VI-3a). Encapsulation efficiency reached up to 27% for a targeted drug loading content of 35 wt%. Additionally, controlled release was demonstrated through the thermoresponsive behavior of the PHPMA block, with cargo release triggered by cooling the vesicles to 0 °C, as demonstrated by SAXS and TEM (Figure VI-3b, c). Similarly, Zhang's group has demonstrated the encapsulation of silica nanoparticles in vesicles obtained by aqueous photo-PISA of HPMA using a PEG macro-CTA as macroinitiator.[8]

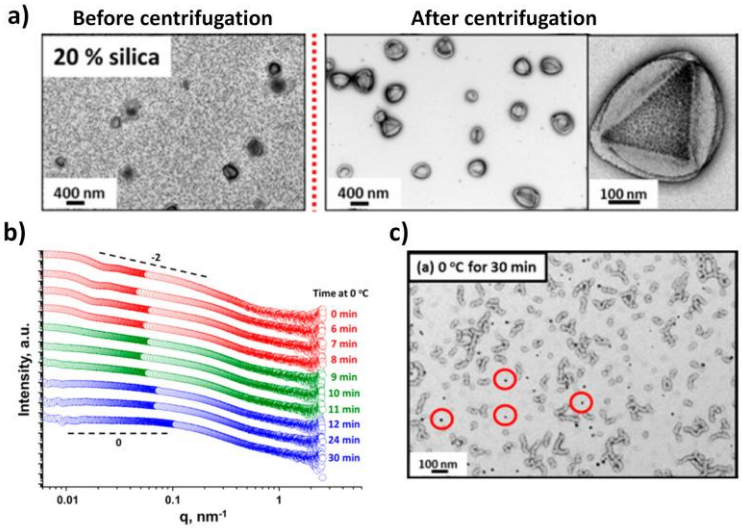

Figure VI-3. (a) Representative TEM images of vesicles in presence of 20% of silica nanoparticles before purification (left) and after purification by centrifugation/redispersion (right). (b) SAXS patterns during vesicles dissociation after being cooled at 0 °C for 30 min (red: vesicles, green: worm-like micelles, blue: spheres). (c) Representative TEM images of particles after having being cooled at 0 °C for 30 min (spheres and free silica nanoparticles). Adapted from Armes *et al.*[6]

Proteins and enzymes have also been investigated for physical *in situ* encapsulation. Armes and colleagues explored the encapsulation of bovine serum albumin (BSA) during RAFT-mediated PISA of HPMA at 37 °C to prevent protein denaturation.[6] After purification by centrifugation and redispersion, TEM analysis confirmed a pure vesicular morphology, indicating that neither the mild polymerization conditions nor the presence of BSA disrupted self-assembly. Although BSA is a monothiol-functional protein theoretically capable of participating in radical polymerization, no adverse effects were detected by SEC, TEM, or ^{1}H NMR. The encapsulation efficiency was estimated at 10.8%. Zhang's group also investigated BSA encapsulation during the photo-PISA of HPMA, following the same procedure used for silica nanoparticle encapsulation.[8] The successful encapsulation was confirmed using fluorescein-labeled BSA. However, the study did not report encapsulation efficiency values.

Building on this approach, more complex systems have been explored, including the encapsulation of green fluorescent protein (GFP), horseradish peroxidase (HRP), and glucose oxidase (GOx) within PEG-*b*-PHPMA vesicles via photo-PISA.[9] The presence of these proteins did not interfere with the polymerization process, and encapsulation efficiencies ranged from 11% for GFP to 54% for HRP and 41%

for GOx. Notably, the encapsulated enzymes retained their activity, with HRP maintaining 57 ± 13% and GOx 46 ± 1% relative to their free counterparts. Furthermore, permeability studies confirmed that substrates for both GOx and HRP could diffuse through the vesicle membrane, enabling the enzymes, compartmentalized within separate vesicle lumens, to participate in a cascade reaction. This system achieved 46 ± 3% of the activity observed for free enzymes, likely due to the restricted diffusion of substrates across the membrane.

Overall, the physical encapsulation of small active molecules, nanoparticles, proteins, and enzymes offers a straightforward approach to obtaining loaded nanocarriers, though encapsulation efficiency remains limited. Additionally, cargo incorporation can impact self-assembly, leading to changes in nanoparticle size or morphology. Furthermore, polymerization conditions may contribute to drug degradation, and some drugs can act as radical scavengers, potentially disrupting the polymerization process.

VI.1.1.2. Chemical encapsulation

To minimize premature leakage and overcome the limitations of physical *in situ* encapsulation mentioned above, covalent cargo loading is considered as an alternative, either within the hydrophobic core (Scheme VI-2a) or on the hydrophilic shell (Scheme VI-2b)

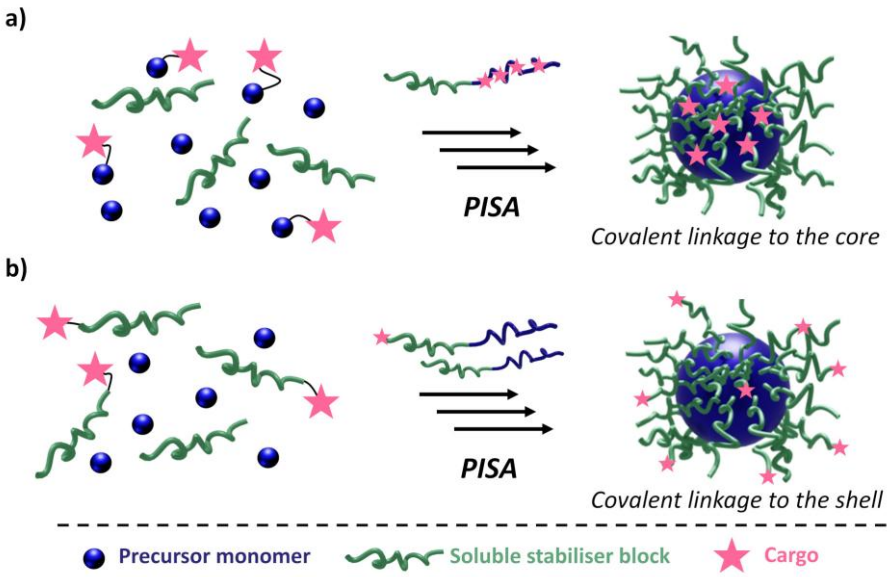

Scheme VI-2. *In situ* chemical encapsulation of cargo through (a) covalent bonding to the core *via* modified monomers or (b) covalent attachment to the shell using a modified macroinitiator.

VI.1.1.2.1. Chemical encapsulation in the core

For covalent loading in the hydrophobic core, drug-conjugated monomers are generally used, enabling precise control over the drug content in the final nanoparticles by adjusting the monomer feed ratio, ultimately leading to the formation of prodrug nanoparticles.

Few examples have been reported, including Pan's group, which developed redox-responsive prodrug nanoparticles via RAFT-mediated PISA.[10] These nanoparticles feature a cross-linked hydrophobic

core composed of benzyl methacrylate (BzMa) and *N,N*-cystaminebismethacrylamide (CBMA), a middle layer with camptothecin (CPT), linked to the polymer chains via reductive-sensitive linkage, and a PEG-based hydrophilic shell for stabilization. The CPT content can be precisely tuned, with final drug loading content up to 12.8 wt%, and drug release is triggered in reductive environments like high intracellular GSH levels.

Gianneschi's group used ROMPISA in water for the one-pot incorporation of a platinum-based drug into nanoparticles.[11] They synthesized spherical micelles by extending poly(oligo ethylene glycol) stabilizer blocks with a cisplatin analogue, achieving high platinum loadings (up to 27 wt%) at high solids content. A pH-responsive version was also designed to study charge and pH effects on cellular uptake. Drug release occurred via ligand exchange, where nucleophiles like chloride or water diffuse into the core. This approach enabled controlled platinum delivery for therapeutic applications.

As discussed in **Chapter I**, Nicolas *et al*. demonstrated that therapeutic cargo can remain active while covalently bound to the polymer backbone.[12] They synthesized paclitaxel (PTX) and gemcitabine (GEM) methacrylate monomers, polymerized via rROPISA with cyclic ketene acetal and lauryl methacrylate (LMA) using POEGMA as a macroinitiator. Drug loading was tunable via the monomer feed ratio, though excess drug disrupted self-assembly, with DLC up to 33 wt% for PTX and 10 wt% for GEM. The covalently bound drugs exhibited slower degradation, likely due to hydrophobic interactions and steric hindrance, and showed enhanced cytotoxicity against A549 cancer cells, with lower IC50 values than free drugs, indicating a controlled release mechanism.

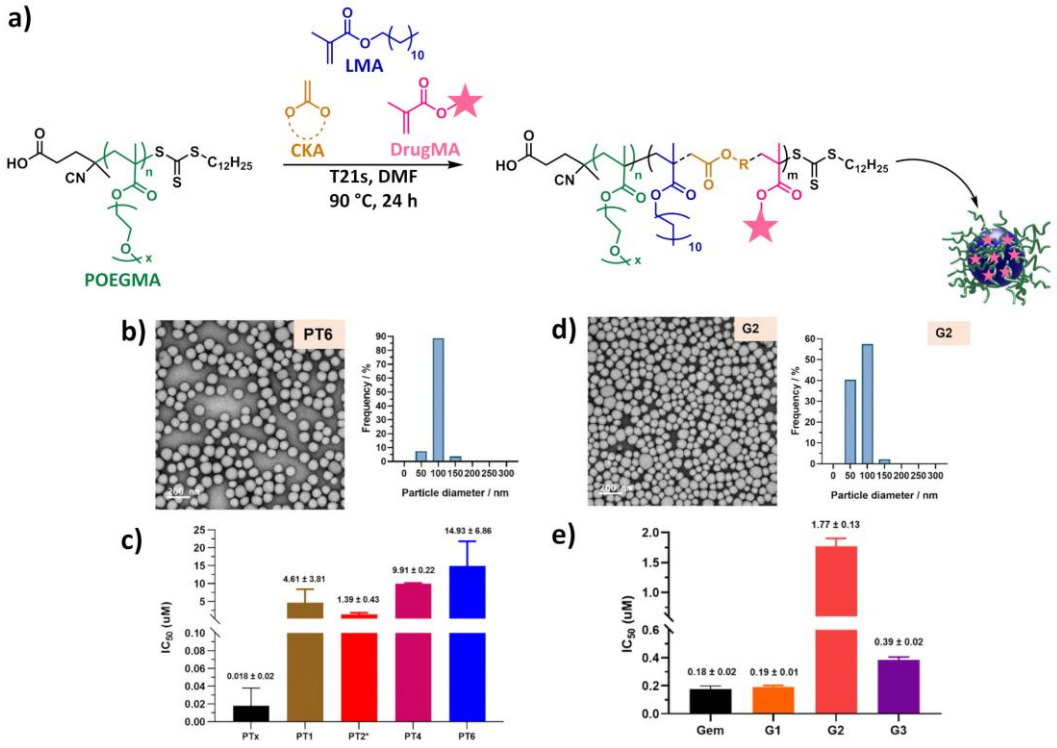

Figure VI-4. (a) RAFT-mediated PISA of LMA, CKA, and drug-bearing methacrylates (paclitaxel and gemcitabine) initiated by POEGMA macro-CTA. (b) Representative TEM image and corresponding histogram of particle diameters for paclitaxel-based nanoparticles. (c) IC50 values after 72 h incubation of A549 cancer cells with paclitaxel-containing nanoparticles. (d) Representative TEM image and corresponding histogram of particle diameters for gemcitabine-based nanoparticles. (e) IC50 values after 72 h incubation of A549 cancer cells with gemcitabine-containing nanoparticles. Adapted from Nicolas *et al.*[12]

Patterson and coworkers also demonstrated the chemical encapsulation of antimicrobial agents during the ROPI-CDSA of *L*-lactide, preserving their antimicrobial activity, this time through its use as catalyst, as discussed in **Chapter I.** [13] Unexpectedly, chlorhexinidine acted both as a catalyst and a co-initiator, leading to the formation of drug-conjugated polymer suspensions, with 100 % conjugation efficiency estimated.

Covalent drug loading within the hydrophobic core represents a promising strategy for achieving controlled and sustained release. However, it necessitates careful consideration of the release mechanisms, which may depend on internal or external stimuli. Although high drug loading contents, up to 30 wt%, can be attained, excessively high loading may disrupt the self-assembly process. Furthermore, while the drug-polymer conjugate may retain its activity, its therapeutic efficacy could be diminished due to slower release kinetics.

VI.1.1.2.2. Chemical encapsulation at the surface

Incorporating cargo into the hydrophilic shell can enhance stability and prolong circulation while maintaining biological accessibility. For instance, Stenzel's group incorporated the anticancer drug PENAO into the hydrophilic block of spherical micelles via copolymerization with 2-methacryloyloxyethyl phosphorylcholine (MPC).[14] In follow-up work,[15] *in vivo* studies showed rapid NP accumulation in the

liver, prompting surface modification with triphenylphosphonium (TPP) for mitochondrial targeting. However, *in vitro* results suggested limited mitochondrial accumulation due to TPP's insufficient surface exposure.

Other examples, such as peptide (KLA)[16] or functional nucleic acid (FNA)[17] incorporation, are detailed in **Chapter I**.

VI.1.2. *Post*-PISA encapsulation

Alternatively, *post*-polymerization encapsulation (*post*-PISA) is preferred when the cargo is sensitive to PISA conditions, limited monomer conversion, or hindered assembly. In physical encapsulation *post*-PISA, the drug is dissolved in the dispersion medium or *via* latex swelling with an organic solvent, offering milder reaction conditions. However, this method requires a strong affinity between the cargo and the nanoparticle core, which can be challenging or requires a specific polymer design to adapt to cargo specific properties (Scheme VI-3, left). In contrast, chemical *post*-PISA encapsulation involves covalent attachment of the cargo within the core or shell *via* coupling reactions with functional groups incorporated into the block copolymer (Scheme VI-3, middle and right).

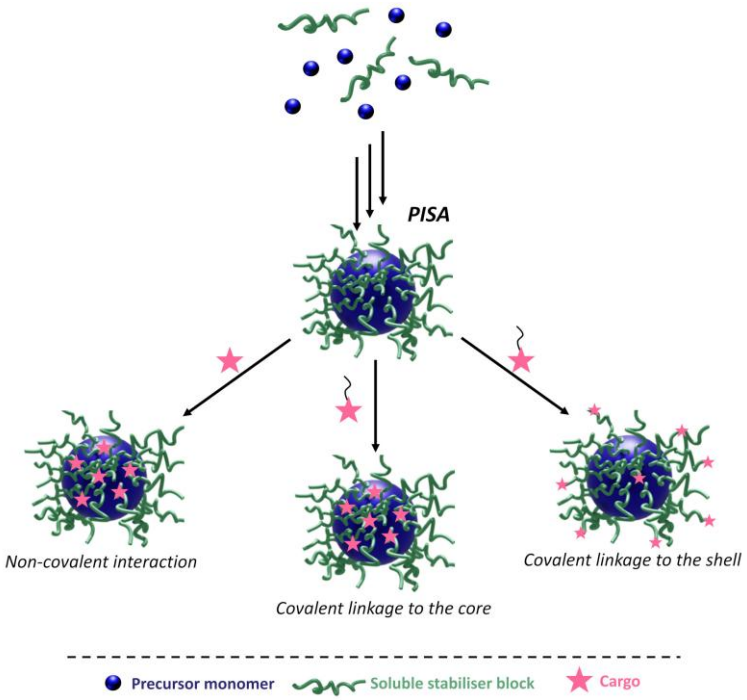

Scheme VI-3. *Post*-PISA loading through physical encapsulation (left) or chemical encapsulation, via covalent linkage in the hydrophobic core (middle) or to the shell (right).

VI.1.2.1. Physical encapsulation

Blasco's group investigated this method by studying the diffusion of Nile Red (NR) into poly(ethylene glycol)-*block*-poly(2,6-diacylaminopyridine)-*block*-poly(2-hydroxypropylmethacrylate)

(PEG-*b*-PDAP-*b*-PHPMA) nanoparticles, which were cross-linked through functionalization with thymine groups.[18] The cross-linked nanoparticles encapsulated 1.4 times more NR than non-cross-linked ones, and exhibited slower NR release, indicating enhanced stability.

Latex swelling with a suitable solvent is another viable loading method, as demonstrated by Chemtob and coworkers.[19] In this approach, Nile Red was dissolved in THF and introduced into an aqueous suspension of poly(hydroxyethyl acrylate)-*block*-poly(o-nitrobenzyl acrylate) (PHEA-*b*-PNBA) nanoparticles obtained by RAFT-PISA.

Crosslinking is highly recommended to maintain nanoparticle stability during swelling and loading, as further demonstrated by Sun *et al.*[20] Building on the aqueous ROPISA of NCA developed by our group, they synthesized cysteine-based nanogels via simultaneous ROPISA and disulfide cross-linking of cysteine *N*-carboxyanhydrides (Cys-NCA) in presence or not of γ-benzyl-*L*-glutamate-NCA (BLG-NCA), followed by indomethacin loading, achieving a drug loading capacity of 22.5 wt% and an encapsulation efficiency of 44.9%. The nanogels exhibited redox responsiveness, disassembling upon disulfide cleavage. *In vitro* studies showed limited drug release in PBS (10% in 50 hours), whereas in the presence of the reductive reagent DL-dithiothreitol (DTT), disulfide bond cleavage triggered a sustained and accelerated release (60% in 60 hours).

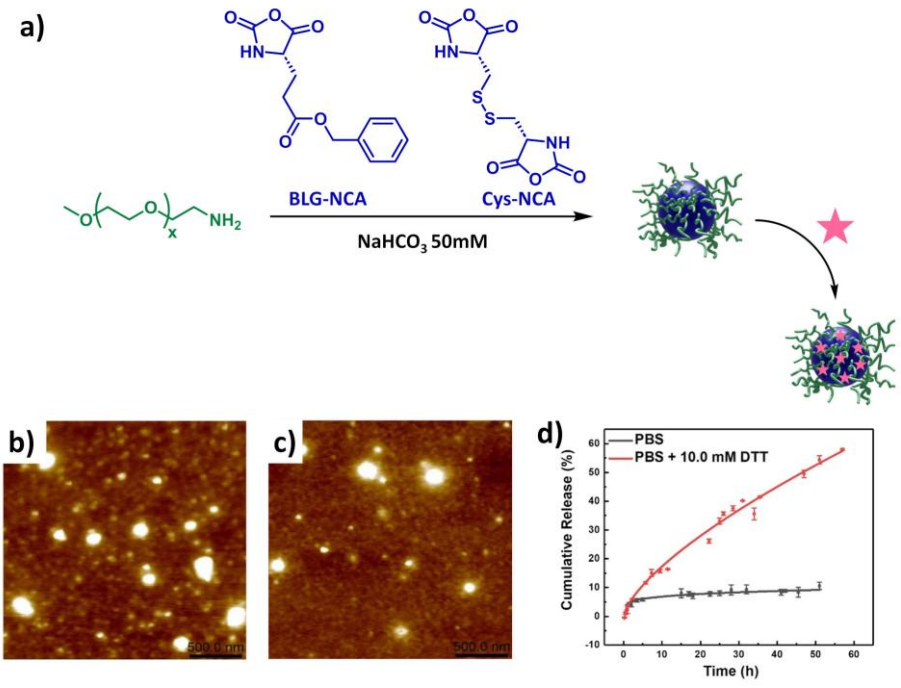

Figure VI-5. (a) Aqueous ROPISA of Cys-NCA (or Cys-NCA and BLG-NCA) initiated by PEG_{5k}-NH_2 in $NaHCO_3$ 50mM leading to core cross-linked nanogels, followed by indomethacin loading by post-PISA diffusion. (b) Representative AFM image of the PEG-*b*-PCys nanogel and (c) PEG-*b*-P(Cys-*co*-BLG) nanogel. (d) Indomethacin drug release profile of the core cross-linked nanogel PEG-*b*-PCys under reduction-sensitve (DTT) and reduction-insensitive conditions. Adapted from Sun *et al.*[20]

Alternatively, hydrophilic cargo can be introduced post-PISA into the aqueous lumen of vesicles using bioinspired methods, akin to cell transfection techniques. Armes *et al*. successfully applied this

approach by incorporating EGFP plasmid DNA into pH-responsive framboidal polymersomes via electroporation.[21]

VI.1.2.2. Chemical encapsulation

Chemical *post*-PISA encapsulation involves covalent attachment of the drug within the core or shell *via* coupling reactions with functional groups incorporated into the block copolymer via (co)monomers or the polymer end groups (Scheme VI-3).

VI.1.2.2.1. Chemical encapsulation in the core

For example, David and coworkers reported the nonaqueous post-PISA chemical conjugation of DOX in the hydrophobic core of poly[oligo(ethylene glycol) methacrylate]-*block*-[poly(styrene)-*co*-poly(vinyl benzaldehyde)] (POEGMA-*b*-P(S-*co*-VBA)) nanoparticles.[3] They used aldehyde groups to attach DOX *via* a pH-sensitive linkage, achieving a drug loading content of 5 wt% and an encapsulation efficiency of 67%. Building on this approach, Pan and colleagues applied a similar strategy to graft DOX in the hydrophobic core of poly((*N,N'*-dimethylamino)ethyl methacrylate)-*block*-poly(p-(methacryloxyethoxy)benzaldehyde) (PDMAEMA-*b*-PMAEBA) nanoparticles.[22] By condensing the primary amine of DOX with aldehyde groups from MAEBA units, they formed acid-labile imine linkages, achieving a drug loading capacity of 11.5–16.2 wt% with reaction efficiencies between 19.3 and 23.7%. Notably, the conjugation did not alter nanoparticle morphology, and DOX release was effectively triggered in acidic environments.

VI.1.2.2.2. Chemical encapsulation at the surface

Couturaud's group explored DOX conjugation *via* a two-step carbodiimide activation.[3] They first synthesized poly((ethylene glycol) methacrylate)-*co*-poly(pentafluorophenyl methacrylate)-*block*-poly(hydroxypropyl methacrylate) (P((PEGMA-*co*-PFBMA)-*b*-PHPMA)) nanoparticles through RAFT-mediated PISA. *N*-acetylcysteine (NAC) was then introduced, leveraging its thiol group to react with the polymer's pentafluorophenyl (PFP) rings via the para-Fluoro-Thiol Reaction (PFTR). DOX was subsequently grafted onto the nanoparticle surface through a carbodiimide reaction without altering the assembly (Figure VI-6). Post-PISA polymer-DOX conjugates exhibited dose-dependent cytotoxicity with IC50 values comparable to free DOX, while confocal microscopy confirmed enhanced cellular uptake of the conjugates.

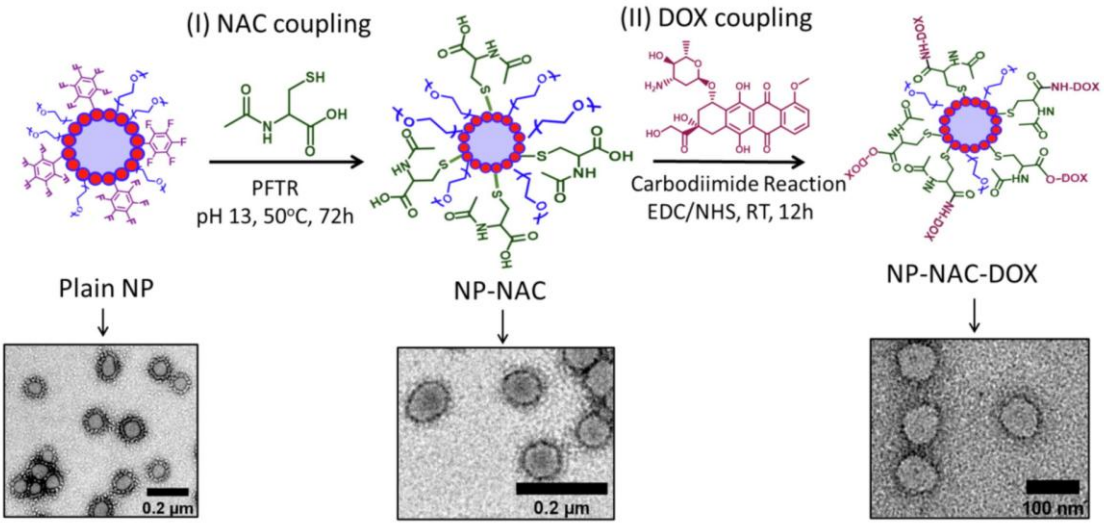

Figure VI-6. Particle surface functionalization with (i) NAC and then (ii) DOX, and corresponding representative TEM images of plain nanoparticles, NAC-functionalized nanoparticles and DOX-NAC-functionalized nanoparticles. Adapted from Couturaud *et al.*[3]

Other strategies for loading and retaining cargo *via* covalent linkages in the core or shell have been developed using various chemical coupling reactions, involving for example hydroxy groups[23] and thiols,[24] in addition of the aldehyde and para-fluorine groups mentioned above. Alternatively, cargo immobilization on the PISA-NP surface can be achieved through complexation, such as Ni^{2+}-NTA/His interactions.[25]

Overall, *post*-PISA chemical encapsulation is a valuable strategy for drug loading without disrupting the PISA process. However, it requires appropriate functional groups, additional synthetic steps, and cleavable linkages to preserve drug activity, although the prodrug approach can be effective. In contrast, physical encapsulation via diffusion into the hydrophobic core faces physical limitations and has been less explored.

Despite the promising potential of PISA for the development of drug delivery systems, several limitations persist. Notably, encapsulation efficiencies often remain moderate (typically below 50%), and achieving optimal drug loading and release profiles continues to be a major challenge. Furthermore, most PISA-based strategies rely on controlled radical polymerization (CRP), which typically produces non-degradable polymer backbones. This lack of biodegradability raises concerns for biomedical applications, where the long-term accumulation of such materials in the body could pose toxicity risks. In contrast, aqueous ROPISA offers a greener and more sustainable alternative for the fabrication of nanocarriers. This approach enables the synthesis of polypeptide-based nanoparticles that are both biocompatible and biodegradable, while also allowing access to anisotropic morphologies, features known to improve tumor accumulation, cellular uptake, and circulation time, as detailed in **Chapter I**. Building on the comprehensive investigations carried out throughout this PhD, **Chapter V** demonstrated that worm-like nanoparticles obtained *via* aqueous ROPISA of BLG-NCA exhibit high cellular internalization, prolonged

blood circulation, and significant tumor accumulation in two tumor models, thereby confirming their strong potential as drug delivery nanocarriers.

Based on these findings, the present chapter explores the use of these anisotropic nanoparticles for the one-pot encapsulation of anticancer drugs. Three model drugs, ellipticine, mitoxantrone, and doxorubicin, were selected due to their varying hydrophobicity and distinct UV-visible absorbance profiles, which facilitate their characterization and quantification. We focused on physical encapsulation strategies, carried out either during nanoparticle formation (*in situ* ROPISA) or after polymerization (*post*-ROPISA), as these approaches do not require additional synthetic steps such as covalent drug conjugation (Scheme VI-4). Each encapsulation protocol was tailored to the specific chemical properties and functional groups of the drugs.

BLG-NCA was chosen as the monomer for this study due to its well-documented polymerization and self-assembly behavior under aqueous ROPISA conditions, as described in **Chapters II** and **V**. The process parameters were carefully optimized to ensure that the anisotropic morphology of the nanoparticles was preserved while achieving the highest possible drug loading efficiency.

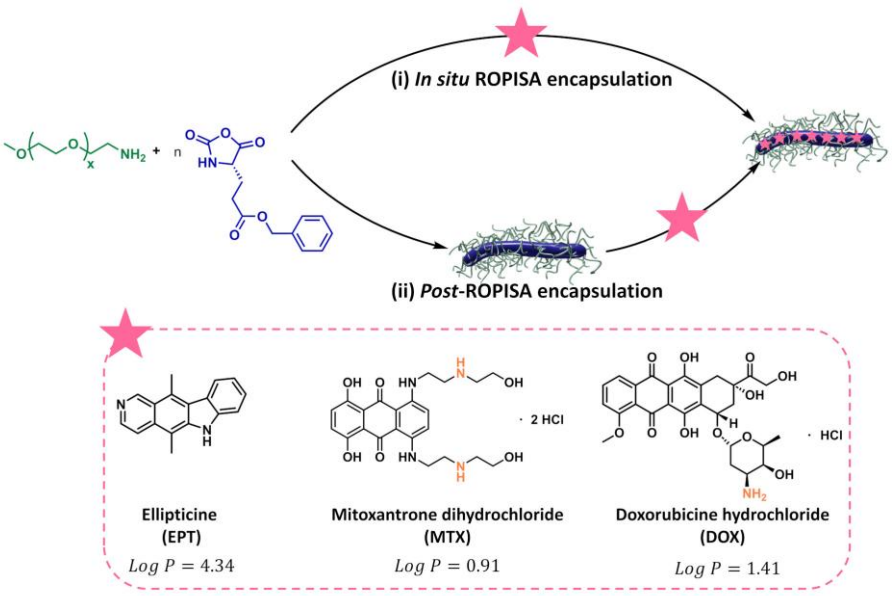

Scheme VI-4. General strategy for encapsulation of anticancer drugs in polypeptide-based nanoparticles through aqueous ROPISA of BLG-NCA.

VI.2. *In-situ* ROPISA encapsulation

VI.2.1. Ellipticine

Ellipticine (EPT) is a potent anticancer agent, naturally produced alkaloid isolated from the leaves of *Ochrosia elliptica*.[26] EPT is known for its high efficacy against various types of cancer but has limited clinical use due to severe side effects at high doses and poor water solubility.[27] To address these limitations, its encapsulation in nanocarriers has been explored as a promising drug delivery strategy.[27–29] We thus investigated the *in situ* encapsulation of EPT during the aqueous ROPISA of BLG-NCA as already

described in previous chapters, using PEG_{5k}-NH_2 as macroinitiator, targeting DP of 30, in a $NaHCO_3$ 50mM solution at a solid content of 7 wt% (% of solution that is not solvent *e.g.*, polymer/monomer and initiator, excluding the drug).

Given the drug's poor water solubility, DMSO, a Class 3 solvent recognized by the International Council for Harmonization of Technical Requirements for Pharmaceuticals for Human Use (ICH) for its low toxicity and absence of health-based exposure limits, was selected as an organic co-solvent.[30] However, even in DMSO, the drug's solubility remains relatively low (≈ 10 $mg.mL^{-1}$). To minimize potential solvent effects on self-assembly, we initially targeted a DMSO volume fraction of 10%. Considering the solubility limit in DMSO, the solid content, and the solvent fraction, the maximum achievable drug loading content was 1.3 wt%. To achieve encapsulation, an EPT solution in DMSO was prepared and added to the monomer simultaneously with the aqueous PEG solution. After overnight stirring, the resulting suspension was purified by multiple centrifugation steps to remove insoluble EPT aggregates, followed by ultrafiltration to eliminate any free soluble drug.

The synthesized copolymer was characterized by ^{1}H NMR and SEC. The obtained degree of polymerization (DP = 20) was lower than the target value, indicating a slight interference of EPT in the polymerization process (Table VI-1, Figure VI-7a). SEC analysis revealed an average molar mass of 10.5 $kg.mol^{-1}$ (PS calibration) with low dispersity ($Đ$ = 1.06) and a higher retention time compared to analogous PEG-*b*-PBLG synthesized without ellipticine, further supporting the influence of EPT on the polymerization (Figure VI-7b).

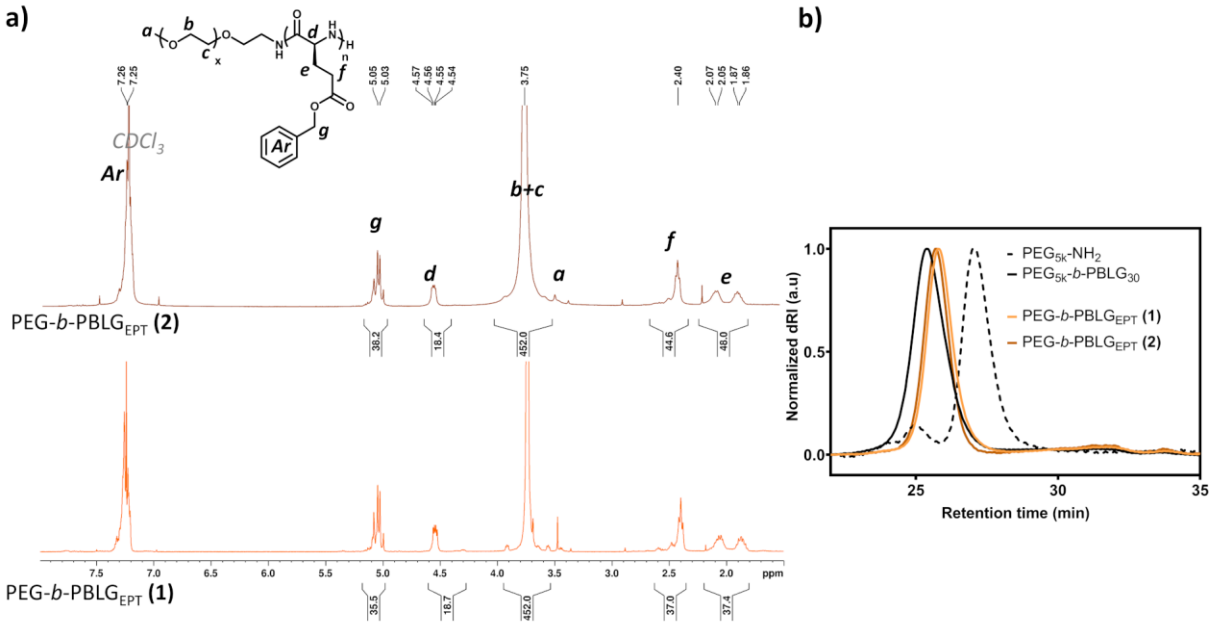

Figure VI-7. (a) ^{1}H NMR spectra of PEG-*b*-$PBLG_{EPT}$ **(1)** and **(2)** in $CDCl_3$ + 15% TFA with targeted DP of 19. The backbone protons from the PEG (b+c) were used as a reference to determine the DP of the PBLG block, with the average integration from the signals of BLG protons. (b) SEC chromatograms of PEG-*b*-$PBLG_{EPT}$ **(1)** and **(2)** upon in situ ROPISA encapsulation (DMF + 1% LiBr, dRI detection).

Nanoparticle characterization by DLS and TEM confirmed the formation of homogeneous nanoparticles with a sphere-equivalent Z-average diameter of 71 nm and a low polydispersity index (0.11) (Figure VI-8a). TEM further revealed the presence of worm-like nanoparticles (Figure VI-8b). These findings indicate that the presence of the drug and the solvent did not interfere with either the polymerization or the self-assembly processes.

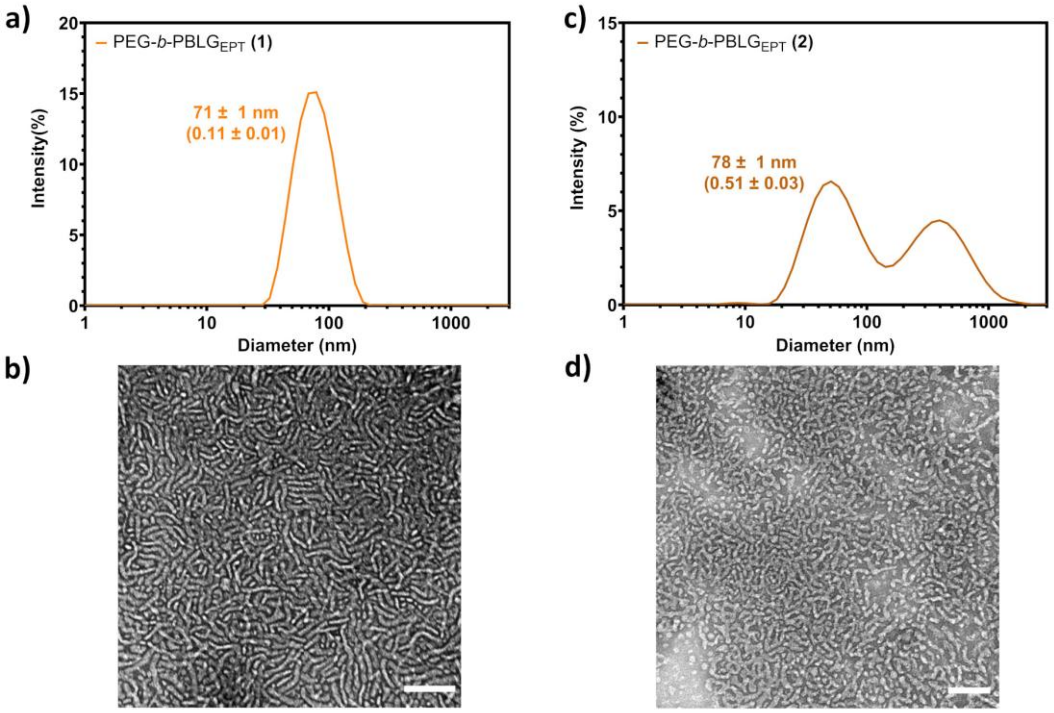

Figure VI-8. DLS profiles of purified (a) PEG-*b*-PBLG$_{EPT}$ **(1)** and (c) PEG-*b*-PBLG$_{EPT}$ **(2)** nanoparticle suspensions, with corresponding representative TEM image of purified (b) PEG-*b*-PBLG$_{EPT}$ **(1)** and (d) PEG-*b*-PBLG$_{EPT}$ **(2)** nanoparticle suspensions. Scale-bar: 200 nm.

The drug loading content and encapsulation efficiency were subsequently determined by UV-Vis spectroscopy, based on the characteristic absorbance peak of EPT at 294 nm. The results indicated a drug loading content of 0.3 wt% and an encapsulation efficiency of 29% (Table VI-1, Figure VI-9).

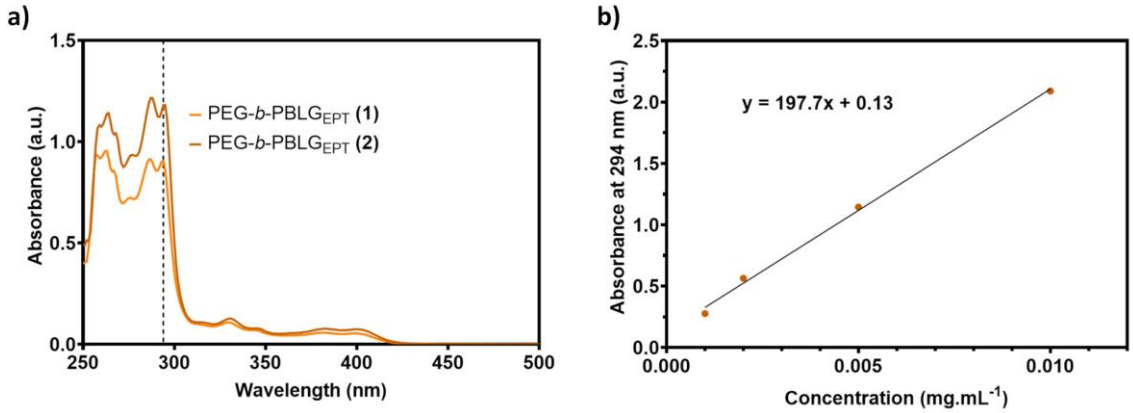

Figure VI-9. (a) UV-Vis spectra of PEG-*b*-PBLG$_{EPT}$ **(1)** and **(2)** upon *in situ* ROPISA encapsulation, purification, lyophilization and solubilization in DMSO. (b) Associated calibration curve of EPT in DMSO for EPT concentration determination.

These initial findings are promising, given the very low solubility of EPT and the inherent polymerization conditions that constrain the feeding ratio. To further enhance the drug loading content, an increased amount of EPT was introduced by raising the DMSO volume fraction to 20%. However, this modification adversely affected the self-assembly process, resulting in heterogeneous nanoparticles (Figure VI-8c,d), while yielding only a marginal improvement in drug loading (DLC = 0.5 wt%, EE = 21 %, Table VI-1, Figure VI-9).

Table VI-1. Characteristics of EPT-loaded PEG-*b*-PBLG nanoparticles after *in situ* PISA encapsulation.

N°	DP^{th}	DMSO [v/v %]	DLC^{th} [a] [wt%]	DP^{RMN} [b]	M_n [c] [kg.mol^{-1}]	$Đ$ [c]	DLC [d] [wt%]	EE [d] [%]	D_Z (σ) [e] [nm]
1	30	10	1.3	18	10.5	1.06	0.3	29	71 ± 1 (0.11 ± 0.01)
2		20	2.5	21	11.2	1.04	0.5	21	78 ± 1 (0.51 ± 0.03)

[a] Theoretical drug loading content (DLC^{th}) targeted with an initial feed weight ratio wt % of EPT to total mass of dispersed materials and EPT. [b] Average degree of polymerization (DP) determined by ^{1}H NMR. [c] Number average molar-mass (M_n) and molar-mass dispersity ($Đ$) determined by SEC in DMF +1% LiBr using PS calibration. [d] Experimental drug loading content (DLC) measured by UV-vis spectrophotometry and corresponding efficiency of encapsulation (EE). [e] Hydrodynamic Z-average diameter (D_Z) and polydispersity (σ) determined by DLS at 90°.

Overall, the encapsulation efficiency of ellipticine was moderate, demonstrating the feasibility of *in situ* drug loading but also highlighting the challenges associated with optimizing this process. These difficulties arise primarily from the poor solubility of the active ingredient and the fixed solid content required for polymerization, which necessitates higher drug concentrations. The use of DMSO also requires careful consideration. *In situ* encapsulation without organic solvents could be explored through alternative approaches such as ultrasonication. This technique could facilitate the homogeneous dispersion of poorly soluble drugs while accelerating self-assembly kinetics.[31] Moreover, it may enable the encapsulation of crystalline drug forms, as previously demonstrated for doxorubicin in vesicle cores.[32] Additionally, selecting a monomer with stronger affinity for the drug could provide an alternative strategy to improve encapsulation efficiency.

VI.2.2. Mitoxantrone

We then investigated the *in situ* encapsulation of a less hydrophobic compound (log P_{oct} = 0.91), mitoxantrone (MTX), an anthracenedione-based anticancer agent structurally related to doxorubicin but with reduced cardiotoxicity. MTX is clinically used in the treatment of breast and prostate cancers, as well as lymphomas and leukemias.[33] The ROPISA procedure previously established for ellipticine encapsulation was adapted for MTX, omitting the use of an organic co-solvent due to its sufficient aqueous solubility. A theoretical drug loading content (DLC) of 1 wt% was targeted at a solid content of 7 wt%. MTX was pre-dissolved in a 50 mM $NaHCO_3$ solution and subsequently mixed with the PEG-$NaHCO_3$ solution before being introduced to the monomer under vigorous stirring. Following overnight stirring, the

resulting blue colloidal suspension was purified via sequential centrifugation and ultrafiltration against ultra-pure water to remove unencapsulated drug and potential aggregates.

The resulting copolymer was first analyzed by ^{1}H NMR a revealing a degree of polymerization of 30, in good agreement with the targeted one (Figure VI-10a). SEC exhibited a monomodal distribution, with a calculated molar mass of 10.8 kg.mol^{-1} (PS calibration) and a narrow dispersity ($Đ$ = 1.05) (Figure VI-10b).

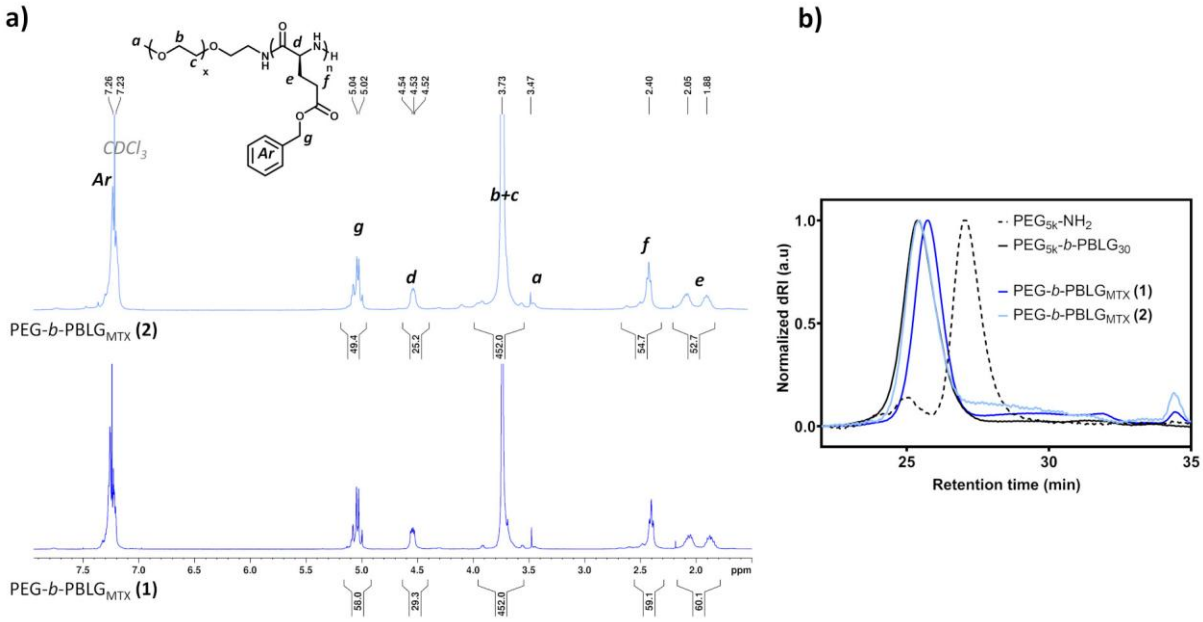

Figure VI-10. (a) ^{1}H NMR spectra of PEG-*b*-PBLG$_{MTX}$ **(1)** and **(2)** in $CDCl_3$ + 15% TFA with targeted DP of 30. The backbone protons from the PEG (b+c) were used as a reference to determine the DP of the PBLG block, with the average integration from the signals of BLG protons. (b) SEC chromatograms of PEG-*b*-PBLG$_{MTX}$ **(1)** and **(2)** upon *in situ* ROPISA encapsulation (DMF + 1% LiBr, dRI detection).

DLS measurements showed a sphere-equivalent Z-average diameter of 141 ± 1 nm with a polydispersity index of 0.28 (Figure VI-11a). TEM analysis confirmed the formation of worm-like nanoparticles, indicating that MTX encapsulation did not disrupt the self-assembly process (Figure VI-11b).

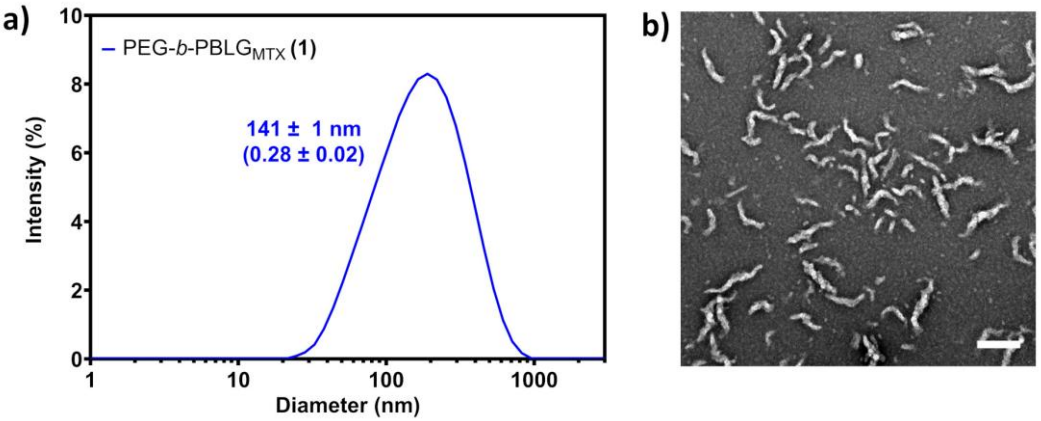

Figure VI-11. (a) DLS profiles of purified PEG-*b*-PBLG$_{MTX}$ **(1)** nanoparticle suspension. (b) Representative TEM image of purified PEG-*b*-PBLG$_{MTX}$ **(1)** nanoparticles suspension. Scale-bar: 200 nm.

Drug loading content and encapsulation efficiency were determined by UV-Vis spectroscopy, using the strong absorbance of MTX at 682 nm. A DLC of 0.8 wt% was achieved, corresponding to a high EE of 79% (Table VI-2,Figure VI-12).

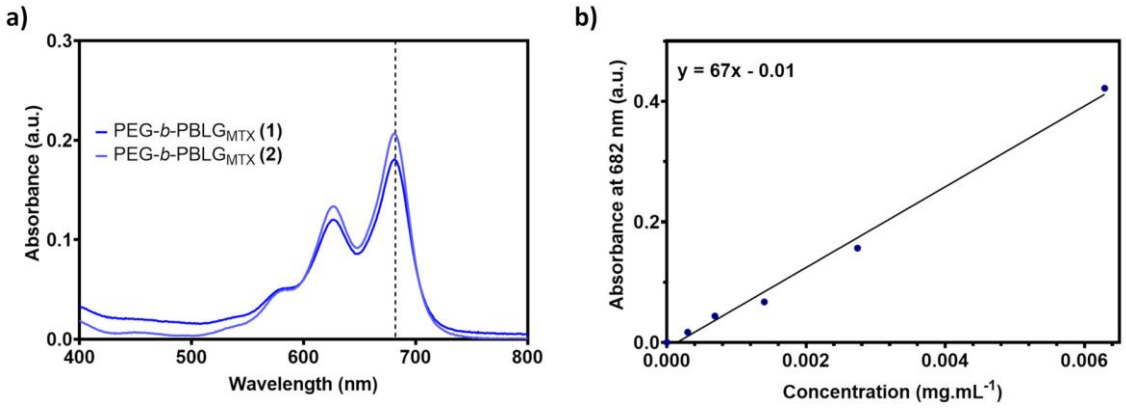

Figure VI-12. (a) UV-Vis spectra of PEG-*b*-PBLG$_{MTX}$ **(1)** and **(2)** upon *in situ* ROPISA encapsulation, purification, lyophilization and solubilization in DMSO. (b) Associated calibration curve of MTX in DMSO for MTX concentration determination.

Table VI-2. Characteristics of MTX-loaded PEG-*b*-PBLG nanoparticles after *in situ* PISA encapsulation.

N°	DPth	DLCth [a] [wt%]	DP^{RMN} [b]	M_n [c] [kg.mol^{-1}]	$Đ$ [c]	DLC [d] [wt%]	EE [d] [%]	D_Z (σ) [e] [nm]
1	30	1	29	10.8	1.05	0.8	79	141 ± 1 (0.28 ± 0.02)
2		10	25	11.8	1.05	2.2	22	207 ± 4 (0.26 ± 0.01)

[a] Theoretical drug loading content (DLCth) targeted with an initial feed weight ratio wt% of MTX to total mass of dispersed materials and MTX. [b] Average degree of polymerization (DP) determined by ^{1}H NMR. [c] Number average molar-mass (M_n) and molar-mass dispersity ($Đ$) determined by SEC in DMF +1% LiBr using PS calibration. [d] Experimental drug loading content (DLC) measured by UV-vis spectrophotometry and corresponding efficiency of encapsulation (EE). [e] Hydrodynamic Z-average diameter (D_Z) and polydispersity (σ) determined by DLS at 90°.

Encouraged by these results, we attempted to increase the DLC by raising the feeding ratio to 10 wt%. However, during ROPISA, a significant amount of aggregates was observed, and SEC analysis revealed an additional population at higher retention times, potentially corresponding to BLG oligomers (Figure VI-10b), even though ^{1}H NMR analysis indicated a DP of 32 (Figure VI-10a). Given that MTX contains secondary amino groups capable of initiating BLG-NCA polymerization (Figure VI-13a), a control experiment was conducted by mixing MTX with BLG-NCA in 50 mM $NaHCO_3$. The resulting mixtures were analyzed by SEC and compared to MTX alone to identify potential initiation effects (Figure VI-13b).

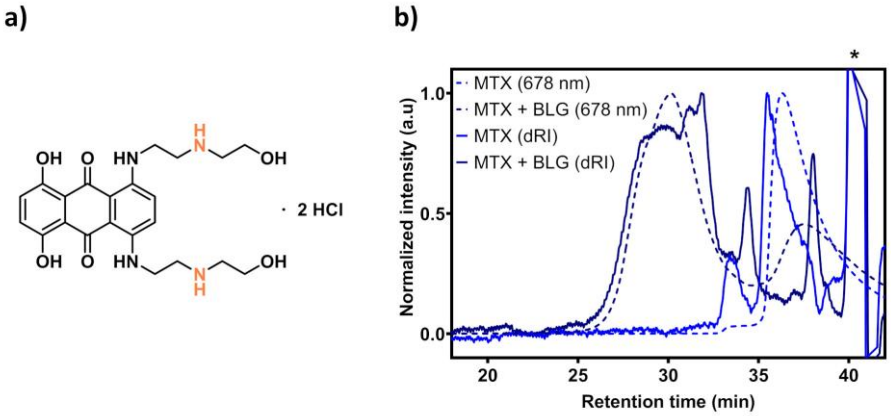

Figure VI-13. (a) MTX chemical structure. (b) SEC chromatograms of MTX and MTX + BLG from the control experiment (full line: dRI detection, dashed line: UV-Vis detection at λ = 678 nm).

MTX alone eluted at approximately 35 minutes, as detected by both dRI and UV-Vis at 678 nm. However, the product obtained from the control experiment eluted earlier, around 30 minutes, suggesting the presence of BLG oligomers covalently linked to MTX, as confirmed by UV-Vis detection. This indicates that side reactions involving MTX-initiated BLG oligomerization may have occurred concomitantly with the ROPISA process, explaining the presence of aggregates observed in the *in situ* encapsulation experiments. Even after the purification, oligomers are still present as indicated by the SEC. The biological activity of these conjugates remains uncertain and requires further investigation. However, previous studies have demonstrated co-initiation events during the encapsulation of antimicrobial active ingredients in ROPI-CDSA process, where antibacterial activity was retained, despite increased MIC values due to drug conjugation.[13] Such prodrug strategies have already demonstrated potential for drug delivery applications[34,35] and could be further explored in PISA encapsulation, as evidenced in the introduction this section with for instance the rROPISA using gemcitabine and paclitaxel-based monomers.[12]

VI.2.3. Doxorubicin

Doxorubicin (DOX) is an anthracycline antibiotic derived from *Streptomyces peucetius*, widely used in cancer therapy for over five decades to treat lymphomas, solid tumors, and leukemias.[36] Despite its broad clinical application, DOX is associated with significant cardiotoxicity and adverse effects on multiple organs, prompting extensive research into drug delivery systems to mitigate these toxicities.[37] One of the most notable advances in this field is *Doxil*®, the first FDA-approved liposomal formulation of DOX, designed to enhance drug bioavailability and reduce systemic toxicity.[37] In its hydrophilic hydrochloride form (DOX·HCl), DOX contains a primary amine group that possibly participate in polymerization by initiating BLG-NCA polymerization, leading to the formation of oligomers. To investigate this potential side reaction, a control experiment was conducted by mixing DOX with BLG-NCA in a $NaHCO_3$ (50 mM) solution overnight, followed by freeze-drying and SEC analysis in DMF (Figure VI-14).

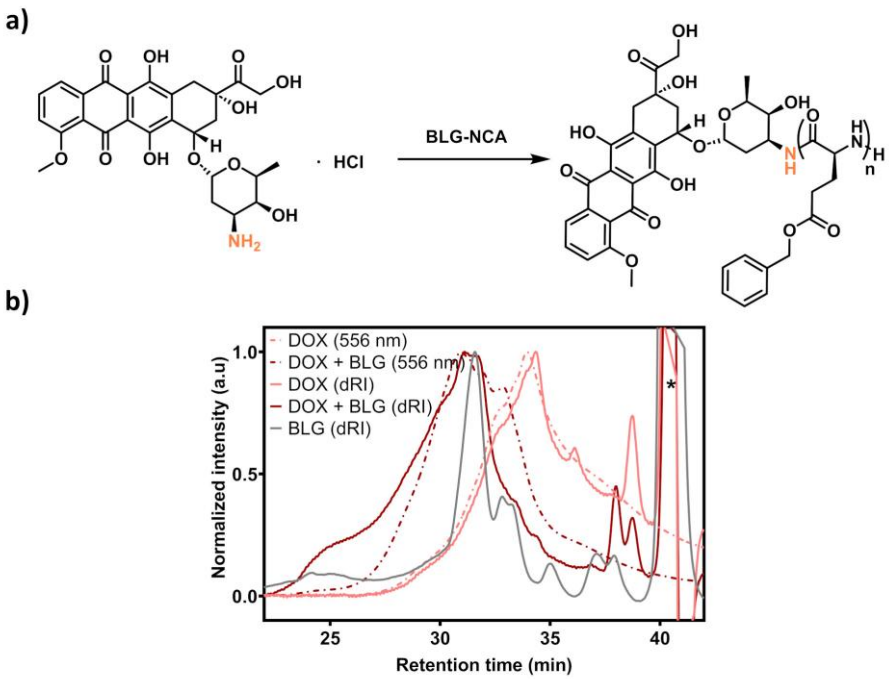

Figure VI-14. (a) Schematic representation of oligomerization of BLG-NCA initiated by DOX. (b) Resulting SEC chromatograms of DOX, water-initiated oligomers of BLG and DOX + BLG from the control experiment (full line: dRI detection, dashed line: UV-Vis detection at λ = 556 nm).

SEC comparisons with free DOX and BLG oligomers obtained from water-initiation revealed that the DOX-BLG mixture eluted at higher retention times than free DOX alone, aligning with BLG oligomers. UV-Vis detection at 556 nm further confirmed that these oligomers contained DOX, supporting the hypothesis that DOX's primary amine can initiate BLG-NCA oligomerization.

Given that the kinetics of polymerization and self-assembly may outcompete these side reactions, we explored the *in situ* encapsulation of DOX during the formation of PEG-*b*-PBLG nanoparticles, targeting an initial DLC^{th} of 10 wt% with a DP of 19, both with (PEG-*b*-$PBLG_{DOX}$ **(2)**) and without a co-solvent (PEG-*b*-$PBLG_{DOX}$ **(1)**). The resulting red colloidal suspension contained significant aggregates, which were removed via centrifugation and ultrafiltration. After analysis by ^{1}H NMR, the calculated DP was 28, higher than the targeted value (Figure VI-15). However, due to overlapping doxorubicin peaks, this calculation may not be accurate.

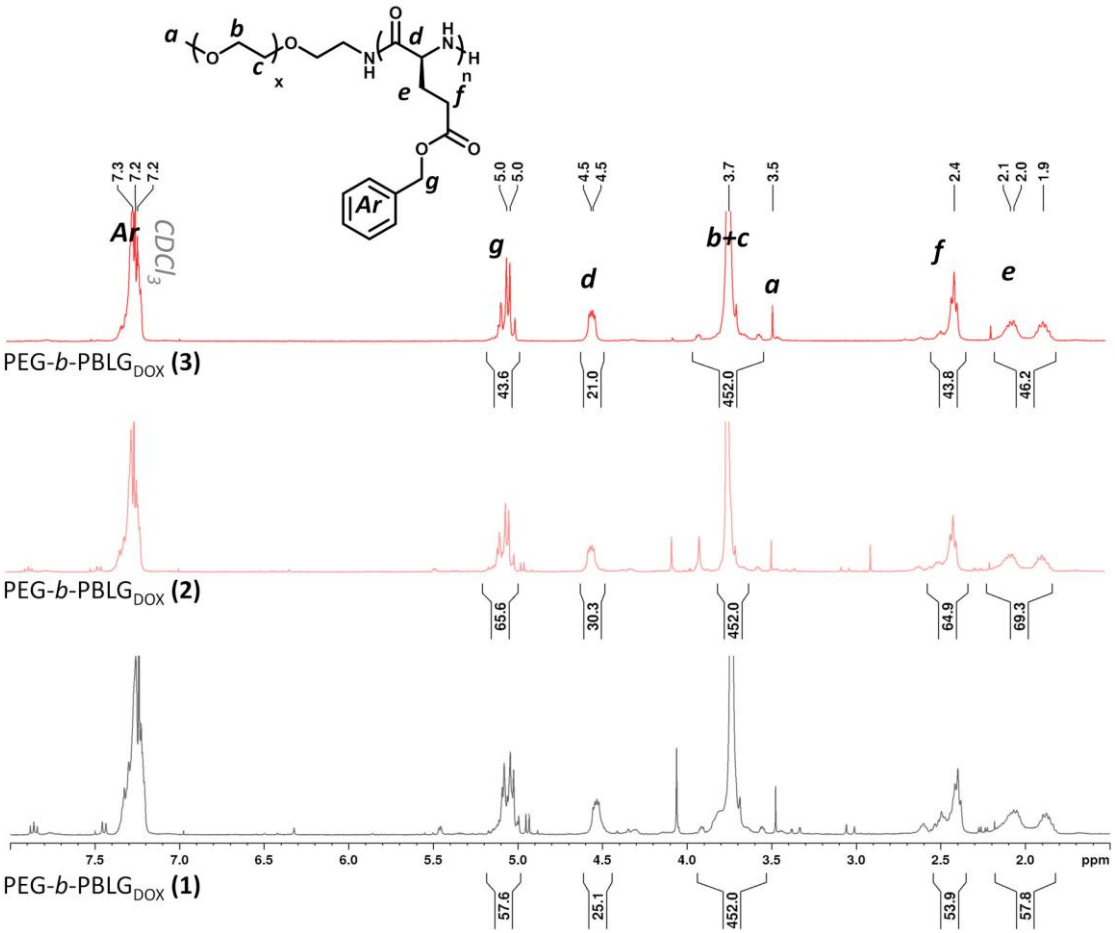

Figure VI-15. ^{1}H NMR spectra of PEG-*b*-PBLG$_{DOX}$ **(1)**, **(2)** and **(3)** in $CDCl_3$ + 15% TFA with targeted DP of 30 for **(1)** and **(2)**, and 19 for **(3)**. The backbone protons from the PEG (b+c) were used as a reference to determine the DP of the PBLG block, with the average integration from the signals of BLG protons.

SEC analysis revealed a high fraction of BLG oligomers when no co-solvent was used, suggesting that side reactions persisted (Figure VI-16). However, these DOX-BLG conjugates may not necessarily hinder the biological activity of the DDS, as previously observed.

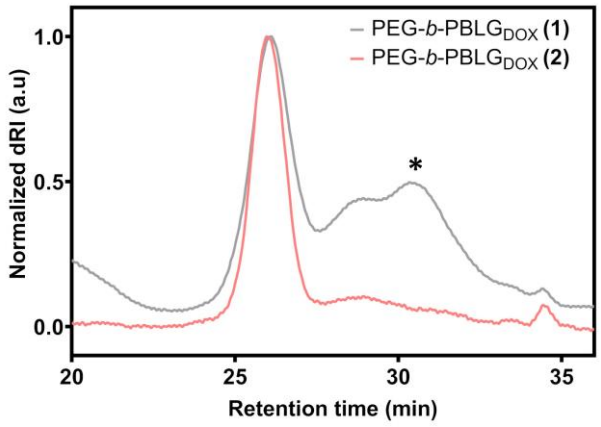

Figure VI-16. SEC chromatograms of PEG-*b*-PBLG$_{DOX}$ **(1)** and **(2)** upon *in situ* ROPISA encapsulation (DMF + 1% LiBr, dRI detection).

Nevertheless, their presence may limit the drug loading capacity. Indeed, DLC of 1.5 wt% was obtained for an EE of 15 % (PEG-*b*-PBLG$_{DOX}$ **(1)**, Table VI-3, Figure VI-17). With 10% of DMSO as co-

solvent (PEG-*b*-PBLG$_{DOX}$ **(2)**), while SEC analysis showed a reduction in oligomer content, the overall DLC did not improve (DLC = 0.9 wt%, EE = 8 %).

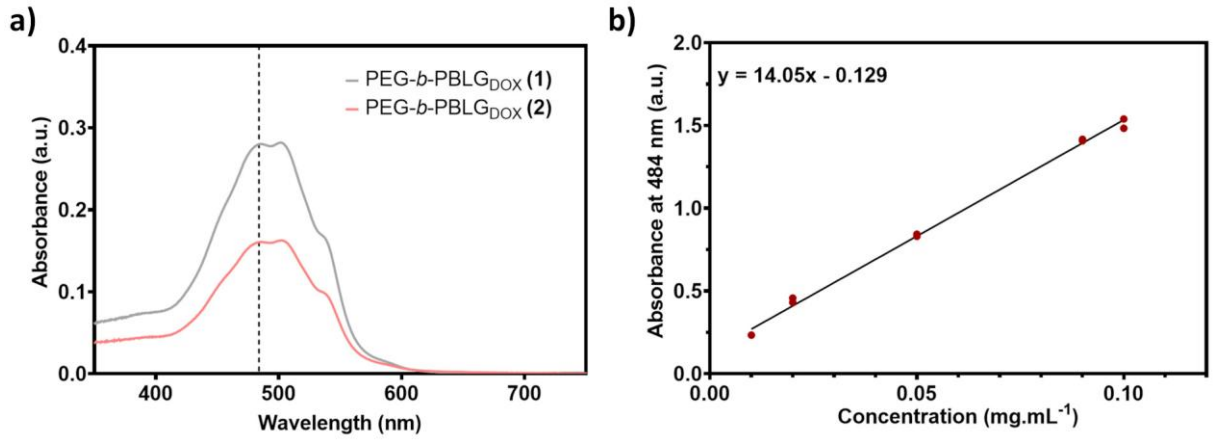

Figure VI-17. (a) UV-Vis spectra of PEG-*b*-PBLG$_{DOX}$ **(1)** and **(2)** upon *in situ* ROPISA encapsulation, purification, lyophilization and solubilization in DMSO. (b) Associated calibration curve of DOX in DMSO for DOX concentration determination.

DLS analysis revealed that nanoparticles formed in the presence of DMSO were less homogeneous than those obtained without DMSO (126 nm, σ = 0.31 *vs.* 191 nm, σ = 0.22) (Table VI-3, Figure VI-18a). TEM further confirmed the formation of homogeneous worm-like nanoparticles in the absence of DMSO, whereas nanoparticles produced with DMSO were fewer in number and displayed greater heterogeneity (Figure VI-18b).

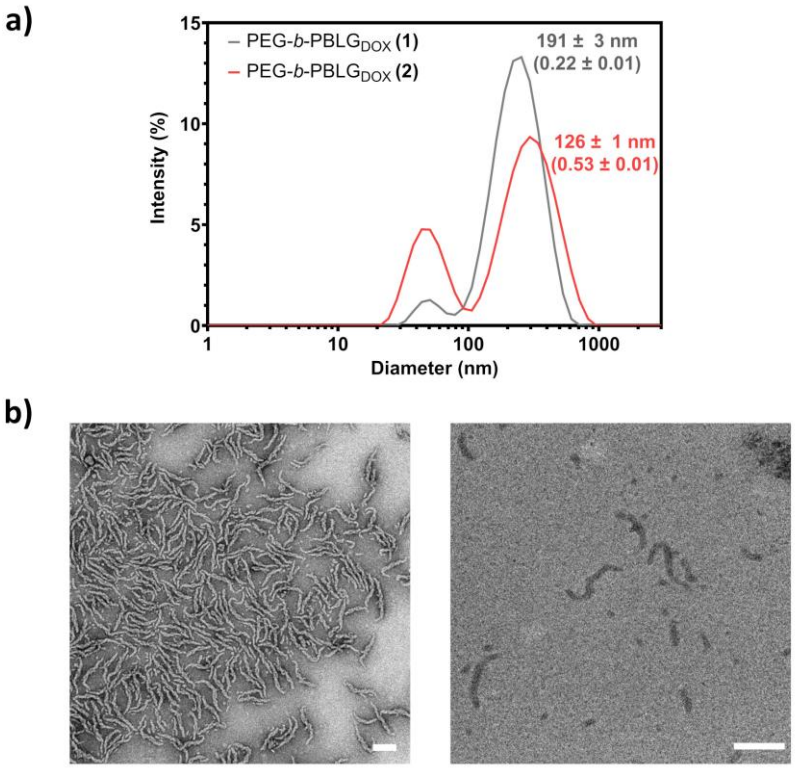

Figure VI-18. (a) DLS profiles of purified PEG-*b*-PBLG$_{DOX}$ **(1)** and **(2)** nanoparticle suspensions. (c) Representative TEM images of purified PEG-*b*-PBLG$_{DOX}$ nanoparticles suspension. Scale-bar: 200 nm.

To further optimize drug loading, we examined the impact of increasing the target DP while reducing the doxorubicin feeding ratio to achieve a DLC^{th} of 1 wt% (PEG-*b*-$PBLG_{DOX}$ **(3)**). Although this strategy resulted in a lower drug loading content (0.3 wt%), it enhanced encapsulation efficiency (26%) (Table VI-3, Figure VI-19a) and significantly reduced oligomer formation, as confirmed by SEC (Figure VI-19b). However, ^{1}H NMR indicated a lower-than-expected DP (Figure VI-15). Additionally, some aggregates persisted, and DLS as well as TEM analyses revealed that the nanoparticles remained less homogeneous (Table VI-3,Figure VI-19c, d).

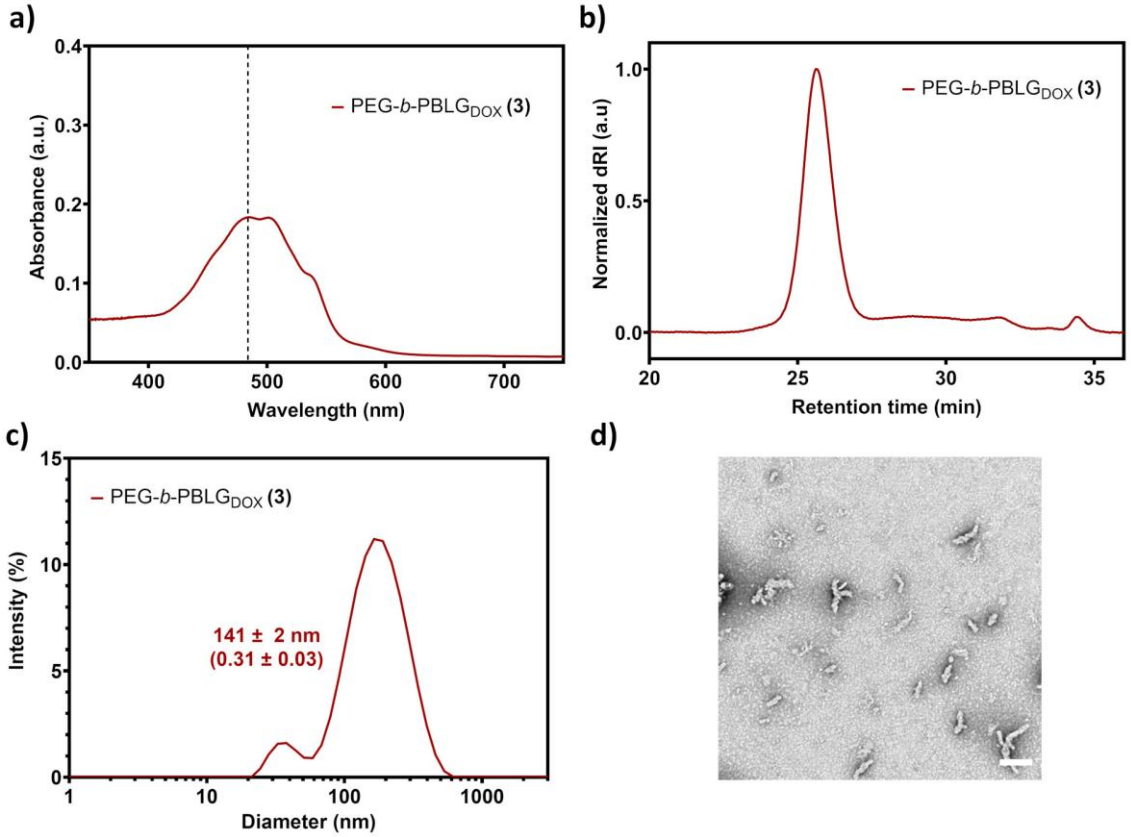

Figure VI-19. (a) UV-Vis spectrum of PEG-*b*-$PBLG_{DOX}$ **(3)** upon *in situ* ROPISA encapsulation, purification, lyophilization and solubilization in DMSO. (b) SEC chromatogram of PEG-*b*-$PBLG_{DOX}$ **(3)** upon *in situ* ROPISA encapsulation (DMF + 1% LiBr, dRI detection). (c) DLS profile of purified PEG-*b*-$PBLG_{DOX}$ **(3)** nanoparticle suspension. (d) Representative TEM images of purified PEG-*b*-$PBLG_{DOX}$ **(3)** nanoparticle suspension. Scale-bar: 200 nm.

Table VI-3. Characteristics of DOX-loaded PEG-*b*-PBLG nanoparticles after *in situ* PISA encapsulation.

N°	DP^{th}	DLC^{th} [a] [wt%]	DMSO [v/v %]	DP^{RMN} [b]	M_n [c] [kg.mol^{-1}]	$Đ$ [c]	DLC [d] [wt%]	EE [d] [%]	D_Z (σ) [e] [nm]
1	19	10	-	28	9.7 (1.6)	1.08 (1.35)	1.5	15	191 ± 3 (0.22 ± 0.01)
2			10	33	10.4	1.04	0.9	8	126 ± 1 (0.31 ± 0.01)
3	30	1	-	22	11.1 (1.6)	1.05 (1.37)	0.3	26	141 ± 2 (0.31 ± 0.02)

[a] Theoretical drug loading content (DLC^{th}) targeted with an initial feed weight ratio wt% of DOX to total mass of dispersed materials and DOX. [b] Average degree of polymerization (DP) determined by ^{1}H NMR. [c] Number average molar-mass (M_n) and molar-mass dispersity ($Đ$) determined by SEC in DMF +1% LiBr using PS calibration. [d] Experimental drug loading content (DLC) measured by UV-vis spectrophotometry and corresponding efficiency of encapsulation (EE). [e] Hydrodynamic Z-average diameter (D_Z) and polydispersity (σ) determined by DLS at 90°.

In summary, *in situ* encapsulation of DOX yielded promising results, with high encapsulation efficiency achieved for low targeted drug loading content (1 wt%). However, further improvement is desired to increase drug loading. A key limitation arises from the side reaction leading to BLG-NCA oligomerization initiated by DOX, which restricts the ability to improve the DLC. Moreover, the formation of these oligomers may compromise the biological activity of doxorubicin.

Although the *in situ* encapsulation strategy can be applied, drugs containing nucleophilic functional groups may hinder achieving high drug loading content due to undesired initiation reactions. To enhance the drug loading of these reactive agents and minimize the formation of potential oligomers, we explored *post*-PISA encapsulation as an alternative approach for incorporating the drug into the hydrophobic core.

VI.3. Post-ROPISA encapsulation

In this section, we focused on the encapsulation of doxorubicin, driven by the promising results obtained from *in situ* encapsulation, its broad therapeutic applications, and the side reactions observed during *in situ* encapsulation. These experiments were conducted by Maura Martinez Morales, a PhD student working on the application of ROPISA in nanomedicine. Based on our previous investigation into the mechanism and kinetics of aqueous ROPISA of BLG-NCA in **Chapter II**, the polymerization is expected to be complete within 2 hours, whereas the self-assembly process continues to evolve overnight under stirring. To optimize DOX encapsulation, we thus investigated the impact of drug addition at two different time point, after 2 hours or 16 hours of reaction, while also assessing the effect of hydrophobic core size by targeting two different degrees of polymerization (DP = 19 and 30). Additionally, two theoretical drug loadings (DLC^{th} = 1.4 and 10 wt%) were explored. Experimental conditions are summarized in Table VI-4.

Table VI-4. Characteristics of DOX-loaded PEG-*b*-PBLG nanoparticles after post-PISA encapsulation.

N°	DPth	DLCth [a] [wt%]	T^{add} [h]	DP^{RMN}	M_n [b] [kg.mol^{-1}]	$Đ$ [b]	DLC [c] [wt%]	EE [c] [%]	D_Z (σ) [d] [nm]
4	19	1.4	2	21	10.9	1.04	1.2	87	86 ± 1 (0.16 ± 0.02)
5			16	21	10.8	1.04	1.4	97	87 ± 1 (0.19 ± 0.02)
6		10	2	22	11.0	1.04	4.6	47	82 ± 1 (0.14 ± 0.01)
7			16	21	10.9	1.04	8.8 ± 0.6*	90 ± 7*	87 ± 4 (0.16 ± 0.02)
8	30		2	36	11.3	1.05	9.1	89	133 ± 1 (0.29 ± 0.03)
9			16	33	11.7	1.05	6.9	69	97 ± 2 (0.18 ± 0.01)

[a] Theoretical drug loading content (DLCth) targeted with an initial feed weight ratio % of DOX to total mass of dispersed materials and DOX. [b] Average degree of polymerization (DP) determined by ^{1}H NMR. [c] Number average molar-mass (M_n) and molar-mass dispersity ($Đ$) determined by SEC in DMF +1% LiBr using PS calibration. [d] Experimental drug loading content (DLC) measured by UV-vis spectrophotometry and corresponding efficiency of encapsulation (EE). * For PEG-*b*-PBLG$_{DOX}$ **(7)**, the experiment was done in triplicate ($n = 3$, mean ± standard deviation). [e] Hydrodynamic Z-average diameter (D_Z) and polydispersity (σ) determined by DLS at 90°.

The aqueous ROPISA was conducted under previously established conditions in **Chapter II**, followed by the addition of an aqueous solution of pre-solubilized DOX. The mixture was then stirred for an additional 16 hours. To remove any potential DOX-BLG aggregates or insoluble DOX precipitates, the resulting colloidal solutions were first purified by centrifugation. Free soluble drug was further eliminated by ultrafiltration against ultra-pure water. Macromolecular and colloidal characterization were performed using SEC and DLS, while drug loading content and encapsulation efficiency were determined by UV-vis spectroscopy. ^{1}H NMR analysis confirmed degrees of polymerization consistent with the targeted values (Table VI-4, Figure VI-20).

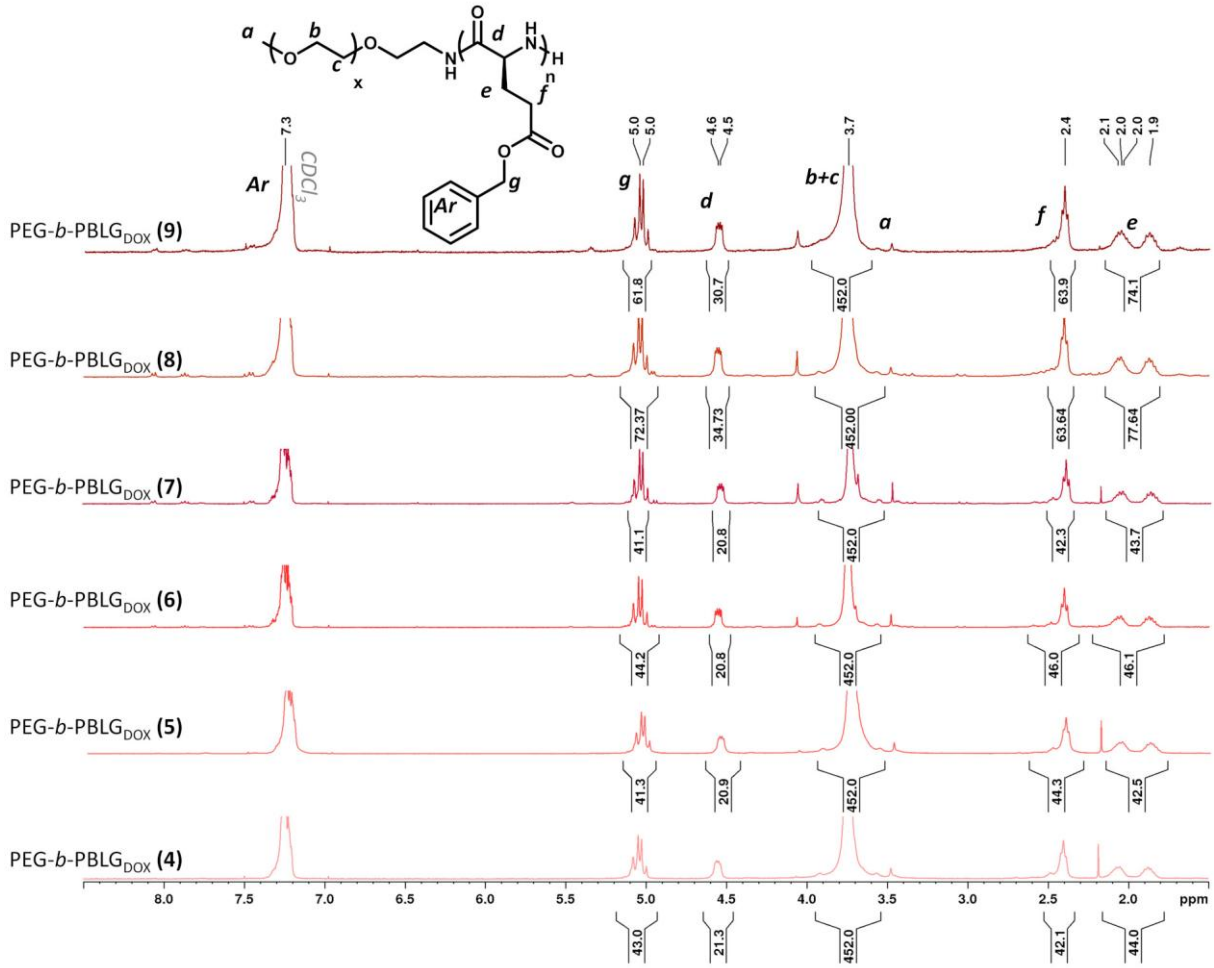

Figure VI-20. ^{1}H NMR spectra of PEG-*b*-PBLG$_{DOX}$ **(4)** to **(9)** in $CDCl_3$ + 15% TFA with targeted DP of 19 for **(4)** to **(7)** and 30 for **(8)** and **(9)**. The backbone protons from the PEG (b+c) were used as a reference to determine the DP of the PBLG block, with the average integration from the signals of BLG protons.

SEC analysis revealed an additional population at higher retention times following DOX addition, eluting at approximately 35 minutes, distinct from the DOX-BLG conjugates which eluted around 30 minutes (Figure VI-21).

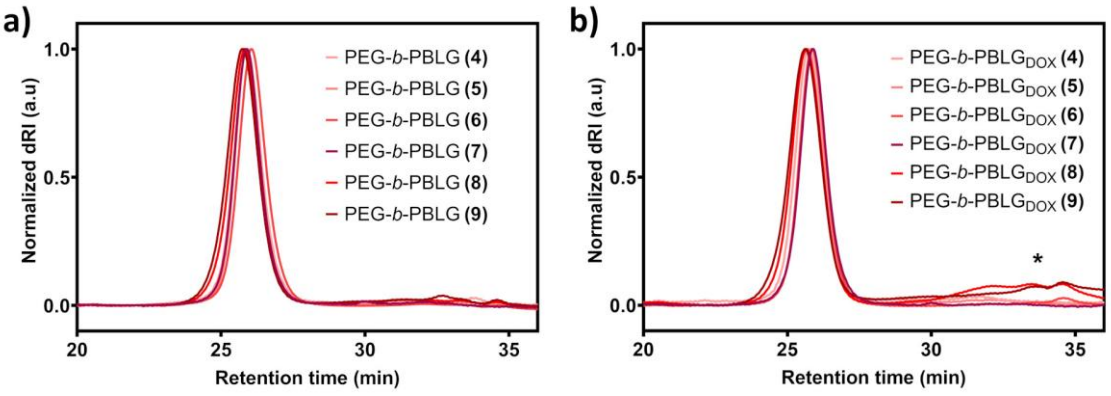

Figure VI-21. (a) SEC chromatograms before and (b) after DOX addition and purification for post-PISA encapsulation experiments (DMF + 1% LiBr, dRI detection).

This suggests that the observed species correspond to encapsulated DOX, which is released upon dissolution in DMF, rather than covalently conjugated drug-polymer complexes. Therefore, SEC confirmed that the addition of DOX, whether after 2 or 16 hours, did not interfere with the polymerization process, further demonstrating the rapid kinetics of polymerization.

DLS measurements confirmed the formation of homogeneous nanoparticles in all cases prior to DOX addition. Furthermore, the addition of DOX did not significantly affect the Z-average diameter or the dispersity of the nanoparticles, indicating that the drug incorporation did not disrupt the overall colloidal stability of the system (Table VI-4, Figure VI-22).

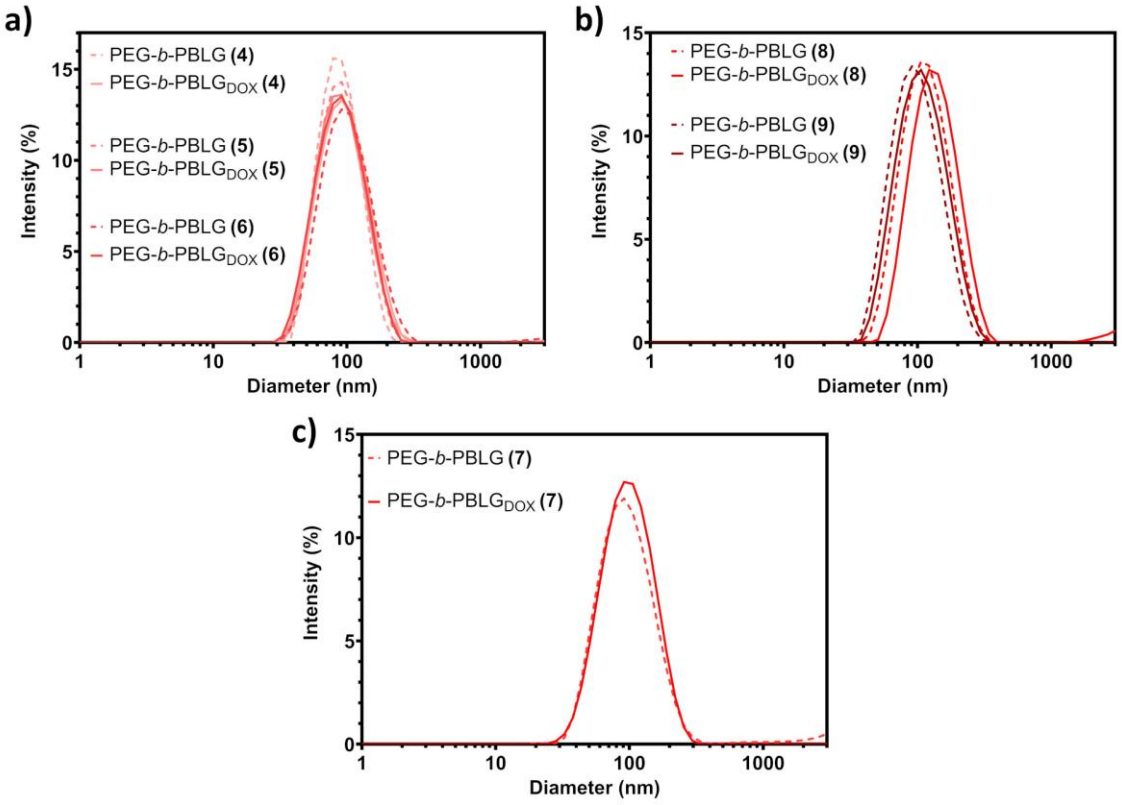

Figure VI-22. DLS profiles of PEG-*b*-PBLG targeting a DP 19 or (a) a DP 30 (b) before and after DOX addition and purification. (c) DLS profile of PEG-*b*-PBLG$_{DOX}$ **(7)** nanoparticle suspension before and after DOX addition and purification.

UV-Vis spectroscopy, using the strong absorbance peak at 484 nm, determined the concentration of DOX encapsulated within the purified nanoparticles, yielding EE values ranging from 47% to 97%, demonstrating a high loading potential (Table VI-4, Figure VI-23). Notably, no significant impact was observed with increasing DP or the size increase of the hydrophobic core. No clear trend in drug loading was also noticed according to the time of addition, except for formulations targeting a DP 19 and a DLCth of 10 wt% (PEG-*b*-PBLG$_{DOX}$ **(6)**, **(7)**, Table VI-4). In these cases, adding the drug after 2 hours yielded significantly lower drug loading compared to addition after 16 hours. This last condition was repeated in triplicate as it was the most promising one, resulting in DLC of 8.8 ± 0.6 wt% and an EE of 90 ± 7%.

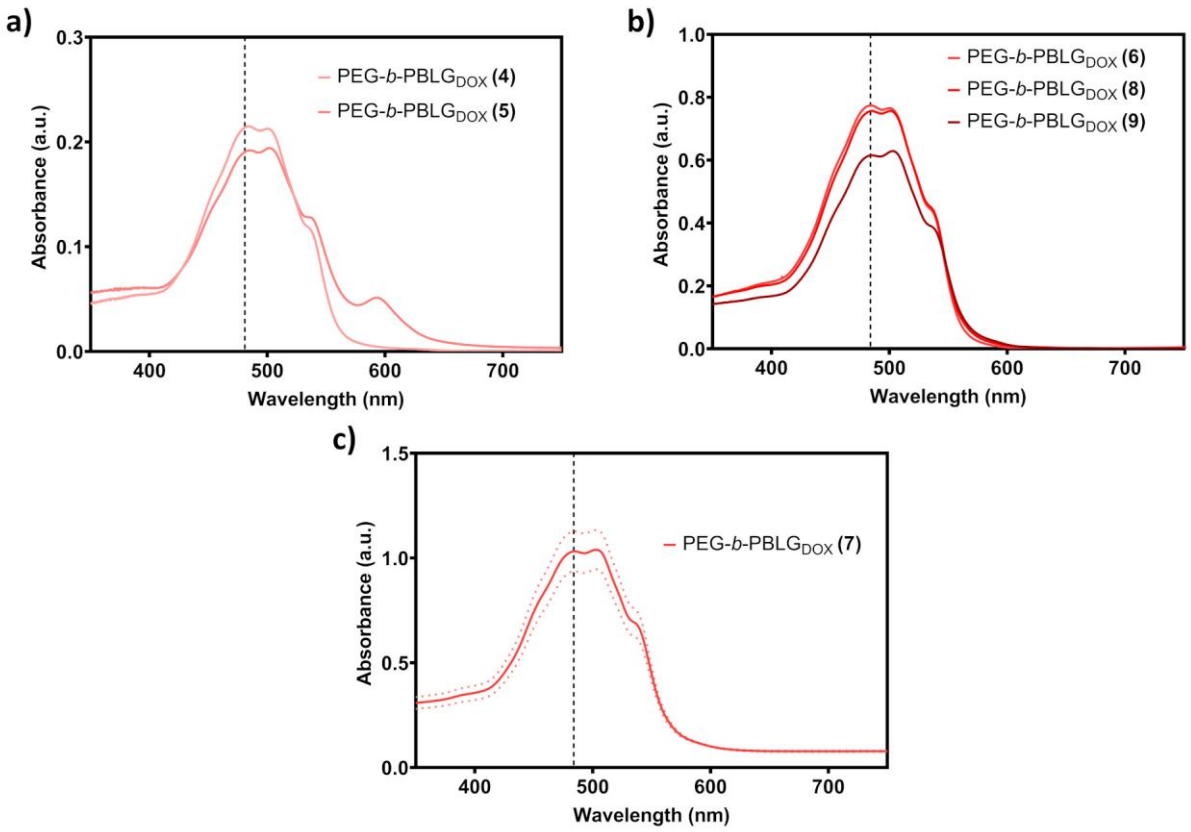

Figure VI-23. Drug loading determination by UV-Vis spectrophotometry. (a) UV-Vis spectra of PEG-*b*-PBLG$_{DOX}$ **(4)**, **(5)**, (b) PEG-*b*-PBLG$_{DOX}$ **(6)**, **(8)**, **(9)** and (c) PEG-*b*-PBLG$_{DOX}$ **(7)** ($n = 3$) upon *post*-ROPISA encapsulation, purification, lyophilization and solubilization in DMSO.

For this last condition, DLS confirmed the presence of homogeneous nanoparticles with an average hydrodynamic diameter of 87 nm and a dispersity of 0.16 (Figure VI-22c). TEM revealed the presence of worm-like nanoparticles, similar to those observed for empty PEG-*b*-PBLG nanoparticles (Figure VI-24).

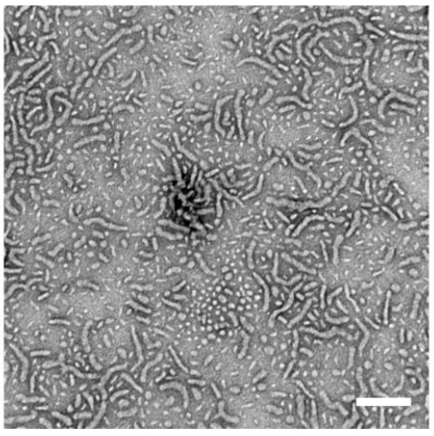

Figure VI-24. Representative TEM images of purified PEG-*b*-PBLG$_{DOX}$ **(7)** nanoparticles suspension. Scale-bar: 200 nm.

One plausible explanation for the observed difference in DLC is the variation of pH during the reaction. Indeed, we highlighted in **Chapter II** that the medium is around pH 6.5 at 2 hours, as the CO_2

release during the ROP remains dissolved in the solution. Under these acidic conditions, doxorubicin becomes more hydrophilic (its pKa being around 9.9) and is therefore less likely to diffuse into the hydrophobic core. In contrast, after 16 hours, the pH returns to its initial value of 8.5 due to the elimination of CO_2. As a result, doxorubicin becomes more hydrophobic, increasing its affinity for the hydrophobic core and thereby enhancing drug loading efficiency.

These results are highly promising and, for the first time, demonstrate exceptionally high drug encapsulation efficiencies for a ROPISA process,[13] and even for PISA.[1,2,38,3] The micellar core appears to be sufficiently flexible to allow drug diffusion into, even in the absence of a plasticizing solvent.

VI.4. Conclusion

In this chapter, we demonstrated that high encapsulation efficiencies for anticancer drugs with varying hydrophobicity can be achieved through two complementary strategies: *in situ* encapsulation during aqueous ROPISA and *post*-polymerization encapsulation (*post*-ROPISA). Our investigation indicates that for drugs with minimal side reactions, such as mitoxantrone, *in situ* encapsulation is effective. In contrast, for more reactive compounds like doxorubicin, where nucleophilic functional groups may trigger unwanted polymerization side reactions, a *post*-ROPISA strategy is more suitable to confine the drug within the hydrophobic core. Moreover, the *in situ* encapsulation of ellipticine, a highly hydrophobic but non-reactive agent, was also demonstrated; however, its encapsulation efficiency was limited by poor solubility in both DMSO and water, resulting in lower drug loading.

These findings underscore the critical influence of a drug's chemical nature and solubility on the encapsulation process and provide a framework for the rational design of polypeptide-based nanocarriers with optimized drug loading and controlled morphology for cancer therapy. Altogether, this study highlights the unique capability of the ROPISA process to produce polypeptide-based nanomedicines with high concentration, high yield, and high drug loading content through a one-pot, two-step procedure conducted entirely in pure water.

Future work will focus on optimizing drug loading capacities by selecting monomers with higher affinity for drugs, such as tyrosine, known for its π-π stacking and hydrogen bonding interactions with hydrophobic compounds. Additionally, further studies will aim to refine drug release profiles and evaluate the therapeutic efficacy of these nanocarriers in relevant biological models.

Beyond physical encapsulation, chemical conjugation also represents a promising strategy, as introduced in the introduction of this chapter. Given our previous demonstration in **Chapter V** of carbodiimide coupling within the hydrophobic core using a fluorescent probe, this functionalization strategy could be extended to therapeutic cargoes of interest.

VI.5. Experimental section

VI.5.1. Materials

γ-benzyl-*L*-glutamate was purchased from PMC Isochem (Vert-le-Petit, France) and stored at -20 °C under argon atmosphere and weighed in the glove box Jacomex GP13 no. 2675. α-methoxy-ω-amino poly(ethylene glycol) PEG_{5k}-NH_2 (M_p = 5000 g.mol^{-1}, $Đ$ = 1.02) was bought from RAPP Polymer Gmbh (Tübingen, Germany).

Doxorubicin hydrochloride (DOX) was purchased from Sigma-Aldrich, mitoxantrone dihydrochloride (MTX) from BLD PHARMATECH GMBH and ellipticine (EPT) from MedChemExpress. All the drugs were stored at 4°C, in the dark.

Dimethylsulfoxide (DMSO) and *N*-*N*-Dimethylformamide (DMF) (for size-exclusion chromatography) were purchased from Sigma-Aldrich. Ultrapure water was obtained from a Milli-Q system (Merck Millipore, France) with a resistivity of 18.2 MΩ. Deuterated solvent ($CDCl_3$) was purchased from Eurisotop.

Amicon Ultra 15mL (cut-off 30kDa, RC) were bought from UGAP. Spectra/Por 6 dialysis membrane 3.5kDa MWCO were purchased from Repligen.

VI.5.2. Instrumentation and methods

VI.5.2.1. Nuclear Magnetic Resonance (NMR)

^{1}H Nuclear Magnetic Resonance (NMR) spectra were recorded on a Bruker Avance III spectrometer equipped with a 5 mm BBFO (broad band fluorine observation) liquid probe, at 298 K. ^{1}H data were acquired at 400.2 MHz observation frequency, with 16 scans and a recycle delay of 1 second. Signals were referred to the signal of residual protonated solvent signals.

VI.5.2.2. Size Exclusion Chromatography (SEC)

Polymer molar masses were determined by SEC using dimethylformamide (DMF + LiBr 1 g.L^{-1}) as eluent. Measurements were performed on an Ultimate 3000 system from ThermoFischer Scientific (Ilkirch, France) equipped with a diode array detector (DAD). The system also includes a multiangle light scattering detector (MALS) and differential refractive index detector dRI from Wyatt technology (Santa Barbara CA, USA). Polymers were separated on three Shodex Asahipack gel columns [GF 310 (7.5 × 300 mm²), GF510 (7.5 × 300 mm²), exclusion limits from 500–300 000 Da] at a flowrate of 0.5 mL.min^{-1}. Columns temperature was held at 50 °C. Easivial™ kit of Polystyrene from Agilent (Santa Clara CA, USA) was used as calibration standard (Mn from 162 to 364 000 Da).

VI.5.2.3. Transmission Electron Microscopy (TEM)

The images were recorded on a Hitachi H7650 microscope working at 80 kV. Samples after dialysis against PBS and filtration with a 0.22 µm CA filter were prepared by deposing a drop of 0.1 mg.mL^{-1} nanoparticles dispersion onto a copper grid (200 mesh coated with carbon) after glow discharge for 45 second and removing excess after 1 minute. Grids were negatively stained with 1.2% uranyl acetate for 1 min.

VI.5.2.4. Dynamic Light Scattering (DLS)

For DLS measurements, nanoparticles were diluted to 1 mg.mL^{-1} and a Zetasizer nano ZS (Malvern Instruments, UK) instrument with a detection angle of 90° and a red laser (633 nm) as the incident beam was used. Measurements were carried out at 25 °C in triplicate.

VI.5.2.5. Drug Loading Content (DLC) and Encapsulation Efficiency (EE) Determination

The purified nanoparticle solution was freeze-dried and obtained powder was solubilized in DMSO to release the loaded drug. Quantification of the amount of loaded drug was determined by UV-vis spectroscopy using a calibration curve performed in the same solvent. EPT was quantified at 294 nm, MTX at 682 nm, and DOX at 484 nm using a calibration curve obtained with known amounts of EPT, MTX, and DOX, respectively.

DOX concentration was measured on a Specord 200 Plus UV-Vis spectrophotometer from Analytik Jena, equipped with two lamps, a deuterium lamp (190 – 320 nm) and a halogen lamp (320 – 1100 nm). Spectral scans were performed with 500 µL of samples in quartz cells of 10 mm optical path length and recorded with the WinAspect Plus software using the following settings: 300 – 750 nm, 0.5 nm sensitivity, 50 nm.s^{-1} scan speed, and correction with the pure solvent as a reference.

For EPT and MTX, the amount was measured on a Cary 100 UV-Vis spectrophotometer equipped with a multi-cell temperature controller from Agilent Technologies. The solutions were placed in 1 cm quartz suprasil micro-cells (500 µL). Data were collected from 250 – 500 nm (EPT) and from 400 – 800 nm (MTX).

Theoretical Drug Loading Content (DLC^{th}), Experimental Drug Loading Content (DLC^{exp}) and Encapsulation Effiency (EE) were calculated using the following equations:

(1) $$DLC^{th} = \frac{Initial\ mass\ of\ drug}{Total\ mass} \times 100$$

(2) $$DLC^{exp} = \frac{Mass\ of\ drug}{Total\ mass} \times 100$$

(3) $$EE = \frac{DLC^{exp}}{DLC^{th}} \times 100$$

VI.5.3. Encapsulation procedures

All the diblock copolymers were synthesized by ring-opening polymerization induced self-assembly (ROPISA) in aqueous buffer, as described previously in **Chapter II** and **III.**

VI.5.3.1. *In-situ* encapsulation of ellipticine (EPT)

A typical procedure for in situ encapsulation of ellipticine is as follows: a solution of EPT at 9 mg.mL^{-1} in DMSO was prepared by dissolving 0.9 mg of EPT in 0.1 mL of DMSO to target a DLCth of 1.28 wt%. At the same time, BLG-NCA (47 mg, 0.18 mmol, 31 eq) was weighed in a dry Schlenk tube a magnetic stirring bar under inert atmosphere. The Schlenk was then removed from the glove box and cooled in an ice bath for at least 10 minutes. A water solution of $NaHCO_3$ 0.05M containing the PEG_{5k}-NH_2 macro-initiator (0.9 mL, 30 mg, 0,006 mmol) was prepared and refrigerated in an ice bath for at least 10 minutes. While remaining in the ice bath, the aqueous solution containing the macroinitiator and 0.1 mL of the solution that contains the drug were added to the NCA powder under strong agitation (τ_s = 7 wt%). The reaction was left to stir 1) first in an ice-cold water bath; 2) then at room temperature overnight. Same procedure was used, and quantities were adapted for a DLCth of 2.54 wt% with a DMSO fraction of 20 %: 1.8 mg of EPT was solubilized in 0.2 mL of DMSO to obtain a solution at 9 mg.mL^{-1}. The yellow colloidal water solution was centrifuged several times to remove aggregates (9 000 g) and ultrafiltrated against ultra-pure water.

VI.5.3.2. *In-situ* encapsulation of mitoxantrone (MTX)

The same procedure used for ellipticine encapsulation was used for MTX, with the drug dissolved in water at 0.75 mg.mL^{-1} for DLCth of 1 wt% and 7.5 mg.mL^{-1} for 10 wt%. The resulting blue colloidal solution was then subjected to multiple centrifugation steps (1 000 g × 2, then 10 000 g) to remove aggregates, and ultrafiltered against ultra-pure water to remove soluble free drug.

VI.5.3.3. *In-situ* encapsulation of doxorubicin (DOX)

30 mg of DOX was solubilized in 3 mL of H_2O to obtain a stock solution at 10 mg.mL^{-1} to target a DLCth of 10 wt%. In parallel, BLG-NCA (150 mg, 0.6 mmol, 19 eq) was weighed in a dry Schlenk tube with a magnetic stirring bar. The Schlenk was removed from the glove box and cooled on ice. PEG_{5k}-NH_2 (150 mg, 0.03 mmol) was solubilized in 4 mL of $NaHCO_3$ (50 mM) and added to the NCA powder under a strong agitation (τ_s = 7 wt%). At the same time, 1 mL of the DOX solution was added to the mixture. The reaction was left to stir 1) first in an ice-cold water bath; 2) then at room temperature overnight. The same procedure was adapted for a targeted DLCth of 1 wt% and a targeted DP of 30, by adjusting the DOX concentration and the feeding ratio. With the use of DMSO as a co-solvent, same procedure was employed, but DOX was pre-solubilized in DMSO to obtain a stock solution at 90 mg.mL^{-1}. 0.4 mL of DOX in DMSO was added to 3.6 mL of the mixture. The resulting red colloidal solution was then subjected to multiple centrifugation steps (1 000 g × 2, then 10 000 g) to remove aggregates, and ultrafiltered against ultra-pure water to remove soluble free drug.

VI.5.3.4. *Post-PISA* encapsulation of doxorubicin (DOX)

A typical aqueous ROPISA of BLG-NCA initiated by PEG_{5k}-NH_2 was performed, targeting a degree of polymerization of 19 or 30, as described in **Chapter II**. After 2 or 16 hours of stirring, an aqueous solution of DOX was added, targeting a DLC^{th} of 1.4 or 10 wt%. The mixture was then stirred for an additional 16 hours.

The resulting red colloidal solution was then subjected to multiple centrifugation steps (1 000 g × 2, then 10 000 g) to remove aggregates, and ultrafiltered against ultra-pure water to remove soluble free drug.

VI.6. References

[1] B. Karagoz, C. Boyer, T. P. Davis, *Macromol. Rapid Commun.* **2014**, *35*, 417–421.
[2] J. Engström, H. Asem, H. Brismar, Y. Zhang, M. Malkoch, E. Malmström, *Macromol.Chem. Phys.***2020**, *221*, 1900443.
[3] H. Phan, M. Cossutta, C. Houppe, C. Le Cœur, S. Prevost, I. Cascone, J. Courty, J. Penelle, B. Couturaud, *J. Colloid Interface Sci.* **2022**, *618*, 173–184.
[4] C. Cao, F. Chen, C. J. Garvey, M. H. Stenzel, *ACS Appl. Mater. Interfaces* **2020**, *12*, 30221–30233.
[5] G. Li, D. C. Barzycki, R. G. Ricarte, *AIChE Journal* **2023**, *69*, e18014.
[6] C. J. Mable, R. R. Gibson, S. Prevost, B. E. McKenzie, O. O. Mykhaylyk, S. P. Armes, *J. Am. Chem. Soc.* **2015**, *137*, 16098–16108.
[7] Y. Huang, P. Li, R. Zhao, L. Zhao, J. Liu, S. Peng, X. Fu, X. Wang, R. Luo, R. Wang, Z. Zhang, *Biomedicine & Pharmacotherapy* **2022**, *151*, 113053.
[8] J. Tan, H. Sun, M. Yu, B. S. Sumerlin, L. Zhang, *ACS Macro Lett.* **2015**, *4*, 1249–1253.
[9] L. D. Blackman, S. Varlas, M. C. Arno, A. Fayter, M. I. Gibson, R. K. O'Reilly, *ACS Macro Lett.* **2017**, *6*, 1263–1267.
[10] W.-J. Zhang, C.-Y. Hong, C.-Y. Pan, *Biomacromolecules* **2016**, *17*, 2992–2999.
[11] D. B. Wright, M. T. Proetto, M. A. Touve, N. C. Gianneschi, *Polym. Chem.* **2019**, *10*, 2996–3000.
[12] C. Zhu, H. Beauseroy, J. Mougin, M. Lages, J. Nicolas, *Chem. Sci.* **2025**, *16*, 2619–2633.
[13] P. Joshua Hurst, K. J. Gassaway, M. Faris Abouchaleh, N. S. Idris, C. R. Jones, C. A. Dicksion, J. S. Nowick, J. P. Patterson, *RSC Applied Polymers* **2024**, *2*, 238–247.
[14] J.-M. Noy, C. Cao, M. Stenzel, *ACS Macro Lett.* **2019**, *8*, 57–63.
[15] J.-M. Noy, F. Chen, D. T. Akhter, Z. H. Houston, N. L. Fletcher, K. J. Thurecht, M. H. Stenzel, *Biomacromolecules* **2020**, *21*, 2320–2333.
[16] H. Sun, W. Cao, N. Zang, T. D. Clemons, G. M. Scheutz, Z. Hu, M. P. Thompson, Y. Liang, M. Vratsanos, X. Zhou, W. Choi, B. S. Sumerlin, S. I. Stupp, N. C. Gianneschi, *Angew. Chem. Int. Ed.* **2020**, *59*, 19136–19142.
[17] T. Lückerath, K. Koynov, S. Loescher, C. J. Whitfield, L. Nuhn, A. Walther, C. Barner-Kowollik, D. Y. W. Ng, T. Weil, *Angew. Chem. Int. Ed.* **2020**, *59*, 15474–15479.
[18] M. Abad, M. Nardi, L. Oriol, M. Piñol, E. Blasco, *Polym. Chem.* **2022**, *14*, 71–80.
[19] E. Chaabouni, V. Tkachenko, L. Vidal, N. Allouche, A. Chemtob, *Eur. Polym. J.* **2021**, *156*, 110633.
[20] S. Xi Huang, Z. Hao Wang, M. Lin, X. Hui Fu, J. Sun, *Polymer Chemistry* **2023**, *14*, 1801–1808.
[21] C. J. Mable, I. Canton, O. O. Mykhaylyk, B. U. Gul, P. Chambon, E. Themistou, S. P. Armes, *Chem. Sci.* **2019**, *10*, 4811–4821.
[22] L. Qiu, C.-R. Xu, F. Zhong, C.-Y. Hong, C.-Y. Pan, *ACS Appl. Mater. Interfaces* **2016**, *8*, 18347–18359.
[23] J.-M. Noy, F. Chen, M. Stenzel, *Beilstein J Org Chem* **2021**, *17*, 2302–2314.
[24] E. Hinde, K. Thammasiraphop, H. T. T. Duong, J. Yeow, B. Karagoz, C. Boyer, J. J. Gooding, K. Gaus, *Nature Nanotech* **2017**, *12*, 81–89.
[25] C. Lee, A. Hwang, L. Jose, J. H. Park, S. Jang, J. K. Song, Y. Kim, Y. Cho, H. B. Jeon, J.-O. Jin, H. Paik, *J. Ind. Eng. Chem* **2020**, *86*, 35–38.
[26] V. M. Dan, T. S. Varghese, G. Viswanathan, S. Baby, *CCDT* **2020**, *20*, 33–46.
[27] R. Indra, T. Černá, Z. Heger, J. Hraběta, M. Wilhelm, S. Dostálová, A. Lengálová, M. Martínková, V. Adam, T. Eckschlager, H. H. Schmeiser, V. M. Arlt, M. Stiborová, *Toxicology* **2019**, *419*, 40–54.
[28] R. M. Al-Nakashli, C. Cao, R. Raveendran, H. Lu, M. H. Stenzel, *Macromol. Chem. Phys.* **2023**, *224*, 2200179.
[29] F. Masood, P. Chen, T. Yasin, N. Fatima, F. Hasan, A. Hameed, *Mater. Sci. Eng. C* **2013**, *33*, 1054–1060.
[30] D. R. Joshi, N. Adhikari, *J. Pharm. Res. Int.* **2019**, 1–18.
[31] B. Liu, R. Fang, W. Li, X. Wu, T. Liu, M. Lin, J. Sun, X. Chen, *J. Am. Chem. Soc.* **2024**, *146*, 16558–16566.
[32] R. Nordström, L. Zhu, J. Härmark, Y. Levi-Kalisman, E. Koren, Y. Barenholz, G. Levinton, D. Shamrakov, *Pharmaceutics* **2021**, *13*, 123.
[33] B. J. Evison, B. E. Sleebs, K. G. Watson, D. R. Phillips, S. M. Cutts, *Medicinal Research Reviews* **2016**, *36*, 248–299.

[34] J. Nicolas, *Chem. Mater.* **2016**, *28*, 1591–1606.
[35] L. Guerassimoff, M. Ferrere, A. Bossion, J. Nicolas, *Chem. Soc. Rev.* **2024**, *53*, 6511–6567.
[36] M. Kciuk, A. Gielecińska, S. Mujwar, D. Kołat, Ż. Kałuzińska-Kołat, I. Celik, R. Kontek, *Cells* **2023**, *12*, 659.
[37] N. Zhao, M. C. Woodle, A. J. Mixson, *J Nanomed Nanotechnol* **2018**, *9*, 519.
[38] H. Asem, W. Zheng, F. Nilsson, Y. Zhang, M. S. Hedenqvist, M. Hassan, E. Malmström, *ACS Appl. Bio Mater.* **2021**, *4*, 1045–1056.

General conclusion

The development of elongated polymeric nanocarriers for drug delivery offers a promising strategy to enhance the efficacy of anticancer agents, as these structures improve tumor penetration and cellular uptake. The self-assembly of amphiphilic block copolymers provides effective control over nanocarrier size, shape, and surface properties. Polypeptide-based systems are particularly attractive due to their biocompatibility and biodegradability. However, while some nanocarriers have reached clinical trials, elongated polypeptide-based systems remain largely unexplored. The synthesis and formulation of these nanocarriers necessitates several steps, which hinders scalability. Regarding the synthesis, the most efficient route to high-molecular-weight polypeptides is ring-opening polymerization (ROP) of α-amino acid *N*-carboxyanhydrides (NCAs). However, conventional ROP is limited by strict anhydrous requirements, complex purification processes, and the utilization of toxic solvents. Recent advances in aqueous polymerization have circumvented these challenges by optimizing conditions to suppress water-induced NCA hydrolysis, leading to the development of ring-opening polymerization-induced self-assembly (ROPISA) at LCPO. This novel one-step process that directly yields amphiphilic copolymers and elongated nanomaterials in a scalable manner. Despite its promise, the process remains complex and not fully understood.

In this PhD project, our objective was to deepen our understanding and expand the potential of aqueous ROPISA of NCAs for nanomedicine applications, with a particular focus on oncology.

In **Chapter II**, we investigated the mechanism of polymerization and self-assembly of aqueous ROPISA of γ-benzyl-*L*-glutamate (BLG-NCA) initiated by α-amino poly(ethylene glycol) (PEG_{5k}-NH_2) using time-resolved *in situ* small angle and wide-angle X-ray scattering (SAXS/WAXS), as well as complementary techniques like size-exclusion chromatography (SEC) and transmission electron microscopy (TEM). Our findings reveal that polymerization occurs at a rate that is faster than hydrolysis, driven by a confined environment that enhances local monomer concentrations and preserves the amino group's nucleophilicity. Furthermore, we have demonstrated that the solubility of NCA exerts a significant influence on the kinetics of polymerization and that early β-sheet formation directs the self-assembly into anisotropic nanostructures, with fiber-like morphologies emerging *via* chain addition or fusion.

In **Chapter III**, we expanded our investigation by systematically varying the NCA monomers, subjected to ROPISA initiated by PEG_{5k}-NH_2. By varying the protecting groups in lysine NCAs and employing amino acids with different hydrophobicity and stacking capabilities, such as glycine, alanine, leucine, phenylalanine, and tyrosine, we observed significant modulation of nanoparticle anisotropy. The hydrophilic/hydrophobic balance, π-π stacking, and hydrogen bonding interactions were found to

influence both polymerization kinetics and self-assembly, ultimately affecting the aspect ratio of the nanostructures. Moreover, the influence of monomer hydrophobicity on polymerization kinetics—where more hydrophilic monomers exhibited ultra-fast polymerization—further supports the hypothesis proposed in **Chapter II** that solubilization is the rate-limiting step in the ROPISA process.

In **Chapter IV**, our studies on various macroinitiators to obtain functional and/or (bio)degradable nanoparticles by taking advantage of the aqueous media, highlighted the critical role of the stabilizing block in the resulting nanostructures. Peptide-based macroinitiators, including poly(*L*-proline) and elastin-like polypeptides, resulted in well-defined anisotropic nanostructures that exhibited unique thermoresponsive properties. In addition, poly(sarcosine), enzyme-polypeptide conjugates, cyclic peptides, self-immolative polymers, and dextran derivatives further emphasized the pivotal role of the stabilizing block in regulating nanoparticle morphology and enhancing polymerization efficiency. Despite the observation of reduced enzymatic activity in some enzyme-polypeptide conjugates due to steric hindrance, these findings validate ROPISA as a promising platform for synthesizing fully peptidic nanoparticles and protein conjugates for drug delivery applications.

In Chapter V, various biological evaluations further confirmed the potential of aqueous ROPISA in nanomedicine. Fluorescent PEG-*b*-PBLG worm-like nanoparticles were synthesized via a one-step aqueous ROPISA of BLG-NCA and dye conjugation, and their performance in *in vitro* and *in vivo* conditions were benchmarked against spherical nanoparticles produced by solvent displacement. Cellular uptake and *in vivo* biodistribution studies using CT26 and 4T1 tumor models revealed efficient internalization for both morphologies, with CT26 exhibiting faster uptake and 4T1 showing higher overall accumulation. In 3D spheroid models, both nanoparticle types demonstrated effective penetration, although 4T1 spheroids exhibited slower kinetics. *In vivo* studies corroborated prolonged circulation and significant tumor accumulation in both models, particularly for the worm-like nanoparticles in 4T1 tumors.

Finally, **Chapter VI** assessed strategies for encapsulating anticancer drugs, including ellipticine, mitoxantrone, and doxorubicin, using both *in situ* and *post*-ROPISA approaches. The results indicated that while *in situ* encapsulation is effective for less reactive drugs, a *post*-ROPISA approach is preferable for reactive compounds like doxorubicin, thereby confining the drug more effectively within the hydrophobic core. These preliminary encapsulation studies further validate the potential of ROPISA for developing efficient nanocarriers.

Overall, this PhD work establishes that aqueous ROPISA is a robust and scalable platform for designing anisotropic, polypeptide-based nanocarriers. It also provides important information about how polymerization, self-assembly, and drug loading work together to improve cancer therapy with nanomedecine.

Perspectives

As this PhD project will progress toward applications in nanomedicine under the work of Maura Martinez Morales, several research directions have been identified and will be briefly presented in the following paragraphs.

Modulating morphology by copolymerization and enhanced drug loading

First, the development of nanocarriers via ROPISA with high drug-loading capacity and controlled drug release remains a key objective. To this end, monomers exhibiting a strong affinity for selected drugs will be investigated. As discussed in **Chapter III**, tyrosine has emerged as a promising candidate due to its advantageous interactions. However, challenges related to its gelation properties impede the efficacy of controlled homopolymerization. In this regard, copolymerization emerges as a promising strategy to integrate tyrosine's properties while maintaining control over both polymerization and self-assembly. Moreover, the incorporation of diverse side chains through copolymerization has the potential to introduce a variety of intermolecular interactions, including hydrogen bonding, π-π stacking, and ionic interactions, thereby further refining the nanocarrier properties. The exploration of random copolymerization *via* ROPISA has been undertaken, employing racemic monomers as the starting point[1,2] The objective of this study is to assess the impact of chirality on the resulting nanoparticle morphology. However, to the best of our knowledge, only one study has reported random copolymerization involving cysteine and BLG-NCA for the formation of nanogels.[3]

Building on this, an effort was made to undertake the copolymerization of BLG-NCA and tyrosine-NCA (Tyr-NCA) using the ROPISA method described in Chapters II and III. Two copolymerizations were performed with initial Tyr-NCA fractions of 0.1 and a target degree of polymerization (DP) of 35 (PEG_{5k}-*b*-P(Tyr_4-*co*-BLG_{31}) and 0.5 with a target DP of 37 (PEG_{5k}-*b*-P(Tyr_{18}-*co*-BLG_{19})), employing the classical procedure of aqueous ROPISA. The chemical structure of each copolymer was determined using ^{1}H NMR. For a target tyrosine fraction of 0.1, ^{1}H NMR revealed a DP of 35 with a tyrosine fraction of 0.09, and 0.44 with a DP of 32 for a target fraction of 0.5 (Figure 1a). SEC chromatograms revealed an effective chain extension with a slightly higher molar mass dispersity for PEG_{5k}-*b*-P(Tyr_{18}-*co*-BLG_{19}) ($Đ$ = 1.14) than PEG_{5k}-*b*-P(Tyr_{18}-*co*-BLG_{19}) ($Đ$ = 1.11) (Figure 1b).

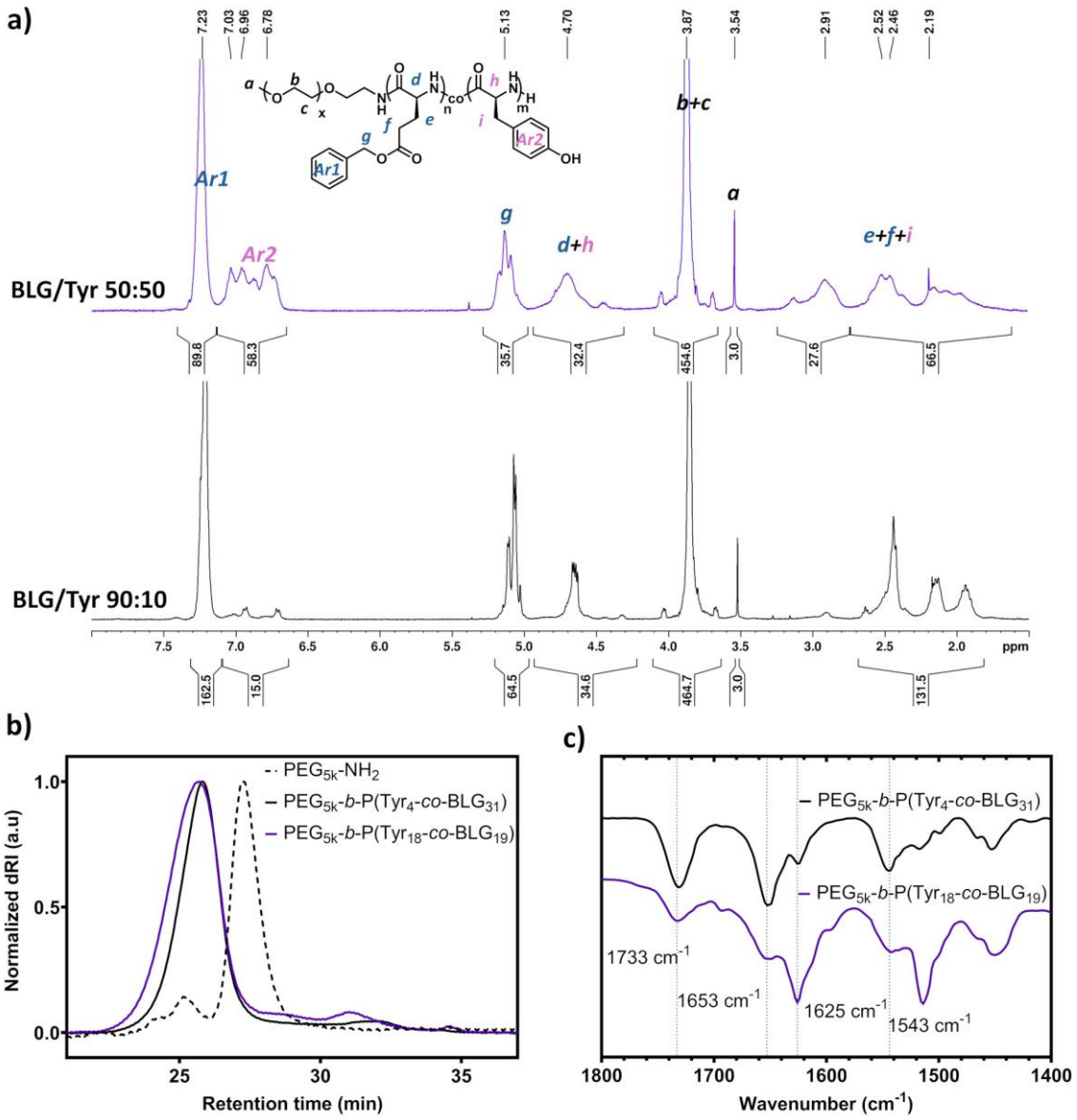

Figure 1. Chemical characterizations of diblock copolymers PEG_{5k}-*b*-P(BLG_x-*co*-Tyr_{1-x})$_n$ for targeted ratios of BLG/Tyr of 50:50 and 90:10. (a) ^{1}H NMR spectra of PEG_{5k}-*b*-P($BLG_{0.9}$-*co*-$Tyr_{0.1}$)$_{35}$ and PEG_{5k}-*b*-P($BLG_{0.5}$-*co*-$Tyr_{0.5}$)$_{37}$ and in TFA-*d*.(b) SEC chromatograms of PEG_{5k}-*b*-P($BLG_{0.9}$-*co*-$Tyr_{0.1}$)$_{35}$ and PEG_{5k}-*b*-P($BLG_{0.5}$-*co*-$Tyr_{0.5}$)$_{37}$ in DMF (+1% LiBr, detection by differential refractive index). (c) ATR-FTIR spectra of lyophilized powders PEG_{5k}-*b*-P($BLG_{0.9}$-*co*-$Tyr_{0.1}$)$_{35}$ and PEG_{5k}-*b*-P($BLG_{0.5}$-*co*-$Tyr_{0.5}$)$_{37}$.

DLS confirmed the presence of nanoparticles with a bimodal population (Figure 2a). TEM images demonstrated the uniform distribution of nanoparticles and indicated that the incorporation of tyrosine reduced the anisotropy, resulting in a more spherical morphology compared to the elongated, anisotropic particles observed for the homogeneous polypeptide-block (Figure 2b). The incorporation of 50% of tyrosine resulted in nanoparticles that were shorter and thinner than those formed with 10% of tyrosine. However, in both cases the aspect ratio was relatively low (Figure 2c).

To investigate further the impact of the conformation, FTIR analyses were conducted to correlate the secondary structure with the anisotropy. As shown in Figure 1c, FTIR spectra revealed the presence of amide I band at 1653 cm^{-1} and 1625 cm^{-1}, showing the co-existence of α-helices and β-sheet

structures, proportional to the amount of BLG and Tyr incorporated. PBLG, as previously substantiated in **Chapter II**, forms α-helix structure, while PTyr, as delineated in **Chapter III**, forms a β-sheet structure. The mixture of these two conformations may explain the less anisotropic structure. These findings suggest that copolymerization could serve as an effective strategy to modulate nanoparticle anisotropy.

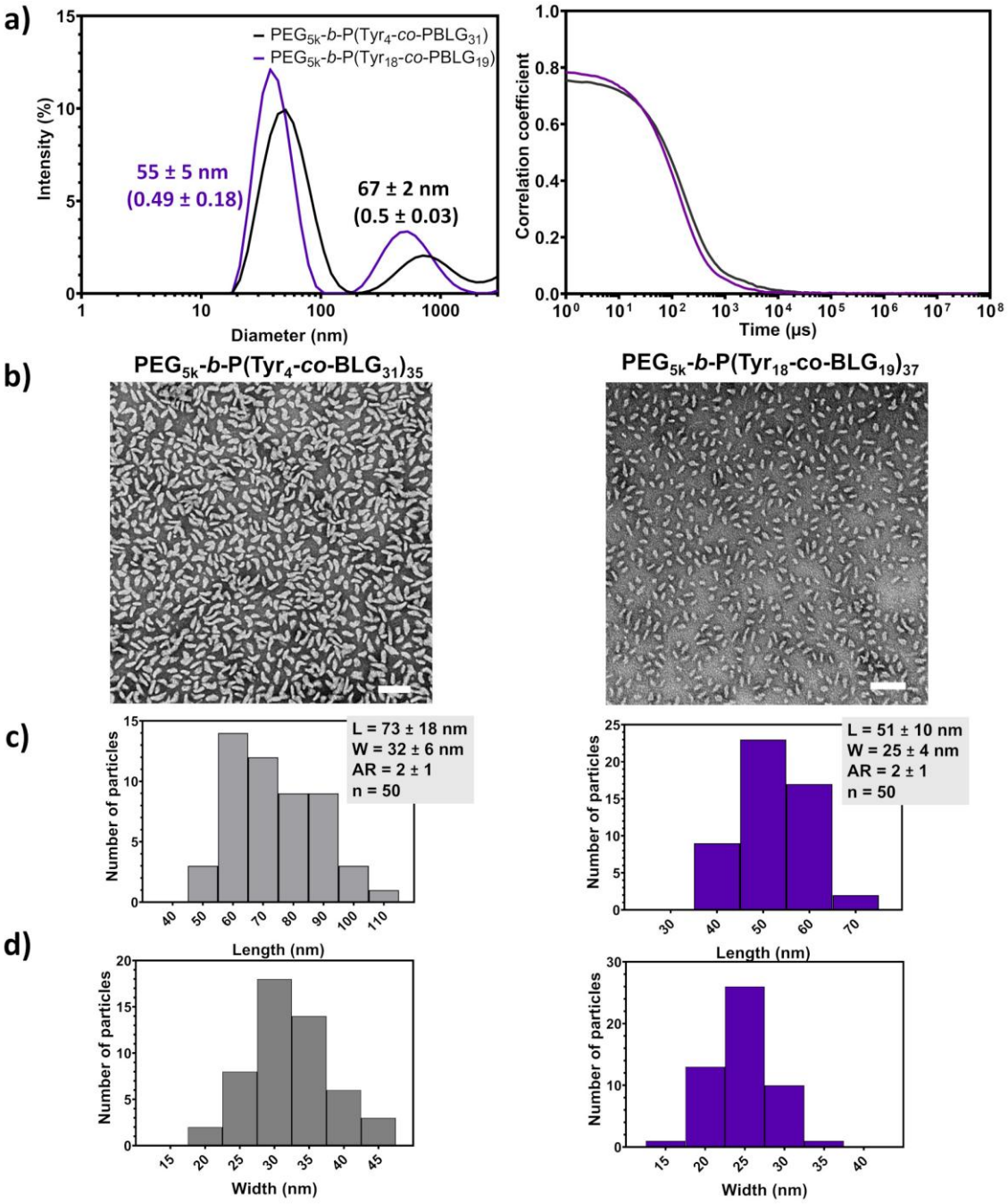

Figure 2. (a) DLS profiles (left) of the PEG_{5k}-*b*-$P(BLG_x$-*co*-$Tyr_{1-x})_n$ suspensions with associated correlograms (right). (b) Representative TEM images of the corresponding nanoparticles. Scale-bar: 200 nm. (c) Length and (d) width distribution of the PEG_{5k}-*b*-$P(BLG_x$-*co*-$Tyr_{1-x})_n$ nanoparticles obtained by analysis of 50 nano-objects by ImageJ on a TEM image.

The process of tyrosine copolymerization has the potential to enhance the drug-loading capacity of nanocarriers. Indeed, the presence of tyrosine residues can introduce additional interactions such as hydrogen bonding and π-π stacking, which may improve the incorporation and retention of drugs within the nanocarriers.

Towards active targeting with hyaluronan as stabilizer block

In light of the encouraging outcomes outlined in **Chapter IV** concerning the versatility of macroinitiators, a rational subsequent step would be to use a macroinitiator that can actively target tumor cells, such as hyaluronan. As previously discussed, hyaluronan is well known for its affinity with CD44 receptors, which are frequently overexpressed in various cancer types.[4] Moreover, previous studies conducted within our research group have highlighted the promise of hyaluronan-based block copolymers in the field of drug delivery. Specifically, the synthesis of hyaluronan-*block*-PBLG polymersomes via copper-catalyzed click chemistry has yielded successful encapsulation of doxorubicin, thereby facilitating efficient intracellular drug delivery and demonstrating significant antitumor activity in both *in vitro* and *in vivo* models.[5–7] However, the synthesis and formulation of these polymersomes required a two-step process. A more straightforward approach would be to use hyaluronan bearing a nucleophilic group to directly initiate the aqueous ROPISA of NCAs. A number of strategies can be devised to introduce the necessary nucleophilic group for polymerization initiation. For instance, hyaluronate amine, which is commercially available and has varying degrees of substitution, could be utilized. Alternatively, functionalization with dihydrazide may also be considered as described by Schatz *et al*.,[8] given that dextran-ADH effectively initiated aqueous ROPISA of NCAs, resulting in well-defined globular morphologies (Scheme 1).

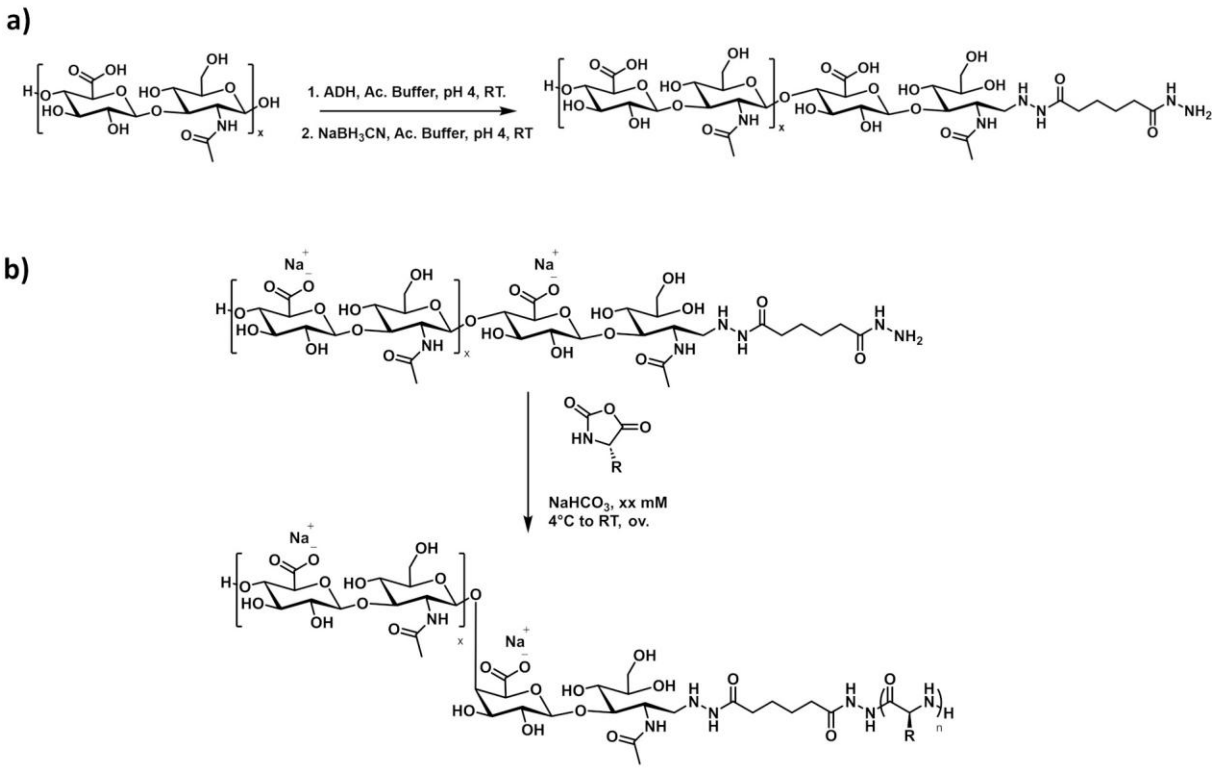

Scheme 1. Potential chemical route to design HA-*b*-PBLG copolymer via aqueous ROPISA. (a) End-functionalization of hyaluronan with ADH. (b) Aqueous ROPISA of NCA in optimized conditions.

However, hyaluronan is a polyanion, which is considered to be negatively charged under ROPISA conditions (pKa between 3 and 4). Consequently, hyaluronan introduces a degree of complexity that remains to be thoroughly explored in the PISA context.[9,10] Amin El Jarroudi Hamou's PhD project, which explores polyelectrolytes as initiators in ROPISA, will offer valuable insights into optimizing polymerization conditions. The investigation encompasses the examination of pivotal factors, including salt concentration and ultrasonication, with the potential to enhance polymerization efficiency and regulate nanoparticle morphology.

Encapsulation optimization and further *in vitro / in vivo* evaluation

In **Chapter VI**, the efficacy of physical encapsulation was demonstrated with the *post*-polymerization process, which resulted in high encapsulation efficiency. However, the drug loading content (DLC) was found limited to 9 wt%, thereby impeding the therapeutic potential of these nanocarriers. To overcome this limitation, further studies are needed to better understand the encapsulation mechanism. Key parameters such as pH must be investigated, as it evolves during ROPISA (**Chapter II**) and influences the hydrophilicity of doxorubicin.[11] This, in turn, affects the drug's affinity for the hydrophobic core and impacts drug loading. Optimizing these conditions is expected to enhance the DLC and improve the overall performance of the nanocarrier. Furthermore, the exploration of alternative monomers with enhanced affinity for doxorubicin is anticipated to result in a

substantial enhancement of the DLC. Once these optimizations are achieved, the drug release profile should be systematically evaluated to assess the nanocarrier's capacity for sustained and controlled drug delivery. Subsequent to these preliminary studies, *in vitro* and *in vivo* evaluations will be carried out using relevant cancer models in collaboration with academic partners. These studies will provide critical insights into the therapeutic efficacy and biodistribution of the optimized nanocarriers, paving the way for their potential translation into clinical applications.

References

[1] C. Grazon, P. Salas-Ambrosio, S. Antoine, E. Ibarboure, O. Sandre, A. J. Clulow, B. J. Boyd, M. W. Grinstaff, S. Lecommandoux, C. Bonduelle, *Polym. Chem.* **2021**, *12*, 6242–6251.

[2] B. Liu, R. Fang, W. Li, X. Wu, T. Liu, M. Lin, J. Sun, X. Chen, *J. Am. Chem. Soc.* **2024**, *146*, 16558–16566.

[3] S. Xi Huang, Z. Hao Wang, M. Lin, X. Hui Fu, J. Sun, *Polym. Chem.* **2023**, *14*, 1801–1808.

[4] V. M. Platt, F. C. Jr. Szoka, *Mol. Pharm.* **2008**, *5*, 474–486.

[5] K. K. Upadhyay, J.-F. L. Meins, A. Misra, P. Voisin, V. Bouchaud, E. Ibarboure, C. Schatz, S. Lecommandoux, *Biomacromolecules* **2009**, *10*, 2802–2808.

[6] K. K. Upadhyay, A. N. Bhatt, A. K. Mishra, B. S. Dwarakanath, S. Jain, C. Schatz, J.-F. Le Meins, A. Farooque, G. Chandraiah, A. K. Jain, A. Misra, S. Lecommandoux, *Biomaterials* **2010**, *31*, 2882–2892.

[7] K. K. Upadhyay, A. K. Mishra, K. Chuttani, A. Kaul, C. Schatz, J.-F. Le Meins, A. Misra, S. Lecommandoux, *Nanomedicine Nanotechnol. Biol. Med.* **2012**, *8*, 71–80.

[8] E. Courtecuisse, S. Bourasseau, B. E. Christensen, C. Schatz, *Carbohydr. Polym.* **2024**, *345*, 122576.

[9] S. M. North, S. P. Armes, *Polym. Chem.* **2020**, *11*, 2147–2156.

[10] V. Ladmiral, A. Charlot, M. Semsarilar, S. P. Armes, *Polym. Chem.* **2015**, *6*, 1805–1816.

[11] L. D. Mayer, L. C. L. Tai, M. B. Bally, G. N. Mitilenes, R. S. Ginsberg, P. R. Cullis, *Biochim. Biophys. Acta BBA - Biomembr.* **1990**, *1025*, 143–151.

Auto-assemblage induit par polymérisation par ouverture de cycle des *N*-carboxyanhydrides en milieu aqueux vers une application en nanomédecine

Les copolymères à blocs amphiphiles permettent de concevoir des nanovecteurs aux propriétés contrôlées (taille, forme, surface), capables de cibler les tumeurs via l'effet de perméabilité et de rétention accrue (EPR) tout en limitant la toxicité des traitements. Les systèmes à base de polypeptides sont particulièrement prometteurs grâce à leur biocompatibilité, leur biodégradabilité et leur capacité à s'auto-assembler via des structures secondaires bien définies. La polymérisation par ouverture de cycle (ROP) des *N*-carboxyanhydrides (NCA) permet d'obtenir ces matériaux, mais impose des conditions rigoureuses et l'usage de solvants toxiques. Le procédé ROPISA en milieu aqueux représente une alternative plus verte, combinant polymérisation et auto-assemblage en une étape. Cette thèse explore les mécanismes de la ROPISA aqueuse, la diversité des monomères et amorceurs utilisables, et la manière dont ces paramètres influencent les morphologies obtenues. Des nanoparticules anisotropes ont été produites et évaluées *in vitro* et *in vivo* sur des modèles tumoraux pertinents. Enfin, des stratégies d'encapsulation de principes actifs ont été développées pour concevoir des nanomédicaments anticancéreux.

Mots clés : *N*-carboxyanhydride d'acides aminés, polymérisation par ouverture de cycle, polypeptide, polymères amphiphiles, auto-assemblage, nanomédecine.

Aqueous ring-opening polymerization-induced self-assembly of *N*-carboxyanhydrides towards nanomedicine

Amphiphilic block copolymers provide a versatile platform for designing nanocarriers with tunable properties (size, shape, surface), capable of targeting tumors through the Enhanced Permeability and Retention (EPR) effect while minimizing drug toxicity. Polypeptide-based systems are particularly attractive due to their biocompatibility, biodegradability, and ability to self-assemble via defined secondary structures. Ring-opening polymerization (ROP) of *N*-carboxyanhydrides (NCAs) is commonly used to synthesize such materials but requires strict anhydrous conditions and toxic solvents. Aqueous ROPISA offers a greener, one-pot alternative by combining polymerization and self-assembly in a single step. This PhD work investigates the polymerization and self-assembly mechanisms of aqueous ROPISA, explores the use of various monomers and macroinitiators to diversify the resulting nanostructures, and evaluates the performance of anisotropic nanoparticles *in vitro* and *in vivo.* Drug encapsulation strategies were also developed to design anticancer nanomedicines based on this platform.

Keywords: Amino-acid *N*-carboxyanhydrides, ring-opening polymerization, polypeptide, amphiphilic polymers, self-assembly, nanomedicine.

Laboratoire de Chimie des Polymères Organiques, UMR 5629

16 Avenue Pey-Berland, F-33607 PESSAC